

PROPERTIES OF

Lithium Niobate

Edited by

K. K. WONG

Northstar Photonics, Inc., USA



Published by: INSPEC, The Institution of Electrical Engineers,
London, United Kingdom

© 2002: The Institution of Electrical Engineers

This publication is copyright under the Berne Convention and the Universal Copyright Convention. All rights reserved. Apart from any fair dealing for the purposes of research or private study, or criticism or review, as permitted under the Copyright, Designs and Patents Act, 1988, this publication may be reproduced, stored or transmitted, in any forms or by any means, only with the prior permission in writing of the publishers, or in the case of reprographic reproduction in accordance with the terms of licences issued by the Copyright Licensing Agency. Inquiries concerning reproduction outside those terms should be sent to the publishers at the undermentioned address:

The Institution of Electrical Engineers,
Michael Faraday House,
Six Hills Way, Stevenage,
Herts. SG1 2AY, United Kingdom

While the authors and the publishers believe that the information and guidance given in this work are correct, all parties must rely upon their own skill and judgment when making use of them. Neither the authors nor the publishers assume any liability to anyone for any loss or damage caused by any error or omission in the work, whether such error or omission is the result of negligence or any other cause. Any and all such liability is disclaimed.

The moral right of the authors to be identified as authors of this work has been asserted by him/her in accordance with the Copyright, Designs and Patents Act 1988.

British Library Cataloguing in Publication Data

A CIP catalogue record for this book
is available from the British Library

ISBN 0 85296 799 3

Introduction

The growth of lithium niobate boules in the late 1960s has resulted in the use of the material in realising signal processing chips for televisions and video cassette recorders. Since then, tremendous progress has been made in the growth of high quality optical grade lithium niobate material by a very small number of crystal growth centres. With this advancement in material quality, high performance integrated optical devices have been demonstrated.

Waveguide devices such as high speed optical modulators (OC-48 and OC-192) have been extensively deployed in today's advanced long distance dense wavelength division multiplex (DWDM) telecommunication systems by various telecommunication companies around the world. The use of such high speed optical modulators are currently being deployed in metro DWDM systems. Another important use of this material is in commercial and military navigation systems where the heart of the system comprises an integrated optical signal processing chip, usually called the gyro chip.

Other uses of lithium niobate in optical dispersion compensators, optical wavelength converters and optical parametric amplifiers employing periodically poled lithium niobate proton exchanged waveguides are being engineered in a number of companies.

Since the previous EMIS book on LiNbO₃ in 1989, an enormous amount of development and manufacturing has been carried out with the benefit of improved material quality. For example, since 1989 over 6,500 research papers on lithium niobate have been published. This new book incorporates and builds on the information in the old book and highlights these new developments. In addition, the format of presentation has also been improved to allow the reader easier access to knowledge of the various properties.

The editor would like to express his sincere thanks to all contributing authors for their time and effort in preparing the various Datareviews. In addition he would like to express his sincere thanks to the Managing Editor of EMIS (Electronic Materials Information Service) for his constant help, encouragement and patience throughout the preparation of this book.

Finally, I would like to thank God for giving the scientific community such wonderful insights into His creation by quoting the first three lines of Psalm 19 from the Holy Bible:

The heavens declare the glory of God; and the firmament sheweth his handywork.
Day unto day uttereth speech, and night unto night sheweth knowledge.
There is no speech nor language, where their voice is not heard.

K.K. Wong
July 2002

Contributing Authors

F. Agullo-Lopez Universidad Autonoma de Madrid Ciudad Universitaria Canto Blanco 28049 Madrid Spain	1.4
J.A. Aust¹ National Institute of Standards and Technology 325 Broadway Boulder CO 80305 USA	13.1
F. Caccavale SAES GETTERS, SPA Group Headquarters Viale Italia, 77 20020 Lainate (MI) Italy	8.10, 12.1 - 12.3, 13.2 - 13.4
D. Ciplys Moscow Institute of Electronic Technology Department of Chemistry Zelenograd Moscow 103498 Russia	10.5
D. Craig CIENA Communications, Inc. 920 Elkridge Landing Road Linthicum MD 21090 USA	5.1 - 5.4, 10.1 - 10.4
T. Fang Crystal Technology, Inc. 1040 East Meadow Circle Palo Alto CA 94303 USA	11.2
V.A. Fedorov Moscow Institute of Electronic Technology Department of Chemistry Zelenograd Moscow 103498 Russia	3.1, 3.2, 8.6 - 8.9, 10.5

¹ Current address is: J.A. Aust, Research Electro-Optics, Inc., 1855 S. 57th Street, Boulder, CO 80301, USA

C. Florea Northstar Photonics, Inc. 6464 Sycamore Court Maple Grove MN 55369 USA	1.1, 4.1 - 4.4, 6.1, 7.2, 7.3, 8.2, 8.4, 9.6, 9.7, 11.4 - 11.6
G. Foulon Crystal Technology, Inc. 1040 East Meadow Circle Palo Alto CA 94303 USA	1.2, 2.1
J. Garcia Sole Universidad Autonoma de Madrid Ciudad Universitaria Canto Blanco 28049 Madrid Spain	1.4
C. Geosling Northrup Grumman 5500 Canoga Avenue Woodland Hills CA 91367 USA	13.5
K.A. Green Northrup Grumman, L5100 600 Hicks Road Rolling Meadows IL 60008 USA	8.3, 9.1 - 9.3, 9.5, 11.3
V. Hinkov Fraunhofer Institut fur Physikalische Messtechnik Heidenhofstrasse 8 D-79110 Freiburg Germany	10.6, 10.7, 15.3
D. Jundt Crystal Technology, Inc. 1040 East Meadow Circle Palo Alto CA 94303 USA	1.2, 2.1, 8.1, 11.1, 11.2

Yu.N. Korkishko	3.1, 3.2, 8.6 - 8.9, 10.5
Moscow Institute of Electronic Technology	
Department of Chemistry	
Zelenograd	
Moscow 103498	
Russia	
S.M. Kostritskii	8.8, 8.9
Moscow Institute of Electronic Technology	
Department of Chemistry	
Zelenograd	
Moscow 103498	
Russia	
F. Laurell	8.7
Royal Institute of Technology (KTH)	
Department of Physics	
SE-16440 Kista	
Stockholm	
Sweden	
I. Mnushkina	2.3
Deltronic Crystal Industries, Inc.	
60 Harding Avenue	
Dover	
NJ 07801	
USA	
R. Rimeika	10.5
Moscow Institute of Electronic Technology	
Department of Chemistry	
Zelenograd	
Moscow 103498	
Russia	
K.H. Ringhofer	14.2, 14.3
University of Osnabruck	
Department of Physics	
PO 4469	
D-4500 Osnabruck	
Germany	
C. Sada	12.2, 13.3, 13.4
University of Padova	
INFM and Physics Department	
Via Marzolo 8	
35131 Padova	
Italy	

N.A. Sanford

13.1

National Institute of Standards and Technology
325 Broadway
Boulder
CO 80305
USA

F. Segato

12.1 - 12.3, 13.3, 13.4

Telsay Telecommunications via dell'Industria
131055 Quinto di Treviso
Italy

E.W. Taylor

14.1

International Photonics Consultants, Inc.
30 Tierra Monte NE
Albuquerque
NM 87122
USA

K.K. Wong

8.5, 15.1, 15.2

Northstar Photonics, Inc.
6464 Sycamore Court
Maple Grove
MN 55369
USA

In producing the present volume Datareviews by the following authors of the previous EMIS book dealing with lithium niobate, *Properties of Lithium Niobate* (INSPEC, 1989), were updated, adapted, merged or reproduced:

M.N. Armenise, A. Ballato, J.C. Brice, Y. Cho, I. Foldvari, E. Fries, L.E. Halliburton, L.I. Ivleva, T. Kanata, C.J.G. Kirkby, L. Kovacs, K. Kubota, S.H. Lee, M.F. Lewis, T.H. Lin, S. Matsumura, D.P. Morgan, R.C. Peach, A. Peter, C.W. Pitt, K. Polgar, N.M. Polozkov, G.T. Reed, J.F. Scott, D. Taylor, I. Tomono, P.D. Townsend, R.S. Weis, B.L. Weiss, C.L. West, K. Yamanouchi.

Abbreviations

AAS	atomic absorption spectroscopy
ABPM	active-beam propagation method
AC	alternating current
ADC	automatic diameter control
ADI	alternated direction implicit
AES	Auger electron spectroscopy
AFM	atomic force microscopy
AO	acousto-optic
APE	annealed proton-exchanged
ASE	amplified spontaneous emission
ATR	attenuated total reflection
BA	benzoic acid
BPM	beam propagation method
CLN	congruent lithium niobate
CPU	central processing unit
CRSS	critical resolved shear stress
CW	continuous wave
CZ	Czochralski
DC	direct current
DCXRD	double-crystal X-ray diffractometry
DI	deionised
DIC	differential interference contrast
DMPE	dilute melt proton exchange
DTA	differential thermal analysis
EFG	edge-defined film-fed grown
ENDOR	electron nuclear double resonance
EPR	electron paramagnetic resonance
ERDA	elastic recoil detection analysis
ESR	electron spin resonance
EXAFS	extended X-ray absorption fine structure
FED	free electroacoustic decay
FTIR	Fourier transform infrared
FWHM	full width at half maximum
GPE	graded proton exchange
HT	high temperature
HTPE	high-temperature proton exchange
ICP	inductively coupled plasma
ICP-AES	inductively coupled plasma atomic emission spectroscopy
ID	identification (of wafers)
IDT	interdigital transducer
IL	insertion loss

IR	infrared
IWKB	inversion of Wentzel-Kramer-Brillouin (approximation technique)
LB	lithium benzoate
LE	lateral excitation
LN	lithium niobate
LNO	lithium niobate
LO	longitudinal optical
LPE	liquid phase epitaxy
LSAW	leaky surface acoustic wave
LT	low temperature
MBE	molecular beam epitaxy
MP	melting point
MPE	melt-phase epitaxy
NF	near field
NLO	non-linear optics
NMR	nuclear magnetic resonance
NRA	nuclear reaction analysis
NS	non-stoichiometry
NSSL	non-synchronous scattering loss
OPO	optical parametric oscillator
PA	pyrophosphoric acid
PAC	perturbed angular correlation
PE	proton-exchange(d)
PI	proportional integral
PID	proportional integral derivative
PIXE	particle induced X-ray emission
PL	photoluminescence spectra
PLD	pulsed laser deposition
PPLN	periodically poled lithium niobate
PRD	photorefractive damage
PRS	photorefractive sensitivity
PRW	photorefractive waveguide
QE	quasi-extensional
QL	quasi-longitudinal
QPM	quasi-phase-matched
QS	quasi-shear
RAC	reflective array compressor
RBS	Rutherford backscattering spectrometry
RE	rare earth
RF	radio frequency
RHEED	reflection high energy electron diffraction
RIBE	reactive ion beam etching
RIE	reactive ion etching
RPE	reverse proton-exchange
RSF	relative sensitivity factor

RSI	rear-shear interferometer
RT	room temperature
SAW	surface acoustic wave
SEM	scanning electron microscopy
SH	second harmonic
SHG	second harmonic generation
SIMS	secondary ion mass spectrometry
SLN	stoichiometric lithium niobate
SNR	signal-to-noise ratio
SPE	soft proton exchange
STM	scanning tunnelling microscopy
SVEA	slowly varying envelope approximation
TCF	temperature coefficient of frequency
TDPAC	time dependent perturbed angular correlation(s)
TE	thickness excitation
TE	transverse electric
TI	titanium indiffusion
TIPE	titanium indiffused proton exchanged
TM	temperature of melting
TM	transition metal
TM	transverse magnetic
TO	transverse optical
TOF	time-of-flight
UHF	ultra-high frequency
UV	ultraviolet
VUV	vacuum ultraviolet
WKB	Wentzel-Kramer-Brillouin (approximation technique)
XRD	X-ray diffraction
XSW	X-ray standing waves

Contents

<i>Introduction</i>	viii
<i>Contributing Authors</i>	ix
<i>Abbreviations</i>	xiii
1. Structure, Stoichiometry and Phase Transitions	1
1.1 Stoichiometry, Defect Structure and Composition of LiNbO ₃	3
1.2 Crystal Structure of LiNbO ₃	8
1.3 Phase Transition Temperatures of LiNbO ₃	13
1.4 Point Defects in LiNbO ₃	15
2. Growth	23
2.1 Boules of LiNbO ₃ Congruently Grown by the Czochralski Technique	25
2.2 Growth of LiNbO ₃ by Stepanov's Technique	28
2.3 Iron-Doped Boules of LiNbO ₃	30
2.4 Epitaxial Growth of LiNbO ₃	38
3. Structure of Modified Material	41
3.1 Structural Phase Diagram of Proton-Exchanged Waveguides in LiNbO ₃	43
3.2 Composition of Different Crystal Phases in Proton-Exchanged Waveguides in LiNbO ₃	50
4. Mechanical Properties	55
4.1 Stiffness and Compliance of LiNbO ₃	57
4.2 Photoelastic Coefficients of LiNbO ₃	61
4.3 Third-Order Elastic Coefficients of LiNbO ₃	65
4.4 Yield Stress of LiNbO ₃	67
5. Thermal Properties	71
5.1 Thermal Expansion Coefficients of LiNbO ₃	73
5.2 Thermal Conductivity Properties of LiNbO ₃	78
5.3 Specific Heat Properties of LiNbO ₃	81
5.4 Thermal Diffusivity of LiNbO ₃	85
6. Electrical and Pyroelectric Properties	89
6.1 Electrical Conductivity of LiNbO ₃	91
6.2 Pyroelectric Coefficients of LiNbO ₃	97

7. Piezoelectric and Electromechanical Properties	99
7.1 Second-Order Piezoelectric Constants of LiNbO ₃	101
7.2 Third-Order Piezoelectric Constants of LiNbO ₃	105
7.3 Electrostrictive Constants of LiNbO ₃	107
7.4 Electromechanical Coupling Factors of LiNbO ₃	108
8. Optical, Dielectric and Electro-Optical Properties	113
8.1 Dispersion Effects in Undoped and MgO-Doped LiNbO ₃	115
8.2 Dispersion Properties of LiNbO ₃ and Tables	119
8.3 Dielectric Constants of LiNbO ₃	129
8.4 Electro-Optic Coefficients of LiNbO ₃	131
8.5 Photorefractive Effects in LiNbO ₃	141
8.6 Refractive Indices of Different Crystal Phases in Proton-Exchanged LiNbO ₃ Waveguides	146
8.7 Second-Order Non-Linear Properties of Different Crystal Phases in Proton-Exchanged LiNbO ₃ Waveguides	153
8.8 IR Reflection Spectra of Proton-Exchanged Waveguides Containing Different H _x Li _{1-x} NbO ₃ Phases	161
8.9 Holographic Gratings in Photorefractive LiNbO ₃ Waveguides Fabricated by Combined Proton and Copper Exchange	169
8.10 Chromium Doping of LiNbO ₃ by Thin Film Diffusion	175
9. Luminescence, Raman and ESR Spectra	183
9.1 Luminescence of LiNbO ₃	185
9.2 Raman Spectra of Undoped LiNbO ₃	188
9.3 Raman Spectra of Doped LiNbO ₃	190
9.4 Magnetic Resonance Spectra of Impurities and Defects in LiNbO ₃	192
9.5 Absorption Spectra of Bulk LiNbO ₃	197
9.6 IR Spectral Presence of OH Ions in LiNbO ₃	200
9.7 Stark Effect for Rare-Earth Dopants in LiNbO ₃	209
10. Acoustic Wave Propagation and Properties	213
10.1 Velocity of Ultrasonic Bulk Waves in LiNbO ₃	215
10.2 Attenuation of Ultrasonic Bulk Waves in LiNbO ₃	241
10.3 SAWs in LiNbO ₃ : Properties of Common Orientations	243
10.4 Attenuation of SAWs in LiNbO ₃	252
10.5 Velocity of SAWs in Proton-Exchanged Waveguides in LiNbO ₃	254
10.6 Velocity of SAWs on LiNbO ₃ : Anisotropy, Temperature and Composition Dependence	263
10.7 Velocity of SAWs on LiNbO ₃ : Ti-Indiffused, PE and Ion-Implanted	265

11. Basic Processing Techniques	271
11.1 Poling of LiNbO ₃	273
11.2 Preparation of LiNbO ₃ Wafers	277
11.3 Chemical Etching of LiNbO ₃	282
11.4 Ion Beam Milling and Reactive Ion Beam Etching of LiNbO ₃	285
11.5 Reactive Ion Etching of LiNbO ₃	288
11.6 Excimer Laser Treatment of LiNbO ₃	290
12. Rare-Earth Doping	293
12.1 Erbium Doping of LiNbO ₃ by Thin Film Diffusion	295
12.2 Erbium Doping of LiNbO ₃ by the Ion Exchange Process	300
12.3 Study of Erbium-Doped LiNbO ₃ Waveguides by the Beam Propagation Method	307
13. Techniques for Material Studies	313
13.1 Uniformity Studies of Congruent LiNbO ₃ by Maker Fringe Analysis	315
13.2 Secondary Ion Mass Spectrometry of LiNbO ₃	325
13.3 Near Field Method for the Characterization of Channel Waveguides in LiNbO ₃	334
13.4 M-Lines Spectroscopy for the Characterization of Slab Waveguides in LiNbO ₃	340
13.5 Microanalytical Techniques for Waveguide Examination in LiNbO ₃	348
14. Special Effects and Holographic Processes	357
14.1 Radiation Effects in LiNbO ₃	359
14.2 Basics of Holographic Processes in LiNbO ₃	372
14.3 Dynamic Properties of LiNbO ₃ , Optical Damage-Related Issues and Stabilization Techniques	377
15. Optical Waveguide Technologies	383
15.1 Proton Exchange in Undoped LiNbO ₃ (Concentrated Melt)	385
15.2 Proton Exchange in Undoped LiNbO ₃ (Dilute Melt)	392
15.3 Proton Exchange in Ti-Indiffused and MgO-Doped LiNbO ₃	396
15.4 Kinetics of Ti-Indiffusion in LiNbO ₃	398
15.5 Characteristics of LiNbO ₃ Optical Waveguides	401
15.6 Ion Implantation in LiNbO ₃	406
Index	411

CHAPTER 1

STRUCTURE, STOICHIOMETRY AND PHASE TRANSITIONS

- 1.1 Stoichiometry, defect structure and composition of LiNbO₃
- 1.2 Crystal structure of LiNbO₃
- 1.3 Phase transition temperatures of LiNbO₃
- 1.4 Point defects in LiNbO₃

1.1 Stoichiometry, defect structure and composition of LiNbO₃

S.C. Abrahams; updated by C. Florea

February 2002

A STOICHIOMETRY AND CRYSTAL GROWTH

Stoichiometric lithium niobate, in common with many oxides, melts incongruently. The composition of a given crystal depends on the proportions used in the starting materials. The congruent composition contains 48.45 mol% Li₂O and 51.55 mol% Nb₂O₅ [1]. Czochralski growth from a series of melts with compositions ranging from 47 mol% to 49 mol% Li₂O results in the composition ranges between the top and bottom of the pulled crystal boule as shown in TABLE 1.

TABLE 1 Composition variations within the melt and the boule in the case of Czochralski growth.

Melt composition (mol% Li ₂ O)		Boule composition (mol% Li ₂ O)	
Initial	Final	Top (initial)	Bottom (final)
47.00	45.45	48.03	47.44
48.00	47.44	48.30	48.10
48.20	47.73	48.41	48.19
48.40	48.21	48.45	48.34
48.60	48.80	48.49	48.51
48.80	49.32	48.56	48.61
49.00	49.86	48.55	48.70

A relationship between the melt composition and the crystal composition has been established [2], being described by the following equation:

$$c_{Li} = 48.5 + 0.3436 \times (c_{Li,melt} - 48.5) - 0.02897 \times (c_{Li,melt} - 48.5)^2$$

Since the crystal composition depends not only on the melt composition but also on other geometrical and growth parameters, such a relationship has only a qualitative significance. The above equation is valid in the range 45 < c_{Li,melt} < 52 mol% Li₂O with an accuracy of 0.3 mol% provided the growth conditions do not differ strongly from the cited reports from which data were collected.

The Curie temperature corresponding to these compositions varies from 1362 K to 1435 K, with T_C = 1411(2) K for the congruent composition. The Li₂O content, C (in mol%), and the T_C of a lithium niobate crystal are empirically related [1] by:

$$T_C = 9368.4 - 369.05 C + 4.228 C^2 \text{ (K)} \quad (1)$$

Li₂O-deficient boules are convertible to stoichiometric LiNbO₃ by equilibration in contact with Li₃NbO₄ + LiNbO₃ powder mix at temperatures approaching but lower than T_C for 300 hours [3].

B VARIABILITY IN COMPOSITION

Crystals grown from compositions other than congruent exhibit variations in composition and the composition actually changes markedly along the growth direction. Measurements of the refractive

1.1 Stoichiometry, defect structure and composition of LiNbO_3

indices, birefringence, the UV absorption edge and lattice constants can all be used as methods for the characterisation of the crystal composition [2].

In particular, the sensitivity of the extraordinary refractive index, n_e , to the composition (a variation of 280×10^{-4} is observed for Li/Nb mole ratios between 0.8 and 1.2) provides a rapid non-destructive method for examining lithium niobate boules [4]. Boules grown from melts with composition ranging between 47.8 and 48.8 mol% Li_2O exhibit a range in n_e of about 50×10^{-4} . In a typical electrooptic switch the index change induced by the electric field is about 16×10^{-4} ; variations in index greater than about 1.6×10^{-4} may adversely influence electrooptic response [5]. In the case of Ti-diffused lithium niobate directional coupler switches for example, index changes of about 2.5×10^{-4} in the crystalline substrate are large enough to cause non-ideal electrooptic behaviour [6]. A change of 0.2 mol% in Li_2O content has thus been reported [7] to correspond to a 20% change in Ti diffusivity near the congruent composition, with resulting impact on the coupling characteristics of coupler devices.

The position of the fundamental absorption edge is very sensitive to the composition of LiNbO_3 . A shift of about 20 nm is found for Li_2O content variation in the range from 47.5 mol% to 50 mol% [8]. From the experimental data, a two-parameter non-linear fit was obtained:

$$E = k\sqrt{50 - c_{\text{Li}}} + E_0$$

where E is the photon energy corresponding to the absorption edge at the chosen value of α , c_{Li} is the Li_2O concentration in mol%, and k and E_0 are the fitting parameters. The values of these parameters are given in TABLE 2.

TABLE 2 Calibration parameters for the absorption edge dependence on the Li_2O content.

Polarisation	k (eV (mol%) $^{1/2}$)	E_0 (eV) (for $\alpha = 20 \text{ cm}^{-1}$)	E_0 (eV) (for $\alpha = 15 \text{ cm}^{-1}$)
Ordinary	-0.189 ± 0.003	4.112 ± 0.002	4.092 ± 0.002
Extraordinary	-0.218 ± 0.003	4.136 ± 0.002	4.119 ± 0.002

A polynomial fit for the dependence of the absorption edge wavelength on the composition has also been proposed [2]. The polynomial fit is given by the following pair of equations:

$$\lambda_{15} = 321.9 - 1.597x - 5.745x^2, \text{ at } 15 \text{ cm}^{-1}$$

and

$$\lambda_{20} = 320.4 - 1.829x - 5.485x^2, \text{ at } 20 \text{ cm}^{-1}$$

Here x is the deviation from the congruent composition (48.38 mol%), expressed in mol%. These two equations are valid for light polarised parallel and propagating perpendicular to the polar c axis. A resolution of 0.02 mol% can easily be obtained.

Differences between stoichiometric and congruent composition lithium niobate are apparent at the unit cell level [9] (see TABLE 3). Both a and c lattice constants at 298 K decrease in length by 0.061% to 0.064% as the crystal composition changes from congruent to stoichiometric. More recent diffraction measurements in the range 47 - 49.8 mol% Li_2O content have shown an overall decrease of 0.004 Å (~0.077 %) and 0.014 Å (~0.1 %) for the lattice constants a and c , respectively [10]. If a linear relationship holds, then accurate lattice constant measurement provides a convenient way to determine composition. The dependences of these constants, however, on the Li content seem to be less linear than that of the unit cell volume. Using the data from [10], the following relationship has been established [2] between the unit cell volume and Li_2O concentration:

$$V (\text{\AA}^3) = 334.7 - 0.3338 c_{\text{Li}} (\text{mol\%})$$

The confidence in such a composition calibration is limited to about 0.2 - 0.3 mol%. Measured and calculated densities vary linearly with Li_2O concentration and could also be used as a criterion of composition; values not significantly different from those in TABLE 3 have been independently reported [7,11]. The precision of the density measurements, however, has to be increased since the experimental error of density measurements is normally $\sim 0.3 \times 10^{-2} \text{ g cm}^{-3}$ while the density was found to change only by $1.5 \times 10^{-2} \text{ g cm}^{-3}$ over the solid solution range [10].

TABLE 3 Unit cell parameters (a , c , V) and density (d) for stoichiometric and congruent LiNbO_3 .

Parameter	Congruent	Stoichiometric
$a (\text{\AA})$	5.15052(6)	5.14739(8)
$c (\text{\AA})$	13.86496(3)	13.85614(9)
$V (\text{\AA}^3)$	318.513	317.941
$d_{\text{measured}} (\text{g cm}^{-3})$	4.648(5)	4.635(5)
$d_{\text{calculated}} (\text{g cm}^{-3})$	4.646	4.6327

It is worth remarking that a further source of compositional uncertainty in growing lithium niobate crystals from the melt is the possibility of a variation from average in the Li-6 concentration of the starting materials [12]. The concentration of this isotope in minerals varies naturally from 6.77% to 9.28%, and may be as low as 0.1% if previous processing has taken place in order to remove Li-6 as a source of neutron shielding material. The resulting maximum error in the expected proportion of Li_2O from average in a lithium niobate crystal is 0.12 mol%, corresponding to a difference of 5 K in T_c .

C STOICHIOMETRY AND DEFECT STRUCTURE

The atomic arrangement within the stoichiometric hexagonal unit cell consists of six LiNbO_3 with Li and Nb ions located on the polar c -axis and the O atoms in general positions; Li occupies an oxygen atom octahedron that shares faces with adjacent similar octahedra on either side along the trigonal axis. One such octahedron is empty, the other is occupied by Nb. The triple octahedron is repeated, with alternating sequences having identical orientation, along the polar axis. The spacing between corresponding atoms in alternate sequences forms the c -axis repeat. The Nb atom is displaced by 0.277 \AA from the centre of its octahedron and the Li atom is displaced by 0.675 \AA from its nearest shared face between octahedra at 295 K. It is these displacements along the polar axis, of identical sense, that give rise to the dipoles producing the spontaneous polarisation. If these displacements become zero, then the polarisation becomes zero and the crystal is paraelectric. Similarly, equal but opposite displacements reverse the spontaneous polarisation sense [13-15].

In stoichiometric LiNbO_3 with $T_c = 1470$ K, the Li atom site is 100% occupied by Li and the Nb site is 100% occupied by Nb, as the O site is 100% occupied by O [9]. X-ray diffraction shows that, in congruent lithium niobate with $T_c = 1415$ K, the Li site contains 94.1(3)% Li and 5.9(3)% Nb whereas the Nb site contains 95.3(3)% Nb and 4.7% vacancies, for the O site containing 100% oxygen [9]. Each of the missing Li^+ ions is hence substituted by an Nb^{5+} ion, with compensating vacancies at the Nb site. Non-stoichiometric lithium niobate may be represented by the chemical formula $[\text{Li}_{(1-5x)}\text{Nb}_{(5x)}]\text{Nb}_{(1-4x)}\text{O}_3$, where Li site occupancy is given within square brackets. The structure remains stable for x up to 0.02 [1]. In congruent material, $x = 0.0118(7)$. An assumed charge of +1 on Li ions and +5 on Nb ions results in charge neutrality; smaller effective charges assumed for Nb are balanced by compensating vacancies at the Nb site (i.e. Schottky vacancies).

The lithium niobate defect structure corresponding to the chemical formula $[\text{Li}_{(1-5x)}\text{Nb}_{(5x)}]\text{Nb}_{(1-4x)}\text{O}_3$ is approximated by a periodic array of unit cells in which one Nb atom in every three cells occupies a Li site and one Nb site in every four cells is unoccupied. The resulting formula for this hypothetical

1.1 Stoichiometry, defect structure and composition of LiNbO_3

defect structure is $[\text{Li}_{(0.945)}\text{Nb}_{(0.055)}]\text{Nb}_{(0.958)}\text{O}_3$, which is comparable to the congruent formula $[\text{Li}_{(0.941)}\text{Nb}_{(0.059)}]\text{Nb}_{(0.953)}\text{O}_3$. The distribution of the two types of defect (substitutional and vacancy) is still under study, with their formation being postulated as due to a near equivalence in free energy of the lithium niobate and ilmenite structures which differ only in the cation packing sequence [16]. An ordering of the distribution may give rise to the anomaly in thermal expansion observed [17] near 395 K. A variety of studies have been conducted on the defect structure in congruent and stoichiometric lithium niobate (see for example [18] and [19]). High resolution electron microscopy has also been used to investigate the intrinsic defect of non-stoichiometric lithium niobate [20], and the existence of clustered defects (clusters of Nb on Li sites and/or clusters of Nb_2O_5 about 1 nm in diameter) has been suggested for crystals around and at congruent composition.

D CURIE TEMPERATURE DEPENDENCE ON DEFECT STRUCTURE

The Curie temperature for compositions within the defect structure range $x = 0$ to 0.02 has been related to the atomic displacement (Δz) of the Nb ions at room temperature from the midpoint between nearest adjacent planes of O atoms normal to the polar axis [9]. The relationship

$$T_C = \frac{K}{2k_B} (\Delta z)^2 [\text{K}]$$

(where the ratio between the force constant (K) and the Boltzmann constant (k_B) is taken as $2 \times 1.93 \times 10^{-4}$) [21] leads on rearrangement to the results shown in TABLE 4, in which the B atom occupancy in the A site is denoted by A(B). The ionic distribution in TABLE 4 is derived from the defect structure chemical formula, with T_C calculated from the relationship to Li_2O as given by EQN (1).

TABLE 4 Curie temperature dependence on the defect structure.

Crystal composition Li_2O mol%	Ionic distribution				T_C (K)	Δz (Å)
	Li(Li)	Li(Nb)	Nb(Nb)	O(O)		
50.0	1	0	1	3	1486	0.277
49.5	0.983	0.017	0.986	3	1460	0.275
49.0	0.967	0.033	0.974	3	1436	0.273
48.5	0.951	0.049	0.961	3	1416	0.271
48.0	0.935	0.065	0.948	3	1395	0.269
47.5	0.919	0.081	0.935	3	1378	0.267
47.0	0.904	0.096	0.923	3	1363	0.266

E DEFECT STRUCTURE MODEL FOR LITHIATION PROCESS AT ABOUT 1300 K

A four-stage lithiation process has been proposed [9]. In the first stage, Li^+ ions enter unit cells at the crystal exterior causing $4x$ of the Nb atoms at the Li site to become less stable than those at the Nb site and resulting in their migration to each Nb site in the formula $[\text{Li}_{(1-5x)}\text{Nb}_{(5x)}]\text{Nb}_{(1-4x)}\text{O}_3$. Such migration can take place either along the 3.068(2) Å path (room temperature value) connecting adjacent Li and Nb octahedra centred on adjacent trigonal axes, or along the 3.064(8) Å path parallel to the trigonal axis. Bond length and energy considerations suggest the former path is more likely than the latter.

In the second stage, vacancies produced at the Li site in the first stage become occupied by entering Li^+ ions, causing the first stage to be repeated throughout the crystal interior.

In the third stage, the remaining x Nb atoms at the Li site exchange with Li^+ ions in unit cells that are probably closer to the crystal exterior. High-temperature exchange of this kind is known to be

1.1 Stoichiometry, defect structure and composition of LiNbO_3

energetically favourable in view of the initial defect structure formation. Continuation of the exchange process results in all Li sites finally becoming 100% occupied by Li^+ ions.

In the final stage, the excess x Nb^{5+} ions reaching the crystal surface form an oriented overgrowth of lithium niobate unit cells in the Li_2O -rich environment. Following first-stage initiation, it is expected that all four stages will subsequently proceed together. Experimental evidence in support of this lithiation model is not yet available.

REFERENCES

- [1] H.M. O'Bryan, P.K. Gallagher, C.D. Brandle [*J. Am. Ceram. Soc. (USA)* vol.68 (1985) p.493]
- [2] M. Wohlecke, G. Corradi, K. Betzler [*Appl. Phys. B (Germany)* vol.63 (1996) p.323]
- [3] P.K. Gallagher, H.M. O'Bryan [*J. Am. Ceram. Soc. (USA)* vol.68 (1985) p.147]
- [4] G.E. Peterson, S.R. Lunt [*Ferroelectrics (Switzerland)* vol.75 (1987) p.99]
- [5] G.E. Peterson, S.R. Lunt [*Electron. Lett. (UK)* vol.22 (1986) p.674]
- [6] L. McCaughan, K.D. Choquette [*IEEE J. Quantum Electron. (USA)* vol.QE-22 (1986) p.947]
- [7] R.J. Holmes, W.J. Minford [*Ferroelectrics (Switzerland)* vol.75 (1987) p.63]
- [8] L. Kovacs, G. Ruschhaupt, K. Polgar, G. Corradi, M. Wohlecke [*Appl. Phys. Lett. (USA)* vol.70 (1997) p.2801]
- [9] S.C. Abrahams, P. Marsh [*Acta Crystallogr. B (Denmark)* vol.42 (1986) p.61]
- [10] N. Iyi et al [*J. Solid State Chem. (USA)* vol.101 (1992) p.340]
- [11] P.K. Gallagher, H.M. O'Bryan [*J. Am. Ceram. Soc. (USA)* vol.71 (1988) p.56]
- [12] J.E. Riley Jr. [*Ferroelectrics (Switzerland)* vol.75 (1987) p.59]
- [13] S.C. Abrahams, J.M. Reddy, J.L. Bernstein [*J. Phys. Chem. Solids (UK)* vol.27 (1966) p.997]
- [14] S.C. Abrahams, W.C. Hamilton, J.M. Reddy [*J. Phys. Chem. Solids (UK)* vol.27 (1966) p.1013]
- [15] S.C. Abrahams, H.J. Levinstein, J.M. Reddy [*J. Phys. Chem. Solids (UK)* vol.27 (1966) p.1019]
- [16] D.M. Smyth [*Proc. 6th IEEE Int. Symp. Application of Ferroelectrics* (1986) p.115]
- [17] P.K. Gallagher, H.M. O'Bryan, E.M. Gyorgy, J.T. Krause [*Ferroelectrics (Switzerland)* vol.75 (1987) p.71]
- [18] A.V. Yatsenko, E.N. Ivanova, N.A. Sergeev [*Physica B (Netherlands)* vol.240 (1997) p.254]
- [19] K. Polgár, Á. Péter, I. Földvári, Zs. Szaller [*J. Cryst. Growth (Netherlands)* vol.218 (2000) p.327]
- [20] Ch. Leroux, G. Nihoul, G. Malovichko, V. Gracev, C. Boulesteix [*J. Phys. Chem. Solids (UK)* vol.59 (1998) p.311]
- [21] S.C. Abrahams, S.K. Kurtz, P.B. Jamieson [*Phys. Rev. (USA)* vol.172 (1968) p.551]

1.2 Crystal structure of LiNbO₃

D.H. Jundt and G. Foulon

May 2001

A INTRODUCTION

The crystal structure of single crystal lithium niobate was investigated by X-ray diffraction [1] as well as neutron diffraction [2] in the mid 1960s. While this work determined the space group and the approximate position of all atoms, the researchers were apparently not aware at that time that lithium niobate can exist over a wide range of compositions. Further work was thus necessary to determine the lattice constants for both congruent and stoichiometric compositions. The results were published in 1984 by Abrahams and Marsh [3].

As shown elsewhere in this book, lithium niobate exists in a wide composition range of Li/Nb ratio. Because of the fast growth and good homogeneity that can be achieved when growing from a melt of congruent composition, it is the most commonly used melt composition. In the solidified crystal, the Li-deficiency (as compared to the stoichiometric formula LiNbO₃) manifests itself by stochastically distributed vacancies and anti-site defects, without changing the symmetry relation of the lattice. To describe the crystal structure, we can therefore treat the crystal as if it were stoichiometric.

B SPACE GROUP OF LITHIUM NIOBATE

The paraelectric high temperature phase ($\overline{R\bar{3}c}$) possesses inversion symmetry. When the crystal is cooled below the Curie temperature, the symmetry of the space group lowers to R3c (space group no. 161) [4]. This trigonal space group can be described by a rhombohedral lattice with three equivalent lattice vectors \mathbf{a}_1 , \mathbf{a}_2 , and \mathbf{a}_3 . The lattice is defined by the length of one of the lattice vectors, and the angle α between any pair of those vectors. The unit cell has the volume

$$a^3 \sqrt{1 - 3 \cos^2 \alpha + 2 \cos^3 \alpha}$$

and contains two formula units. The coordinates of only one formula unit need to be specified; the others follow from applying the symmetry operations.

It is more convenient to describe the lattice using hexagonal axes because it naturally decouples the polar axis from the direction perpendicular to it [5]. This triples the volume of the unit cell as compared to the rhombohedral description. The unit cell in the hexagonal lattice is defined by one of the three equivalent \mathbf{a}_H lattice vectors, and the polar \mathbf{c}_H lattice vector. Here, the angle between the \mathbf{a} axes and the \mathbf{c} axis is 90°. The volume is given by

$$\sqrt{3}/2 \times a^2 c$$

and it contains six formula units. Again, giving the lattice positions of the atoms for one formula unit is sufficient to fully describe the structure. Because this lattice description contains three times more atoms than necessary, two-thirds of the Miller-Bravais indices in the indirect lattice are phantoms of the hexagonal lattice description, and have no significance for the actual crystal.

Given a crystal plane (hkl) in rhombohedral coordinates, it can be converted to the hexagonal set (HKL) by the following transformation:

1.2 Crystal structure of LiNbO_3

$$\mathbf{H} = \mathbf{h} - \mathbf{k}$$

$$\mathbf{K} = \mathbf{k} - \mathbf{l}$$

$$\mathbf{L} = \mathbf{h} + \mathbf{k} + \mathbf{l}$$

It follows that

$$\mathbf{K} - \mathbf{H} + \mathbf{L} = 3\mathbf{k} \quad (2)$$

and the expression $\mathbf{K} - \mathbf{H} + \mathbf{L}$ must always be an integral multiple of three. For example, the cleavage planes are given by $\{0\ 1\ .\ 2\}$, but there are no meaningful crystal planes with index $\{1\ 0\ .\ 2\}$. The angle ϕ between two planes with indices $(\mathbf{H}_1 \mathbf{K}_1 \mathbf{L}_1)$ and $(\mathbf{H}_2 \mathbf{K}_2 \mathbf{L}_2)$ can be calculated as:

$$\cos \phi = \frac{\mathbf{H}_1 \mathbf{H}_2 + \mathbf{K}_1 \mathbf{K}_2 + \frac{1}{2}(\mathbf{H}_1 \mathbf{K}_2 + \mathbf{H}_2 \mathbf{K}_1) + \frac{3a^2}{4c^2} \mathbf{L}_1 \mathbf{L}_2}{\left(\mathbf{H}_1^2 + \mathbf{K}_1^2 + \mathbf{H}_1 \mathbf{K}_1 + \frac{3a^2}{4c^2} \mathbf{L}_1^2 \right)^{1/2} \left(\mathbf{H}_2^2 + \mathbf{K}_2^2 + \mathbf{H}_2 \mathbf{K}_2 + \frac{3a^2}{4c^2} \mathbf{L}_2^2 \right)^{1/2}} \quad (3)$$

where a and c stand for the hexagonal lattice vector lengths. For a set of Miller-Bravais indices $(\mathbf{H}\mathbf{K}\mathbf{L})$, the spacing d of the corresponding planes is given by:

$$d = \left(\frac{4}{3} \left(\frac{\mathbf{H}^2 + \mathbf{H}\mathbf{K} + \mathbf{K}^2}{a^2} \right) + \frac{\mathbf{L}^2}{c^2} \right)^{-1/2} \quad (4)$$

C CRYSTAL LATTICE AND ATOMIC POSITIONS

The atomic positions for a formula unit have been measured by X-ray analysis at room temperature for a crystal grown from a stoichiometric melt [1]. These measurements were refined [3] for congruent LN as well as LN at the high temperature phase-boundary close to stoichiometry. The coordinates are given as fractions of the hexagonal unit vectors \mathbf{a}_{1H} , \mathbf{a}_{2H} and \mathbf{c}_H . Both the Li and Nb atoms are located on the three-fold symmetry axis. Symmetry relationships do not restrict the placement of the origin (0,0,0) along the three-fold symmetry axis. It thus can be chosen to coincide with the Nb site as assumed in the values in TABLE 1. The oxygen atom is in a general, not restricted position, resulting in a multiplicity of three as compared to either Nb or Li. The coordinates of the original X-ray study along with the refinements for congruent and stoichiometric crystals are shown in TABLE 1. Because crystal growth capabilities have improved since the mid 1960s, the later values are likely to be better estimates. This assumption is supported by the smaller R-values for the later fits to the X-ray data [1,3].

TABLE 1 Fractional atomic coordinates as expressed in hexagonal lattice units.

	Stoichiometric melt [1]	Congruent crystal [3]	Stoichiometric crystal [3]
Nb (\mathbf{a}_{1H})	0	0	0
Nb (\mathbf{a}_{2H})	0	0	0
Nb (\mathbf{c}_H)	0	0	0
Li (\mathbf{a}_{1H})	0	0	0
Li (\mathbf{a}_{2H})	0	0	0
Li (\mathbf{c}_H)	0.2829	0.2791	0.2787
O (\mathbf{a}_{1H})	0.0492	0.0479	0.0476
O (\mathbf{a}_{2H})	0.3446	0.3430	0.3433
O (\mathbf{c}_H)	0.0647	0.06385	0.06336

1.2 Crystal structure of LiNbO_3

The room temperature lattice vector lengths have been measured [3] for both congruent and stoichiometric composition. The crystal measured for the congruent composition was grown from a melt containing 48.6 mol% Li, a value that was generally assumed to be congruent until 1991 when the estimate was refined to 48.38 mol% [6]. The crystal composition however (48.45 mol%, estimate of [3]) is close to true congruency, and the values given can be assumed to be correct for currently grown congruent crystals. The results are shown in TABLE 2 together with the density measured by dilatometry. The unit cell contains six formula units.

TABLE 2 Hexagonal lattice unit cell vector lengths and density for two crystal compositions.

Lattice vector length	Congruent crystal [3]	Stoichiometric crystal [3]
a_{H}	5.15052 Å	5.14739 Å
c_{H}	13.86496 Å	13.85614 Å
Density ρ	4.648 g/cm ³	4.635 g/cm ³

The lattice spacing is dependent not only on crystal composition, but also on temperature. The temperature dependence of both lattice cell vector lengths has been determined in the temperature range from room temperature to 500°C by Kim and Smith [7]. The resulting thermal expansion can be expressed in a quadratic function:

$$d_T/d_{25C} = 1 + \alpha(T - 25) + \beta(T - 25)^2 \quad (5)$$

where the coefficients α and β are given in TABLE 3 and d is any length tied to the crystal lattice such as a crystal length. The values are normalised to a temperature of 25°C.

TABLE 3 Thermal expansion (EQN (5)) for the polar direction c_{H} as well as perpendicular to it.

	Linear coefficient α	Quadratic coefficient β
Direction perpendicular to c_{H}	1.54×10^{-5}	5.3×10^{-9}
Direction along c_{H}	0.75×10^{-5}	-7.7×10^{-9}

D GEOMETRICAL INTERPRETATIONS OF LATTICE STRUCTURE

While Section C above gives a complete description of the atomic positions, it can be advantageous to interpret the structure as distorted perovskite or hexagonal close-packing. This helps to visualise fundamental physical phenomena or properties such as the phase-transition, the relationship to perovskites or thermal expansion [8,9]. To do so, the origin is best centred between two oxygen planes that are spaced by $c_{\text{H}}/6$. This leads to the following parameters for the congruent crystal lattice:

	Congruent crystal [3]
Nb ($a_{1\text{H}}$)	0
Nb ($a_{2\text{H}}$)	0
Nb (c_{H})	$w = 0.0195$
Li ($a_{1\text{H}}$)	0
Li ($a_{2\text{H}}$)	0
Li (c_{H})	$1/3 + w' = 1/3 - 0.0347$
O ($a_{1\text{H}}$)	$u = 0.0479$
O ($a_{2\text{H}}$)	$1/3 + v = 1/3 + 0.0097$
O (c_{H})	1/12

w , w' , u and v are small quantities that describe the deviation from an idealised structure having the oxygen atoms arranged in a hexagonal close-packed arrangement [8]. There are six octahedral interstices along the three-fold symmetry axis, one between each pair of oxygen layers. The first and fourth contain Nb, the second and fifth are empty, and the third and sixth contain Li. The simplest distortion from this high symmetry structure is a non-zero value for u , while the other parameters remain zero. This will lower the symmetry of the space group to R3c, that of the para-electric phase. The oxygen octahedra containing Li rotate around the three-fold axis, with the rotation direction reversing every $c_H/2$. In order to keep the octagons regular in shape, the ratio c/a will need to be decreased. The value for u above corresponds to about 6° of rotation. If that rotation were increased to 30° , the ideal cubic perovskite structure would result.

This lattice description is well suited to compare characteristics of lithium niobate with other materials such as PrAlO_3 , LaCoO_3 , KNbO_3 , NaNbO_3 or $\text{Pb}(\text{Zr}, \text{Ti})\text{O}_3$, and is helpful to theoretically predict or compare materials properties.

E CRYSTAL PROPERTIES

Crystal properties are best described in tensor form in a rectilinear coordinate system. The conventional choice of coordinate system for lithium niobate is a right-handed system with the X-axis along one of the hexagonal a_H axes, the Z-axis along the c_H axis, and the Y-axis along the direction given by the vector product $Z \wedge X$. The polarity of Z and Y are defined such that the piezoelectric tensor coefficients d_{33} and d_{22} are positive. The polarity of +X follows from the choice of a right-handed system. All the crystal properties have to satisfy the symmetry relationships of point group 3m. There is a three-fold symmetry axis (a 120° rotation maps each atom onto an atom of the same type), and three mirror planes perpendicular to the three equivalent X-axes. Vector properties such as spontaneous polarisation and pyroelectricity can exist only along the Z-axis. Symmetric second order tensors [10], such as dielectric constant, thermal expansion etc., have two independent elements, one along the polar axis and the other perpendicular to it. Third order tensors such as the ones describing the electro-optic, piezo-electric or non-linear optic effect have four independent elements. They are most conveniently expressed in contracted notation [10] as shown for the piezoelectric effect in EQN (6b).

$$P_i = \sum_{j,k=1}^3 d_{ijk} T_{jk} \quad (6a)$$

$$P_i = \sum_{l=1}^6 d_{il} T_l \quad (6b)$$

$$d_{il} = \begin{pmatrix} 0 & 0 & 0 & 0 & d_{15} & -2d_{22} \\ -d_{22} & d_{22} & 0 & d_{15} & 0 & 0 \\ d_{31} & d_{31} & d_{33} & 0 & 0 & 0 \end{pmatrix} \quad (6c)$$

where T is the applied stress, d the piezoelectric tensor and P the resulting electric polarisation [11]. As an example, consider a thin crystal plate that has a surface normal rotated from the +Y-axis to the +Z-axis by an angle θ . If a stress is applied across the thin dimension, the resulting polarisation across the plate is given by the 'longitudinal piezo-effect':

$$d_{eff} = d_{22} \cos^3 \theta + (2d_{15} + d_{31}) \cos^2 \theta \sin \theta + d_{33} \sin^3 \theta \quad (7)$$

F CONCLUSION

X-ray analysis has been used to determine atomic positions and lattice vector lengths in both stoichiometric and congruent LiNbO_3 . The structure is treated as hexagonal. Thermal expansion data are also presented. Crystal properties, e.g. electro-optic, piezo-electric and non-linear optical effects, are described by tensors.

REFERENCES

- [1] S.C. Abrahams, J.M. Reddy, J.L. Bernstein [*J. Phys. Chem. Solids (UK)* vol.27 (1966) p.997]
- [2] S.C. Abrahams, W.C. Hamilton, J.M. Reddy [*J. Phys. Chem. Solids (UK)* vol.27 (1966) p.1013]
- [3] S.C. Abrahams, P. Marsh [*Acta Crystallogr. B (Denmark)* vol.42 (1986) p.61]
- [4] R.S. Weis, T.K. Gaylord [*Appl. Phys. A (Germany)* vol.37 (1985) p.191]
- [5] N.F.M. Henry, K. Lonsdale (Eds.) [*International Tables for X-Ray Crystallography* (Kynoch Press, Birmingham, UK, 1965)]
- [6] P.F. Bordui, R.G. Norwood, C.D. Bird, G.D. Calvert [*J. Cryst. Growth (Netherlands)* vol.113 (1991) p.61]
- [7] Y.S. Kim, R.T. Smith [*J. Appl. Phys. (USA)* vol.40 (1969) p.4637]
- [8] H.D. Megaw [*Acta Crystallogr. A (Denmark)* vol.24 (1968) p.583]
- [9] H.D. Megaw, C.N.W. Darlington [*Acta Crystallogr. A (Denmark)* vol.31 (1975) p.161]
- [10] J.F. Nye [*Physical Properties of Crystals* (Oxford, UK, 1985)]
- [11] [*IEEE Trans. Sonics Ultrason. (USA)* vol.SU-31 (1984) p.ANSI/IEEE STd 176]

1.3 Phase transition temperatures of LiNbO₃

J.C. Brice

This Datareview appeared in *Properties of Lithium Niobate* (INSPEC, IEE, London, UK, 1989) and is reproduced here for the reader's convenience.

A INTRODUCTION

All samples of lithium niobate show a phase transition at high temperatures (1050 to 1210°C depending on the ratio of Li to Nb). Very pure samples show only this transition. Many doped samples show one or more phase changes at low temperatures (typically 60 to 130°C).

B THE HIGH TEMPERATURE PHASE CHANGE

The transition discussed here is the one involved in the change from the ferroelectric phase with a 3-fold axis to the para-electric phase with an inverse 3-fold axis.

References [1-7] and the papers which they quote give widely scattered data but there is a clear trend for the transition temperature to rise with the lithium content of the crystals. The data in TABLE 1 are the result of fitting the data to a linear relation.

TABLE 1 The high temperature transition.

Solid composition (molar % lithium oxide)	Transition temperature (Celsius)	Conditions
45.7	1054 ± 25	Nb saturated solid
46.0	1064 ± 20	
47.0	1098 ± 15	
48.0	1131 ± 10	
48.4	1145 ± 10	Congruent melting composition
49.0	1165 ± 10	
50.0	1198 ± 5	
50.2	1205 ± 5	Li saturated solid

Gallagher and O'Bryan [7] explain this linear relation in terms of the cation vacancy content which they can vary also by doping with titanium dioxide. The curve which they obtain lies within the error limits given in TABLE 1. These limits are deduced on the basis that the errors are random. It is not possible, on the basis of existing data, to exclude variations caused by other factors, e.g. impurities or oxygen partial pressure during growth and processing.

Since it is easier to grow high quality crystals near to the maximum (congruent) melting composition, most crystals can be expected to have transition temperatures near to 1145°C.

The compositions corresponding to the conditions shown in TABLE 1 have uncertainties of about 0.1%.

C LOW TEMPERATURE TRANSITIONS

Many authors have reported phase changes at various temperatures below those given in TABLE 1. For example, Ismailzade et al [8] report eleven such transitions. See also [10,11]. Transitions in the

1.3 Phase transition temperatures of $LiNbO_3$

range 60 to 80°C have been found in crystals doped with iron, nickel and manganese [9,12] while [9] also reports a transition at 125°C in a crystal doped with 0.22% ferric oxide. In the case of manganese-doped crystals, a first order phase change with a significant latent heat occurs. In view of the established fact [12] that pure samples show no low temperature transitions, it is reasonable to assume that uncharacterised crystals which show transitions are impure. Since less than 0.1% impurity makes the phase changes obvious, only very small amounts of critical impurities may be needed. Further study of this topic is needed so that potentially destructive phase changes at processing temperatures can be avoided at minimum cost.

REFERENCES

- [1] K. Nassau [*J. Phys. Chem. Solids (UK)* vol.27 (1966) p.989]
- [2] J.R. Carruthers, G.E. Peterson, M. Grasso, P.M. Bridenbaugh [*J. Appl. Phys. (USA)* vol.42 (1971) p.1846-51]
- [3] J.C. Brice [*Curr. Top. Mater. Sci. (Netherlands)* vol.4 (1980) p.237]
- [4] Landolt-Bornstein [*Numerical Data and Functional Relations in Science and Technology* vol.15a (Springer, Berlin, 1981) p.489]
- [5] P.K. Gallagher, H.M. O'Bryan [*J. Am. Ceram. Soc. (USA)* vol.68 no.3 (1985) p.147-50]
- [6] Yu.K. Voron'ko, A.B. Kudryavtsev, V.V. Osiko, A.A. Sobol, E.V. Sorokin [*Sov. Phys.-Solid State (USA)* vol.29 no.5 (1987) p.711-5]
- [7] P.K. Gallagher, H.M. O'Bryan [*J. Am. Ceram. Soc. (USA)* vol.71 no.1 (1988) p.C-56-9]
- [8] I.G. Ismailzade, V.I. Nesterenko, F.A. Mirishi [*Sov. Phys.-Crystallogr. (USA)* vol.13 (1968) p.25]
- [9] Zhou Hengnan, Shen Huimin, Yuan Fang, Qiu Dirong, Wang Yening [*Chin. Phys. Lett. (China)* vol.3 no.8 (1986) p.373-6]
- [10] P.K. Gallagher, H.M. O'Bryan, E.M. Gyorgy, J.T. Krause [*Ferroelectrics (UK)* vol.75 no.1-2 (1987) p.71-8]
- [11] H. Engelmann, N. Gramer, Hsia Yuanfu, Liu Rongchuan, U. Gonser [*Ferroelectrics (UK)* vol.69 (1986) p.217]
- [12] V.E. Vasil'ev, B.B. Ped'ko, V.M. Rudyak [*Sov. Phys.-Solid State (USA)* vol.29 no.8 (1987) p.1474]

1.4 Point defects in LiNbO₃

F. Agulló-Lopez and J. García Solé

August 2001

A INTRODUCTION

As in other oxides, defects can be introduced in LiNbO₃ by a variety of methods including: crystal growth, impurity diffusion, ion implantation, radiation damage and thermochemical reduction. In this Datareview we will present a short overview of our present knowledge of the main properties and structural features of point defects, i.e. those having dimensions comparable to atomic size. The emphasis will be on new developments since the publication of the previous EMIS Datareview on this subject [1]. The focus will be on the defects themselves (type and structure), more than on the experimental techniques used for their production and detection.

B INTRINSIC DEFECTS

B1 Cation Sublattice

Intrinsic or structural defects are those related to the host crystal lattice. Particularly important are the non-stoichiometry (NS) defects that accommodate the deviations from nominal stoichiometry in the congruent and, to a lesser extent, in the near-stoichiometric crystals. The defect structure in congruent crystals (with a Li-deficiency given by [Li]/[Nb] = 0.945) has been discussed for many years and our view has evolved considerably with time. Two basic models have been proposed and investigated. In both models it is generally accepted that the Li-deficiency is compensated by a certain number of Nb⁵⁺ ions located in Li⁺ sites, the so called antisites, Nb_{Li}. The controversy emerges with those defects that are created to compensate the excess of charge introduced by the Nb_{Li} antisites.

In the Nb-vacancy model, generally accepted after the work by Abrahams and Marsh [2], charge compensation is at the cost of Nb-vacancies, V_{Nb}. Therefore the NS defects are: Nb_{Li} (4.6%) and V_{Nb} (3.7%). On the other hand, in the Li-vacancy model [3] charge compensation is by Li-vacancies, V_{Li}, and the NS defects are now: Nb_{Li} (3.7%) and V_{Li} (0.9%) (see FIGURE 1). Recently this second model has been in better accordance with experiments [4-6]. In any case, both models lead to the same number of non-regular Li sites (4.6%), which is important to account for the so called 'threshold effect' (see examples of this effect in Section C). On the other hand, evidence for two different Li⁺ sites has been derived from ion beam methods and experiments on hyperfine time dependent perturbed angular correlations (TDPAC) [7]. They probably correspond to regular Li⁺ ions and Li⁺ ions at Nb⁵⁺ octahedrons that give rise to a local reordering of the cation sequence along the c-axis so as to resemble the one occurring in the ilmenite structure [8] (see

Nb	Nb	Nb	Nb
Li	Li	Li	Li
Nb	Nb	Nb	Li
Li	Nb _{Li}	Nb _{Li}	Nb
Nb	V _{Nb}	Nb	Nb
Li	Li	V _{Li}	Li

FIGURE 1 Schematic representation of the cation stacking sequence along the c axis (first column) including the possible NS defects, Nb_{Li} and V_{Nb} (second column), Nb_{Li} and V_{Li} (third column), and the ilmenite-like cation stacking sequence (fourth column).

FIGURE 1). These results add new complicating features to our picture and suggest that the two basic models should be considered as ideal limiting schemes. The actual situation may probably contain features of both models.

In near-stoichiometric crystals where a ratio $[\text{Li}]/[\text{Nb}] \approx 1$ has been achieved, the defect structure is simpler. The concentration of Nb_{Li} defects is strongly reduced and only a Li site is observed [8]. However, one should be aware that a substantial concentration of defects is still present in these crystals since the ratio $[\text{Li}]/[\text{Nb}]$ is not known with an accuracy better than 0.1%.

B2 Anion Sublattice

Scarce information is available on the behaviour of the anionic (oxygen) sublattice, although it appears to be less defective. Oxygen vacancies exist in most oxides and so are expected to occur in LiNbO_3 . Ionising radiation may turn these vacancies into colour centres, such as F or F^+ , that can be identified by their optical absorption spectra. In fact, several bands in thermochemically reduced or irradiated crystals have been associated with colour centres. A relevant result supporting this view comes from electron irradiation experiments [9], showing that the optical bands appear just for electron energies above the threshold required for displacement of oxygen ions. Moreover the spectra and annealing behaviour of these bands are the same as found after heating in a reducing atmosphere. However, this interpretation is not generally accepted and alternative proposals involving polaron or bipolaron states have been advanced to account for the colouring. Self-trapped electrons as $\text{Nb}_{\text{Li}}^{+4}$ have been identified by EPR at low temperature and they have been correlated with an optical band at 1.6 eV. Bipolaron states resulting from the covalent coupling between polarons in close proximity have also been inferred from experimental data. It is argued that although vacancies are created by the irradiation, they remain empty as the corresponding electronic trap levels lie above those for the polarons. Detailed arguments can be found in [10]. One should note here that the two views might be reconciled if the colour centres in LiNbO_3 are viewed as polarons and/or bipolarons trapped at oxygen vacancies, although apparently this is not supported by the EPR data.

C CHEMICAL IMPURITIES

C1 Hydrogen

Hydrogen is a very common impurity in oxides, generally associated with host O^{2-} ions forming the OH^- molecular ion. It is a very interesting impurity for optoelectronic applications particularly in relation to photorefractive fixing and proton exchange waveguides (see Chapter 15). Most structural information has been derived from infrared (IR) spectra. It is now accepted that hydrogen lies in any of the four shortest O-O bonds connecting O^{2-} neighbours in planes perpendicular to the c-axis. In doped crystals the positions of the IR bands are shifted with respect to the pure crystals due to the change in the local environment of the protons. Further details on structural data, properties and applications can be consulted in [11].

C2 Closed-Shell Ions (Mg, Zn, Sc etc.)

Much work has been performed on these ions (particularly on Mg^{2+}) because of their role in inhibiting the photorefractive effect. At low concentrations Mg^{2+} substitutes for Li^+ host ions. This substitution is accompanied by a corresponding decrease in the number of antisites Nb_{Li} . Thus, 4.6% MgO-doped crystals resemble stoichiometric crystals. This is also confirmed by the UV spectra and other physical properties. However, for concentrations higher than the previous threshold (4.6%), Mg^{2+} ions also enter Nb^{5+} octahedral sites [12]. Although the lattice positions of other photorefractive inhibiting ions

such as Zn^{2+} [13], In^{3+} [13] and Sc^{3+} [14] have not been definitively identified, they presumably occupy the same lattice positions as Mg^{2+} ions.

C3 Transition-Metal and Rare-Earth Ions

Transition metal (TM) and rare earth (RE) ions are the most interesting defects since they play a key role in optoelectronic applications, especially laser and amplifier systems and non-linear photorefractive properties. The majority of these devices are based on trivalent lanthanide RE ions although some TM ions are also of great relevance. For instance $\text{Fe}^{3+}/\text{Fe}^{2+}$ ions play a special role in the photorefractive effect, while Ti^{4+} ions are used to fabricate waveguides.

C3.1 Valence states

TM ions are known to occur in several stable charge states in the LiNbO_3 host, e.g. titanium (Ti^{4+} , Ti^{3+}), iron (Fe^{2+} , Fe^{3+}), manganese (Mn^{4+} , Mn^{3+}), copper (Cu^+ , Cu^{2+}), nickel (Ni^+ , Ni^{2+}) and cobalt (Co^{2+}) [10,15]. Multiple valence states are very relevant to photorefractive and photochromic properties. On the other hand most lanthanide RE ions have only a stable triplet charge state. However, the actinic uranium ions can be present with higher stable charge states (U^{5+} and U^{6+}) [16,17].

C3.2 Lattice location

Four lattice sites are, in principle, candidates to be occupied by foreign ions in LiNbO_3 : three octahedral sites (Li^+ , Nb^{5+} , and an empty structural octahedron) and an interstitial tetrahedral site. Due to the low concentration of these foreign ions, X-ray diffraction cannot be used and other methods become necessary to detect their location. Much progress has been recently achieved on this problem because of the use of advanced characterisation techniques such as: electron double nuclear resonance (ENDOR) [18], EPR [19,20], extended X-ray absorption fine structure (EXAFS) [21,22], TDPAC [7,8], X-ray standing waves (XSW) [23] and particularly ion-beam methods [24-28]. All these methods have allowed a clear picture of the sites that are occupied by TM and RE ions to be obtained, although problems still remain in relation to the underlying physical mechanisms and driving forces that determine the location. The advantage of ion-beam methods, particle induced X-ray emission (PIXE) [24,25] and especially Rutherford backscattering spectrometry (RBS) [26], over other sophisticated spectroscopic tools, is that they essentially rely on geometrical arguments to a large extent, independent of physical assumptions.

RBS/channelling has been particularly useful for determining the lattice location of a variety of trivalent RE ions, as they are heavier than Nb^{5+} , the heaviest constituent ion in LiNbO_3 [26]. However, this experimental technique is no longer applicable for detecting the location of TM ions, and PIXE [24,25] together with spectroscopic techniques (EXAFS [21,22], EPR [19,20] and ENDOR [18]) has been applied.

It has been concluded that RE³⁺ and TM (Mn^{2+} , Cr^{3+} , Fe^{3+} , Ni^{3+} , Ti^{4+} and Hf^{4+}) ions replace Li⁺ octahedral sites in congruent crystals [18-20,26-30]. However, RE³⁺ ions shift their position with respect to the regular Li⁺ location, along the c ferroelectric axis towards the empty octahedral site [26-29,31]. The amount of this off-centre shift is represented as a function of the RE³⁺ ionic radius in FIGURE 2, where a roughly linear dependence is observed. This behaviour points to strain effects as responsible for the shift. For the particular case of Er³⁺ ions, a certain fraction is forming clusters or precipitates in the lattice and then not replacing regular Li⁺ sites [31]. This is likely to produce inaccuracy in the measured shift, so that the reported Er³⁺ ion displacement deviates from the linear dependence in FIGURE 2.

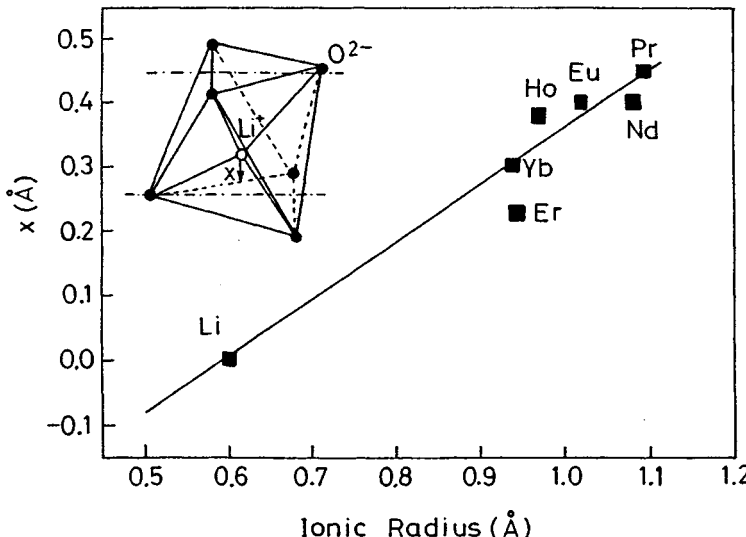


FIGURE 2 Displacement from the Li^+ position as a function of the ionic radius of the active RE^{3+} ion measured by RBS/channelling (after [26,28]).

So far we can conclude that divalent, trivalent and tetravalent TM and RE ions lie in Li^+ sites. In fact, evidence for Nb^{5+} site occupancy has only been found for pentavalent or hexavalent ions: Ta^{5+} [27,32], W^{6+} [33], U^{6+} and U^{5+} ions [16,17] lie in this site. This suggests that electrostatic effects may also be relevant in determining lattice location.

C3.3 Change of site by codoping or stoichiometry changes

As we have said above, the cations of the codopant oxides (Mg^{2+} , Zn^{2+} , Sc^{3+} etc.) prefer to occupy Li^+ sites in congruent crystals, so that a competition with RE and TM ions appears in doubly-doped lithium niobate crystals. This fact produces a reduction in the segregation coefficient of the RE and TM ions. However, the main effect of codoping is to remove TM (Cr^{3+} and Hf^{4+}) ions from the Li^+ to the Nb^{5+} site. Thus a double occupancy of these two lattice sites has been reported to occur for Cr^{3+} ions in $\text{LiNbO}_3:\text{MgO:Cr}$ crystals when the MgO concentration is higher than 4.6% [19] (see FIGURE 3(a)). On the other hand, a full conversion in the occupancy from Li^+ to Nb^{5+} sites has been found in congruent $\text{LiNbO}_3:\text{MgO:Hf}$ crystals for a 6% MgO concentration [34], as can be seen in FIGURE 3(b). This figure shows a gradual transfer of Hf^{4+} ions from Li^+ to Nb^{5+} sites and the threshold effect (4.6% MgO concentration) is also clearly appreciated.

This redistribution of sites has also been reported to occur in near-stoichiometric crystals. As in the previous case, this remarkable result is related to the interaction of the dopant ion with the intrinsic defects accommodating the Li deficiency. As an example, Hf, Fe and Cr ions move from Li^+ to Nb^{5+} sites as the crystal approaches the stoichiometric composition [35-37]. For Hf this behaviour is inferred from the combined results from ion-beam channelling and PAC techniques.

At this point it should also be mentioned that in both congruent and stoichiometric crystals the location of TM ions may depend on concentration. Indeed, this has been ascertained for Hf^{4+} . In stoichiometric crystals with 1 mol% of HfO_2 and in congruent crystals doped with 6% HfO_2 , the Hf^{4+} ions occupy both Li^+ and Nb^{5+} sites. In fact, it has been proposed that well above a threshold concentration the distribution of Hf^{4+} ions among these two sites tends to be in accordance with the ratio 1/3 needed to assure electrical neutrality [7].

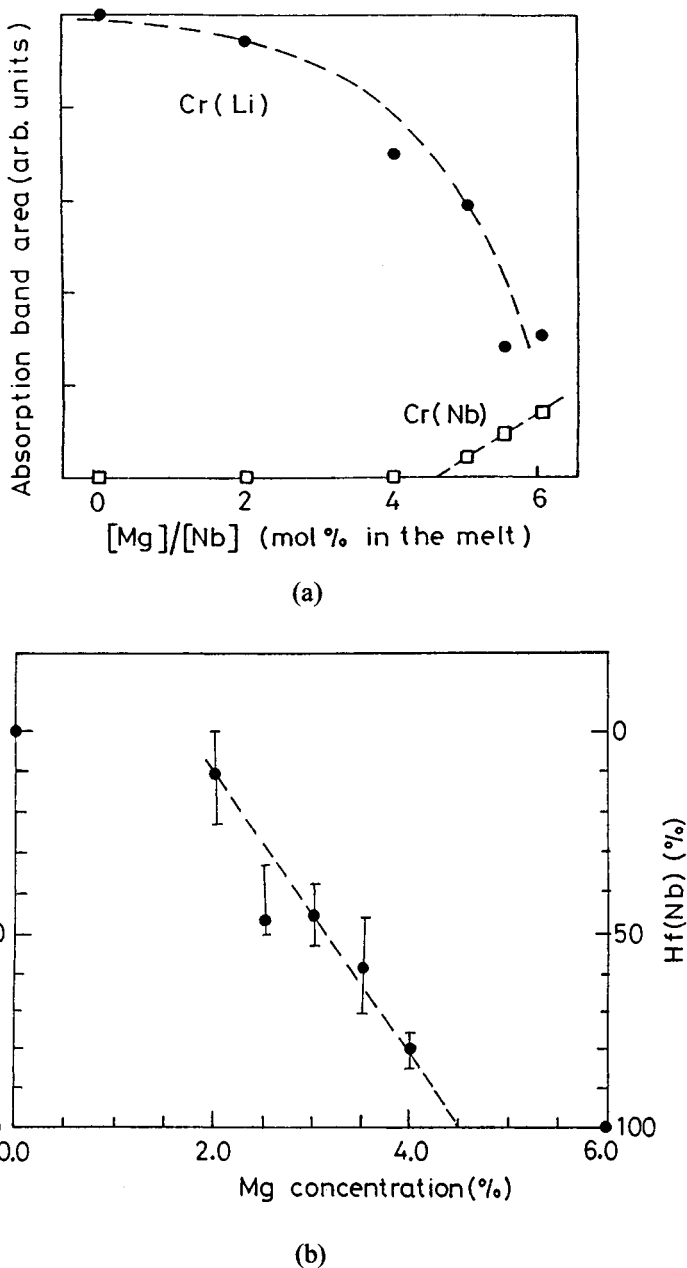


FIGURE 3 Transfer of TM ions from Li^+ to Nb^{5+} sites by MgO codoping. Evidence from (a) absorption of Cr^{3+} ions, (b) RBS/channelling of Hf^{4+} ions (bars include the results for several axial directions. (After [19,34].)

Finally, it should be noted that the previous redistribution effect has not been observed for RE^{3+} ions. For these ions the situation must be different. In fact, the large ionic radius may explain that for both codoped and near-stoichiometric crystals RE^{3+} ions remain at Li^+ sites.

C3.4 Non-equivalent centres

The presence of non-equivalent centres is a common feature in ion doped LiNbO_3 crystals. Evidence for these centres has been found for a variety of RE (Pr^{3+} , Nd^{3+} , Eu^{3+} , Dy^{3+} , Ho^{3+} , Er^{3+} , Tm^{3+} and Yb^{3+}) and Cr^{3+} ions by using optical spectroscopy, as far as they present optical spectra (optically active ions). In fact, the optical absorption and fluorescence bands of these ions are broader in LiNbO_3 than

in other crystals and some specific sensitive inter-Stark optical transitions display a clear structure (see FIGURE 4) that reveals the presence of non-equivalent centres. These centres can be individually excited by laser site selective spectroscopy. A summary of the present understanding of the nature and structure of TM and RE ion centres in LiNbO_3 can be found in [26,29,38]. It is important to recall here that the term 'centre' is related to ions in specific local environments. Therefore centres may occur even when the TM or RE ions occupy only the Li^+ site, giving rise to non-equivalent optical spectra, i.e. non-equivalent optical centres. Thus, each TM or RE ion centre has a set of energy levels related to a particular crystalline field [26].

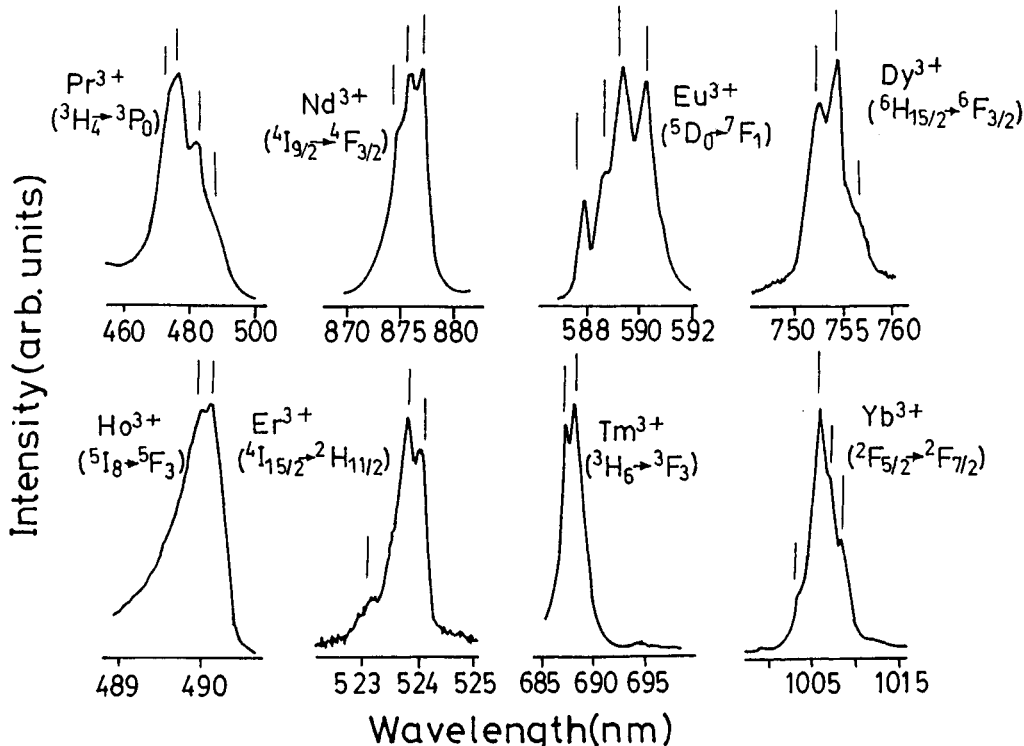


FIGURE 4 Low temperature optical spectra corresponding to single inter-Stark transitions of RE^{3+} ions in congruent LiNbO_3 (the states involving these single transitions are displayed). (After [29,38].)

The structure of the non-equivalent RE ion centres has been related to different off-centre positions around the average position given by RBS (see FIGURE 2) as a result of different local environments. These local environments are very likely created by different configurations of the NS defects (antisites and related vacancies) around the RE^{3+} ions devoted to achieving a local charge compensation better than statistical distributions of these NS defects around the RE^{3+} ions [29].

D CONCLUSION

Point defects arise in LiNbO_3 during crystal growth, impurity diffusion, ion implantation, radiation damage and thermochemical reduction. Intrinsic defects on both cation and anion sublattices are discussed. Impurity elements covered include hydrogen, a very common impurity, group II (e.g. Mg, Zn and Sc), which inhibit the photorefractive effect, and transition-metal and rare-earth ions. The latter play key roles in optoelectronic applications and non-linear photorefractive properties.

REFERENCES

- [1] [*Properties of Lithium Niobate* EMIS Datareview Series No.5 (INSPEC, IEE, London, UK, 1989)]
- [2] S.C. Abrahams, P. Marsh [*Acta Crystallogr. B (Denmark)* vol.42 (1986) p.61]
- [3] P. Lerner, C. Legras, J.P. Dumas [*J. Cryst. Growth (Netherlands)* vol.314 (1968) p.231]
- [4] J. Blumel, E. Born, Th. Metzger [*J. Phys. Chem. Solids (UK)* vol.55 (1994) p.589]
- [5] Y. Watanabe, T. Sota, K. Suzuki, N. Iyi, K. Kitamura, S. Kimura [*J. Phys., Condens. Matter (UK)* vol.7 (1995) p.3627]
- [6] A. Kling et al [*Nucl. Instrum. Methods Phys. Res. B (Netherlands)* vol.113 (1996) p.293]
- [7] J.G. Marques et al [*Nucl. Instrum. Methods Phys. Res. B (Netherlands)* vol.136-138 (1998) p.431]
- [8] J.G. Marques et al [*8th Europhysical Conf. on Defects in Insulating Materials* Keele, UK, 6-11 July 1998 (Gordon and Breach, Switzerland, 1999)]
- [9] E.R. Hodgson, F. Agulló-López [*Solid State Commun. (USA)* vol.64 (1987) p.965]
- [10] O.F. Schirmer, H.J. Reyher, M. Wöhlecke [*Insulating Materials for Optoelectronics* Ed. F. Agulló-López (World Scientific, 1995) p.93]
- [11] J.M. Cabrera, J. Olivares, M. Carrascosa, J. Rams, R. Muller, E. Dieguez [*Adv. Phys. (UK)* vol.45 (1996) p.349]
- [12] A. Kling, D. Kollewe, B.C. Grabmaier [*Nucl. Instrum. Methods Phys. Res. B (Netherlands)* vol.64 (1992) p.232]
- [13] T. Volk, N. Rubinina, M. Wöhlecke [*J. Opt. Soc. Am. B (USA)* vol.11 no.9 (1994) p.1681]
- [14] J.K. Yamamoto, K. Kitamura, N. Iyi, S. Kimura, Y. Furukawa, M. Sato [*Appl. Phys. Lett. (USA)* vol.61 (1992) p.2156]
- [15] O.F. Schirmer, O. Thiemann, M. Wöhlecke [*J. Phys. Chem. Solids (UK)* vol.52 (1991) p.185]
- [16] A. Kling et al [*8th Europhysical Conference on Defects in Insulating Materials* Keele, UK, 6-11 July 1998 (Gordon and Breach, Switzerland, 1999)]
- [17] D. Bravo, L.E. Bausá, F.J. López [*8th Europhysical Conference on Defects in Insulating Materials* Keele, UK, 6-11 July 1998 (Gordon and Breach, Switzerland, 1999)]
- [18] G. Corradi, H. Söthe, J.M. Spaeth, K. Polgár [*J. Phys., Condens. Matter (UK)* vol.3 (1991) p.1901]
- [19] J. Diaz-Caro, J. García Solé, D. Bravo, J.A. Sanz-García, F.J. López, F. Jaque [*Phys. Rev. B (USA)* vol.54 (1996) p.13042]
- [20] J. Diaz-Caro, J. García Solé, D. Bravo, T.P.J. Han, F. Jaque, B. Henderson [*Ferroelectr. Lett. Sect. (Switzerland)* vol.23 (1997) p.27]
- [21] C. Zaldo, F. Agulló-Lopez, J. García, A. Marielli, S. Mobilio [*Solid State Commun. (USA)* vol.71 (1989) p.243]
- [22] C. Zaldo, C. Prieto, H. Dexpert, P. Fessler [*J. Phys., Condens. Matter (UK)* vol.3 (1991) p.4135]
- [23] T. Gog, G. Materlik [*Insulating Materials for Optoelectronics* Ed. F. Agulló (World Scientific, 1995) ch.8 p.201]
- [24] L. Rebouta et al [*Europhys. Lett. (France)* vol.14 (1991) p.557]
- [25] L. Rebouta, M.F. da Silva, J.C. Soares, J.A. Sanz García, E. Dieguez, F. Agulló-Lopez [*Nucl. Instrum. Methods Phys. Res. B (Netherlands)* vol.64 (1992) p.189]
- [26] A. Lorenzo et al [*Opt. Mater. (Netherlands)* vol.8 (1997) p.55]
- [27] L. Rebouta, P.J.M. Smulders, D.O. Boerma, F. Agulló-Lopez, M.F. Da Silva, J.C. Soares [*Phys. Rev. B (USA)* vol.48 (1993) p.3600]

1.4 Point defects in LiNbO_3

- [28] A. Lorenzo, H. Jaffrezic, B. Roux, G. Boulon, J. García Solé [*Appl. Phys. Lett. (USA)* vol.67 no.25 (1995) p.3735]
- [29] J. García Solé, L.E. Bausá, D. Jaque, E. Montoya, H. Murrieta, F. Jaque [*Spectrochim. Acta A (Netherlands)* vol.54 (1998) p.1571]
- [30] B. Hauer et al [*J. Phys., Condens. Matter (UK)* vol.6 (1994) p.267]
- [31] L. Rebouta et al [*Appl. Phys. Lett. (USA)* vol.70 no.9 (1997) p.1070]
- [32] C. Prieto, C. Zaldo, P. Fessler, H. Dexpert, J.A. Sanz García, E. Diéguez [*Phys. Rev. B (USA)* vol.43 (1991) p.2594]
- [33] A. Kling, J.G. Marques, M.F. da Silva, E. Dieguez, F. Agulló-López, J.C. Soares [*Nucl. Instrum. Methods Phys. Res. B (Netherlands)* vol.127-128 (1997) p.520]
- [34] L. Rebouta, M.F. da Silva, J.C. Soares, M.T. Santos, E. Diéguez, F. Agulló-López [*Radiat. Eff. Defects Solids (UK)* vol.136 (1995) p.137]
- [35] G.A. Torchia et al [*J. Phys., Condens. Matter (UK)* vol.10 (1998) p.L341]
- [36] G.I. Malovichko, V.A. Grachev, O.F. Schirmer, B. Faust [*J. Phys., Condens. Matter (UK)* vol.5 (1993) p.3971]
- [37] J.G. Marques et al [*Mater. Sci. Forum (Switzerland)* vol.248-249 (1997) p.395]
- [38] J. García Solé [*Phys. Scr. Vol. T (Sweden)* vol.55 (1994) p.30]

CHAPTER 2

GROWTH

- 2.1 Boules of LiNbO₃ congruently grown by the Czochralski technique
- 2.2 Growth of LiNbO₃ by Stepanov's technique
- 2.3 Iron-doped boules of LiNbO₃
- 2.4 Epitaxial growth of LiNbO₃

2.1 Boules of LiNbO₃ congruently grown by the Czochralski technique

D.H. Jundt and G. Foulon

July 2001

A INTRODUCTION

Lithium niobate is a synthetic crystal, first grown in the early 1960s using the Czochralski technique [1]. Other growth techniques such as Verneuil, flux, Bridgman or Stepanov methods can also be used. Initially, the phase diagram was not known well, and growth was performed from a stoichiometric melt (i.e. having a molar ratio Li/Nb = 1). Growth is most easily initiated along the Z axis, but other orientations can also be grown by providing a seed of the correct orientation.

B CZOCHRALSKI GROWTH METHOD

The Czochralski growth method is widely used for industrial crystal growth, most notably that of silicon. The pure compound of the material to be grown is melted in a crucible in the growth station. A seed crystal suspended from a rotating seed rod is then lowered into the furnace cavity, and the tip is touched into the melt. If the melt temperature is in the appropriate range just slightly above the melting point of the material (1250°C for lithium niobate), growth of a crystal can be initiated by starting to slowly withdraw the seed rod. New crystal material will attach to the solid seed, cooled by conducting heat through the seed rod. As the growth progresses, the diameter of the growing crystal is controlled by adjusting the crucible temperature. Lowering the heating power will accelerate the crystallisation and lead to a diameter increase, while increasing the power will act to decrease the crystal diameter. Growth furnace configurations and parameters for successful lithium niobate growth have been described by various groups [1-5].

The components of a Czochralski system are: the crucible containing the melt, the heat generation with surrounding insulation, seed pull and rotation mechanism, and a feedback system for diameter control.

Growth is typically performed from platinum crucibles. For larger diameter crystals, the crucibles need thicker walls to counteract the increased static fluid pressure of the larger melt that tends to deform the crucibles at high temperatures. Alternatively, the platinum can be stabilised by additives such as zirconia or yttria grains. Rhodium is not typically used since it gets incorporated, leading to coloured crystals. The growth is typically conducted in air. In an atmosphere that lacks oxygen, the thermal transport conditions are radically altered, requiring a completely different set of growth parameters [6].

The ideal melt composition for growth is at the congruency point. For several decades, this composition was assumed to be 48.6 mol% lithium [7]. More recent studies have corrected this to somewhat lower values [3,8]. In order to reproducibly achieve melt fraction conversions above around 90%, the melt composition must be controlled very precisely. This requires good control of impurities such as sodium, exact weighing of the powders, control of the isotopic ratio of Li, and control of moisture content, e.g. by complete drying of the powders [3]. For applications demanding high wafer quality and low compositional variation from one crystal to another, the maximal melt fraction conversion typically is chosen below 50%.

2.1 Boules of LiNbO_3 congruently grown by the Czochralski technique

Two types of heating can be used to grow lithium niobate: resistive heating and inductive heating. Resistive heating is generally more efficient because no conversion or coupling losses are involved. The heating elements are arranged in an insulated cavity containing the crucible. The geometry of the cavity as well as the refractory materials used to provide insulation determine the temperature gradients within the cavity [9]. In inductive heated growth (also commonly referred to as RF growth), the electric power radiated by a coil arranged around the crucible is coupled to the crucible and other metal receptors that might be present, and the induced eddy currents there generate heat. The thermal gradients are influenced by the insulation that is placed around the crucible and the space above. Secondary receptors (active after heaters) can be used to further reduce the gradients.

Lithium niobate is a fragile crystal and has non-isotropic thermal expansion coefficients. Cracking is a serious problem in LN crystal growth, often occurring during the cool-down of the grown crystal. The thermal gradients within the crystal during growth determine how much strain is incorporated into the crystal [10,11]. A careful balance should be maintained so that a controlled crystal shape can be achieved while keeping the strain manageable. The heat enthalpy released at the growth interface during growth must be effectively removed for growth to proceed at a reasonable rate without causing constitutional supercooling (deviations from congruency are small, but always present). This requires sufficiently large gradients within the melt, typically aided by the rotation of the crystal pumping a forced convection. In the space above the melt, the gradients should be optimised so that seeding can be achieved, while at the same time assuring that low dislocation densities can be achieved during the bulk of the crystal growth cycle. Very low gradients narrow the temperature range for successful seeding so growth becomes impractical. Low radial melt gradients are also undesirable because such conditions lead to poor shape control as facets develop in a growth influenced by interface attachment kinetics. High radial gradients in the crystal on the other hand will lead to generation of dislocations leading to sub-grain boundaries.

As the crystal is grown, the melt level in the crucible drops. This alters the thermal gradients at the location of the interface. To compensate for this effect, the crucible often is lifted or the heating coil (in an RF system) is lowered. The crystal rotation can also be adjusted to maintain the desired interface shape [12]. In the absence of rotation, the melt convection will be driven by natural buoyancy. At the correct crystal rotation, the forced convection induced by crystal rotation defines a stable convection pattern, leading to a crystal interface less convex than it would be without rotation. To get additional control over convection patterns, the crucible can also be rotated.

Growing a crystal requires the following steps. First, the crucible with the reacted lithium niobate powder (or crystal fragments) is heated up in the furnace cavity to a temperature above the melting point. The melt is soaked for a while to ensure that all crystal agglomerates are melted. Then, the melt is cooled to a temperature close to, but still above, the melting temperature. The actual temperature depends on the gradients in the melt and furnace. The seed of the desired orientation is then lowered to the melt level. During the growth setup, the seed must be carefully oriented to avoid non-centred rotation. To avoid dislocations propagating from the seed into the growing crystal, seeds are typically cut from previously grown crystals with low dislocation densities. After successful seeding, the crystal diameter is increased from the seed diameter to that of the useful portion of the crystal. This is generally achieved by programming a steady cooling rate for the heating system. After the crystal has achieved a certain diameter, around 2 - 4 cm, the crystal weighing system signal is strong enough for the automatic diameter control (ADC) to be switched on. The ADC circuit derives an error signal from the difference between the measured crystal weight and that of the pre-defined ideal weight increase curve. This error signal is fed into a PI or PID controller adjusting the heating power.

After the necessary crystal length has been achieved, the crystal is separated from the melt by accelerated pulling. Tapering the crystal bottom to avoid heat shock is typically not necessary. An annealing stage follows, to reduce the risk of cracking. The crystal is brought into a space of low thermal gradients at a temperature where dislocations move easily. The dislocations will adjust to

2.1 Boules of LiNbO_3 congruently grown by the Czochralski technique

lower the strain energy of the crystal. In highly strained crystals, dislocations typically will form grain boundaries. After completion of the annealing step, the crystal is slowly cooled to room temperature in order to avoid thermally induced cracking.

C CONCLUSION

Details of the Czochralski growth process for LiNbO_3 are outlined. Ideally, the melt composition should be near to stoichiometric and must be controlled precisely. The cool-down process is critical and the non-isotropic thermal expansion coefficients lead to cracking. Large temperature gradients in the melt are used, together with controlled gradients above the melt to minimise dislocations. Both crystal and crucible can be rotated. Automatic diameter control is used once the crystal is 2 - 4 cm long. An annealing step is included.

REFERENCES

- [1] K. Nassau, H.J. Levinstein, G.M. Loiacono [*J. Phys. Chem. Solids (UK)* vol.27 (1966) p.983]
- [2] M. Thirumavalavan et al [*Ferroelectrics (UK)* vol.102 (1990) p.15]
- [3] P.F. Bordui, R.G. Norwood, C.D. Bird, G.D. Calvert [*J. Cryst. Growth (Netherlands)* vol.113 (1991) p.61]
- [4] D. Cochet-Muchy [*J. Phys. IV, Colloq. (France)* vol.4 no.C2 (1994) p.33]
- [5] K. Shigematsu, Y. Anzai, S. Morita, N. Yamada, H. Yokoyama [*Jpn. J. Appl. Phys. I, Regul. Pap. Short Notes (Japan)* vol.26 (1987) p.1988]
- [6] Y. Okano, Y. Tsuji, D.H. Yoon, K. Hoshikawa, T. Fukuda [*J. Cryst. Growth (Netherlands)* vol.141 (1994) p.383]
- [7] R.L. Byer, J.F. Young, R.S. Feigelson [*J. Appl. Phys. (USA)* vol.41 (1970) p.2320]
- [8] H.M. O'Brian, P.K. Gallagher, C.D. Brandle [*J. Am. Ceram. Soc. (USA)* vol.68 (1985) p.493]
- [9] J.C. Rojo, E. Dieguez, J.J. Derby [*J. Cryst. Growth (Netherlands)* vol.200 (1999) p.329]
- [10] T. Tsukada, K. Kakinoki, M. Hozawa, N. Imaishi, K. Shimamura, T. Fukuda [*J. Cryst. Growth (Netherlands)* vol.180 (1997) p.543]
- [11] Z. Galazka [*J. Cryst. Growth (Netherlands)* vol.178 (1997) p.345]
- [12] N. Miyazaki, H. Uchida, T. Tsukada, T. Fukuda [*J. Cryst. Growth (Netherlands)* vol.162 (1996) p.83]

2.2 Growth of LiNbO₃ by Stepanov's technique

N.M. Polozkov and L.I. Ivleva

This Datareview appeared in *Properties of Lithium Niobate* (INSPEC, IEE, London, UK, 1989) and is reproduced here for the reader's convenience.

The first report on shaped LiNbO₃ crystal growth by the EFG method (which is, in our opinion, a version of Stepanov's method suggested in 1938, where the general principles of shaped crystal growth were described [1]) was published by LaBell in 1971 [2]. However, the technological parameters have not been considered. The first detailed paper on this question by Fukuda and Hirano appeared in 1975 [3]. The pulling speed of such crystals was 18 cm/h, that is about forty times as fast as that of the conventional Czochralski technique. The size of these crystals was 20 × 1.5 × 40 mm. The values of dielectric and pyroelectric parameters of these shaped crystals were the same as those of a plate cut from boule crystal grown by the Czochralski technique. It was also noted that under high thermal gradients (approximately 200 grad/cm) the plate crystal may be grown at a faster pulling speed, but the crystal tends to be cracked during growth. Characteristic crystal defects depending on the growth conditions, such as microvoids and subgrain boundaries, were often observed in the crystals obtained. The growth of shaped LiNbO₃ crystals 20 × 3 × 200 mm in size was also reported in [4]. The optically homogeneous crystals were grown with the pulling speed 2 - 4 cm/h.

We have used Stepanov's technique to grow shaped LiNbO₃ crystals in the form of 20 × 1.5 × 105 mm plates, and rods with square cross-section 15 × 15 × 80 mm in size. Single crystals were grown (on an installation by RF heating from platinum crucibles and platinum dies) with the orientations [0001] and [1010] along the growth axes. Charges with stoichiometric and congruent compositions were used. The rate of solidification varied from 1 to 11 cm/h [5,6].

When growing LiNbO₃ single crystals by Stepanov's technique at a rate of more than 1.5 cm/h the development of 5 - 100 micron microinclusions is observed in the crystal bulk, independent of the temperature gradient, direction of growth, or charge. In the same crystal, microinclusions may be parallel or perpendicular to the pulling direction. With increasing pulling rates up to 7 cm/h and higher, microinclusions develop long intertwining chains.

One of the possible effects causing the development of microinclusions in LiNbO₃ crystals may be dissociation of the melt at the overhead walls of the crucible. To grow these LiNbO₃ crystals, we have used an additional platinum screen placed between the inductor coil and the crucible. In this case the platinum screen was heated by RF heating. The crucible was heated by thermal radiation, thus avoiding overheating of the crucible walls. The LiNbO₃ crystals grown under these conditions with the pulling rate 2 cm/h had microinclusions. Attempts to grow crystals in vacuum of 1×10^{-4} to 10^{-5} torr have not been successful. The LiNbO₃ shaped crystals grown in vacuum were black. After annealing in air they became transparent. In the bulk of the crystals thus grown with a pulling rate 2 cm/h there were microinclusions. The development of microinclusions in LiNbO₃ shaped crystals may be associated with the purity of the charge. We used recrystallised LiNbO₃ as a charge. In this case, crystals free of microinclusions have been obtained at a pulling rate of 11 cm/h.

Thus, we may conclude that the presence of microinclusions in the LiNbO₃ crystals is due to uncontrollable contaminating impurities in the melt, and is due to constitutional supercooling related to the growth conditions of the crystals by the following equation by Tiller [7]:

$$\frac{G}{R} = -\frac{m(1-K)Co}{DK}$$

2.2 Growth of LiNbO_3 by Stepanov's technique

where K is the equilibrium coefficient of impurity segregation, D is the liquid diffusion coefficient, G is the temperature gradient in the melt at the crystallisation front, R is the growth rate, Co is the initial liquid composition and m is the inclination of the liquidus line. While the crystallisation front is plane, the microinclusions are rejected into the melt. When the crystallisation front becomes cellular, the microinclusions start to be pulled into the crystal and into the boundaries of the cells. The shapes and sizes of the microinclusions in LiNbO_3 shaped crystals grown by Stepanov's method depend on the growth rate, and their location depends on the die construction [8].

REFERENCES

- [1] A.V. Stepanov [*Budushee Metalloobrabotki* (L. Lenizdat, 1963)]
- [2] H.E. LaBell Jr., A.I. Mlavsky [*Mater. Res. Bull. (USA)* vol.6 (1971) p.571]
- [3] T. Fukuda, H. Hirano [*Mater. Res. Bull. (USA)* vol.10 no.8 (1975) p.801-6]
- [4] Z.J. Shi, Z.G. He, C.F. Ying [*Ultrasonics (UK)* vol.18 no.2 (1980) p.57-60]
- [5] Yu.S. Kuz'minov, S.V. Lavrishchev, N.M. Polozkov, N.V. Tkachenko [*Izv. Akad. Nauk. SSSR Ser. Fiz. (USSR)* vol.47 no.2 (1983) p.392-4]
- [6] L.I. Ivleva, Yu.S. Kuz'minov, V.V. Osiko, N.M. Polozkov, A.M. Prochorov [*Dokl. Akad. Nauk SSSR (USSR)* vol.268 no.1-3 (1983) p.69-72]
- [7] W.A. Tiller, K.A. Jackson, J.W. Rutter, B. Chalmers [*Acta Metall. (USA)* vol.1 (1953) p.428]
- [8] B.S. Red'kin, G.A. Satunkin, V.A. Tatarchenko, L.M. Umarov, L.I. Gubina [*Izv. Akad. Nauk SSSR Ser. Fiz. (USSR)* vol.47 no.2 (1983) p.386-91]

2.3 Iron-doped boules of LiNbO₃

I. Mnushkina

August 2001

A INTRODUCTION

LiNbO₃ (LN), one of the most technologically important oxide single crystals, has an unusual combination of ferroelectric, electro-optic, acoustic and piezoelectric properties.

The photorefractive properties of LiNbO₃ are of considerable interest for such applications as holographic volume data storage, optical image and signal processing, phase conjugation, real time interferometry, beam deflection and novelty filters [1]. However, the optical storage sensitivity of the pure congruent LiNbO₃ single crystal is rather poor. Two approaches have been pursued in order to improve its optical storage performance:

- (1) LN crystals have been optimised through doping with transition metal impurities, especially iron [1]. It has been reported that Fe ions in the LN crystals are a cause of the photorefractive phenomena [2].
- (2) Non-stoichiometry of LN single crystal (undoped and Fe-doped) has been controlled. It has been demonstrated that the structure and densities of the intrinsic (non-stoichiometric) defects substantially influence the optical properties, including the photorefractive effects [3-5].

The growth methods of Fe-doped congruent and stoichiometric materials each have their own special characteristics and will be described in this Datareview.

B GROWTH OF Fe-DOPED CONGRUENT LN

According to the Li₂O-Nb₂O₅ phase diagram [6], the Fe:LN crystals can be grown from the congruent melt with a composition ratio of Li:Nb = 48.6:51.4 and doped with 0.010 - 0.7 mol% Fe.

A typical growth of Fe-doped LN was demonstrated by He et al [7] and is very similar to the growth of undoped LN. The mixed raw material powder was pressed into a cylindrical sample, then sintered at 800°C for four hours and later at 1100°C for six hours in order to let the solid phase reaction complete. The purities of Nb₂O₅ and Li₂CO₃ materials used were 99.95% and 4N respectively. If the amount of fluorine content in the raw material is high, it causes the composition of the melt to deviate from its congruent composition and supercool the melt. In this manner, inclusions and bubbles would appear in the crystal, and high quality Fe-LN crystal could not be obtained. Therefore, the authors concluded that the fluorine content in raw Nb₂O₅ should be low or Nb₂O₅ should be sintered at 900 - 1000°C for ten hours before being used.

Fe:LN crystals are usually grown along the c-axis by the Czochralski (CZ) technique. The proper crystal growth rate and low temperature fluctuations are two of the most important factors for obtaining crystals without striae. Generally speaking, the pull rate for Fe-LN growth is slower than that for pure LiNbO₃ and closely related to the temperature gradient in the chamber of the furnace. A vertical temperature gradient of 40°C/cm and a pull rate of 5 mm/hr have been used by He et al [7]. The inclusion structure appeared throughout the whole crystal. This inclusion structure, deep brown in

2.3 Iron-doped boules of LiNbO_3

colour, extended from the top of the crystal to the bottom. Inclusions may be caused by a mismatch between the temperature gradient and the crystal growth rate. The same authors obtained a large size, high optical quality Fe-LN single crystal, with diameter of about 75 mm, using the crucible weighing method. The vertical temperature gradient was $70^\circ\text{C}/\text{cm}$ and the pulling rate 3 - 4 mm/hr. No striations occurred in such a crystal, and the crystal showed uniform transmission.

Large (>75 mm diameter) LN crystals with various iron concentrations (0.01 - 0.1 mol%) have been grown by Latore et al [8] by the CZ method with automatic weight control. All crystals were grown along the c-axis with a growth rate of 2 mm/hr and rotation rate of 5 - 7 rpm. Dopant Fe_2O_3 was added in excess to the congruent melt composition. Crystals were characterised using several techniques: transmission X-ray topography, ICP spectroscopy, optical absorption and DTA. TABLE 1 and FIGURES 1 and 2 represent these results.

TABLE 1

Wt % of iron			
Run #	Melt	Crystal	Tc ($^\circ\text{C}$)
LN138	0.00%	0.00%	1136.0
Fe:LN16	0.01%	0.01%	1135.5
Fe:LN13D	0.03%	0.02%	1139.9
Fe:LN247Z	0.05%	0.04%	1141.4
Fe:LN14	0.11%	0.07%	1141.5

As determined by ICP emission spectroscopy.

One of the major factors affecting the photorefractive properties is the charge state change of Fe [9]. Therefore, in order to grow LN crystals for optical applications with high homogeneity and high reproducibility, it is necessary to understand the segregation phenomena and establish techniques for controlling the concentration and charge state distribution profiles of Fe ions.

Values of the effective distribution coefficient of Fe in LN have been reported as 0.7 and 0.9 [10]. Takei and Katsumata [11] noted that the Fe concentration in crystals is 60 - 75% less than that in the melt. Dutov [12] reported that the Fe concentration in the 0.1 at% Fe-doped LN single crystal increased linearly with solidification fraction.

Kawasaki and co-authors [13] grew 0.019 mol% Fe-doped LN single crystals in order to investigate the uniformity of the crystal along the growth direction. The effective distribution coefficient k_{eff} , equilibrium distribution coefficient k_0 , and Fe^{2+} distribution along the growth direction in the crystal were clarified. They discussed the Fe^{2+} profile in the grown crystal from the viewpoint of the thermal history of the boule. As grown crystal was dark brown in colour and had changed from dark to light along the growth direction. FIGURE 3 [11] shows the absorption spectrum of the upper part (solidification fraction $g = 0.1$) and lower part ($g = 0.63$) of the crystal. For the Fe-doped crystal, absorption peaks were observed around 480 nm, whereas they were not observed for the undoped crystal. There is a consensus that peaks in the 480 nm region are caused by Fe^{2+} [14,15]. Kawasaki et al noticed that the peak intensities depend on solidification fraction. The absorption coefficient decreased from 13.5 to 4.6 cm^{-1} with the increase of solidification fraction from 0.10 to 0.63. In FIGURE 4, Fe concentration is plotted against the solidification fraction g of the crystal. The effective distribution coefficient k_{eff} was obtained from the following equation [16]:

$$C_s / C_0 = k_{\text{eff}} \left((1-g)^{k_{\text{eff}}} \right)^{-1}$$

2.3 Iron-doped boules of LiNbO_3

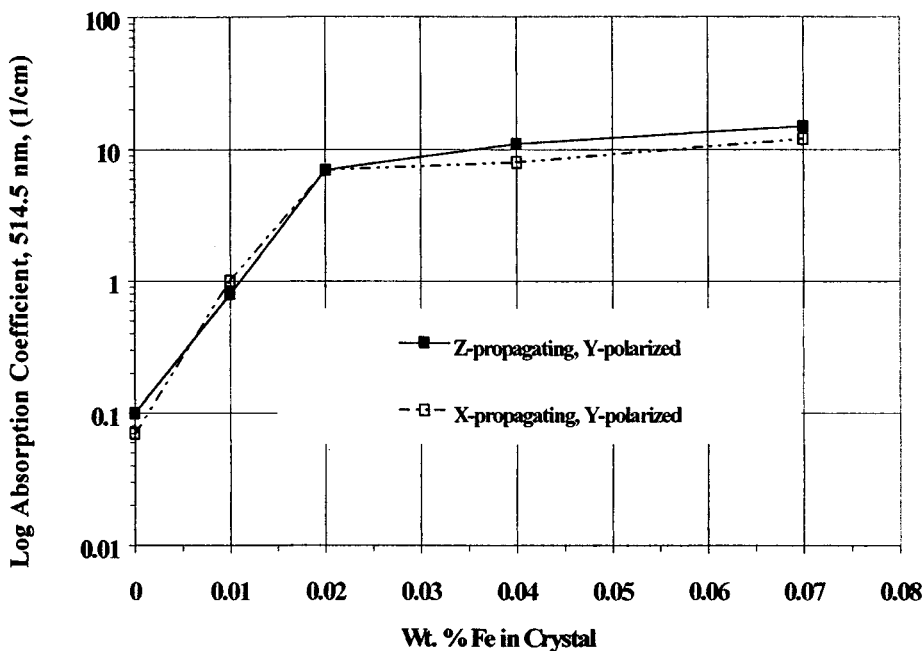


FIGURE 1 Log absorption coefficient dependence on Fe content in the crystal.

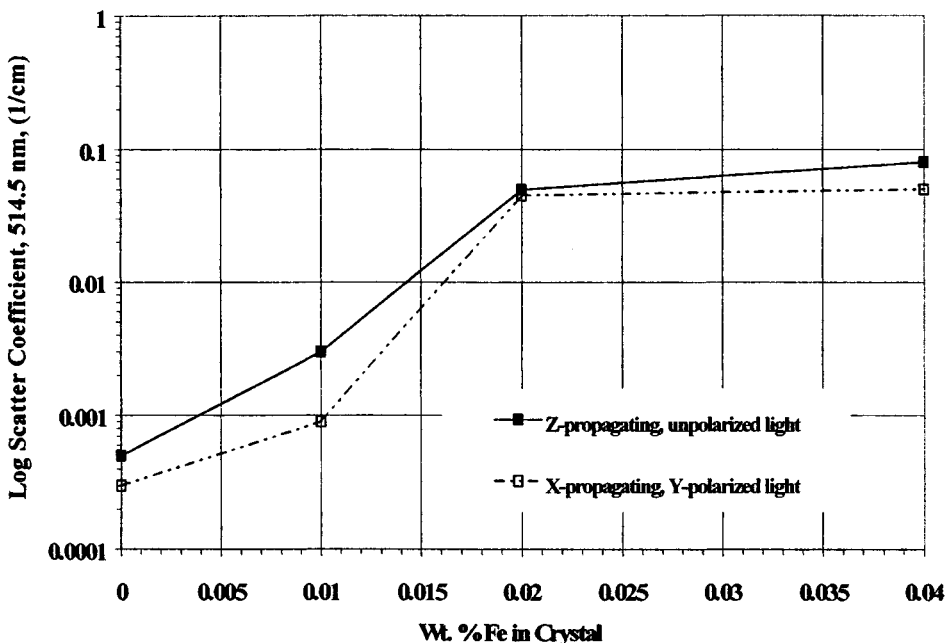


FIGURE 2 Log scatter coefficient dependence on Fe content in the crystal.

2.3 Iron-doped boules of LiNbO_3

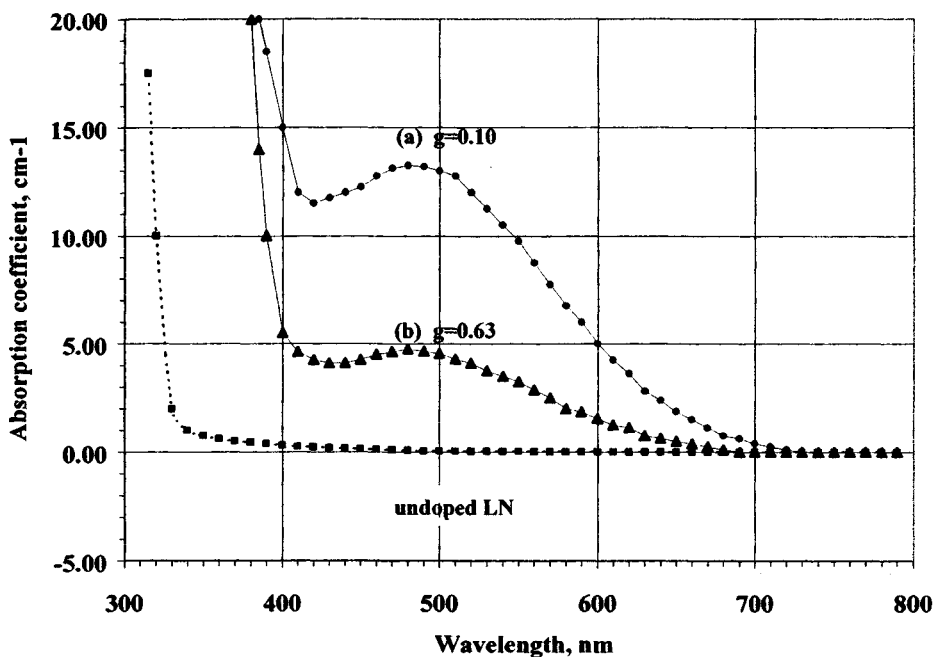


FIGURE 3 Absorption spectra of (a) upper part ($g = 0.10$) and (b) lower part ($g = 0.63$) of 0.019 mol% Fe-doped LN crystal grown with pulling rate of 5.0 mm/hr. The absorption spectrum of an undoped crystal is shown for comparison.

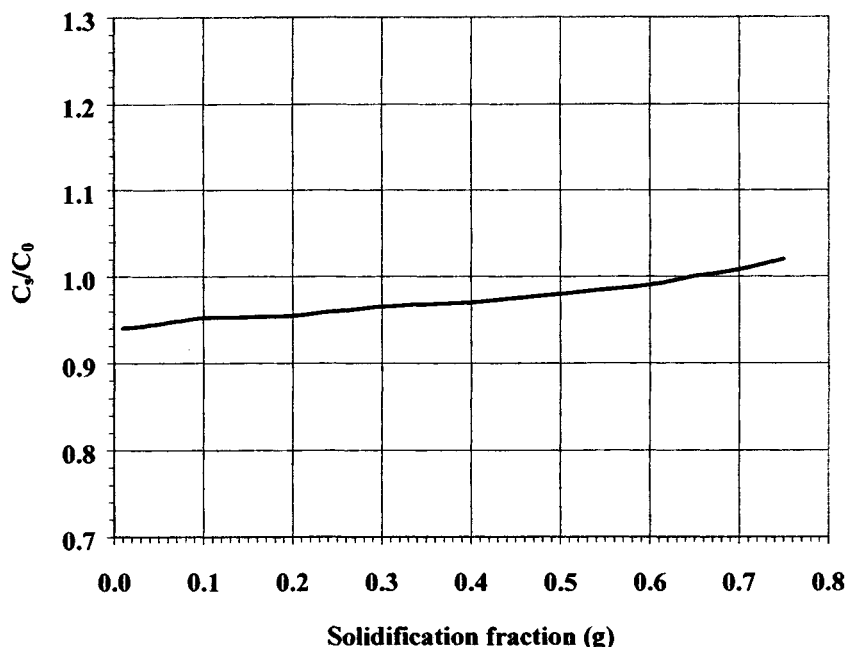


FIGURE 4 Fe concentration dependence on solidification fraction of the crystal grown with pulling rate of 5.0 mm/hr. C_s and C_0 are the Fe concentration in the crystal and in the melt, respectively.

2.3 Iron-doped boules of LiNbO₃

where C_s and C₀ are the Fe concentration in the crystal and in the melt, respectively. The equilibrium distribution coefficient k₀ was calculated from the following equation [17]:

$$k_{\text{eff}} = k_0 / [k_0 + (1 - k_0) \exp(-fd/D)]$$

where f, d and D are the solidification rate, thickness of the diffusion layer and diffusion constant of solute atom in the liquid phase, respectively.

Values of k_{eff} = 0.94, 0.94 and 0.95 corresponded to pull rates of 1.0, 3.0, and 5.0 mm/hr, respectively, and k₀ was determined to be 0.94. These results support the reported value of k_{eff} = 0.9 rather than 0.7 and suggest that the Fe concentration dependence on the solidification fractions is not as strong as reported by Dutov [12].

The result that k_{eff} is smaller than unity means that the Fe concentration in the lower parts of the crystal ends up higher than the concentration in the upper parts. Kawasaki et al [13] investigated absorption coefficients of the crystal along the growth direction at 480 nm. They observed a decrease in the absorption coefficient along the growth direction, which could not be explained by the increase in the amount of Fe. The authors concluded that there is a variation of the charge state of the Fe ions in the crystal, because of the difference in thermal history between the lower and upper parts. To achieve absorption homogeneity from one end to the other it is necessary to perform post growth crystal annealing in oxygen in a low gradient furnace at 950 - 1000°C. This procedure converts most of the Fe back to the trivalent state [9].

In summary, the homogeneity of the composition and optical perfection of the Fe-doped CZ-grown crystals are determined by the following main factors:

- Proper crystal growth rate
- Low temperature fluctuations
- Pull rate (generally slower than for undoped LN) closely related to the temperature gradient
- Diameter or weight control
- Postgrowth annealing in oxygen

C GROWTH OF Fe-DOPED STOICHIOMETRIC LN

The CZ method described above can be used only for growing the congruent composition of Fe-doped LN. This composition has an excess of Nb with respect to the stoichiometric composition (51.4%). The deficiency of Li ions leads to the formation of Nb_{Li} and (V_{Nb}Nb_{Li}) defects.

The Fe concentration in LN crystals (0.001 - 0.1 wt%) is usually much smaller than the concentration of the intrinsic defects n_{def}. Therefore, experiments with congruent LN would not help to answer the question as to how Fe impacts the defect structure of LN.

Recently, two methods have been identified that allow the growth of undoped and Fe-doped LN crystals with very low n_{def}. The first one relies on crystal growth from melts containing K₂O [18], and the second one uses the double crucible CZ method with an automatic powder supply system [19].

It was shown [5] that LN pulled from the congruent melt composition ($x = [\text{Li}] / ([\text{Li}] + [\text{Nb}]) = 48.6\%$) with 6 wt% of K₂O leads to crystals with $x = 50 \pm 0.15\%$. Potassium enters the material only to a very low extent (0.022 ± 0.004 wt%), as determined by electron microprobe [5]. Crystals have been doped with 0.05 wt% of Fe₂O₃, corresponding to 420 mol ppm in the crystal (a distribution coefficient of 0.9

2.3 Iron-doped boules of LiNbO_3

was assumed) [20]. EPR and optical absorption measurements were performed on these crystals and crystals grown from congruent melts and various K_2O concentrations [21]. It was found that the linewidth ΔB of low field lines of Fe^{3+} decreases monotonically with increasing K_2O content in the respective melt. The lowest ΔB was reached for nominally undoped LN grown from a melt with 6 wt% of K_2O . For LN doped with 0.05% Fe_2O_3 , the relative changes of ΔB were smaller and saturated on approaching 6 wt% K_2O . The profound changes in the linewidths resulting from small increases in the Fe concentration are of extreme importance. Malovichko and co-authors showed [21] that the incorporation of Fe drastically changes the properties of LN. A small concentration of about 420 ppm of Fe_2O_3 is sufficient to introduce lattice perturbations corresponding to a decrease in Li content from 50% to 49.5%, i.e. to a doping of 5000 ppm.

Another technique for obtaining stoichiometric Fe-doped LN crystals is the double crucible CZ method. This method utilises the ordinary CZ furnace equipped with a radio frequency generator and a platinum crucible with a double chamber structure, which divides the melt into two parts. The inner crucible is a platinum cylinder (90 mm diameter, 100 mm height) placed on the bottom of the outer crucible (140 mm diameter, 70 mm height). The outer melt can enter the inner crucible through a small gap between the bottom of the outer crucible and the inner cylinder. In order to grow stoichiometric LN crystals, the compositions of the inner melt and outer one should be kept Li-rich (~58.5 Li_2O mol%) and stoichiometric, respectively. In order to keep the melt composition constant, stoichiometric LN powder is supplied to the outer melt by an automatic supply system. In this supply system, the stoichiometric LN powder is placed in a holding container (hopper). The powder is delivered from the bottom of the container by a 'cork-screw' mechanism. The weight of the holding container, including the powder, is monitored every second by an electronic balance. The decrease per unit time in the weight of powder in the hopper is adjusted to equal the desired supply rate by automatically changing the rotation rate of the cork-screw mechanism. A load cell is equipped with the apparatus to monitor the weight change of the growing crystal, and this information is used for an automatic diameter control. At the same time, the powder supply rate is also automatically set to follow the weight increase of the growing crystal. Details of the supply system are described in [22,23].

Crystals were grown along the c-axis at a pull rate of 0.5 mm/hr. The starting materials were high purity Li_2CO_3 (>4N) and Nb_2O_5 (>5N) powder. Growth was accomplished in an oxygen/nitrogen gas mixture flow with volume ratio of oxygen to nitrogen 5:100. The seed rotation rate was about 5 rpm, and the crucible was rotated at a rate of 0.05 - 0.1 rpm in the opposite direction. Stoichiometric Fe-doped crystals of more than 40 mm in diameter and about 100 mm in length were typically obtained. The crystal composition over the whole diameter, and over the whole length of crystal grown, was estimated to be stoichiometric from both its chemical analysis and its Curie temperature, calculated with the equation proposed by O'Bryan et al [24]. Iron concentration in the crystal was analysed by inductively coupled plasma atomic emission spectroscopy (ICP-AES) and found to be homogeneous. Photorefractive properties of stoichiometric Fe-doped LN were compared with those of crystals grown from the congruent melt composition [25,26]. TABLE 2 shows the comparison in properties between stoichiometric (SLN) and congruent (CLN) Fe-doped LN crystals.

TABLE 2 Properties of congruent (CLN) and stoichiometric (SLN) Fe-doped LN crystals.

	Fe-doped CLN	Fe-doped SLN
Curie temperature ($^{\circ}\text{C}$)	1137	1198
Fe concentration in the crystal (wt. ppm)	500	270
Absorption at 532 nm (cm^{-1})	9.3	5.8
Exponential gain coefficient (Γ/cm^{-1})	15	27
Writing time at 1 W/cm^2 (s)	1.5	0.6
Photorefractive sensitivity S_{nl} ($\text{cm}^3 \text{J}^{-1}$)	$2.2 \times 10^{-7}*$	$4.9 \times 10^{-7}**$

Fe concentration: *300 wt. ppm, **150 wt. ppm.

2.3 Iron-doped boules of LiNbO_3

These results are clear evidence that non-stoichiometric defect control in lithium niobate crystals is of key importance for the improvement of their photorefractive properties. It is essential to continue the search for optimum conditions for growth of high quality single crystals from off-congruent compositions because Fe-doped stoichiometric LN has a great deal of potential for use as a holographic data storage material.

D CONCLUSION

This Datareview outlines the growth and properties of both congruent and stoichiometric LiNbO_3 doped with iron. Large diameter (>75 mm) congruent crystals with a range of iron levels can be grown by the Czochralski technique. Distribution coefficient values are in the range 0.7 - 0.9, although recent data suggest a value of ~0.94. Stoichiometric material has been produced by growth from melts containing K_2O and by the double crucible Czochralski technique. Crystals of 40 mm diameter and 100 mm length have been grown by the latter method. Fe-doped LiNbO_3 has potential as a holographic data storage material.

REFERENCES

- [1] P. Gunter, J.-P. Huignard [*Photorefractive Materials and Their Applications I and II* (Springer-Verlag, Heidelberg, 1988,1989)]
- [2] G.E. Peterson, A.M. Glass, T.J. Negran [*Appl. Phys. Lett. (USA)* vol.13 (1968) p.223]
- [3] Y. Furukawa, M. Sato, K. Kitamura, Y. Yajima, M. Minakata [*Appl. Phys. (Germany)* vol.72 (1992) p.3250]
- [4] N.B. Anghert, V.A. Pashkov, N.M. Solov'yeva [*Zh. Eksp. Teor. Fiz. (USSR)* vol.26 (1972) p.1666]
- [5] G.I. Malovichko et al [*Appl. Phys. A (Germany)* vol.56 (1993) p.103]
- [6] R.L. Byer, J.F. Young, R.S. Feigelson [*J. Appl. Phys. (USA)* vol.41 (1970) p.2320]
- [7] X.M. He, X.L. Fang, Y.N. Zhu, B.Y. Shu, L.Y. Xu [*J. Cryst. Growth (Netherlands)* vol.76 (1986) p.701]
- [8] J.R. Latore, S. Samuelson, R. Uhrin, F. Nitanda, Y. Furukawa [*1993 Topical Meeting on Photorefractive Materials, Effects, and Devices Ukraine*, 1993]
- [9] W. Philips, D.L. Staebler [*J. Electron. Mater. (USA)* vol.3 (1974) p.601]
- [10] A. Rauber [*Curr. Top. Mater. Sci. (Netherlands)* vol.1 (1978) p.551]
- [11] H. Takei, T. Katsumata [*Jpn. J. Appl. Phys. (Japan)* vol.7 (1982) p.994]
- [12] A.G. Dutov [*Vestn. Akad. Nauk SSSR Ser. Fiz.-Mat. Nauk (USSR)* vol.3 (1982) p.107]
- [13] K. Kawasaki, Y. Okano, S. Kan, M. Sakamoto [*J. Cryst. Growth (Netherlands)* vol.119 (1992) p.317]
- [14] M.G. Clark, F.J. DiSalvo, A.M. Glass, G.E. Peterson [*J. Chem. Phys. (USA)* vol.59 (1973) p.6209]
- [15] H. Kurz, E. Kratzig [*Appl. Phys. (Germany)* vol.12 (1977) p.355]
- [16] J.S. Shah [in *Crystal Growth and Characterization Vol.6* Ed. B.R. Pamplin (Pergamon, Oxford, 1975) ch.4 p.114]
- [17] J.A. Burton, R.C. Prim, W.P. Slichter [*J. Chem. Phys. (USA)* vol.21 (1953) p.1987]
- [18] G.I. Malovichko, V.G. Grachev, L.P. Yurchenko, V.Y. Proshko, E.P. Kokonyan, V.T. Gabrialyan [*Phys. Status Solidi A (Germany)* vol.133 (1992) p.K29]
- [19] K. Kitamura, Y. Furukawa, Y.Ji. Montomezzani, M. Zgonik, C. Medrano, P. Gunter [*J. Appl. Phys. (USA)* vol.82 (1997) p.1006]
- [20] E. Kratzig, O.F. Shirmer [in *Photorefractive Materials and their Applications* Eds. P. Gunter, J.P. Huignard (Springer, Berlin, 1988) p.131]

2.3 Iron-doped boules of LiNbO_3

- [21] G.I. Malovichko, V.G. Grachev, O.F. Shirmer [*Solid State Commun. (USA)* vol.89 (1994) p.195]
- [22] K. Kitamura, J.K. Yamamoto, N. Yi, S. Kimura, T. Hayashi [*J. Cryst. Growth (Netherlands)* vol.116 (1992) p.327]
- [23] K. Kitamura [*Ceramic Transactions* Eds. R.K. Padly, R. Guo (The American Ceramic Society, Westerville, OH, USA, 1995) vol.60 p.37]
- [24] H.M. O'Bryan, P.K. Gallagher, C.D. Brandle [*J. Am. Ceram. Soc. (USA)* vol.68 (1985) p.493]
- [25] M. Garrett, I. Mnushkina, Y. Furukawa, K. Kitamura, L.E. Halliburton, N.C. Giles, S.D. Setzler [*1997 Topical Meeting on Photorefractive Mat., Effects and Devices Japan*, p.295]
- [26] K. Kitamura, Y. Furukawa, S. Tanaka, T. Yamaji, H. Hatano [*Proc. SPIE (USA)* vol.3291 (1998) p.115]

2.4 Epitaxial growth of LiNbO₃

C.W. Pitt

This Datareview appeared in *Properties of Lithium Niobate* (INSPEC, IEE, London, UK, 1989) and is reproduced here for the reader's convenience.

There have been several reasons suggested for attempting the growth of epitaxial layers of lithium niobate. One has been the expectation of improved optical properties. For example, applications in integrated optics have required the introduction of dopants into the crystal by diffusion in order to increase the refractive index to form an optical waveguide. Some dopants, for example titanium, decrease the optical damage threshold, and increase the optical absorption and scattering of the waveguide, especially in the visible spectrum. Operation of integrated optical devices at infrared wavelengths, and the use of proton exchange have tended to mitigate optical damage. Nevertheless homoepitaxial layers in which the refractive index may be controlled by oxygen stoichiometry control [1], or in which co-dopants such as neodymium or chromium [2] may readily be incorporated, or of improved crystallinity, still appear attractive for some optical applications.

Heteroepitaxy of lithium niobate on substrates such as sapphire [1,2,6,10], silicon [3], or lithium tantalate [4,5,9] would appear to offer advantages for optical devices in which, for example, improved access to the electro-optic properties may be arranged. Acoustic wave devices employing either bulk or surface waves might similarly benefit; the former from thin deposited piezoelectric layers rather than mechanically thinned or etched bulk material, and the latter from more efficient electrode configurations in SAW devices. However, there is little evidence in the literature that such SAW devices have been successfully attempted; most reported work has been directed at integrated optics applications.

Epitaxy has been achieved by a number of processes - recently using molecular beam deposition (MBE) [1], RF sputtering [2,6] and solid-phase implantation/thermal annealing [7]. Rather earlier attempts were made using melt-phase growth (MPE) [4,5], indiffusion regrowth [8], liquid-phase growth (LPE) [9], sputtering [10] and vapour-phase epitaxy [11].

Melt-phase epitaxy [4,5], the first process to be attempted, utilised the higher melting point of lithium tantalate compared with that of lithium niobate, and the relatively small lattice mismatch (0.08% for a(H) and 0.57% for c(H)). Layers have been grown on x, y and z-plane lithium tantalate by covering the surface of prepared substrates with lithium niobate powder produced from congruent grown crystal (Li/Nb = 0.942), heating in a furnace to 1300°C and cooling at 20°C/hour past 1250°C (MP of lithium niobate). The layers, from 3 to 6 microns, were grown with refractive indices of $n_o = 2.288$ and $n_e = 2.207$ at helium-neon laser wavelength. The refractive index profile was graded from the surface of the epilayer to the interface, giving a value for $dn = 0.07$. Optical waveguiding losses in the layers were not measured, but appeared to be ~10 dB/cm, mainly scattering either from surface roughness (as grown) or from point defects in the epilayer (after polishing the surface); x-plane growth produced cracks along the (102) planes.

Heteroepitaxial layers of graded niobate-on-tantalate were achieved without melting, by use of solid-state diffusion in the indiffusion regrowth process [9]. Niobium metal thin films (15 to 150 nm thick) were evaporated onto lithium tantalate substrates (x-z and y-z planes) and heated in air to 1100°C for times up to six hours. During this period some niobium replaced tantalum in the lattice giving $\text{LiNb}_x\text{Ta}_{1-x}\text{O}_3$ where x was estimated to be up to 0.35 at the surface; the corresponding surface refractive index change was measured as approximately +1% at helium-neon laser wavelength. Measurement of the optical waveguides formed by this technique gave an effective refractive index for the TE mode of 2.188; this compares with the substrate index of 2.179 and a quoted value for

2.4 Epitaxial growth of LiNbO_3

lithium niobate of 2.237, again at the same laser wavelength. Losses in the guiding layers were 1 dB/cm at 633 nm, 4.3 dB/cm at 559 nm and 6.7 dB/cm at 485 nm. The surface layer was used to fabricate an electro-optic modulator after re-poling; for propagation of light in the x-z plane and with a transverse electric field, the electro-optic coefficient appeared to be approximately as expected from the $\text{Li}(\text{TaNb})\text{O}_3$ solid mixed layer.

The vapour transport technique [11] appeared in 1974. One end of an evacuated (10^{-5} mm Hg) sealed quartz tube containing lithium niobate powder (and sulphur as a transport agent) was heated to 1000°C; the deposition end of the tube was maintained at 910°C. Heating was sustained for seven days; small ($0.5 \times 0.5 \times 0.5$ mm) rhombohedral crystals covered by (102) plane faces were deposited. When optically flat plates of lithium niobate in (102) and (010) orientations were placed in the cooler position, epitaxial layers from 2 to 10 microns were deposited. No optical evaluation of the layers was reported.

LPE growth of lithium niobate on tantalate was reported [9] by Miyazawa et al in 1975. The melt consisted of 50 mol% of Li_2O , 40 mol% V_2O_5 as fluxing agent, and 10 mol% Nb_2O_5 ; this was heated to 1100°C, then cooled to 850°C, at which point substrates of c- LiTaO_3 were dipped. Uniform refractive index epitaxial layers of lithium niobate, ~3 microns thick, were produced with indices of $n_o = 2.2884$ and $n_e = 2.1914$ (633 nm). Similarly by waveguiding measurement, the losses were determined at TM_o mode = 5 dB/cm and TR_o mode = 11 dB/cm.

The earliest report of sputter deposited epitaxial layers was from Takada et al [10] and was contemporary with much of the work on other epitaxy techniques. A 9 cm sputtering target was made by sintering lithium enriched lithium niobate powder; this was energised with 50 W RF power in an atmosphere of 60% Ar/40% O_2 at 2×10^{-2} torr. LiNbO_3 was deposited onto c-plate sapphire held at 600°C, at the rate of 250 Å per hour. A layer of thickness 1800 Å waveguided helium-neon laser light giving the film indices as $n_o = 2.324 \pm 0.02$ and $n_e = 2.18 \pm 0.04$ and loss of 9 dB/cm; the appearance of the streak of guided light indicated strong scattering. The layer thinness precluded examination of the epitaxial nature of the film. Later use of this technique, with similar process parameters, by Meek, Holland and Townsend [6] again produced layers of lithium-niobium oxide with refractive indices similar to those of stoichiometric lithium niobate. However, the authors are cautious about claiming true epitaxy for the layers; they suggest that the optical refractive index values could also be attributed to oriented polycrystalline film. In a 1987 paper [2] Kanata, Kobayashi and Kubota report the use of RF magnetron sputtering (30 mm target of lithium niobate enriched with 25 mol% di-lithium oxide, 100 W RF power input, plasma gas 50% Ar/50% O_2 , 500°C substrate temperature), claiming confirmation of epitaxial layers on both c- and a-plane sapphire by X-ray diffraction and Raman scattering. Chromium and neodymium were incorporated into grown layers as dopants and multiple lithium niobate/lithium tantalate layers were grown without interdiffusion. The latter layers were used to demonstrate second harmonic generation. The ordinary-ray refractive index values for the epitaxial layers (measured by Abeles method at a wavelength of 633 nm) was quoted as: lithium niobate = 2.288, lithium niobate with 10 wt% Cr^{+++} = 2.334, lithium niobate with 10 wt% Nd^{+++} = 2.303.

Molecular beam epitaxy [1,3] has been used to grow homoepitaxial layers (z and y cut), heterolayers on sapphire (z-plane) and tantalate (z cut), and oriented polycrystalline layers on silicon (111). The process followed the principles of MBE developed for III-V semiconductors and other materials; the layer was deposited onto a substrate carefully prepared by ion etching and thermal annealing to give an atomically clean (fractional monolayer contamination) and single-crystal-structured surface (confirmed by RHEED and SIMS) in an ultra-high vacuum environment. The lithium and niobium beams were produced by electron-beam guns and the oxygen beam was supplied by a multi-microchannel effusion source creating a beam of molecular oxygen, or by an oxygen radical source. A mass analyser enabled the three beams to be set to give the Li/Nb/O ratio of 1/1/3; the beams were directed at the substrate held at 560 - 680°C. Composition of the layers was examined by AES and IR spectrometry and the structure was determined by X-ray diffraction, transmission electron diffraction

2.4 Epitaxial growth of LiNbO_3

and optical waveguiding. Films grown on sapphire exhibited a cubic structure rather than the rhombohedral structure of layers grown on niobate. Although most layers were oxygen deficient, giving a slightly higher refractive index than bulk material, optical waveguiding was only achieved in the non-birefringent layers grown on sapphire. Refractive index values for the cubic phase material were 2.20 - 2.30 at 633 nm and the optical loss was 16 dB/cm.

Graded index layers of $\text{Li}(\text{NbTi})\text{O}_3$ have been grown [7] by implanting rather large doses of titanium (doses from 1.2 to 2.5×10^{17} atoms/cm² at energies of 360 and 540 kV, substrate held at liquid nitrogen temperature) into lithium niobate and then performing thermal annealing and redistribution (1000°C for one hour). The optical waveguides produced by this technique had a half-width half-maximum profile of one micron and a surface concentration of 12%, implying very much narrower optical mode confinement than titanium diffused structures. The refractive index increase in the y-propagation direction was +0.030. The best stripe guide losses reported were 1 dB/cm. Single crystal regrowth in x-cut niobate was confirmed by ion scattering/channelling spectra in the solid-state regrowth region.

REFERENCES

- [1] R.A. Betts, C.W. Pitt [*Electron. Lett. (UK)* vol.21 no.21 (1985) p.960-2]
- [2] T. Kanata, Y. Kobayashi, K. Kubota [*J. Appl. Phys. (USA)* vol.62 no.7 (1987) p.2989-93]
- [3] M. Petrucci, C.W. Pitt, H. Robinson [*Proc. Electrochem. Soc. (USA)* vol.88-8 (1988) p.191-204]
- [4] P.K. Tien, S. Riva-Sanseverino, R.J. Martin, A.A. Ballman, H. Brown [*Appl. Phys. Lett. (USA)* vol.24 no.10 (1974) p.503-6]
- [5] S. Miyazawa [*Appl. Phys. Lett. (USA)* vol.23 no.4 (1973) p.198-200]
- [6] P.R. Meek, L. Holland, P.D. Townsend [*Thin Solid Films (Switzerland)* vol.141 no.2 (1986) p.251-60]
- [7] Ch. Buchal, P.R. Ashley, B.R. Appleton [*J. Mater. Res. (USA)* vol.2 no.2 (1987) p.222-30]
- [8] J.M. Hammer, W. Philips [*Appl. Phys. Lett. (USA)* vol.24 no.11 (1974) p.545-7]
- [9] S. Miyazawa, S. Fushimi, S. Kondo [*Appl. Phys. Lett. (USA)* vol.26 no.1 (1975) p.8-10]
- [10] S. Takada, M. Ohnishi, H. Hayakawa, N. Mikoshiba [*Appl. Phys. Lett. (USA)* vol.24 no.10 (1974) p.490-2]
- [11] S. Fushimi, K. Sugii [*Jpn. J. Appl. Phys. (Japan)* vol.13 no.11 (1974) p.1895-6]

CHAPTER 3

STRUCTURE OF MODIFIED MATERIAL

- 3.1 Structural phase diagram of proton-exchanged waveguides in LiNbO₃
- 3.2 Composition of different crystal phases in proton-exchanged waveguides in LiNbO₃

3.1 Structural phase diagram of proton-exchanged waveguides in LiNbO₃

Yu.N. Korkishko and V.A. Fedorov

July 1999

A INTRODUCTION

We present the structural phase diagram of proton-exchanged LiNbO₃ optical waveguides [1], where the surface index increase Δn_e is plotted as a function of the strain normal to the substrate surface, ϵ''_{33} . We present these diagrams for the different useful orientations of LiNbO₃ and give some general comments and a brief description of different H_xLi_{1-x}NbO₃ crystal phases, generated by proton exchange.

Rice and Jackel [2,3] described in detail the H_xLi_{1-x}NbO₃ powder solid solutions. X-ray diffraction measurements for these materials showed complex structural behaviour, with two distinct rhombohedral phases and one monoclinic phase. The relationships between lattice parameters and proton concentration were obtained for the α - and β -H_xLi_{1-x}NbO₃ stress-free (powder) phases [1,2].

However, the results obtained for powders cannot be applied directly to the single crystalline waveguides. Indeed, the strains induced by the substrate/guide interface substantially modify the proton concentration and the crystal structure of the exchanged layer (FIGURE 1). Our work [4-12] allowed identification of the different crystallographic phases H_xLi_{1-x}NbO₃ which can be realised in the proton exchanged layers, considering that there is a phase jump on gradually varying the proton concentration in the exchange layer, causing a sudden variation of the cell parameters, even if the crystallographic system is conserved. Most interesting for waveguide fabrication is that most of these discontinuities and phase jumps can already be seen on a rather simple diagram, which we called the structural phase diagram [9], where the surface index increase Δn_e is plotted as a function of the strain normal to the substrate surface, ϵ''_{33} . The methods used to determine refractive index and strains were reported in [9] and [11].

B EXPERIMENTAL RESULTS

In most cases we observed that PE LiNbO₃ waveguides on X- and Z-cuts have only one non-zero component ϵ''_{33} of deformation tensor in the 'technological' coordinate system of axes x₁"x₂"x₃" attached to the substrate orientation (where the axis x₃" is normal to the plane of the interface and the planar orthogonal axes x₁" and x₂" define this plane and are chosen arbitrarily to form together with x₃" a right-handed orthogonal set of axes (FIGURE 1)), while waveguides on Y- and rotated Y-cuts have only two non-zero strain components ϵ''_{23} and ϵ''_{33} in this coordinate system.

FIGURE 2 shows the structural phase diagram for the Z-cut and X-cut substrates. The seven regions on Z-cut LiNbO₃, corresponding to the seven crystal phases α , κ_1 , κ_2 , β_1 , β_2 , β_3 and β_4 -H_xLi_{1-x}NbO₃, can be clearly recognised. The phase transitions are characterised by a discontinuity of either the index variation (Δn_e), or/and the deformations along axis x₃" perpendicular to the surface plane (ϵ''_{33}).

3.1 Structural phase diagram of proton-exchanged waveguides in LiNbO_3

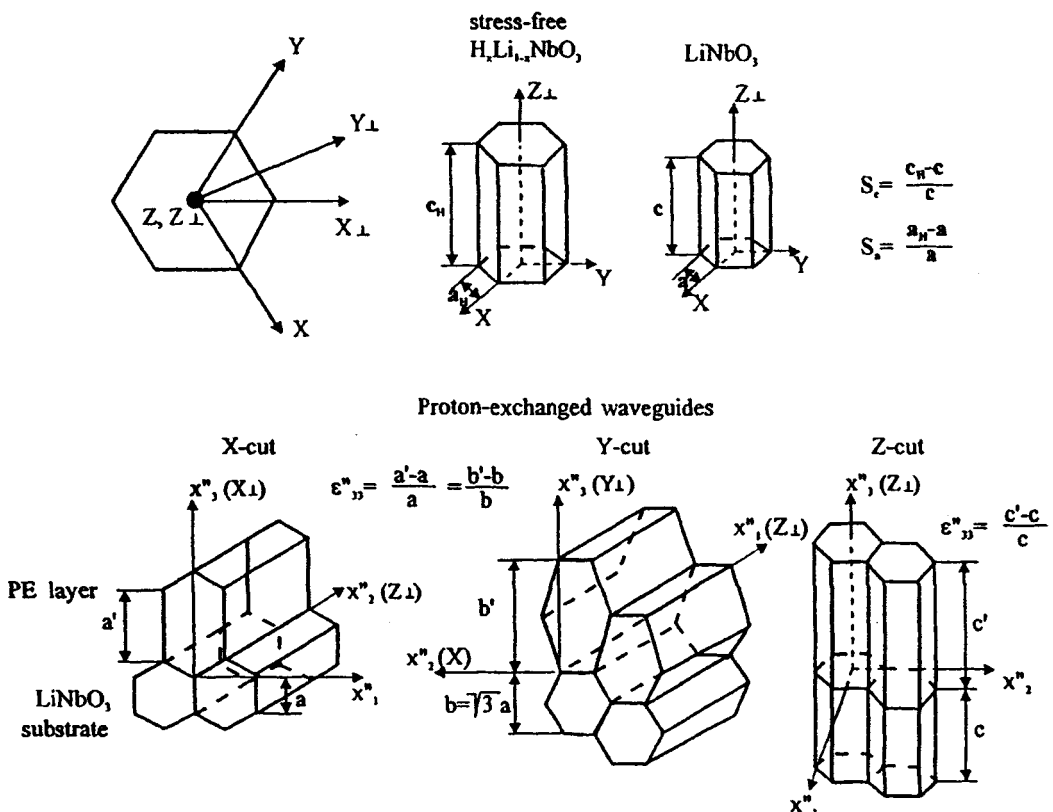


FIGURE 1 Schematic of the cell expansion in $\text{H}_x\text{Li}_{1-x}\text{NbO}_3$ powders and in strained $\text{H}_x\text{Li}_{1-x}\text{NbO}_3$ solid solutions formed at the surface of X-, Y- and Z-cut LiNbO_3 by proton exchange.

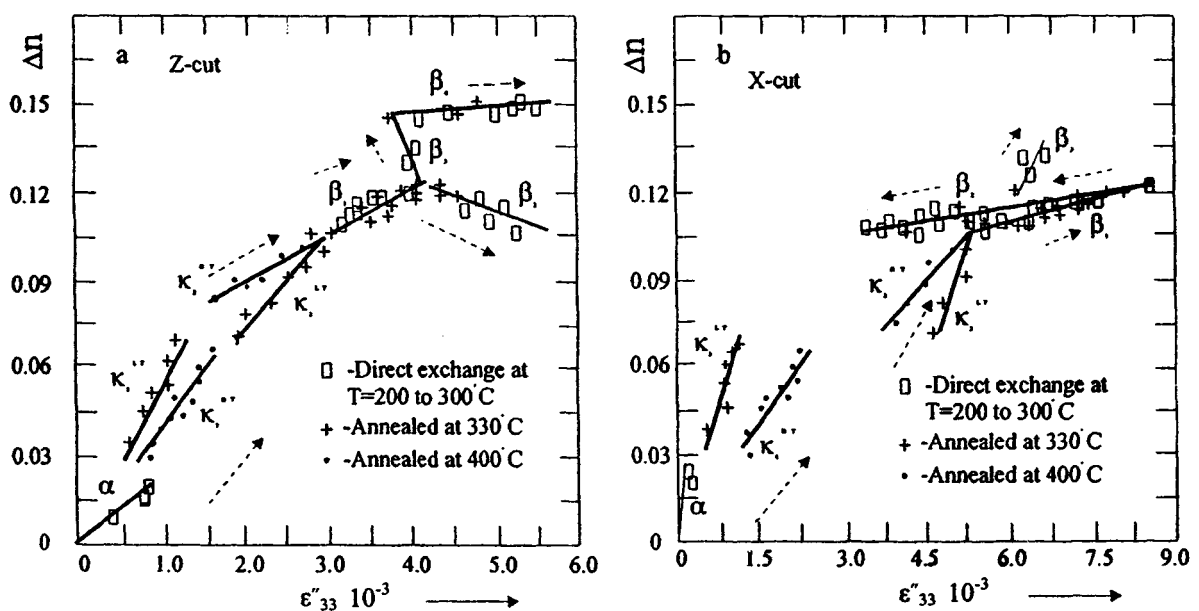


FIGURE 2 Structural phase diagrams of $\text{H}_x\text{Li}_{1-x}\text{NbO}_3$ on Z-cut (a) and X-cut (b) substrates. They give the dependence of the extraordinary index variation Δn_e measured at $\lambda = 633 \text{ nm}$ on the surface value of deformation ϵ''_{33} normal to the surface plane. The arrows show the directions in which proton concentration increases.

3.1 Structural phase diagram of proton-exchanged waveguides in LiNbO_3

On the X-cut substrates one can observe the same phases. However, the β_4 phase can exist only as a very thin layer. The X-cut LiNbO_3 exhibits surface damage when immersed for prolonged periods in high acidity melts (e.g. pyrophosphoric acid). The β_4 phase appearing in this way can exist as a single crystalline layer ($h < 0.2 \mu\text{m}$) only for the short period of PE. The Δn_e of this phase has not been measured, as a layer thick enough to be optically characterised cannot be formed on the X-cut.

A very thin layer of the β_4 phase with deformations $\varepsilon''_{33} > 10 \times 10^{-3}$ was also observed on X-ray rocking curves from samples fabricated in molten benzoic acid at temperatures below $\sim 250^\circ\text{C}$. However, this layer gives a negligible effect in the common refractive index profile due to its small thickness. Probably, this layer was detected by Ito and Kawamoto [13] with a special diffractometer.

The structural phase diagram for Y-cut LiNbO_3 is similar to the diagram for X-cut except for the regions where waveguides cannot be obtained due to surface damage. Only two phases, β_1 and α , with sufficient depth to be characterised both optically and structurally can be realised by direct exchange on Y-cut substrates. Subsequent increasing of proton concentration in the melt leads to surface damage. However, single-mode PE waveguides on Y-cut LiNbO_3 ($\lambda = 633 \text{ nm}$) can be made without producing surface damage by using very short exchange times in benzoic acid with subsequent annealing [14].

Therefore, the structural phase diagrams presented in FIGURE 2 reflect only the phases which are able to be realised as relatively thick layers in which refractive index can be measured. Depending on fabrication conditions very thin layers of phases with higher proton concentration can also be realised on the surface of PE LiNbO_3 waveguides.

TABLE 1 shows the typical fabrication conditions for different $\text{H}_x\text{Li}_{1-x}\text{NbO}_3$ phases. As shown in TABLE 1, one goes from the β_1 to the β_4 phase by increasing the acidity of the melt. We see that by varying the proton concentration in the melt, it is possible to obtain by low temperature direct proton exchange up to five different crystalline phases (α and β_1 to β_4) on Z-cut, up to four phases (α and β_1 to β_3) on X-cut and only two phases (α and β_1) on Y-cut LiNbO_3 substrates.

TABLE 1 Direct proton exchange fabrication conditions to obtain different $\text{H}_x\text{Li}_{1-x}\text{NbO}_3$ phases.

Phase	LiNbO_3 cut	LB + LB (300°C)	KHSO ₄ in glycerin (220°C)	Other PE sources
α	X, Y, Z	>2.5%		stearic acid + lithium stearate (>0.3%)
β_1	X, Y, Z	1 to 2.5%	0 to 1 g/l	stearic, palmetic, oleic, octanolic, toluic acids
β_2	X, Z	0%	2 to 4 g/l	miristic acid
β_3	X, Z		8 to 15 g/l	lauric acid
β_4	Z		>20 g/l	phosphoric, pyrophosphoric acids, ammonium dihydropophosphate, cinnamic acid, potassium hydrosulphate, sulphuric acid
κ_2^{HT}	X, Y, Z	-	-	$\text{ZnSO}_4\text{-K}_2\text{SO}_4\text{-Na}_2\text{SO}_4\text{-KHSO}_4$ ($C_{\text{KHSO}_4} = 0.04$ to 0.07 mol/kg)
κ_1^{HT}	X, Y, Z	-	-	$\text{ZnSO}_4\text{-K}_2\text{SO}_4\text{-Na}_2\text{SO}_4\text{-KHSO}_4$ ($C_{\text{KHSO}_4} = 0.01$ to 0.04 mol/kg)
η	(0̄14)	0%	>2 g/l	phosphoric, pyrophosphoric acids, ammonium dihydropophosphate, cinnamic acid

The β_i and α phases can be fabricated by direct proton exchange or by annealing of $\text{H}_x\text{Li}_{1-x}\text{NbO}_3$ phases with higher proton concentration, as follows: $\beta_4 \rightarrow \beta_3 \rightarrow \beta_2 \rightarrow \beta_1 \rightarrow \alpha$. The κ_i phases, characterised by Δn_e from 0.025 to 0.08, can be formed by post-exchange annealing of the β_i phases

3.1 Structural phase diagram of proton-exchanged waveguides in LiNbO_3

only. Annealing is an important fabrication parameter in the fabrication of PE waveguides. Actually, most of the published results were obtained using heavily annealed PE waveguides (APE [15]), whose index profiles indicate that they are in the α -phase. The corresponding waveguides are very low loss and characterised by graded refractive index profiles with $\Delta n_e < 0.03$. However, the APE process, as was reported recently [16-18], can reduce or even destroy the non-linear coefficients and the periodic domain orientation in a portion of the waveguiding structure.

The α -phase generated in PE LiNbO_3 waveguides, which corresponds to the α -phase identified by Rice and Jackel [2] and Rice [3], can be obtained using low acidic bath such as benzoic acid (BA) melts at temperatures from 200 to 350°C, containing from 2.5 to 3.5 mol % of lithium benzoate (LB). This value depends on the temperature of PE [19]. This process has recently been called soft proton exchange (SPE) [20]. The main advantage of the SPE process is that it indicates no phase transitions. This allows preservation of both the non-linear coefficient and the domain orientation while fully benefiting from the power confinement associated with the guided wave configuration. The SPE processes were performed in benzoic acid diluted by lithium benzoate. The proton-lithium interdiffusion coefficient in the α -phase is some orders of magnitude smaller than that for the β_1 phases, and one has to use very long processes to make single mode waveguides at 1.55 μm wavelength (three days at 300°C [20]). Therefore, it is important to increase the intensity of the SPE process. This intensity can be increased by increasing the exchange temperature; however the boiling point of benzoic acid is only 249°C, and its high vapour pressure limits the temperature that can be used for SPE. By choosing an appropriate proton exchange source with higher melting point and smaller vapour pressure one can increase the temperature of the PE process, and therefore increase the interdiffusion coefficient in the α -phase. What would be more convenient is a source with higher boiling point and lower vapour pressure. Possible candidates include stearic acid (boiling point 374°C), palmetic acid (360°C), oleic acid (369°C) and erucic acid (358°C). Recently, we proposed the high-temperature proton exchange process (HTPE) in a new melt, a mixture of stearic acid and lithium stearate [21].

As an alternative, the melt for HTPE could be a sulphate mixture with a relatively low acidity, realised by adding a small amount of KHSO_4 , the so-called graded proton exchange (GPE) method [22]. However, the relatively high melting temperature for the $\text{K}_2\text{SO}_4\text{-Na}_2\text{SO}_4\text{-ZnSO}_4$ eutectic (384°C) makes it inconvenient to use for practical waveguide designs.

The three phases β_1 to β_3 , produced by low temperature direct PE, are associated with a step index presenting an extraordinary index increase higher than 0.09. However, waveguides containing the β_4 phase exhibit graded refractive index profiles in the region from $\Delta n_e = 0.15$ to 0.12.

Note, that exchanged layers in different crystalline phases can present similar index profiles and differ considerably when other physical properties are taken into account.

Only the β_1 phase can be found alone on top of the structure; the exchanged layer is then homogeneous, the rocking curves present a clear narrow peak for the exchanged layer and the index profile has a step-like form. The β_2 and β_3 phases can be found only in combination with the β_1 phase, organised as a sublayer, the rocking curves presenting two peaks. The β_4 phase can be found only in combination with two phases β_3 and β_1 with lower proton concentrations. The exchanged layer is then stratified in two or three single phase layers presenting two or three different indices, which has been verified by slowly removing the surface layer by successive polishing.

The propagation losses, which are higher than 1 dB/cm when the β_2 phase is present, are of the order 0.5 dB/cm only in the β_1 phase. One has also to expect very different electro-optic and non-linear properties of these waveguides [11,18]. This possibility of having waveguides presenting the same refractive index profile but with very different structural properties is responsible, we think, for the

3.1 Structural phase diagram of proton-exchanged waveguides in LiNbO_3

great variety of discussions concerning PE waveguides one can find in the literature of the past ten years [11].

It is possible by annealing either to involve protons in a given phase or to go from a high concentration phase to a low concentration phase. For example, starting in the β_2 phase one can reach the β_1 phase. By further annealing at temperatures up to 330°C we were able to observe two layers in the crystallographic phases we call here κ_1^{LT} and κ_2^{LT} , phases (low temperature modifications) which cannot be observed by low temperature ($T_{\text{PE}} < 350^\circ\text{C}$) direct proton exchange. By annealing at temperatures above 380°C, the high temperature modification of these phases, that we call κ_1^{HT} and κ_2^{HT} , were observed. The κ_2 phases can be found only in combination with the κ_1 phases, the X-ray rocking curves presenting two peaks with more or less signal in a graded intermediate area. In contrast to the κ_1 phase, where for similar $\Delta n_e \varepsilon''_{33} (\kappa_1^{\text{LT}}) < \varepsilon''_{33} (\kappa_1^{\text{HT}})$, the low temperature κ_2 phase is characterised by larger deformations where $\varepsilon''_{33} (\kappa_2^{\text{LT}}) > \varepsilon''_{33} (\kappa_2^{\text{HT}})$.

It should be noted that the $\kappa_1^{\text{LT}} \rightarrow \kappa_1^{\text{HT}}$ phase transition is not too sharp, and in waveguides annealed at intermediate temperatures from 340 to 380°C the deformations increase continuously [9].

Early on we observed the evaporation of Li_2O from PE LiNbO_3 waveguides in high temperature processing ($T_A > 400^\circ\text{C}$) [23]. As a result, the lithium deficient monoclinic phase LiNb_3O_8 forms when the refractive index change in the initial PE region achieves the value $\Delta n_e = 0.037$. In this case the mixed ($\text{LiNb}_3\text{O}_8 + \kappa_1^{\text{HT}}\text{-H}_x\text{Li}_{1-x}\text{NbO}_3$) phase is realised. Long treatment at temperatures above 400°C leads to surface damage of samples [23,24]. However, in the region with $\Delta n_e > 0.037$ formation of the LiNb_3O_8 phase has not been observed even for waveguides annealed at $T > 400^\circ\text{C}$ [23]. We never observed this phase in APE samples annealed up to $\Delta n_e = 0.005$ at temperatures lower than 340°C. These results can explain the difference between κ_i^{LT} and κ_i^{HT} phases. Indeed, because of Li_2O evaporation at high temperature the stoichiometry of the surface region changes: the v in the stoichiometric formula $\{(\text{Li}_2\text{O})_{1-x}(\text{H}_2\text{O})_x\}_v(\text{Nb}_2\text{O}_5)_{1-v}$ decreases. Therefore, the main reason for differences between the κ_i^{LT} and κ_i^{HT} phases is, probably, the difference in their stoichiometry: $v (\kappa_i^{\text{LT}}) > v (\kappa_i^{\text{HT}})$.

Probably, stresses appearing due to lattice parameter mismatch lead to dividing of the equilibrium β phase reported in [2,3] into four different phases (FIGURE 3). The single crystalline phases κ_1 and κ_2 are realised in the proton concentration interval corresponding to an $(\alpha + \beta)$ phase mixture in the stress-free state (powders). Waveguides containing the κ_1 and κ_2 phases are characterised by high losses (more than 10 dB/cm [25]).

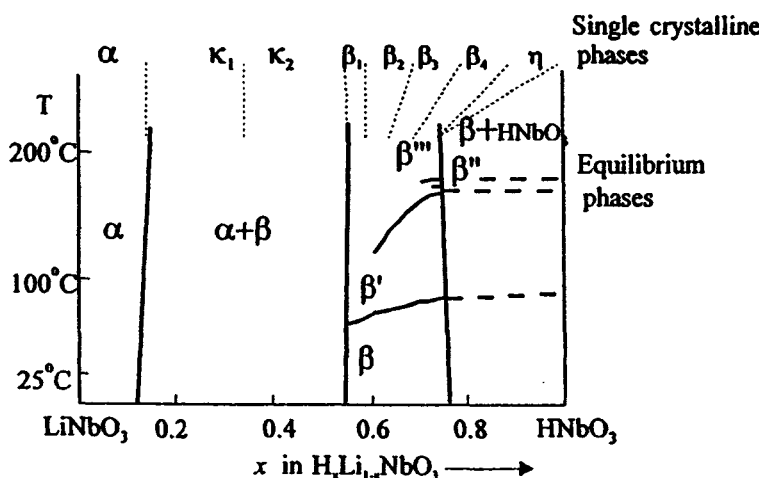


FIGURE 3 Equilibrium [3] and stressed phase diagrams of $\text{H}_x\text{Li}_{1-x}\text{NbO}_3$.

3.1 Structural phase diagram of proton-exchanged waveguides in LiNbO_3

Finally, proton exchange is a very simple and attractive technique for making optical waveguides in LiNbO_3 , but varying the fabrication parameters leads to very different waveguides that are impossible to identify just by measuring the index profile. Knowledge of $\text{H}_x\text{Li}_{1-x}\text{NbO}_3$ single crystal phase diagrams for the popular crystal cuts enables one to predict the properties of the waveguides and to optimise the fabrication process.

C CONCLUSION

This Datareview has summarised the structural phase diagrams of proton-exchanged waveguides made in LiNbO_3 . Several different orientations are discussed. These phase diagrams can help in predicting waveguide properties and in optimising fabrication processes.

ACKNOWLEDGEMENTS

This work was supported by the Russian Foundation of Basic Research under grants 96-15-96978 and 99-15-96110 for Young Doctors of Sciences and grant 96-15-98220 for Leading Science Schools and by the «Russian Universities - Basic Researches» program under grant 248-1998. This investigation is also part of the project A-0102 supported by the «Integration» Foundation (Russia).

REFERENCES

- [1] J.L. Jackel, C.E. Rice, J.J. Veselka [*Appl. Phys. Lett. (USA)* vol.41 (1992) p.607-8]
- [2] C.E. Rice, J.L. Jackel [*Mater. Res. Bull. (USA)* vol.19 (1984) p.591]
- [3] C.E. Rice [*J. Solid State Chem. (USA)* vol.64 (1986) p.188]
- [4] V.A. Fedorov, Yu.N. Korkishko [*Proc. SPIE (USA)* vol.2291 (1994) p.243]
- [5] V.A. Fedorov, Yu.N. Korkishko [*Proc. SPIE (USA)* vol.2401 (1995) p.216]
- [6] Yu.N. Korkishko, V.A. Fedorov [*Opt. Mater. (Netherlands)* vol.5 (1996) p.175]
- [7] Yu.N. Korkishko, V.A. Fedorov, M.P. De Micheli, P. Baldi, K. El Hadi, A. Leycuras [*Appl. Opt. (USA)* vol.35 (1996) p.7060]
- [8] M.P. De Micheli, D.N. Ostrowsky, Yu.N. Korkishko, P. Bassi [in *Insulating Materials for Optoelectronics* Ed. F. Agullo-Lopez (World Scientific, Singapore, 1995) p.329]
- [9] Yu.N. Korkishko, V.A. Fedorov [*IEEE J. Sel. Top. Quantum Electron. (USA)* vol.2 (1996) p.187]
- [10] Yu.N. Korkishko, V.A. Fedorov [*J. Appl. Phys. (USA)* vol.82 (1997) p.171]
- [11] Yu.N. Korkishko, V.A. Fedorov [*Ion exchange in single crystals for integrated optics and optoelectronics* (Cambridge International Science Publishing, Cambridge, UK, 1999)]
- [12] Yu.N. Korkishko, V.A. Fedorov, S.M. Kostritskii [*J. Appl. Phys. (USA)* vol.84 (1998) p.2411]
- [13] K. Ito, K. Kawamoto [*Jpn. J. Appl. Phys. (Japan)* vol.31 (1992) p.3882]
- [14] M. Goodwin, C. Stewart [*Electron. Lett. (UK)* vol.19 (1983) p.223]
- [15] P.G. Suchoski, T.K. Findakly, F.J. Leonberger [*Opt. Lett. (USA)* vol.13 (1988) p.1050]
- [16] K. El Hadi et al [*J. Opt. Soc. Am. B (USA)* vol.14 (1997) p.3197]
- [17] Yu.N. Korkishko, V.A. Fedorov, F. Laurell [*Proc. 9th European Conference on Integrated Optics Italy* (1999) p.127]
- [18] Yu.N. Korkishko, V.A. Fedorov, F. Laurell [*IEEE J. Sel. Top. Quantum Electron. (USA)* submitted 1999]
- [19] M.J. Li, M.P. De Micheli, D.N. Ostrowsky, M. Papuchon [*J. Opt. (France)* vol.18 (1987) p.139]
- [20] L. Chanvillard et al [*Proc. 9th European Conference on Integrated Optics Italy* (1999) p.513]

3.1 Structural phase diagram of proton-exchanged waveguides in LiNbO₃

- [21] Yu.N. Korkishko, V.A. Fedorov, O.Yu. Feoktistova [*J. Lightwave Technol. (USA)* vol.18 no.4 (2000) p.562-8]
- [22] V.A. Ganshin, Yu.N. Korkishko [*Phys. Status Solidi A (Germany)* vol.119 (1990) p.11]
- [23] V.A. Ganshin, Yu.N. Korkishko [*Opt. Commun. (Netherlands)* vol.86 (1991) p.523]
- [24] V.A. Ganshin, Yu.N. Korkishko, V.Z. Petrova [*Sov. Phys.-Tech. Phys. (USA)* vol.30 (1985) p.1313]
- [25] S. Chen, P. Baldi, M.P. De Micheli, D.B. Ostrowsky, A. Leycuras, P. Bassi [*J. Lightwave Technol. (USA)* vol.12 (1994) p.862]

3.2 Composition of different crystal phases in proton-exchanged waveguides in LiNbO₃

Yu.N. Korkishko and V.A. Fedorov

July 1999

A INTRODUCTION

We present measurements of the dependence of the extraordinary refractive index increase, Δn_e , on hydrogen concentration for PE LiNbO₃ waveguides. A correlation between the crystal structure, hydrogen concentration and ordinary and extraordinary refractive indices has been experimentally determined that allows us to explain some optical phenomena observed and to predict the characteristics of the great variety of proton exchanged waveguides.

The first careful measurement of the dependence of extraordinary refractive index increase, Δn_e , on hydrogen concentration in PE LiNbO₃ waveguides, using the elastic recoil detection (ERD) method and the prism coupling technique, was performed by Howerton et al [1]. Also, many attempts have been made to estimate the proton concentration in PE LiNbO₃ waveguides using different methods of analysis. The published results are summarised in TABLE 1. Although the majority of researchers reported that the dependence of Δn_e on hydrogen concentration is non-linear, the values of proton concentration obtained even for PE LiNbO₃ samples prepared under similar conditions are quite different in different studies. This is not surprising, as the existence of various phases in PE LiNbO₃ waveguides has not been taken into account. In the case of PE, the strong change in the physico-chemical properties induced by the appearance of a variety of crystalline phases makes the matrix effects prevail, and the profiles obtained consequently quite unreliable (for example, an increase of the Nb signal was observed). This could explain the large discrepancy between results obtained by different researchers.

In [15] we have examined the refractive index profiles and the areas under the refractive index increment distribution, $\Delta n_e(z)$, of a series of PE LiNbO₃ waveguides, as-exchanged, as well as after furnace annealing, and demonstrated a method of determination of hydrogen concentration in different H_xLi_{1-x}NbO₃ phases, generated in PE LiNbO₃ waveguides.

B PROCEDURE

The method is based on measuring the area under the refractive index profile curve. The area under the evolving refractive index curves does not remain constant during annealing. Various research groups (see, for example [1,16-18]) have used this area change as a qualitative criterion for assessing the non-linearity of the relationship between the hydrogen concentration and extraordinary refractive index in PE LiNbO₃ waveguides. A very large non-linearity has been observed for waveguides containing initially the β_2 and the β_4 phases. When the exchange layer is in the β_2 , β_3 or β_4 phase, the -O-H absorption spectra exhibit not only one sharp peak polarised perpendicular to the c axis, but also a broad unpolarised absorption band centred at 3240 cm⁻¹, associated with interstitial hydrogen. The area under the index profile does show an initial increase with annealing due to protons moving from optically inactive interstitial positions to active substitutional sites [4,5].

3.2 Composition of different crystal phases in proton-exchanged waveguides in LiNbO_3

TABLE 1 Proton concentration for the different $\text{H}_x\text{Li}_{1-x}\text{NbO}_3$ phases.

Cut	PE source	Annealing temperature	$\text{H}_x\text{Li}_{1-x}\text{NbO}_3$ phase	Δn_e	x	Method	Ref
Z	BA	-	β_2	-	0.4 - 0.5	SIMS	[2]
		275°C	β_1	0.11	0.32		
X	BA	-	β_2	0.12	0.85 ^(a)	SIMS	[3]
Z	BA	400°C	κ_2^{HT} to κ_1^{HT}	-	<0.22	SIMS	[4]
Z	BA	-	β_2	-	0.3	SIMS	[5]
		400°C	β_1 κ_1^{HT}		0.26 <0.2		
Z	BA	275°C 400°C	β_1 κ_1^{HT}	0.11 0.047	0.32 0.14	SIMS	[6]
Z, X	BA	400°C	β_2	0.11	0.65 - 0.75	NR	[7]
			β_1 κ_1^{HT}	0.105	0.6		
			κ_1^{HT}	0.07	0.4		
			κ_1^{HT}	0.02	0.15		
Z, X	BA	-	β_2	-	0.65 - 0.75	NR	[8]
Z	BA	-	β_2	-	0.75	AAS	[9]
Z	BA	-	β_2	-	0.33	AAS	[10]
X	BA + 1% LB	300°C 320°C 340°C 400°C	κ_2^{LT} κ_1^{LT} α or κ_1^{LT} κ_1^{HT}	0.081 0.039 0.039 0.0035	0.315 0.315 0.275 0.020	ERD	[11]
Z	BA	300 to 370°C	α $\kappa_1^{\text{LT}} + \kappa_1^{\text{HT}}$ $\kappa_2^{\text{LT}} + \kappa_2^{\text{HT}}$ β_1 β_2	0 - 0.02 0.02 - 0.075 0.075 - 0.105 ~0.11 ~0.11	0 - 0.12 0.12 - 0.4 0.4 - 0.55 0.55 - 0.65 0.65 - 0.8		
Z	PA	- 200°C 260°C 280°C 300°C 320°C 340°C 360°C	β_4 β_4 or β_3 β_1 β_1 β_1 κ_2^{LT} $\kappa_2^{\text{LT}} + \kappa_2^{\text{HT}}$	0.132 0.124 0.114 0.113 0.110 0.104 0.099 0.092	0.68 0.68 0.65 0.64 0.55 0.55 0.51 0.41	Raman	[12]
Z	PA	- 250°C	β_4 β_3 or β_1	0.148 0.12	0.75 0.66		
Z	PA	- 300°C 300°C	β_4 β_3 or β_1 β_1	>0.14 -	0.9 0.5 0.4	FRD	[14]

^(a)Only Li concentration has been determined. BA - benzoic acid, LB - lithium benzoate, PA - pyrophosphoric acid.

The method is based on three assumptions:

- (i) The first assumption is that the change in the refractive index, Δn_e , is a linear function of the proton concentration, C_H , within each crystal phase without interstitial protons (α , κ_1 , κ_2 and β_1 - $\text{H}_x\text{Li}_{1-x}\text{NbO}_3$):

$$C_H^i = A(i) \Delta n_e^i + E(i) \quad \text{or} \quad x = B(i) \Delta n_e^i + D(i) \quad (1)$$

where $A(i)$, $B(i)$, $E(i)$ and $D(i)$ are constants for each i - $\text{H}_x\text{Li}_{1-x}\text{NbO}_3$ phase.

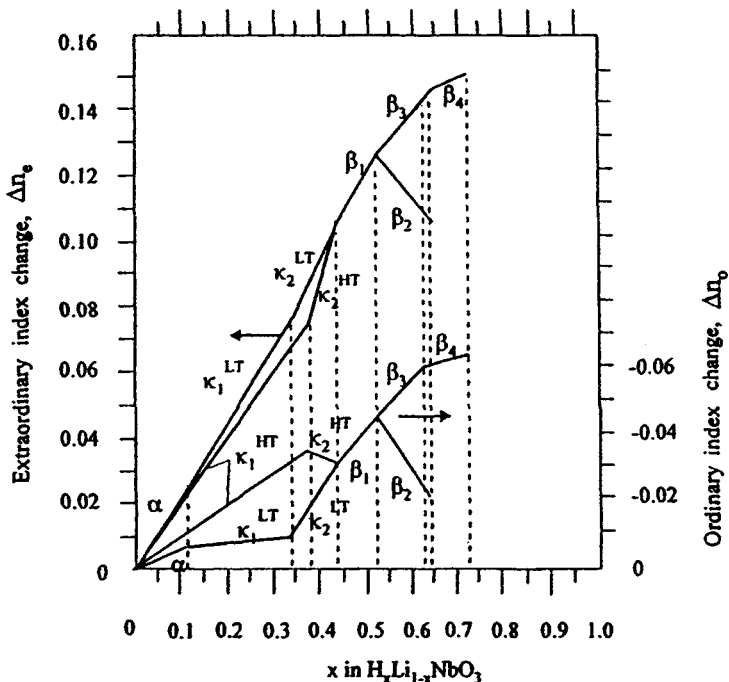


FIGURE 1 Extraordinary and ordinary refractive indices versus hydrogen concentration for the different $\text{H}_x\text{Li}_{1-x}\text{NbO}_3$ phases.

The α phase samples are characterised by the lowest proton concentration and one can expect a very small matrix effect in the analytical determination (SIMS, ERD etc.) of proton concentration in this phase. Most of the researchers reported that $x \leq 0.12$ for the α phase waveguides where $\Delta n_e \leq 0.025$, which is in good agreement with basic work [19,20]. Therefore, the value of $B(\alpha) = 4.8$ has been chosen as an average of all data reported. It is evident that $D(\alpha) = 0$.

- (ii) The second assumption is that the total hydrogen content does not change on annealing in a dry atmosphere. Note, that Zavada et al [5] reported that wet flowing oxygen acts as a constant source of interstitial protons; however we did not observe any hydrogen incorporation while annealing in dry air. Indeed, starting from one of the phases β_1 , κ_1 , κ_2 or α , we did not observe any change of total O-H band intensity around 3500 cm^{-1} on IR spectra (an increase is observed after annealing of the β_2 , β_3 and β_4 phases).
- (iii) Next, we assume that there are no jumps of proton concentration on the α - κ_1^{LT} , κ_1^{LT} - κ_2^{LT} and κ_2^{LT} - β_1 phase boundaries, which is a fairly good assumption owing to the absence of noticeable jumps of Δn_e on phase boundaries [21-23]. Under these assumptions we are able to compare the experimental refractive index profiles for samples obtained after annealing steps, when the κ_1^{LT} or α phases exist on top of the PE LiNbO_3 waveguide.

Thus, assuming that the total hydrogen content Q is conserved during the annealing process the following expression can be written:

$$Q = S \int_0^\infty C_H(z) dz = S \sum_i^N \int_{z_{i-1}}^{z_i} (A(i) \Delta n_e^i(z) + E(i)) dz = \text{const} \quad (2)$$

where $i = 1, \dots, N$ denotes the crystal phases without interstitial hydrogen, realised in PE LiNbO_3 waveguides ($N_{\max} = 4$). These phases are organised as individual layers. The z_{i-1} and z_i are depth

3.2 Composition of different crystal phases in proton-exchanged waveguides in LiNbO_3

coordinates of upper and lower concentration i-phase boundaries, respectively ($z_0 = 0$ and for the α phase $z_i = \infty$); $S = \text{const}$ is an area of the sample.

It is then possible to compare the areas under the experimental $\Delta n_e(z)$ curve for one and the same sample which passes continuously from the β_1 phase through the κ_2^{LT} and κ_1^{LT} phases to the α phase during the annealing process, and calculate coefficients $A(i)$ and $E(i)$ for all phases.

By solving the system of equations for experimental refractive index profiles and taking into account the assumption made above and for experimental $\Delta n_e(z)$ profiles, the constants $B(i)$ and $D(i)$ were found.

C RESULTS

The results are presented in TABLE 2.

TABLE 2 Parameters of model for different phases.

Phase	B(i)	D(i)	Δn_e	X
β_4	15.0	-1.54	0.145 - 0.15	0.65 - 0.71
β_3	5.91	-0.22	0.125 - 0.145	0.52 - 0.65
β_2	-6.5	1.33	0.125 - 0.105	0.52 - 0.65
β_1	4.17	0	0.105 - 0.125	0.44 - 0.52
κ_2^{LT}	3.18	0.11	0.075 - 0.105	0.34 - 0.44
κ_1^{LT}	4.55	0.003	0.025 - 0.075	0.12 - 0.34
κ_2^{HT}	2.3	0.2	0.075 - 0.105	0.36 - 0.44
κ_1^{HT}	4.9	0	0 - 0.075	0 - 0.36
α	4.8	0	0 - 0.025	0 - 0.12

In the described approach, we have assumed a linear relationship between the extraordinary refractive index increment and the proton concentration in the low proton concentration phases: α , κ_1 , κ_2 and $\beta_1\text{-H}_x\text{Li}_{1-x}\text{NbO}_3$. This is valid because protons in these phases are ‘active’, i.e. sited in oxygen planes (substitutional positions), and a linear relationship between Δn_e and substitutional hydrogen concentration was established [17]. However, in the β_2 , β_3 and $\beta_4\text{-H}_x\text{Li}_{1-x}\text{NbO}_3$ phases protons occupy both substitutional and interstitial positions, so as interstitial protons are optically ‘inactive’ [17] the relationship between Δn_e and x may have a non-linear character even for individual phases. However, as a first approximation we have used a linear dependence of Δn_e on total hydrogen concentration x (both substitutional and interstitial positions) for the β_2 , β_3 and β_4 phases. The procedure for determination of hydrogen concentration for these phases is described carefully in [15].

FIGURE 1 shows the dependence of proton concentration on extraordinary refractive index increment for different $\text{H}_x\text{Li}_{1-x}\text{NbO}_3$ phases generated in PE LiNbO_3 waveguides.

D CONCLUSION

Measurements of the extraordinary refractive index versus hydrogen concentration in proton-exchanged LiNbO_3 waveguides are reported. A correlation is demonstrated between the refractive indices, the hydrogen concentration and the crystal structure. This helps to predict waveguide characteristics and to explain some of the observed optical phenomena.

ACKNOWLEDGEMENTS

This work was supported by the Russian Foundation of Basic Research under grants 96-15-96978 and 99-15-96110 for Young Doctors of Sciences and grant 96-15-98220 for Leading Science Schools and by the «Russian Universities - Basic Researches» program under grant 248-1998. This investigation is also part of the project A-0102 supported by the «Integration» Foundation (Russia).

REFERENCES

- [1] M. Howerton, W.K. Burns, P.R. Skeath, A.S. Greenblatt [*IEEE J. Quantum Electron. (USA)* vol.QE-27 (1991) p.593]
- [2] S.W. Wilson, S.W. Novak, J.M. Zavada, A. Loni, R.M. De La Rue [*J. Appl. Phys. (USA)* vol.66 (1989) p.6055]
- [3] R. Richter, T. Bremer, P. Hertel, E. Krätzig [*Phys. Status Solidi A (Germany)* vol.114 (1989) p.765]
- [4] J.M. Zavada, H.C. Casey Jr., Ch.Ho. Chen, A. Loni [*Appl. Phys. Lett. (USA)* vol.62 (1993) p.2769]
- [5] J.M. Zavada, H.C. Casey Jr., R.J. States, S.W. Novak, A. Loni [*J. Appl. Phys. (USA)* vol.77 (1995) p.2697]
- [6] A. Loni, R.M. De La Rue, J.M. Zavada, S.W. Wilson [*Electron. Lett. (UK)* vol.27 (1991) p.1245]
- [7] K. Ito, K. Kawamoto [*Jpn. J. Appl. Phys. (Japan)* vol.31 (1992) p.3882]
- [8] C. Canali et al [*J. Appl. Phys. (USA)* vol.59 (1986) p.2643]
- [9] A. Loni, R.M. De La Rue, J.M. Winfield [*J. Appl. Phys. (USA)* vol.61 (1987) p.64]
- [10] A. Loni, R.M. De La Rue, M.A. Foad, J.M. Winfield [*Proc. IGWO (UK)* (1989) p.258]
- [11] M. Rottchalk, T. Bachmann, A. Witzmann [*Nucl. Instrum. Methods Phys. Res. B (Netherlands)* vol.61 (1991) p.91]
- [12] I. Savatinova, S. Tonchev, M. Kuneva [*Appl. Phys. A (Germany)* vol.56 (1993) p.81]
- [13] C. Ziling et al [*J. Appl. Phys. (USA)* vol.73 (1993) p.3125]
- [14] G.R. Paz-Pujalt, D.D. Tuschel, G. Braunstein, T. Blanton, S. Tong Lee, L.M. Salter [*J. Appl. Phys. (USA)* vol.76 (1994) p.3981]
- [15] Yu.N. Korkishko, V.A. Fedorov [*J. Appl. Phys. (USA)* vol.82 (1997) p.171]
- [16] S.T. Vohra, A.R. Mickelson, S.E. Asher [*J. Appl. Phys. (USA)* vol.65 (1989) p.1429]
- [17] J. Nikolopoulos, G.L. Yip [*Proc. SPIE (USA)* vol.1583 (1991) p.71]
- [18] J. Nikolopoulos, G.L. Yip [*J. Lightwave Technol. (USA)* vol.LT-9 (1991) p.864]
- [19] C.E. Rice, J.L. Jackel [*Mater. Res. Bull. (USA)* vol.19 (1984) p.591]
- [20] C.E. Rice [*J. Solid State Chem. (USA)* vol.64 (1986) p.188]
- [21] Yu.N. Korkishko, V.A. Fedorov [*IEEE J. Sel. Top. Quantum Electron. (USA)* vol.2 (1996) p.187]
- [22] Yu.N. Korkishko, V.A. Fedorov, M.P. De Micheli, P. Baldi, K. El Hadi, A. Leycuras [*Appl. Opt. (USA)* vol.35 (1996) p.7060]
- [23] Yu.N. Korkishko, V.A. Fedorov [*Ion Exchange in Single Crystals for Integrated Optics and Optoelectronics* (Cambridge International Science Publishing, Cambridge, UK, 1999)]

CHAPTER 4

MECHANICAL PROPERTIES

- 4.1 Stiffness and compliance of LiNbO₃**
- 4.2 Photoelastic coefficients of LiNbO₃**
- 4.3 Third-order elastic coefficients of LiNbO₃**
- 4.4 Yield stress of LiNbO₃**

4.1 Stiffness and compliance of LiNbO₃

I. Tomeno and S. Matsumura; updated by C. Florea

September 2001

A INTRODUCTION

The symbols and definitions used here are in accordance with the IRE standards [1]. The second-order elastic constants are relevant to the vibration modes in a piezoelectric material as follows [2,3].

The equation of motion for particle displacements u_k ($k = x, y, z$) associated with a plane wave in a piezoelectric medium may be written:

$$(c'_{jk} - \delta_{jk}\rho V^2)u_k = 0$$

where V is the velocity of the plane wave propagating along the direction n in the medium of density ρ and the piezoelectrically stiffened elastic constant c'_{jk} is given by:

$$c'_{jk} = [c_{ijkl}^E + (e_{pij}\epsilon_{qkl}n_p n_q)]/(\epsilon_{rs}^S n_r n_s) n_i n_l$$

where c^E , e , ϵ^S denote the elastic constant (stiffness) at constant electric field, the piezoelectric stress constant, and the dielectric constant at constant strain (clamped permittivity), respectively. The vector components n_q are projections along the crystal axes of a unit vector perpendicular to the piezoelectric plate. If an elastic constant depends on any piezoelectric constants, it is called piezoelectrically stiffened, while, if it does not, it is called unstiffened.

The second-order elastic constants are determined, in general, either by resonance techniques [2,3] or through measurements of sound velocity [3,4]. They can also be determined by Fourier analysis of the free electroacoustic decay (FED) caused by applying an RF electric-field pulse in a piezoelectric crystal [10]. This last method is useful when anharmonic effects are considered.

The measurement of the stiffness constants will implicitly determine the elastic compliances, these two sets of constants being interconnected through straightforward relationships. The elastic compliances relate the stress on a plate with the strain and the plate dimensions.

B STIFFNESS AT CONSTANT ELECTRIC FIELD

The most often cited measured values for the elastic constant at constant electric field (at room temperature) are indicated chronologically in TABLE 1, along with the references. Note that, except in [10] and [9], c_{66}^E is not measured but computed as $(c_{11}^E - c_{12}^E)/2$ and it is shown here only for completeness. The most comprehensive sets of data are given in [2] and [3] but the measurements from different samples have shown slight non-uniformity [2] and there was not much attention given to the crystal stoichiometry. The only mention of stoichiometry is made in [6], where samples from a congruent melt with Li/Nb ratio of 0.942 were used. Recent data [6-9] are important as the quality of the samples and the control of the stoichiometry have improved markedly. The data from [7] may be best for surface acoustic wave (SAW) devices as the data were determined from SAW measurements on modern quality crystals. Some of the data from [8] were refined further in [9].

4.1 Stiffness and compliance of LiNbO_3

TABLE 1 Elastic stiffness at constant electric field (10^{11} N m^{-2}).

Constant	[2]	[3]	[4]	Ref. 19 from [5]	[6]	[7]	[8]	[9]	[10]
Density \rightarrow (10^3 kg m^{-3})	4.7	4.64	-	4.628	-	4.628	4.64	4.64	4.622
c_{11}^E	2.03	2.030	2.059	1.990	1.987	1.9839 ± 0.0089	2.031	-	1.987 ± 0.002
c_{12}^E	0.53	0.573	0.565	0.538	-	0.5472 ± 0.0097	0.53	-	-
c_{13}^E	0.75	0.752	0.75	0.714	-	0.6513 ± 0.0193	0.742	-	-
c_{14}^E	0.09	0.085	0.083	0.0785	-	0.0788 ± 0.0004	0.085	-	-
c_{33}^E	2.45	2.424	2.49*	2.372	2.509	2.2279 ± 0.0324	2.413	2.435	-
c_{44}^E	0.60	0.595	0.607	0.601	0.595	0.5960 ± 0.0008	0.646	0.61	0.593 ± 0.002
c_{66}^E	0.75	0.728	0.733	0.726	0.719	0.7183	0.75	0.756	0.792 ± 0.002

*Based on the fact that all the other constants in [4] are in very good general agreement with the other literature data, a presumed typographical error in [4] is corrected here for c_{33}^E ('2.49' in the original should perhaps be '24.9').

The temperature variation of the elastic stiffness at constant electric field was investigated in [3] in the range from 273 K to 383 K for all the stiffness constants and the results are shown in TABLE 2. In [6] an extended temperature range was covered, from 300 K to 1200 K, but only for c_{11}^E , c_{44}^E , and c_{66}^E . While c_{11}^E maintained a linear variation with the temperature, dropping from about $2 \times 10^{11} \text{ N m}^{-2}$ at 300 K to about $1.7 \times 10^{11} \text{ N m}^{-2}$ at 1200 K, the c_{44}^E and c_{66}^E behaved non-linearly with temperature. More precisely (see [6], plots on pages 166, 167), c_{44}^E exhibited a minimum of about $0.566 \times 10^{11} \text{ N m}^{-2}$ at around 840 K and then slowly increased up to 1040 K, while c_{66}^E decreased non-linearly between 500 K and 1100 K and became practically independent of temperature beyond 1190 K with a value of about $0.657 \times 10^{11} \text{ N m}^{-2}$.

TABLE 2 Normalised stiffness temperature coefficients
(defined as $\alpha_{jk} = (dc_{jk}^E/dt)/c_{jk}^E$ in 10^{-4} deg^{-1}).

α_{11}	α_{12}	α_{13}	α_{14}	α_{33}	α_{44}	α_{66}
-1.74	-2.52	-1.59	-2.14	-1.53	-2.04	-1.43

C STIFFNESS AT CONSTANT POLARISATION

Valuable information regarding the interaction between strain and the order parameter characterising the structural phases of LiNbO_3 can be derived from the difference between the elastic constant at constant polarisation (or electric displacement for $E = 0$) and at constant electric field [6]. The available literature data are shown in TABLE 3 along with the references.

TABLE 3 Elastic stiffness at constant polarisation (in 10^{11} N m^{-2}).

Elastic stiffness	c_{11}^P	c_{12}^P	c_{13}^P	c_{14}^P	c_{33}^P	c_{44}^P	c_{66}^P
[2]	2.19	0.37	0.76	-0.15	2.52	0.95	0.91
[6]	2.15 (estimated)	-	-	-	2.509	0.95 (estimated)	0.88 (estimated)

4.1 Stiffness and compliance of LiNbO_3

The temperature variation of the elastic stiffness at constant polarisation was investigated in [6] from 300 K to 1200 K but only for c_{33}^P , which decreases linearly with the temperature from about $2.5 \times 10^{11} \text{ N m}^{-2}$ at 300 K to about $2.28 \times 10^{11} \text{ N m}^{-2}$ at 1080 K.

Notes:

- (1) The effect of the stoichiometry on the elastic properties of lithium niobate has also been studied (for example, see [12]). As a main result, it was found that, for the $[\text{Li}]/[\text{Nb}]$ ratio range from 0.908 to 0.988 (inside the crystal), the c_{44} constant presents a minimum of $0.586 \times 10^{11} \text{ N m}^{-2}$ at a $[\text{Li}]/[\text{Nb}]$ ratio of 0.948.
- (2) The elastic constants of lithium niobate have also been measured in the hypersonic range (for example, see [13]). The values of the elastic constants are not in full agreement with ultrasonic data with the largest differences being in the case of c_{12} (8.5%) and c_{13} (5.2%).

D COMPLIANCE AT CONSTANT ELECTRIC FIELD

The values for the elastic compliances at constant electric field reported in [2], [3], and reference 9 in [11] are presented in TABLE 4. The temperature variation of the elastic compliance at constant electric field was investigated in [3] in the range from 273 K to 383 K for all the compliance constants and the results are shown in TABLE 5.

TABLE 4 Elastic compliance at constant electric field.

Constant (units)		[2]	[3]	Ref. 9 from [11]
Density \rightarrow (10^3 kg m^{-3})	ρ	4.7	4.64	-
Elastic compliance $(10^{-12} \text{ m}^2 \text{ N}^{-1})$	s_{11}^E	5.78	5.831	5.8
	s_{12}^E	-1.01	-1.150	-1.05
	s_{13}^E	-1.47	-1.452	-1.46
	s_{14}^E	-1.02	-1.000	-1.01
	s_{33}^E	5.02	5.026	5.02
	s_{44}^E	17.0	17.10	17.05
	s_{66}^E	13.6	13.96	13.8

TABLE 5 Normalised compliance temperature coefficients
(defined as $\beta_{jk} = (ds_{jk}^E/dt)/s_{jk}^E$ in 10^{-4} deg^{-1}).

β_{11}	β_{12}	β_{13}	β_{14}	β_{33}	β_{44}	β_{66}
1.66	0.28	1.94	1.33	1.60	2.05	1.43

E COMPLIANCE AT CONSTANT POLARISATION

The values for the elastic compliances at constant polarisation reported in the literature [2] are presented in TABLE 6.

TABLE 6 Elastic compliance at constant polarisation.

Elastic compliance $(10^{-12} \text{ m}^2 \text{ N}^{-1})$	s_{11}^P	s_{12}^P	s_{13}^P	s_{14}^P	s_{33}^P	s_{44}^P	s_{66}^P
	5.20	-0.44	-1.45	0.87	4.89	10.8	11.3

F CONCLUSION

Both elastic and stiffness constants are tabulated in this Datareview. Temperature coefficients of the stiffness and elastic constants at constant electric field are also given. Similar data are presented under constant polarisation conditions.

REFERENCES

- [1] Standards on Piezoelectric Crystals [*Proc. IRE (USA)* vol.37 (1949) p.1378 and vol.46 (1958) p.764]
- [2] A.W. Warner, M. Onoe, G.A. Coquin [*J. Acoust. Soc. Am. (USA)* vol.42 (1967) p.1223]
- [3] R.T. Smith, F.S. Welsh [*J. Appl. Phys. (USA)* vol.42 (1971) p.2219]
- [4] L.P. Avakyants, D.F. Kiselev, N.N. Shchitov [*Sov. Phys.-Solid State (USA)* vol.6 (1976) p.899]
- [5] J.G. Gualtieri, J.A. Kosinski, A. Ballato [*IEEE Trans. Ultrason. Ferroelectr. Freq. Control (USA)* vol.41 (1994) p.53]; reference [19] in this citation is given as: I.A. Dan'kov, E.F. Tokarev, G.S. Kudryashov, K.G. Belobaev [*Inorg. Mater. (Russia)* vol.19 (1983) p.1049]
- [6] I. Tomono, S. Matsumura [*J. Phys. Soc. Jpn. (Japan)* vol.56 (1987) p.163]
- [7] G. Kovacs, M. Anhorn, H.E. Engan, G. Visintini, C.C.W. Ruppel [*IEEE Ultrason. Symp. (USA)* vol.1 (1990) p.435]
- [8] R.V. Damle [*J. Phys. D, Appl. Phys. (UK)* vol.25 (1992) p.1091]
- [9] R.V. Damle [*J. Phys. D, Appl. Phys. (UK)* vol.27 (1994) p.1933]
- [10] R.E. de Souza, M. Engelsberg, G.C. do Nascimento [*J. Appl. Phys. (USA)* vol.76 (1994) p.2399]
- [11] C.E. Greninger [*J. Appl. Phys. (USA)* vol.85 (1999) p.7037]; reference [9] in this citation is given as: A. Rauber [*Current Topics in Material Science* Ed. E. Kaldis, vol.1 (North-Holland, 1978) ch.7, p.253]
- [12] A. de Bernabe, C. Prieto, A. de Andres [*J. Appl. Phys. (USA)* vol.79 (1996) p.143]
- [13] T. Blachowicz, Z. Kleszczewski [*J. Acoust. Soc. Am. (USA)* vol.104 (1998) p.3356]; reference [5] from this citation is indicated for the lithium niobate data in the hypersonic regime: R.J. O'Brien, G. Rosasco, A. Weber [*Light Scattering Spectra of Solids - Proceedings of the International Conference on Light Scattering Spectra of Solids* New York, Ed. G.B. Wright (Springer-Verlag, 1969) p.623]

4.2 Photoelastic coefficients of LiNbO₃

R.S. Weis; updated by C. Florea

May 2001

A INTRODUCTION

The use of lithium niobate for the fabrication of acoustic transducers and acousto-optic devices makes a knowledge of its photoelastic constants imperative.

A change in the refractive index of a material as a result of a strain in the material is known as the photoelastic effect. The anisotropic photoelastic relationship between the strain and the refractive index is usually written as:

$$\Delta\left(\frac{1}{n_{ij}^2}\right) = \sum_{k,l} p_{ijkl} S_{kl}$$

where n_{ij} is the second-rank tensor describing the refractive index (relative permittivity) of the material, S_{kl} is the second-order strain tensor, and p_{ijkl} is the fourth-rank strain photoelastic tensor. The independent elastic variable is not actually the strain but the displacement gradient [1]. This rotation (of volume elements varying within an acoustic wavelength) as well as strain contributes to the change in refractive index of a material experiencing acoustic shear waves. Therefore, the previously assumed symmetry of photoelastic coefficients upon interchange of the two elastic indices is incorrect for coefficients corresponding to acoustic shear waves [2]. For lithium niobate, the photoelastic coefficients p_{44} and p_{55} , which are numerically equal, consist of symmetric and anti-symmetric components (with respect to the elastic indices) [2]. All other photoelastic coefficients contain only symmetric components.

B PHOTOELASTIC COEFFICIENTS

Since the available data do not allow the resolution of the components of p_{44} , the interchange of elastic indices will be used here for ease of notation. Also, it can be shown that $\Delta(n_{ij}^{-2}) = \Delta(n_{ji}^{-2})$ [3]. Using these two observations the fourth-rank strain photoelastic tensor of 81 elements can be reduced to 36 independent elements which can be written as a 6×6 matrix using the following substitutions in notation:

$$\begin{array}{lll} jk = 11 \rightarrow 1, & jk = 22 \rightarrow 2, & jk = 33 \rightarrow 3, \text{ and} \\ jk = 23 \text{ or } 32 \rightarrow 4, & jk = 31 \text{ or } 13 \rightarrow 5, & jk = 12 \text{ or } 21 \rightarrow 6 \end{array}$$

The application of Neumann's principle ([3], page 115) to the p_{ijkl} tensor along with the reduced-subscript notation will yield:

4.2 Photoelastic coefficients of LiNbO_3

$$P_{ijkl} = \begin{bmatrix} P_{11} & P_{12} & P_{13} & P_{14} & 0 & 0 \\ P_{12} & P_{11} & P_{13} & -P_{14} & 0 & 0 \\ P_{31} & P_{31} & P_{33} & 0 & 0 & 0 \\ P_{41} & -P_{41} & 0 & P_{44} & 0 & 0 \\ 0 & 0 & 0 & 0 & P_{44} & \frac{P_{41}}{2} \\ 0 & 0 & 0 & 0 & P_{14} & \frac{(P_{11} - P_{12})}{2} \end{bmatrix}$$

Note that there are only eight independent coefficients with p_{66} being given by $(p_{11} - p_{12})/2$.

When determining the values of these coefficients, the contribution of the secondary (indirect) photoelastic effect must also be taken into account. This secondary effect, while it manifests itself just like the primary effect, is actually the coupling of the piezoelectric effect with the linear electro-optic effect. The applied strain causes an electric field through the piezoelectric effect and this electric field then causes a change in the crystal's refractive index through the linear electro-optic effect [4]. Thus, to the observer who applied the strain and is measuring the change in the refractive index, this secondary contribution is inseparable from the primary photoelastic effect. This indirect photoelastic effect cannot be represented as an ordinary tensor but instead it must be expressed as a tensor that is dependent on the acoustic wave direction [1]. In lithium niobate the secondary effect is significant when determining the values of p_{13} and p_{33} . The relationships between the measured, effective coefficients (p^{eff}) and those describing only the primary effect are [5]:

$$p_{13} (\text{primary}) = p_{13}^{\text{eff}} - 0.043$$

and

$$p_{33} (\text{primary}) = p_{33}^{\text{eff}} - 0.154$$

The values of the primary photoelastic coefficients reported in the literature are given chronologically in TABLE 1. The data from the references which present effective values have been modified accordingly such that the table contains only primary values (for p_{13} and p_{33}) [4].

TABLE 1 Strain photoelastic coefficients (dimensionless) at constant electric field.

p_{11}	p_{12}	p_{13}	p_{14}	p_{31}	p_{33}	p_{41}	p_{44}	Ref
0.036	0.072	0.135 ^(a)	-	0.178	0.066 ^(a)	0.155	-	[6]
0.034	0.072	0.139 ^(a)	0.066	0.178	0.060 ^(a)	0.154	0.30	[7]
0.045	0.096	0.149 ^(a)	0.055	0.138	0.078 ^(a)	0.12	0.019	[8]
0.025	0.079	0.132 ^(a)	0.1	0.168	0.068 ^(a)	0.158	-	[9]
-0.02	+0.08	+0.13	-0.08	+0.17	+0.07	-0.15	+0.12	[10]
- ^(b)	0.088	0.126	0.080	0.176	0.069	0.134	0.152	[5]
-0.026	+0.090	+0.133	-0.075	+0.179	+0.071	-0.151	+0.146	[4] ^(c)

(a) Primary coefficient obtained from the reported effective coefficient;

(b) instead of p_{11} [5] gives $p_{66} = 0.055$; (c) [4] also gives $p_{66} = -0.053$.

As an aside, the signs of the strain photoelastic coefficients were not determined completely until 1976 and therefore in TABLE 1 [5-9] give only absolute values of these coefficients.

C FIGURES OF MERIT

To compare the usefulness of acousto-optic materials [11] for device applications various figures of merit have been developed [12]. Perhaps four of the most used are:

$$M_1 = \frac{n^7 \cdot p^2}{\rho \cdot v} \quad M_2 = \frac{n^6 \cdot p^2}{\rho \cdot v^3}$$

$$M_3 = \frac{n^7 \cdot p^2}{\rho \cdot v^2} \quad M_4 = \frac{n^8 \cdot p^2 \cdot v}{\rho}$$

where n is the average refractive index, p is the applicable photoelastic coefficient, ρ is the bulk mass density, and v is the bulk acoustic wave velocity given by:

$$v = \frac{1}{\sqrt{\rho \cdot s}}$$

with s the applicable elastic compliance coefficient.

M_1 is proportional to the product of the bandwidth and diffraction efficiency associated with a bulk acoustic wave for a given level of acoustic power if the height of the acoustic wave is constant [13]. It is appropriately used to select materials for devices such as modulators requiring optimum efficiency and bandwidth.

M_2 is proportional to the diffraction efficiency associated with a bulk acoustic wave for a given level of acoustic power and is appropriately used to select materials for narrow-band devices.

M_3 is proportional to the diffraction efficiency associated with a bulk acoustic wave for a given level of acoustic power if the acoustic beam height can be made as small as the optical beam size in the interaction region [6].

M_4 is proportional to the product of the square of the bandwidth and diffraction efficiency associated with a bulk acoustic wave for a given acoustic power density. It is appropriately used to select materials for wide-band applications where power density is the limiting factor [12].

As an example, for a longitudinal bulk acoustic wave propagating in the x-direction in LiNbO₃ ($n = 2.20$, $\rho = 4.7 \times 10^3 \text{ kg m}^{-3}$, $v = 6.57 \times 10^3 \text{ m s}^{-1}$), and an optical beam extraordinarily polarised at an angle of 35° relative to the y-axis (measured in the y-z plane) the following typical values of the figures of merit have been reported:

$$M_1 = 6.65 \times 10^{-7} \text{ m}^2 \text{ s kg}^{-1} [6], \quad M_2 = 6.99 \times 10^{-15} \text{ s}^3 \text{ kg}^{-1} [6],$$

$$M_3 = 1.01 \times 10^{-16} \text{ m s}^2 \text{ kg} [6], \quad M_4 = 62.9 \text{ m}^4 \text{ s}^{-1} \text{ kg}^{-1} [12].$$

D CONCLUSION

The change in refractive index caused by an applied stress, the photoelastic effect, is described by a tensor quantity. There is also a secondary effect due to the coupling of the piezoelectric effect with the linear electro-optic effect. The primary photoelastic coefficients are tabulated. Various figures of merit are defined that can be used to compare various acousto-optic materials when used in device applications.

REFERENCES

- [1] D.F. Nelson, M. Lax [*Phys. Rev. B (USA)* vol.3 (1971) p.2778]; see also Erratum [*Phys. Rev. B (USA)* vol.4 (1971) p.3779]
- [2] D.F. Nelson, M. Lax [*Phys. Rev. Lett. (USA)* vol.24 (1970) p.379]
- [3] J.F. Nye [*Physical Properties of Crystals* (Oxford University Press, 1957) p.248]
- [4] L.P. Avakyants, D.F. Kiselev, N.N. Shchitov [*Sov. Phys.-Solid State (USA)* vol.6 (1976) p.899]
- [5] L. Marculescu, G. Hauret [*C. R. Hebd. Seances Acad. Sci. B (France)* vol.276 (1973) p.555]
- [6] R.W. Dixon [*J. Appl. Phys. (USA)* vol.38 (1967) p.5149]
- [7] R.J. O'Brien, G.J. Rosasco, A. Weber [*J. Opt. Soc. Am. (USA)* vol.60 (1970) p.716]
- [8] V.V. Kludzin [*Sov. Phys.-Solid State (USA)* vol.13 (1971) p.540]
- [9] V.V. Lemanov, O.V. Shakin, G.A. Smolenskii [*Sov. Phys.-Solid State (USA)* vol.13 (1971) p.426]
- [10] G.A. Coquin [cited in D.A. Pinnow *Handbook of Lasers with Selected Data on Optical Technology* Ed. R.J. Pressley (Chemical Rubber Co., 1971) p.482]
- [11] A.A. Oliner (Ed.) [*Acoust. Surf. Waves, Top. Appl. Phys. (Germany)* vol.24 (1978) ch.6]
- [12] I.C. Chang [*IEEE Trans. Sonics Ultrason. (USA)* vol.SU-23 (1976) p.2]
- [13] E.I. Gordon [*IEEE J. Quantum Electron. (USA)* vol.2 (1966) p.104]
- [14] T.M. Smith, A. Korpel [*IEEE J. Quantum Electron. (USA)* vol.1 (1965) p.283]

4.3 Third-order elastic coefficients of LiNbO₃

Y. Cho and K. Yamanouchi; updated by C. Florea

September 2001

Third-order elastic constants play an important role in a quantitative analysis of the non-linear effects in finite amplitude acoustic waves such as second-harmonic generation, acoustical mixing and parametric oscillation.

Lithium niobate, crystallographic class 3m, has fourteen third-order elastic constants. TABLE 1 gives the measured constant-electric-field coefficients at room temperature (20°C) as reported in the literature [1,2]. The short notation system was used where $c_{(ij)(kl)(mn)} = c_{IJK}$, with i, j, k, l, m, n = 1 ... 3 and I, J, K = 1 ... 6.

TABLE 1 Third-order elastic coefficients (in 10^{11} N m^{-2}).

Coefficient	[1]		[2]	
	Value	Standard error	Value	Standard error
c_{111}^E	-21.2	4.0	-5.12	1.94
c_{112}^E	-5.3	1.2	4.54	0.76
c_{113}^E	-5.7	1.5	7.28	1.72
c_{114}^E	2.0	0.8	-4.10	0.44
c_{123}^E	-2.5	1.0	7.19	1.47
c_{124}^E	0.4	0.3	0.55	0.13
c_{133}^E	-7.8	1.9	-0.34	1.73
c_{134}^E	1.5	0.3	-0.01	0.26
c_{144}^E	-3.0	0.2	-0.37	0.2
c_{155}^E	-6.7	0.3	-5.99	0.26
c_{222}^E	-23.3	3.4	-4.78	1.87
c_{333}^E	-29.6	7.2	-3.63	6.90
c_{334}^E	-6.8	0.7	-5.40	0.29
c_{444}^E	-0.3	0.4	-0.41	0.92

The values from [1] are for the congruent composition. In [1] the coefficients were determined from the measured values of the velocity variation of small-amplitude ultrasonic waves as functions of applied static uniaxial compressive stresses. Also [1] uses the measured values of third-order piezoelectric and electrostrictive constants.

The values from [2] are determined via the same method as in [1], but these were determined using measured values of other kinds of non-linear constants (second-order elastic and piezoelectric constants).

The c_{111} coefficient was also determined by measuring the amplitude of the second-harmonic wave of the longitudinal wave propagating along the x-axis [3]. This method does not need the corrections that are applied to other kinds of non-linear constants because the longitudinal wave propagating along the x-axis has no electromechanical coupling.

The measured value in [3] is $c_{111} = -16.1 \times 10^{11} \text{ N m}^{-2}$. The large value of this coefficient confirms the larger values of the c_{111} (as well as c_{222} and c_{333}), measured in [1] and [2], when compared with the other coefficients even though the standard errors are quite high.

4.3 Third-order elastic coefficients of LiNbO₃

REFERENCES

- [1] Y. Cho, K. Yamanouchi [*J. Appl. Phys. (USA)* vol.61 (1987) p.875]
- [2] Y. Nakagawa, K. Yamanouchi, K. Shibayama [*J. Appl. Phys. (USA)* vol.44 (1973) p.3969]
- [3] J. Philip, M.A. Breazeale [*IEEE Symp. Proc. (USA)* vol.2 (1982) p.1022]

4.4 Yield stress of LiNbO₃

A. Peter and E. Fries; updated by C. Florea

May 2001

The plastic deformation of LiNbO₃ was first examined by Vere [1]. He studied ferroelectric multidomain stoichiometric crystal specimens deformed by compression in the temperature range 1150°C to 1250°C, along [0001] and [0110] axes. He found the material was very brittle even at temperatures approaching its melting point and deformed mainly by twinning on a (1012) [1011] pyramidal system, the onset of mechanical twinning and the nucleation of fracture being almost simultaneous. Fracture planes were (1012) and (0110), the first one being predominant in as-grown crystals and the second one predominant in deformed specimens. A description of the nucleation of microcracks at the twin band intersections was also given.

Deformation twinning was further examined [2,3] by making uniaxial compression tests of monodomain samples at temperatures above 400°C. The crystallographic elements of two pyramidal twinning systems were determined:

$$K_1 = (10\bar{1}2), \quad \eta_1 = [\bar{1}011], \quad K_2 = (10\bar{1}4), \quad \eta_2 = [\bar{2}02\bar{1}],$$

for which S = (1210), s = 0.19, and

$$K_1 = (1014), \quad \eta_1 = [2021], \quad K_2 = (1012), \quad \eta_2 = [1011],$$

for which S and s are not specified.

Here, K₁ and η₁ are the twinning plane and twinning direction, K₂ and η₂ are the invariant plane and direction, respectively, S is the shear plane, and s is the shear magnitude. The shear plane is also (1210); considering the interatomic arrangements in the [1011] and [2021] directions, the s values are 0.13 and 0.09 for the first and second twinning systems, respectively.

To avoid twinning and to achieve plastic deformation of single crystals in [4] the studies from [2,3] were taken into account by choosing stress directions from the twinning zones on a stereographic projection; these zones contain stress directions where twinning can be activated by compression as the operating twin systems would produce contraction. To avoid fracture they also chose ferroelectric monodomain crystals [5] as multidomain crystals contain excess twins that induce cracks during deformation [6]. Compression tests were performed in air on congruent composition samples [7]. In view of the various possible slip systems common in hcp structures, five different stress orientations were selected (see TABLE 1). For the orientations X, Y and 45° X contained in the basal plane prismatic, pyramidal glide could be activated, while for the orientation 36° Y, contained in the YZ plane, basal and prismatic glide could be activated. Finally Z was chosen in the area where twinning systems could be activated.

TABLE 1 Compression axes σ in the orthohexagonal and hexagonal conventions.

Orthohexagonal	Hexagonal
X	[2110], ‘a’
Y	[0110]
Z	[0001], ‘c’
36° X	[0221]
45° Y	45° off ‘a’ in (0001)

4.4 Yield stress of LiNbO_3

The specimens were parallelepipeds about $4 \times 4 \times 9 \text{ mm}^3$ compressed with a constant cross head velocity of $20 \mu\text{m min}^{-1}$ ($d\varepsilon/dt = 3$ to $4 \times 10^{-5}/\text{s}$) in an Instron machine up to 1170°C (0.9 TM), which is the Curie temperature for congruent composition samples. Stress relaxations were also recorded after stopping the cross head motion. Stress-strain curves for different orientations and temperatures can be found in [4] and [7].

Along the Z-axis, only mechanical twinning could be obtained, typical oscillations being observed at 1000°C on the stress-strain curve. The yield stress value is quite independent of temperature:

37 MPa at 1000°C
30 MPa at 1120°C

For other orientations, plastic deformation could be obtained above 1000°C (0.8 TM) without failure or twinning. Yield drops were observed, even when reloading after high-temperature deformation; except for the X compression, their amplitudes decrease with increasing temperature. The stress-strain curves exhibit a linear work-hardening stage from $\varepsilon \approx 2\%$ with low $\theta = d\sigma/d\varepsilon$ values:

30 MPa for $\sigma \parallel 36^\circ \text{ Y}$
50 MPa for $\sigma \parallel \text{X}$
100 MPa for $\sigma \parallel 45^\circ \text{ X}$
150 MPa for $\sigma \parallel \text{Y}$

Some of the key observations are outlined below.

- (i) The critical yield stress σ_c was studied versus temperature for different orientations. In the case of a yield drop the lower value was plotted, such that in the case of X the $\sigma = 0.2$, for $\varepsilon = 0.2\%$, was plotted. It can be seen that the softest direction is 36° Y with σ_c varying from 44 MPa at 1010°C to 12 MPa at 1170°C , while the hardest direction is X with σ_c varying from 60 MPa at 1070°C to 35 MPa at 1170°C , with the 45° X and the Y directions looking very similar with σ_c varying from 60 MPa at 1020°C to 30 MPa at 1170°C .
- (ii) Analysing stress relaxations gives information on the thermal activation of the deformation process [8]. At 1050°C the mean value of the activation volume is $5.8 \times 10^{-27} \text{ m}^3$ which corresponds to 20 V_{uc} ($V_{uc} = 3 \times 10^{-28} \text{ m}^3$ is the hexagonal unit cell and gives an idea of the volume involved when a dislocation overcomes an obstacle).
- (iii) Characterisation of the slip systems was made by optical observations, chemical etching and Berg-Barrett topography. A detailed analysis of glide planes and glide systems along with mechanical considerations will be found in [7]. The slip systems and their corresponding critical resolved shear stress (CRSS), τ , values are given in TABLE 2. The CRSS is defined as $\tau = \sigma_c f$ (at 1070°C) with σ_c being the critical yield stress mentioned above and f being the Schmid number for the slip system and the corresponding compression axis [7].

4.4 Yield stress of $LiNbO_3$

TABLE 2 Slip systems and their corresponding CRSS
(at 1070°C) for compression along different directions.

$\sigma \parallel$	Slip planes	Slip directions	CRSS (MPa)
36° Y	(0001)	[12̄10] [1̄120]	13
	(11̄20)	[1101]	15
	(1̄210)	[1011]	15
	X	[1̄101] [1012]	20 20
Y	(011̄1)	[0112]	18
45° X	(1̄012)	[1011]	17

REFERENCES

- [1] A.W. Vere [*J. Mater. Sci. (UK)* vol.3 (1968) p.617]
- [2] A.A. Blistanov, I.V. Nosova, M.M. Tagieva [*Krystallografiya (Russia)* vol.20 (1975) p.666]
- [3] A.A. Blistanov, I.V. Nosova, M.M. Tagieva [*Krystallografiya (Russia)* vol.21 (1976) p.217]
- [4] E. Fries, J. Deschamps, A. Peter, K. Polgar [*Cryst. Lattice Defects Amorphous Mater. (UK)* vol.16 (1987) p.111]
- [5] K. Polgar, L. Jeszenszky, K. Rakasanyi, E. Hartman [*Acta Phys. Acad. Sci. Hung. (Hungary)* vol.47 (1979) p.125]
- [6] N. Niizeki [in *Crystal Growth and Characterization* Eds R. Ueda, J.B. Mullin (North-Holland, 1975) p.97]
- [7] E. Fries, A. Peter [*Rev. Phys. Appl. (France)* vol.22 (1987) p.1353]
- [8] T. Bretheau, J. Castaing, J. Rabier, P. Veyssiere [*Adv. Phys. (UK)* vol.28 (1979) p.829]

CHAPTER 5

THERMAL PROPERTIES

- 5.1 Thermal expansion coefficients of LiNbO₃
- 5.2 Thermal conductivity properties of LiNbO₃
- 5.3 Specific heat properties of LiNbO₃
- 5.4 Thermal diffusivity of LiNbO₃

5.1 Thermal expansion coefficients of LiNbO₃

D. Taylor; updated by D. Craig

August 2001

A INTRODUCTION

The phase diagram for Li₂O-Nb₂O₅ shows a range of non-stoichiometry for LiNbO₃ extending from about 46 mole % Li₂O to the stoichiometric composition [1,2]. Stoichiometric LiNbO₃ melts incongruently below its Curie point and the congruently melting composition, 48.45 mole % Li₂O, has a Curie point of 1411 K [2]. Many properties, including thermal expansion [3,4], are significantly affected by the stoichiometry and so it is important that specimens of lithium niobate are properly characterised.

B EXPERIMENTAL RESULTS

Axial expansion data have been reported for lithium niobate from X-ray diffraction [5-10], dilatometer [3,4,6,11-14], interferometer [15] and capacitance dilatometer [16,17] measurements. Unfortunately, the compositions, and hence stoichiometry, were only given for the most recent data sets [3,4]. However, Gallagher et al [3,4] observed that changes in stoichiometry only have a significant effect on the thermal expansion of the c-axis; the expansion of the a-axis is virtually identical for stoichiometric and congruently melting compositions.

Phase transitions and anomalous thermal expansion behaviour have been observed in thermal expansion studies of lithium niobate compositions [4,9,10,12,13,15] and affect the thermal expansion coefficients. The anomalous behaviour at 348 K reported by Hsu et al [15] was not observed by Gallagher et al [4]. Gallagher et al [4] reported a change in expansion coefficient in the c-axis of congruently melting lithium niobate at 393 K, which also coincides with anomalous behaviour in the c-axis curve of Hsu et al [15], although not commented on by the latter. These anomalies at 348 and 393 K are barely detectable and were not observed by Zhdanova et al [11] and Browder and Ballard [16]. Reports of phase transitions [9,10,12,13] at other temperatures below the Curie point appear to be erroneous. The phase transition at the Curie point affects the thermal expansion behaviour, and has been observed in three studies [3,10,12,13].

The general form of the expansion curves of lithium niobate compositions is that the a-axis expands with an increasing rate of expansion, whereas the c-axis reaches a maximum at about 925 K and decreases thereafter. Several data sets [9,10,12,13] do not conform to this behaviour and are regarded as erroneous. Shapiro et al [9] report a decreasing c-axis throughout the range of experimental temperatures (293 to 973 K) and the other data sets report an increasing c-axis up to the Curie temperature.

The data for the a-axis [3-7,10,11,14,15] were combined for the stoichiometric and congruently melting composition and normalised to an a-parameter (equivalent to that of the stoichiometric composition) of 5.148 Å at 298 K. The different sets of a-axis data appeared to be consistent with one another when the data below 190 K in [11] were rejected. The maximum scatter in the normalised a-axis data, 0.005 Å, occurred at temperatures greater than 773 K.

5.1 Thermal expansion coefficients of LiNbO_3

There is a problem in analysing the literature data for the c-axis because of the lack of compositional data, except for the recent data of Gallagher et al [3,4]. The majority of the literature data are for commercial melt-grown crystals, which are assumed to be close to the congruent-melting composition, an assumption which was also made by Gallagher et al [3]. Thus, the data for the c-axis were divided into two sets: one for the congruently melting composition [3-7,11,14-17], which was normalised to a c-parameter of 13.865 Å at 298 K, and one for the stoichiometric composition [3,4] which was normalised to a c-parameter of 13.856 Å at 298 K. The c-axis data for the stoichiometric composition showed a difference of 0.004 Å between the normalised data of the two studies by Gallagher et al [3,4] at 523 K. The c-axis data for the congruently melting composition showed a difference of 0.003 Å between the normalised data of the two studies by Gallagher et al [3,4] at 523 K, and gave a maximum scatter for all the normalised data of 0.004 Å at 673 K and above 1273 K. The scale for the change in length of the c-axis in [7] seems to be out by a factor of 5 and was corrected prior to analysis. Data in the vicinity of the Curie point of the congruently melting composition [3,10,12,13] were not considered reliable enough to be used.

The data were fitted by the method of least squares to a third-order polynomial and then converted to the form:

$$x = a(1 + bT + cT^2 + dT^3) \quad (T \text{ in } ^\circ\text{C})$$

A better fit to the data was obtained by dividing the data into sets with shorter temperature ranges. In order to report regression data for the a-axis of the congruently melting composition the combined regression data for the a-axis were normalised to an a-parameter of 5.151 Å at 298 K. The results of the regression analyses are given in TABLE 1 and FIGURE 1.

The instantaneous expansion coefficients obtained by differentiating the regression data in TABLE 1 were plotted against temperature and a smooth curve drawn through them by eye. The expansion coefficients thus obtained are given in TABLE 2. The expansion coefficients given for the c-axis of the

TABLE 1 Regression data for lithium niobates. The figures in parentheses are one standard deviation and refer to the least significant digits, SE is the standard error of the estimate and R the multiple correlation coefficient.

Range (K)	a	b ($\times 10^6$)	c ($\times 10^9$)	d ($\times 10^{12}$)	SE	R
a-axis, stoichiometric						
60 - 220	5.1460	13.00(15)		-98.1(15)	0.0001	0.9995
220 - 553	5.1460	13.43(13)	17.55(58)	16.3(40)	0.0004	0.9990
523 - 1373	5.1460	16.29(28)	4.83(30)		0.0013	0.9989
c-axis, stoichiometric						
213 - 323	13.8541	6.22(16)			0.004	0.9961
323 - 1073	13.8544	6.86(15)	-5.53(16)		0.0012	0.9933
1073 - 1273	13.8500	5.53(12)		-3.80(7)	0.0002	0.9990
a-axis, congruent						
60 - 220	5.1490	13.00(15)		-98.1(15)	0.0001	0.9995
220 - 523	5.1490	13.43(13)	17.55(58)	-16.3(40)	0.0004	0.9990
523 - 1373	5.1485	16.29(28)	4.83(30)		0.0013	0.9989
c-axis, congruent						
60 - 373	13.8673	4.09(11)	4.40(40)	-20.2(32)	0.0007	0.9947
373 - 1373	13.8633	4.40(8)		-3.69(9)	0.0010	0.9887

5.1 Thermal expansion coefficients of LiNbO_3

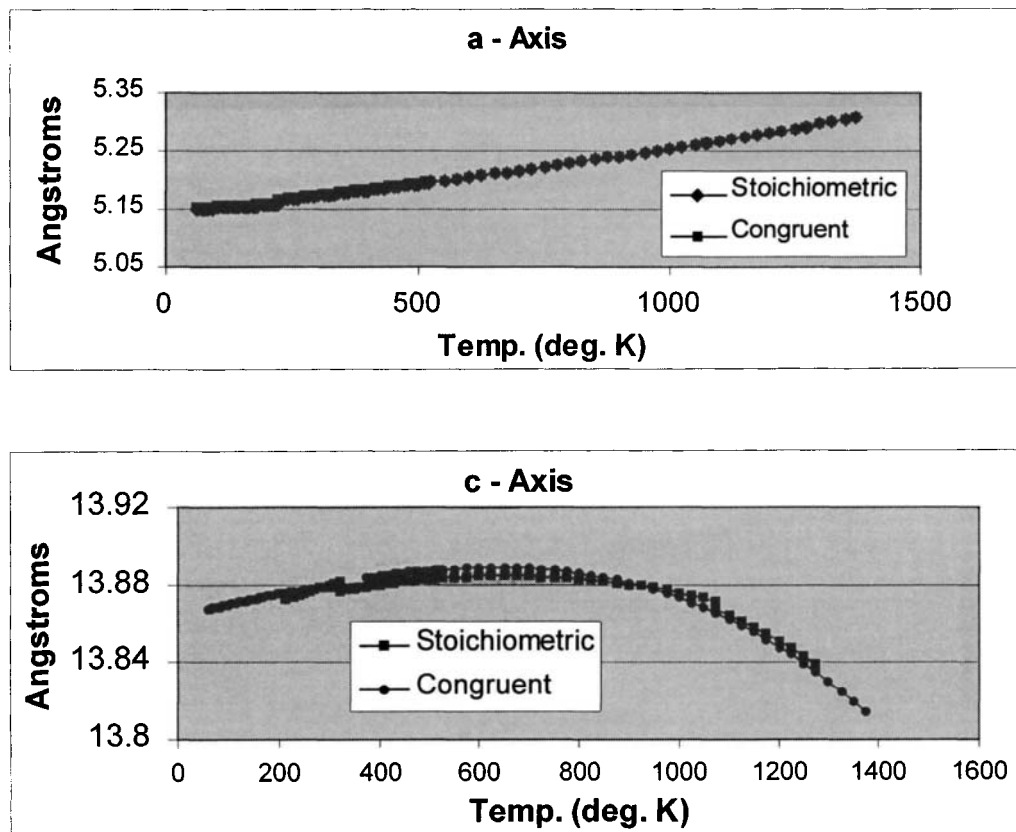


FIGURE 1 Regression data for lithium niobates.

congruently melting composition between 60 and 120 K were taken from [16] because the regression data do not adequately represent the expansion data in this temperature range. Percentage expansions, relative to 298 K, were calculated from the regression data and are given in TABLE 2 and FIGURE 2. Mean linear expansion coefficients and percentage linear expansions are also given in TABLE 2 for the congruently melting composition. Expansion coefficients at 298 K are compared with coefficients from the literature in TABLE 3.

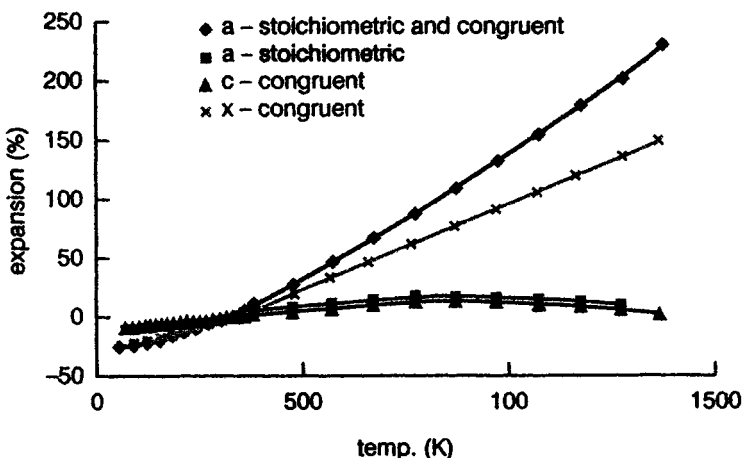


FIGURE 2 Percentage expansions relative to 298 K for stoichiometric and congruently melting lithium niobate (see TABLE 2). x refers to the mean cell parameter calculated from the volume; hence $\partial x / \partial t$ (%) is the mean percentage linear expansion.

5.1 Thermal expansion coefficients of LiNbO_3

TABLE 2 Percentage expansions relevant to 298 K and instantaneous expansion coefficients for stoichiometric and congruently melting lithium niobate. x refers to the mean cell parameter calculated from the volume; hence $\partial x/\partial T$ (%) is the mean percentage linear expansion.

Stoichiometric and congruent			Stoichiometric		Congruent		Congruent	
T (K)	$\partial a/\partial T$ (%)	$\partial a/a\partial T$ ($10^6/\text{K}$)	$\partial c/\partial T$ (%)	$\partial c/c\partial T$ ($10^6/\text{K}$)	$\partial c/\partial T$ (%)	$\partial c/c\partial T$ ($10^6/\text{K}$)	$\partial x/\partial T$ (%)	$\partial x/x\partial T$ ($10^6/\text{K}$)
60	-0.216	1.2			-0.063	4.3	-0.166	
80	-0.214	2.6			-0.058	0.7	-0.164	1.5
100	-0.208	4.2			-0.057	0.7	-0.158	3.4
120	-0.198	5.9			-0.055	1.3	-0.150	4.6
140	-0.184	7.3			-0.052	1.7	-0.140	5.7
160	-0.166	8.8			-0.048	2.1	-0.128	6.7
180	-0.147	10.0			-0.043	2.6	-0.113	7.4
200	-0.125	10.8			-0.037	3.0	-0.097	8.3
220	-0.101	11.6	-0.049	6.2	-0.031	3.3	-0.080	9.0
240	-0.077	12.3	-0.036	6.1	-0.023	3.5	-0.060	9.6
260	-0.052	13.0	-0.024	6.1	-0.016	3.8	-0.041	10.1
280	-0.025	13.5	-0.011	6.0	-0.008	4.0	-0.019	10.7
298	-0.000	14.1	0.000	6.0	0.000	4.1	0.000	11.1
320	0.032	14.6	0.016	5.9	0.010	4.2	0.025	11.6
340	0.063	15.2	0.029	5.8	0.018	4.3	0.048	12.0
360	0.094	15.7	0.041	5.7	0.027	4.3	0.072	12.3
380	0.127	16.1	0.053	5.6	0.035	4.3	0.098	12.6
473	0.297	17.8	0.100	4.8	0.073	4.0	0.222	13.7
573	0.489	19.0	0.140	3.9	0.105	3.5	0.360	14.1
673	0.686	20.1	0.171	3.0	0.139	2.7	0.502	14.4
773	0.892	21.0	0.192	2.0	0.160	1.6	0.647	14.6
873	1.108	22.0	0.202	0.9	0.171	0.4	0.795	14.8
973	1.334	23.0	0.207	-0.4	0.168	-1.1	0.943	15.0
1073	1.569	23.9	0.202	-1.9	0.149	-2.8	1.093	15.0
1173	1.814	24.9	0.175	-3.7	0.113	-4.6	1.243	15.0
1273	2.068	25.9	0.127	-5.9	0.057	-6.7	1.393	14.9
1373	2.333	26.9			-0.021	-9.0	1.542	14.8

TABLE 3 Expansion coefficients at 298 K for lithium niobate.
C = congruent, S = stoichiometric.

Ref	Date	Type	$(\partial a/a\partial T)$ ($10^6/\text{K}$)	$(\partial c/c\partial T)$ ($10^6/\text{K}$)
[11]	1968	C	14.2	7.5
[6]	1969	C	14.4	4.3
[16]	1977	C	14.8	4.1
[15]	1980	C	14.0	3.8
[4]	1987	C	15.2	4.8
		S	14.3	6.5
		C	14.1	4.1
		S	14.1	6.0

The general features of the expansion curves are an a-axis with an increasing rate of expansion and a c-axis which reaches a maximum expansion at 903 K for the congruently melting composition and 953 K for the stoichiometric composition. There are no phase transitions or expansion anomalies between 400 K and the Curie point in the case of the congruently melting composition, and the incongruent melting point in the case of the stoichiometric composition. The data of TABLE 2 do not take account of the expansion anomalies observed at 348 K [15] and 393 K [4,15]. The latter has been

5.1 Thermal expansion coefficients of LiNbO_3

attributed to a defect order/disorder process [4]. There is reasonable agreement between the expansion coefficients at 298 K (TABLE 3), except for the c-axis coefficient of [6]. The a-axis coefficient of the congruently melting composition calculated from the regression data of [4] seems high, because its expansion curve has essentially the same slope as the stoichiometric form at 298 K: see Figure 1 of [4].

There is a need for careful expansion studies below 100 K and above 1373 K for the congruently melting composition: the former temperature range to explore the expansion anomalies seen in Figure 3 of Browder and Ballard [16] and the latter temperature range to explore, preferably by X-ray diffraction, the behaviour in the vicinity of the Curie point. More detailed studies to confirm the anomalies seen at 348 and 393 K and studies on compositions with lower stoichiometries than the congruently melting composition would give a more complete picture of the thermal expansion behaviour of this technically important compound.

C CONCLUSION

Several techniques have been used to measure the thermal expansion coefficients of LiNbO_3 . Stoichiometry has an effect on the values along the c-axis but not along the a-axis. Phase transitions in some temperature ranges also lead to problems in data interpretation. Further work is required at both low and high temperatures to resolve the observed anomalies.

REFERENCES

- [1] J.R. Carruthers, G.E. Peterson, M. Grasso, P.M. Bridenbaugh [*J. Appl. Phys. (USA)* vol.42 (1971) p.1846-51]
- [2] H.M. O'Bryan, P.K. Gallagher, C.D. Brandle [*J. Am. Ceram. Soc. (USA)* vol.68 no.9 (1985) p.493-6]
- [3] P.K. Gallagher, H.M. O'Bryan [*J. Am. Ceram. Soc. (USA)* vol.68 no.3 (1985) p.147-50]
- [4] P.K. Gallagher, H.M. O'Bryan, E.M. Gyorgy, J.T. Krause [*Ferroelectrics (UK)* vol.75 no.1-2 (1987) p.71-7]
- [5] G. Bayer [*Proc. Br. Ceram. Soc. (UK)* no.22 (1973) p.39-53]
- [6] Y.S. Kim, R.T. Smith [*J. Appl. Phys. (USA)* vol.40 (1969) p.4637-41]
- [7] F.C. Lissalde, J.C. Peuzin [*J. Appl. Crystallogr. (Denmark)* vol.7 pt.6 (1974) p.572-6]
- [8] S.C. Abrahams, H.J. Levinstein, J.M. Reddy [*J. Phys. Chem. Solids (UK)* vol.27 (1966) p.1019-26]
- [9] Z.I. Shapiro, S.A. Fedulov, Yu.N. Venevtsev, L.G. Rigerman [*Sov. Phys.-Crystallogr. (USA)* vol.10 (1966) p.725-8]
- [10] I.G. Ismailzade, V.I. Nesterenko, F.A. Mirishli [*Sov. Phys.-Crystallogr. (USA)* vol.13 (1968) p.25-8]
- [11] V.V. Zhdanova, V.P. Klyeuv, V.V. Lemanov, I.A. Smirnov, V.V. Tikhonov [*Sov. Phys.-Solid State (USA)* vol.10 (1968) p.1360-2]
- [12] G.A. Smolenski, N.N. Krainik, N.P. Khuchua, V.V. Zhdanova, I.E. Mylnikova [*Phys. Status Solidi (Germany)* vol.13 (1966) p.309-14]
- [13] N.N. Krainik, N.P. Khuchua, V.V. Zhdanova, I.E. Myl'nikova, N.N. Parfenova [*Proc. Int. Mtg. on Ferroelectrics* vol.1 (1966) p.377-86]
- [14] W.L. Bond [reported in [8]]
- [15] T.-J. Hsu, H.-M. Sun, Y.-N. Wang [*K'o Hsueh Tlung Pao (China)* vol.25 (1980) p.586-8]
- [16] J.S. Browder, S.S. Ballard [*Appl. Opt. (USA)* vol.16 no.12 (1977) p.3214-7]
- [17] S.S. Ballard, S.E. Brown, J.S. Browder [*Appl. Opt. (USA)* vol.17 no.7 (1978) p.1152-4]

5.2 Thermal conductivity properties of LiNbO₃

T.H. Lin and S.H. Lee; updated by D. Craig

August 2001

A INTRODUCTION

Thermal conductivity is a basic material property and is defined as the quantity of heat transmitted per unit time in the direction normal to a surface of unit area, due to unit temperature gradient under steady-state conditions, and is expressed as

$$k = \frac{Q}{A} \frac{\Delta X}{\Delta T} \quad (1)$$

where Q is the heat transfer rate, ΔX is the thickness of the sample, A is the cross-sectional area of the material through which heat is transmitted, and ΔT is the temperature difference between the two surfaces of the material. The data on thermal conductivity for lithium niobate are obtained from this fundamental definition. It should be noted that the solid composition of lithium niobate, $x(\text{Li}_2\text{O})(1-x)(\text{Nb}_2\text{O}_5)$, can be varied based on the mole fraction x (x can be 0.455 as niobate-saturated solid or 0.484 as congruent composition from melt or 0.500 as stoichiometric composition or 0.503 as lithium-saturated solid), which changes the concentration of vacancies in the crystal lattice. Basically, thermal conduction is due to phonon transport and since phonon scattering depends on defects of the crystal, e.g. vacancies, the thermal conductivity is affected by solid composition.

B EXPERIMENTAL RESULTS

Zhdanova et al [1] used an instrument called 'Arrangement A' [2] in which they used the product of current and voltage across a heating element to measure power into the element. Heat is transferred through two lithium niobate samples (of unspecified solid composition) attached on both sides of the heating element. Temperatures are measured at the heating element and the two opposite sides of the lithium niobate samples. Incorporating these data with the cross-sectional area, the thicknesses of the samples and the heat flow rate, the thermal conductivity can be calculated from the definition. This measurement ranges from -173°C to 127°C and is shown in TABLE 1 and FIGURE 1. As can be seen from this table, there is only about 5% difference between the thermal conductivities which are parallel and perpendicular to the c-axis.

Lin et al [3] measured the thermal conductivity of a congruent lithium niobate (0.484(Li₂O)0.516(Nb₂O₅)) with Lee's classical technique [4] in which a hot chuck is used as a constant temperature source, and the temperatures are measured on both sides of the samples. Thermal conductivity is then calculated from the definition. The data were taken from 100°C to 250°C, which is shown in TABLE 2. The data at temperatures above 127°C follow consistently with the tendency of the data in TABLE 1. Inconsistencies between TABLES 1 and 2 in the temperature region between 100°C and 127°C may come from systematic errors in the measurements. Zhdanova reported a ±5% inaccuracy for their measurement based on their calculation [2]. In addition to this, the heat conducted through the electrical conducting wire may cause considerable inaccuracy. In general, the data follow a curve without fluctuation which indicates a small defect (vacancy) concentration lithium niobate being used. The measurements using the classical Lee's technique are performed in ambient atmosphere, in which air flow is a possible cause of fluctuation and error in the temperature reading.

5.2 Thermal conductivity properties of LiNbO_3

TABLE 1 Thermal conductivity of lithium niobate measured with 'Arrangement A'. (1) is measured along the trigonal axis, (2) and (3) are measured perpendicular to the trigonal axis. Solid composition is not specified in the original reference.

T (°C)	k (10^{-3} cal/s/cm/°C)		
	(1)	(2)	(3)
-188	-	34.5	-
-186	-	-	33.5
-183	36.0	-	-
-178	-	28.5	-
-173	29.5	-	-
-171	-	27.0	-
-163	24.5	-	22.5
-150	-	21.5	-
-143	19.5	-	-
-138	-	17.8	-
-113	16.5	-	-
-73	13.0	-	-
-71	-	12.5	-
-68	13.5	-	-

T (°C)	k (10^{-3} cal/s/cm/°C)		
	(1)	(2)	(3)
-66	-	12.3	-
-58	12.5	-	-
-48	12.0	11.3	-
27	-	10.0	-
31	11.0	-	-
34	-	-	9.7
42	10.7	-	-
52	10.0	-	-
67	-	9.2	-
110	-	8.7	-
112	10.0	-	-
117	9.5	-	-
123	-	8.2	-
127	9.5	-	-

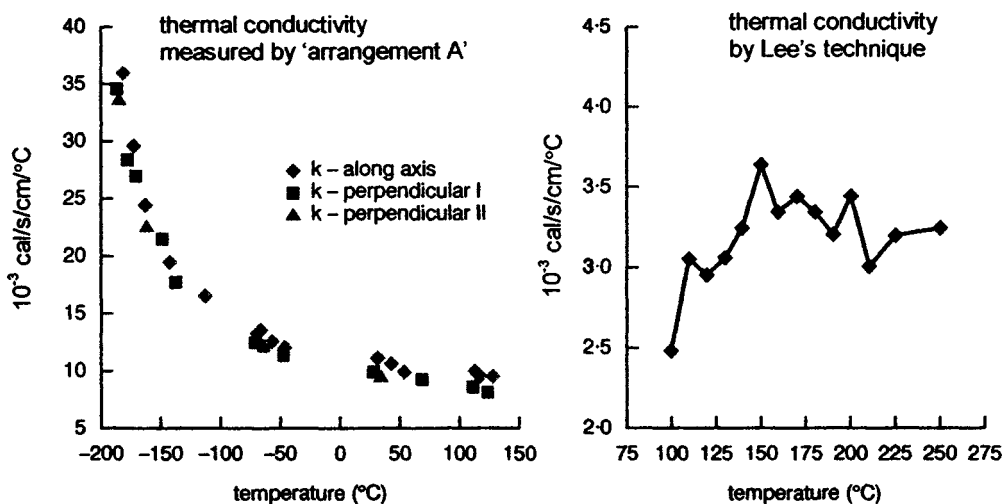


FIGURE 1 Graphs of TABLE 1 and TABLE 2.

TABLE 2 Thermal conductivity of congruent lithium niobate measured with Lee's classical technique [3].

T (°C)	k* (10^{-3} cal/s/cm/°C)
100	2.4
110	3.0
120	2.9
130	3.0
140	3.2
150	3.6
160	3.3

T (°C)	k* (10^{-3} cal/s/cm/°C)
170	3.40
180	3.30
190	3.15
200	3.40
210	2.95
225	3.15
250	3.20

(*Data reported with error bar of $\pm 10\%$.)

5.2 Thermal conductivity properties of LiNbO_3

Thermal conductivity is useful both for material processing and for understanding thermal constraints of optoelectronic devices. During crystal pulling with the Czochralski method, limits on diameter and pulling rates are closely related to thermal conductivity [5]. After the crystal is pulled, thermal conductivity and diameter are the factors limiting the cooling rate to prevent cracking [6]. Silicon devices integrated on lithium niobate may be achieved through laser crystallisation of silicon layers on lithium niobate substrates [7]. Thermal conductivity must be known in order to prevent damage to the lithium niobate substrate during the crystallisation process [8]. After this film is crystallised, electronic circuits may be fabricated for optoelectronic devices utilising lithium niobate. The thermal conductivity of lithium niobate will put limits on the operational speed of the circuits if thermal runaway is to be avoided. The thermal conductivity can also be used in calculating thermal diffusivity which is another important thermal property. Explanation of this calculation is given in another Datareview [9].

C CONCLUSION

Values for the thermal conductivity of LiNbO_3 are affected by solid composition and are given over the temperature range -200 to +250°C. This knowledge is important for crystal growth, for cooling of the crystals, for fabrication of devices and in the operational speed of these devices.

REFERENCES

- [1] V.V. Zhdanova, V.P. Klyuev, V.V. Lemanov, I.A. Smirnov, V.V. Tikhonov [*Sov. Phys.-Solid State (USA)* vol.10 (1968) p.1360]
- [2] E.D. Devyamkova, A.V. Pemrov, I.A. Smirnov, B.Ya. Moizhes [*Sov. Phys.-Solid State (USA)* vol.2 (1960) p.681]
- [3] T.H. Lin, D. Edwards, R.E. Reedy, K. Das, W. McGinnis, S.H. Lee [*Ferroelectrics (UK)* vol.77 (1988) p.153-60]
- [4] J. Duncan, S.G. Starling [*A Text Book of Physics* (Macmillan, New York, 1957) p.355]
- [5] S.A. Fedulov, Z.I. Shapiro, P.B. Ladyzhinskii [*Sov. Phys.-Crystallogr. (USA)* vol.10 (1965) p.218]
- [6] J.C. Brice [*J. Cryst. Growth (Netherlands)* vol.42 (1977) p.42730]
- [7] R.E. Reedy [Silicon Transistors and Photodetectors Integrated on a Lithium Tantalate Substrate, Ph.D. dissertation (UCSD, San Diego, 1983) ch.2 p.12]
- [8] R.E. Reedy [Silicon Transistors and Photodetectors Integrated on a Lithium Tantalate Substrate, Ph.D. dissertation (UCSD, San Diego, 1983) ch.2 p.25]
- [9] T.H. Lin, S.H. Lee [Datareview in this book: 5.4 Thermal diffusivity of LiNbO_3]

5.3 Specific heat properties of LiNbO₃

T.H. Lin and S.H. Lee; updated by D. Craig

August 2001

A INTRODUCTION

When a quantity of heat H is added to a piece of lithium niobate of mass ' m ' so that its temperature is changed by $T_2 - T_1$, then the mean heat capacity is given by

$$c(\text{mean}) = \frac{H}{T_2 - T_1} \quad (1)$$

EQN (1) can be divided by the mass ' m ' to obtain a mass-independent quantity,

$$C = \frac{c(\text{mean})}{m} = \frac{H}{m(T_2 - T_1)} \quad (2)$$

The limiting value of the above ratio as the temperature is changed by ∂T is defined as the true specific heat

$$C = \frac{1}{m} \frac{\partial' H}{\partial T} \quad (3)$$

where $\partial' H$ is used instead of ∂H to indicate that the value is not an exact differential [1]. Usually the measurement of the specific heat is done either under constant pressure C_p or constant volume C_v . Specific heat measurements on materials with low vapour pressure, such as lithium niobate, can be considered as being done under constant pressure. Classical physics predicts a value of 24.9 J/gram-atom/°C for the heat capacity at constant volume [2]. The theoretical value of C_p can then be obtained from the relationship [3]

$$C_p = C_v + (5 \pm 1) \times 10^{-3} \times (C_p)^2 (T/T_m) \quad (4)$$

with melting point T_m at 1242°C, which makes C_p differ from C_v by a variation of 0.25% at room temperature to 12.5% at the melting point. To obtain the specific heat of lithium niobate, the heat capacity can be divided by 29.57 g/gram-atom and 4.186 J/cal, which reaches a value of C_v of 0.202 cal/g/°C. Basically, as the specific heat depends on the number of atoms per unit weight, we can expect 4% variation in C_p due to different solid composition. However, in none of the reported data is the solid composition of the sample specified.

B EXPERIMENTAL RESULTS

Zhdanova et al [4] presented their data in terms of heat capacity, which can easily be transformed to specific heat using EQN (2), i.e. by dividing EQN (2) by molecular weight 147.85 g/mole. The instrument used is an adiabatic specific heat calorimeter. The measurements were made from -193°C

5.3 Specific heat properties of LiNbO_3

to 117°C, as shown in TABLE 1 and FIGURE 1. This report covers the widest range of temperatures for the heat capacity measurement of lithium niobate to date.

TABLE 1 Specific heat of lithium niobate measured with adiabatic calorimeter [4].
Solid composition is not specified in the original reference.

T (°C)	C _p (cal/g/°C)	T (°C)	C _p (cal/g/°C)
-193	0.032	-33	0.138
-183	0.041	-23	0.141
-173	0.052	-13	0.144
-163	0.060	-3	0.148
-153	0.068	7	0.150
-143	0.076	17	0.153
-133	0.083	27	0.155
-123	0.091	37	0.157
-113	0.097	47	0.159
-103	0.104	57	0.161
-93	0.110	67	0.163
-83	0.117	77	0.165
-73	0.122	87	0.167
-63	0.127	97	0.168
-53	0.131	107	0.169
-43	0.135	117	0.171

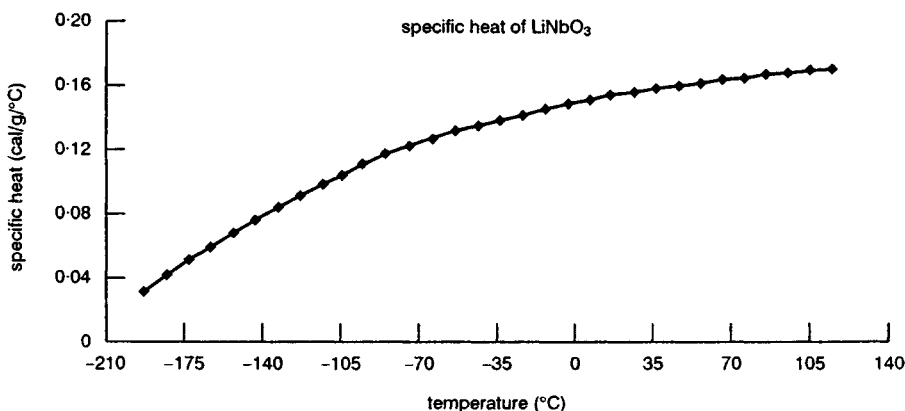


FIGURE 1 Specific heat of lithium niobate measured with adiabatic calorimeter [4].

Beerman [5] measured his data using the thermoelectric cooling/heating facility at Goddard Space Flight Center. Measurements at -25°C and 100°C are reported with the units of $\text{J}/\text{cm}^3/\text{°C}$. They are divided by 4.2 J/cal and 4.64 g/cm³ for conversion into cal/g/°C, which are shown in TABLE 2. Lin et al [6] also reported specific heat data of congruent lithium niobate at room temperature by using water as a calorimeter in an adiabatic system. The value reported is approximately 0.1 cal/g/°C at 25°C.

5.3 Specific heat properties of LiNbO_3

TABLE 2 Specific heat of lithium niobate measured with thermo-electric cooling/heating facility at Goddard Space Flight Center [5]. Solid composition is not specified in the original reference.

T (°C)	C _p (cal/g/°C)
-25	0.154
100	0.14

Investigation of the physical properties of LiNbO_3 crystals doped with metal impurities is also desirable because of the extensive use of these crystals. Vasil'ev et al [7] reported data on specific heat of 0.1 at.% manganese-doped LiNbO_3 , which is shown in TABLE 3 and FIGURE 2. The measurements were made by the calorimeter method employing a UNTO-26 system [7]. The data were taken from 38°C to 82°C. Note that there is an anomaly at 63.9°C, which is attributed to a possible phase transition initiated by the introduction of the metal impurity. In general, specific heat depends on the

TABLE 3 Temperature dependence of the specific heat of $\text{LiNbO}_3 + 0.1$ at.% Mn single crystals under (1) short-circuit C_p(E) and (2) open-circuit C_p(D) conditions [7].

T (°C)	C _p (E) (cal/g/°C)	C _p (D) (cal/g/°C)	T (°C)	C _p (E) (cal/g/°C)	C _p (D) (cal/g/°C)
37.2	0.125	0.095	62.5	0.303	0.265
41.3	-	0.110	63.1	0.378	0.275
41.8	0.136	-	63.6	0.468	0.280
44.3	-	0.120	63.9	0.578	0.283
45.5	0.147	-	64.1	0.378	0.278
48.0	-	0.136	64.5	0.232	0.267
49.2	0.158	-	65.3	0.196	0.239
50.5	-	0.147	66.7	-	0.196
52.0	0.163	-	67.6	0.220	-
53.75	-	0.161	69.2	0.242	0.214
55.5	0.163	-	73.1	0.250	-
57.0	-	0.169	74.0	-	0.223
58.5	0.167	-	76.1	0.252	-
59.4	-	0.191	77.2	-	0.228
61.0	0.191	0.225	80.9	-	0.232
62.0	0.220	0.254	81.1	0.255	-

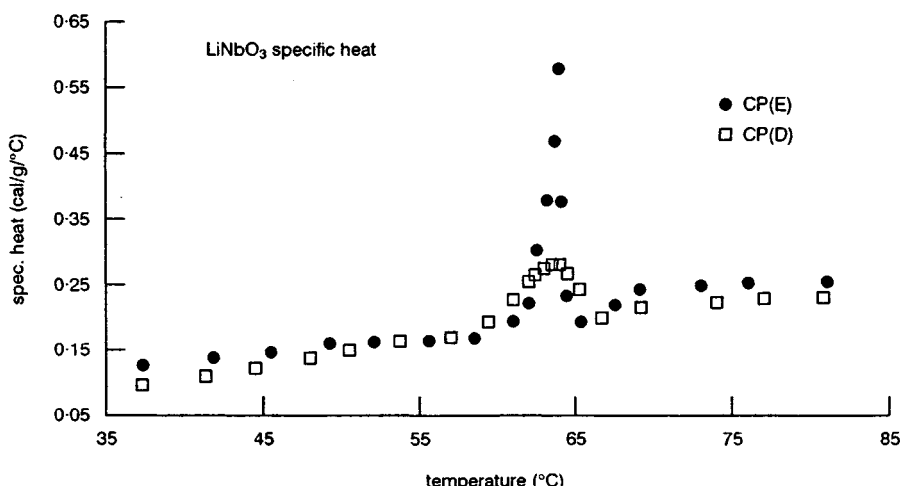


FIGURE 2 Temperature dependence of the specific heat of $\text{LiNbO}_3 + 0.1$ at.% Mn single crystals under (1) short-circuit C_p(E) and (2) open-circuit C_p(D) conditions [7].

5.3 Specific heat properties of LiNbO_3

number of atoms per unit weight. The weight of 0.1 at.% Mn-doped single crystal LiNbO_3 will be different from that of the pure LiNbO_3 by 0.594%, which is negligible. Therefore, the data on the manganese-modified lithium niobate should be comparable with the pure material. In fact, the data in TABLE 3 are in good agreement with those in TABLE 1 at temperatures below 63.9°C. The fact that the specific heat is higher in doped material above 63.9°C may be due to a different phase or increment with respect to temperature.

Due to technical difficulties of measurement at temperatures above 120°C, data reported are below this temperature. Brice [3] suggested that electrons may contribute to the specific heat at temperatures higher than the Debye temperature. Based on the measurements done by Zhdanova et al [4], the Debye temperature lies between 27°C and 327°C. In ionic lithium niobate crystals, the electronic contribution to the specific heat can be described by a formula [3],

$$C_p = 0.202 \pm 0.004 + (0.000034 \pm 0.000014)T \quad (5)$$

where the ± 0.004 comes from the variation of the average atomic weight of different solid compositions.

This formula can be used in the future to verify the electronic contribution of the specific heat of lithium niobate at higher temperature. One important application of this physical property is to infrared detectors made from pyroelectric materials [5]. The specific heat can also be used in calculating thermal diffusivity, which is another important thermal property. Explanation of this calculation is given in another Datareview [8].

C CONCLUSION

Heat capacity data are presented for LiNbO_3 over the temperature range -193 to +117°C. Data are also presented for Mn-doped material from 38 to 82°C. These data are useful when the material is used in pyroelectric infrared detectors.

REFERENCES

- [1] Y.S. Touloukian, E.H. Buyco [in *Thermal Properties of Matter, vol.5 Specific Heat, Nonmetallic Solids* (IFI/Plenum, New York-Washington, 1970) p.3a]
- [2] C. Kittel [*Introduction to Solid State Physics* (John Wiley and Sons Inc., New York, 1976) p.111]
- [3] J.C. Brice [*The Growth of Crystals from Liquid* (North Holland, Amsterdam, 1973) p.66-7]
- [4] V.V. Zhdanova, V.P. Klyuev, V.V. Lemanov, I.A. Smirnov, V.V. Tikhonov [*Sov. Phys.-Solid State (USA)* vol.10 (1968) p.1360]
- [5] H.P. Beerman [*Infrared Phys. (UK)* vol.15 no.3 (1975) p.225]
- [6] T.H. Lin, D. Edwards, R.E. Reedy, K. Das, W. McGinnis, S.H. Lee [*Ferroelectrics (UK)* vol.77 (1988) p.153-60]
- [7] V.E. Vasil'ev, B.B. Ped'ko, V.M. Rudyak [*Sov. Phys.-Solid State (USA)* vol.29 no.8 (1987) p.1474]
- [8] T.H. Lin, S.H. Lee [Datareview in this book: 5.4 Thermal diffusivity of lithium niobate]

5.4 Thermal diffusivity of LiNbO₃

T.H. Lin and S.H. Lee; updated by D. Craig

August 2001

A INTRODUCTION

Consider that heat flows through lithium niobate in the x direction. The differential form for thermal conductivity is

$$\frac{Q}{A} = k \frac{\partial T}{\partial x} \quad (1)$$

When the thermal properties are independent of temperature, and the temperature varies with time t, EQN (1) can be differentiated with respect to x to obtain

$$\rho C_p \frac{\partial T}{\partial t} = k \frac{\partial}{\partial x} \left(\frac{\partial T}{\partial x} \right) \quad (2)$$

or

$$\frac{\partial T}{\partial t} = D \frac{\partial}{\partial x} \left(\frac{\partial T}{\partial x} \right) \quad (3)$$

where ρ is the density of the material, C_p is the specific heat at constant pressure, and D (equivalent to $k/(\rho C_p)$), is called the thermal diffusivity [1]. If heat is generated in the lithium niobate at a rate G per unit time per unit volume, EQN (3) is replaced by

$$\frac{\partial T}{\partial t} = D \frac{\partial}{\partial x} \left(\frac{\partial T}{\partial x} \right) + G \quad (4)$$

The dimension of 'D' is (length)²/time, which is the dimension of a diffusion constant. The quantity 'D' determines how fast the temperature redistributes in a system when there is a thermal disturbance.

B EXPERIMENTAL RESULTS

All the reported data about thermal diffusivity of lithium niobate are recent because of its increasing usefulness to advanced technology such as non-linear optics and laser processing of silicon integrated on lithium niobate. Morgan et al [2] used two-beam interferometry to measure this thermal property. An instrument called a rear-shear interferometer (RSI) uses front and rear reflections off the test crystal. Lithium niobate is inserted into the RSI and the crystal heated via its absorption of an input pulse from a focused CO₂ laser at 10.6 μm. As the heat diffuses outward in the crystal, the refractive index increases and the crystal expands. The resulting small changes in optical path can be monitored interferometrically in real time, and the fringe data can be analysed by computer to determine the thermal diffusivity. The data were measured from room temperature to 500°C, which covers the widest range of thermal diffusivity for lithium niobate (see TABLE 1). Lin et al [3] used the Forbes' bar

5.4 Thermal diffusivity of LiNbO_3

method and the modified Angstrom method to measure thermal diffusivity. These measurements are compared with a value calculated from thermal conductivity and specific heat to verify the order of magnitude [3]. In the Forbes' bar method [4], one end of the lithium niobate sample is clamped to a hot chuck at a constant temperature and the other end is monitored by a thermocouple and a chart recorder. Using the transient data from the chart recorder and the definition of thermal diffusivity, i.e.

$$D \text{ is equivalent to } \frac{k}{(\rho C_p)} \quad (5)$$

the thermal diffusivity can be calculated (see TABLE 2). In the modified Angstrom method [5], a sinusoidal heat wave generator with frequency Ω is attached to one end of the sample, and two thermocouples with separation l are attached to the sample. The ratio of the two amplitudes of the temperatures (Φ) and the phase difference of the two sinusoidal variations (δ) are read from the chart recorder connected to the thermocouples. Thermal diffusivity can then be determined from

$$D = \frac{\Omega l * 2}{\delta \ln(\Phi)} \quad (6)$$

TABLE 1 Thermal diffusivity of congruent lithium niobate obtained with optical interferometry [2].

T (°C)	D ($10^{-3} \text{ cm}^2/\text{s}$)
20	14.00
125	10.10
150	7.70
375	6.50
500	5.95

TABLE 2 Thermal diffusivity of congruent lithium niobate measured with the modified Angstrom method [3].

T (°C)	D ($10^{-3} \text{ cm}^2/\text{s}^*$)
30	7.5
80	9.0
200	7.5
375	6.50
305	8.6

(*Data reported with error bar of $\pm 10\%$.)

The temperature range reported is from room temperature to 300°C, as shown in TABLE 3. The fourth method utilises the definition in EQN (5) with the existing specific heat and thermal conductivity data for lithium niobate to calculate thermal diffusivity. For example, at 117°C, $k \sim 1.0 \times 10^{-2}$ cal/cm/s/°C (see Table 1 in [12]), $C_p = 0.171 \text{ cal/g/}^\circ\text{C}$ (see Table 1 in [13]), and $\rho = 4.64 \text{ g/cm}^3$. These values lead to a calculated thermal diffusivity value of $12.6 \times 10^{-3} \text{ cm}^2/\text{s}$. The data calculated from thermal conductivity and specific heat are listed in TABLE 4 [6]. The data presented in TABLES 1-4 are in reasonable agreement ($\pm 20\%$) with each other (see FIGURE 1). The differences among the data obtained from the three measurement techniques may come from the possible errors discussed in [2] and [3].

5.4 Thermal diffusivity of LiNbO_3

TABLE 3 Thermal diffusivity of congruent lithium niobate with Forbes' bar method [3].

T (°C)	D ($10^{-3} \text{ cm}^2/\text{s}^*$)
67	8.1
78	9.5
115	9.2
140	9.3
165	9.7
200	10.8

(*Data reported with error bar of $\pm 10\%$.)

TABLE 4 Thermal diffusivity of lithium niobate (solid composition is not specified in the original reference) calculated from the existing thermal conductivity and specific heat data [6].

T (°C)	D ($10^{-3} \text{ cm}^2/\text{s}^*$)
-187	189.2
-173	122.3
-163	88.0
-143	55.3
-113	36.7
-73	23.0
117	12.0

(*Data reported with error bar of $\pm 10\%$.)

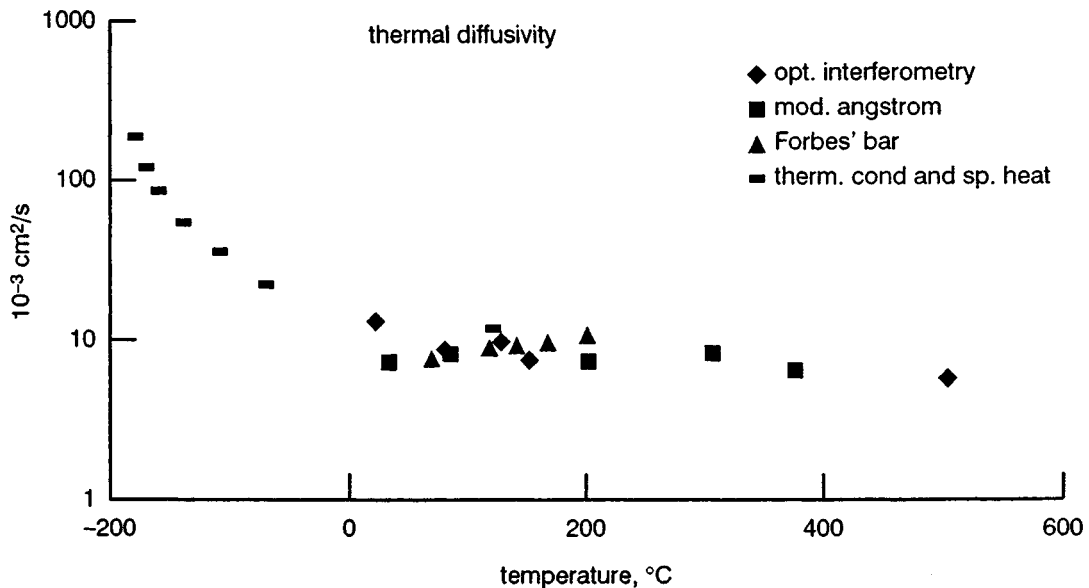


FIGURE 1 Comparison of data from TABLES 1-4.

The optical interferometer has a number of drawbacks. First, the logarithmic scale used as a part of the regression procedure resulted in poorer precision near room temperature. Second, the noise in the optics may cause ambiguous readings. Possible errors in the Forbes' bar method are the heat loss to the ambient through air conduction which may cause serious systematic errors at high temperature and the measurement of the sample length due to the epoxy used to attach the thermocouples. Several

5.4 Thermal diffusivity of LiNbO_3

sources of error may occur in the modified Angstrom method. First, the length of the sample may not be sufficient, and the heat wave reflects at the end of the sample. The second source of error is in measuring the phase difference. The amplitude of the temperature variation of the thermocouple farther away from the heating source is small and slightly distorted, which enhances the uncertainty in finding the exact location of the peak. Finally, the estimation of the distance between the two thermocouples may have an error due to the area of the epoxy used to attach them.

One of the important applications of thermal diffusivity is related to second-harmonic generation [2]. Optical absorption from a laser causes heating and a temperature gradient in second-harmonic crystals. The resulting changes in the temperature and beam profile are detrimental to the phase-matching condition. Thermal diffusivity helps to establish a guideline on the limit on the power through the crystal. Knowledge of thermal diffusivity is also useful in simulating the temperature distribution in the structure of silicon on electro-optic materials [7]. Estimates of the temperature gradient in the structure and of the highest temperature experienced by the electro-optic material during laser treatment helps to prevent material cracking or surface damage. Laser crystallisation of silicon on lithium tantalate [8] and PLZT [9] have been reported. Laser crystallisation of silicon on lithium niobate has been studied by Chen [10] for the implementation of the integrated optics spectrum analyser proposed by Wu [11].

C CONCLUSION

Thermal diffusivity values for LiNbO_3 over the temperature range 20 to 500°C, measured by a variety of techniques, are given. These data are useful in second-harmonic generation studies and in establishing the temperature limits which can be used in device fabrication and applications.

REFERENCES

- [1] Y.S. Touloukian, R.W. Powell, C.Y. Ha, M.C. Nicalarow [in *Thermal Properties of Materials, vol.10 Thermal Diffusivity* (IFI/Plenum, New York and Washington, 1973) p.3a]
- [2] R.A. Morgan, K.I. Kang, C.C. Hsu, C.L. Koliopoulos, N. Peyhambarian [*Appl. Opt. (USA)* vol.26 (1987) p.5266]
- [3] T.H. Lin, D. Edwards, R.E. Reedy, K. Das, W. McGinnis, S.H. Lee [*Ferroelectrics (UK)* vol.77 (1988) p.153-60]
- [4] Y.S. Touloukian, R.W. Powell, C.Y. Ha, M.C. Nicalarow [in *Thermal Properties of Materials, vol.10 Thermal Diffusivity* (IFI/Plenum, New York and Washington, 1973) p.16a]
- [5] N. Savvides, W. Murray [*J. Phys. E (UK)* vol.11 no.9 (1978) p.941]
- [6] V.V. Zhdanova, V.P. Klyuev, V.V. Lemanov, I.A. Smirnov, V.V. Tikhonov [*Sov. Phys.-Solid State (USA)* vol.10 (1968) p.1360]
- [7] M.L. Burgener, R.E. Reedy [*J. Appl. Phys. (USA)* vol.53 no.6 (1982) p.4357-63]
- [8] R.E. Reedy, S.H. Lee [*10th Int. Opt. Computing Conf. (Cambridge, 1983)* p.MA6-8]
- [9] T.H. Lin, M.L. Burgener, S.C. Esener, S.H. Lee [*Mater. Res. Soc. Symp. Proc. (USA)* vol.74 (1987) p.135]
- [10] Sun-Ming Chen [*Laser Recrystallization of Silicon on Lithium Niobate*, Ph.D. dissertation (University of Cincinnati, 1987)]
- [11] R. Wangin Wu [*Optical Wave Guide Detection: Photodetector Array Formed on the Wave Guide Utilizing Laser Recrystallization Silicon-on-Insulator Technology*, Ph.D. dissertation (University of Cincinnati, 1984) p.5]
- [12] T.H. Lin, S.H. Lee [Datareview in this book: 5.2 Thermal conductivity properties of LiNbO_3]
- [13] T.H. Lin, S.H. Lee [Datareview in this book: 5.3 Specific heat properties of LiNbO_3]

CHAPTER 6

ELECTRICAL AND PYROELECTRIC PROPERTIES

- 6.1 Electrical conductivity of LiNbO₃**
- 6.2 Pyroelectric coefficients of LiNbO₃**

6.1 Electrical conductivity of LiNbO₃

L. Kovacs and K. Polgar; updated by C. Florea

February 2002

A INTRODUCTION

The investigation of the electrical conduction processes in insulating materials plays an important role in the understanding of both intrinsic and extrinsic defect formation and migration mechanisms. In non-stoichiometric lithium niobate the electrical conductivity measurements yield valuable information about the defect structure of the crystal.

The conductivity of LiNbO₃ has been studied in a wide temperature range that can be divided into three parts according to the different dominant conduction mechanisms. At low temperatures (below about 400 K) a hopping mechanism of small electrons or small polarons is assumed. At temperatures between 400 K and 1000 K the conduction is governed by mobile protons, while in the high temperature region (above 1000 K) the conduction is intrinsic. Similar divisions can be found in other reviews [1,2].

B CONDUCTIVITY BELOW 350 - 400 K

The electrical conductivity of lithium niobate at room temperature was found to be about 10⁻¹⁸ (mΩ cm)⁻¹ as estimated from the thermal decay of a hologram written into the crystal [3]. The thermally activated ionic transport obeys an Arrhenius-type dependence on the temperature, the conductivity being given by

$$\sigma = \sigma_0 \exp\left(-\frac{E_a}{k_B T}\right)$$

where E_a is the activation energy and σ₀ = enu₀, where n is the ion density, u₀ the ion mobility and e the elementary charge. The rather low value of σ₀ makes it very difficult to measure the DC (direct current) conductivity in this temperature range. Moreover, the displacement current resulting from the pyroelectric effect during the random temperature fluctuations of the sample is comparable with or exceeds the conduction current [4]. Therefore the electrical conductivity of LiNbO₃ near room temperature is usually measured by indirect methods as listed in [5].

The kinetics of charge transport is studied in this temperature range by methods involving, for example, optically induced birefringence [6] and external electric fields influencing the optical properties of the crystal [7]. A diffraction method can also be used that measures the thermal decay of a grating created by the photorefractive effect [3]. Direct compensation measurements of the pyroelectric field screened by free charges were reported in [5]. TABLE 1 contains the activation energy of the electrical conductivity of LiNbO₃ determined using the methods mentioned above.

The results obtained confirmed the hypothesis of electron hopping as the conduction mechanism in lithium niobate below or near room temperature [5,8]. The value of the activation energy of the electrical conductivity was found to be consistent with the small polaron model in lithium niobate [9]. Mobility measurements on reduced LiNbO₃ also support the theory of hopping motion of small polarons [10].

6.1 Electrical conductivity of LiNbO_3

TABLE 1 Activation energy (E) of the electrical conductivity of lithium niobate near room temperature.

	E (eV)	Ref
t < 60°C	0.49	[5]
t < 100°C	0.20	[6]
	0.1 - 0.3	[7]
t < 60°C	0.36	[11]

The AC (alternating current) conductivity has also been measured in wide frequency (10^2 - 10^7 Hz) and temperature (77 - 790 K) ranges [12,13]. In the low temperature range, below about 400 K, a strong frequency dependence was observed, $\sigma \propto \omega^s$ (σ is the conductivity, ω the angular frequency) with the value of s being determined as approximately 1 [12] or 0.8 [13]. The frequency dependence disappeared with increasing temperature. The results were interpreted as the polaron conduction mechanism [11] and random hopping of electrons [13].

In the 300 - 400 K range lithium niobate crystals doped with B, Zn or Gd have also been studied [14] and an anomalous increase in the conductivity at ~ 370 K has been reported for different frequencies. The effect is more pronounced in the Gd-doped samples.

C CONDUCTIVITY BETWEEN 400 AND 1000 K

The electrical conductivity in this range can easily be measured directly by both DC and AC methods. A number of papers present electrical conductivity data in pure and doped LiNbO_3 [3-5,12-28]. The authors agree on the extrinsic character of the conduction; nevertheless, only a few papers give an interpretation of the mechanism by determining the charge carriers [19,26,29,30]. The electrical conductivity in the presence of static fields up to 15 kV cm $^{-1}$ was also measured along with the temperature dependence of the dark conductivity under the same conditions for the 300 - 650 K temperature range [31].

The electrical conductivity of pure and doped LiNbO_3 was usually measured along the crystallographic c axis. In some cases the electrical conductivity was found to be identical for directions parallel and perpendicular to the c axis, e.g. [23]. In most cases the authors do not mention the composition of the samples.

The values of the electrical conductivity presented by different authors for as-grown LiNbO_3 fall into the relatively narrow range of 10^{-6} - 10^{-5} (m Ω m) $^{-1}$ at 400°C. Neither the Mg and transitional metal dopants nor compositional changes influence drastically the electrical conductivity of lithium niobate. In the 400 - 1000 K temperature range $\log(\sigma)$ gives a straight line versus the reciprocal temperature. The values of the activation energy calculated from the Arrhenius equation fall in the 1 - 1.5 eV range, as seen in TABLE 2. The scattering of the data shown in TABLE 2 is most probably due partly to the different crystal samples and to the inaccuracy of the measurements.

A detailed study of the electrical conductivity of LiNbO_3 crystals of different stoichiometries was performed [19]. Annealing samples at high temperatures in water vapour, it was found that the conductivity is clearly proportional to the hydroxyl content of the crystal. The 1.12 ± 0.03 eV and the 1.08 ± 0.02 eV activation energies (measured on samples grown from melts of different Li/Nb ratios) were attributed to OH $^-$ ions substituting for oxygen ions and to OH $^-$ interstitial ions, respectively.

The dependence of the activation energy on the starting material and the dependence on the stoichiometry of the crystal were observed by others as well [23,24]. It was shown that the activation energy decreases with increasing Li/Nb ratio [24], confirming earlier results [19]. Chemically reduced LiNbO_3 has also been studied and enhanced electrical conductivity is reported [32].

6.1 Electrical conductivity of LiNbO_3

TABLE 2 Activation energy (E) of the electrical conductivity of pure and doped lithium niobate between 330 K and 1000 K ('-' represents undoped material).

Dopant	Temperature	E (eV)	Ref
-, Mg, Cu, Mo, Mn, W	80 - 250°C	1.00 - 1.41	[4]
-	>90°C	1.26	[5]
-	>60°C	1.0	[11]
-, Cr, Co, Fe	130 - 310°C	1.1	[3]
-	<600°C	1.5	[15]
-, Cr, Ni	200 - 400°C	1.4	[16]
-	<700°C	1.06 - 1.23	[17]
Li deficient	20 - 400°C	1.31	[18]
Excess Li	20 - 400°C	1.1	[18]
-	400 - 800°C	1.08, 1.12	[19]
-	620 - 790°C	1.15	[20]
Fe	>400°C	1.1	[21]
-, Mg, Mg + Fe	190 - 315°C	1.21	[22]
-, Fe, Mo, Cr	230 - 560°C	1.13 - 1.26	[23]
-, Mg	300 - 500°C	1.10 - 1.32	[24-26]
H	350 - 700°C	1.08	[30]

The combined effect of Mg and OH ions on the electrical conductivity has also been measured between 340 and 460°C [25,26]. At 400°C the electrical conductivity was found to be linearly proportional to the OH absorption of the 'as grown' samples confirming earlier results [19]. In LiNbO_3 containing Mg, however, a non-linear behaviour of the electrical conductivity and of the activation energy with respect to the doping level has been reported [26]. This non-linearity may be a consequence of the formation of Mg-OH complexes in these crystals. The data of [26] are shown in TABLE 3.

TABLE 3 Electrical conductivity of Mg-doped lithium niobate (400°C) [26].

Li/Nb ratio in melt	Mg conc. (mol%)	Activation energy (eV)	Conductivity ($10^{-6} (\text{m}\Omega \text{ m})^{-1}$)
0.945	undoped	1.16	3.0
	1	1.20	2.7
	2.7	1.22	2.5
	5.4	1.24	2.2
1.1	undoped	1.10	2.8
	2	1.14	2.7
	3	1.19	2.0
	3.5	1.31	1.1
	4	1.30	1.4
	1.2	2.7	1.1

Additional dark conductivity measurements for various dopants (Ce, Co, Cr, Cu, Fe, Mn, Ni, Rh, Tb) and co-dopants (Fe:Ce, Fe:Mn) in lithium niobate were also reported [27].

The thermal fixing of holograms is realised by ionic migration between 100 and 200°C. The activation energy for this ion migration was found to be about 1.1 eV [33]. It was demonstrated, by spatially resolved absorption spectroscopy, that in the thermal fixing process the protons are the mobile ions in $\text{LiNbO}_3:\text{Fe}$ crystals [29]. It was also shown [34] that the protons are the only mobile ions in the LiNbO_3 under the experimental conditions applied (600°C, 100 V cm⁻¹), whereas lithium ions do not move under these conditions.

The case of Fe: LiNbO_3 is particularly important due to the interest in archival holographic data storage [34]. The dark conductivity for Fe: LiNbO_3 planar waveguides was found to be in the 8×10^{-17}

6.1 Electrical conductivity of LiNbO_3

- $5 \times 10^{-12} (\Omega \text{ cm})^{-1}$ range for iron doping levels in the range $0 - 10 \times 10^{20} \text{ ions cm}^{-3}$ [28]. A long lifetime of the fixed space-charge hologram is required for practical applications. The ionic hologram lifetime in dehydrated LiNbO_3 crystals doped with about 0.01 wt% Fe was extrapolated to be as long as ~ 2 years at room temperature (24°C) [34]. Additionally, preliminary research seems to indicate that actually the use of copper doping instead of iron doping may be more advantageous due to the much smaller dark conductivity observed in the case of copper-doped samples when compared with iron-doped samples [28].

The number of protons incorporated into the air-grown crystal was estimated to be about $10^{18} \text{ ions cm}^{-3}$ [35] or even $3 \times 10^{19} \text{ ions cm}^{-3}$ [36]. The OH concentration, however, is higher by at least one order of magnitude in crystals annealed in water vapour atmosphere at elevated temperatures [19].

Li^+ ionic conductivity of LiNbO_3 has also been observed in the $50 - 300^\circ\text{C}$ temperature range using metallic lithium as anode in vacuum or argon atmosphere [37]. The DC conductivity of LiNbO_3 was found to be more than two orders of magnitude higher than for passive contacts. Activation energies of 0.5 eV and 0.7 eV were determined for directions perpendicular and parallel to the c axis, respectively.

D CONDUCTIVITY ABOVE 1000 K

The first high temperature electrical conductivity measurements on lithium niobate crystals were performed in 1968 [1]. The slope of the plot of $\log(\sigma)$ versus T^{-1} (T being the temperature) at constant O_2 pressure yielded an activation energy of 2.15 eV. Additional data on the activation energy are provided in TABLE 4. The dependence $\sigma \propto p^{1/4}$ (p is the O_2 pressure) was attributed to singly ionised oxygen vacancies. Evidence was found for a considerable fraction of ionic conductivity.

TABLE 4 Activation energy (E) of the electrical conductivity of lithium niobate above 1000 K.

E (eV)	2.15	2.12	2.05 - 2.34	2.5
Ref	[15]	[38]	[17]	[39]

A detailed study on electrical conductivity [38] confirmed the early results. The study showed that the electrical conductivity is completely ionic at 1 atm of oxygen pressure and 1000 K, while for low partial pressure the electrical conductivity (at 1000 K) becomes completely electronic. Thermoelectric power measurements indicated that LiNbO_3 is n-type. At 1 atm of oxygen pressure the ionic conductivity is cationic and most probably due to lithium ions, a conclusion confirmed by a different study [17]. An additional study [40] concluded from the comparison of lithium ion diffusion and electrical conductivity measurements that the ionic conductivity is determined solely by lithium ions.

The electrical conductivity was also studied in LiNbO_3 as a function of temperature, oxygen partial pressure and Li/Nb ratio [39]. The conductivity was found to be dependent on the Li/Nb ratio in the low oxygen pressure region as well as in the region of ionic conduction at high oxygen pressure. The conductivity decreased with increasing Li_2O content in both regions in contrast to the results previously reported [38]. The results are consistent with the electron concentration being approximately proportional to the Li_2O deficiency at a given oxygen pressure and temperature. The increase in ionic conductivity with increasing Li_2O deficiency indicates that it is likely that the lithium vacancies are the mobile species [41]. In addition it was shown that the oxygen vacancies are not the major defects in LiNbO_3 [39,41]. Further experiments are needed to decide whether the Li ions or Li vacancies are the charge carriers at high oxygen pressure.

REFERENCES

- [1] A. Rauber [*Curr. Top. Mater. Sci. (Netherlands)* vol.1 (1978) p.481]
- [2] Yu.S. Kuzminov [*Electro-Optical and Nonlinear-Optical Lithium Niobate Crystal* (Izd. Nauka, Moscow, 1987)]
- [3] D.L. Staebler, J.J. Amodei [*Ferroelectrics (UK)* vol.3 (1972) p.107]
- [4] A.A. Blistanov, E.V. Makarevskaya, V.V. Geras'kin, O. Kamalov, M.M. Koblova [*Fiz. Tverd. Tela (USSR)* vol.20 (1978) p.2575; *Sov. Phys.-Solid State (USA)* vol.20 (1978) p.1489]
- [5] A.A. Blistanov, V.V. Geras'kin, A.V. Stepanova, M.V. Puchkova, N.G. Sorokin [*Sov. Phys.-Solid State (USA)* vol.26 (1984) p.684]
- [6] V.A. Pashkov, N.M. Solov'eva, N.G. Angert [*Sov. Phys.-Solid State (USA)* vol.21 (1979) p.54]
- [7] A.A. Blistanov, V.V. Geras'kin, S.V. Kudasova [*Sov. Phys.-Crystallogr. (USA)* vol.26 (1981) p.202]
- [8] I.Sh. Akhmadullin, V.A.K. Golenischchev, S.A. Migachev, S.P. Mironov [*Bull. Russ. Acad. Sci., Phys. (USA)* vol.62 (1998) p.1297]
- [9] A. Zylbersztein [*Appl. Phys. Lett. (USA)* vol.29 (1976) p.778]
- [10] P. Nagels [in *The Hall Effect and Its Applications* Eds C.L. Chien, C.R. Wedlake (Plenum, USA, 1980)]
- [11] A.A. Blistanov, V.V. Geras'kin, A.V. Stepanova [*Sov. Phys.-Solid State (USA)* vol.28 (1986) p.166]
- [12] T.M. Glushkova, D.F. Kiselev, M.M. Firsova [*Fiz. Tverd. Tela (USSR)* vol.13 (1971) p.2753]
- [13] A. Mansingh, A. Dhar [*J. Phys. D (UK)* vol.18 (1985) p.2059]
- [14] M.N. Palatnikov, V.A. Sandler, N.V. Sidorov, A.V. Gur'yanov, V.T. Kalinnikov [*Phys. Solid State (Russia)* vol.42 (2000) p.1499]
- [15] G. Bergmann [*Solid State Commun. (USA)* vol.6 (1968) p.77]
- [16] M.B. Roitberg, V.K. Novik, N.D. Gavrilova [*Kristallografiya (USSR)* vol.14 (1969) p.938]
- [17] L.I. Ivleva, Yu.S. Kuzminov, V.V. Osiko [*Izv. Akad. Nauk Neorg. Mater. (USSR)* vol.7 (1971) p.1377]
- [18] W. Bollman, M. Gernand [*Phys. Status Solidi A (Germany)* vol.9 (1972) p.301]
- [19] W. Bollman, H.-J. Stohr [*Phys. Status Solidi A (Germany)* vol.39 (1977) p.477]
- [20] S.N. Kaul, K. Singh [*Solid State Commun. (USA)* vol.26 (1978) p.365]
- [21] I.B. Barkan, I.M. Baskin, M.V. Entin [*Phys. Status Solidi A (Germany)* vol.59 (1980) p.K97]
- [22] R. Gerson, J.F. Kirchhoff, L.E. Halliburton, D.A. Bryan [*J. Appl. Phys. (USA)* vol.60 (1986) p.3553]
- [23] V. Trnovcova, L. Simoncic, E. Mariani [*Phys. & Appl. Bratislava (Czechoslovakia)* vol.9 (1982) p.195]
- [24] L. Kovacs [PhD Thesis, R. Eotvos University, Hungary (1986)]
- [25] K. Polgar, L. Kovacs, I. Foldvari, I. Cravero [*Solid State Commun. (USA)* vol.59 (1986) p.375]
- [26] L. Kovacs, I. Foldvari, K. Polgar [*Acta Phys. Hung. (Hungary)* vol.61 (1987) p.223]
- [27] D.K. McMillen et al [*Proc. SPIE - Int. Soc. Opt. Eng. (USA)* vol.3137 (1997) p.39]
- [28] D. Kip, J. Hukriede, E. Kräitzig [*Phys. Status Solidi A (Germany)* vol.168 (1998) p.R3]
- [29] H. Vormann, G. Weber, S. Kapphan, E. Kräitzig [*Solid State Commun. (USA)* vol.40 (1981) p.543]
- [30] N. Schmidt, K. Betzler, M. Grabs, S. Kapphan, F. Klose [*J. Appl. Phys. (USA)* vol.65 (1989) p.1253]
- [31] L.K. Bunina, E.P. Guenok, A.Yu. Kudzin, G.Kh. Sokolyanskii, A.S. Yudin [*Sov. Phys.-Solid State (USA)* vol.33 (1991) p.1387]
- [32] E.M. Standifer, D.H. Jundt, R.G. Norwood, P.F. Bordui [*Proc. IEEE Inter. Freq. Control Symp.* (1998) p.470]
- [33] J.J. Amodei, D.L. Staebler [*RCA Rev. (USA)* vol.33 (1972) p.71]

6.1 Electrical conductivity of LiNbO₃

- [34] S. Orlov, A. Yariv [*Conf. on Lasers and Electro-Optics* (Opt. Soc. America, 1996) paper CTuA3, p.71]
- [35] O.W. Johnson, J. DeFord, J.W. Shaner [*J. Appl. Phys. (USA)* vol.44 (1973) p.3008]
- [36] W. Bollman, K. Schlothauer, J. Zogal [*Krist. Tech. (Germany)* vol.11 (1976) p.1327]
- [37] H. Franke [*Phys. Status Solidi A (Germany)* vol.83 (1984) p.K73]
- [38] P.J. Jorgensen, R.W. Bartlett [*J. Phys. Chem. Solids (UK)* vol.30 (1969) p.2639]
- [39] Y. Limb, K.W. Cheng, D.M. Smyth [*Ferroelectrics (UK)* vol.38 (1981) p.813]
- [40] V.B. Ptashnik, T.Yu. Dunaeva, I.V. Myasnikov [*Izv. Akad. Nauk Neorg. Mater. (USSR)* vol.21 (1985) p.2076]
- [41] D.M. Smyth [*Ferroelectrics (UK)* vol.50 (1983) p.419]

6.2 Pyroelectric coefficients of LiNbO₃

R.S. Weis

This Datareview appeared in *Properties of Lithium Niobate* (INSPEC, IEE, London, UK, 1989) and is reproduced here for the reader's convenience.

Since lithium niobate is a pyroelectric solid, the thermal stability of optical devices fabricated using it is largely determined by the pyroelectric effect.

A pyroelectric solid exhibits a change in spontaneous polarisation as a function of temperature. The relationship between the change in temperature, ΔT , and the change in spontaneous polarisation vector, ΔP , is linear and can be written as $\Delta P = p\Delta T$ where p is the pyroelectric tensor. In tensor component form this may be written as $\Delta P(i) = p(i)\Delta T$. In lithium niobate this effect is due to the movement of the lithium and niobium ions relative to the oxygen layers. Since the Li and Nb ions move only in a direction parallel to the c-axis, the pyroelectric tensor is of the form

$$p(i) = \begin{vmatrix} 0 \\ 0 \\ p_3 \end{vmatrix}$$

One value from the literature which explicitly states both the magnitude and sign of p_3 for stoichiometric lithium niobate ($T_c = 1483$ K) is $p_3 = -4 \times 10^{-5}$ C/K/m² [1]. Note that the negative value of p_3 indicates that upon cooling the +c crystal face will become more positively charged. Two magnitudes of p_3 indirectly referred to in the literature are $|p_3| = 4 \times 10^{-5}$ C/K/m² [2], and $|p_3| = 8.3 \times 10^{-5}$ C/K/m² [3]. A magnitude that can be derived from the data presented in [4], using the unclamped relative permittivity value $\epsilon_{33} = 28.1$ [5], is $|p_3| = 6.8 \times 10^{-5}$ C/K/m².

REFERENCES

- [1] A. Savage [*J. Appl. Phys. (USA)* vol.37 (1966) p.3071-2]
- [2] V.K. Novik, N.D. Gavrilova, N.D. Fel'dman [*Pyroelectric Convertors* in Russian (Sovetskoe Radio, Moscow, 1979)]; cited in V.V. Lemanov, B.V. Sukharev [*Sov. Tech. Phys. Lett. (USA)* vol.9 no.4 (1983) p.218-9]
- [3] [*Optical Crystals* brochure (Crystal Technology Inc., Palo Alto, CA) cited in [4]]
- [4] C.H. Bulmer, W.K. Burns, S.C. Hiser [*Appl. Phys. Lett. (USA)* vol.48 no.16 (1986) p.1036-8]
- [5] R.S. Weis, T.K. Gaylord [*Appl. Phys. A (Germany)* vol.37 no.4 (1985) p.191-203]

CHAPTER 7

PIEZOELECTRIC AND ELECTROMECHANICAL PROPERTIES

- 7.1 Second-order piezoelectric constants of LiNbO₃
- 7.2 Third-order piezoelectric constants of LiNbO₃
- 7.3 Electrostrictive constants of LiNbO₃
- 7.4 Electromechanical coupling factors of LiNbO₃

7.1 Second-order piezoelectric constants of LiNbO₃

A. Ballato

This Datareview appeared in *Properties of Lithium Niobate* (INSPEC, IEE, London, UK, 1989) and is reproduced here for the reader's convenience.

Piezoelectricity couples the mechanical stress (T) and strain (S) fields with the electric intensity (E) and displacement (D) fields. Depending on variable choice, four sets of constitutive relations are defined in [1,2] for the linear case; these are, in compressed matrix form:

$$[T] = [cE] [S] - [e]' [E]; [T] = [cD] [S] - [h]' [D]$$
$$[D] = [e] [S] + [\epsilon S] [E]; [E] = -[h] [S] + [\beta S] [D]$$

$$[S] = [sE] [T] + [d]' [E]; [S] = [sD] [T] + [g]' [D]$$
$$[D] = [d] [T] + [\epsilon T] [E]; [E] = -[g] [T] + [\beta T] [D]$$

[cE], [cD] and [sE], [sD] are (6×6) symmetric elastic stiffness, compliance matrices at constant E and D; [ϵS], [ϵT] and [βS], [βT] are symmetric (3×3) dielectric permittivity, impermeability matrices at constant [S] and [T]; [e], [h], [d], and [g] are (3×6) piezoelectric matrices. A prime denotes transpose. Equivalent sets are defined with polarisation [P] as variable, leading to piezoelectric matrices [a] and [b], [3,15,16]; these are less often used.

The following relations exist amongst the material constants:

$$[c] [s] = [I]; [\epsilon] [\beta] = [I]; [I] = \text{identity matrix}$$

$$[cD] - [cE] = [e]' [h] = [h]' [e]; [\epsilon T] - [\epsilon S] = [e] [d]' = [d] [e]'$$
$$[sE] - [sD] = [d]' [g] = [g]' [d]; [\beta S] - [\beta T] = [g] [h]' = [h] [g]'$$

$$[e] = [\epsilon S] [h] = [d] [cE]; [g] = [\beta T] [d] = [h] [sD]$$
$$[d] = [\epsilon T] [g] = [e] [sE]; [h] = [\beta S] [e] = [g] [cD]$$

Resonance measurements on thickness mode plate vibrators and pulse-echo (transit time) measurements lead to values for [cE], [e] and [ϵS] from whence the other values are computed. Resonance measurements on bar and rod vibrators lead to determination of the [sE], [d] and [ϵT] set. These dynamic techniques are both more accurate and more precise than static methods.

For lithium niobate the symmetry elements of point group 3m require that the piezoelectric [e] matrix has the form

$$\begin{bmatrix} 0 & 0 & 0 & 0 & e15 & -e22 \\ -e22 & e22 & 0 & e15 & 0 & 0 \\ e31 & e31 & e33 & 0 & 0 & 0 \end{bmatrix}$$

The [h] matrix is identical in form, while the [d] and [g] matrices have a multiplying factor 2 in the 16 position.

Determinations of greatest significance are those of [4-10]; results are summarised in TABLES 1 - 10. Usually [e] is determined, sometimes [d] or a combination of [e] and [d]: [h] and [g] have been

7.1 Second-order piezoelectric constants of LiNbO_3

calculated from these. Variations in values are strongly suspected to be largely due to sample differences, particularly stoichiometry [12-14]. The determinations of [5] (resonance) and [7] (transit-time) remain today the most consistent and carefully made, although the samples used were certainly not of the congruent composition [12] now universally grown. The Curie point of the material of [7] was measured to be 1165°C.

The preferred set of piezoelectric values to date is still that of Smith and Welsh [7].

TABLE 1 Piezoelectric stress constant [e] (C/m^2).

e15	e22	e31	e33	T (°C)	Ref
3.7	2.5	0.2	1.3	RT	[5]
3.60	2.52	0.747	1.67	RT	[6]
3.76	2.43	0.23	1.33	25	[7]
3.8	2.5	0.35	1.42	20	[8]
3.83	2.37		1.80	RT	[9]
3.61	2.40	0.28	1.59	RT	[10]

Estimated errors: e15, e22: 3%; e31: 60%; e33: 15%.

TABLE 2 Piezoelectric strain coefficient [d] (10^{-12} C/N).

d15	d22	d31	d33	T (°C)	Ref
74.0	20.8	-0.863	16.2	20	[4]
68	21	-1	6	RT	[5]
64.3	20.6	+1.15	6.53	RT	[6]
69.2	20.8	-0.85	6.0	25	[7]
68.9	20.9	+0.003	5.8	20	[8]
65.36	20.29	-1.22	8.27	RT	[10]

TABLE 3 Piezoelectric stress modulus [h] (10^9 N/C).

h15	h22	h31	h33	T (°C)	Ref
9.5	6.4	0.8	5.1	RT	[5]
9.04	6.33	3.07	6.86	RT	[6]
9.59	6.20	0.93	5.38	25	[7]
9.2	6.1	1.3	5.87	20	[8]
9.16	6.09	1.2	6.88	RT	[10]

TABLE 4 Piezoelectric strain constant [g] ($10^{-3} \text{ m}^2/\text{C}$).

g15	g22	g31	g33	T (°C)	Ref
91	28	-4	23	RT	[5]
87.7	28.1	+4.79	24.4	RT	[6]
91.8	27.6	-3.3	23.6	25	[7]
92.5	28.1	+0.01	23.5	20	[8]
89.5	27.8	-4.87	33.0	RT	[10]

TABLE 5 Hydrostatic strain coefficient d(h) (10^{-12} C/N).

d(h) = d33 + 2 d31	T (°C)	Ref
14.5	20	[4]
4.0	RT	[5]
8.8	RT	[6]
4.3	25	[7]
6.31	21	[11]
5.8	20	[8]
5.83	RT	[10]

7.1 Second-order piezoelectric constants of LiNbO_3

TABLE 6 Temperature coefficient of e ($10^{-6}/\text{K}$).

Te15	Te22	Te31	Te33	T ($^{\circ}\text{C}$)	Ref
147	79	221	887	25	[7]

$$Te = (de/dT)/e$$

TABLE 7 Temperature coefficient of d ($10^{-6}/\text{K}$).

Td15	Td22	Td31	Td33	T ($^{\circ}\text{C}$)	Ref
280	240	1100	290	20	[4]
345	234	1910	1130	25	[7]

$$Td = (dd/dT)/d$$

TABLE 8 Temperature coefficient of h ($10^{-6}/\text{K}$).

Th15	Th22	Th31	Th33	T ($^{\circ}\text{C}$)	Ref
-235	-303	-450	+216	25	[7]

$$Th = (dh/dT)/h$$

TABLE 9 Temperature coefficient of g ($10^{-6}/\text{K}$).

Tg15	Tg22	Tg31	Tg33	T ($^{\circ}\text{C}$)	Ref
-37	-148	1239	459	25	[7]

$$Tg = (dg/dT)/g$$

TABLE 10 Temperature coefficient of d(h) ($10^{-6}/\text{K}$).

Td(h)	T ($^{\circ}\text{C}$)	Ref
193	20	[4]
822	25	[4]

$$Td(h) = (dd(h)/dT)/d(h)$$

REFERENCES

- [1] [Proc. IRE (USA) vol.37 no.12 (1949) p.1378-95]
- [2] [Proc. IRE (USA) vol.46 no.4 (1958) p.764-78]
- [3] R. Bechman [in *Piezoelectricity* (HMSO, London, 1957) Report 1, p.1-11]
- [4] T. Yamada, N. Niizeki, H. Toyoda [Jpn. J. Appl. Phys. (Japan) vol.6 no.2 (1967) p.151-5]
- [5] A.W. Warner, M. Onoe, G.A. Coquin [J. Acoust. Soc. Am. (USA) vol.42 no.6 (1967) p.1223-31]
- [6] A.P. Korolyuk, L.Ya. Matsakov, V.V. Vasil'chenko [Sov. Phys.-Crystallogr. (USA) vol.15 no.5 (1971) p.893-6]
- [7] R.T. Smith, F.S. Welsh [J. Appl. Phys. (USA) vol.42 no.6 (1971) p.2219-30]
- [8] Y. Nakagawa, K. Yamanouchi, K. Shibayama [J. Appl. Phys. (USA) vol.44 no.9 (1973) p.3969-74]
- [9] R.A. Graham [J. Appl. Phys. (USA) vol.48 no.6 (1977) p.2153-63]
- [10] I.A. Dan'kov, E.F. Tokarev, G.S. Kudryashov, K.G. Belobaev [Inorg. Mater. (USA) vol.19 no.7 (1983) p.1049-54]
- [11] R.A. Graham [Ferroelectrics (UK) vol.10 no.1-4 (1976) p.65-9]
- [12] A. Rauber [Curr. Top. Mater. Sci. (Netherlands) vol.1 ch.7 p.481-601]

7.1 Second-order piezoelectric constants of LiNbO_3

- [13] E. Born, E. Willibald, R. Veith [*Proc. IEEE Ultrasonics Symposium* Dallas, TX, Nov. 1984 (IEEE, New York, 1984) p.268-70]
- [14] R.S. Weis, T.K. Gaylord [*Appl. Phys. A (West Germany)* vol.37 no.4 (1985) p.191-203]
- [15] W.R. Cook, H. Jaffe [in *Landolt-Bornstein Numerical Data and Functional Relationships in Science and Technology* Ed. K.-H. Hellwege (Springer, 1979) vol.III/11 ch.3 p.291]
- [16] D.F. Nelson [in *Landolt-Bornstein Numerical Data and Functional Relationships in Science and Technology* Ed. K.-H. Hellwege (Springer, 1979) vol.III/11 ch.5 p.499-503]

7.2 Third-order piezoelectric constants of LiNbO₃

Y. Cho and K. Yamanouchi; updated by C. Florea

May 2001

Third-order piezoelectric (stress) constants e_{ijklm} are fifth-rank tensors. They combine the non-linear electric displacement D_i^{NL} with the product of two strain fields, S_{jk} and S_{lm} , in the state of zero electric fields ($E = 0$) as:

$$D_i^{NL} = \frac{1}{2} e_{ijklm} S_{jk} S_{lm}$$

or the non-linear total thermodynamic tension T_{jk}^{NL} [1] with the product of the electric field E_i and strain S_{lm} as:

$$T_{jk}^{NL} = e_{ijklm} E_i S_{lm}$$

where all these field quantities are defined in the material frame [2].

The third-order piezoelectric constants (as well as the third-order elastic, dielectric and electrostrictive constants) are important in a quantitative analysis of non-linear effects of acoustic waves, especially in optimising non-linear acoustic devices such as SAW convolvers and correlators.

Lithium niobate has thirteen third-order piezoelectric constants that are fully or partially reported in [1] and [3] (see TABLE 1, where the simplified notation has been used such that $e_{ijk(lm)} \rightarrow e_{ijk(lm)}$ with $i, j, k, l, m = 1 - 3$ and $J, K = 1 - 6$).

TABLE 1 The measured values of the piezoelectric stress constants $e_{ijk(lm)}$ (C m⁻²).

Constant	[1]	[3]
e_{222}	15.0 (12.3)*	21 (10)*
e_{115}	17.1 (6.6)	-
e_{125}	19.9 (2.1)	-
e_{126}	-15.9 (5.3)	-
e_{135}	19.6 (2.7)	-
e_{136}	-0.9 (2.7)	-
e_{145}	20.3 (5.7)	-
e_{311}	14.7 (6.0)	-
e_{312}	13.0 (11.4)	-
e_{313}	-10.0 (8.7)	-
e_{314}	11.0 (4.6)	-
e_{333}	-17.3 (5.9)	-21 (7)
e_{344}	-10.2 (5.6)	-

*Indicated in parentheses are the standard error values.

In [1], all thirteen constants of the congruently melting composition crystal were determined at room temperature from measured values of the velocity variation of small-amplitude ultrasonic waves (referred to the material frame as functions of applied static electric fields) and from the measured values of third-order elastic, dielectric and electrostrictive constants.

7.2 Third-order piezoelectric constants of LiNbO_3

In [3], only e_{222} and e_{333} were given, from measuring the non-linearities of piezoelectric polarisation as a function of momentarily applied compressive strain (impact-loading technique). In the case of determining e_{222} and e_{333} , this method does not need correction using other kinds of non-linear constants.

REFERENCES

- [1] Y. Cho, K. Yamanouchi [*J. Appl. Phys. (USA)* vol.61 (1987) p.875]
- [2] D.F. Nelson [*Electric, Optic and Acoustic Interaction in Dielectrics* (Wiley, New York, USA, 1979)]
- [3] R.A. Graham [*J. Appl. Phys. (USA)* vol.48 (1977) p.2153]

7.3 Electrostrictive constants of LiNbO₃

Y. Cho and K. Yamanouchi; updated by C. Florea

May 2001

Electrostrictive constants, l_{ijkl} , are fourth-rank tensors that combine the non-linear total thermodynamic tension T_{jk}^{NL} [1] with the product of two electric fields, E_i and E_j , in the state of zero strain fields ($S = 0$) as

$$T_{kl}^{NL} = -\frac{1}{2} l_{ijkl} E_i E_j$$

or the non-linear electric displacement D_{ii}^{NL} with the product of the electric field E_j and strain S_{kl} as

$$D_{ii}^{NL} = l_{ijkl} E_j S_{kl}$$

where all these field quantities are defined in the material frame [2].

They can be determined directly without the knowledge of other kinds of higher-order constants by measuring the variation of capacitance in the state of constant strain, that is, the variation of clamped dielectric constant when the directed stress is applied to the crystal.

In [1], all eight electrostrictive constants of the congruently melting composition crystal were determined at room temperature. The data are presented in TABLE 1, where the simplified notation has been used such that $l_{(ij)(kl)} \rightarrow l_{IJ}$ with $i, j, k, l = 1 - 3$ and $I, J = 1 - 6$.

TABLE 1 The measured values of the electrostrictive constants $l_{(ij)(kl)}$ (in 10^{-9} F m^{-1}) from [1].

Constant	l_{11}	l_{12}	l_{13}	l_{31}	l_{33}	l_{14}	l_{41}	l_{34}
Measured value	1.11 (0.39)	2.19 (0.56)	2.32 (0.67)	0.19 (0.61)	-2.76 (0.41)	1.51 (0.17)	1.85 (0.17)	-1.83 (0.11)

Indicated in parentheses are the standard error values.

Finally, readers should note that there are different definitions of electrostrictive constants (as well as other higher-order constants) when we use different sets of field quantities as the independent variables, as for example (S, D) versus (T, D).

REFERENCES

- [1] Y. Cho, K. Yamanouchi [*J. Appl. Phys. (USA)* vol.61 (1987) p.875]
- [2] D.F. Nelson [*Electric, Optic and Acoustic Interaction in Dielectrics* (Wiley, New York, USA, 1979)]

7.4 Electromechanical coupling factors of LiNbO₃

A. Ballato

This Datareview appeared in *Properties of Lithium Niobate* (INSPEC, IEE, London, UK, 1989) and is reproduced here for the reader's convenience.

A INTRODUCTION

Electromechanical coupling factors k are dimensionless measures of efficacy of piezoelectric transduction. They appear in considerations of bandwidth and insertion loss in transducers and signal processing devices, and in location and spacing of critical frequencies of resonators. General features are given in [1-4]. A distinction is made between 'material coupling factors' and 'mode coupling factors' [3] according to whether geometrical factors are included in the definition to take into account distributions of stress or strain in the specimen. With the exception of the coupling factors for acoustic surface waves, the values given here represent material coupling factors containing only ratios of elastic, piezoelectric and dielectric quantities. Numerical values are computed from the lithium niobate data of Smith and Welsh [5].

B LENGTH EXTENSION OF THIN RODS AND BARS

Single longitudinal component of stress.

$$k_{22} = d_{22}/(\epsilon T_{11} sE_{11})^{1/2} = 31.4\%, \text{ electric field along Y axis, bar length along either X or Y axis.}$$

$$k_{31} = k_{32} = d_{31}/(\epsilon T_{33} sE_{11})^{1/2} = 2.21\%, \text{ electric field along Z axis, bar length along Y axis.}$$

$$k_{33} = d_{33}/(\epsilon T_{33} sE_{33})^{1/2} = 16.8\%, \text{ electric field along Z axis, bar length along Z axis.}$$

d , ϵT , and sE are components of piezoelectric strain coefficient, dielectric permittivity at constant stress, and elastic compliance at constant electric field.

C SIMPLE THICKNESS MODES OF THIN PLATES

Simple thickness modes have no variations in motion lateral to the thickness direction. Three modal types are distinguished, the quasi-extensional (QE), designated 'a mode', fast quasi-shear (QS), designated 'b mode', and slow quasi-shear, designated 'c mode'. The methods of piezoelectric excitation are further distinguished by direction of electric field: thickness excitation (TE), field along thickness from electrodes on major surfaces, and lateral excitation (LE), field parallel to the major surfaces from electrodes placed along the edges. In (LE) the azimuth direction is also specified. References [7,8] describe the procedure for obtaining the TE and LE material electromechanical coupling coefficients in the most general cases.

D SIMPLE THICKNESS MODES OF X-CUT PLATES

IEEE notation [6] for plate orientation: (xy) or (xz).

Thickness excitation (mode b):

$$k_{15} = e_{15''}/(\epsilon S_{11} cb)^{1/2} = 68.9\%$$

7.4 Electromechanical coupling factors of LiNbO_3

Misleadingly called the ‘41° X-cut’; the cut is unrotated, but the coupling between the shears results in a shear polarisation in the YZ plane at an angle of 37.7° to the Z axis in the -Y direction. $e15''$ is an effective piezoelectric stress constant, ϵS_{11} the 11 component of dielectric permittivity at constant strain, and c_b the piezoelectrically stiffened b mode elastic stiffness eigenvalue. This mode of the X-cut accounts for more than 80% of the lithium niobate shear mode transducer market. The slower shear mode, with polarisation in the YZ plane normal to the b mode, is also excited with TE; its coupling is $k_{16} = 6.9\%$. The pure compressional mode a is not driven by TE, $k_{11} = 0$.

Lateral excitation (mode a):

$k(\text{LE})_{21} = 27.2\%$, electric field along Y axis.

$k(\text{LE})_{31} = 3.2\%$, electric field along Z axis.

The two shear modes are inert to lateral fields at any azimuth.

E SIMPLE THICKNESS MODES OF Z-CUT PLATES

IEEE notation [6] for plate orientation: (zx) or (zy).

Thickness excitation (mode a), pure extension:

$$k_{33} = k_{t3} = e_{33}/(\epsilon S_{33} c_{33})^{1/2} = 16.9\%$$

$c_{33} = \underline{cE}_{33} + e_{33}^2/\epsilon S_{33}$ is the piezoelectrically stiffened elastic stiffness. k_{33} is to be distinguished from \underline{k}_{33} . This mode of the Z-cut accounts for about 10% of the lithium niobate extensional mode transducer market. Pure shear modes b, c are inert: $k_{34} = k_{35} = 0$.

Lateral excitation (modes b and c), pure shear:

$$k(\text{LE})_{15} = k(\text{LE})_{25} = e_{15}/(\epsilon S_{11} cE_{44})^{1/2} = 77.9\%, \text{ electric field at any azimuth.}$$

These shear modes have the same frequency and possess the highest coupling of any thickness mode in lithium niobate. The extensional mode which is driven by TE is inert to lateral excitation, $k(\text{LE})_{13} = k(\text{LE})_{23} = 0$.

F SIMPLE THICKNESS MODES OF ROTATED Y-CUT PLATES

IEEE notation [6] for plate orientation: (yx1) θ .

Thickness excitation, angle $\theta = 0$ (Y-cut):

$k_{22} = k_{t2} = 30.8\%$, QE mode a coupled to QS mode b.

$k_{24} = 56.8\%$, QS mode b coupled to QE mode a.

$k_{26} = 0$, mode c, X-directed pure shear mode.

Lateral excitation, angle $\theta = 0$ (Y-cut):

$k(\text{LE})_{12}$ (mode a) = $k(\text{LE})_{14}$ (mode b) = 0;

$k(\text{LE})_{16}$ (mode c) = $e_{16}/(\epsilon S_{11} cE_{66})^{1/2} = 45.5\%$, electric field in X-direction.

$k(\text{LE})_{32}$ (mode a) = 3.1%; $k(\text{LE})_{34}$ (mode b) = 0.6;

7.4 Electromechanical coupling factors of LiNbO_3

$k'(\text{LE})36$ (mode c) = 0, electric field in Z-direction.

The unrotated Y-cut is not of commercial interest.

Thickness excitation, angle $\theta = -16.38^\circ$ (163° rotated Y-cut):

$k'22 = k't2 = 0$, QE mode a; condition defining θ .

$k'24 = 61.8\%$, QS mode b coupled to QE mode a. This mode accounts for less than 10% of the lithium niobate shear mode transducer market.

$k'26 = 0$.

Lateral excitation, angle $\theta = -16.38^\circ$:

$k'(\text{LE})12$ (mode a) = $k'(\text{LE})14$ (mode b) = 0;

$k'(\text{LE})16$ (mode c) = 66.1%, pure shear mode, electric field in X-direction.

$k'(\text{LE})32$ (mode a) = 4.6%; $k'(\text{LE})34$ (mode b) = 8.4%; $k'(\text{LE})36$ (mode c) = 0, electric field in Z'-direction.

Thickness excitation, angle $\theta = +36.26^\circ$ (36° rotated Y-cut):

$k'22 = k't2 = 48.7\%$, QE mode a. This mode accounts for more than 90% of the lithium niobate extensional mode transducer market. $k'24 = 0$, pure shear mode b; $k'26 = 0$, QS mode c, condition that defines θ .

Lateral excitation, angle $\theta = +36.26^\circ$:

$k'(\text{LE})12$ (mode a) = $k'(\text{LE})14$ (mode c) = 0; $k'(\text{LE})16$ (mode b) = 4.8%, electric field in X-direction.

$k'(\text{LE})32$ (mode a) = 18.9%, $k'(\text{LE})34$ (mode c) = 13.1%; $k'(\text{LE})36$ (mode b) = 0, electric field in Z'-direction.

Graphs of k for TE are given in [7] for doubly rotated cuts of lithium niobate; [11] also presents TE graphs of k for doubly rotated cuts, but based upon the approximate velocity-shift relation given below in Section H. The availability of lateral-field transducers with very large coupling factors is apparently not widely recognised.

G HYDROSTATIC COUPLING FACTOR $k(h)$

$$k(h) = d(h)/(\epsilon T33 sE(h))^{1/2} = 9.21\%$$

$d(h) = 2d31 + d33$ = hydrostatic strain coefficient.

$sE(h) = 2(sE11 + sE12) + 4sE13 + sE33$ = hydrostatic elastic compliance at constant electric field.

H SURFACE ACOUSTIC WAVE (SAW) COUPLING FACTORS

Because of the complex wave shape, mode coupling factors are used instead of material coupling factors. These are defined by the approximate relation $k(\text{SAW}) = (2\Delta v/v(o))^{1/2}$, where $\Delta v = (v(o) - v(m))$ is the difference in the SAW velocities when propagating on an unmetallised $v(o)$ and metallised $v(m)$ substrate. More accurate formulas are given in [9,10]; [10] also contains a discussion of stoichiometry differences and other material considerations possibly implicated in departures from agreement among investigators in certain SAW parameters.

$k(\text{SAW}) = 7.1\%$, Z-cut, X-propagation; no commercial use.

$k(\text{SAW}) = 23.5\%$, (yx1) + 41.5° , rotated Y-cut, X-propagation. Maximum coupling for zero power flow angle; no longer used commercially.

$k(\text{SAW}) = 21.9\%$, Y-cut, Z-propagation; zero power flow angle. Small fraction of commercial SAW demand.

$k(\text{SAW}) = 23.7\%$, (yx1) + 127.8° , rotated Y-cut, X-propagation. Zero power flow angle, zero spurious bulk mode. Most popular commercial cut.

I TEMPERATURE COEFFICIENTS OF COUPLING

Bars: $Tk_{22} = -40$, $Tk_{31} = Tk_{32} = +1492$, $Tk_{33} = +715$

Plates: X-cut $Tk(\text{LE})_{21} = +4.5$, $Tk(\text{LE})_{31} = -5.5$

Y-cut $Tk(\text{LE})_{16} = -11$

Z-cut $Tk_{33} = Tkt_3 = +551$, $Tk(\text{LE})_{15} = Tk(\text{LE})_{25} = +88$

Reference [12] plots k_{22} , k_{33} and k_{31} for bars, and Tkt_3 for plates over the range 100 - 700 K.

$Tk = (dk/dT)/k$

Units: $10^{-6}/\text{K}$

REFERENCES

- [1] [Proc. IRE (USA) vol.46 no.12 (1958) p.764-78]
- [2] D.A. Berlincourt, D.R. Curran, H. Jaffe [in *Physical Acoustics* Ed. W.P. Mason (Academic, 1964) vol.1A ch.3 p.169-270]
- [3] W.R. Cook, H. Jaffe [in *Landolt-Bornstein Numerical Data and Functional Relationships in Science and Technology* Ed. K.-H. Hellwege (Springer, 1979) vol.III/11 ch.3 p.287-470]
- [4] [IEEE Standard on Piezoelectricity ANSI/IEEE Std 176-1987 (IEEE, New York, 1987)]
- [5] R.T. Smith, F.S. Welsh [*J. Appl. Phys. (USA)* vol.42 no.6 (1971) p.2219-30]
- [6] [Proc. IRE (USA) vol.37 no.12 (1949) p.1378-95]
- [7] A. Ballato [in *Physical Acoustics* Eds W.P. Mason, R.N. Thurston (Academic, 1977) vol.13 ch.5 p.115-81]
- [8] A. Ballato, E.R. Hatch, M. Mizan, T.J. Lukaszek [*IEEE Trans. Ultrason. Ferroelectr. Freq. Control (USA)* vol.33 no.4 (1986) p.385-92]
- [9] R.C. Smythe, R.S. Wagers [in *Precision Frequency Control* Eds E.A. Gerber, A. Ballato (Academic, 1985) vol.1 ch.5 p.228-57]
- [10] C.S. Hartmann, S. Jen, M.A. Domalewski, J.C. Andle [*Proc. IEEE 1987 Ultrasonics Symp.* Denver, CO, USA, Oct. 1987 (IEEE, New York, 1987) p.161-7]
- [11] A.P. Korolyuk, L.Ya. Matsakov, V.V. Vasil'chenko [*Sov. Phys.-Crystallogr. (USA)* vol.15 no.5 (1978) p.893-6]
- [12] I.A. Dan'kov, E.F. Tokarev, G.S. Kudryashov, K.G. Belobaev [*Inorg. Mater. (USA)* vol.19 no.7 (1983) p.1049-54]

CHAPTER 8

OPTICAL, DIELECTRIC AND ELECTRO-OPTICAL PROPERTIES

- 8.1 Dispersion effects in undoped and MgO-doped LiNbO₃
- 8.2 Dispersion properties of LiNbO₃ and tables
- 8.3 Dielectric constants of LiNbO₃
- 8.4 Electro-optic coefficients of LiNbO₃
- 8.5 Photorefractive effects in LiNbO₃
- 8.6 Refractive indices of different crystal phases in proton-exchanged LiNbO₃ waveguides
- 8.7 Second-order non-linear properties of different crystal phases in proton-exchanged LiNbO₃ waveguides
- 8.8 IR reflection spectra of proton-exchanged waveguides containing different H_xLi_{1-x}NbO₃ phases
- 8.9 Holographic gratings in photorefractive LiNbO₃ waveguides fabricated by combined proton and copper exchange
- 8.10 Chromium doping of LiNbO₃ by thin film diffusion

8.1 Dispersion effects in undoped and MgO-doped LiNbO₃

D.H. Jundt

June 2000

A INTRODUCTION

The most commonly used compositions of lithium niobate (LN) for optical applications are congruent (undoped), and magnesium-doped LN.

Congruent LN can be grown in large sizes with excellent homogeneity and virtually free of striations [1]. This makes it a good choice for substrates of integrated optics devices, and for applications where the large birefringence of LN is utilised, such as in walk-off plates (e.g. in fibre isolators), optical low-pass filters (e.g. in digital still cameras), or in polarising prisms (e.g. in magneto-optic pick-up heads). More recently, congruent LN has also found applications in periodically poled devices for frequency conversion such as mid-IR generating OPOs. Accurate index of refraction data are necessary to model the light propagation and phase-matching properties of such devices.

MgO-doped LN is used primarily for optical elements where congruent LN suffers from photorefractive effects. This is the case for laser beams such as those encountered when producing red, green or blue light by sum-frequency generation.

Light propagation in LN is governed by the refractive index n_e for light polarised along the polar Z-axis, and n_o for light polarised in the X-Y-plane [2,3]. The refractive index is dependent not only on the polarisation of the light, but also on the wavelength, the material composition and temperature. Small changes in the index of refraction can be induced by the electro-optic (electric field) and piezo-optic (strain) effect. The refractive index (real part of the susceptibility) is determined by the absorption (imaginary part) in the material [3]. However, the exact absorption characteristic over the whole spectral range is not easily measured. Within the transmission window, a very precise approximation of the refractive index can be attained by assuming just a few absorption points (oscillators) at fixed wavelengths outside the transparency range [4]. This leads to an expression for the polarisability $n^2 - 1$ in the form of a Sellmeier equation. Each such oscillator is characterised by its absorption strength and the frequency (wavelength). Absorption bands far in the UV can be approximated by a constant, and bands far in the IR by a term proportional to the square of the wavelength.

B CONGRUENT LITHIUM NIOBATE

The refractive indices of LN were measured and expressed in Sellmeier equations soon after the discovery of LN [5,6]. However, accurate data were only available after more homogeneous crystals could be grown from melt compositions close to congruency [7,8]. The most widely used Sellmeier equations are cast in a form for calculating the index as a function of both wavelength and temperature, and are given in EQN (1) and TABLE 1 [9]. They are based on room-temperature measurements ranging from 400 nm to 3 μ m and on the temperature-dependence of the indices at two wavelengths, 633 nm and 3.39 μ m. The temperature dependence for the blue-green spectral region as well as that for the mid-IR beyond 3.39 μ m is extrapolated, and thus less accurate.

$$n^2 = A_1 + \frac{A_2 + B_1 F}{\lambda^2 - (A_3 + B_2 F)^2} + B_3 F - A_4 \lambda^2 \quad (1a)$$

8.1 Dispersion effects in undoped and MgO-doped LiNbO₃

$$F = (T - T_0)(T + T_0 + 546) \text{ with } T_0 = 24.5^\circ\text{C} \quad (1b)$$

In EQN (1), the wavelength λ is given in μm , and the temperature T in degrees Celsius. The coefficients A and B are given in TABLE 1.

TABLE 1 Coefficients for EQN (1) for congruent LN.

	A ₁	A ₂	A ₃	A ₄	B ₁	B ₂	B ₃
n _o	4.9048	0.11775	0.21802	0.027153	2.2314×10^{-8}	-2.9671×10^{-8}	2.1429×10^{-8}
n _e	4.5820	0.09921	0.21090	0.021940	5.2716×10^{-8}	-4.9143×10^{-8}	2.2971×10^{-7}

As PPLN was more widely used in optical parametric oscillator (OPO) applications generating wavelengths in the mid-IR out to 5 μm , a more accurate Sellmeier equation for the mid-IR was derived [10]. This refined Sellmeier equation for n_e is shown in EQN (2) and TABLE 2 based on the same measured data with the addition of phase-matching results from an OPO.

$$n_e^2 = A_1 + B_1 F + \frac{A_2 + B_2 F}{\lambda^2 - (A_3 + B_3 F)^2} + \frac{A_4 + B_4 F}{\lambda^2 - A_5^2} - A_6 \lambda^2 \quad (2a)$$

$$F = (T - T_0)(T + T_0 + 546.32) \text{ with } T_0 = 24.5^\circ\text{C} \quad (2b)$$

TABLE 2 Coefficients for EQN (2) for the extraordinary index of congruent LN.

Parameter	A ₁	A ₂	A ₃	A ₄	A ₅
Value	5.35583	0.100473	0.20692	100	11.34927

Parameter	A ₆ (10 ⁻²)	B ₁ (10 ⁻⁷)	B ₂ (10 ⁻⁸)	B ₃ (10 ⁻⁸)	B ₄ (10 ⁻⁵)
Value	1.5334	4.629	3.862	-0.89	2.657

The transparency range for congruent LN extends from the UV edge around 350 nm to around 4.5 μm where multi-phonon absorption starts to be significant. The measured absorptivity [11] for congruent LN in the wavelength range from 2.5 to 7 μm is shown in FIGURE 1. The peak at 2.87 μm is due to the OH absorption band, and does not affect light polarised along the Z-axis.

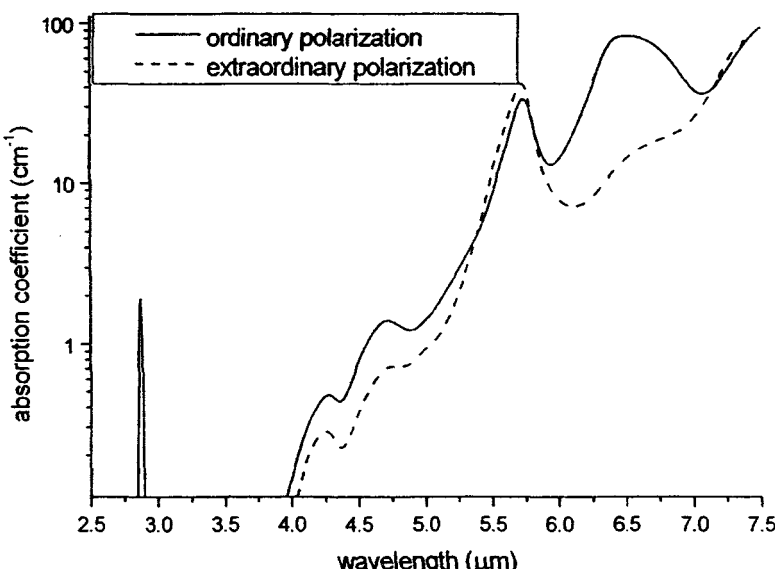


FIGURE 1 Absorption coefficient for light polarised along the Z-axis (extraordinary) or perpendicular to the Z-axis (ordinary).

C MAGNESIUM-DOPED LITHIUM NIOBATE

The indices of magnesium-doped LN can vary depending on the starting melt compositions. The most widespread composition uses the same Li₂O/Nb₂O₅ ratio as for a congruent crystal, but with the addition of approximately 5 mol% of MgO. The room-temperature indices of such a crystal have been measured for wavelengths from 400 nm to 5 μm [12]. The corresponding Sellmeier equation is shown in EQN (3) and TABLE 3.

$$n^2 = 1 + \frac{A\lambda^2}{\lambda^2 - B} + \frac{C\lambda^2}{\lambda^2 - D} + \frac{E\lambda^2}{\lambda^2 - F} \quad (3)$$

TABLE 3 Coefficients for EQN (3) for MgO-doped LN.

	A	B	C	D	E	F
n _o	2.4272	0.01478	1.4617	0.05612	9.6536	371.216
n _e	2.2454	0.01242	1.3005	0.05313	6.8972	331.33

D LITHIUM-RICH COMPOSITIONS

Stoichiometric LN has been studied for its low defect densities and its increased photorefractive properties that might be useful for optical storage applications. The refractive index and its temperature dependence have been measured for LN equilibrated at high temperature to the lithium-rich phase-boundary [13]. TABLE 4 lists the coefficients for EQN (1) that can be used to calculate the refractive indices for such crystals.

TABLE 4 Coefficients to be inserted into EQN (1) for stoichiometric LN.

	A ₁	A ₂	A ₃	A ₄	B ₁	B ₂	B ₃
n _o	4.913	0.1163	0.2201	0.0273	0.94 × 10 ⁻⁸	3.98 × 10 ⁻⁸	1.6 × 10 ⁻⁸
n _e	4.546	0.0917	0.2148	0.0303	1.93 × 10 ⁻⁸	5.3 × 10 ⁻⁸	2.72 × 10 ⁻⁷

As LN can exist over a wide range of Li-compositions, it is useful to be able to estimate the effect of a slight deviation in stoichiometry on the refractive indices. By taking the index of refraction measurements of congruent and stoichiometric crystals as input, and adding some index data for intermediate compositions [14], a recipe was derived to estimate the index of refraction as a function of composition, wavelength and temperature [15]. EQN (4) shows the definitions for the calculations, and TABLE 5 lists the parameters to be inserted. To calculate the index of refraction, one first calculates the parameter β depending on the crystal composition x given in mol% of lithium oxide. β ranges from 0 (congruent) to 1 (stoichiometric), and is negative for compositions poorer in lithium than congruency. Next, the interpolation parameter c is calculated from β, and the value for each parameter P is calculated as the interpolation between the corresponding values for the congruent and stoichiometric crystal. These interpolated values are then inserted into EQN (4c). The definition of F is given in EQN (1b).

$$\beta = \frac{x - x_0}{x_1 - x_0} \text{ and } c = \frac{\exp(\alpha\beta) - 1}{\exp(\alpha) - 1} \text{ where } \begin{cases} \alpha = 1.04918 \\ x_0 = 48.253 \\ x_1 = 49.970 \end{cases} \quad (4a)$$

$$\bar{P}_i = (1 - c)P_i^{\text{congr}} + cP_i^{\text{stoich}} \text{ for } i = 1 \dots 7 \quad (4b)$$

$$n^2 = \bar{P}_1 + \frac{\bar{P}_2 + \bar{P}_5 F}{\lambda^2 - (\bar{P}_3 + \bar{P}_6 F)^2} + \bar{P}_7 F - \bar{P}_4 \lambda^2 \quad (4c)$$

TABLE 5 Coefficients for EQN (4b) to calculate the index of composition x.

	P ₁	P ₂ (10 ⁻²)	P ₃	P ₄ (10 ⁻²)	P ₅ (10 ⁻⁸)	P ₆ (10 ⁻⁸)	P ₇ (10 ⁻⁸)
n _o (congr)	4.90511	11.7610	0.218043	2.72232	-1.25245	18.1829	2.0867
n _o (stoich)	4.89750	11.9382	0.217367	1.64003	0.21774	4.71382	3.4653
n _e (congr)	4.58237	9.88953	0.21150	2.20292	5.14087	-3.43904	23.19289
n _e (stoich)	4.54104	9.30126	0.213044	2.69934	3.70377	3.67027	21.3666

E CONCLUSION

Variations in the refractive indices of LiNbO₃, both congruent and stoichiometric, with wavelength and temperature are described. More accurate data in the mid-IR region have been acquired recently because of the use of LiNbO₃ as an OPO material. Data for magnesium-doped material is also given in this Datareview.

REFERENCES

- [1] J.A. Aust, N.A. Sanford, J. Amin [*LEOS'97* San Francisco, USA, 10-13 Nov. 1997 (IEEE, New York, NY, USA, 1996) p.114]
- [2] J.F. Nye [*Physical Properties of Crystals* (Oxford University Press, Oxford, 1985)]
- [3] M. Born, E. Wolf [*Principles of Optics* 3rd Ed. (Pergamon, Oxford, 1965)]
- [4] A.E. Siegman [*Lasers* (University Science, Mill Valley, California, 1986)]
- [5] M.V. Hobden, J. Warner [*Phys. Lett. (USA)* vol.22 (1966) p.243]
- [6] G.D. Boyd, W.L. Bond, H.L. Carter [*J. Appl. Phys. (USA)* vol.38 (1967) p.1941]
- [7] D.S. Smith, H.D. Riccius, R.P. Edwin [*Opt. Commun. (Netherlands)* Erratum in vol.20, p.188 (1977) vol.17 (1976) p.332]
- [8] D.F. Nelson, R.M. Mikulyak [*J. Appl. Phys. (USA)* vol.45 (1974) p.3688]
- [9] G.J. Edwards, M. Lawrence [*Opt. Quantum Electron. (UK)* vol.16 (1984) p.373]
- [10] D.H. Jundt [*Opt. Lett. (USA)* vol.22 (1997) p.1553]
- [11] L.E. Myers, W.R. Bosenberg [*J. Quantum Electron. (USA)* vol.33 (1997) p.1663]
- [12] D.E. Zelmon, D.L. Small, D. Jundt [*J. Opt. Soc. Am. B (USA)* vol.14 (1997) p.3319]
- [13] D.H. Jundt, M.M. Fejer, R.L. Byer [*IEEE J. Quantum Electron. (USA)* vol.26 (1990) p.135]
- [14] P.F. Bordui, R.G. Norwood, D.H. Jundt, M.M. Fejer [*J. Appl. Phys. (USA)* vol.71 (1992) p.875]
- [15] D.H. Jundt [PhD Thesis, Stanford University, 1991]

8.2 Dispersion properties of LiNbO₃ and tables

C.J.G. Kirkby; updated by C. Florea

February 2002

A THEORY

In a dielectric material the relationship between the electric flux density, D, and field, E, is determined by the oscillatory behaviour of the electrons contained within the material; at low field strengths the relationship is linear, being defined by the permittivity, which has the general form of a second rank tensor. For non-gyrotropic materials, only the diagonal elements are non-zero. At optical frequencies, the permittivity of a material is usually described in terms of the refractive index, a complex quantity with real and imaginary components connected on causality arguments via the Kramers-Kronig relationship. The imaginary component, representing absorptive processes, is the subject of a separate review. Only the real component, generally referred to as 'refractive index', is considered here. For lithium niobate this has two components, the ordinary (n_o) and the extraordinary (n_e) indices.

The spectral dispersion of the refractive index of a material is intimately related to the energy-band structure, reflecting the characteristic Lorentzian frequency dependence of the electronic oscillators. For lithium niobate, limited early experimental absorption-edge spectral data [1,2] and theoretical energy-band calculations [3] exist. In summary, pure, well oxidised lithium niobate is transparent from the fundamental bandgap absorption band-edge around 350 nm to about 5 μm , where phonon absorption (extending to nearly 80 μm) sets in. In the far-infrared the absorption shows little structure, the phonon influence fading. The visible refractive indices, together with their temperature dependence, can be explained on the basis of a single UV oscillator, together with several IR oscillators of lesser significance [4].

A widely used and convenient representation of refractive index dispersion is the Sellmeier oscillator [5], having the form:

$$n^2 = 1 + \sum_{j=1}^N \frac{A_j^2}{\lambda^2 - B_j^2} \quad (1)$$

where λ is the wavelength, and A_j and B_j represent the strengths and wavelengths of the N assumed oscillators, respectively. For many purposes, a single oscillator representation is adequate.

B MATERIAL CONSIDERATIONS

Lithium niobate is not completely represented by the generic chemical formula LiNbO₃. The generic formula can be rewritten as (Li₂O)_v(Nb₂O₅)_{1-v} where v represents the mol% LiO₂ content of the crystal, which can take values in the interval 0.480 - 0.500. In the case of $v = 0.5$ one obtains the generic formula, LiNbO₃, and the respective composition is therefore named stoichiometric.

Large deviations from this stoichiometric composition may exist, characterised by two independent variables: the Li/Nb ratio and the ratio between the sum of the metals and the oxygen content. The important case of the congruent composition is represented by the crystals that have $v = 0.486$, i.e. 48.6 mol% Li₂O (meaning a Li-to-Nb ratio of 0.9455).

C REFRACTIVE INDEX DATA

Refractive index data for lithium niobate are available over a very broad wavelength range, from VUV to millimetric wavelength, with emphasis on the visible and near-infrared. Extensive reviews covering various wavelength/energy ranges have been presented in the literature [6-8], with the latter being the most complete.

C1 Ultraviolet

Ordinary and extraordinary indices were derived by Kramers-Kronig transformation of UV reflection data [9], with the measurements being made on cleaved surfaces of material of unspecified stoichiometry at room temperature (293 K) over the wavelength range 120 - 310 nm (4 - 10 eV). The data are presented in TABLE 1.

TABLE 1 Ultraviolet refractive index data for lithium niobate of unspecified stoichiometry [9].

E (eV)	E (cm^{-1})	λ (nm)	n_o	n_e
10.00	80645	124.0	1.67	1.73
9.75	78629	172.2	1.88	1.97
9.50	76613	130.5	2.04	2.14
9.25	74597	124.1	2.19	2.32
9.00	72581	137.8	2.32	2.42
8.75	70565	141.7	2.12	2.17
8.50	68548	145.9	1.82	1.89
8.25	66532	150.3	1.58	1.63
8.00	64516	153.0	1.43	1.48
7.50	60484	165.3	1.38	1.48
7.00	56452	177.1	1.54	1.75
6.50	52419	190.8	1.82	2.07
6.00	48387	206.7	2.16	2.30
5.75	46371	215.7	2.36	2.46
5.50	44355	225.5	2.68	2.76
5.25	42339	236.2	3.22	2.98
5.00	40323	248.0	3.62	3.10
4.75	38306	261.1	3.52	2.99
4.50	36290	275.6	3.19	2.79
4.25	34274	291.8	2.91	2.59
4.00	32258	310.0	2.76	2.49

Subsequent determinations [10,11] used unpolarised light, and are thus not strictly representative of a uniaxial, birefringent material, although the covered range of 3 - 35 eV [11] is far wider than in the case of the data presented above.

C2 Visible and Near-Infrared

Refractive index measurements in the visible region are generally performed using the minimum deviation method with a prism of accurately known angle [12]; this gives absolute measurements, with a precision determined by the precision with which the prism angle and the wavelength are known.

C2.1 Stoichiometric LiNbO_3

The spectral dependence (dispersion) of the refractive index in stoichiometric material has been reported by a number of workers [13-16], along with the temperature dependence of the dispersion. The refractive index was measured in the wavelength range 447 - 707 nm, for temperatures between

8.2 Dispersion properties of LiNbO_3 and tables

19°C and 374°C [17], but no explicit data were presented. Instead, a Sellmeier-type equation was derived for each of n_o and n_e , where T is the absolute temperature (K) and λ is the free-space wavelength (nm):

$$n^2(\lambda, T) = a_1 + \frac{a_2 + b_1 T^2}{\lambda^2 - (a_3 + b_2 T^2)^2} + b_3 T^2 + a_4 \lambda^2 \quad (2)$$

where the coefficients are given below:

	a_1	a_2	a_3	a_4	b_1	b_2	b_3
n_o	4.9130	1.173×10^5	2.12×10^2	-2.78×10^{-8}	1.65×10^{-2}	2.7×10^{-5}	0
n_e	4.5567	0.970×10^5	2.01×10^2	-2.24×10^{-8}	2.70×10^{-2}	5.4×10^{-5}	2.605×10^{-7}

Similar relationships derived in [14] and [15] lack the temperature dependence and therefore are not given here.

Measurements over a wider range of wavelengths, 420 - 4000 nm, have also been reported [13]. The temperature was not specified although subsequent measurements [14], reported by the same authors, provided data on MgO-stabilised (0.5 wt%) stoichiometric lithium niobate at 25°C and 80°C. The results of [13] and [14] were summarised in [14] by means of third-order polynomial functions for two wavelength subsets (500 - 1200 nm and 500 - 2000 nm) and for the total wavelength range noted above. Temperature dependences of the polynomial coefficients, in a linear approximation, were also derived. TABLE 2 presents the results of [14] at 25°C. Similar measurements were reported at 20°C

TABLE 2 Visible and near-IR refractive index data for stoichiometric lithium niobate (25°C) [14].

E (eV)	E (cm^{-1})	λ (nm)	n_o	n_e
2.9524	23810	420	2.4144	2.3038
2.7556	22222	450	2.3814	2.2765
2.4800	20000	500	2.3444	2.2446
2.2545	18182	550	2.3188	2.2241
2.0667	16667	600	2.3002	2.2083
1.9077	15385	650	2.2862	2.1964
1.7714	14286	700	2.2756	2.1874
1.5500	12500	800	2.2598	2.1741
1.3778	11111	900	2.2487	2.1647
1.2400	10000	1000	2.2407	2.1580
1.0333	8333	1200	2.2291	2.1481
0.8857	7143	1400	2.2208	2.1410
0.7750	6250	1600	2.2139	2.1351
0.6689	5556	1800	2.2074	2.1297
0.6200	5000	2000	2.2015	2.1244
0.5636	4545	2200	2.1948	2.1187
0.5167	4167	2400	2.1882	2.1138
0.4769	3846	2600	2.1814	2.1080
0.4429	3571	2800	2.1741	2.1020
0.4133	3333	3000	2.1663	2.0955
0.3875	3125	3200	2.1580	2.0866
0.3647	2941	3400	2.1493	2.0814
0.3444	2778	3600	2.1398	2.0735
0.3263	2632	3800	2.1299	2.0652
0.3100	2500	4000	2.1193	2.0564

8.2 Dispersion properties of LiNbO_3 and tables

and 100°C over a limited wavelength range of 447.1 - 706.5 nm [15]. Sellmeier relationships are presented for these two temperatures, together with temperature coefficients of the two indices

A wide temperature range, from room temperature to nearly 1000°C, has been covered in [16], although for a narrow wavelength range of 404.7 - 587.6 nm. The reported results are in relatively poor agreement with the results of the other groups. The temperature dependences are presented graphically, without adequate resolution to confirm agreement with the Sellmeier equations.

The mean differences between the predicted refractive index values, based on equation (2) of [17], and the values from the cited literature [13-16] are tabulated in TABLE 3.

TABLE 3 Mean differences between predicted [17] and measured [13-16] visible and near-IR refractive index data for stoichiometric lithium niobate (see text).

	Ref [13] ^(a)	Ref [14] ^(b)	Ref [15]	Ref [16]
n_o	0.0017	0.0064	0.0037	0.0110
n_e	0.0021	0.0010	0.0069	0.0110

^(a)Assumed temperature of 20°C; also these figures are for the 400 - 1000 nm range.

^(b)For the 25°C data.

As seen from TABLE 3, the predictions agree relatively well with most of the experimental data. The Sellmeier model is expected to fit experimental data better at longer wavelengths, i.e. remote from the assumed UV oscillator; this is indeed found to be the case.

C2.2 Congruent LiNbO_3

The ordinary and extraordinary refractive indices in congruent material were measured at 24.5°C over the wavelength range 404.63 - 3051.48 nm [18]. These data were confirmed by others [19] and are presented in TABLE 4.

The data of [18], and the temperature-dependent measurements at two wavelengths (632.8 nm and 3392.2 nm) reported in [19], were fitted to temperature-dependent Sellmeier equations [20]. Converting to the format of [17], the generic equation becomes:

$$n^2(\lambda, t) = a_1 + \frac{a_2 + b_1 f(t)}{\lambda^2 - (a_3 + b_2 f(t))^2} + b_3 f(t) + a_4 \lambda^2 \quad (3)$$

where λ is the free-space wavelength (nm), and $f(t) = (t - t_0)(t + t_0 + 546)$ with $t_0 = 24.5^\circ\text{C}$, the temperature of the original measurements of [18]. The coefficients appearing in the above Sellmeier expression (EQN (3)) are given below for the ordinary (n_o) and extraordinary (n_e) polarisations:

	n_o	n_e
a_1	4.9048	4.5820
a_2	1.1775×10^5	0.9921×10^5
a_3	2.1802×10^2	2.1090×10^2
a_4	-2.7153×10^{-8}	-2.1940×10^{-8}
b_1	2.2314×10^{-2}	5.2716×10^{-2}
b_2	-2.9671×10^{-5}	-4.9143×10^{-5}
b_3	2.1429×10^{-8}	2.2971×10^{-8}

Since EQN (3) is based on room-temperature data for wavelengths ranging from 404.6 nm to 3.39 μm , it is expected that this equation is inadequate for wavelengths beyond 3.3 μm , particularly at

8.2 Dispersion properties of LiNbO_3 and tables

TABLE 4 Visible and near-IR refractive index data for congruent lithium niobate (24.5°C) [18].

E (eV)	E (cm^{-1})	λ (nm)	n_o	n_e
3.0645	24714	404.63	2.4317	2.3260
2.8451	22944	435.84	2.3928	2.2932
2.6506	21376	467.82	2.3634	2.2683
2.5834	20834	479.99	2.3541	2.2605
2.4382	19663	508.58	2.3356	2.2488
2.2708	18313	546.07	2.3165	2.2285
2.1492	17332	576.96	2.3040	2.2178
2.1417	17272	578.97	2.3032	2.2171
2.1104	17020	587.56	2.3002	2.2147
1.9259	15532	643.85	2.2835	2.2002
1.8568	14974	667.82	2.2778	2.1953
1.7551	14154	706.52	2.2699	2.1886
1.5323	12357	809.26	2.2541	2.1749
1.4225	11472	871.68	2.2471	2.1688
1.3253	10688	935.64	2.2412	2.1639
1.2917	10417	959.99	2.2393	2.1622
1.2229	9862	1014.00	2.2351	2.1584
1.1354	9156	1092.14	2.2304	2.1545
1.0746	8666	1153.92	2.2271	2.1517
1.0709	8636	1157.94	2.2269	2.1515
0.9630	7766	1287.70	2.2211	2.1464
0.8611	6945	1439.97	2.2151	2.1413
0.7569	6104	1638.21	2.2083	2.1356
0.6488	5232	1911.25	2.1994	2.1280
0.5677	4578	2184.28	2.1912	2.1211
0.5167	4167	2399.95	2.1840	2.1151
0.4742	3824	2615.04	2.1765	2.1087
0.4542	3663	2730.35	2.1724	2.1053
0.4280	3451	2897.33	2.1657	2.0999
0.4064	3277	3051.48	2.1594	2.0946

elevated temperatures. Due to the interest in quasi-phase matching (QPM) in periodically poled lithium niobate (PPLN), accurate knowledge of the extraordinary refractive index in the $3 - 5 \mu\text{m}$ range becomes necessary. EQN (3) has therefore been improved so that QPM temperature and period (or wavelength) predictions are reliable for wavelengths in the $3 - 5.5 \mu\text{m}$ range [21]. The extended Sellmeier expression, which contains an added oscillator at wavelength a_5 in the mid-IR spectral region, is given by [21]:

$$n_e^2(\lambda, t) = a_1 + \frac{a_2 + b_1 f(t)}{\lambda^2 - (a_3 + b_2 f(t))^2} + b_3 f(t) + \frac{a_4 + b_4 f(t)}{\lambda^2 - a_5^2} + a_6 \lambda^2 \quad (4)$$

where λ is the free-space wavelength (nm), and $f(t) = (t - t_0)(t + t_0 + 546.32)$ with $t_0 = 24.5^\circ\text{C}$. The coefficients for the extraordinary polarisation (n_e) are given below, with the designation of b_1 , b_2 , b_3 being adjusted for consistent notation within this Datareview:

a_1	5.35583	b_1	3.8620×10^{-2}
a_2	1.0047×10^5	b_2	-0.8900×10^{-5}
a_3	2.0692×10^2	b_3	4.6290×10^{-7}
a_4	1×10^8	b_4	2.6570
a_5	1.1349×10^4		
a_6	-1.5334×10^{-8}		

C2.3 Dependence on stoichiometry

From comparison of the early measurements, it became apparent that the observed large scatter in results was due to the compositional differences between the samples used. It was shown [22] that whereas the ordinary refractive index is nearly independent of crystal composition, the extraordinary refractive index changes by up to 0.03 when varying the Li/Nb ratio (r). At 632.8 nm, for example, the extraordinary refractive index decreases linearly from 2.2187 at $r = 0.8$ to 2.2190 at $r = 1.20$.

Composition dependent refractive index data for the top and bottom of a single boule have been presented [23], indicating index gradients dependent on the melt composition (see Datareview 1.1 in this book). It was also shown that adding MgO to the melt will induce index changes as well [15], which is consistent with the fact that the presence of MgO in the melt will change the stoichiometry of the grown boule. The location of the UV absorption edge also changes with the stoichiometry. More details are provided in Datareview 1.1 in this book. Also some data on Li-rich LiNbO_3 can be found in the second reference cited in [8].

C2.4 Thin-film and amorphous LiNbO_3

Refractive index data from sputtered polycrystalline and amorphous material [24] and from sputtered single-crystal film [25] have been reported. Amorphous material exhibits an isotropic index significantly below that for single-crystal material, while polycrystalline films exhibit anisotropic indices falling between those for stoichiometric and congruent material. Both classes of material are generally well-behaved with respect to the spectral dispersion. Since these materials are in general of indeterminate stoichiometry, it is therefore not relevant to tabulate the refractive index data here.

C2.5 Doped LiNbO_3

The influence of impurity doping on the refractive index has been studied by a number of groups. Tabulated data are given for Mg at 20°C [15] and for Sc, Ti, Cr, Mn, Fe, Co, Ni, Cu and Zn at room temperature [16]. Room temperature data from [16] are given in TABLE 5. We present the data from [16] because of its completeness but one should note the caveat regarding this reference (see Section C2.1).

Additional data, over different wavelength ranges, for Cr around 25 - 30°C [26] and for MgO at 21°C [27], have been recently reported. The data from [26], given in TABLE 6, were obtained for Li-rich material ($v = 0.495$, i.e. Li concentration in the crystal of 49.5%). A two-oscillator Sellmeier equation is also proposed, which provides good agreement with the experimental data (as demonstrated for the extraordinary refractive index, in the particular case of 0.01 wt% doping).

The MgO -doped lithium niobate data from [27] were fitted to a three-oscillator Sellmeier equation of the form:

$$n^2(\lambda) = 1 + \frac{A\lambda^2}{\lambda^2 - B} + \frac{C\lambda^2}{\lambda^2 - D} + \frac{E\lambda^2}{\lambda^2 - F} \quad (5)$$

8.2 Dispersion properties of LiNbO_3 and tables

TABLE 5 Visible and near-IR refractive index data for stoichiometric doped lithium niobate [16].
All doping levels are 0.1 at% except for Cu (0.5 at%) and Zn (0.2 at%).

(a) Ordinary refractive index.

Dopant	404.7 nm	471.3 nm	480.0 nm	546.1 nm	585.2 nm	587.6 nm
Sc	2.3935	2.3466	2.3436	2.3172	2.3100	2.3040
Ti	2.3928	2.3462	2.3432	2.3167	2.3043	2.3036
Cr	2.3926	-	-	2.3167	2.3042	2.3035
Mn	2.3944	-	-	2.3180	2.3056	2.3047
Fe	2.3930	2.3464	2.3434	2.3166	2.3044	2.3036
Co	2.3942	-	-	2.3176	2.3052	2.3046
Ni	2.3933	2.3466	2.3437	2.3170	2.3046	2.3038
Cu	-	-	-	2.3176	2.3051	2.3043
Zn	2.3929	-	-	2.3171	2.3046	2.3038

(b) Extraordinary refractive index.

Dopant	404.7 nm	471.3 nm	480.0 nm	546.1 nm	585.2 nm	587.6 nm
Sc	2.2833	2.2495	2.2471	2.2249	2.2143	2.2137
Ti	2.2881	2.2491	2.2468	2.2241	2.2136	2.2129
Cr	2.2852	-	-	2.2217	2.2112	2.2105
Mn	2.2868	-	-	2.2232	2.2128	2.2119
Fe	2.2878	2.2487	2.2464	2.2234	2.2135	2.2128
Co	2.2899	-	-	2.2262	2.2154	2.2147
Ni	2.2879	2.2488	2.2468	2.2240	2.2136	2.2129
Cu	-	-	-	2.2247	2.2141	2.2134
Zn	-	-	-	2.2243	2.2137	2.2131

TABLE 6 Visible and near-IR refractive index data for Cr-doped lithium niobate [23].

Doping		1079.8 nm	1084.4 nm	1140.9 nm	1152.3 nm	1176.7 nm
0.01 wt%	n_o	2.228	2.228	2.226	2.224	2.222
0.01 wt%	n_e	2.142	2.141	2.140	2.139	2.138
0.05 wt%	n_o	2.227	2.228	2.225	2.223	2.222
0.05 wt%	n_e	2.143	2.142	2.141	2.139	2.138
0.275 wt%	n_o	2.231	2.231	2.227	2.227	2.226
0.275 wt%	n_e	2.143	2.144	2.143	2.140	2.139

with λ being the free-space wavelength (μm). The coefficients, at 21°C, for both ordinary and extraordinary refractive indices are given below:

	n_o	n_e
A	2.2454	2.4272
B	0.01242	0.01478
C	1.3005	1.4617
D	0.05313	0.05612
E	6.8972	9.6536
F	331.33	371.216

A similar expression was developed in [27] for undoped congruently grown LiNbO_3 , with coefficients given for comparison between the doped and undoped crystals.

In [28] a variety of dopants (Co, Mn, Cr, Fe, Ni, Cu) are considered at room temperature. The refractive index change is predicted based on the doping-induced lattice distortion, and also the dopant-ion radius is correlated to this index change, at 546 nm, relative to the undoped material.

8.2 Dispersion properties of LiNbO_3 and tables

Numerical data are limited to graphical representation of the extraordinary refractive index only for Cu and Co over the 450 - 650 nm spectral range.

In the case of Ti doping, data on changes in n_o and n_e as functions of mass concentration were summarised [29] and it was shown that at Ti concentrations of 0.2% - 0.7% (i.e. 1.3×10^{20} - 4×10^{20} ions cm^{-3}) the n_e slope decreases abruptly. A common linear relationship was found to hold for n_o and for n_e below the point of slope anomaly. A similar analysis [30] provides more detailed polynomial expressions incorporating non-linearities and wavelength dispersion and the non-linearity was confirmed from X-ray absorption as well [31]. In [31] it was found that the Ti-centre is concentration dependent, an anomaly in the concentration range 5×10^{20} - 2×10^{21} ions cm^{-3} being associated with displacement in the xy plane. This displacement results in bilinear dependence of n_o , and, since no z-displacement occurs, n_e remains essentially linearly dependent on concentration.

C3 Infrared Region

In [4] the refractive index dispersion of lithium niobate was derived by direct analysis of reflectivity data in the transparent region (by fitting oscillator models using the data of [14]). This type of derivation resulted in a poor fit between theory and experiment at long wavelengths. Different authors [32,33] used Kramers-Kronig analysis on data obtained, at a temperature of 25°C, from a material of unspecified composition (perhaps near-stoichiometric). In TABLE 7, refractive index data are presented, as obtained from the graphical representations of the dispersion provided in the cited references ([4] for 5 - 11 μm , [32] for 12.5 - 250 μm , and [34] for 250 - 1000 μm).

TABLE 7 Infrared refractive index data for stoichiometric lithium niobate [4,25,28] (see text).

E (eV)	E (cm^{-1})	λ (μm)	n_o	n_e
0.2480	2000	5.00	2.05	2.00
0.2067	1666	6.00	1.97	1.92
0.1771	1428	7.00	1.84	1.83
0.1550	1250	8.00	1.71	1.72
0.1378	1111	9.00	1.52	1.55
0.1240	1000	10.00	1.20	1.30
0.1127	909	11.00	0.60	0.81
0.0992	800	12.50	0.20	0.46
0.0868	700	14.29	0.54	0.56
0.0644	600	16.67	1.10	4.02
0.0620	500	20.00	3.27	2.67
0.0496	400	25.00	1.01	0.83
0.0434	350	28.57	2.64	-
0.0372	300	33.33	2.80	1.20
0.0310	250	40.00	6.79	6.58
0.0248	200	50.00	2.54	6.78
0.0186	150	66.67	7.96	6.33
0.0124	100	100.00	8.57	5.66
0.0099	80	125.00	7.87	5.52
0.0074	60	166.67	7.34	5.38
0.0062	50	200.00	6.90	5.17
0.0050	40	250.00	6.80	5.13
0.0037	30	333.33	6.70	5.10
0.0025	20	500.00	6.64	5.07
0.0012	10	1000.00	6.61	5.06

In the far-infrared, [34] and [35] used channel-spectrum measurements to deduce the refractive index, with virtually identical results, the latter presenting an analytic expression for the refractive index energy dispersion:

$$n^2(E) = 1 + \frac{a - bE^2}{c - E^2} \quad (6)$$

where E is the photon energy (cm^{-1}). The determined coefficients are given below for both ordinary and extraordinary refractive indices:

	n_o	n_e
a	1.12×10^6	1.19×10^6
b	4.64	4.98
c	4.41×10^4	2.72×10^4

C4 Microwave Region

In the millimetric wavelength range, Fourier-transform spectroscopy was used to determine ordinary and extraordinary refractive indices over the wavelength range 0.25 - 0.06 cm (i.e. 4 - 18 cm^{-1}) [36]. For both polarisations, the squared values of the measured refractive indices ($n_o = 6.68$ and $n_e = 5.13$) approximated the values of the clamped dielectric constants, as expected. These values are in good agreement with the long-wavelength results of [34]. A slight tendency for the refractive index to increase with the frequency is the result of approaching the higher frequency infrared active modes of the material.

REFERENCES

- [1] D. Redfield, W.J. Burke [*J. Appl. Phys. (USA)* vol.45 (1974) p.4566]
- [2] I. Foldvari, K. Polgar, A. Mecseki [*Acta Phys. Hung. (Hungary)* vol.55 (1984) p.321]
- [3] L. Hafid, F.M. Michel-Clendini [*J. Phys. C (UK)* vol.19 (1986) p.2907]
- [4] A.S. Barker, R. Loudon [*Phys. Rev. (USA)* vol.158 (1967) p.433]
- [5] B. Tatian [*Appl. Opt. (USA)* vol.23 (1984) p.4477]
- [6] A. Rauber [*Curr. Top. Mater. Sci. (Netherlands)* vol.1 (1978) p.481]
- [7] R.S. Weis, T.K. Gaylord [*Appl. Phys. A (Germany)* vol.37 (1985) p.191]
- [8] E.D. Palik [*Handbook of Optical Constants of Solids* (Academic Press, 1985) p.695]; see also V.G. Dmitriev [*Handbook of Nonlinear Optical Crystals* (Springer, 1999) section 2.11]
- [9] E. Weisendanger, G. Guntherodt [*Solid State Commun. (USA)* vol.14 (1974) p.303]
- [10] K. Barner, R. Braunstein, H.A. Weakliem [*Phys. Status Solidi B (Germany)* vol.68 (1975) p.525]
- [11] A.M. Mamedov [*Opt. Spectrosc. (USA)* vol.56 (1984) p.645]
- [12] W.L. Bond [*J. Appl. Phys. (USA)* vol.36 (1965) p.1674]
- [13] G.D. Boyd, R.C. Miller, K. Nassau, W.L. Boyd, A. Savage [*Appl. Phys. Lett. (USA)* vol.5 (1964) p.234]
- [14] G.D. Boyd, W.L. Boyd, H.L. Carter [*J. Appl. Phys. (USA)* vol.38 (1967) p.1941]
- [15] J.E. Midwinter [*J. Appl. Phys. (USA)* vol.39 (1968) p.3033]
- [16] N.N. Sirota, V.P. Yarunchiev, I.T. Bondar [*J. Appl. Spectrosc. (USA)* vol.31 (1979) p.1165]
- [17] M.V. Hobden, J. Warner [*Phys. Lett. (Netherlands)* vol.22 (1966) p.243]
- [18] D.F. Nelson, R.M. Mikulyak [*J. Appl. Phys. (USA)* vol.45 (1974) p.3688]
- [19] S.D. Smith, H.D. Riccius, R.P. Edwin [*Opt. Commun. (Netherlands)* vol.17 (1976) p.332 and vol.20 (1977) p.188 (errata)]
- [20] G.J. Edwards, M. Lawrence [*Opt. Quantum Electron. (Netherlands)* vol.16 (1984) p.373]
- [21] D.H. Jundt [*Opt. Lett. (USA)* vol.22 (1997) p.1553]
- [22] J.G. Bergman, A. Ashkin, A.A. Ballman, J.M. Dziedzic, H.J. Levinstein, R.G. Smith [*Appl. Phys. Lett. (USA)* vol.12 (1968) p.92]
- [23] G.E. Peterson, S.R. Lunt [*Ferroelectrics (UK)* vol.75 (1987) p.99]
- [24] G.H. Hewig, K. Jain, F.O. Sequeda, R. Tom, P.-W. Wang [*Thin Solid Films (Switzerland)* vol.88 (1982) p.67]

8.2 Dispersion properties of LiNbO_3 and tables

- [25] G.H. Hewig, K. Jain [*J. Appl. Phys. (USA)* vol.54 (1983) p.57]
- [26] K. Chah, M. Aillerie, M.D. Fontana, G.I. Malovichko, K. Betzler, E. Kokanyan [*Opt. Commun. (Netherlands)* vol.136 (1997) p.231]
- [27] D.E. Zelmon, D.L. Small, D. Jundt [*J. Opt. Soc. Am. B (USA)* vol.14 (1997) p.3319]
- [28] I.T. Bodnar, V.P. Yarunichev [*Cryst. Res. Technol. (Germany)* vol.18 (1983) p.1161]
- [29] J. Ctyroki, M. Hofman, J. Janta [*IEEE J. Quantum Electron. (USA)* vol.20 (1984) p.400]
- [30] S. Fouchet, A. Carenco, C. Daguet, R. Guigliemi, L. Riviere [*J. Lightwave Technol. (USA)* vol.5 (1987) p.700]
- [31] P. Skeath, W.T. Elam, W.K. Burns, F.A. Stevie, T.H. Briggs [*Phys. Rev. Lett. (USA)* vol.59 (1987) p.1950]
- [32] J.D. Axe, D.F. O'Kane [*Appl. Phys. Lett. (USA)* vol.9 (1966) p.58]
- [33] Yu.M. Poplavko, V.V. Meriakri, V.N. Aleshechkin, V.G. Tsyalov, E.F. Ushatkin, A.S. Kynazev [*Sov. Phys.-Solid State (USA)* vol.15 (1973) p.991]
- [34] K. Sakai [*Appl. Opt. (USA)* vol.11 (1972) p.2894]
- [35] D.R. Bosomworth [*Appl. Phys. Lett. (USA)* vol.9 (1966) p.330]
- [36] P.S. Brody, J.P. Sattler, G.J. Simonis [*Ferroelectrics (UK)* vol.50 (1983) p.645]

8.3 Dielectric constants of LiNbO₃

I. Tomeno and S. Matsumura; updated by K.A. Green

July 2001

A FREQUENCY DEPENDENCE

The RF dielectric constants of lithium niobate, a piezoelectric material, fall into two general categories, low frequency (unclamped/constant stress) and high frequency (clamped/constant strain). At electrical frequencies below approximately 100 kHz, the crystal strain follows the electric field changes, and the constant-stress dielectric constant is labelled ϵ_{ii}^T . The subscript refers to the direction of the force and response: $i = 1,2,3$ for the x,y,z directions. Constant-strain dielectric constants ϵ_{ii}^S are obtained at frequencies above approximately 10 MHz, where the strain is unable to follow the fields. Room-temperature ϵ_{ii} values were reported in [1-4,11]. The data are compared in Landolt-Börnstein [5,6]. Room-temperature average values for ϵ_{ii} are obtained from [1-4]. The clamped dielectric constant ϵ_{11}^S is approximately half as large as the free dielectric constant ϵ_{11}^T . In contrast to ϵ_{11} , there is only a slight difference between ϵ_{33}^T and ϵ_{33}^S . Dielectric constants in the GHz range were determined by Ohmachi et al [7], and Teague and Rice [8]. High-frequency dielectric constants can be estimated from light scattering experiments [9,10]. These data are summarised in TABLE 1.

TABLE 1 Dielectric constants of LiNbO₃.

Frequency	ϵ_{11}	ϵ_{33}	Ref
Low (100 kHz)	84.6	29.1	[1-4]
High (10 MHz)	44.3	27.6	[1-4]
0.1 GHz	44.1	23	[8]
1.0 GHz	43.9	23.7	[8]
9.0 GHz	42.5	26	[7]
IR	41.5	44	[9]
Raman	26.0	29	[10]

B TEMPERATURE DEPENDENCE

Tomeno and Matsumura [4] determined the temperature dependence of dielectric constants. Both free and clamped dielectric constants ϵ_{11} increase gradually with increasing temperature. At 1200 K, ϵ_{11}^T is 133 and ϵ_{11}^S is 90. The dielectric constant ϵ_{33} obeys the Curie-Weiss law:

$$\epsilon_{33} = C/(T - T_c) \quad T > T_c$$

$$\epsilon_{33} = C'/(T_c - T) \quad T < T_c$$

The slope for $1/\epsilon_{33}$ at 1 MHz above T_c yields a Curie constant $C = 2.7 \times 10^5$ K, which is a typical value for the displacive phase transition. The ratio $C/C' = 2.6$ indicates that LiNbO₃ undergoes a nearly second-order phase transition. The Curie temperature T_c is 1410 K for LiNbO₃ with a congruent melt composition. The ϵ_{33} value at T_c is 2×10^5 at 100 kHz.

The normalised temperature coefficients for ϵ_{ii}^T are reported by Smith and Welsh [3] in the temperature range between 273 and 383 K:

8.3 Dielectric constants of LiNbO_3

$$(\text{d}\varepsilon_{11}/\text{dT})/\varepsilon_{11} = 3.82 \times 10^{-4} \text{ K}, (\text{d}\varepsilon_{33}/\text{dT})/\varepsilon_{33} = 6.71 \times 10^{-4} \text{ K}$$

C DIELECTRIC LOSS

The loss tangent is small in the temperature range between 293 and 573 K up to 9 GHz. Ohmachi et al [7] reported that tan delta is 1.3×10^{-3} . Tomono and Matsumura [4] observed that tan delta at 10 kHz increases considerably with increasing temperature above 600 K.

D CONCLUSION

Both low-frequency and high-frequency dielectric constants of LiNbO_3 are reviewed. These values increase with increasing temperature and the temperature coefficients are reported. The loss tangent is small in the temperature range 293 to 573 K, up to 9 GHz.

REFERENCES

- [1] A.W. Warner, M. Onoe, G.A. Coquin [*J. Acoust. Soc. Am. (USA)* vol.42 no.6 (1967) p.1223-31]
- [2] T. Yamada, N. Niizeki, H. Toyoda [*Jpn. J. Appl. Phys. (Japan)* vol.6 no.2 (1967) p.151-5]
- [3] R.T. Smith, F.S. Welsh [*J. Appl. Phys. (USA)* vol.42 no.6 (1971) p.2219-30]
- [4] I. Tomono, S. Matsumura [*J. Phys. Soc. Jpn. (Japan)* vol.56 no.1 (1987) p.163-77]
- [5] [*Landolt-Börnstein Numerical Data and Functional Relationships in Science and Technology* vol.III/11 (Springer, 1979) p.341]
- [6] [*Landolt-Börnstein Numerical Data and Functional Relationships in Science and Technology* vol.III/9 (Springer, 1975) p.152]
- [7] Y. Ohmachi, K. Sawamoto, H. Toyoda [*Jpn. J. Appl. Phys. (Japan)* vol.6 (1967) p.1467-8]
- [8] J.R. Teague, R.R. Rice [*J. Appl. Phys. (USA)* vol.46 no.7 (1975) p.2864-6]
- [9] A.S. Barker Jr., R. Loudon [*Phys. Rev. (USA)* vol.158 no.2 (1967) p.433-45]
- [10] I.P. Kaminow, W.D. Johnston Jr. [*Phys. Rev. (USA)* vol.160 (1967) p.519]
- [11] A. Mansingh, A. Dhar [*J. Phys. D (UK)* vol.18 (1985) p.2059]

8.4 Electro-optic coefficients of LiNbO₃

C.J.G. Kirkby; updated by C. Florea

February 2002

A ELECTRO-OPTIC EFFECTS

A1 Introduction

A full theoretical treatment of electro-optic behaviour is given in [1]. Electro-optic effects are generally discussed phenomenologically in terms of the optical indicatrix, an ellipsoidal surface with axes related to the major crystal axes and in which the major and minor axes of the central section normal to the propagation direction represent the principal refractive indices. The behaviour of the indicatrix can be presented as a power series in electric field, E, by:

$$\Delta \frac{1}{n_{ij}^2} = \sum_k r_{ijk} E_k + \sum_{k,l} R_{ijkl} E_k E_l + \dots \quad (1)$$

where E_k are Cartesian components. Alternatively, dielectric polarisation, P_k, is regarded as the driving term, giving:

$$\Delta \frac{1}{n_{ij}^2} = \sum_k f_{ijk} P_k + \sum_{k,l} g_{ijkl} P_k P_l + \dots \quad (2)$$

The tensors r_{ijk} and R_{ijkl}, generally contracted to r_{mk} and R_{mn}, represent the linear and quadratic electro-optic coefficients; the polarisation optic coefficients f_{mk} and g_{mn} are also used, particularly in dealing with polar materials.

From symmetry, twenty of the twenty-one acentric classes, class 432 being the sole exception, are piezoelectric and exhibit a linear electro-optic effect.

Lithium niobate, with symmetry 3m and point group C3v, exhibits four independent linear electro-optic coefficients, r₁₃ (= -r₂₃), r₂₂ (= -r₁₂ = -r₆₁), r₃₃ and r₅₁ (= r₄₂), their signs and magnitudes being determined by the symmetry and relative orientation of the BO₆ octahedra in the crystal structure. In [2] it was shown that r₂₂, r₅₁ and (r₁₃ - r₃₃) must all have the same sign.

All materials, regardless of symmetry, exhibit quadratic and higher order effects, although these are rarely significant.

A2 Measurement

Determinations of electro-optic coefficient generally involve measurement of induced refractive index changes via corresponding optical phase changes. With the external field along the crystal z-axis, the principal axes of the indicatrix coincide with the crystallographic axes and are given by:

$$n_x = n_y = n_o + n_o^3 r_{13} E_x / 2 \quad (3a)$$

$$n_z = n_e + n_e^3 r_{33} E_z / 2 \quad (3b)$$

whence r₁₃ and r₃₃ can be determined directly, assuming knowledge of the refractive indices. Defining

8.4 Electro-optic coefficients of LiNbO_3

$$r_z = r_{13} - (n_e/n_o)^3 r_{33} \quad (4)$$

the birefringence B_{xz} becomes:

$$B_{xz} = (n_e - n_o) + n_o^3 r_z E_z / 2 \quad (5)$$

providing confirmation of consistency.

With the field along the x-axis, the indicatrix axes become, to first order,

$$n_x = n_o + n_o^3 r_{22} E_x / 2 \quad (6a)$$

$$n_y = n_o - n_o^3 r_{22} E_x / 2 \quad (6b)$$

$$n_z = n_e \quad (6c)$$

allowing determination of r_{22} . In this configuration, the ellipsoid axes are related to the crystalline axes by a 45° rotation about the z-axis, followed by small identical rotations, θ , about the x and y axes given by:

$$\theta = \frac{r_{51} E_x n_e^2 n_o^2}{1.414 (n_o^2 - n_e^2)} \quad (7)$$

permitting determination of r_{51} , which is consequently regarded most difficult to determine precisely.

A3 Measurement Conditions

At excitation frequencies below mechanical resonance, the ‘unclamped’ state, an electro-optic crystal deforms freely under piezoelectric forces and the measured electro-optic coefficient includes an additional photo-elastic contribution; above mechanical resonance, the crystal is effectively clamped in the sense that mechanical deformation induced by acoustic modes cannot be sustained, and all piezo-optic contributions vanish. Formally, the relationship between clamped and unclamped coefficients may be written:

$$r_{ijk}(T) = r_{ijk}(S) + \sum_{m,n} p_{ijmn}(E) d_{kmn}(T) \quad (8)$$

where $r(T)$ and $r(S)$ are measured at zero stress (unclamped, $T = 0$) and zero strain (clamped, $S = 0$) respectively, $p_{ijmn}(E)$ is the zero-field photo-elastic coefficient and $d_{kmn}(T)$ is the zero-stress piezoelectric coefficient. Similar relationships obtain for the tensors R, f and g.

At frequencies extending up to the interband absorption, optical and acoustic phonons are effectively clamped, the electro-optic effect possessing purely electronic origins. Although usually treated in the context of non-linear optics, electronic electro-optic phenomena are equally the high frequency extension of the basic electro-optic effect and may be characterised by an ‘electronic’ linear electro-optic tensor $r(e)$, related to the SHG coefficient d by:

$$d_{kji} = -0.25 (n_i n_j)^2 r_{ijk}(e) \quad (9)$$

In reporting data, it is thus clearly important to specify measurement conditions.

B MATERIAL CONSIDERATIONS

Lithium niobate is not completely defined by the stoichiometric formula LiNbO_3 . Large deviations from this composition may exist, characterised by two independent variables, namely the Li/Nb ratio and the ratio between the sum of the metals and oxygen. Two extreme compositions are commonly encountered:

- (i) Stoichiometric material represents the strict chemical formula LiNbO_3 , with Li/Nb = 1.0 (Li_2O mole fraction = 0.5).
- (ii) Congruently melting material grows in the same composition as its melt, with Li/Nb = 0.945 (Li_2O mole fraction = 0.486).

Pure, well oxidised lithium niobate is transparent from the fundamental bandgap absorption edge around 350 nm [3] to about 5 μm , where phonon absorption, extending to nearly 80 μm , sets in; the far infrared absorption spectrum shows little structure, the phonon influence fading. Since electro-optic behaviour as commonly understood implies optical transparency, it is meaningful to consider only spectral regions in which significant transparency occurs.

Since lithium niobate is a ferroelectric material, capable of exhibiting a well defined domain structure, it is important to ensure that the material is fully poled to a single domain state before measuring electro-optic coefficients.

C LINEAR ELECTRO-OPTIC COEFFICIENTS

C1 Ultraviolet

With an interband optical absorption edge around 350 nm [3], lithium niobate is essentially absorbing in the ultraviolet; no data for electro-optic coefficients in this region appear to have been reported.

C2 Visible and Near Infrared

C2.1 General

C2.1.1 Low frequency (unclamped)

Low frequency (DC and 60 Hz) measurements of r_{22} and r_{51} were reported in [4], together with r_z defined in EQN (4), at room temperature at a wavelength of 632.8 nm. Conflicting data for r_{22} were reported in [5]. Zook et al [6] measured r_{33} , r_{13} and r_{22} at 100°C and their temperature dependences (Section C2.4). The absolute signs of r_{33} and r_{13} were determined experimentally; the signs of the other components remain undetermined. In [7] low frequency half wave voltage data were reported, from which a value for r_z can be derived. An interferometric technique was used in [8] to determine r_{13} , r_{33} and r_z . Holmes et al [9] measured r_{13} and r_{33} in a range of samples at unspecified frequency, the data being compatible with unclamped conditions. With the development of improved measurement methods very accurate values of these coefficients (in particular, r_{13} and r_{33} for congruent LiNbO_3 , at 632.8 nm) have been recently reported [46,47].

Review collations, of varying accuracy, exist. Reference [11] presents data of [4,5] and subsequently ([12]) of [8]. Reference [13] tabulates data of [4-6] and [14], correcting errors appearing in another Landolt-Bornstein tabulation [15]. Reference [16] contains some erroneous references while [17] presents data of uncertain origin, not apparently derived consistently from any one of the above sources.

8.4 Electro-optic coefficients of LiNbO_3

Data from accessible primary sources, together with results from certain secondary collations, are presented in TABLE 1. Agreement between the different workers is reasonably good, with accuracies of the order of 10% generally acceptable. The differences might also be due to the different stoichiometry of the crystals used for measurements, especially for the earlier data where the crystal stoichiometry was more difficult to control and/or to assess. The dependence on the stoichiometry of the electro-optic coefficients is discussed in Section C2.3.

TABLE 1 Visible and near infrared (unclamped) electro-optic coefficients of LiNbO_3 .

$r_{13}(T)$	$r_{22}(T)$	$r_{33}(T)$	$r_{51}(T)$	$r_z(T)$	Ref
-	3.3	-	32	17.4	[4]
-	6.7	-	-	19	[5]
+10.0	6.8	+32.6	32.6	-	[6]
-	-	-	-	17.8	[7]
10.9	-	34.0	-	19.4	[8]
-	-	-	-	17	[41]
-	6.4	-	-	-	[25]
11.0	-	36.7	-	-	[9]
-	5.1	22.3	-	-	[10]
9.6	6.7	31	32	-	[17]
-	6.7	-	-	18	[14]
9.5	-	31.2	-	-	[46]
10.5	-	31.4	-	-	[47]

Numerical data for r_{ij} presented in units of 10^{-12} m/V .

C2.1.2 High frequency (clamped)

Turner [18] used a heterodyne technique to determine clamped r_{13} , r_{22} , r_{33} , r_{51} and r_z ; r_{51} is probably least accurate. Turner et al [7] subsequently reported $n^3 r_{ij}$ products at 76 MHz, allowing r_{13} and r_{33} to be determined from knowledge of the refractive indices. Kaminow et al [19] determined r_{51} via a waveguide technique, and in the same paper reported hitherto unpublished figures, due to Turner, for r_{33} , r_{13} and r_{22} .

In reviews, the data of Turner are reported by [11,13,16] (erroneously citing the unclamped data of [4]), and [17]. Adachi [20], reproducing Turner's data indirectly via [11], introduces the non-existent component r_{52} in place of r_{51} .

Data from primary sources, essentially results of Turner and his various collaborators, together with results from certain secondary collations, are presented in TABLE 2.

TABLE 2 Visible and near infrared (clamped) electro-optic coefficients of LiNbO_3 .

$r_{13}(S)$	$r_{22}(S)$	$r_{33}(S)$	$r_{51}(S)$	$r_z(S)$	Ref
+8.6	3.4	+30.8	+28	20.58	[18]
8.56	-	30.47	-	18.54	[7]
-	7.9	-	-	+18.2	[19]
10.9	-	34.0	-	-	[14]
7.7	3.4	28.8	-	-	unpub.

Numerical data for r_{ij} presented in units of 10^{-12} m/V .

C2.1.3 Optical frequency (NLO)

In the case of lithium niobate, application of the Kleinmann symmetry rule renders d_{31} and d_{15} equal, implying approximate equality of $r_{13}(e)$ and $r_{15}(e)$. Data on electronic electro-optic coefficients are generally derived from SHG measurements; although absolute determinations exist, such measurements are difficult and many workers report data relative to standard characterised materials. First measurements [21-23] were relative to KDP. Miller et al [23] showed d_{22} and d_{33} essentially independent of stoichiometry, d_{31} increasing by 50% as melt Li/Nb ratio increases from 0.852 to 1.083. The d-tensor components were determined at a range of wavelengths, both indirectly and directly [24]; $r_{ij}(e)$, derived from these data using EQN (9), are shown in TABLE 3. Broadly similar figures are given in [1].

TABLE 3 Visible and near infrared (electronic) electro-optic coefficients derived from [24].

Wavelength (nm)	$r_{13}(e)$	$r_{22}(e)$	$r_{33}(e)$
448	0.88	0.57	-
1060	0.92	0.62	5.34
1150	0.90	0.53	5.34
1318	0.98	0.62	5.60
2120	-	-	5.36

Numerical data for r_{ij} presented in units of 10^{-12} m/V .

C2.2 Wavelength dependence

Wavelength dependence of electro-optic coefficients is related to the factors defining refractive index dispersion; a full treatment appears in [1]. Analytically, the parameter $P = r/(1 - 1/n^2)^2$, where r is probably strictly the electronic component $r(e)$, exhibits quadratic dependence on normalised photon energy (E/E_o), with coefficients generally, but not necessarily, increasing towards the bandgap energy, E_o :

$$P = P_o + Q(E/E_o)^2 \quad (10)$$

Early determinations of electro-optic coefficients were performed at an optical wavelength of 632.8 nm, the only generally accessible CW laser line. Reference [25] reported $r_{22}(T)$ at 436, 546, 589 and 632.8 nm, indicating inverse wavelength dependence, linearly proportional to the refractive index term $(n^2 - 1)^2/n^4$, and showing the sign to be negative. Reference [9] reported r_{13} and r_{33} , apparently unclamped, at 632.8 and 1320 nm, indicating inverse wavelength dependence. In [26] r_{13} , r_{22} and r_{51} were determined indirectly by Raman scattering at 587 nm; comparison with direct measurement was poor. The same group [27], citing [28], claim r_{22} constant at $1.2 \times 10^{-12} \text{ m/V}$ over 700 - 2500 nm.

Reference [13] tabulates clamped and unclamped data from a number of sources [4-6,14,18,19,38] at wavelengths in the range 632.8 nm to 3390 nm, correcting errors for $r(T)$ at 633 nm cited in [15]; reference [12] quotes [25] for r_{22} .

TABLE 4 presents a collation of available wavelength dependence data. For $r_{22}(T)$, assuming $E_o = 6.74 \text{ eV}$, the following parameters in EQN (10) can be derived: $P_o = 6.13$, $Q = 42.01$; unfortunately, insufficient data are available to make realistic calculations for the remaining coefficients.

8.4 Electro-optic coefficients of LiNbO_3

TABLE 4 Visible and near infrared wavelength dependence of electro-optic coefficients.

nm	$r_{ij}(T)$				$r_{ij}(S)$				Ref
	r_{13}	r_{22}	r_{33}	r_{51}	r_{13}	r_{22}	r_{33}	r_{51}	
436	-	-9.1	-	-	-	-	-	-	[25]
548	-	-7.7	-	-	-	-	-	-	[25]
589	-	-6.9	-	-	-	-	-	-	[25]
633	-	-6.3	-	-	-	-	-	-	[25]
633	-	6.7	-	-	-	-	-	-	[5]
633	+10.0	6.8	+32.2	-	-	-	-	-	[6]
633	-	3.3	-	32	-	-	-	-	[4]
633	-	6.7	-	-	10.9	-	34.0	-	[14]
633	-	-	-	-	-	-	-	+18.2	[19]
633	-	-	-	-	+7.7	3.4	+28.8	-	(a)
633	-	-	-	-	8.6	3.4	30.8	28	[18]
633	11.0	-	36.7	-	-	-	-	-	[9]
1150	-	5.4	-	-	-	-	-	-	[14]
1320	10.3	-	34.1	-	-	-	-	-	[9]
3390	-	3.1	-	-	-	-	-	-	[14]
3390	-	-	-	-	6.5	3.1	28	23	[18]

Numerical data for r_{ij} presented in units of 10^{-12} m/V .

(a) E.H. Turner, unpublished, cited in [19].

C2.3 Stoichiometry dependence

The influence of crystal stoichiometry on electro-optic coefficients in lithium niobate has been disputed. Hirano [29] reported unclamped half-wave voltage decreasing appreciably with any departure from stoichiometric composition, the value at a Li/Nb ratio of 1.10 being 56% of that in stoichiometric material. Turner et al [7] refuted this claim, reporting unclamped and clamped values of r_{13} , r_{33} and r_z essentially unchanged over a Li/Nb ratio range from 0.91 to 1.083 and presenting theoretical backing for their findings. Recent accurate measurements, however, seem to indicate that the unclamped values (modulation at 1000 Hz) for the quasi-stoichiometric LiNbO_3 are indeed lower by about 10% when compared with the values for the congruent LiNbO_3 [47]. In particular, $r_{13} = 9.25 \pm 0.07 \text{ pm V}^{-1}$ and $r_{33} = 29.4 \pm 0.2 \text{ pm V}^{-1}$ for quasi-stoichiometric LiNbO_3 ([Li]/[Nb] ratio of 0.992) while $r_{13} = 10.49 \pm 0.07 \text{ pm V}^{-1}$ and $r_{33} = 31.4 \pm 0.2 \text{ pm V}^{-1}$ for congruent LiNbO_3 ([Li]/[Nb] ratio of 0.942) as measured by the same authors.

C2.4 Temperature dependence

Reference [6] measured $r_{22}(T)$, $r_{13}(T)$ and $r_{33}(T)$ at 633 nm over the temperature range 20 to 200°C, characterising the dependence by a parameter $(1/r)\partial r/\partial t$. Iwasaki et al [25] reported $r_{22}(T)$ over a comparable range, presenting graphical data at four wavelengths. Sonin et al [41] measured r_z over 0 - 900°C. No determination of the temperature dependence of $r_{51}(T)$ or the clamped coefficients appears to have been reported.

The results of [6,25,41] (over the range 0 to 400°C) can be expressed as:

$$\log[r(t)] = at + b \quad (11)$$

where the constants a and b characterise the temperature dependence to within experimental error. Relevant values of these parameters and digitised selections from the results of [25] are presented in TABLE 5.

8.4 Electro-optic coefficients of LiNbO_3

TABLE 5 Linear electro-optic coefficients: temperature dependence.

(a) Analytical representation: $-\log[r(t)] = at + b$.

Coefficient	Wavelength	a ($\times 10^{-4}$)	b
$r_{22}(T)$	436	1.57	0.95
$r_{22}(T)$	546	1.76	0.88
$r_{22}(T)$	589	2.30	0.82
$r_{22}(T)$	633	2.47	0.80
$r_{13}(T)$	633	4.9	1.46
$r_{33}(T)$	633	4.6	0.99
$r_z(T)$	633	1.91	1.24

(b) Tabulation of $-r_{22}(T)$.

Temperature (°C)	436 nm	546 nm	589 nm	633 nm
20	9.11	7.72	6.85	6.34
50	9.08	7.64	6.87	6.36
75	9.10	7.67	6.92	6.41
100	9.18	7.74	6.97	6.49
125	9.23	7.79	7.05	6.59
150	9.35	7.90	7.18	6.72
175	8.46	8.05	7.33	6.89
200	9.70	8.31	7.56	7.11
225	9.90"	8.56"	7.79"	7.33

Values marked " are extrapolations.

(c) Temperature dependence coefficients $(1/r)dr/dt$ (from [6]).

	$(1/r)dr/dt$ (°C)
$r_{13}(T)$	0.00046
$r_{22}(T)$	0
$r_{33}(T)$	0.00049
$r_{51}(T)$	-

Numerical data for r_{ij} presented in units of 10^{-12} m/V .

C2.5 Doped material

C2.5.1 Proton doping

Proton doping, by ion exchange from organic acid solution [30], is believed to quench the electro-optic properties of lithium niobate. Using a waveguide technique, [31] showed r_{33} decreasing by a factor of 2.7 in material of unspecified proton doping, the degradation depending qualitatively on the exchange time, and hence presumably on the dopant concentration. A limited determination of the concentration dependence of r_{33} was reported in [32], indicating a structural mechanism for the reduction, which reached a factor of 10 at 1% H/Li substitution.

Reference [43] confirmed this reduction in r_{33} using a technique based on electro-optic prism deflection in slab waveguides and taking into account the electro-optic properties of the substrate. The reduction could be virtually completely reversed by controlled annealing of the material. Similar response to annealing was reported in [44,45].

8.4 Electro-optic coefficients of LiNbO_3

No determinations of the remaining coefficients appear to have been made.

C2.5.2 Helium doping

In [33] a 70% decrease in r_{13} on He^+ implantation was reported while, more recently, [34] reported a somewhat smaller decrease of 20% ($r_{13} = 8.13 \times 10^{-12} \text{ m/V}$) in 1.2 MeV implanted waveguides. The difference is attributed to differing techniques for lateral confinement. Measurements of the other coefficients do not appear to have been made.

C2.5.3 Metallic doping

C2.5.3.1 Titanium doping

Although the principal vehicle for contemporary lithium niobate waveguide technology, the influence of titanium doping on electro-optic behaviour does not appear to have been fully investigated. Holmes et al [9] measured r_{13} and r_{33} at 2.9 mol% doping at 632.8 nm and 1320 nm, apparently under unclamped conditions. Within the limits of experimental accuracy, the two coefficients were unchanged on doping.

Reference [43] showed from waveguide measurements that Ti doping reduces r_{33} to around two thirds of the value in virgin material, possibly associated with the increased OH content of the diffused region.

C2.5.3.2 Magnesium doping

Magnesium doping is a recent strategy to reduce the susceptibility of lithium niobate to ‘optical damage’ [35]. r_{13} and r_{33} were measured at 10.7 mol% doping at wavelengths of 632.8 nm and 1320 nm, apparently under unclamped conditions [9]. Within the limits of experimental accuracy, the two coefficients were unchanged on doping.

C2.5.3.3 Iron doping

Iron doping enhances the photorefractive response of lithium niobate and is widely used in holographic data storage studies. Reference [40] used undoped r_{33} and r_{51} results of [18] in analysing results.

C2.5.3.4 Other dopants

Rh, W, V, Mo and Mn doping have been explored for holographic storage studies [36]; no data on electro-optic coefficients have been reported.

C2.6 Thin film and amorphous material

Second harmonic generation in RF-sputtered thin films [42], a linear electro-optic effect in RF-sputtered thin films [48], and quadratic electro-optic behaviour in epitaxially grown thin films [49] have all been demonstrated. Polycrystalline lithium niobate thin films were RF-sputtered on glass substrates and the effective electro-optical coefficient was reported to be 1.34 pm V^{-1} , which is about 4% of the bulk value of r_{33} [48]. In the case of the higher quality epitaxial lithium niobate films grown on sapphire, the quadratic electro-optic effect (characterised by s_{13} and s_{33} for the grown (1120) LiNbO_3 films) was larger by a factor of 41 than the linear effect. An effective quadratic coefficient

$$\frac{1}{2} (n_e^3 s_{33} - n_o^3 s_{13})$$

of about 2.38×10^{-3} pm V⁻¹ was estimated [49].

C3 Infrared

Klein [37] reported values for the parameter $R_{ij} = n^3 r_{ij}$ at 94 GHz (3.13 cm⁻¹); utilising these data, together with n_o and n_e from the same work, r_{22} , r_{13} and r_{33} can be derived. Brody et al [38] report r_{33} , indicating the spectral dependence of the resultant phase shift over the energy range 5 - 15 cm⁻¹. Available data are listed in TABLE 6.

TABLE 6 Infrared (3.13 cm⁻¹, 94 GHz)
electro-optic coefficients.

r_{13}	16.0	[37]
r_{22}	18.9	[37]
r_{33}	35.6	[37]
r_{33}	44.0	[38]

Numerical data for r_{ij} presented in units of 10^{-12} m/V.

D QUADRATIC ELECTRO-OPTIC COEFFICIENTS

Since the Nb ions are surrounded by octahedra of six O ions in a manner similar to the B ions in the ABO₃ cubic perovskite structure, it is of interest to relate the linear electro-optic effect to the quadratic effect in the paraelectric perovskites. Indeed, the linear electro-optic effect in ferroelectric perovskites may be regarded as fundamentally a quadratic effect biased by the spontaneous polarisation [1]. Zook et al [6] derived g_{11} , g_{12} and g_{44} , together with an estimate for the spontaneous polarisation in good agreement with that derived from pyroelectric measurements. Calculations from first principles have also been reported [1], as indicated in TABLE 7.

TABLE 7 Polarisation-optic coefficient (quadratic).
Numerical data for g_{ij} presented in units of m⁴ C⁻².

	T [1]	S [1]	e [1]	Exp. [6]
g_{11}	+0.16	0.20	+0.087	+0.209
g_{12}	+0.04	0.01	+0.082	+0.064
g_{44}	+0.11	0.10	+0.16	+0.145

REFERENCES

- [1] S.H. Wemple, M. DiDomenico [*Appl. Solid State Sci. (USA)* vol.4 (1972) p.263-383]
- [2] L.B. Kreutzer [*Appl. Phys. Lett. (USA)* vol.10 (1967) p.336]
- [3] D. Redfield, W.J. Burke [*J. Appl. Phys. (USA)* vol.45 no.10 (1974) p.4566-71]
- [4] E. Bernal, G.D. Chen, T.C. Lee [*Phys. Lett. (Netherlands)* vol.21 no.3 (1966) p.259-60]
- [5] P.V. Lenzo, E.G. Spencer, K. Nassau [*J. Opt. Soc. Am. (USA)* vol.56 no.5 (1966) p.633-5]
- [6] J.D. Zook, D. Chen, G.N. Otto [*Appl. Phys. Lett. (USA)* vol.11 no.5 (1967) p.159-61]
- [7] E.H. Turner, F.R. Nash, P.M. Bridenbaugh [*J. Appl. Phys. (USA)* vol.41 (1970) p.5278-81]
- [8] K. Onuki, N. Uchida, T. Saku [*J. Opt. Soc. Am. (USA)* vol.62 no.9 (1972) p.1030-2]
- [9] R.J. Holmes, Y.S. Kim, C.D. Brandle, D.M. Smyth [*Ferroelectrics (UK)* vol.51 no.1/2 (1983) p.41-5]
- [10] Bong-Ho Moon, Jae-Hyeon Lee, Min-Su Jang [*New Phys. (Korean Phys. Soc.) (South Korea)* vol.25 no.2 (1985) p.180-5]
- [11] T. Ikeda [*Landolt-Bornstein New Series Gp.III* vol.3 (Springer, Berlin, 1981) p.89-92 and p.356-9]

- [12] N. Niizeki, M. Marutake [*Landolt-Bornstein New Series Gp.III* vol.9 (Springer, Berlin, 1981) p.S79-82 and p.S281-4]
- [13] R.S. Weis, T.K. Gaylord [*Appl. Phys. A (Germany)* vol.37 no.4 (1985) p.191-203]
- [14] P.H. Smakula, P.C. Claspy [*Trans. Metall. Soc. AIME (USA)* vol.239 (1967) p.421-3]
- [15] T. Yamada [*Landolt-Bornstein New Series Gp.III* vol.16a (Springer, Berlin, 1981) p.149-56 and p.489-99]
- [16] A. Rauber [*Curr. Top. Mater. Sci. (Netherlands)* vol.1 (1978) p.481-601]
- [17] A.J. Moses [*The Practising Scientist's Handbook* (Van Nostrand Reinhold, London, UK, 1978, ISBN 0 442 25584 5)]
- [18] E.H. Turner [*Appl. Phys. Lett. (USA)* vol.8 no.11 (1966) p.303-4]
- [19] I.P. Kaminow, E.H. Turner, R.L. Barns, J.L. Bernstein [*J. Appl. Phys. (USA)* vol.51 no.8 (1980) p.4379-84]
- [20] M. Adachi, T. Shiosaki, A. Kawabata [*Ferroelectrics (UK)* vol.27 no.1-4 (1980) p.89-92]
- [21] G.D. Boyd, R.C. Miller, K. Nassau, W.L. Bond, A. Savage [*Appl. Phys. Lett. (USA)* vol.5 (1964) p.234-6]
- [22] R.C. Miller, A. Savage [*Appl. Phys. Lett. (USA)* vol.9 no.4 (1966) p.169-71]
- [23] R.C. Miller, W.A. Nordlund, P.M. Bridenbaugh [*J. Appl. Phys. (USA)* vol.42 (1971) p.4145]
- [24] M.M. Choy, R.L. Byer [*Phys. Rev. B (USA)* vol.14 no.4 (1976) p.1693-706]
- [25] H. Iwasaki, H. Toyoda, N. Niizeki, H. Kubota [*Jpn. J. Appl. Phys. (Japan)* vol.6 no.12 (1967) p.1417-22]
- [26] V.S. Gorelik, O.G. Zolotukhin, M.M. Sushchinskii [*Sov. Phys.-Solid State (USA)* vol.22 no.4 (1980) p.598-600]
- [27] V.S. Gorelik, L.G. Reznik, B.S. Umarov [*Sov. Phys.-JETP (USA)* vol.58 no.2 (1983) p.267-9]
- [28] L.A. Kulevskii, A.M. Prokhorov, V.V. Smirnov [*Sov. Phys.-JETP (USA)* vol.28 (1969) p.217]
- [29] H. Hirano [*Jpn. J. Appl. Phys. (Japan)* vol.8 (1969) p.399]
- [30] J.L. Jackel, C.E. Rice, J.J. Veselka [*Ferroelectrics (UK)* vol.50 no.1-4 (1983) p.491-6]
- [31] R.A. Becker [*Appl. Phys. Lett. (USA)* vol.43 no.2 (1983) p.131-3]
- [32] M. Minakata, K. Kumagai, S. Kawakami [*Appl. Phys. Lett. (USA)* vol.49 no.16 (1986) p.992-4]
- [33] G.L. Destefanis et al [*J. Appl. Phys. (USA)* vol.50 no.12 (1979) p.7898-905]
- [34] G.T. Reed, B.L. Weiss [*Electron. Lett. (UK)* vol.23 no.8 (1987) p.424-5]
- [35] D.A. Bryan, R.R. Rice, R. Gerson, H.E. Tomaschke, K.L. Sweeney, L.E. Halliburton [*Opt. Eng. (USA)* vol.24 no.1 (1985) p.138-43]
- [36] W.J. Burke [RCA Report N00010-74-C-0321 (1974)]
- [37] M.B. Klein [*Int. J. Infrared Millim. Waves (USA)* vol.2 no.2 (1981) p.239-46]
- [38] P.S. Brody, J.P. Sattler, G.J. Simonis [*Ferroelectrics (UK)* vol.50 no.1-4 (1983) p.645-50]
- [39] E.H. Turner [*J. Opt. Soc. Am. (USA)* vol.56 (1966) p.1426]
- [40] S.G. Odulov [*JETP Lett. (USA)* vol.35 no.1 (1982) p.10-13]
- [41] A.S. Sonin, L.G. Lomova [*Sov. Phys.-Solid State (USA)* vol.9 (1968) p.2607]
- [42] G.H. Hewig, K. Jain [*J. Appl. Phys. (USA)* vol.54 no.1 (1983) p.57-61]
- [43] M. Rottchalk, A. Rasch, W. Karthe [*J. Opt. Commun. (Germany)* vol.9 (1988) p.19-23]
- [44] A. Loni, R.M De La Rue, J.M. Winfield [*Tech. Digest of 9th Topical Meeting on Integrated and Guided Wave Optics* Santa Fe, NM, USA (1988) p.84-7]
- [45] P.G. Suchoski, T.K. Findakly, F.J. Leonberger [*Opt. Lett. (USA)* vol.13 no.11 (1988) p.1050-2]
- [46] P. Ney, A. Maillard, M.D. Fontana, K. Polgar [*J. Opt. Soc. Am. B (USA)* vol.17 (2000) p.1158]
- [47] J.A. deToro, M.D. Serrano, A.G. Cabanes, J.M. Cabrera [*Opt. Commun. (Netherlands)* vol.154 (1998) p.23]
- [48] G. Griffel, S. Ruschin, N. Croitoru [*Appl. Phys. Lett. (USA)* vol.54 (1989) p.1385]
- [49] S.-H. Lee, T.W. Noh, J.-H. Lee [*Appl. Phys. Lett. (USA)* vol.68 (1996) p.472]

8.5 Photorefractive effects in LiNbO₃

K.K. Wong

March 2002

A PHOTOREFRACTIVE EFFECTS IN LITHIUM NIOBATE CRYSTALS

The photorefractive effects in bulk lithium niobate (LiNbO₃) crystals are described in this section. The sensitivity of optical waveguides fabricated in LiNbO₃ to photorefractive effects is discussed in the next section of this Datareview.

The term photorefractive effect commonly also known as optical damage refers to an optically induced change of the refractive indices observed when an intense blue or green laser beam was focused into LiNbO₃. This effect was first reported by Ashkin et al [1] and then by Chen et al [2]. Chen postulated that the change in refractive index of the crystal was caused by photoexcited carriers being transported along the polar axes of the crystals and subsequently being trapped [3]. Chen assumed the carriers to originate from impurities or defects in the LiNbO₃ crystal.

The displacement of photoexcited carriers may be attributed to four separate effects. They are:

- (a) bulk photovoltaic effect [4], even in the absence of an applied electric field,
- (b) photoconductivity [5], only in the presence of an electric field,
- (c) diffusion [6], only in some cases, and
- (d) pyroelectricity [51,52].

Since the resistivity of LiNbO₃ is high at room temperature, even a small current flowing in the crystal can cause a high space charge field which will modify the refractive indices of the crystal via the electro-optic effect [7]. This change in the refractive index of the crystal, ΔN , is reversible. The magnitude of ΔN which can vary from 10^{-6} to 10^{-3} depends on the laser radiation intensity ($10^{-1} - 10^3$ W/cm²) and its dose ($1 - 10^3$ J/cm²) [1-3,8,9]. The time of relaxation of ΔN is dependent on the temperature of the crystal [10,11] and the impurity concentration and can range from 10^{-4} seconds to several months [12,13]. Also it was reported that ΔN relaxes when the LiNbO₃ crystal is illuminated with photoactive radiation due to photoconductivity [14,15]. In most cases the relaxation time is a function of the specific resistance of the crystal.

There is general agreement that the photoexcited carriers come from Fe⁺⁺ impurities in the LiNbO₃ crystal [4,14,16] and that the photorefractive sensitivity of the crystal is proportional to its Fe⁺⁺ concentration [9]. Phillips et al reported that the photorefractive sensitivity can be increased by two or three orders by doping the crystal with iron or copper impurities [14].

On the contrary, by addition of 4.6 mol% of MgO to undoped LiNbO₃ crystal, Zhong et al reported a hundred-fold increase in the resistance against optical damage over the pure crystal [17]. The above improvement was found to be due to a hundred-fold increase in the photoconductivity of the crystal with negligible changes in the photovoltaic current [18-21]. Using UV and IR spectrophotometry and AC conductivity, Polgar et al confirmed also that the above behaviour was observed above the concentration of about 4.5 mol% of MgO [22]. Wen et al found that in connection with photorefractive effects, the Li-rich LiNbO₃:Mg (5 mol% MgO) was able to withstand higher laser light intensities than the congruent LiNbO₃:Mg (5 mol% MgO) [23]. This improvement was due to increased photoconductivity with little change in photovoltaic current [23]. Chang et al reported the ability of Li-rich LiNbO₃:Mg (5 mol% MgO):Fe (0.1 wt% Fe₂O₃) to resist optical damage and the result was found to be comparable to that measured for LiNbO₃:Mg (5 mol% MgO), even though the

photorefractive sensitive dopant Fe was added [24]. The enhanced optical damage resistance reported may be due to the change in occupation sites of Fe ions [24].

Quantitative measurements of the photorefractive effects in LiNbO_3 were accomplished by three common techniques. They are:

- (a) birefringence measurement: the measurement of the change in birefringence using conventional compensation techniques [3],
- (b) holographic technique [25], and
- (c) electrostatic technique: the optically generated space charge field can be measured directly using an electrometer probe [26].

Recently Kim and Rhee reported the determination of the photorefractive constant and photoconductivity in $\text{LiNbO}_3:\text{Fe}$ using Maker fringes [53], i.e. utilising the electric field dependence of non-phase-matched second harmonic generation. Bian [54] used the Z-scan technique to estimate the photovoltaic field in iron-doped lithium niobate crystal. This method is based on the saturable photorefractive non-linearity for photovoltaic crystals under short-circuit condition: the general (on- and off-axis) Z-scan formula for a one-dimensional Gaussian laser beam is derived. The possibility of using the Z-scan technique to detect and measure the bulk photovoltaic effects in pyroelectric crystals with photorefraction is discussed.

All the above described reversible photorefractive effects can be known as volume photorefractive effects. A new phenomenon in optical damage characterised by a strong irreversible change in refractive index of LiNbO_3 with a measured ΔN of -0.2 occurring in a surface layer of thickness 30 nm was first reported by Markan et al [27,28]. The effect was observed when high power UV laser radiation was used (provided by a KrF* excimer laser with a lasing wavelength of 249 nm, pulse duration of 5 ns and a power density of up to 20 MW/cm^2). This surface photorefractive effect was observed in undoped LiNbO_3 as well as crystals doped with iron and chromium. The change in ΔN was reported to be two to three orders of magnitude larger than that reported for the volume photorefractive effect. This new effect may be important in the realisation of integrated optical devices in LiNbO_3 .

The photorefractive effects in LiNbO_3 have been used to develop high volume stationary [10,14] and dynamic [29] holograms and have possible use in real-time optical processing applications such as phase conjugation with gain, dynamic holographic interferometry and self-induced optical cavities [30].

High-intensity single-beam photorefractive data on lithium niobate indicated the occurrence of a well-defined intensity threshold for enhanced fanning of the output beam. Rams et al [55] described that the threshold markedly rises with temperature in the range 20 - 160°C. Below threshold, the beam profile is only slightly changed during propagation and it remains essentially independent of the light intensity. These results offer an insight into the beam degradation in applications whereby high light density powers are used. The data indicate that the threshold effect is thermally activated with an activation energy of 0.24 eV within the range of values found for the conductivity.

B PHOTOREFRACTIVE EFFECTS IN OPTICAL WAVEGUIDES

Optical waveguides in LiNbO_3 can be fabricated by three methods, namely titanium indiffusion [31], proton exchange [32] and ion implantation [33]. The photorefractive/optical damage effects in channel waveguides can be attributed to the photovoltaic and the photoconductive effects. Researchers have found that the optical damage resistance of proton exchange and ion implanted

waveguides is at least two orders of magnitude greater than that of titanium indiffused waveguides evaluated under the same experimental conditions [34-36]. Recently Fujiwara [56] reported a comparison of the photorefractive effect in proton-exchanged (PE) and annealed proton-exchanged (APE) LiNbO_3 optical waveguides at the irradiation wavelength of 488 nm. In APE waveguides the photorefractive sensitivity is about three times that of PE waveguides up to an irradiation intensity of 100 W/cm². It was found that the contribution of the dark conductivity to the photorefractive effect in PE and APE waveguides was dominant in the intensity range used in the experiments. Ion beam implantation has been used by Robertson [57] as a postprocessing method to dramatically reduce the photorefractive effect in APE LiNbO_3 channel waveguides. It is postulated that the observed decrease in photorefractive susceptibility can be explained by the implant changing the defect structure and hence the photovoltaic properties of the material. Steinberg [58] reported a quantitative comparison of the photorefractive effect in APE channel waveguides in MgO-doped and congruent LiNbO_3 at the 633 and 830 nm wavelengths. The results show that doping with 7 mol% MgO reduces the photorefractive effect at 633 nm by two orders of magnitude. The photorefractive effect in the doped substrate shows only a weak dependence on the guided power. Doping with 4 mol% MgO has only little effect on the photorefractive effect compared with that on the congruent material. A reduced photovoltaic current is responsible for the small photorefractive effect in the 7 mol%-doped substrate. Higher optical damage thresholds were measured with the use of titanium indiffused waveguides whereby the laser light was propagated along the Z-direction of the crystal [37-40]. The reason for the reduced photorefractive sensitivity can be attributed to the different values associated with the different electro-optic coefficients of the LiNbO_3 crystal.

Recent use of periodically poled lithium niobate (PPLN) devices for frequency conversion has resulted in the study of their sensitivity to photorefractive effects. Taya and co-workers [59] reported a quantitative analysis of the steady-state photorefractive index perturbations caused by a given optical irradiance distribution in a PPLN structure. They showed that the photogalvanic fields responsible for whole-beam effects are strongly reduced in periodically poled crystals. Xu [60] used a novel two-beam technique to study the photorefractive damage (PRD) of PPLN convertors whereby the second harmonic generation tuning curve of a broadband probe beam was monitored. They found that the quasi-phase-matched (QPM) condition and wavelength conversion efficiency change markedly even for low irradiation power (<20 mW), indicating that the PRD effect is non-negligible in PPLN wavelength convertors.

The use of optically induced refractive index changes in waveguides for the realisation of integrated optical devices such as gratings for optical switches and wavelength division multiplexers has been reported [41-43]. Unfortunately the photorefractive effect is in general an unwanted effect which can cause serious degradation in the performance of integrated optical components. Researchers have shown that the optical damage in Ti:LiNbO₃ waveguides is caused by the presence of Fe⁺⁺ centres [44]. Their results show that Fe⁺⁺ centres are stabilised against oxidation in the region of large titanium concentration near the surface thus increasing the sensitivity to optical damage considerably. This undesired effect may be largely eliminated by additional indiffusion of protons [44].

The photorefractive effect in optical waveguides is strongly wavelength dependent and can be substantially reduced by using longer wavelengths. For low voltage long interaction length directional couplers, the main contributing factor to optical damage is the photovoltaic mechanism. Work by Schmidt et al on directional couplers operated at 830 nm with field strengths of about 10 kV/cm showed a mainly photoconductive mechanism [45]. In the case of work done by Becker, the photovoltaic current was equivalent to the photoconductive current with the experiments performed at field strengths of 1 kV/cm [46]. Bulmer reported optical damage in slightly asymmetric Mach-Zehnder interferometers at 830 nm due to photovoltaic effects [47]. Optical damage effects in Ti:LiNbO₃ directional couplers and Mach-Zehnder interferometers were reported by Harvey at a wavelength of 1300 nm with optical power levels of the order of 20 mW (measured at device output) [48]. The tested directional couplers showed a considerable reduction in modulation efficiency. The dominant mechanism for the optical damage of the directional couplers is the photovoltaic effect

which affects both the bias point and the extinction ratio of the coupler. The Mach-Zehnder interferometers showed only a slight drift in the bias voltage at the same optical power level with no change in the extinction ratio. Here the dominant mechanism is the photoconductive effect.

A common method used for the characterisation of photorefractive effects in optical waveguides is to measure the attenuation of the laser light beam as it scatters [37]. However this method is incapable of generating a quantitative measure of the magnitude and dynamics of the effects. Techniques reported by Becker et al [49] and Fujiwara et al [50] employing some form of Mach-Zehnder interferometer have been shown to provide excellent vehicles to quantify optical damage effects.

REFERENCES

- [1] A. Ashkin et al [*Appl. Phys. Lett. (USA)* vol.9 (1966) p.72]
- [2] F.S. Chen [*J. Appl. Phys. (USA)* vol.38 (1967) p.3418]
- [3] F.S. Chen [*J. Appl. Phys. (USA)* vol.40 no.8 (1969) p.3389-96]
- [4] A.M. Glass, D. von der Linde, T.J. Negram [*Appl. Phys. Lett. (USA)* vol.25 no.4 (1974) p.233-5]
- [5] J.B. Thoxer [*Appl. Phys. Lett. (USA)* vol.15 (1969) p.210]
- [6] J.J. Amodei, D.L. Staebler [*RCA Rev. (USA)* vol.33 no.1 (1972) p.71-93]
- [7] I.P. Kaminow [in *An Introduction to Electrooptic Devices* (USA, 1974) p.40]
- [8] R.G. Smith, D.B. Fraser, R.T. Denton, T.C. Rich [*J. Appl. Phys. (USA)* vol.39 (1968) p.4600]
- [9] G.E. Peterson, A.M. Glass, T.J. Negran [*Appl. Phys. Lett. (USA)* vol.19 (1971) p.130]
- [10] D.L. Staebler, J.J. Amodei [*Ferroelectrics (UK)* vol.3 no.2-4 (1972) p.107-13]
- [11] I.B. Barkan, S.I. Marenikov, M.V. Entin [*Phys. Status Solidi A (East Germany)* vol.38 (1976) p.139]
- [12] A.M. Glass [*Opt. Eng. (USA)* vol.17 no.5 (1978) p.470]
- [13] P. Gunter, H.J. Eichler [in *Electro-Optic and Photorefractive Materials* vol.18, Ed. P. Gunter (Springer-Verlag, Germany, 1987) p.206]
- [14] W. Phillips, J.J. Amodei, D.L. Staebler [*RCA Rev. (USA)* vol.33 no.1 (1972) p.94-109]
- [15] H. Kurz [*Ferroelectrics (UK)* vol.8 no.1-2 (1974) p.437-9]
- [16] A.M. Glass, G.E. Peterson, T.J. Negran [*Laser Induced Damage in Optical Materials* Boulder, CO, USA, 14-15 June 1972, Eds A.J. Glass, A.H. Guenther (Nat. Bur. Stand., Washington DC, USA, 1972) p.15-26]
- [17] G.G. Zhong, J. Jin, Z.K. Wu [*Proc. 11th Int. Quantum Electronic Conf. (USA, 1980)* p.631]
- [18] Wang Huafu, Shi Guotong, Wu Zhongkang [*Phys. Status Solidi A (East Germany)* vol.89 no.2 (1985) p.K211-4]
- [19] D.A. Bryan, R. Gerson, H.E. Tomaschke [*Appl. Phys. Lett. (USA)* vol.44 no.9 (1984) p.847-9]
- [20] R. Sommerfeldt, L. Holtmann, E. Kratzig, B.C. Grabmaier [*Phys. Status Solidi A (East Germany)* vol.106 (1988) p.89]
- [21] R. Gerson, J.F. Kirchhoff, L.E. Halliburton, D.A. Bryan [*J. Appl. Phys. (USA)* vol.60 no.10 (1986) p.3553-7]
- [22] K. Polgar, L. Kovacs, I. Foldvari, I. Cravero [*Solid State Commun. (USA)* vol.59 no.6 (1986) p.375-80]
- [23] J.K. Wen, L. Wang, Y.S. Tang, H.F. Wang [*Appl. Phys. Lett. (USA)* vol.53 no.4 (1988) p.260-1]
- [24] T.J. Chang, J.K. Wen, Y.P. Zhu, Z.F. Wang, Y.S. Tang, H.F. Wang [*Chin. Phys. Lett. (China)* vol.5 no.10 (1988) p.449-52]
- [25] F.S. Chen, J.T. LaMacchia, D.B. Fraser [*Appl. Phys. Lett. (USA)* vol.13 (1968) p.223]
- [26] P.J. Cressman, L.B. Schein [*Integrated & Guided Optics Conf. (USA, 1978)* p.WA4-1]
- [27] I.B. Barkan, V.N. Ishchenko, S.A. Kochubei, D.I. Lunenok, A.M. Razhev [*Sov. J. Quantum Electron. (USA)* vol.16 (1986) p.553]

- [28] I.B. Barkan, V.N. Ishchenko, S.A. Kochubei, D.I. Lunenok, A.M. Razhev [*Appl. Phys. A (West Germany)* vol.44 no.2 (1987) p.167-70]
- [29] I.B. Barkan, S.I. Marennikov, M.V. Entin [*Phys. Status Solidi A (East Germany)* vol.45 (1978) p.K17]
- [30] J.P. Huignard, G. Roosen [in *Nonlinear Optics: Materials and Devices* Eds C. Flytzanis, J.L. Oudar (Springer-Verlag, Germany, 1986) p.128]
- [31] R.V. Schmidt, I.P. Kaminow [*Appl. Phys. Lett. (USA)* vol.25 no.8 (1974) p.458-60]
- [32] J.L. Jackel, C.E. Rice, J.J. Veselka [*Appl. Phys. Lett. (USA)* vol.41 no.7 (1982) p.607-8]
- [33] G.L. Destefanis, J.P. Gailliard, E.L. Ligeon, S. Valette, B.W. Farmery, P.D. Townsend [*J. Appl. Phys. (USA)* vol.50 no.12 (1979) p.7898-905]
- [34] J.L. Jackel, A.M. Glass, G.E. Peterson, C.E. Rice, D.H. Olson, J.J. Veselka [*J. Appl. Phys. (USA)* vol.55 no.1 (1984) p.269-70]
- [35] K.K. Wong [*GEC J. Res. (UK)* vol.3 no.4 (1985) p.243-50]
- [36] E. Glavas, P.D. Townsend, G. Droungas, M. Dorey, K.K. Wong, L. Allen [*Electron. Lett. (UK)* vol.23 no.2 (1987) p.73]
- [37] R.L. Holman, J. Busch, M. Parmenter, P.J. Cressman [*Ferroelectrics (UK)* vol.50 no.1-4 (1983) p.497-503]
- [38] S. Thaniyavarn [*Appl. Phys. Lett. (USA)* vol.47 no.7 (1985) p.674-7]
- [39] S. Thaniyavarn [*Opt. Lett. (USA)* vol.11 (1986) p.39]
- [40] N.A. Sanford, J.M. Connors, W.A. Dyes [*J. Lightwave Technol. (USA)* vol.6 no.6 (1988) p.898]
- [41] R.P. Kenan, D.W. Vahey, N.F. Hartman, V.E. Wood, C.M. Verber [*Opt. Eng. (USA)* vol.15 (1976) p.12]
- [42] C.M. Verber, V.E. Wood, R.P. Kenan, N.F. Hartman [*Ferroelectrics (UK)* vol.10 no.1-4 (1976) p.253-6]
- [43] C.M. Verber, N.F. Hartman, A.M. Glass [*Appl. Phys. Lett. (USA)* vol.30 no.6 (1977) p.272-3]
- [44] V. Gericke, P. Hertel, E. Kratzig, J.P. Nisius, R. Sommerfeldt [*Appl. Phys. B (West Germany)* vol.44 (1987) p.155]
- [45] R.V. Schmidt, P.S. Cross, A.M. Glass [*J. Appl. Phys. (USA)* vol.51 no.1 (1980) p.90-3]
- [46] R.A. Becker [*Proc. SPIE - Int. Soc. Opt. Eng. (USA)* vol.578 (1985) p.12]
- [47] C.H. Bulmer, W.K. Burns, S.C. Hiser [*Tech. Digest of 7th Topical Meeting on Integrated & Guided-Wave Optics* Kissimmee, Florida, USA, 24-26 Apr. (Opt. Soc. Am., Washington DC, 1984) p. WC1-1]
- [48] G.T. Harvey [*J. Lightwave Technol. (USA)* vol.6 (1988) p.872]
- [49] R.A. Becker, R.C. Williamson [*Appl. Phys. Lett. (USA)* vol.47 no.10 (1985) p.1024-8]
- [50] T. Fujiwara, S. Sato, H. Mori [*Appl. Phys. Lett. (USA)* vol.54 no.11 (1989) p.975-7]
- [51] V.I. Belinicher, I.F. Kanaev, V.K. Malinovskii, B.I. Sturman [*Bull. Acad. Sci. USSR Phys. Ser. (USA)* vol.41 no.4 (1977) p.67-72]
- [52] V.I. Belinicher, I.D. Kanaev, V.K. Malinovskii, B.I. Sturman [*Sov. Phys.-Solid State (USA)* vol.18 no.8 (1976) p.2256-61]
- [53] B.G. Kim, B.K. Rhee [*Opt. Commun. (Netherlands)* vol.198 (2001) p.193-7]
- [54] S. Bian [*Opt. Commun. (Netherlands)* vol.141 (1997) p.292-7]
- [55] J. Rams, A. Alcazar-de-Velasco, M. Carrascosa, J.M. Cabrera, F. Agullo-Lopez [*Opt. Commun. (Netherlands)* vol.178 (2000) p.211-6]
- [56] T. Fujiwara, X. Cao, R. Srivastava, R.V. Ramaswamy [*Appl. Phys. Lett. (USA)* vol.61 no.7 (1992) p.743-5]
- [57] E.E. Robertson, R.W. Eason, Y. Yokoo, P.J. Chandler [*Appl. Phys. Lett. (USA)* vol.70 no.16 (1997) p.2094-6]
- [58] S. Steinberg, R. Goring, T. Hennig, A. Rasch [*Opt. Lett. (USA)* vol.20 no.7 (1995) p.683-5]
- [59] M. Taya, M.C. Bashaw, M.M. Fejer [*Opt. Lett. (USA)* vol.21 no.12 (1996) p.857-9]
- [60] C.Q. Xu, H. Okayama, Y. Ogawa [*J. Appl. Phys. (USA)* vol.87 no.7 (2000) p.3203-8]

8.6 Refractive indices of different crystal phases in proton-exchanged LiNbO₃ waveguides

Yu.N. Korkishko and V.A. Fedorov

July 1999

A INTRODUCTION

Our preliminary studies [1-5] allowed us to identify the different crystallographic phases H_xLi_{1-x}NbO₃ that can be realised in proton-exchanged (PE) waveguides, considering that a phase jump occurs when the proton concentration in the exchanged layer is gradually varied, which causes a sudden variation of the cell parameters, even if the crystallographic system is conserved. Each phase is characterised by its own values of ordinary and extraordinary refractive indices. In this Datareview we present the results of measuring ordinary and extraordinary refractive indices for different H_xLi_{1-x}NbO₃ phases, generated in proton-exchanged LiNbO₃ waveguides.

B EXPERIMENTAL PROCEDURE

To realise the PE waveguides, one can use either a simple exchange, varying the temperature and the acidity of the bath and the duration of the exchange to modify the parameters of the waveguide, or a two-step process, where the exchange is followed by annealing, whose duration and temperature further modify the waveguide parameters.

PE waveguides were fabricated in optical grade virgin LiNbO₃ substrates of X-, Y- and Z-cuts. As the sources of PE we used a solution of KHSO₄ in glycerine, benzoic acid, whose acidity can be reduced by adding up to 5 wt% of lithium benzoate, stearic acid, whose acidity can be reduced by adding up to 1 wt% of lithium stearate, pyrophosphoric acid, and ammonium dihydrophosphate.

In order to find mode-effective indices, we measured excitation angles of dark m-lines of modes with one prism-coupler set-up at the 633 nm wavelength. The extraordinary refractive-index profiles throughout the guide depth were reconstructed by the IWKB technique proposed by White and Heidrich [6] and improved by Dikaev et al [7]. The calculation procedure proposed by Chiang [8] has also been used. The surface increments Δn_e were determined as the average between values obtained by using these two methods.

With PE, an increase of the extraordinary refractive index and a decrease of the ordinary index are observed relative to the values of LiNbO₃ substrates [9]. Thus, the prism-coupling technique and the IWKB method can be used only to determine the extraordinary index profiles.

To measure the ordinary index change in the LiNbO₃ guides the dark-mode reflectivity technique has been used [10-12] (FIGURE 1). We used the input polarisation decoupled orientation for guides on X- and Y-cut in which light propagates along the optical axis and the input TE polarisation for guides on Z-cut. For these orientations, the light sees a value of n_o in the layer smaller than that of the substrate, and there exist no critical reflections, but only partial reflections on the guide/substrate interface. This condition is similar to the guided mode condition for TE modes, except for the phase changes on the guide/substrate interface arising from total reflections:

$$\frac{2\pi}{\lambda} h \sqrt{(n_o^2 - n_{\text{eff}}^2)} = \arctg \left(\zeta \sqrt{\frac{(n_{\text{eff}}^2 - 1)}{(n_o^2 - n_{\text{eff}}^2)}} \right) + m\pi \quad (1)$$

$\zeta = n_o^2$ for TM modes and $\zeta = 1$ for TE modes.

Sharpness of the layer/substrate interface of as-exchanged proton-exchanged samples produces relatively high reflectivity. The fringe visibility is improved by putting a pressure onto the prism higher than the 'normal' one used for the observation of guiding modes [12]. This makes it possible to observe 'dark-modes' at the input angles corresponding to EQN (1).

Measurements were taken of the angular positions (ϕ_m , FIGURE 1) of the interference fringes arising from those partial reflections. By measuring effective indices n_{eff} of at least two 'dark' ordinary polarisation modes with mode number $m = 0, 1, \dots$, the surface values of n_o and film thickness h are easily obtained by solving the system of equations (EQN 1).

However, the annealed PE LiNbO_3 waveguides (APE) [13] exhibit graded refractive index profiles and, therefore, the interference analysis cannot be used. To measure the ordinary index increments in the APE waveguides we have used the reverse proton-exchange (RPE) technique [14-16]. The method consists in preparing samples by pairs. The initial exchange is identical on both samples; one of them is reverse exchanged in LiNO_3 (37.5 mol%)- KNO_3 (44.5 mol%)- NaNO_3 (18.0 mol%) melt (melting point of this eutectic mixture is 120°C) or pure LiNO_3 (melting point -261°C) melts at temperatures from 250 to 330°C, while the second ('control sample') is annealed at the same temperature and for the same time $t_{\text{APE}} = t_{\text{RPE}}$.

On the RPE and the APE waveguides, we characterised the surface-guiding layers using the prism-coupling technique. In this process we neglect the fact that the ordinary waveguide is only due to an index barrier and that the ordinary index increases again at a certain depth in the substrate. This is a good approximation when the barrier is deep enough to prevent significant evanescent tails of the ordinary modes reaching the region of the substrate where the index increases again. We thus introduce a fictitious value of the ordinary substrate index n_o^b equal to the minimal measurable value of the ordinary index profile, i.e. observed at the turning point z_0 of the last ordinary polarisation mode (FIGURE 2). It was found that essentially pure lithium niobate is formed at the surface after RPE, which is confirmed by SIMS measurements [17] showing the hydrogen concentration at the surface is similar to that in the initial LiNbO_3 [17]. This indicates that the surface ordinary index of the RPE waveguide can be taken as the bulk value so that $n_o = n_o^s$. Therefore, $\Delta n_o(z_0) = n_o^s - n_o^b$.

In most of the cases, the effective indices of the extraordinary RPE waveguide can also be measured by the prism-coupling technique but the index profile, which is no longer monotonic, cannot be reconstructed by IWKB. We then made the following approximation. In the barrier region, which, as was obtained recently [17], is not affected by the reverse exchange, the extraordinary index profiles of the 'control' APE and RPE waveguides are identical. In particular, we can say that at depth z_0 , the influence of the RPE process is negligible and so $\Delta n_e^{\text{APE}}(z_0) = \Delta n_e^{\text{RPE}}(z_0) = \Delta n_e(z_0)$. The dependence of

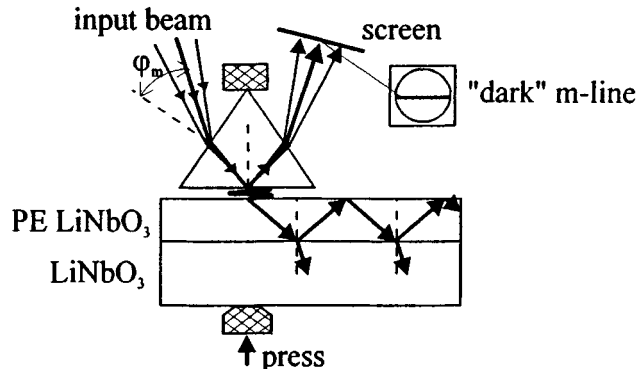


FIGURE 1 Experimental set-up to measure 'dark' ordinary polarisation modes.

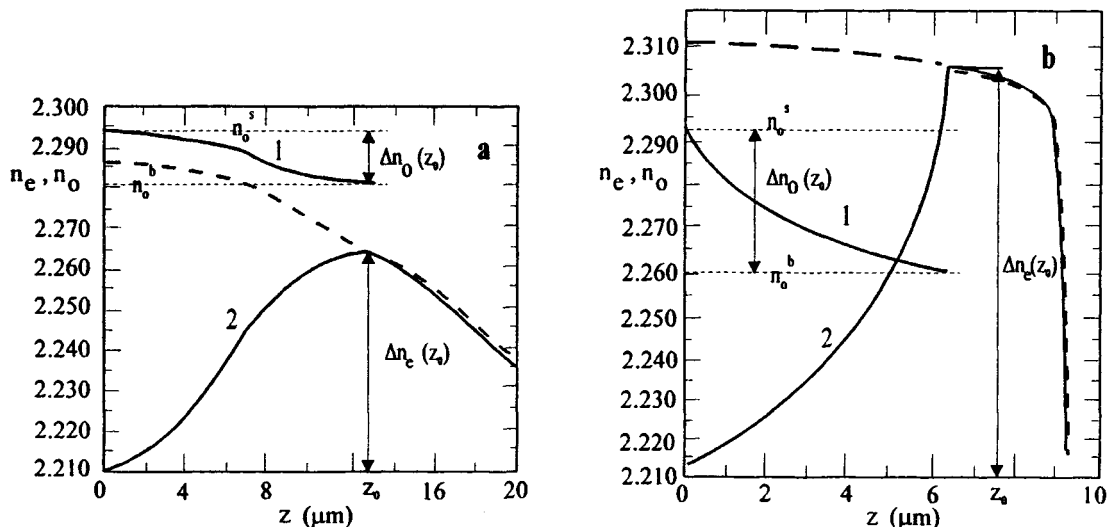


FIGURE 2 Ordinary (1) and extraordinary (2) refractive-index profiles in RPE waveguides on Z-cut LiNbO_3 prepared under the following conditions: (a) PE in ammonium dihydrophosphate melt at $T_{\text{PE}} = 220^\circ\text{C}$, $t_{\text{PE}} = 14$ hr, post-exchanged annealing: $T_A = 330^\circ\text{C}$, $t_A = 110$ hr; RPE in LiNO_3 melt: $T_R = 300^\circ\text{C}$, $t_R = 100$ hr; (b) PE in solution of KHSO_4 in glycerin ($C = 1 \text{ g/l}$) $T_{\text{PE}} = 240^\circ\text{C}$, $t_{\text{PE}} = 50$ hr, RPE in LiNO_3 melt: $T_R = 300^\circ\text{C}$, $t_R = 50$ hr. Dashed lines show extraordinary refractive index profiles in 'control' samples.

$\Delta n_o(z_0)$ on $\Delta n_e(z_0)$ obtained in this way is thought to be close to a general relationship between Δn_o and Δn_e in APE waveguides with graded refractive index profiles [14-16].

The validity of this approximation is established by the interference method. Indeed, if the RPE technique was used to measure Δn_o in PE waveguides with step-like refractive index profiles (FIGURE 2(b)), the values of Δn_o obtained by using the above-described method were equal (± 0.003) to those measured by an interference analysis.

C EXPERIMENTAL RESULTS

By using the dark m-line technique for waveguides with step-like index profiles and the reverse proton-exchange method for graded waveguides the relationship between changes of ordinary and extraordinary refractive indices has been obtained for various $\text{H}_x\text{Li}_{1-x}\text{NbO}_3$ phases (TABLE 1, FIGURE 3) [1,4,5].

TABLE 1 Ordinary and extraordinary refractive indices for different $\text{H}_x\text{Li}_{1-x}\text{NbO}_3$ phases.

Phase	Type of refractive-index profile	Interval of Δn_e	Interval of Δn_o	Relationship between Δn_e and Δn_o
β_4	graded	0.14 to 0.15	$\Delta n_o \approx 0.065$	
β_3	step-like	0.125 to 0.135	-0.04 to -0.048	$\Delta n_o = -0.08 \times \Delta n_e - 0.038$
β_2	step-like	0.01 to 0.12	-0.025 to -0.045	$\Delta n_o = -0.20 \times \Delta n_e - 0.005$
β_1	step-like	0.095 to 0.12	-0.03 to -0.045	$\Delta n_o = -0.40 \times \Delta n_e + 0.007$
κ_1^{HT}	graded	0 to 0.05	0 to -0.03	$\Delta n_o = -0.64 \times \Delta n_e$
κ_1^{LT}	graded	0.04 to 0.07	-0.007 to -0.01	$\Delta n_o = -0.08 \times \Delta n_e - 0.004$
α	graded	0 to 0.025	0 to -0.005	$\Delta n_o = -0.2 \times \Delta n_e$

Note that the obtained results are close to early reported ones of Olivares et al [12] $\Delta n_o = -0.40 \times \Delta n_e + 0.007$, obtained for the β_1 -phase.

The relationship determined between Δn_e and Δn_o can explain the following phenomenon. In thick β_2 - β_1 two-layer waveguides on X-cut and Z-cut ($h \geq 3 \mu\text{m}$) we were able to excite not only extraordinary polarisation modes (TE for X-cut and TM for Z-cut), but also weak ordinary polarisation modes (TM for X-cut and TE for Z-cut) with $n_{\text{eff}} \approx 2.25$ [18]. Similar results have been reported for X-cut samples proton exchanged in benzoic acid melt [19]. FIGURE 3 shows that under the condition $\Delta n_e(\beta_1) = \Delta n_e(\beta_2)$ (real index profile has a step-like form), the ordinary refractive index in the β_1 -phase is lower than that in the surface β_2 layer such that, when the thickness of the structure is large enough, the ordinary polarisation mode can be excited [1]. High optical losses of more than 85 dB/cm (absorption $\alpha > 2 \text{ mm}^{-1}$) have been measured for weak TM modes [19]. These large losses point to the excitation of substrate modes resulting from the low width of the second layer (β_1 -phase), which acts as an ordinary refractive index barrier [1].

A prerequisite for the numerical calculation of the proton-exchanged layer data is the knowledge of material dispersion of the various phases in the HNbO_3 - LiNbO_3 single crystalline system. Only a few papers have reported on refractive-index dispersion of PE LiNbO_3 structures [20-22].

Based on the few known measured values of refractive indices, it does not seem to be possible to calculate the Sellmeier coefficients for $\text{H}_x\text{Li}_{1-x}\text{NbO}_3$ solid solutions. In addition, PE sample morphology has been studied by the RBS (Rutherford backscattering) method in the aligned configuration and showed the presence of niobium dislocations in the β_2 - and β_4 -phases [23-27]. Therefore, the displacement of Nb^{+5} ions should modify some oscillators in the Sellmeier equation [22].

$$n^2(\lambda) = 1 + \sum_s a_s \frac{\lambda^2 \lambda_s^2}{\lambda^2 - \lambda_s^2} + \dots \quad (2)$$

Hagner et al [22] reported on a study of material dispersion using normalisation

$$K_\lambda = \frac{\Delta n_e^\lambda}{\Delta n_e^{\lambda=0.63 \text{ nm}}} \quad (3)$$

The Sellmeier equation (EQN 2) and EQN (3) were connected by Hagner et al [22] with an error $\delta K < 10^{-4}$ to:

$$K_\lambda = \frac{n_{e,s}^\lambda}{n_{e,s}^{\lambda=0.63 \text{ nm}}} \left[1 + a_{UV} f(\lambda, \lambda_{UV}, n_{e,s}^\lambda, n_{e,s}^{\lambda=0.63 \text{ nm}}) \right] \quad (4)$$

8.6 Refractive indices of different crystal phases in proton-exchanged LiNbO₃ waveguides

if Δn_e is merely caused by an additional resonance wavelength λ_{UV} in the near UV. The function f is independent of the oscillation strength a_{UV} , but it is slightly dependent on the dispersion of substrate index n_s .

The results of material dispersion for some PE LiNbO₃ samples containing different phases are represented in TABLE 2.

TABLE 2 Normalisation K_λ of the surface increase of the extraordinary refraction index Δn_e^λ , in various phases in the H_xLi_{1-x}NbO₃ system [22].

Phase	$\Delta n_e^\lambda = 633 \text{ nm}$	$K_\lambda = 568 \text{ nm}$	$K_\lambda = 514 \text{ nm}$	$K_\lambda = 488 \text{ nm}$
β_1	0.110	1.060	1.141	1.205
κ_1	0.0366	1.082	1.164	1.227
κ_1	0.0266	1.056	1.134	1.183
α	0.0173	1.055	1.134	1.184
α	0.0175	1.049	1.119	1.171
α	0.0079	1.043	1.114	1.156
α	0.0045	1.020	1.093	1.135
Bulk LiNbO ₃	2.2027	1.008	1.018	1.024

One can see that material dispersion is decreased with decreasing proton concentration [22].

The dispersion of the extraordinary refractive-index increase (Δn_e) of PE LiNbO₃ waveguides measured from 405 to 1319 nm was also reported in [28,29]. Different types of proton-exchanged waveguide, prepared under different conditions, were studied. FIGURE 4 shows the dispersion of Δn_e for the different PE LiNbO₃ waveguides. As can be seen, Δn_e for the β_2 - and β_1 -PE LiNbO₃ waveguides, as well as for the α -phase waveguides, fabricated by the APE method, increases by approximately a factor of two as one moves from 1300 to 400 nm. However, in the case of the α -phase waveguides fabricated by the soft proton exchange (SPE) [30] method, Δn_e increases by more than a factor of five as we go from 1300 to 400 nm.

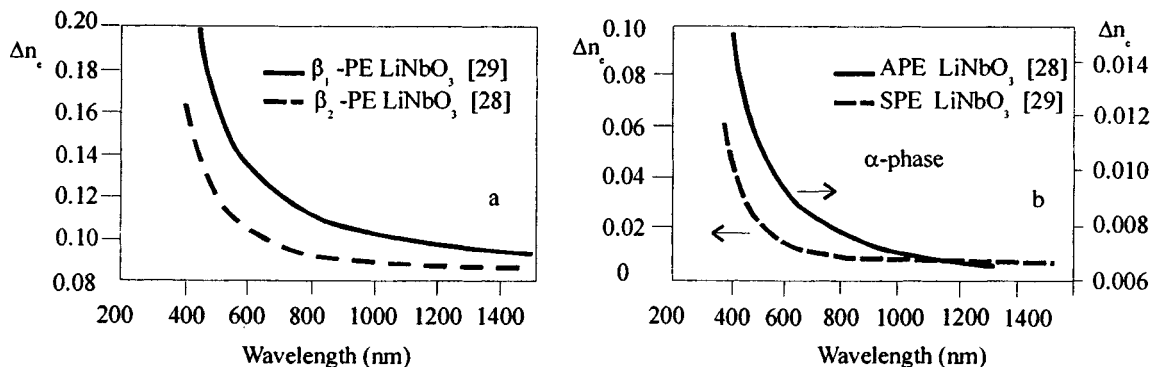


FIGURE 4 Dispersion of Δn_e for (a) β_2 , β_1 and (b) α -phase PE LiNbO₃ waveguides.

D CONCLUSION

This Datareview presents measured results of ordinary and extraordinary refractive indices for several H_xLi_{1-x}NbO₃ phases, generated in proton-exchanged waveguides. Both step-like index profile and graded waveguides were studied. Material dispersion is found to increase with decreasing proton concentration.

ACKNOWLEDGEMENTS

This work was supported by the Russian Foundation of Basic Research under grants no.96-15-96978 and no.99-15-96110 for Young Doctors of Sciences and grant no.96-15-98220 for Leading Science Schools and by the 'Russian Universities - Basic Researches' program under grant no.248-1998. This investigation is also part of the project A-0102 supported by the 'Integration' Foundation (Russia).

REFERENCES

- [1] Yu.N. Korkishko, V.A. Fedorov [*IEEE J. Sel. Top. Quantum. Electron. (USA)* vol.2 (1996) p.187]
- [2] Yu.N. Korkishko, V.A. Fedorov, M.P. De Micheli, P. Baldi, K. El Hadi, A. Leycuras [*Appl. Opt. (USA)* vol.35 (1996) p.7060]
- [3] Yu.N. Korkishko, V.A. Fedorov [*J. Appl. Phys. (USA)* vol.82 (1997) p.171]
- [4] Yu.N. Korkishko, V.A. Fedorov [*Opt. Mater. (Netherlands)* vol.5 (1996) p.175]
- [5] Yu.N. Korkishko, V.A. Fedorov [*Ion Exchange in Single Crystals for Integrated Optics and Optoelectronics* (Cambridge International Science Publishing, Cambridge, UK, 1999)]
- [6] J.M. White, P.F. Heidrich [*Appl. Opt. (USA)* vol.15 (1976) p.151]
- [7] Y.M. Dikaev, Yu.A. Kopylov, I.M. Kotelyanskii [*Kvantovaya Elektron. (Russia)* vol.8 (1981) p.378]
- [8] K.S. Chiang [*IEEE J. Lightwave Technol. (USA)* vol.3 (1985) p.385]
- [9] M. De Micheli, J. Boteneau, S. Neveu, P. Sibillot, D.B. Ostrowsky [*Opt. Commun. (Netherlands)* vol.42 (1982) p.101]
- [10] V.A. Ganshin, Yu.N. Korkishko, V.Z. Petrova [*Sov. Phys.-Tech. Phys. (USA)* vol.30 (1985) p.1313]
- [11] V.A. Ganshin, V.Sh. Ivanov, Yu.N. Korkishko, V.Z. Petrova [*Sov. Phys.-Tech. Phys. (USA)* vol.31 (1986) p.1313]
- [12] J. Olivares, M.A. Díaz-Garsía, J.M. Cabrera [*Opt. Commun. (Netherlands)* vol.92 (1992) p.40]
- [13] P.G. Suchoski, T.K. Findakly, F.J. Leonberger [*Opt. Lett. (USA)* vol.13 (1988) p.1050]
- [14] Yu.N. Korkishko, V.A. Fedorov [*Pis'ma Zh. Tekh. Fiz. (Russia)* vol.21 (1995) p.61]
- [15] Yu.N. Korkishko, V.A. Fedorov, S.V. Katin, A.V. Kondrat'ev [*Proc. SPIE (USA)* vol.2401 (1995) p.149]
- [16] Yu.N. Korkishko, V.A. Fedorov, S.V. Katin, A.V. Kondrat'ev [*Proc. 7th European Conf. on Integrated Optics* Delft, Netherlands, 3-6 April 1995 (Delft Univ. Press, 1995) p.395]
- [17] Yu.N. Korkishko, V.A. Fedorov, T.M. Morozova, F. Caccavale, F. Gonella, F. Segato [*J. Opt. Soc. Am. A (USA)* vol.15 (1998) p.1838]
- [18] V.A. Ganshin, Yu.N. Korkishko [*J. Opt. Commun. (Germany)* vol.13 (1991) p.2]
- [19] F. Rickerman, D. Dip, B. Gather, E. Krätzig [*Phys. Status Solidi A (Germany)* vol.150 (1995) p.763]
- [20] N.A. Sanford, W.E. Lee [*Proc. SPIE (USA)* vol.578 (1985) p.7]
- [21] Y. Handa, M. Miyawaki, S. Ogura [*Proc. SPIE (USA)* vol.460 (1984) p.101]
- [22] G. Hagner, A. Rasch, W. Karthe [*Phys. Status Solidi A (Germany)* vol.123 (1991) p.K159]
- [23] M. De Micheli et al [*IEEE J. Lightwave Technol. (USA)* vol.LT-4 (1986) p.743]
- [24] C. Canali, A. Carnera, G. Della Mea, R.M. De La Rue, A.C.G. Nutt, J.R. Tobin [*Proc. SPIE (USA)* vol.460 (1984) p.49]
- [25] C. Canali, A. Carnera, P. Mazzoldi, R.M. De La Rue [*Proc. SPIE (USA)* vol.517 (1984) p.119]
- [26] C. Canali et al [*J. Appl. Phys. (USA)* vol.59 (1986) p.2643]
- [27] G.R. Paz-Pujalt, D.D. Tuschel, G. Braunstein, T. Blanton, S. Tong Lee, L.M. Salter [*J. Appl. Phys. (USA)* vol.76 (1994) p.3981]

8.6 Refractive indices of different crystal phases in proton-exchanged LiNbO₃ waveguides

- [28] M.L. Bortz, M.M. Fejer [*Opt. Lett. (USA)* vol.16 (1987) p.1844]
- [29] K. El Hadi, V. Rastogi, M.R. Shenoy, K. Thyagarajan, M. De Micheli, D.B. Ostrowsky [*Appl. Opt. (USA)* vol.37 (1998) p.6463]
- [30] L. Chanvillard et al [*Proc. 9th European Conf. on Integrated Optics Italy* (1999) p.513]

8.7 Second-order non-linear properties of different crystal phases in proton-exchanged LiNbO₃ waveguides

Yu.N. Korkishko, V.A. Fedorov and F. Laurell

July 1999

A INTRODUCTION

Sources of coherent light in the blue and green spectral regions are required in many different applications such as colour printing, high-definition projection displays, medicine for fluorescence studies of biological systems and optical data storage. Second harmonic generation (SHG) in non-linear optical waveguides either using conversion from a guided mode at the fundamental frequency into an SH guided-mode (guided-guided type of SHG) or through conversion of a fundamental guided mode into an SH radiation mode (so-called Cherenkov-type SHG), offers a means of direct and efficient generation of short-wavelength light by frequency doubling of low-cost laser diodes and compact diode-pumped solid-state lasers currently available around 1 μm and longer wavelengths. By using non-linear optical waveguides, high conversion efficiencies can be obtained even for moderate input powers because of the high optical power density and long interaction lengths provided by guided-wave structures. Lithium niobate (LiNbO₃) is an excellent optical material, most commonly used as a substrate for applications in integrated electro-optic and non-linear optical devices. In single-mode channel LiNbO₃ guides, which provide tight optical confinement, even a modest CW power of 2 mW coupled into a guided mode will result in a power density of the order of 10⁶ W/cm². During the last few years the quasi-phase-matching (QPM) technique [1], in which the ferroelectric domains of the material are periodically inverted to compensate for dispersion, has received much attention for SHG of blue [2] and green [3] light in non-linear LiNbO₃ waveguides.

A suitable waveguide for a frequency-conversion device in LiNbO₃ should preserve the non-linear susceptibility of the crystal, have low loss, be resistant to photorefractive damage and be compatible with the inverted domain structure. Titanium in-diffusion and proton exchange are the two techniques readily available for fabricating waveguides in LiNbO₃ [4]. However, the well-studied titanium-diffused LiNbO₃ waveguides are not generally suitable for SHG non-linear optics for several reasons. The Ti:LiNbO₃ waveguide fabrication is performed at elevated temperatures (~950 - 1100°C), which could modify the domain structure of the crystal. Also, Ti:LiNbO₃ waveguides display photorefractive damage at near-infrared power levels exceeding tens of milliwatts, making them impractical for non-linear optical applications. As an alternative, the proton-exchange (PE) process and annealed proton exchange (APE) in LiNbO₃ provide excellent waveguides for these purposes. PE waveguides have a step-index profile with a large extraordinary refractive index change ($\Delta n \approx 0.1 - 0.14$), and are fabricated at temperatures below 350°C. Furthermore the best PE and APE LiNbO₃ waveguides were reported to have low propagation losses and resistance to photorefractive damage orders of magnitude greater than that of Ti:LiNbO₃ [5].

B EFFECT OF PROTON EXCHANGE ON NON-LINEAR OPTICAL PROPERTIES

There have been numerous efforts to quantify the effect of proton exchange on the non-linear susceptibilities and to measure the d₃₃ non-linear optical coefficient of PE LiNbO₃ and APE LiNbO₃ [6-16]. However, a number of approaches report partly contradictory results. The measured SHG efficiencies in both waveguided QPM and Cherenkov generation suggest that the non-linear

susceptibility $\chi^{(2)}$ in the direct-exchanged guiding region should be substantially smaller than that of the untreated LiNbO_3 [6-11]. The d_{33} coefficient of PE LiNbO_3 waveguides prepared by PE in pure benzoic acid has been measured to be ≈ 0 [6-8], 0.45 [9], 0.5 [10], and 0.63 [11] of the bulk value. The effect of annealing on the non-linear properties of the PE waveguides has also been the object of some controversy. Some authors claim that it is possible to restore the non-linearity after annealing [9,11], whereas others have observed the opposite behaviour [6], with measurements of d_{33} on the surface of APE LiNbO_3 varying from 1/30 [6] to 0.65 [9] and 0.9 [11] of the bulk value. Hsu et al [8] observed a recovery (up to $\sim 50\%$) in the short-time proton-exchanged sample only (benzoic acid, 0.5 h at 180°C) of LiNbO_3 under thermal annealing at 350°C for 1 h, while the long-time (1 h and 1.5 h) exchanged samples did not show any recovery of the non-linear coefficient under thermal annealing. Bortz et al [12] reported depth profiling of the d_{33} non-linear coefficient using reflected SHG from angle-lapped samples in APE LiNbO_3 waveguides fabricated on X-cut LiNbO_3 by PE in pure benzoic acid and annealed in air for varying times. At depths greater than the initial PE depth the d_{33} coefficient retained nearly its bulk LiNbO_3 value, but within the initial PE region the value of d_{33} varied with annealing time and no reflection was observed for an unannealed sample [12]. The absence of any reflected SH from the unannealed region was explained by formation of a PE LiNbO_3 phase with either inversion symmetry or a different $\chi^{(2)}$ tensor that did not result in any reflected SH. Paz-Pujalt et al [13] established by Raman measurements that non-linear properties are lost upon PE due to the formation of paraelectric centres and changes in the chemical bonding. Non-linear activity was partly recovered by annealing [13]. The fact that QPM SHG devices work with PE waveguides after annealing also suggests some recovery of the non-linearity. Second-order optical non-linearities in waveguides prepared using a dilute melt PE method, using a solution of KHSO_4 and lithium benzoate in glycerine, were measured by Veng et al [14] by detecting the 266 nm reflected SHG signal. It was found for this kind of waveguide that in the waveguide region all the second-order susceptibilities take values of at least 90% of the original LiNbO_3 values for refractive-index changes less than ~ 0.115 , whereas the susceptibilities are strongly reduced for larger index changes. Recently, El Hadi et al [15,16] carefully studied the influence of the PE process on the non-linear properties of the three different types (high-acidity exchanged, annealed and highly dilute melt exchanged) of periodically poled LiNbO_3 waveguides. They found that for PE waveguides prepared in the β_1 -phase the reflected SH signal measured in the exchange region is less than 5% of the value registered for the bulk region. It was also observed that the APE process can restore the non-linearity but will erase the periodic domain structure. This erasure can be avoided by use of a highly diluted proton-exchange melt [15,16].

A summary of the reported results of measurement of the non-linear optic d_{33} coefficient in PE and APE LiNbO_3 waveguides is given in TABLE 1. As one can see, publications on the subject report rather different results of the non-linear properties of the PE and APE waveguides, which are related to the difficult task of probing the non-linear properties of a PE thin layer at the surface of the LiNbO_3 crystal as well as to the existence of various phases in PE LiNbO_3 waveguides that have not been taken into account in the previous studies.

C NON-LINEAR SUSCEPTIBILITY OF DIFFERENT PROTON-EXCHANGED PHASES

Our latest studies [18-20] have shown that seven different crystallographic phases of $\text{H}_x\text{Li}_{1-x}\text{NbO}_3$, the α , κ_1 , κ_2 , β_1 , β_2 , β_3 and β_4 phases, can be realised in proton-exchanged LiNbO_3 layers depending on exchange and annealing conditions. For the design, fabrication and optimising of the PE LiNbO_3 non-linear optical devices it is essential to determine the non-linearity of proton-exchanged waveguides with different $\text{H}_x\text{Li}_{1-x}\text{NbO}_3$ phases and correlate it to the waveguides' processing conditions and their linear optical properties (refractive index change and optical losses). To clarify the situation, we performed an investigation of the influence of the phase state of $\text{H}_x\text{Li}_{1-x}\text{NbO}_3$ waveguides on the second-order

TABLE 1 Reported values of non-linear optic d_{33} coefficient in PE and APE LiNbO_3 waveguides.
The results are given as the value normalised to that of the bulk.

Reference	SHG technique	Proton exchange	Annealing	Phase on the surface (expected)	Non-linear optic coefficient d_{33}
Suhara et al [10]	Transmitted grating	BA, 230°C, 2 h	-	β_2	0.5 ± 0.08
Keys et al [9]	Transmitted grating	BA, 235°C, 1 h	350°C, 0.5 h	$\frac{\beta_2}{\kappa_2^{\text{LT-HT}}}$	0.45 ± 0.05 0.65 ± 0.02
Cao et al [11]	Reflection ($\lambda_{\omega} = 1.064 \mu\text{m}$)	BA, 180°C, 1 h	350°C, 10 h	β_2	0.62 0.88
Laurell et al [6]	Reflection ($\lambda_{\omega} = 0.532 \mu\text{m}$)	BA, 180°C, 1 h	350°C, 10 h	$\frac{\beta_2}{\kappa_2^{\text{LT-HT}}}$	<0.03 <0.03
Ohlfeldt et al [17]	End-face reflection ($\lambda_{\omega} = 1.064 \mu\text{m}$)	PA, 260°C, 6 h	400°C, 16 h	$\frac{\beta_4}{\kappa_2^{\text{HT}}}$	≈ 0 Restored
Bortz and Fejer [7]	Reflection ($\lambda_{\omega} = 1.064 \mu\text{m}$)	BA, 220°C, 2 h (X-cut)		β_1	≤ 0.01
Bortz et al [12]	Reflection ($\lambda_{\omega} = 0.532 \mu\text{m}$)	BA, 173°C, 1 h	333°C, 3 - 63 h	$\frac{\beta_2}{\kappa_2^{\text{LT}} - \kappa_1^{\text{LT}}}$	See text
Li et al [24]	Cherenkov SHG	BA, 300°C, 0.5 h		β_2	0.2 (X-cut) 0.3 (Z-cut)
Hsu et al [8]	Reflection ($\lambda_{\omega} = 0.532 \mu\text{m}$)	BA, 180°C, 0.5 h	300°C, 1 - 17 h	$\frac{\beta_2}{\kappa_2^{\text{LT}} - \kappa_1^{\text{LT}}}$	≈ 0 ~ 0.5

BA - benzoic acid, PA - pyrophosphoric acid

optical non-linearity [21,22], by using reflected SHG measurements from the polished waveguide end face using the experimental setup proposed by Ohlfeldt [17]. This technique circumvents the restrictions of the reflection SHG technique with contribution from the waveguide bulk interface and allows the spatial variation in the non-linear coefficient in the waveguides to be measured. 1.064 μm light polarised parallel to the Z-axis of LiNbO₃ from a mode-locked and Q-switched Nd:YAG laser was focused using a lens (NA = 0.65) onto the polished end face of the waveguide. The waveguide sample was mounted on a piezo-electrically driven translation stage (Melles Griot X-Y-Z Nanoblock), which permitted vertical scanning of both the waveguide and the bulk region. The reflected fundamental beam and the generated reflection-SH beam were separated using beamsplitters and an interference filter, and detected with a germanium detector and a photomultiplier tube, respectively. The reflected IR intensity, which was used to determine the position of the air/sample interface, was monitored using a lock-in amplifier, and the SH signal from the photomultiplier tube was analysed with a gated integrator. The intensity of the reflected SH signal is proportional to the square of the second-order non-linearity, and therefore the measurement of harmonic power I(2 ω) in both the exchanged and unexchanged regions by vertical edge scanning can be used to compare the waveguide non-linearity with its substrate value. From the response versus the depth of an untreated sample, the radius of the focused spot was estimated by the knife-edge technique [23] to be approximately 1 μm , which gives a reasonable spatial resolution for the characterisation of the samples in this study.

FIGURES 1 - 4 show the dependences of the refractive index (a) and the end-face reflected SH intensity (b) versus depth into the waveguide for some PE LiNbO₃ samples studied. For the S1, S2 and S4 samples, where the β_4 , β_3 and β_1 -phases were generated at the surface, the reflected SHG signal in the as-exchanged region is less than ~3% of the value registered for the bulk region (FIGURE 1(b)), indicating that, in this case, the non-linear coefficient in the guide is less than ~15% of the bulk value. Li et al [24] showed theoretically that the reduction of non-linear coefficients in the guiding layer

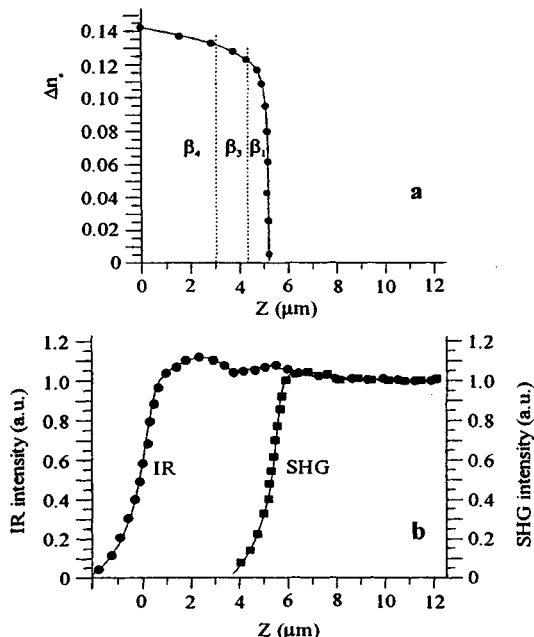


FIGURE 1 (a) Refractive index and (b) reflected SH and IR intensities versus depth into the S1 sample with the $\beta_4\text{-H}_x\text{Li}_{1-x}\text{NbO}_3$ phase at the surface.

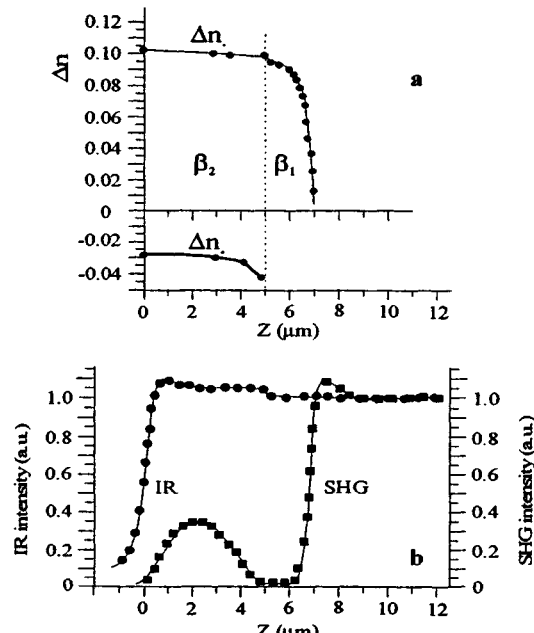


FIGURE 2 (a) Refractive index and (b) reflected SH and IR intensities versus depth into the S3 sample with the $\beta_2\text{-H}_x\text{Li}_{1-x}\text{NbO}_3$ phase at the surface.

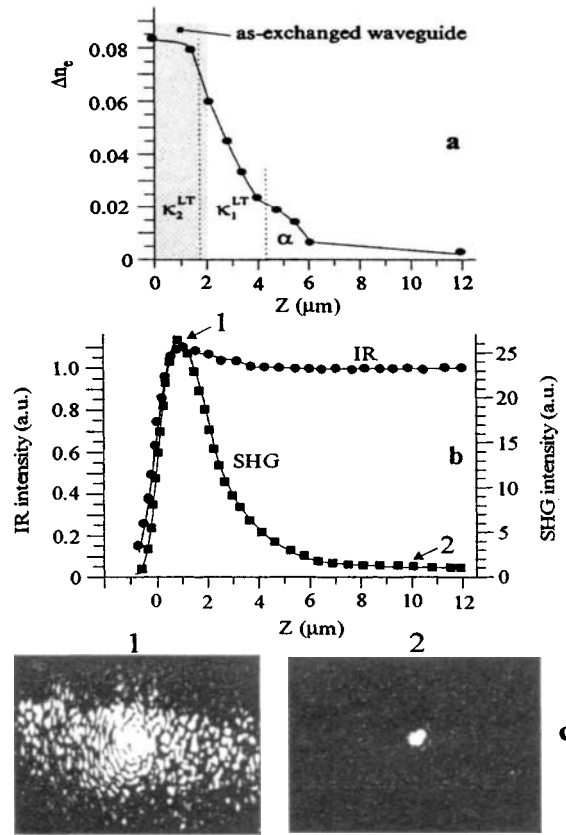


FIGURE 3 (a) Refractive index and (b) reflected SH and IR intensities versus depth into the S5 sample with the κ_2^{LT} - $H_xLi_{1-x}NbO_3$ phase at the surface. (c) Pictures of the reflected SH beam (1) in the as-exchanged waveguide region (point 1 on FIGURE 3(b)) and (2) in the bulk (point 2).

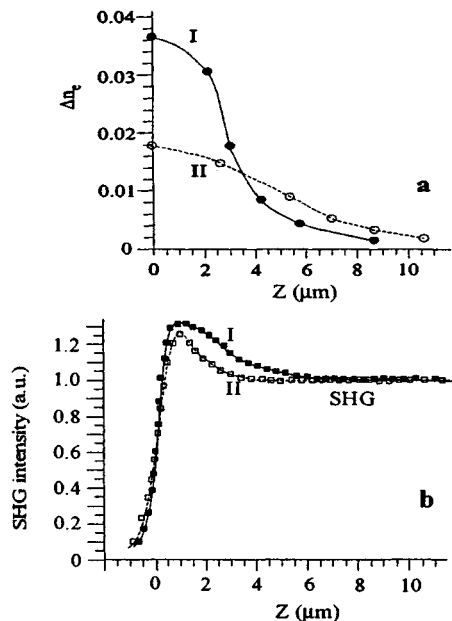


FIGURE 4 (a) Refractive index and (b) reflected SH intensity versus depth into the S13 sample (I) and S14 sample (II) prepared by the graded proton exchange method.

increases the conversion efficiency of SHG, in the form of Cherenkov-type radiation, in the step-index PE waveguides. This result is consistent with earlier experimental results of Arvidsson et al [25], who had noted the possibility of increased efficiencies with reduced non-linear coefficients. Taniuchi and Yamamoto [26] have also found the SHG in unannealed PE waveguides to be more efficient in a Cherenkov configuration than in the phase-matched scheme using the same non-linear coefficient. Therefore, the step-like β_i -phase PE $LiNbO_3$ waveguides with large refractive index increase are advantageous for efficient SHG in Cherenkov configuration. Efficient Cherenkov SHG [27-29] as well as sum-frequency generation [30,31] have been obtained in high-index PE $LiNbO_3$ and $Mg:LiNbO_3$ waveguides with a maximum conversion efficiency of $1\% W^{-1} cm^{-1}$ [29], producing up to 1 mW of 420 nm output from 65 mW of infrared power [26]. It is known that the reduction of non-linear coefficients in the step-index guiding layer increases the conversion efficiency of SHG in the form of Cherenkov-type radiation. Therefore, the step-like β_i -phase PE $LiNbO_3$ waveguides with large refractive index increase are advantageous for efficient SHG in the Cherenkov configuration.

For the PE LiNbO_3 waveguide prepared in the β_2 -phase (sample S3) the results are rather different (FIGURE 2). FIGURE 2(b) shows that the registered non-linear signal in the surface region occupied by the β_2 -phase is approximately 30% of the bulk value and that the SHG signal practically disappears when the β_1 sublayer is reached. The quality of the reflected SHG beam in the β_2 -phase region was similar to the quality of the beam reflected from the bulk region [22]. The results obtained indicate that for the β_2 -phase the d_{33} non-linear coefficient is approximately 55% of the bulk value, in contrast to other direct exchanged high-concentrated β_1 , β_3 and β_4 -phases with strongly reduced non-linearity.

For the waveguides S5-S7, formed by an annealing process from the β_i -phase structures and exhibited in the κ_2^{LT} , κ_1^{LT} and $\alpha \text{H}_x\text{Li}_{1-x}\text{NbO}_3$ phases at the surface, the results are rather complicated. For these samples, the measured intensity of the reflected SH signal that was strongly reduced after the initial proton exchange seems to be restored and even increased after annealing (FIGURE 3(b)). However, this apparent increase of non-linearity is accompanied by a strong degradation of the quality of the SHG reflected beam in the region of initial β_i -phase PE waveguides due to the beam scattering (FIGURE 3(c1)). For the regions below the depth of initial β_i -phase the value of the SHG intensity and the quality of the SHG reflected beam are close to those from the bulk region (FIGURE 3(c2)). For the samples S8 and S9, prepared by high-temperature annealing, which exhibited the κ_2^{HT} , κ_1^{HT} phases at the surface, the general behaviour of the SHG signal is similar to that for low-temperature annealed samples S5, S6 and S7, but the apparent increase of the non-linearity due to the scattering is noticeably smaller. As the examination of the edge of the samples from S5 to S9 under an optical microscope indicates that the quality of the end face in all samples is equivalent to that of untreated LiNbO_3 samples, we believe that the relaxation-induced dislocations are generated during the annealing process at the highly strained and stressed surface region initially filled by high-concentrated β_i phases, causing the large optical losses and the scattering of the SHG reflected beam observed in the APE waveguides, and that, in this case, the crystal structure of the surface region could not be completely restored even by a long annealing process. The optical losses estimated by using a two-prism coupling technique were about 10 dB/cm for κ_i -phase waveguides and less than 1 dB/cm for an α -phase waveguide. In the last case, the depth of the region with poor crystallographic quality (originally β_i -phase) is small compared to the total depth of the APE waveguide and does not significantly affect the light scattering. For κ_1 and, especially, for κ_2 -phase waveguides the depth of this light scattering initial as-exchanged region is comparable with the waveguide thickness, and therefore such waveguides exhibit high optical losses. Therefore, the results obtained indicate that the possibility of making stable, annealed κ_i -phase waveguides with low losses and restored non-linearity is very doubtful. Furthermore, annealed proton exchange, the most commonly used technique to prepare the waveguides in LiNbO_3 , is shown to interfere strongly with previously patterned domains [16,32] leading to domain-structure erasure, which explains why APE waveguides for quasi-phase-matched SHG and optical parametric oscillator devices present a conversion efficiency significantly lower [34], and power threshold considerably higher [16], than theoretically expected.

Another high-temperature technique used to fabricate PE LiNbO_3 waveguides is the so-called graded PE method [33] using melts of K_2SO_4 - Na_2SO_4 - ZnSO_4 - KHSO_4 at temperatures above 400°C. FIGURE 4 shows refractive-index profiles, and the intensity of the reflected SH signal, versus the depth for the graded proton-exchanged samples S13 and S14. One can see only an insignificant increase of the registered non-linear signal due to the scattering (FIGURE 4(b)) and a small degradation of the quality of the reflected beam at the surface region (FIGURE 4(c)). Also, the graded PE was demonstrated [32] to leave the ferroelectric domain structure of poled LiNbO_3 intact during the waveguide fabrication. Thus, use of the graded PE technique makes it possible to produce high-quality waveguides with undegraded non-linear optical properties and without affecting the domains.

Recently, El Hadi et al [16] reported that direct PE in a diluted benzoic acid melt (3% of lithium benzoate) completely preserves the non-linear optical properties of the material. Under these conditions

the α -phase is reached. The authors did not observe any difference in SH reflected beam quality between the waveguide and the bulk regions. So, the direct PE in a diluted melt can preserve all the non-linear optical and structural properties of LiNbO₃ and is a way to produce high-quality LiNbO₃ waveguides, available for non-linear applications.

At present, we have also established [35] that the non-linear properties of PE LiNbO₃ waveguides can be effectively recovered by the reverse proton-exchange technique. Thus, reverse proton exchange [36,37] has been demonstrated as a simple and attractive technique for fabricating buried optical waveguides with symmetrical refractive-index profiles and undegraded non-linear coefficients.

D CONCLUSION

The non-linear optical properties of proton-exchanged waveguides in different H_xLi_{1-x}NbO₃ phases are summarised in this Datareview. The results obtained are believed to be useful for the design, fabrication and optimising of guided-wave non-linear optical devices in LiNbO₃.

ACKNOWLEDGEMENTS

This work was supported by the Russian Foundation of Basic Research under grants no.96-15-96978 and no.99-15-96110 for Young Doctors of Sciences and grant no.96-15-98220 for Leading Science Schools and by the 'Russian Universities - Basic Researches' program under grant no.248-1998. This investigation is also part of the project A-0102 supported by the Integration Foundation (Russia).

REFERENCES

- [1] J.A. Armstrong, N. Bloembergen, J. Ducuing, P.S. Pershan [*Phys. Rev. (USA)* vol.127 (1962) p.1918]
- [2] J. Webjörn, F. Laurell, G. Arvidsson [*IEEE Photonics Technol. Lett. (USA)* vol.1 (1989) p.316]
- [3] E.J. Lim, M.M. Feier, R.L. Byer [*Electron. Lett. (UK)* vol.25 (1989) p.174]
- [4] M.N. Armenise, K.K. Wong, V. Hinkov, G.T. Reed, B.L. Weiss [in *Properties of Lithium Niobate* (INSPEC, IEE, London, UK, 1989) ch.8 p.237-66]
- [5] E. Glavas, J.M. Cabrera, P.D. Townsend [*J. Phys. D, Appl. Phys. (UK)* vol.22 (1989) p.611]
- [6] F. Laurell, M.G. Roelofs, H. Hsiung [*Appl. Phys. Lett. (USA)* vol.60 (1992) p.301]
- [7] M.L. Bortz, M.M. Feier [*Opt. Lett. (USA)* vol.17 (1992) p.704]
- [8] W.-Y. Hsu, C.S. Willand, V. Gopalan, M.C. Gupta [*Appl. Phys. Lett. (USA)* vol.61 (1992) p.2263]
- [9] R.W. Keys, A. Loni, R.M. De La Rue [*Electron. Lett. (UK)* vol.26 (1990) p.625]
- [10] T. Suhara, H. Tazaki, H. Nishihara [*Electron. Lett. (UK)* vol.25 (1989) p.1326]
- [11] X. Cao, R. Srivastava, R.V. Ramaswamy, J. Natour [*IEEE Photonics Technol. Lett. (USA)* vol.3 (1991) p.25]
- [12] M.L. Bortz, L.A. Eyres, M.M. Feier [*Appl. Phys. Lett. (USA)* vol.62 (1993) p.2012]
- [13] G.R. Paz-Pujalt, D.D. Tusche, G. Braunstein, T. Blanton, S. Tong Lee, L.M. Salter [*J. Appl. Phys. (USA)* vol.76 (1994) p.3981]
- [14] T. Veng, T. Skettrup, K. Pedersen [*Appl. Phys. Lett. (USA)* vol.69 (1996) p.2333]
- [15] K. El Hadi, P. Baldi, M.P. De Micheli, D.B. Ostrowsky, F. Laurell [in *Proc. 8th Euro. Conf. Integrated Optics (ECIO'97)* Stockholm, Sweden, 1997, p.358]
- [16] K. El Hadi et al [*J. Opt. Soc. Am. B (USA)* vol.14 (1997) p.3197]
- [17] H. Ohlfeldt [*J. Appl. Phys. (USA)* vol.76 (1994) p.3255]

- [18] Yu.N. Korkishko, V.A. Fedorov [*Ion Exchange in Single Crystals for Integrated Optics and Optoelectronics* (Cambridge International Science Publishing, Cambridge, UK, 1999)]
- [19] Yu.N. Korkishko, V.A. Fedorov [*IEEE J. Sel. Top. Quantum Electron. (USA)* vol.2 (1996) p.187]
- [20] Yu.N. Korkishko, V.A. Fedorov [Datareview in this book: 3.1 Structural phase diagram of proton-exchanged waveguides in $LiNbO_3$]
- [21] Yu.N. Korkishko, V.A. Fedorov, F. Laurell [*Proc. 9th Europ. Conf. Integrated Optics* Torino, Italy, April 1999, p.127]
- [22] Yu.N. Korkishko, V.A. Fedorov [*IEEE J. Sel. Top. Quantum Electron. (USA)* vol.6 no.1 (2000) p.132]
- [23] D.K. Cohen, B. Little, F.S. Luecke [*Appl. Opt. (USA)* vol.23 (1984) p.637]
- [24] M.J. Li, M. De Micheli, Q. He, D.B. Ostrowsky [*IEEE J. Quantum Electron. (USA)* vol.26 (1990) p.1384]
- [25] G. Arvidsson et al [in *Digest of Topical Meeting of Nonlinear Guidewave Phenomena* Houston, USA, 1989, paper THA3-1]
- [26] T. Taniuchi, K. Yamamoto [*Proc. SPIE (USA)* vol.864 (1987) p.9]
- [27] N.A. Sanford, J.M. Connors [*J. Appl. Phys. (USA)* vol.65 (1989) p.1429]
- [28] R.W. Keys, A. Loni, R.M. De La Rue [*J. Mod. Opt. (UK)* vol.37 (1990) p.545]
- [29] M.J. Jongerius, R.R. Drenten, R.B.J. Droste [*Philips J. Res. (Netherlands)* vol.46 (1992) p.231]
- [30] K. Yamamoto, H. Yamamoto, T. Taniuchi [*Appl. Phys. Lett. (USA)* vol.58 (1991) p.1227]
- [31] Q. He et al [*Opt. Commun. (Netherlands)* vol.89 (1992) p.54]
- [32] J. Webjörn [*IEEE J. Lightwave Technol. (USA)* vol.11 (1993) p.589]
- [33] V.A. Ganshin, Yu.N. Korkishko [*Phys. Status Solidi A (Germany)* vol.119 (1990) p.11-25]
- [34] S. Helmfrid, G. Arvidsson, J. Webjörn [*J. Opt. Soc. Am. B (USA)* vol.10 (1993) p.222]
- [35] Yu.N. Korkishko, V.A. Fedorov [submitted to *J. Appl. Phys. (USA)* (1999)]
- [36] V.A. Ganshin, Yu.N. Korkishko [*Sov. Phys.-Tech. Phys. (USA)* vol.35 (1990) p.1095]
- [37] Yu.N. Korkishko, V.A. Fedorov, T.M. Morozova, F. Caccavale, F. Gonella, F. Segato [*J. Opt. Soc. Am. A (USA)* vol.15 (1998) p.1838]

8.8 IR reflection spectra of proton-exchanged waveguides containing different $H_xLi_{1-x}NbO_3$ phases

S.M. Kostritskii, Yu.N. Korkishko and V.A. Fedorov

August 1999

A INTRODUCTION

In this Datareview, we report on results of the experimental study of lattice vibration spectra of proton-exchanged waveguiding near-surface layers. Spontaneous polarisation and a microscopic lattice contribution in the electro-optic effect are estimated for each $H_xLi_{1-x}NbO_3$ phase from the IR spectroscopy data.

Previous studies [1-3] have allowed us to identify the seven different $H_xLi_{1-x}NbO_3$ phases generated in proton-exchanged (PE) optical waveguides depending on fabrication conditions. A transition from any phase to another is characterised by a jump of unit cell parameters [1,2] and, therefore, each phase has its own specific dependence of refractive index on unit cell parameters and proton concentration [2,3]. Thus, some change of the chemical bonding should be expected at such phase transitions. It is well known that the lattice vibration spectrum gives direct information about the crystal structure and chemical bonding of intrinsic atoms and extrinsic defects (e.g. hydrogen) in both the bulk crystal and its separate fragments. Therefore, a study of the lattice vibrational spectra of a PE waveguiding layer presents some interest for $H_xLi_{1-x}NbO_3$ phase identification. The infrared (IR) reflection and IR attenuated total reflection (ATR) spectroscopy methods are known to be most efficient for studying the lattice vibration spectrum of a near-surface region with depth S comparable to the waveguide thickness d (FIGURE 1). To provide the measurement of IR-reflection and IR-ATR spectra in PE waveguides the IR-spectrophotometer 'Specord M80' with standard attachments for the reflection and ATR experiments has been used. All measurements were performed at a fixed spectral resolution of 2.4 cm^{-1} .

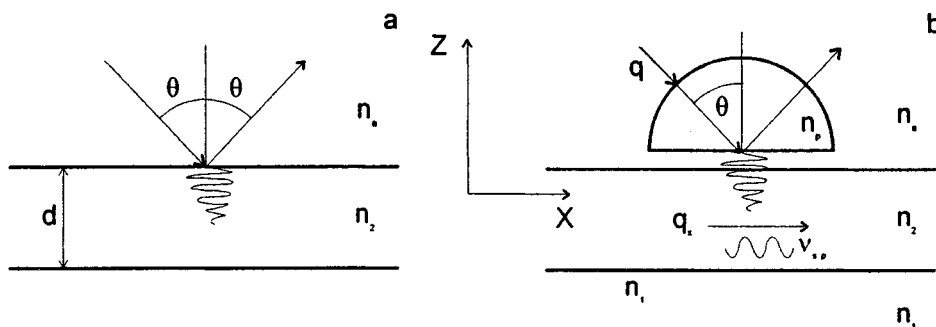


FIGURE 1 Schematic sketch of measurements of (a) IR reflection and (b) ATR of IR radiation.

B EXPERIMENT

To realise the PE planar waveguides, one can use either a simple exchange, varying the temperature and the acidity of the bath and the duration of the exchange to modify the parameters of the waveguide, or a two-step process, where the exchange is followed by annealing, whose duration and temperature further modify the waveguide parameters [1-4].

PE waveguides were fabricated in optical grade virgin $LiNbO_3$ of X- and Z-cuts. The fabrication conditions and sample notation are the same as in our previous investigations [4,5]. FIGURE 2 shows the positions of the samples studied on the structural phase diagrams of proton-exchanged Z-cut (FIGURE 2(a)) and X-cut (FIGURE 2(b)) $LiNbO_3$ waveguides. The surface values of the extraordinary index increment Δn_e and the deformation ϵ''_{33} normal to the surface plane, determined by the IWK technique from the effective indices of guided modes and double-crystal X-ray diffractometry (DCXRD), are presented here. This means that the phase state of a top (surface) part is identified in FIGURE 2, whereas some of the studied samples are multiphase [1,3], i.e. contain other phases in a deeper part of the waveguiding layer. All of the studied samples functioned as multimode optical waveguides.

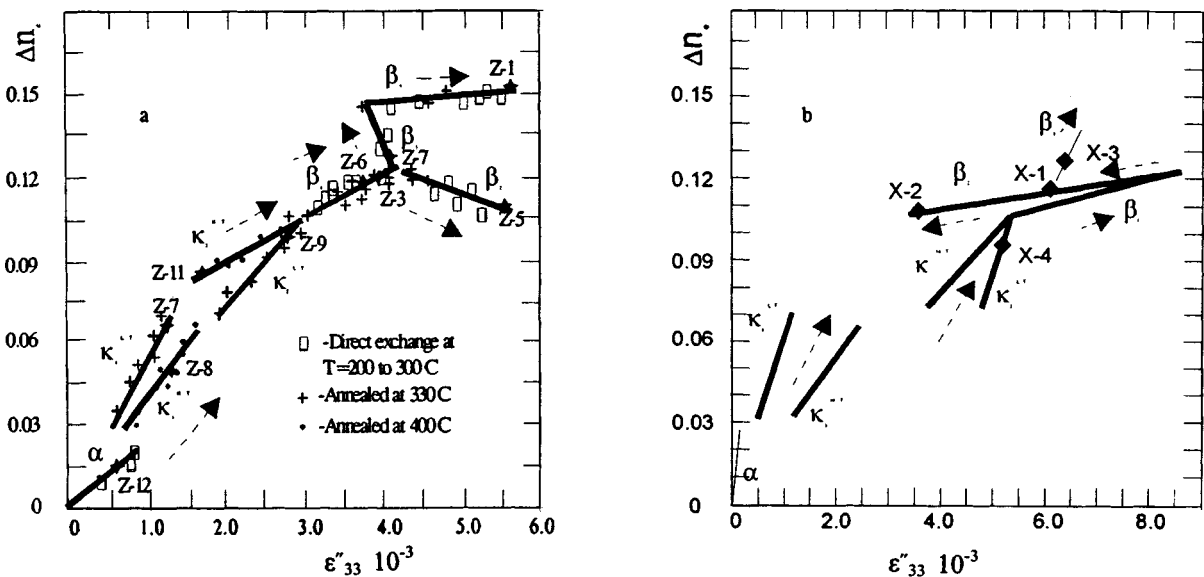
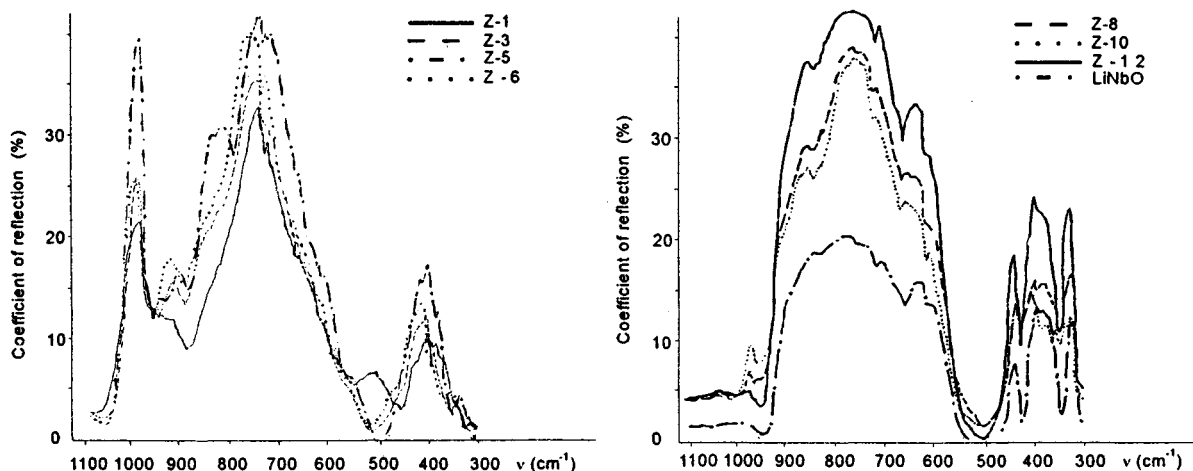


FIGURE 2 Structural phase diagram of (a) Z-cut and (b) X-cut $H_xLi_{1-x}NbO_3$ substrates with positions of studied samples. These give the dependence of the extraordinary index variation Δn_e measured at $\lambda = 633$ nm versus the surface value of deformation ϵ''_{33} normal to the surface plane.

The arrows show the directions in which proton concentration increases.

C EXPERIMENTAL RESULTS

Analysis of the experimental IR reflection data in the low-frequency range indicates the very strong changes in the lattice vibration spectrum caused by proton exchange (FIGURE 3). A direct comparison of spectra obtained in samples containing the various $H_xLi_{1-x}NbO_3$ phases in the top part of the waveguiding layer shows that each phase has its own specific spectrum, which may be used to identify the presence of this phase in samples with unknown phase contents. In the case of multiphase layered waveguides, the IR-reflection spectrum observed depends on an angle θ (FIGURE 1(a)) of incidence of the IR-radiation on the crystal surface. We used the standard attachment to the IR-spectrophotometer that permitted incidence of the radiation at angles of 20° and 70° . The IR-reflection spectra measured at $\theta = 70^\circ$ are not affected by the presence of the various phases in deep parts of the waveguiding layer and, therefore, only give information about a surface phase. At $\theta = 20^\circ$ the spectrum changes induced by proton-exchange depend on an integral phase composition of the waveguiding layer and, therefore, it is rather difficult to separate different phase contributions in the IR reflection spectra. Such an angular dependence is evidently caused by much deeper penetration of IR radiation beyond the surface at $\theta = 20^\circ$ in comparison with that at $\theta = 70^\circ$ [4]. This is why, to analyse the lattice vibration spectrum changes, we have used only the data obtained at $\theta = 70^\circ$, FIGURE 3. These changes are more apparent in the range of intrinsic vibration of the NbO_6

FIGURE 3 IR reflection spectra in the range $300 - 1000 \text{ cm}^{-1}$ at $\theta = 70^\circ$ for different phases.

octahedra. The frequency range for TO phonons of the NbO_6 vibrational mode observed in Raman spectra was reported previously [6]. It has been found that the Raman band in the frequency region from 800 to 900 cm^{-1} is attributed to the NbO_6 octahedra with a large distortion coming from the non-bridging oxygen ions. The broad bands in the range from 600 to 800 cm^{-1} are attributed to less-distorted NbO_6 octahedra in the absence of non-bridging oxygen ions [6]. In the case of IR reflection, the frequencies of TO phonons correspond to the low-frequency edges of the IR spectrum bands [7]. Thus, our experimental data show, in accordance with the well-established assignment [6], less-distorted NbO_6 octahedra with no non-bridging oxygen ions present in the α , κ_1 , and κ_2 phases, as well as in pure $LiNbO_3$. The appearance of weak extra bands in the region of IR reflection spectra from 800 to 900 cm^{-1} for all β_i phases (FIGURE 3) points to the presence of more distorted NbO_6 octahedra with non-bridging oxygen ions. It is also important to note that each β_i phase is 'marked' by a very specific lattice vibration spectrum with unique characteristic bands. Thus, a significant difference should exist between the crystalline structures of different β_i phases, which is introduced by the added chemical bonds with characteristic frequencies of vibration. This feature can be used for accurate identification of β_i phases in any $H_xLi_{1-x}NbO_3$ waveguide.

The theoretical modelling of the electronic structure of $LiNbO_3$ has demonstrated [8] that the optical properties and spontaneous polarisation of $LiNbO_3$ may be evaluated with good approximation in the framework of the quasimolecular model, considering an NbO_6 octahedron cluster as a separate structural fragment. This cluster gives the main contribution to the spontaneous polarisation P_s , which is proportional to the distortion of the octahedra in the real crystal structure of lithium niobate [8]. Moreover, it was established [9,10] that each polar-lattice optic mode in $LiNbO_3$ contributes separately to the electro-optic effect an amount proportional to the product of the Raman scattering efficiency and infrared oscillator strength. Since the contributions of the Nb-O bonds to the linear and non-linear susceptibility are substantially larger than the corresponding contribution of the Li-O bonds [11], we may use the single-oscillator approach, taking into account the fundamental optical mode of the intrinsic vibration of NbO_6 octahedra. The Raman scattering measurement in PE $LiNbO_3$ has shown the small change of the Raman scattering efficiency for this mode [12]. Therefore, to estimate the microscopic lattice contribution in the electro-optic effect and a relative value of P_s in the different $H_xLi_{1-x}NbO_3$ phases, it is enough to determine the LO-TO splitting of this mode in a given phase, as infrared oscillator strength is related [7] to the value of such splitting. It should be noted that the pure electronic contribution in the electro-optic effect, which can be estimated from second-harmonic-generation experiments, is less than 10% of the lattice contribution in the case of $LiNbO_3$ crystal [9,10].

We have established that the LO-TO splitting of the fundamental polar mode associated with NbO_6 octahedra vibrations, which is proportional to the width of the main band ranged from 580 to 900 cm^{-1} , appears to depend on hydrogen concentration x and has quite different specific values for different crystal phases (FIGURE 3). To determine the hydrogen concentration, a recently proposed method was used [3,13]. Our data show that a strong decrease of the LO-TO splitting for this polar mode occurs in $H_xLi_{1-x}NbO_3$ phases with high hydrogen concentration. According to the above mentioned theory [9,10] and our arguments, the reduction of the LO-TO splitting of this vibrational mode points to the degradation of ferroelectric properties and electro-optic coefficients r of the crystal:

$$P_s \sim (v_{\text{LO}}^2 - v_{\text{TO}}^2) / v_{\text{TO}}^2 \quad (1)$$

$$r \sim [(v_{\text{LO}}^2 - v_{\text{TO}}^2) / v_{\text{TO}}^2]^{1/2} + d$$

where P_s is the spontaneous polarisation of the crystal, v_{LO} is the frequency of the LO phonon, v_{TO} is the frequency of the TO phonon, and d is the pure electronic contribution, which can be neglected in the approximated estimation because of its small value.

The Kramers-Kroning analysis of the IR-reflection spectra was used to evaluate the LO- and TO-phonon frequencies. FIGURE 4 shows the dependence of the frequency of the LO phonon for the NbO_6 vibrational mode polarised perpendicular to the optical axis c , versus the calculated hydrogen concentration x for $H_xLi_{1-x}NbO_3$ samples containing different phases at the surface. It is found that the α , κ_1 and κ_2 phases demonstrate a notable gradual change in the lattice vibrational spectrum, even though these phases do not exhibit, in contrast to β_i phases, any characteristic bands in the lattice vibration range. It should be noted that the IR reflection spectra were studied only for $\nu > 300 \text{ cm}^{-1}$, with the low limit of the spectral range being set by the spectrometer used in our experiments. Therefore, the accuracy of the TO-phonon frequency determination was not high; however, it was quite adequate for phases with relatively low hydrogen concentration, such as the α , κ_1 and κ_2 phases. The results of calculations based on EQN (1) are presented in TABLE 1. In the case of the β_i phases, the phonon dampening is very strong, which is direct evidence, according to the established theory [7], of a blurred low-frequency band edge. Therefore, the choice of boundary conditions, i.e. the values of the real and imaginary part of the dielectric permittivity at the lower limit of 300 cm^{-1} of the range of measurements, is crucial. As such, the TO-phonon frequency needs to be properly chosen according to the model used in the calculations. In approximate estimations, however, the Raman frequency of the TO phonon may be used, which, for PE- $LiNbO_3$ waveguides, has been observed at 690 cm^{-1} [12], which is very near to any value calculated from our IR reflection spectra, FIGURE 3. By using the data of LO phonon frequencies (FIGURE 4) and the value of $v_{\text{TO}} = 690 \text{ cm}^{-1}$, the electro-optical coefficients r_{33} and r_{13} and P_s for the fabricated samples can be estimated.

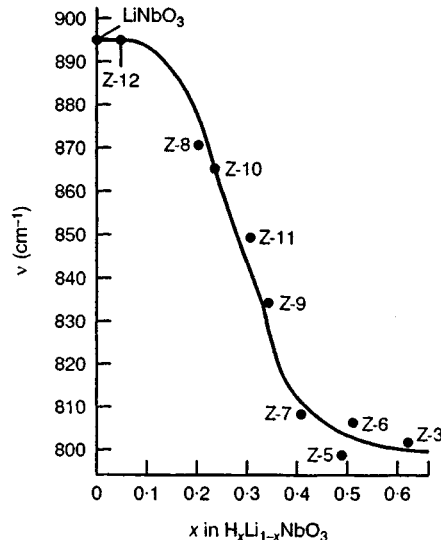


FIGURE 4 The dependence of the frequency of the LO phonon for the NbO_6 vibrational mode polarised perpendicular to the optical axis c versus calculated proton concentration x .

8.8 IR reflection spectra of proton-exchanged waveguides containing different $H_xLi_{1-x}NbO_3$ phases

TABLE 1 The main parameters of the OH-librational band in IR-reflection spectra of proton-exchanged $LiNbO_3$ waveguides, containing the different $H_xLi_{1-x}NbO_3$ phases.

$H_xLi_{1-x}NbO_3$ phase	Frequency of reflectance peak, ν (cm^{-1})	Relative value of reflectance ^(a) at ν (arb. units)
β_1	975	0.6
β_2	980	1.0
β_3	980	0.8
β_4	970	0.5
κ_2^{LT}	955 and 970	0.3
κ_2^{HT}	955 and 970	0.15
κ_1^{LT}	965	0.15
κ_1^{HT}	965	≤ 0.06
α	965	≤ 0.005

^(a)All values of reflection coefficient are normalised to reflectance value in β_2 phase (the maximum value observed).

The sample with the β_4 -phase is outside the range of FIGURE 4. The value $\nu_{LO} = 745 - 750 cm^{-1}$ and a very small LO-TO splitting ($55 - 60 cm^{-1}$) were observed for this phase. The obtained results point to a strong degradation of ferroelectric properties in the β_4 -phase.

The main conclusion of the present study is that all $H_xLi_{1-x}NbO_3$ phases are ferroelectric. Moreover, a comparison of our IR reflection data with previously obtained Raman data [12] for the β_4 -phase confirms the conclusion that this phase is also ferroelectric. In fact, the frequencies of NbO_6 octahedra bands in Raman spectra reported in [12] and acquired from our IR reflection spectra (FIGURE 3) are in good agreement. At the same time, it is well known [7] that if the β_4 -phase is paraelectric then the IR active vibration mode should be forbidden to appear in the Raman spectrum. However, the ferroelectric properties of the β_4 -phase degrade severely due to the extremely small value of the LO-TO splitting. Therefore, this phase is not suitable for use in non-linear and electro-optic devices.

Note that the electro-optical coefficients estimated from IR spectra for the β_i phases are larger than those measured by direct methods [2,14]. The difference may be attributed to the effect of screening in strongly non-uniform layers, which reduces the 'effective' (measured) value of r , but IR spectroscopy provides information about local changes of oscillators, which are responsible for the electro-optical effect.

Note that the lattice vibration spectra of any $H_xLi_{1-x}NbO_3$ phase are similar for the samples of X- and Z-cuts in terms of the vibration mode frequency, excluding the new OH librational modes.

The IR reflection spectra of all studied samples contain the new band at $890 - 985 cm^{-1}$ which is additional to the lattice spectrum of $LiNbO_3$. We assign this band to a direct OH librational mode; as previously reported [15] in a proton-exchanged surface layer of $LiNbO_3$ with a very high proton concentration the direct OH librational mode at $960 cm^{-1}$ was observed by Raman scattering. According to fabrication parameters reported in [15], we assume that the β_1 -phase was studied. The observed OH librational wavenumber is in agreement with a description of the libration by a simple harmonic oscillator model [15]. As is well known [2], the proton in $LiNbO_3$ forms with the oxygen of the crystal lattice an OH complex, revealing its existence by a characteristic IR-active stretching vibration at $\sim 3500 cm^{-1}$. In proton-exchanged $LiNbO_3$ layers this stretching vibration is completely polarised perpendicular to the ferroelectric z-axis. In contrast to this, the OH librational band was displayed [15] at the same frequency components parallel and perpendicular to the z-axis, indicating the energetically isotropic, three-dimensional nature [16] of the libration in strongly proton-exchanged $LiNbO_3$. Analogous to calculations performed in [17] for TiO_2 , where libration plays the role of the attempt frequency for the thermally activated hopping motion of the protons, the present case leads to

an expected isotropic proton conductivity. This is in excellent agreement with the isotropic activation energy found in conductivity measurements for the hopping motion of protons and deuterons in proton-exchanged $LiNbO_3$ with a very high proton concentration, obtained by a direct proton exchange in weakly diluted benzoic acid melt [15,18].

Our experimental studies of polarised IR reflection at OH librational band frequencies for any β_i -phase on Z-cut $LiNbO_3$ showed that the librational energy is the same for absorption either parallel or perpendicular to the optical axis of $LiNbO_3$ [4], which confirms the results obtained by using Raman spectroscopy for the β_1 phase [15]. The IR reflection study of the α , κ_1 and κ_2 -phases on Z-cut $LiNbO_3$ shows that the OH librational mode in these phases is predominantly polarised perpendicular to the c-axis in contrast to that observed for the β_i -phases. Moreover, for the κ_2^{LT} and κ_2^{HT} phases, this band has a pronounced splitting on two components, 955 and 970 cm^{-1} , which are shifted to the low-frequency side with respect to the band position in the β_i -phases [4]. This fact clearly indicates the existence of two energetically non-equivalent OH complexes in the κ_2 -phases. Thus, all the aforementioned results and speculations allow one to assume an anisotropic proton conductivity for the α , κ_1 and κ_2 -phases.

In contrast to observations for the β_i -phases on Z-cut $LiNbO_3$, the librational bands for these phases generated in X-cut $LiNbO_3$ substrates in directions parallel to the c-axis and perpendicular to this axis were found to be very different. The IR reflection spectra show two components with different frequencies and different intensities for incident light of two orthogonal polarisations (FIGURE 5). The component at $960 - 970\text{ cm}^{-1}$ is clearly isotropic, but the component at $890 - 940\text{ cm}^{-1}$ is polarised perpendicularly to the polar axis. Note that the position of the second band, i.e. a splitting magnitude of the libration mode, depends on a phase composition of $H_xLi_{1-x}NbO_3$ (see FIGURES 3 and 5). These experimental facts point to the energetically anisotropic nature of the libration for the β_i - $H_xLi_{1-x}NbO_3$ phases in X-cut $LiNbO_3$ and one would expect an anisotropic proton conductivity for these structures.

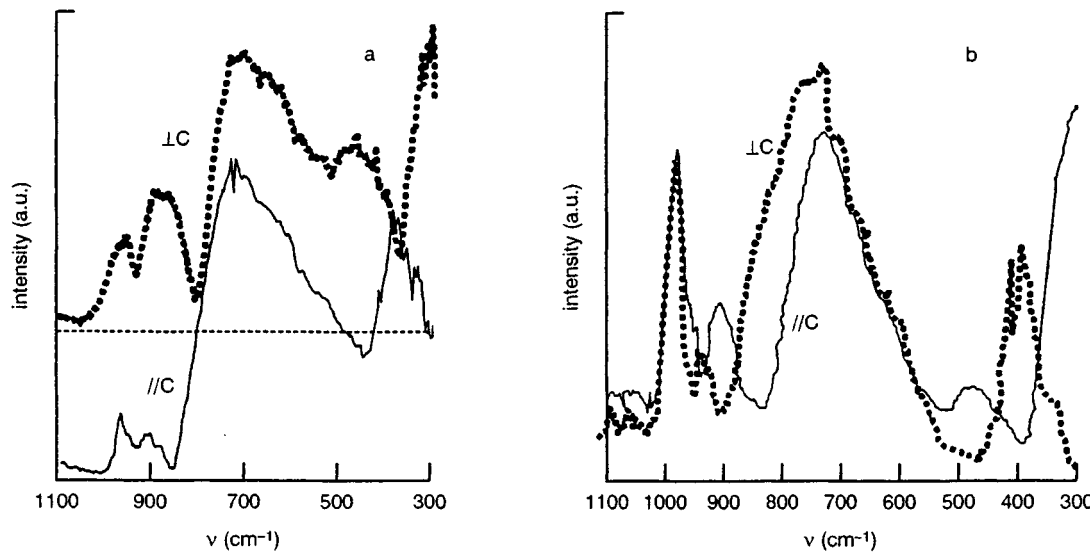


FIGURE 5 IR reflection spectra in the range $300 - 1000\text{ cm}^{-1}$ for (a) the β_3 - $H_xLi_{1-x}NbO_3$ phase at the surface (sample X-3) and (b) the β_2 - $H_xLi_{1-x}NbO_3$ phase at the surface (sample X-2).

The IR reflection study of the α , κ_1 and κ_2 -phases on X-cut $LiNbO_3$ shows that the OH librational mode in these phases is strongly anisotropic as well as for the Z-cut samples.

Quite an interesting result was obtained when the reflection coefficient at the frequencies of the OH librational band at $955 - 985\text{ cm}^{-1}$ was measured in the Z-cut samples. The reflectance in this range turns out to vary significantly for different phases (FIGURE 3, TABLE 2), while the reflectance

8.8 IR reflection spectra of proton-exchanged waveguides containing different $H_xLi_{1-x}NbO_3$ phases

increment at frequencies of the OH stretching band has a similar value for all the studied samples. Besides, the analysis of these data indicates that the dependence of the OH librational band reflectance on exchange ratio, x , is expressly non-monotonic and exhibits leaps at the phase boundaries. An exception to this rule is noted in comparing the α and κ_1^{HT} phases, where reflectance is nearly proportional to hydrogen concentration. Thus, modifications in the OH librational band may be ascribed to changes of effective charge of the corresponding IR-active vibration due to the relocation of protons. The latter is, in turn, caused by the phase transitions in the $H_xLi_{1-x}NbO_3$ system that are triggered by changes in exchange ratio, x .

TABLE 2 Calculated spontaneous polarisation and electro-optical coefficients for different $H_xLi_{1-x}NbO_3$ phases.

Sample	Phase at the surface	P_S/P_S^0 and r_{ij}/r_{ij}^0
Z-12	α	0.99
Z-8	κ_1^{HT}	0.925
Z-10	κ_1^{LT}	0.91
Z-11	κ_2^{HT}	0.88
Z-9	κ_2^{LT}	0.83
Z-6	β_1	0.61
Z-3	β_1	0.59
Z-7	β_3	0.61
Z-5	β_2	0.58
Z-1	β_4	0.19 - 0.28

P_S^0 and r_{ij}^0 are spontaneous polarisation and electro-optical coefficients of pure $LiNbO_3$ respectively.

For detailed studies of the layered structure of waveguides, the ATR method of IR spectroscopy was used. The ATR measurements were made using a KRS-5 prism to couple IR radiation with frequencies from 600 to 900 cm^{-1} into a waveguide. The characteristic feature of ATR spectra is that the band with attenuated reflectance of IR radiation that appears depends on the angle θ (FIGURE 1(b)) of incidence [4]. According to the ATR theory as applied to multilayer structures [19,20], this phenomenon is associated with excitation of surface polaritons on the sample surface as well as on the interface in the near surface region. A simple model gives the following relationship for the frequency of the main mode:

$$v_{sp} = v_{TO} \{ (\epsilon_{2,s} + \coth(q_x d)) / (\epsilon_{2,\infty} + \coth(q_x d)) \} \quad (2)$$

where v_{sp} is the frequency of the double-interface polariton; $\epsilon_{2,s}$ and $\epsilon_{2,\infty}$ are the static and high-frequency (optical frequencies) permittivities of the near-surface layer with thickness d . In experiments, the IR wave-vector component $q_x \sim \sin \theta$ was varied by adjusting the incident angle θ at which light enters the prism (FIGURE 1(b)). The spectral dependence of reflectance from the prism/air interface was measured. EQN (2) was used to analyse the observed dependence of the frequencies of reflectance minima on θ . As follows from EQN (2), for a given value of θ , these frequencies will depend on the waveguide thickness. Experimentally, we did observe such a dependence for waveguides with the α , κ_1 and κ_2 -phases [4]. In waveguides with other phases, a correlation between v_{sp} and d cannot be discerned, being obscured by the much stronger influence of changes in ϵ_2 that are caused by small variations in hydrogen concentration x . If detectable, this dependence can be used to determine the waveguide thickness in unknown samples. According to theory [19], the hops on the $v_{sp}(\theta)$ dependence [4] demonstrate the existence of interfaces between some sublayers with different lattice vibration spectra inside the waveguiding layer. A comparison of these results with the data of the DCXRD measurements shows that the hops on the dependences of v_{sp} on θ are observed in the multiphase samples only. Evidently, these hops point to the presence of interfaces between layered phases. Thus, the results of the ATR spectra study show that the $H_xLi_{1-x}NbO_3$ phases formed in PE $LiNbO_3$ waveguides are structured as individual layers, not as a

8.8 IR reflection spectra of proton-exchanged waveguides containing different $H_xLi_{1-x}NbO_3$ phases

mixture of different phases, as has been supposed by many researchers. Previously, it has been suggested [19,20] that one can determine the thickness of each sublayer in the multilayered system by studying the discontinuities on the dependences of v_{sp} on θ . This work is currently in progress.

D CONCLUSION

This Datareview outlines the lattice vibrational spectra of photon-exchanged waveguides in $LiNbO_3$. Both spontaneous polarisation and microscopic lattice contributions are summarised for each of the phases. Both IR reflection and attenuated total reflection techniques are used to determine values.

ACKNOWLEDGEMENTS

This work was supported by INTAS project 0009-98 and NATO project HTECH.LG 974730.

REFERENCES

- [1] Yu.N. Korkishko, V.A. Fedorov [*IEEE J. Sel. Top. Quantum Electron. (USA)* vol.2 (1996) p.187]
- [2] Yu.N. Korkishko, V.A. Fedorov [*Ion Exchange in Single Crystals for Integrated Optics and Optoelectronics* (Cambridge International Science Publishing, Cambridge, UK, 1999)]
- [3] Yu.N. Korkishko, V.A. Fedorov [*J. Appl. Phys. (USA)* vol.82 (1997) p.1010]
- [4] Yu.N. Korkishko, V.A. Fedorov, S.M. Kostritskii [*J. Appl. Phys. (USA)* vol.84 (1998) p.2411]
- [5] Yu.N. Korkishko, V.A. Fedorov, S.M. Kostritskii [*Appl. Phys. B (Germany)* vol.67 (1998) p.577]
- [6] K. Fukumi, S. Sakka [*J. Mater. Sci. (UK)* vol.23 (1988) p.2819]
- [7] H. Poulet, J.-P. Mathieu [*Spectres de Vibration et Symetrie des Cristaux* (Gordon and Breach, New York, USA, 1970)]
- [8] L. Hafid, F.M. Michel-Calendini [*J. Phys. C, Solid State Phys. (UK)* vol.19 (1986) p.2907]
- [9] I.P. Kaminow, W.D. Johnston Jr. [*Phys. Rev. (USA)* vol.160 (1967) p.519]
- [10] W.D. Johnston Jr. [*Phys. Rev. B (USA)* vol.1 (1970) p.3494]
- [11] S.H. Wemple, M. Di Domenico Jr. [*J. Appl. Phys. (USA)* vol.40 (1969) p.720]
- [12] G.R. Paz-Pujalt, D.D. Tuschel, G. Braunstein, T. Blanton, S. Tong Lee, L.M. Salter [*J. Appl. Phys. (USA)* vol.76 (1994) p.3981]
- [13] Yu.N. Korkishko, V.A. Fedorov, V.V. Nosikov, S.M. Kostritskii, M.P. De Micheli [*Proc. SPIE (USA)* vol.2997 (1997) p.234]
- [14] F. Rickerman, D. Dip, B. Gather, E. Krätzig [*Phys. Status Solidi A (Germany)* vol.150 (1995) p.763]
- [15] A. Gröne, S. Kapphan [*Ferroelectrics (UK)* vol.186 (1996) p.177]
- [16] A. Gröne, S. Kapphan [*J. Phys., Condens. Matter (UK)* vol.7 (1995) p.3051]
- [17] J.B. Bates, J.C. Wang, R.A. Perkins [*Phys. Rev. B (USA)* vol.19 (1979) p.4130]
- [18] S. Klauer, M. Wöhlecke, S. Kapphan [*Phys. Rev. B (USA)* vol.45 (1992) p.2786]
- [19] V.M. Agranovich, D.L. Mills, Eds [*Surface Polaritons* (Elsevier, New York, 1982; Moscow, Russia, 1985)]
- [20] E.A. Vinogradov, I.I. Khammadov [*Spectroscopy of Volume and Surface Crystal Phonons* (Tashkent, USSR, 1989)]

8.9 Holographic gratings in photorefractive LiNbO₃ waveguides fabricated by combined proton and copper exchange

S.M. Kostritskii, Yu.N. Korkishko and V.A. Fedorov

August 1999

A INTRODUCTION

In this Datareview, we present results on the influence of phase composition on the rate of copper exchange and photorefractivity in H_xLi_{1-x}NbO₃ planar waveguides. The holographic recording efficiency is found to depend on the phase composition.

Photorefractive non-linear optical crystals are currently used for a wide range of applications in optical phase-conjugation and two- and four-wave mixing techniques. The fabrication of photorefractive waveguides (PRW) is desirable as it provides compatibility with other miniaturised integrated-optical waveguide devices which are in common use today, in particular laser diodes and fibre geometries. Additionally, the optical confinement inherent to waveguide structures allows a high intensity to be maintained within crystalline waveguides, and this increased intensity-length product leads to an appreciable decrease in the effective photorefractive response time for a given input power [1].

Holographic gratings in integrated optics have been extensively employed for the realisation of couplers, reflectors, beam splitters, resonant filters and wavelength-division multiplexers [2]. The formation of highly efficient holographic gratings in lithium niobate is possible because of the large photorefractive effect in this crystal, as has been previously reported for Li-outdiffused [3], Ti-indiffused [4] and proton-exchanged (PE) [5] planar optical waveguides. These holographic components are recorded in situ and can automatically compensate for wavefront distortions introduced by the mode structure or imperfections of the waveguide. To utilise the photorefractive properties of the waveguides, enhancement of light-induced refractive index changes is particularly important. This may be realised by additional appropriate doping with some transition ions (Fe^{2+/3+}, Cu⁺²⁺) [2].

B PHOTOREFRACTIVE PROTON- AND COPPER-EXCHANGED WAVEGUIDES

The PE waveguides have the very evident advantage over alternatives of fabrication simplicity. The previous studies of the PE LiNbO₃ waveguides [6] allowed us to identify the different crystallographic phases H_xLi_{1-x}NbO₃, considering that the phase transitions occur when the proton concentration x in the exchanged-layer is gradually varied, which causes a sudden variation of the cell parameters. The results obtained previously demonstrated the substantial difference in the chemical bonding [7], and the electro-optical [7] and non-linear-optical properties [8] of the PE waveguides containing different phases. Evidently, variations of other fundamental properties of the H_xLi_{1-x}NbO₃ phases should be expected. Our interest is focused on the phase dependence of an additional copper exchange, as the promising prospects of the combined proton and copper exchange for fabrication of PRW in LiNbO₃ were discovered [9-11]: the light-induced refractive-index changes may reach the extremely high value of 3×10^{-3} [10], an increase of one and two orders of magnitude compared to samples fabricated by Ti-indiffusion and proton exchange, respectively. This value is larger even than the maximal possible values reached in the iron- and copper-doped Ti-indiffused PRW [2]. Therefore, the largest diffraction efficiencies of holographic gratings recorded in LiNbO₃ waveguides

8.9 Holographic gratings in photorefractive LiNbO_3 waveguides

were reached in samples fabricated by combined proton and copper exchange (TABLE 1) [12]. Moreover, the additional copper exchange of the PE LiNbO_3 waveguides allows us to increase its photorefractive sensitivity (PRS) up to one thousand times. Also, it was reported [9,13] that the PRS depends on a proton concentration x in a very complex manner. However, this dependence was not investigated in detail, as the structural phase diagram for the system is not yet taken into account in investigations of proton-assisted copper exchange and holographic-grating recording in optical waveguides realised in this way. Thus, a new possibility in optimisation of fabrication and photorefractive properties of PRW is provided by appropriate choice of $\text{H}_x\text{Li}_{1-x}\text{NbO}_3$ phase for a given application.

TABLE 1 Experimental results [12] for diffraction efficiency η^s (obtained with two, either TM or TE, modes) of holographic gratings written up to saturation in different LiNbO_3 waveguides.

These results were obtained at a fixed interaction length of 2.5 mm.

Waveguide	Cut	Doping	η^s (TM)	η^s (TE)
Ti-indiffused	Z	Fe-indiffusion	0.089	0.021
Ti-indiffused	Z	Cu-indiffusion	0.047	0.014
Proton-exchanged	Z	Cu-exchange	0.95	-

In the present study we used Z-cut PE LiNbO_3 waveguides investigated in our previous work [6] and marked as Z1 - Z12 (TABLE 2). The successive copper exchange was carried out in a melt of benzoic acid mixed with 1 mol% Cu_2O and 1.2 mol% lithium benzoate at 230°C for ten minutes. The lithium benzoate was added in the mixture for suppression of the marked extra proton exchange, which can change a phase state and a refractive index profile.

TABLE 2 Extraordinary refractive index increment δn_e at the surface, deformation ε''_{33} values normal to the surface plane and phase state of $\text{Li}_{1-x}\text{H}_x\text{NbO}_3$ waveguiding layer in the different samples before and after copper exchange.

Sample notation	Before copper exchange			After copper exchange		
	δn_e	$\varepsilon''_{33}, 10^{-3}$	phase	δn_e	$\varepsilon''_{33}, 10^{-3}$	phase
Z1 top layer	0.1513	5.69	β_4	0.117	3.41	β_1
middle layer		4.23	β_3		3.41	β_1
bottom layer		4.15	β_1		3.41	β_1
Z3	0.121	3.85	β_1	0.119	3.500	β_1
Z5 top layer	0.106	5.57	β_2	0.115	4.35	β_2
bottom layer		3.86	β_1		3.38	β_1
Z6	0.116	3.62	β_1	0.118	3.33	β_1
Z7 top layer	0.124	4.08	β_3	0.118	3.25	β_1
bottom layer		3.67	β_1		3.25	β_1
Z8	0.049	1.15	κ_1^{LT}	0.03	0.80	κ_1^{HT}
Z9 top layer	0.092	2.74	κ_2^{LT}	0.088	2.20	κ_2^{LT}
bottom layer		1.26	κ_1^{LT}		0.80	κ_1^{LT}
Z10	0.055	1.24	κ_1^{LT}	0.058	1.70	κ_1^{LT}
Z11	0.064	1.46	κ_2^{HT}	0.063	1.49	κ_2^{HT}
Z12	0.016	0.46	α	0.016	0.46	α

The phase states of the $\text{H}_x\text{Li}_{1-x}\text{NbO}_3$ waveguiding layers before and after copper exchange have been determined by using double crystal X-ray diffraction (DCXRD), IR-reflection and m-lines modal spectroscopy methods (TABLE 2). DCXRD measurements show that the treatment in the Cu-containing melt of benzoic acid induces significant changes of the X-ray rocking curve for all samples studied. In the samples Z1, Z7 and Z9 the decrease in the extra peaks is observed. Simultaneously,

the evident change of the surface value of the extraordinary refractive index increment δn_e was observed. As the Cu concentration in the waveguides is small (less than 1 mol%) we have assumed that copper doping did not significantly modify the structural phase diagram of PE LiNbO_3 waveguides. Therefore, the experimental data on ϵ''_{33} and δn_e allow us to determine, according to the structural phase diagram [6], the phase state of each sample before and after treatment in a Cu-containing melt (TABLE 2). It is important to note that, in many cases, the change of a phase state of the waveguiding layer was induced by this treatment. This conclusion is a clear consequence of the characteristic changes of the relationship between a crystal deformation ϵ''_{33} and a refractive index increment δn_e . Moreover, this conclusion was confirmed clearly by IR-reflection data, where a drastic change of the lattice vibrational spectra (in the range $300 - 1000 \text{ cm}^{-1}$) is observed, as each phase is 'marked' by a very specific lattice vibration spectrum.

The optical absorption of the samples in the UV and the visible region was measured by using a Cary 17D spectrometer and the data obtained allowed us to determine the copper content in the waveguides. The use of a differential-spectroscopy technique enabled us to resolve the absorption bands connected with the Cu impurities. We have found that the copper exchange induces a new composite band in the absorption spectrum between 320 and $\sim 600 \text{ nm}$. The intensity and shape of this band were very different in the waveguides, which contained the different $\text{H}_x\text{Li}_{1-x}\text{NbO}_3$ phases before copper exchange. The most intensive copper-induced absorption was observed in the Z1 sample. The computer fitting of the difference spectrum (optical density D versus photon energy) measured between the sample Z1 and the standard undoped LiNbO_3 substrate demonstrates two pronounced bands at 2.6 and 3.3 eV (FIGURE 1).

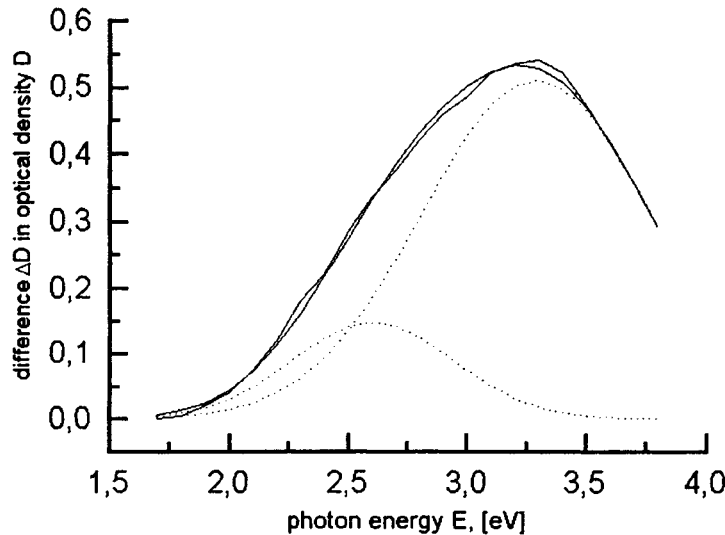


FIGURE 1 Difference optical spectrum of the Cu-doped sample Z1 (solid line) and an unprocessed Z-cut LiNbO_3 substrate. The dotted curves show the fitting result of the observed composite band into the elementary ones.

In accordance with the well-known data (see citations in [9,10]) the band at 3.3 eV corresponds to absorption on the Cu^+ ions. The nature of the second band is not known yet. However, our current study allows us to assume that the new band at 2.6 eV may be assigned to the new type of defect complexes, involving Cu^+ ions, as well as molecular OH^- ions, which are characterised by the component of the OH band at 3474 cm^{-1} in IR-absorption spectra.

It was established that the main difference between the samples studied is the ratio between the intensities of the bands at 2.6 and 3.3 eV. In the spectrum of copper-doped sample Z12 the band at 2.6 eV has a minimum value of relative intensity, but in the other samples this band is much more intense, and it has a maximum contribution in shape of the composite band for the Z1 sample.

(FIGURE 1). These data allow us to assume that a valence state of Cu defects, appearing in proton-exchanged LiNbO_3 waveguides caused by additional copper exchange, depends on the initial phase state of the $\text{Li}_{1-x}\text{H}_x\text{NbO}_3$ layer. Moreover, a value of the integral intensity of the copper-induced absorption has the specific values for samples containing different phases before the Cu exchange. This fact indicates that the rate of the copper exchange depends clearly on the phase state of a $\text{Li}_{1-x}\text{H}_x\text{NbO}_3$ waveguiding layer and for a given phase this rate is proportional to the exchange ratio x . We found that the rates of the Cu exchange for different phases varied by up to twenty times.

C HOLOGRAPHIC GRATINGS

Holographic gratings were written in planar LiNbO_3 waveguides utilising an argon-ion laser (wavelengths of 457.9 and 488 nm). For this purpose, two slightly focused beams were coupled into and out of the waveguide using two rutile prisms. During the build-up of the refractive index grating, the diffraction efficiency η was measured as a function of time by blocking one of the beams for a short time (50 ms) and measuring the ratio of diffracted and total light intensity of the outcoupled beams. In the steady state, the saturation value of diffraction efficiency η^s was reached. We have observed that the effective holographic recording in any sample becomes possible only after the additional Cu doping. An increase of the diffraction efficiency η^s of a recorded photorefractive hologram in the steady state [11,13] with increasing input light power P_{in} occurs in all Cu-exchanged waveguides, and the maximum value $\eta^s(\text{max})$ varies in quite different ranges for waveguides initially containing different $\text{H}_x\text{Li}_{1-x}\text{NbO}_3$ phases. The highest values of $\eta^s(\text{max})$ were obtained in the Cu-exchanged Z11 and Z12 samples (see FIGURE 2), and for the other samples the $\eta^s(\text{max})$ has the following values: $\leq 0.03\%$ for Z1, Z3, Z5, Z6 and Z7, 0.1% for Z9, 0.23% for Z10 and 1.2% for the Z8 sample. The comparison with undoped samples shows that Cu presence increases the efficiency of holographic recording $\eta^s(\text{max})$ by more than fifty times (e.g., from ~ 0.01 to 5.1% for the sample Z11) and essentially decreases a characteristic time of the photorefractive response in all waveguides, e.g. the effective holographic recording becomes possible for two to five seconds in the Z11 and Z12 samples after the copper exchange (FIGURE 2). At the same time a strong difference between the different TM_i modes was observed. Also, it was seen that the change of the $\eta^s(\text{max})$ at the variation of mode order i is very different for the waveguides containing different $\text{Li}_{1-x}\text{H}_x\text{NbO}_3$ phases (FIGURE 3). To compare the different TM_i modes of different waveguides, we determine the values of the holographic sensitivity R from the rate of hologram build-up to the initial stage:

$$R = d\{\eta^{1/2}\}/d(P_{\text{in}} t) \Big|_{t \rightarrow 0} \quad (1)$$

The measurements show that R depends clearly on input power P_{in} , so that we can write:

$$R = R_l + R_q P_{\text{in}} \quad (2)$$

The R determined by EQN (1) is proportional to photorefractive sensitivity [14] and, therefore, may be used as an important parameter to characterise the photorefractive properties.

We have found that there is a crucial influence of the phase generated in the waveguiding layer on the values of R_l , R_q and the ratio R_q/R_l . The maximum values of R_l and R_q were reached in samples Z12 and Z11, respectively. At $\lambda = 488$ nm we have observed: $R_l = 13.2 \times 10^{-3}$ (W s^{-1}) and $R_q = 1.72 \times 10^{-2}$ ($\text{W}^2 \text{s}^{-1}$) in the copper-doped Z12 sample, and $R_l = 0.49 \times 10^{-3}$ (W s^{-1}) and $R_q = 6.8 \times 10^{-2}$ ($\text{W}^2 \text{s}^{-1}$) in the copper-doped Z11 sample. It should be noted that for these initial samples (before copper exchange), the values of R did not exceed 10^{-5} (W s^{-1}) at the same experimental conditions. Moreover, from the dependence of holographic sensitivity on input power for samples Z8, Z9, Z10, Z11 and Z12, we can conclude that there is an evident correlation between the relative intensity of the new band in optical absorption spectra at 2.6 eV and R_q/R_l : the larger the integral band intensity, the higher

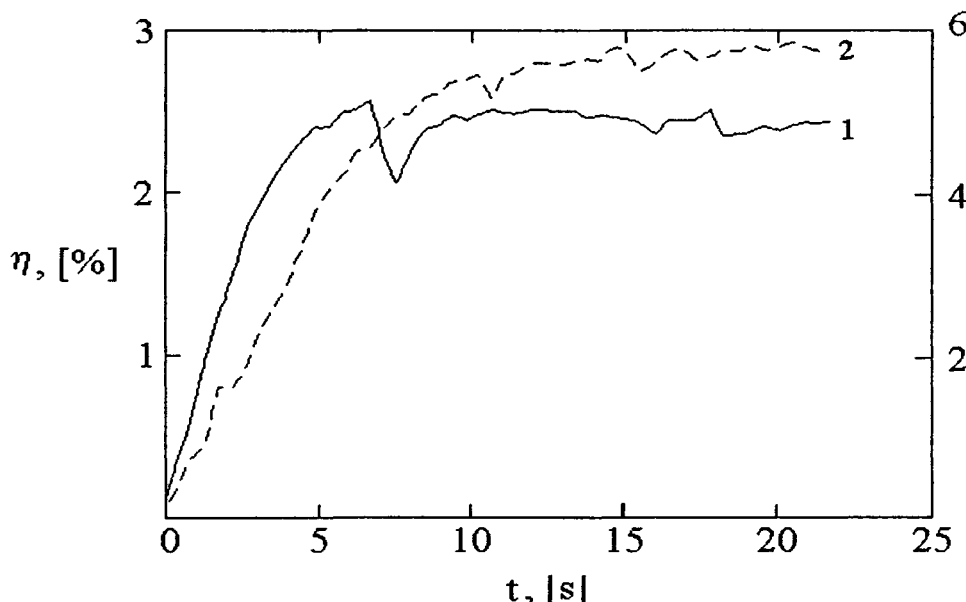


FIGURE 2 Time evolution of writing of a holographic grating at $\lambda = 488 \text{ nm}$ and $P_{\text{in}} = 700 \text{ mW}$ for the copper-exchanged waveguides fabricated by processing of sample Z11 (curve 1, the result obtained with two TM_3 modes) and sample Z12 (curve 2 obtained with two TM_2 modes). There are shown the results for TM_i modes, allowing us to reach the highest value of η^s (max) in a given waveguide. The right and left scales correspond to curves 1 and 2, respectively.

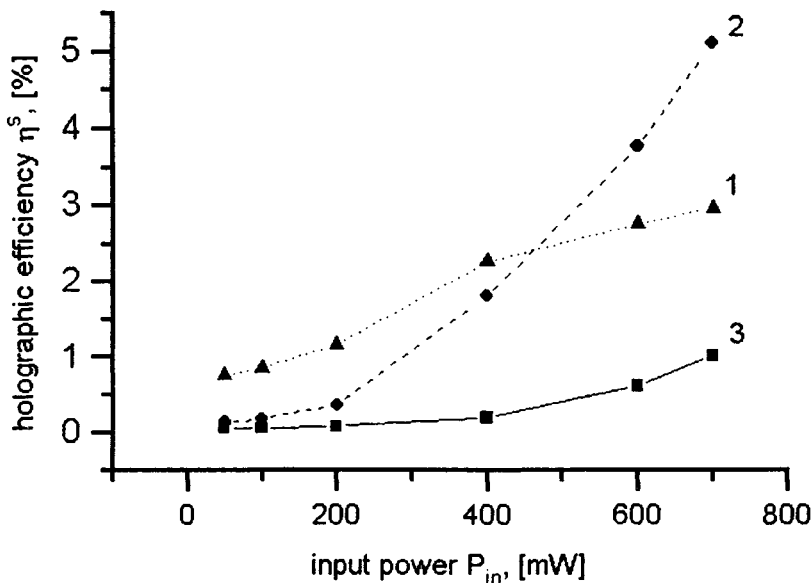


FIGURE 3 Dependence of the steady state diffraction efficiency η^s on input power P_{in} for different copper-exchanged waveguides. 1 - sample Z12, the phase holograms were recorded using TM_2 modes; 2 - sample Z11, TM_3 modes were used; 3 - sample Z8, TM_4 modes were used. These curves are merely guides for the eye through the experimental values shown by solid symbols. Here we have used the TM_i modes, allowing us to obtain a best result.

the R_q/R_l value. However, there is not a direct proportionality between R_q/R_l and the copper-induced absorption, because many factors may influence simultaneously both R_q and R_l [15].

In our opinion, the effective value of the light intensity, J , in the crystal can have a critical effect on the light absorption properties in the material. Hence, when the critical threshold level is reached, the

copper-induced absorption increases with increasing J and in so doing quenches the formation of the holographic recording efficiency in the Cu:H: LiNbO_3 waveguides (e.g. see FIGURE 3, as $J \sim P_{\text{in}}$). The light absorption depends on both the wavelength of laser irradiation used for holographic recording and the valence state of Cu impurities [9], and it may be reduced either by the use of laser irradiation in the red-near IR region or by the valence state variation [9,10,13]. It should be taken into account that the difference of the $\eta^s(\text{max})$ and R values observed in different waveguides may be caused partially also by degradation of the electro-optic effect in proton-exchanged LiNbO_3 crystals, so there is a drastic reduction of the electro-optic coefficients without an increase of exchange ratio x in the $\text{H}_x\text{Li}_{1-x}\text{NbO}_3$ structures [10,17]. Therefore, according to [9,13], we may expect that the photorefractive properties of the samples Z1 to Z10 should be considerably improved by additional treatment in the LiNO_3 melt, when the changes of the hydrogen concentration inside the crystal and the copper valence state occur simultaneously. Therefore, copper-exchanged $\text{Li}_{1-x}\text{H}_x\text{NbO}_3$ waveguides with any phase state may have, in principle, interest for fabrication of photorefractive integrated-optical devices for a given application.

D CONCLUSION

This Datareview summarises the combined effect of copper and proton exchange on the photorefractivity of LiNbO_3 waveguides. A variety of electro-optical devices based on holographic gratings made in such waveguides can be produced. The holographic recording efficiency is shown to be dependent on the phase composition.

REFERENCES

- [1] K.E. Younden, S.W. James, R.W. Eason, P.J. Chandler, L. Zhang, P.D. Townsend [*Opt. Lett. (USA)* vol.17 (1992) p.1509]
- [2] D. Kip [*Appl. Phys. B (Germany)* vol.67 (1998) p.131]
- [3] V.E. Wood, N.F. Hartman, C.M. Verber, R.P. Kenan [*J. Appl. Phys. (USA)* vol.46 (1975) p.1214]
- [4] A.M. Glass, I.P. Kaminow, A.A. Ballman, D.H. Olson [*Appl. Opt. (USA)* vol.19 (1980) p.276]
- [5] L. Wan, Y. Yuan, G. Assanto [*Opt. Commun. (Netherlands)* vol.74 (1990) p.361]
- [6] Yu.N. Korkishko, V.A. Fedorov [*IEEE J. Sel. Top. Quantum Electron. (USA)* vol.2 (1996) p.187]
- [7] Yu.N. Korkishko, V.A. Fedorov, S.M. Kostritskii [*J. Appl. Phys. (USA)* vol.84 (1998) p.2411]
- [8] K. El Hadi, P. Baldi, M.P. De Micheli, D.B. Ostrowsky, F. Laurell [*Proc. 8th Euro. Conf. Integrated Optics Stockholm, Sweden, 1997*, p.358]
- [9] S.M. Kostritskii, O.M. Kolesnikov [*J. Opt. Soc. Am. B (USA)* vol.11 (1994) p.1674]
- [10] F. Rickermann, D. Kip, B. Gather, E. Krätzig [*Phys. Status Solidi A (Germany)* vol.150 (1995) p.763]
- [11] Yu.A. Solomonov, S.M. Shandarov, V.M. Shandarov, A.I. Bashkirov [*Opt. Spectrosc. (Russia)* vol.80 (1996) p.342]
- [12] D. Kip, F. Rickermann, E. Krätzig [*Opt. Lett. (USA)* vol.20 (1995) p.1139]
- [13] S.M. Kostritskii [*J. Nonlinear Opt. Phys. Mater. (Singapore)* vol.6 (1997) p.321]
- [14] S.M. Kostritskii, D. Kip, E. Krätzig [*Appl. Phys. B (Germany)* vol.65 (1997) p.517]
- [15] S.M. Kostritskii, D. Kip [*Phys. Status Solidi A (Germany)* vol.169 (1998) p.171]
- [16] S.M. Kostritskii, P. Moretti [*Appl. Phys. B (Germany)* vol.68 (1999) p.767]
- [17] R. Narayan [*IEEE J. Sel. Top. Quantum Electron. (USA)* vol.3 (1997) p.796]

8.10 Chromium doping of LiNbO₃ by thin film diffusion

F. Caccavale

August 1999

A INTRODUCTION

Laser action in chromium-doped bulk crystals with broad tunability has been demonstrated using various hosts, such as LiCaAlF₆ (LiCAF), LiSrAlF₆ (LiSAF), Gd₃Sc₂Ga₃O₁₂ (GSGG) [1] and Y₃Al₅O₁₂ (YAG) [2].

Waveguide lasers and optical amplifiers have been fabricated in bulk and film lithium niobate substrates doped with the rare earths Nd and Er [3-7]. Optical amplification in proton-exchanged bulk chromium-doped lithium niobate has also been measured [8]. These results indicate a significant potential for an integrated, broad-band tunable laser in the 750 - 1150 nm spectral range, with the additional prospect of diode laser pumping.

The particular attraction of Cr as a laser-active ion is that it has a broad emission spectrum and, combined with the electro-optic properties of lithium niobate, offers the possibility of high-speed electro-optic tuning of the laser to produce a wavelength-agile laser. Furthermore, with Cr ions it is possible to pump the material around 670 nm with a laser diode.

There are also significant drawbacks associated with lithium niobate as a laser host material. It suffers photorefractive damage at shorter wavelengths. It also has a short upper laser state lifetime, less than 1 μ s, compared to typical values to 100 μ s for other Cr host materials [1].

From published data on the spectroscopy of Cr-doped host crystals, a very different behaviour of Cr in LiNbO₃ is expected, compared to other hosts referred to above [1,2,9-13]. However, the potential for tunable laser action and monolithic integration with performant devices in the same LiNbO₃ substrate is rather attractive, due to the well-established technology involving this material [14,15].

Diffusion of the active dopant from a film into the crystal offers the possibility of tailoring doping profiles, avoiding important limitations imposed by a doped bulk substrate. It should become possible to exploit undoped LiNbO₃ substrates with excellent optical quality and large dimensions, with the definition of active areas at any position in the substrate and efficient pump/signal interaction through tailoring of the doping depth profile. Optical amplification and laser action in doped LiNbO₃ will preferably be obtained in locally diffusion-doped substrates, rather than bulk ones.

A process to fabricate chromium-doped lithium niobate substrates, in which chromium ions are introduced by thermal diffusion from a film, has been developed [16]. The corresponding diffusion profiles of Cr in LiNbO₃, as obtained from secondary ion mass spectrometry (SIMS) measurements, are presented. Application of standard diffusion theory enables the extraction of fundamental data for optimisation of the device design, such as diffusion depth and surface concentration. Data obtained from samples fabricated at different temperatures and times provide the effective diffusion coefficient and the activation energy for chromium diffusion into Z-cut LiNbO₃. Using a simple model of waveguide optical amplification, an estimate of the behaviour of the gain attainable has been carried out.

B EXPERIMENT

B1 Sample Preparation

Samples were fabricated by using optical grade Z-cut wafers of LiNbO_3 . After cleaning, the samples were coated with a 10 nm thick layer of chromium by thermal evaporation using an electron beam.

Diffusion was carried out in a tubular furnace with a flow of dry oxygen at a rate of approximately 60 l/h. Diffusion temperatures from 950°C to 1100°C and diffusion times from 1 h to 24 h were used.

Planar-diffused samples fabricated in this way were used to measure the Cr concentration profiles. TABLE 1 presents the parameters (time and temperature) used in the fabrication of a set of samples for SIMS analysis.

TABLE 1 Times and temperatures used in the fabrication of a set of samples for SIMS analysis.

Temperature (°C)	950	1000	1050
Time (h)	8	4	1
	10	6	2
	12	8	4
	14	10	6

In order to measure the waveguide fluorescence spectrum and the lifetime of the upper laser level, proton-exchanged and Ti-indiffusion channel waveguides were fabricated on top of these structures. For proton-exchanged waveguides [17], pure benzoic acid was employed with annealing in a dry oxygen atmosphere. For Ti indiffusion a layer of Ti was electron-beam evaporated and subsequently diffused in a dry oxygen atmosphere. The mask widths for channel waveguide fabrication were from 1 to 10 μm .

B2 Characterisation

The diffused samples were measured by SIMS using a CAMECA IMS 4f ion microscope equipped with a normal-incidence electron flood gun used to compensate the surface-charge build-up while profiling insulating samples like LiNbO_3 crystals. Concentration profiles were obtained using 14.5 keV Cs^+ bombardment and negative secondary ion detection. The caesium beam current was 200 nA over a rastered area of $125 \times 125 \mu\text{m}^2$ and the secondary ions, emitted from a central circular area (10 μm diameter), were collected by the spectrometer. The erosion speed was evaluated by measuring the depth of the crater at the end of each analysis by means of a Tencor Alpha-step profilometer. The depth resolution in our case was mainly determined by the roughness of the crater under analysis, being $\leq 30 \text{ nm}$.

The calibration of the chromium profiles was made by means of the measurement of the total Cr dose in the as-deposited films using Rutherford backscattering spectrometry (RBS) analysis with a 2.2 MeV ${}^4\text{He}^+$ beam ($\Theta = 160^\circ$) and invoking mass conservation in the diffusion process.

C RESULTS AND DISCUSSION

C1 Modelling of the Concentration Profile

In order to interpret the experimental results and extract useful data, a diffusion model of the fabrication technique was applied.

The diffusion equation for a one-dimensional process is [18]:

$$\frac{\partial C}{\partial t} = D \frac{\partial^2 C}{\partial x^2} \quad (1)$$

where C is the concentration and D is the diffusion coefficient. For constant D and a planar source, a solution to EQN (1) is:

$$C = \frac{A}{\sqrt{t}} \exp\left(-\frac{x^2}{4Dt}\right) \quad (2)$$

where A is an arbitrary constant. For an initial state (thin film layer of thickness τ) $C(x)$ is defined by

$$C(x) = \begin{cases} C_0, & -\tau < x < 0 \\ 0, & x > 0 \end{cases} \quad (3)$$

The diffusion profile can be calculated by considering the extended-source distribution to be composed of an infinite number of line sources and by application of the principle of superposition [19]. This leads us to the concentration profile:

$$C(x) = C_0 \left(\operatorname{erf} \frac{x + \tau}{2\sqrt{Dt}} - \operatorname{erf} \frac{x}{2\sqrt{Dt}} \right) \quad (4)$$

If the film thickness is small, the profile can be approximated by:

$$C(x) = \frac{C_0 \tau}{\sqrt{\pi Dt}} \exp\left(-\frac{x^2}{4Dt}\right) = C_{\text{surf}} \exp\left(-\frac{x^2}{d^2}\right) \quad (5)$$

where C_{surf} is the surface concentration and d is the diffusion depth.

The diffusion coefficient D is related to the diffusion temperature by the well-known Arrhenius equation

$$D = D_0 \exp\left(-\frac{Q}{kT}\right) \quad (6)$$

where D_0 is the diffusion constant, Q is the activation energy, k is the Boltzmann constant and T is the diffusion temperature in Kelvin. Knowing D at different temperatures, one can calculate D_0 and Q .

C2 SIMS Results

The main parameters that affect and control the chromium concentration depth profiles are the initial thickness of the Cr film, the diffusion temperature, and diffusion time.

FIGURE 1 shows SIMS concentration profiles of chromium atoms in lithium niobate after the diffusion process, performed for 10 nm thick Cr film, at the same temperature (1000°C), but for various diffusion times.

FIGURE 2 presents SIMS concentration profiles of diffused chromium atoms in lithium niobate for the same diffusion time (10 h) but for two different diffusion temperatures (950 and 1000°C). The Cr distribution is seen to be strongly affected by the temperature. According to the concentration profile

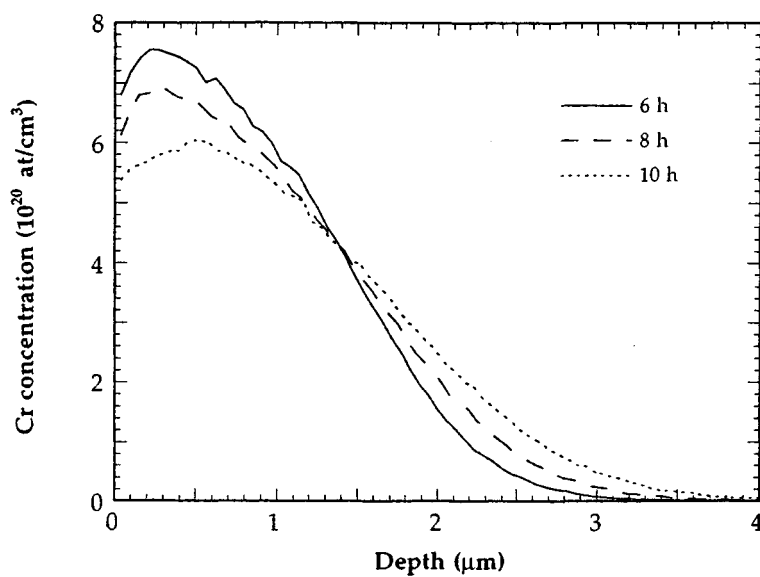


FIGURE 1 Concentration profiles obtained by SIMS for samples doped with 10 nm of Cr and diffused at 1000°C for different times.

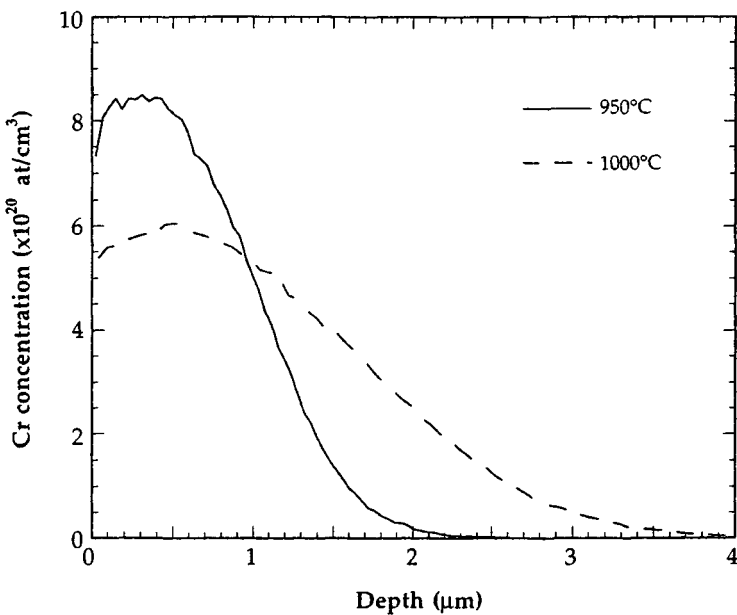


FIGURE 2 Concentration profile obtained by SIMS for a sample doped with 10 nm of Cr and diffused at 10 h at different temperatures.

model, the Cr ion distribution in LiNbO_3 should have the form given by EQN (5). Using the set of analysed samples (TABLE 1) we found the parameters C_{surf} and d that give the best fit of the experimental values to this function.

FIGURE 3 shows the plot of chromium surface concentration versus diffusion time. The lines in FIGURE 3 represent the theoretical behaviour from mass conservation.

The diffusion depth, similarly found by fitting Gaussian functions to the experimental data as obtained by SIMS, is plotted against the square root of the diffusion time in FIGURE 4.

8.10 Chromium doping of LiNbO_3 by thin film diffusion

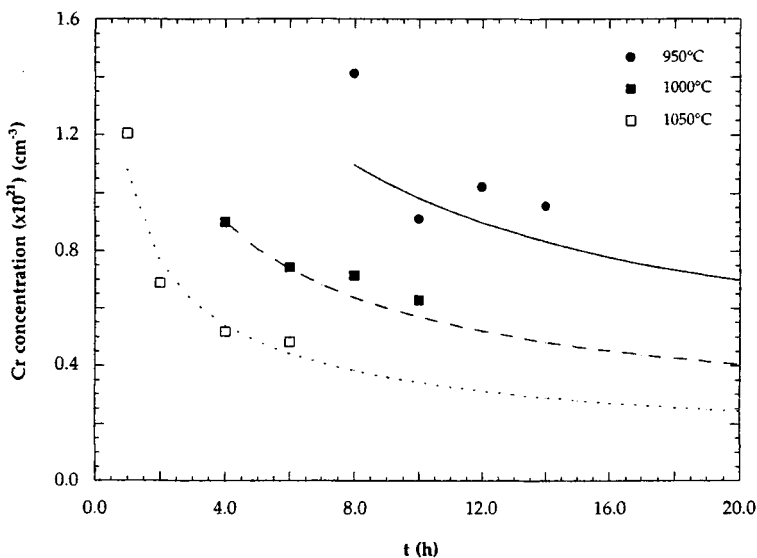


FIGURE 3 Plot of chromium surface concentration versus diffusion time, plotted using the values obtained from Gaussian fits to the experimental points. The lines represent the theoretical behaviour from mass conservation.

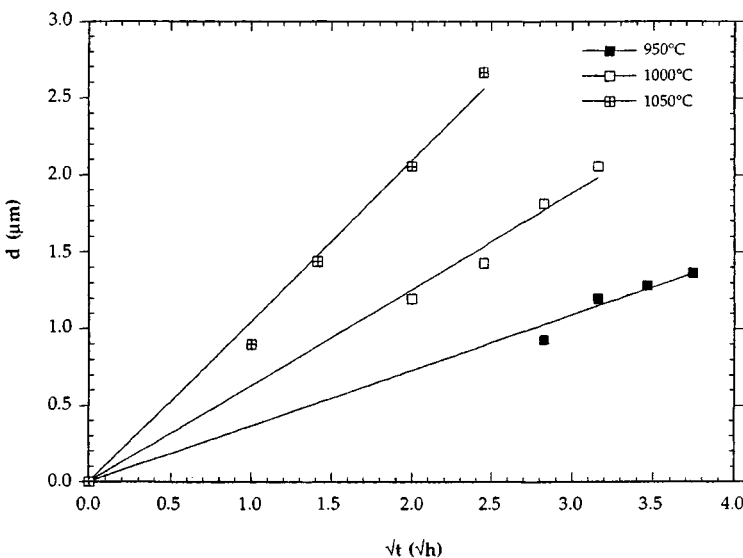


FIGURE 4 Plot of the diffusion depth found by fitting Gaussian functions to the experimental data (as obtained by SIMS) against the square root of the diffusion time.

From the slopes of the straight lines in FIGURE 4 we calculate the average diffusion coefficients for three temperatures, TABLE 2.

TABLE 2 Calculated diffusion coefficients for three diffusion temperatures.

T (°C)	D ($\mu\text{m}^2 \text{ h}^{-1}$)
950	0.033
1000	0.098
1050	0.273

Using these values, an Arrhenius plot was made, FIGURE 5, from which we calculated the diffusion constant D_0 and the activation energy Q . The obtained values for these constants are $4.7 \times 10^{10} \mu\text{m}^2 \text{ h}^{-1}$ and 2.95 eV, respectively.

8.10 Chromium doping of LiNbO_3 by thin film diffusion

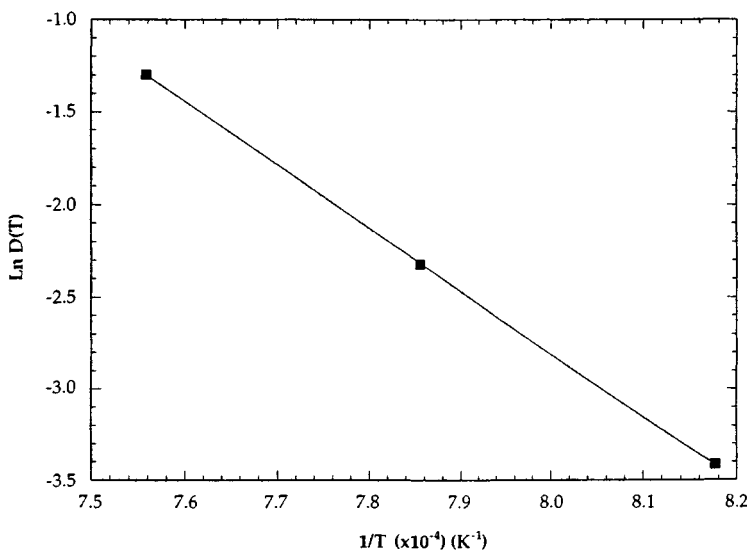


FIGURE 5 Arrhenius plot made using the values presented in TABLE 2.

C3 Guided Wave Fluorescence

In order to measure the waveguide, a sample was coated with 10 nm of Cr and diffused at 1050°C for 4 h, and then a channel waveguide was fabricated by proton exchange (in pure benzoic acid at 220°C for 4 h followed by annealing at 400°C for 2 h in a dry oxygen atmosphere), using an 8 μm window mask width. The corresponding fluorescence spectrum is shown in FIGURE 6. For comparison, the fluorescence spectra of Cr bulk-doped Z-cut LiNbO_3 (Cr concentration $3.2 \times 10^{20} \text{ cm}^{-3}$, supplied by Union Carbide) and of waveguides fabricated by Ti-indiffusion and proton exchange in the same material were also measured, and all presented similar features. The pump, in all cases, was the 488 nm line from an argon-ion laser; the polarisation of the pump beam was parallel to the c-axis of the crystal for all the samples measured.

The lifetime of the upper laser level has been measured on the same samples, using a fast mechanical chopper and a laser beam focused in the plane of the chopper blade, together with a fast amplified silicon detector giving a time resolution of 100 ns [16]. In all cases, and at room temperature, the value obtained was 900 ± 100 ns. These results are in close agreement with the published value [10].

C4 Optical Amplification

A simple model of laser amplification was applied to estimate the behaviour of Cr:LiNbO₃ channel waveguides in both bulk- and diffusion-doped structures, using the parameters measured as above and reasonable estimates for the scattering losses and waveguide modal profiles for pump and signal.

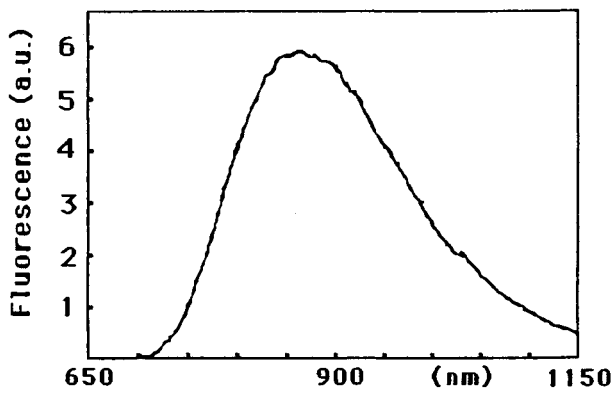


FIGURE 6 Waveguide fluorescence spectrum for a sample doped with 10.0 nm of Cr and diffused at 1050°C for 4 h.

8.10 Chromium doping of LiNbO_3 by thin film diffusion

The rate equations for a four-level laser system in the steady state were used, as in [20], for the cases of bulk- and locally doped amplifiers.

For the waveguide bulk-doped amplifier a Cr concentration of $1.0 \times 10^{20} \text{ cm}^{-3}$ was used, and for the waveguide locally doped amplifier a crystal doped with 10 nm of Cr and diffused at 1050°C for 4 h was assumed. For both waveguides we consider scattering losses on the order of 0.4 dB/cm, an effective pump area equal to $15 \mu\text{m}^2$ and a lifetime of 1 μs (room-temperature operation). We also considered a signal wavelength of 910 nm (peak of the fluorescence intensity) and a pump wavelength of 670 nm (close to the peak of the absorption spectrum and compatible with laser diode pumping) [16].

For these wavelengths, the signal emission and pump absorption cross-sections are, respectively, 1.15×10^{-18} and $1.43 \times 10^{-20} \text{ cm}^2$ [10].

It was found that, for a launched pump power of 10 mW, theoretical maximum gains of 0.18 and 0.33 were obtained for waveguide lengths around 8 and 6 mm, in bulk- and locally doped amplifiers, respectively (the gain factor being defined as the natural logarithm of the amplitude of the signal power as a function of the length).

D CONCLUSION

A study of Cr diffusion in LiNbO_3 crystal has been made as a function of diffusion parameters, i.e. temperature and time. SIMS measurements were performed in order to obtain detailed information on concentration depth profiles.

The chromium diffusion process has been analysed in terms of the classical mathematical diffusion model. Consequently, the diffusion constant and activation energies have been derived. The strongest factor that controls the diffusion process is found to be the temperature.

The fluorescence behaviour of the diffusion-doped Cr:LiNbO_3 has been compared with that of bulk-doped Cr:LiNbO_3 , and found to be similar in practically all respects.

The possibilities of designing and fabricating channel waveguide amplifiers based on chromium-doped LiNbO_3 have now been established - with major advantages being apparent for diffusion-doped Cr:LiNbO_3 .

REFERENCES

- [1] R. Scheeps [*Opt. Mater. (Netherlands)* vol.1 (1992) p.1]
- [2] H. Eilers et al [*IEEE J. Quantum Electron. (USA)* vol.QE-29 (1993) p.2508]
- [3] E. Lallier [*Appl. Opt. (USA)* vol.31 (1992) p.5276]
- [4] D.C. Hanna [*Proc. Europ. Conf. on Integrated Optics ECIO'93* Neuchatel, Switzerland (1993) p.3.1-3.3]
- [5] R.M. De La Rue [*Photonics Optoelectron. (USA)* vol.1 (1993) p.67]
- [6] M. Dinand, W. Sohler [*IEEE J. Quantum Electron. (USA)* vol.QE-30 (1994) p.1267]
- [7] E. Lallier, D. Papillon, J.P. Pocholle, M. Papuchon, M. De Micheli, D.B. Ostrowsky [*Electron. Lett. (UK)* vol.29 (1993) p.175]
- [8] F. Zhou, R.M. De La Rue, C.N. Ironside, T.P.J. Han, B. Henderson, A.I. Ferguson [*Electron. Lett. (UK)* vol.28 (1992) p.2041]
- [9] F. Beaud, M.C. Richardson, Y.F. Chen, B.H.T. Chai [*IEEE J. Quantum Electron. (USA)* vol.QE-30 (1994) p.1259]

8.10 Chromium doping of LiNbO_3 by thin film diffusion

- [10] V.G. Babadjanyan, E.P. Kokanyan, R.B. Kostanyan, V.R. Nikogosyan [*Opt. Commun. (Netherlands)* vol.78 (1990) p.257]
- [11] A.M. Glass [*J. Chem. Phys. (USA)* vol.50 (1969) p.1501]
- [12] W. Jia, H. Liu, R. Knutson, W.M. Yen [*Phys. Rev. B (USA)* vol.41 (1990) p.10906]
- [13] J.F.H. Nicholls, T.P.J. Han, B. Henderson, F. Jaqué [*Chem. Phys. Lett. (Netherlands)* vol.202 (1993) p.560]
- [14] M. Lawrence [*Rep. Prog. Phys. (UK)* vol.56 (1993) p.363]
- [15] L. McCaughan [*Integrated Optics and Optoelectronics* vol.VR45 (SPIE, 1993) p.15-43]
- [16] J.M. Almeida et al [*J. Appl. Phys. (USA)* vol.78 (1995) p.2193-7]
- [17] A. Loni, G. Hay, R.M. De La Rue, J.M. Winfield [*IEEE J. Lightwave Technol. (USA)* vol.7 (1989) p.911]
- [18] J. Crank [*The Mathematics of Diffusion* (Clarendon Press, Oxford, UK, 1975)]
- [19] F. Caccavale, P. Chakraborty, I. Mansour, G. Gianello, M. Mazzoleni [*J. Appl. Phys. (USA)* vol.76 (1994) p.7552-8]
- [20] W. Sohler [*NATO ASI Ser. E (Netherlands)* vol.226 (1992)]

CHAPTER 9

LUMINESCENCE, RAMAN AND ESR SPECTRA

- 9.1 Luminescence of LiNbO₃
- 9.2 Raman spectra of undoped LiNbO₃
- 9.3 Raman spectra of doped LiNbO₃
- 9.4 Magnetic resonance spectra of impurities and defects in LiNbO₃
- 9.5 Absorption spectra of bulk LiNbO₃
- 9.6 IR spectral presence of OH ions in LiNbO₃
- 9.7 Stark effect for rare-earth dopants in LiNbO₃

9.1 Luminescence of LiNbO₃

P.D. Townsend; updated by K.A. Green

July 2001

A INTRINSIC EMISSION BANDS

After the initial report of luminescence in LiNbO₃ [15] there have been a variety of additional studies including excitation by photons [1-3,13], X-rays [4-6], electrons [7] and ion beams [8] as well as thermoluminescence [9,10], electroluminescence [11], time-resolved luminescence [14] and shock waves [12]. In general, the signal levels are relatively weak and barely visible to the eye. In stoichiometric LiNbO₃ there is an intrinsic blue band at 440 nm. This band occurs in both pure and doped crystals (e.g. with Ni, Co, Eu and Mg) as well as during low-temperature thermoluminescence. The signal level is greatly enhanced by Mg impurities and by 5% doping; the luminescence is 100 times brighter than in pure crystals. The blue band originates from an intrinsic electron (Nb⁴⁺) hole (O⁻) recombination at a regular niobate group. In the case of Mg-doped LiNbO₃ the Mg ions may aid the process by acting as electron traps.

Luminescence in congruent (non-stoichiometric) lithium niobate shows a strong emission near 520 nm. This appears to be due to antisite defects Nb_{Li}⁴⁺. Such a proposition is supported by the appearance of the signal in reduced crystals and in those that have lost lithium by heat treatment or changes in the Li:Nb stoichiometry. The more recent use of ion beams to stimulate luminescence produces not only the signals found with X-rays or electrons but also a variety of signals that are apparent under conditions of high excitation density. Foremost among these are a series of lines at 375, 360, 310 and 300 nm ascribed to an exciton decay series [8]. Other strong emission lines in the region of the band edge at 330 and 290 nm have a different temperature dependence and radiation stability. The full width half maximum line widths are typically 0.20 eV and do not show vibrational structure even at 4.2 K. The exciton lines show a thermally activated decrease in intensity with higher temperatures of 0.35 ± 0.05 eV. By contrast, the previously noted features near 440, 470 and 520 nm vary with activation energies of 0.21, 0.20 and 0.17 ± 0.01 eV, respectively.

Addition of impurity ions has some influence on the relative intensities of the 'intrinsic type' luminescence and Mg ions enhance the signals, whereas some ions such as Ni, Eu or Ti either depress the overall signal levels or selectively decrease certain features. Lifetime resolution of component features shows that the majority of the broader emission bands are composites of many components. The presence of Mg apparently allows the operation of a mechanism that liberates lithium ions. The lithium metal is characterised by a line emission near 671 nm.

At low temperatures (77 K) with ion beam excitation the 440, 475 and 520 nm bands all grow with radiation damage. However, in some crystals these bands are present even at the commencement of the damage. Thus, the model of e⁻ - h⁺ recombination at niobate groups for the blue emission and Li-deficient groups for the green light needs minor modification, and suggests that a distortion of a normal group by a defect is required.

One might expect that in an anisotropic crystal structure such as LiNbO₃ the luminescence would be polarised. Hence, one might offer more specific defect models. Few studies of this anisotropy have been made but the ion beam work shows clear evidence for polarised emission. Indeed there are significant differences between the intensity of component emission bands in the X, Y and Z cut crystals.

B THERMOLUMINESCENCE

Both standard and time-resolved thermoluminescence in LiNbO₃ have been successful in the temperature range 10 - 450 K and several glow peaks are noted after X-ray and electron beam excitation. Intrinsic defects exist that can associate to impurities since the strong 70 K peak is seen in both pure and Mg-doped samples. However there is a change in activation energy for the radioluminescence signal from 0.049 to 0.062 ± 0.002 eV.

C IMPURITY AND STOICHIOMETRY EFFECTS

As previously noted, both extrinsic impurities and changes in stoichiometry influence the intensity of the 'intrinsic' emission features. Some impurities also show additional emission typical of the impurity ion. The early study [1,2] of laser-excited fluorescence produced a strong signal near 770 nm. This is linked to Fe impurities and hence one might consider this signal as an indicator of sensitivity to optical damage.

In order to stimulate luminescence with X-rays, electrons or ion beams one provides sufficient energy to cause lattice displacements. Hence, the defect state of the sample changes with irradiation dose. This is informative, as the intensity of the initial signal and the dose dependence are directly related to the original purity, stoichiometry and state of perfection of the crystal. Ion-beam excitation produces these changes over a relatively short time scale (e.g. 20 min) and in a series of studies [8] it has been shown that one may not only separate the behaviour of pure and doped samples but also distinguish between crystals of 'pure' LiNbO₃ from different manufacturers. Variations in quality and impurity segregation have been noted along the length of a single boule.

D CONCLUSION

Luminescence from LiNbO₃ is due to charge-transfer in the niobate octahedron, and is strongly affected by the concentration of Li vacancies. For stoichiometric LiNbO₃, the emission maximum is 440 nm, while the non-stoichiometric (congruent) material maximum is at 520 nm. It is possible to separate effects from the interior of perfect material and damaged or surface layers. Luminescence decay times and intensity variations give a qualitative measure of both purity and crystal quality.

REFERENCES

- [1] A. Hordvik, H. Schlossberg [*Appl. Phys. Lett. (USA)* vol.20 (1972) p.197]
- [2] R. Parsons, W.D. Cornish, L. Young [*Appl. Phys. Lett. (USA)* vol.27 no.12 (1975) p.654-6]
- [3] D.M. Krol, G. Blasse, R.C. Powell [*J. Chem. Phys. (USA)* vol.73 (1980) p.163]
- [4] L. Arizmendi, J.M. Cabrera, F. Aguiillo-Lopez [*Ferroelectrics (UK)* vol.26 no.1-4 (1980) p.823-6; *Solid State Commun. (USA)* vol.40 no.5 (1981) p.583-5; *J. Phys. C (UK)* vol.17 (1984) p.515]
- [5] K.L. Sweeney, L.E. Halliburton, D.A. Bryan, R.R. Rice, R. Gerson, H.E. Tomaschke [*J. Appl. Phys (USA)* vol.57 no.4 (1985) p.1036-44]
- [6] M. Scripsick, P.D. Townsend, L.E. Halliburton [*Radiat. Eff. (UK)* vol.98 no.1-4 (1986) p.259-68]
- [7] J. Llopis, C. Ballesteros, R. Gonzalez, Y. Chen [*J. Appl. Phys. (USA)* vol.56 no.2 (1984) p.460-2]
- [8] P.W. Haycock, P.D. Townsend [*Radiat. Eff. (UK)* vol.98 no.1-4 (1986) p.243-8; *J. Phys. C (UK)* vol.20 no.2 (1987) p.319-28]

9.1 Luminescence of LiNbO_3

- [9] K.A. Mirza, P.D. Townsend, G.L. Destefanis [*Phys. Status Solidi A (Germany)* vol.47 no.1 (1978) p.K63-6]
- [10] K.S.V. Nambi, S.D. Rao, M.P. Chougaonkar [*Nucl. Tracks Radiat. Meas. (UK)* vol.10 (1985) p.243]
- [11] C. Paracchini, J. Rosa [*Solid State Commun. (USA)* vol.51 no.4 (1984) p.239-41]
- [12] P.J. Brannon, R.W. Morris, J.R. Asay [*J. Appl. Phys. (USA)* vol.57 no.5 (1985) p.1676-9]
- [13] M.H.J. Emond, M. Wiegel, G. Blasse [*Mater. Res. Bull. (USA)* vol.28 (1993) p.1025-8]
- [14] V. Pankratov, L. Grigorjeva, D. Millers, G. Corradi, K. Polgar [*Ferroelectrics (UK)* vol.239 (2000) p.241-50]
- [15] G. Blasse, A. Bril [*Z. Phys. Chem. Neue Folge (Germany)* vol.57 (1968) p.187]

9.2 Raman spectra of undoped LiNbO₃

J.F. Scott; updated by K.A. Green

August 2001

Many studies of the Raman spectra of the ferroelectric phase of undoped LiNbO₃ have been reported [1,4,5,25]. Although there was some ambiguity in phonon assignments in the early Raman work, the assignments and approximate wavenumbers by Sidorov et al in 1996 [24] are listed in TABLE 1. Additional lines commonly found near 95, 630, 668 and 740 cm⁻¹ are most likely due to crystal growth, structure and chemical composition that differs from the ideal crystal, including point and extended defects (intrinsic and impurities), and ilmenite-like stacking defects [26].

TABLE 1 Raman line frequencies (cm⁻¹) of fundamental lattice modes in a perfect LiNbO₃ crystal.

A ₁ (TO)	E(TO)	A ₁ (LO)	E(LO)
254	152	278	196
274	237	333	242
333	265	432	296
630	322	875	370
	368		425
	431		455
	580		880

A number of reports were published concluding that the ferroelectric-paraelectric phase transition is mainly order-disorder rather than a displacive mechanism [2,3,6]. Not only is there a large phonon softening (temperature dependence), the spectral response exhibits a dynamic central mode, i.e. quasi-elastic Rayleigh scattering. This central mode can be characterised by a width that is the reciprocal of a temperature-dependent relaxation time. The behaviour of this relaxation time with increasing temperature is quite different for stoichiometric lithium niobate and for congruent samples. For stoichiometric specimens the relaxation time increases linearly with inverse reduced temperature, which is the functional form expected for critical slowing down in the classical order-disorder approximation. By comparison, in congruent lithium niobate specimens it is independent of temperature. This suggests that in congruent lithium niobate the central mode is of defect origin.

Other Raman studies of undoped lithium niobate have emphasised the angular dependences and asymmetries of scattering cross-sections with respect to scattering geometry [10-13], general properties of polaritons [14-17], precise measurement of cross sections [18], asymmetry [7], and both temperature [19,20] and pressure [21] dependences of phonon frequencies.

REFERENCES

- [1] W.D. Johnston Jr., I.F. Kaminow [*Phys. Rev. (USA)* vol.168 (1968) p.1045]
- [2] A. Ridah, M.D. Fontana, P. Bourson [*Phys. Rev. B (USA)* vol.56 no.10 (1997) p.5967]
- [3] A.F. Penna, S.P.S. Porto, E. Wiener-Avnear [*Solid State Commun. (USA)* vol.23 (1977) p.377]
- [4] Y. Ge, C. Zhao [*Spectrosc. Lett. (USA)* vol.31 no.8 (1998) p.1677]
- [5] V.S. Gorelik, A.L. Karuzskii, A.V. Perestoroin, P.P. Sverbil' [*Bull. Lebedev Phys. Inst. (Russia)* no.10 (1999) p.3]

9.2 Raman spectra of undoped LiNbO_3

- [6] J.L. Servoin, F. Gervais [*Solid State Commun. (USA)* vol.31 (1979) p.387]
- [7] U.T. Schwarz, M. Maier [*Phys. Rev. B (USA)* vol.55 no.17 (1997) p.11041]
- [8] S.M. Schapiro, J.D. Axe, G. Shirane, T. Riste [*Phys. Rev. B (USA)* vol.6 (1972) p.4332]
- [9] Ming-Sheng Zhang, J.F. Scott [*Phys. Rev. B (USA)* vol.34 no.3 (1986) p.1880-3]
- [10] R.J. Holmes, D.M. Smyth [*J. Appl. Phys. (USA)* vol.55 (1984) p.353]
- [11] V.S. Gorelik, O.G. Zolotukhin, M.M. Sushchinskii [*Opt. Spectrosc. (Russia)* vol.52 (1982) p.611]; V.A. Klimenko, I.I. Kondilenko, P.A. Korotkov, G.S. Felinskii [*Ukr. Fiz. Zh. (Ukraine)* vol.26 (1981) p.1557]
- [12] V.S. Gorelik, L.G. Reznik, B.S. Umarov [*Opt. Spectrosc. (Russia)* vol.52 (1982) p.236]
- [13] V.I. Belitskii, A.V. Gol'tsev, I.G. Lang, S.T. Pavlov [*Sov. Phys.-Solid State (USA)* vol.25 (1983) p.703]
- [14] H.E. Ponath, A. Lau, W. Wercke [*Ann. Phys. (Germany)* vol.34 (1977) p.229]
- [15] L.G. Reznik, A. Anikiev, V.S. Gorelik, B.S. Umarov [*Opt. Spectrosc. (Russia)* vol.51 (1981) p.171]
- [16] S. Kojima, T. Nakamura [*Ferroelectrics (UK)* vol.37 (1981) p.677]
- [17] V.A. Orlov, Yu.N. Fomin, S.I. Marennikov, A.I. Parkhomenko [*Sov. J. Quantum Electron. (USA)* vol.8 (1978) p.1026]
- [18] M. Nippus [*Z. Naturforsch. A (Germany)* vol.A31 (1976) p.231]
- [19] V.S. Gorelik, S.V. Ivanova, I.P. Kucheruk, B.A. Strukov, A.A. Khalezov [*Sov. Phys.-Solid State (USA)* vol.18 (1976) p.1340]; S.V. Ivanova, V.S. Gorelik, B.A. Strukov [*Ferroelectrics (UK)* vol.21 (1978) p.563]
- [20] A.A. Adkamov, A.A. Anikiev, B.S. Umarov, M. Umarov [*Dokl. Akad. Nauk SSSR (Russia)* vol.286 (1985) p.606 and vol.221 (1983) p.1112]
- [21] A. Jayaraman, A.A. Ballman [*J. Appl. Phys. (USA)* vol.60 (1986) p.1208]; J. Mendes-Filho, V. Lemos, F. Cerdeira [*J. Raman Spectrosc. (UK)* vol.15 (1984) p.367]
- [22] F. Claus, F.X. Winter [*Polaritons* Eds E. Burstein, F. De Martini (Pergamon, New York, 1972) p.41]; M. Posledovich, F.X. Winter, G. Borstel, R. Claus [*Phys. Status Solidi B (Germany)* vol.55 (1973) p.711]
- [23] E.J. Baran, I.L. Botto, F. Muto, N. Kumada, N. Kinomura [*J. Mater. Sci. Lett. (UK)* vol.5 (1986) p.671]
- [24] N. Sidorov, M. Palatnikov, V. Kalinnikov [*Optika I Spektroskopiya (Russia)* vol.82 no.1 (1997) p.38-45]
- [25] A. Barker, R. Loudon [*Phys. Rev. (USA)* vol.158 no.2 (1967) p.433]
- [26] Y. Kong, J. Xu, X. Chen, C. Zhang, W. Zhang, G. Zhang [*J. Appl. Phys. (USA)* vol.87 no.9 (2000) p.4410]

9.3 Raman spectra of doped LiNbO₃

J.F. Scott; updated by K.A. Green

August 2000

Raman spectroscopy of doped lithium niobate concentrates on dopants useful for such applications as optical damage and optical storage (Fe, Mg) and planar waveguides (Ti). Following early reports [1,2] that light illumination altered small-angle (polariton) spectra, additional studies of this effect were made by other groups. Detailed quantitative studies by Anikiev et al [3,4] showed unambiguously that symmetry loss (morphology) in the illuminated region caused these spectral changes. In the presence of strong illumination ($\sim\text{kW/cm}^2$) the Fe ions produce local crystal electric fields perpendicular to the optical c-axis [5] and reduce the local three-fold symmetry [6,7]. This morphic effect of lowering the local symmetry is explained by the theory of Odoulov and Soskin [20] for photorefraction in Fe- or Cu-doped lithium niobate, which shows that B31 and B15 off-diagonal components are also non-zero.

Through this model, Anikiev et al were able to account quantitatively for the number and intensity of all the additional new lines in their small-angle Raman spectra of Fe-doped lithium niobate. In addition, they were able to account for the fact that these lines could be made to disappear [8] in specimens in which a strong (1000 K/cm) thermal gradient was applied; the effect of the latter was that the thermoelectric voltage cancelled the photoelectric voltage.

In addition to the polariton studies of iron-doped lithium niobate summarised above and in [9], there have been a number of phonon studies of the effect of Fe- [10-14] and Ti-doping [15,16], and of asymmetry and temperature dependence of the linewidth [23]. Reference [15] shows an increase in intensity up to a factor of 3.4 for E-symmetry modes relative to Al-symmetry in Ti-doped planar waveguides. The use of Raman spectroscopy to determine the general composition of lithium niobate (and, in particular, the Fe/Nb percentage) was shown earlier [17,18]. Although the technique seems useful for Ti and Fe, Mg-doping [19,21,22] yields only small linewidth increases.

REFERENCES

- [1] V.S. Gorelik, B.S. Umarov, L.G. Reznik [*Phys. Status Solidi B (Germany)* vol.105 no.2 (1981) p.K73]
- [2] V.S. Gorelik, L.G. Reznik, B.S. Umarov [*Sov. Phys.-Solid State (USA)* vol.24 no.10 (1982) p.1803]
- [3] A.A. Anikiev, L.G. Reznik, B.G. Umarov, J.F. Scott [*J. Raman Spectrosc. (UK)* vol.14 no.1 (1984) p.60-6]
- [4] A.A. Anikiev, L.G. Reznik, B.S. Umarov, J.F. Scott [*Ferroelectr. Lett. Sect. (UK)* vol.3 no.4 (1985) p.89]
- [5] A.P. Levanyuk, E.M. Uyukin, V.A. Pashkov, N.M. Solov'eva [*Sov. Phys.-Solid State (USA)* vol.22 no.4 (1980) p.675]
- [6] F.S. Chen [*J. Appl. Phys. (USA)* vol.40 no.8 (1969) p.3389]
- [7] Liu Si-Min, Zhang Guang-Yin, Wu Zhong-Kang, Huang Zhi-Ming, Xu Liang-Ying [*Acta Phys. Sin. (China)* vol.34 no.12 (1985) p.1595]
- [8] L.G. Reznik, A.A. Anikiev, B.S. Umarov, J.F. Scott [*Ferroelectrics (UK)* vol.64 no.4 (1985) p.215]; cf reference [2]
- [9] V.S. Gorelik, L.G. Reznik, B.S. Umarov, V.T. Gabrielyan, E. Koyanan [*Sov. Phys.-Solid State (USA)* vol.25 no.6 (1983) p.1057]

9.3 Raman spectra of doped LiNbO_3

- [10] Liu Si-Min et al [*Acta Phys. Sin. (China)* vol.33 no.1 (1984) p.105]
- [11] M. Nippus, R. Claus [*Z. Naturforsch. A (Germany)* vol.33A no.8 (1978) p.924]
- [12] A.E. Semenov, E.V. Cherkasov [*Sov. Phys.-Solid State (USA)* vol.22 no.6 (1980) p.1105]
- [13] P.A. Korotkov, V.V. Obukhovskii, G.N. Dmitrik, P.S. Radchenko [*Opt. Spectrosc. (Russia)* vol.52 no.3 (1982) p.342]
- [14] B.A. Kolesov, A.E. Semyonov, E.V. Cherkasov [*Opt. Spectrosc. (Russia)* vol.50 no.5 (1981) p.551]
- [15] I.I. Kondilenko, P.A. Korotkov, V.A. Klimenko, G.S. Felinskii [*Opt. Spectrosc. (Russia)* vol.49 no.5 (1980) p.552]
- [16] P.A. Korotkov, G.S. Felinskii [*Kvantovaya Elektron. Kiev (Ukraine)* vol.22 (1982) p.66]
- [17] A.A. Vinogradova, D.P. Krindach, V.S. Maiorov, N.M. Rubinina [*Vestn. Mosk. Univ. Fiz. Astron. (USSR)* vol.17 no.3 (1976) p.352]
- [18] A.E. Balanovskaya, L.I. Pyatigorskaya, Z.I. Shapiro, L.N. Margolin, E.A. Bovina [*J. Appl. Spectrosc. (USA)* vol.38 no.4 (1983) p.491]
- [19] Liu Si-Min, Zhang Guang-Yin [*Acta Phys. Sin. (China)* vol.32 no.1 (1983) p.103]
- [20] S. Odoulov, M. Soskin [in *Laser Optics of Condensed Matter* Eds J.L. Birman, H.Z. Cummins, A.A. Daplyanskii (Plenum, New York, 1988) p.391]
- [21] Y.-F. Xu, Y.-C. Ge, C.-Z. Zhao, C.-X. Guan, D.-M. Li [*Spectrosc. Lett. (USA)* vol.29 no.5 (1996) p.851]
- [22] S. Kojima [*Ferroelectrics (UK)* vol.152 (1994) p.301]
- [23] U.T. Schwarz, M. Maier [*Phys. Rev. B (USA)* vol.55 no.17 (1997) p.11041]

9.4 Magnetic resonance spectra of impurities and defects in LiNbO₃

L.E. Halliburton; updated by C. Florea

May 2001

A INTRODUCTION

Magnetic resonance spectra (electron spin resonance - ESR, electron paramagnetic resonance - EPR) from transition-metal ions and rare-earth ions, along with radiation-induced defects, have all been observed in LiNbO₃. The most striking feature of most of these spectra is their rather large linewidths (up to 100 G or more in many cases). Random internal crystalline fields associated with significant departures from stoichiometry are responsible for these large linewidths [1]. Each paramagnetic centre (i.e. impurity ion or radiation-induced defect) sees a crystalline field slightly different from other similar centres on equivalent sites. These internal fields affect the linewidth either directly through the fine structure terms in the spin-Hamiltonian or indirectly through the influence of spin-orbit couplings on g values. A practical result of these large linewidths is a decrease in the sensitivity of the ESR technique when applied to LiNbO₃. Furthermore, subtle effects, such as slight departures from the axial symmetry, are often undetected and overlapping spectra from different impurities cannot be quantified.

The ESR technique often provides direct information about the lattice site occupied by a paramagnetic ion. However, this is not the case in LiNbO₃. There are three obvious choices (a Li⁺ site, an Nb⁵⁺ site, and an interstitial site) for incorporation of an isolated impurity ion, and they all possess trigonal symmetry. This means that the site symmetry obtained from the angular dependence of the ESR spectrum does not help distinguish between possible sites in the lattice. Other indirect factors such as the net charge, ionic size, and charge compensation mechanisms must be used in arguing for or against incorporation of an impurity on a specific lattice site. An interesting paper [2] raises the possibility of using the temperature dependence of the spin-Hamiltonian parameters to determine the site identities. However, to date, no one has provided direct proof of the site occupied by any impurity in LiNbO₃. Future work must focus on this critical issue. The best hope for a breakthrough in this area rests with the ENDOR (electron nuclear double resonance) technique and its ability to resolve the super-hyperfine interactions with the surrounding lithium and niobium nuclei. Some results regarding the lattice sites occupied by some of the impurities have already been obtained when experimental data are investigated with more complete calculational methods [34,35].

Many of the transition-metal ions appear as trace impurities at the 1 to 20 ppm level in nearly all LiNbO₃ boules. However, ESR studies of impurities have usually focused on crystals doped at the 0.01% to 0.5% level, thus maximising the ESR spectrum of interest and discriminating against the spectra of other impurities inadvertently present. The initial ESR studies in LiNbO₃ were completed in the late 1960s and early 1970s. Because their S-state nature makes them easy to observe, Fe³⁺ and Mn²⁺ received much of the initial attention. Also studied in the first round of experiments were Cr³⁺ and various rare-earth ions. Very few papers describing ESR experiments in LiNbO₃ were published during the mid and late 1970s, but the field was revived in the 1980s with in-depth studies of lower symmetry spectra, Jahn-Teller effects, and electric-field-induced spectra. The late 1980s brought the first reports of ENDOR spectra.

The main results obtained from specific impurities are presented below, followed by results on radiation-induced defects. The values of the main parameters describing the spin-Hamiltonian are given in the way they were reported in the references, and therefore they will have different units

depending on how the Hamiltonian was defined and what units were used in the respective experiments.

B 3d IONS

The 3d¹ ion Ti^{3+} has been studied in [3]. Its ESR spectrum is axially symmetric about the c-axis with $g(\parallel) = 1.96$ and $g(\perp) = 1.84$, and its linewidth varies from 30 to 52 G with magnetic field orientation. No hyperfine from the Ti-47 and Ti-49 isotopes is reported. The Ti^{3+} spectrum is produced either by heating the crystal in a reducing atmosphere at high temperature ($>700^\circ\text{C}$) or by exposing the crystal to ionising irradiation at low temperatures (<125 K). In each case, it is assumed that the Ti^{4+} is converted to Ti^{3+} . There have been suggestions as to the site of the Ti^{3+} or its environment.

The 3d³ ion Cr^{3+} was initially studied in [4] and [5]. They describe an axially symmetric spectrum with parameters $g(\parallel) = 1.969$, $g(\perp)_{\text{eff}} = 3.870$, and $D = 0.45 \text{ cm}^{-1}$. In [6] this spectrum is attributed to Cr^{3+} at an Nb^{5+} site, and also a second weaker axial spectrum ($g = 1.97$, $D = 0.21 \text{ cm}^{-1}$) is attributed to Cr^{3+} on a Li^+ site. The crystal field splitting parameter D increases with temperature for the less-intense axial spectrum and this supports its assignment to Cr^{3+} on a Li^+ site [7]. Later [8] reported additional lower symmetry spectra and suggested they were due to Cr^{3+} ions on Li^+ sites with adjacent Nb^{5+} vacancies. The first ENDOR study in LiNbO_3 on axial Cr^{3+} [9] revealed the presence of a weak Al-27 hyperfine and suggested charge-compensation mechanisms heretofore not considered. Also, the ESR from exchange-coupled Cr^{3+} - Cr^{3+} pairs has been observed [9].

The 3d⁵ ions Fe^{3+} and Mn^{2+} are well characterised in LiNbO_3 .

In [10] the Mn^{2+} ion was studied at 9.3 GHz and room temperature. It was found it has an axial spectrum with $g = 1.998$ and $D = 783$ G. The hyperfine parameters for the Mn-55 nucleus were $A(\parallel) = 86.1$ G and $A(\perp) = 82.4$ G. An uneven spacing of the hyperfine sextet was shown to result from the relatively large D value. In [11] a 35 GHz spectrometer was used and similar spin-Hamiltonian parameters were obtained. Also in [11] the temperature dependence of the parameters (from -176 to 55°C) was measured and it was concluded that Mn^{2+} substitutes for Nb^{5+} because D decreases with increasing temperature. The forbidden hyperfine lines appearing in the Mn^{2+} spectrum have been explained [12] in terms of the large D parameter. A later ENDOR study [13] suggests that Mn^{2+} occupies a Li^+ site, a result that was later backed by a theoretical analysis [34].

The results of complete angular studies of Fe^{3+} were reported nearly simultaneously by three groups [14-16]. An axially symmetric spectrum was observed at room temperature (both at 9 GHz and 35 GHz): the spectrum was described by $g = 2.0024$ and $D = 0.1659 \text{ cm}^{-1}$. Additional crystal field terms in the spin-Hamiltonian are small but not negligible. The reported linewidths are approximately 200 G. Two additional lower symmetry Fe^{3+} spectra were described [8] and it was suggested they have adjacent oxygen vacancy. In Mg-doped LiNbO_3 , it was shown [17] that the axial Fe^{3+} spectrum normally present is replaced with a considerably different one, which has not yet been analysed in detail. Theoretical models [35] seem to indicate that the impurity Fe^{3+} substituted the Nb^{5+} rather than the Li^+ .

The 3d⁷ ion Co^{2+} has been studied in [18] and [19]. The spectrum from this impurity can be observed at temperatures up to 25 K although the lines begin to broaden above 13 K. The exponential increase in linewidth with temperature indicates an Orbach relaxation via an excited state approximately 100 cm^{-1} above the ground state. This unexpectedly small energy separation is caused by a dynamic Jahn-Teller effect [19]. The Co^{2+} spectrum is axially symmetric about the c-axis and is explained in terms of an effective electron spin $S = 1/2$ and nuclear spin $I = 7/2$ with parameters $g(\parallel) = 2.59$, $g(\perp) = 5.04$, $A(\parallel) = 0$, and $A(\perp) = 153 \times 10^{-4} \text{ cm}^{-1}$. It is assumed that the Co^{2+} substitutes for Li^+ . Additional lower symmetry lines accompanying the main Co^{2+} spectrum are attributed to Co^{2+} ions with nearby charge compensators, perhaps Li^+ vacancies [19].

The $3d^8$ ion Ni^{2+} has been studied in [20] and [21]. The spectrum of this $S = 1$ ion exhibits a very large crystal field splitting because of the trigonal symmetry of the LiNbO_3 lattice. Using a frequency-tunable ESR spectrometer, the two $\Delta m(S) = \pm 1$ transitions were observed [20] and it was found that $D = 152.1$ G and $g(\parallel) = 2.24$. The linewidths of these two transitions were approximately 1400 G. In [21] it was demonstrated that the $\Delta m(S) = \pm 2$ transitions could be observed at 9 GHz when induced by the electric component of the microwave field in the cavity. These latter transitions have an effective value of 4.52 and a linewidth of 20 G when the magnetic field is parallel to the crystal's c-axis.

The $3d^9$ ions Cu^{2+} and Ni^+ have also been studied, with Cu^{2+} receiving the most attention.

Below 77 K, the principal g values for Cu^{2+} are $g_1 = 2.095$, $g_2 = 2.111$, and $g_3 = 2.428$ with the principal axis 3 directed 51° from the crystallographic c-axis and towards the nearest-neighbour oxygen ion. A model was proposed [22] in which Cu^{2+} replaces Nb^{5+} , with a nearest-neighbour oxygen vacancy providing the charge compensation. It was observed [23,24] that the Cu^{2+} spectrum undergoes a transition from C1 to C3 symmetry as the temperature increases. Based on these additional observations, a model was proposed wherein the Cu^{2+} replaces a Li^+ with no adjacent charge compensator [23,24]. A static Jahn-Teller effect reduces the symmetry at lower temperatures and a dynamic averaging occurs at higher temperatures.

The ESR spectrum of Ni^+ exhibits a temperature dependence similar to that of Cu^{2+} . Below 77 K the principal g values are $g_1 = 2.246$, $g_2 = 2.217$, and $g_3 = 2.061$ with the principal axis 3 directed 55° from the crystallographic c-axis and towards the nearest-neighbour oxygen ion [24]. At room temperature this spectrum appears as a single nearly isotropic line at $g = 2.19$. Also, its linewidth is strongly angularly dependent at room temperature; the width is 40 G when the magnetic field is parallel to the c-axis and increases significantly for other orientations. As in the case of the Cu^{2+} , the Ni^+ is proposed to replace a Li^+ in the otherwise unperturbed lattice with a static Jahn-Teller effect occurring at lower temperatures and a dynamic averaging at higher temperatures [24]. Earlier [25] it was suggested that this particular ESR spectrum was due to Ni^{3+} , but in [24] this assignment was convincingly ruled out. In [24] the authors used ionising radiation at 77 K to produce Ni^+ and a subsequent thermal annealing destroyed the centres near 400 K.

C 4f IONS

The rare-earth ions Nd^{3+} , Gd^{3+} , Dy^{3+} , Er^{3+} and Yb^{3+} have been studied in LiNbO_3 , and of these, Nd^{3+} and Gd^{3+} appear the most interesting because they each give two distinct spectra, which indicates these ions have more than one charge-compensation mode.

The $4f^3$ ion Nd^{3+} was observed at 4.2 K [26]. For spectrum I $g(\parallel) = 1.43$ and $g(\perp) = 2.95$ were found while for spectrum II the values were $g(\parallel) = 1.33$ and $g(\perp) = 2.95$. It was suggested that spectrum II may have slight deviations (no more than 10°) from the c-axis.

In the case of $4f^7$ ion Gd^{3+} , two spectra have been observed [27] at 9 GHz and room temperature. The Gd^{3+} spectra were complex at this microwave frequency because of the large crystal field splitting term. The same two spectra have been studied also at 35 GHz and room temperature [28]. It was found that the two spectra have the same $g = 1.9916$ and similar $b_2(0)$ values, 0.1185 cm^{-1} and 0.1260 cm^{-1} . The latter spectrum has a slight orthorhombic component. The linewidths for the two spectra were of the order of 50 G.

The $4f^9$ ion Dy^{3+} has been observed at 9 GHz and 4.2 K [26]. It is axial about the crystal three-fold axis and is described by $g(\parallel) = 8.7$ and $g(\perp) = 1.3$. The spectrum consists of a single line and its width and intensity are strongly dependent on the angle between the magnetic field and the symmetry axis.

The intensity is a maximum and the linewidth a minimum (of about 80 to 100 G) for the field parallel to the c-axis.

The $4f^{11}$ ion Er^{3+} also has been observed at 9 GHz and 4.2 K [26]. Its axial spectrum is described by $g(\parallel) = 15.4 \pm 0.1$ and $g(\perp) = 2.1 \pm 0.1$ and is otherwise similar to the Dy^{3+} spectrum. The linewidth is 20 G when the magnetic field is parallel to the c-axis. The axial symmetry along the c-axis and the principal g values were confirmed later in [37], $g(\parallel) = 15.14$ and $g(\perp) = 2.15$, and [36], $g(\parallel) = 15.14 \pm 0.05$ and $g(\perp) = 2.2 \pm 0.9$. Also in [36], the g values for MgO-doped, $g(\parallel) = 4.3 \pm 0.2$ and $g(\perp) = 7.6 \pm 0.3$, and ZnO-doped material, $g(\parallel) = 4.26 \pm 0.05$ and $g(\perp) = 7.8 \pm 0.1$, were given. Although the position for the Er^{3+} in the lattice is not clarified it seems that only one trigonal site is occupied by the rare earth [37].

The $4f^{13}$ ion Yb^{3+} has been studied in [5,38] and the g values were measured as $g(\parallel) = 4.86$ and $g(\perp) = 2.69$ in [5] and more recently [38] as $g(\parallel) = 4.70$ and $g(\perp) = 2.70$ in the 7 - 10 K range. Also [38] reports data on $\text{LiNbO}_3:\text{MgO}$ doped with Yb^{3+} .

D RADIATION-INDUCED DEFECTS

Several radiation-induced effects have been characterised in LiNbO_3 using the ESR technique. The crystal is exposed to ionising radiation (two-photon excitation or X-rays) at 20 K and Nb^{4+} and O are formed [29]. The former are trapped electrons and the latter are trapped holes. The Nb^{4+} spectrum is axially symmetric about the c-axis with $g(\parallel) = 1.90$ and $g(\perp) = 1.72$. It has a well-resolved ten-line hyperfine structure ($A(\parallel) = 0.011 \text{ cm}^{-1}$ and $A(\perp) = 0.023 \text{ cm}^{-1}$) resulting from the 100% abundant Nb-93 isotope ($I = 9/2$). The O-spectrum is an isotropic line at $g = 2.0294$ with a width of approximately 200 G. Both these defects are thermally unstable at room temperature. It was shown [30] that the Nb^{4+} spectrum can be produced by optically bleaching a reduced crystal at 77 K, as opposed to subjecting the crystal to ionising radiation.

A second type of trapped hole centre has been observed [31]. Its complex hyperfine pattern is best explained as one hole interacting equally with three Nb-93 nuclei. It is also thermally unstable at room temperature. Finally, another electron trap has been observed in Mg-doped LiNbO_3 [17]. It is attributed to an Mg^+ complex and it has a g(c) value of 1.82.

Radiation effects in doped LiNbO_3 have been investigated at 9.4 GHz over a temperature range from 4 to 300 K [32,33]. For Fe-doped (0.1 at.%) LiNbO_3 no change in the ESR spectra after γ - and electron-irradiation was observed [32]. On the other hand Cu-doped (0.03 at.%), Cr-doped (0.5 at.%), Mn-doped (0.05 at.%) and Dy-doped (0.3 - 1.7 at.%) LiNbO_3 all exhibited changes in the ESR spectra after γ - and/or electron-irradiation.

E CONCLUSION

Electron spin resonance and electron paramagnetic resonance techniques provide information on site occupancy of transition-metal and rare-earth ions, as well as radiation-induced defects. Ions studied include Ti, Cr, Fe, Mn, Co, Ni, Nb, Gd, Dy, Er and Yb. More detailed information will be obtained when the electron nuclear double resonance technique is applied in the future.

REFERENCES

- [1] G.I. Malovichko, V.G. Grachev, V.T. Gabrielyan, E.P. Kokanyan [Sov. Phys.-Solid State (USA) vol.28 (1986) p.1453]
- [2] V.G. Grachev, G.I. Malovichko [Sov. Phys.-Solid State (USA) vol.27 (1985) p.424]

9.4 Magnetic resonance spectra of impurities and defects in LiNbO_3

- [3] S. Juppe, O.F. Schirmer [*Phys. Lett. A (USA)* vol.117 (1986) p.150]
- [4] G. Burns, D.F. O'Kane, R.S. Title [*Phys. Lett. (USA)* vol.23 (1966) p.56]
- [5] G. Burns, D.F. O'Kane, R.S. Title [*Phys. Rev. (USA)* vol.167 (1968) p.314]
- [6] D.G. Rexford, Y.M. Kim, H.S. Story [*J. Chem. Phys. (USA)* vol.52 (1970) p.860]
- [7] H.K. Choh, S.H. Choh, D. Choi [*J. Kor. Phys. Soc. (Korea)* vol.19 (1986) p.217]
- [8] G.I. Malovichko, V.G. Grachev, S.N. Lukin [*Sov. Phys.-Solid State (USA)* vol.28 (1986) p.553]
- [9] V.G. Grachev, G.I. Malovichko, V.V. Troitskii [*Sov. Phys.-Solid State (USA)* vol.29 (1987) p.349]
- [10] T. Takeda, A. Watanabe, K. Sugihara [*Phys. Lett. A (USA)* vol.27 (1968) p.114]
- [11] M.P. Petrov [*Sov. Phys.-Solid State (USA)* vol.10 (1969) p.2574]
- [12] D.G. Rexford, Y.M. Kim [*Phys. Lett. A (USA)* vol.35 (1971) p.215]
- [13] G. Korradi, H. Sothe, J.-M. Spaeth, K. Polgar [*Abstracts Int. Conf. on Defects in Insulating Crystals Parma, Italy* (1988) p.419]
- [14] H.H. Towner, Y.M. Kim, K.S. Story [*J. Chem. Phys. (USA)* vol.56 (1972) p.3676]
- [15] J.B. Herrington, B. Dischler, J. Schneider [*Solid State Commun. (USA)* vol.10 (1972) p.509]
- [16] F. Mehran, B.A. Scott [*Solid State Commun. (USA)* vol.11 (1972) p.15]
- [17] K.L. Sweeney, L.E. Halliburton, D.A. Bryan, R.R. Rice, R. Gerson, H.E. Tomaschke [*J. Appl. Phys. (USA)* vol.57 (1985) p.1036]
- [18] A.A. Mirzakhanyan, A.K. Petrosyan [*Sov. Phys.-Solid State (USA)* vol.28 (1986) p.904]
- [19] H.J. Donnerberg, O.F. Schirmer [*Solid State Commun. (USA)* vol.63 (1987) p.29]
- [20] A.A. Mirzakhanyan [*Sov. Phys.-Solid State (USA)* vol.23 (1981) p.1434]
- [21] O. Thiemann, O.F. Schirmer [*Phys. Status Solidi B (Germany)* vol.143 (1987) p.K115]
- [22] T. Kobayashi, K. Muto, J. Kai, A. Kawamori [*J. Magn. Reson. (USA)* vol.34 (1979) p.459]
- [23] A.K. Petrosyan, R.M. Khachatryan, E.G. Sharoyan [*Sov. Phys.-Solid State (USA)* vol.26 (1984) p.12]
- [24] G. Korradi et al [*Sov. Phys.-Solid State (USA)* vol.28 (1986) p.412]
- [25] J. Rosa, K. Polak, J. Kubatova [*Phys. Status Solidi B (Germany)* vol.111 (1982) p.K85]
- [26] N.F. Evlanova, L.S. Kornienko, L.N. Rashkovich, A.O. Rybaltovskii [*Sov. Phys.-JETP (USA)* vol.26 (1968) p.1090]
- [27] P.F. McDonald, C.P. Tam, Y.W. Mok [*J. Chem. Phys. (USA)* vol.56 (1972) p.1007]
- [28] B. Dischler, J.R. Herrington, A. Rauber, J. Schneider, W. Urban [*Solid State Commun. (USA)* vol.12 (1973) p.737]
- [29] O.F. Schirmer, D. von der Linde [*Appl. Phys. Lett. (USA)* vol.33 (1978) p.35]
- [30] J.L. Ketchum, K.L. Sweeney, L.E. Halliburton, A.F. Armington [*Phys. Lett. A (Netherlands)* vol.94 (1983) p.450]
- [31] T. Miki, M.R. Hantehzadeh, L.E. Halliburton [*J. Phys. Chem. Solids (UK)* vol.50 (1989) p.1003]
- [32] R. Jablonski et al [*Spectrochim. Acta A (Netherlands)* vol.54 (1998) p.1701]
- [33] S.M. Kaczmarek et al [*J. Alloys Comp. (Switzerland)* vol.275-277 (1998) p.105]
- [34] Y.-Y. Zhou [*Phys. Rev. B (USA)* vol.43 (1991) p.11374]
- [35] M.G. Zhao, M. Chiu [*Phys. Rev. B (USA)* vol.49 (1994) p.12556]
- [36] D. Bravo, A. Martin, F.J. Lopez [*Solid State Commun. (USA)* vol.112 (1999) p.541]
- [37] D.M.B.P. Milori et al [*Phys. Rev. B (USA)* vol.51 (1995) p.3206]
- [38] C. Bonardi et al [*J. Alloys Comp. (Switzerland)* vol.323-324 (2001) p.340]

9.5 Absorption spectra of bulk LiNbO₃

T. Kanata and K. Kubota; updated by K.A. Green

August 2001

Optical absorption in LiNbO₃ has been investigated experimentally and theoretically [1-6]. Redfield and Burke [1], and Weakliem et al [2] investigated the temperature and stoichiometry dependence of the UV absorption edge, while Foldvari et al [3] investigated the dependence of UV-absorption edge on stoichiometry and MgO doping level for the temperature range 10 - 300 K. They make clear the following three features:

- (a) The UV absorption edge shifts to higher energy with increasing temperature in the range 10 - 667 K. At elevated temperatures, the edge is broad and structureless, which is characteristic of ionic crystals; however, it differs in that it remains this way even at low temperature. In particular, the absorption edge is significantly different from that of SrTiO₃ at low temperature in spite of the similarity of these reflection spectra. These broadened features are due to the effects of electric microfields arising from charged point defects (Li and O deficiencies) in the congruently grown lattice.
- (b) The absorption edges in MgO-doped congruent crystals and in stoichiometric crystals are shifted to higher energy compared to undoped congruent crystals, and the edge shapes are similar. For about 2.7×10^{-2} mole/mole MgO the spectroscopic properties of stoichiometric and MgO-doped congruent material are similar. The reasons for this are still unproven, but may involve lattice defects caused by the altered (stoichiometric) melt composition becoming a source of electronic microfields, and/or localised excitons caused by excess Nb in Li sites in congruent material being compensated by the high distribution coefficient of MgO.
- (c) Measured at both 10 and 300 K the maximum separation of the absorption edge curves parallel and perpendicular to the C-axis is less than 10 meV and the curves actually cross at $\alpha = 10^3/\text{cm}$. Thus, there is very little dichroism despite the fact that the crystal structure and near-UV reflectance is anisotropic, and there is birefringence of visible refractive indices. Moreover, a comparative material, such as BaTiO₃, has a marked dichroism (about 0.1 eV) in the ferroelectric state [8]. However, there is some support in the fact that the electric conductivity of the material is isotropic [9], and the Kramers-Kronig analysis of the reflectivity leads to absorption curves for the two polarisations that merge near the absorption edge [10].

Mamedov [5] made a fairly complete study of the optical properties of LiNbO₃. He presents data on absorption coefficient for the energy range 1.0 - 35.0 eV relating the observed behaviour to the electric properties of the crystal. Since LiNbO₃ contains NbO₆ octahedra, the band structure should be characterised by the octahedral structure, as seen in SrTiO₃. From this consideration, he assigned the fundamental optical oscillators at 5.1 and 9.8 eV to optical transitions from the valence band (O 2p) to the conduction band (Nb 4d) consisting of two subbands (d epsilon and d gamma). The smaller structures observed in the energy range 3.0 - 12.0 eV relate to the distortion of the NbO₆ octahedron on the structure transition from perovskite to rhombohedral lattice. In his article, he also presents other transitions in the region of energies >14 eV.

Hafid and Michel-Calendini [6] calculated electronic structure of LiNbO₃ such as densities of states, optical anisotropy and spontaneous polarisation from the X molecular orbital method.

LiNbO₃ has no significant absorption in the visible region. However, reduced LiNbO₃ [11-19,22] has typical broad absorption bands at about 2.5 eV and 3.2 eV. These bands do not change position significantly as the temperature is varied between 10 K and room temperature. The absorption coefficient of the band increases with the degree of the reduction. When X-ray, laser light, tungsten- or Xe-lamps irradiate the reduced material at low temperature, the absorption band at about 2.5 eV disappears and a different band appears at 1.6 eV. On heating the crystal after the irradiation, its new absorption band disappears and the 2.5 eV band again appears. Sweeney and Halliburton [12] explained these phenomena as follows. The oxygen vacancies labelled as F-centres have two electrons initially. These neutrally charged defects are responsible for the absorption band at about 2.5 eV. By irradiation with light at low temperature, one of these electrons is trapped at Nb(5+) and the Nb(4+) ion is formed. The vacancy with its remaining electron, which has an effective positive charge, is labelled as an F+ centre. They assigned the 1.6 eV-band to this F+ centre. Arizmendi et al [13] assigned the 2.5 eV and 3.2 eV bands to F and F+ centres, respectively. Under light irradiation at low temperature, because of the electrons trapped at oxygen vacancies and ejecting electrons into the conduction band, these electrons become self-trapped as polaron states, Nb(4+), and give rise to the 1.6 eV band. However, in contrast to the oxygen vacancies model, Jhans et al [14] and Bernhardt [15] explained that the absorption bands are caused by a variety of electron polaron states. Furthermore, Schirmer et al [16] explained the effect in relation to the bipolaron. These suggestions are in accordance with a reduction model of Smyth and co-workers [20,21]. Garcia-Cabanes et al [22] proposed that the two reduction models are simultaneously operative, that is, oxygen-vacancy F-centres and normal bipolarons could be simultaneously generated. OH⁻ absorption spectra are described in another Datareview in this book [7].

The hydrogen, forming OH⁻ ions, is important not only in fixing of holograms [32] but may also be related to the increase of the laser damage resistance [33]. Herrington et al [34] studied the infrared absorption band (near 2.87 microns) of stretching vibration of the OH⁻ ions which may be formed during the growth process. In the Mg-doped LiNbO₃, the infrared absorption band of OH⁻ ions is also found at about 2.83 microns [35]. For Mg doping of LiNbO₃ it is well known that the resistance to laser damage increases [36]. In an experiment by Kovacs et al [35], when undoped LiNbO₃ is heated to 130°C and cooled back to room temperature, a temperature hysteresis of this OH band is observed. However, in the Mg-doped LiNbO₃, the band returns immediately to its initial state. They considered that this may relate to the increased resistance to laser damage.

There are many important properties introduced by other impurities. For optical application in the transparent region, i.e. in the visible and near-infrared region, impurity doping effects are noticed by several authors [28-31]. Saito and Suganomata [28] have studied the optical absorptive properties of metal ion implanted materials in the wavelength range 400 - 700 nm. The implanted ions were Ti, V, Cr, Fe, Co, Cu, Zr, Nb and Mo. Burns et al [29] studied the optical absorption of Yb⁺⁺⁺, Nd⁺⁺⁺ and Cr⁺⁺⁺ in LiNbO₃ in the infrared region together with the fluorescence and the ESR. Johnson and Ballman [30] measured the absorption of Nd⁺⁺⁺-, Tm⁺⁺⁺- and Ho⁺⁺⁺-doped materials in the wavelength range 500 - 900 nm for Nd⁺⁺⁺ and 350 - 1800 nm for Tm⁺⁺⁺ and Ho⁺⁺⁺. They also demonstrated the coherent emission and the second harmonic generation (SHG). Glass [31] studied the detailed optical spectra of Cr⁺⁺⁺ at wavelengths from 333 to 1000 nm. In his article, much important information about the impurity ions is presented.

REFERENCES

- [1] D. Redfield, W.J. Burke [*J. Appl. Phys. (USA)* vol.45 no.10 (1974) p.4566-71]
- [2] H.A. Weakliem, W.J. Burke, D. Redfield, V. Korsun [*RCA Rev. (USA)* vol.36 no.1 (1975) p.149-62]

- [3] I. Foldvari, K. Polgar, A. Mesceki [*Acta Phys. Hung. (Hungary)* vol.55 no.1-4 (1984) p.321-7]
- [4] I. Foldvari, K. Polgar, R. Voszka, R.N. Balasanyan [*Cryst. Res. Technol. (Germany)* vol.19 no.12 (1984) p.1659]
- [5] A.M. Mamedov [*Opt. Spectrosc. (Russia)* vol.56 no.6 (1984) p.645-9]
- [6] L. Hafid, F.M. Michel-Calendini [*J. Phys. C (UK)* vol.19 no.16 (1982) p.2907-17]
- [7] L. Kovacs, I. Foldvari (updated by C. Florea) [Datareview in this book: 9.6 IR spectral presence of OH ions in LiNbO₃]
- [8] S.H. Wemple [*Phys. Rev. B (USA)* vol.2 (1970) p.2679]
- [9] W. Bollman, M. Gernand [*Phys. Status Solidi A (Germany)* vol.9 no.1 (1972) p.301-8]
- [10] E. Weisendanger, G. Guntherodt [*Solid State Commun. (USA)* vol.14 no.4 (1974) p.303-6]
- [11] J.L. Ketchum, K.L. Sweeney, L.E. Halliburton, A.F. Armington [*Phys. Lett. A (USA)* vol.94A no.9 (1983) p.450-3]
- [12] K.L. Sweeney, L.E. Halliburton [*Appl. Phys. Lett. (USA)* vol.43 no.4 (1983) p.336-8]
- [13] L. Arizmendi, J.M. Cabrera, F. Agullo-Lopez [*J. Phys. C (UK)* vol.17 no.3 (1984) p.515-29]
- [14] H. Jhans, J.M. Honig, C.N.R. Rao [*J. Phys. C (UK)* vol.19 no.19 (1986) p.3649-58]
- [15] Hj. Bernhardt [*Phys. Status Solidi A (Germany)* vol.54 no.2 (1979) p.597-603]
- [16] O.F. Schirmer, S. Juppe, J. Koppitz [*Cryst. Lattice Defects Amorphous Mater. (UK)* vol.16 (1987) p.63]
- [17] M.G. Clark, F.J. DiSalvo, A.M. Glass, G.E. Peterson [*J. Chem. Phys. (USA)* vol.59 no.12 (1973) p.6209-19]
- [18] W. Bollmann [*Phys. Status Solidi A (Germany)* vol.40 no.1 (1978) p.83-91]
- [19] O.F. Schirmer, D. von der Linde [*Appl. Phys. Lett. (USA)* vol.33 no.1 (1978) p.35-8]
- [20] Y. Limb, K.W. Cheng, D.M. Smyth [*Ferroelectrics (UK)* vol.38 no.1-4 (1981) p.813-16]
- [21] D.M. Smyth [*Ferroelectrics (UK)* vol.50 no.1-4 (1983) p.419-28]
- [22] A. Garcia-Cabanes et al [*Phys. Rev. B (USA)* vol.37 no.11 (1988) p.6085-61]
- [23] H. Vormann, G. Weber, S. Kapphan, E. Kratzig [*Solid State Commun. (USA)* vol.40 no.5 (1981) p.543-5]
- [24] R.G. Smith, D.B. Fraser, R.T. Denton, T.C. Rich [*J. Appl. Phys. (USA)* vol.39 (1968) p.4600]
- [25] J.R. Herrington, B. Dischler, A. Rauber, J. Schneider [*Solid State Commun. (USA)* vol.12 no.5 (1973) p.351-4]
- [26] L. Kovacs, K. Polgar, R. Capelletti [*Cryst. Lattice Defects Amorphous Mater. (UK)* vol.15 (1987) p.115]
- [27] D.A. Bryan, R. Gerson, H.E. Tomaschke [*Appl. Phys. Lett. (USA)* vol.44 no.9 (1984) p.847-9]
- [28] Y. Saito, S. Suganomata [*Jpn. J. Appl. Phys. I (Japan)* vol.26 no.11 (1987) p.1941-2]
- [29] G. Burns, D.F. O'Kane, R.S. Title [*Phys. Rev. (USA)* vol.167 (1968) p.314]
- [30] L.F. Johnson, A.A. Ballman [*J. Appl. Phys. (USA)* vol.40 (1969) p.297]
- [31] A.M. Glass [*J. Chem. Phys. (USA)* vol.50 (1969) p.1501]
- [32] H. Vormann, G. Weber, S. Kapphan, E. Kratzig [*Solid State Commun. (USA)* vol.40 no.5 (1981) p.543-5]
- [33] R.G. Smith, D.B. Fraser, R.T. Denton, T.C. Rich [*J. Appl. Phys. (USA)* vol.39 (1968) p.4600]
- [34] J.R. Herrington, B. Dischler, A. Rauber, J. Schneider [*Solid State Commun. (USA)* vol.12 no.5 (1973) p.351-4]
- [35] L. Kovacs, K. Polgar, R. Capelletti [*Cryst. Lattice Defects Amorphous Mater. (UK)* vol.15 (1987) p.115]
- [36] D.A. Bryan, R. Gerson, H.E. Tomaschke [*Appl. Phys. Lett. (USA)* vol.44 no.9 (1984) p.847-9]

9.6 IR spectral presence of OH ions in LiNbO₃

L. Kovacs and I. Foldvari; updated by C. Florea

February 2002

A OH ABSORPTION IN FERROELECTRIC OXIDES

OH impurities in most oxide materials have an influence on chemical and physical properties useful for device applications. The generally accepted role of OH in oxide crystals is the compensation of the charge deviation due to impurities and compositional faults. The OH is assumed to be present in the form of hydroxyl ions sitting either on a regular O²⁻ lattice site or in an interstitial position.

The presence of OH in ferroelectric oxide crystals can be monitored using absorption spectroscopy in the infrared range between 2.8 and 3.0 μm (about 3400 - 3600 cm⁻¹). TABLE 1 summarises the absorption bands found in several ferroelectric oxides.

TABLE 1 Absorption bands of OH vibrations in several ferroelectric oxide crystals measured at room temperature.

Crystal	Band (cm ⁻¹)	Ref
Ba ₂ NaNb ₅ O ₁₅	3425, 3480, 3500	[1]
	3425, 3486, 4392	[2]
BaTiO ₃	3465, 3487.5, 3503, 3512, 3462.5, 3485.5, 3492.5	[3]
	3501.0, 3509.5	[4]
SrTiO ₃	3490	[5]
	3495	[6]
	3497, 3505, 3511, 3519	[7]
KTaO ₃	3472.4, 3480.8	[8]
	3472, 3481, 3488	[7]
KNbO ₃	3504, 3507	[9]
LiTaO ₃	3450	[10]
	3500	[11]
	3466, 3480	[12]
LiNbO ₃	3490	[13]
	3478, 3491	[14]
	3467, 3481, 3492	[15]

The absorption bands originate from the 0 - 1 transition of the stretching vibration of the OH⁻ ion. Intrinsic and extrinsic defects present in the crystal give rise to the appearance of usually more than one absorption band due to the different environments available for the OH in the crystal lattice.

B INCORPORATION OF OH INTO LiNbO₃

Hydroxyl ions are always present in LiNbO₃ crystals grown by the Czochralski method in air. OH⁻ ions can be introduced into the LiNbO₃ after the growth process as well. It was found [11] that hydrogen (forming OH⁻ in the crystal) diffuses into the crystal during an annealing procedure at 600 - 700°C under an electric field. Annealing in water vapour (10 to 30 atm at 750°C) can also increase the absorption of OH⁻ by about an order of magnitude [16].

Hydrogen may diffuse not only into, but also out of the LiNbO₃ crystals. On annealing the LiNbO₃ crystals in vacuum at higher temperatures, the OH absorption decreases and practically disappears near 800°C [17].

9.6 IR spectral presence of OH ions in LiNbO₃

The concentration of OH⁻ in undoped LiNbO₃ crystals can be evaluated from nuclear magnetic resonance (NMR) data [18]. The relation between the OH ion concentration and the absorption coefficient (α) at the main band maximum near 3484 cm⁻¹ can be written in the form:

$$n = (3 \pm 1) \times 10^{19} (\text{cm}^{-2}) \times \alpha (\text{cm}^{-1})$$

In the as-grown crystals, α was found to be between 1 and 3 cm⁻¹ [15,16,19], corresponding to 3×10^{19} - 9×10^{19} OH⁻ ions cm⁻³. Other authors accept the estimation based upon accurate density measurements in rutile made by Johnson et al [20].

Different OH absorption bands appear in undoped (3470 - 3490 cm⁻¹), Mg-doped (3530 - 3540 cm⁻¹), double-doped (3500 - 3510 cm⁻¹), proton-exchanged (3500 - 3510 cm⁻¹) and neutron-irradiated LiNbO₃ crystals as a consequence of the different incorporation mechanisms and the different environments for the OH ions in the lattice (see TABLE 2). The peak positions given by several authors vary by a few wavenumbers, which is certainly within the error bars.

TABLE 2 Absorption bands of OH vibrations in pure and undoped LiNbO₃ crystals.

Crystal	Band (cm ⁻¹)	Ref
LiNbO ₃ (congruent) (nearly stoichiometric)	3478, 3491	[14]
	3467, 3481, 3492	[15]
	3468, 3482, 3488	[21]
LiNbO ₃ :Mg	3534	[22]
	3530, 3540	[23]
	3525, 3536	[21]
LiNbO ₃ :Mg, Fe	3507, 3537	[24]
	3504, 3536	[25]
LiNbO ₃ :Mg, Cr	3506, 3539	[26,46]
LiNbO ₃ :Mg, Nd	3522, 3539	[46]
LiNbO ₃ (proton-exchanged)	3510	[27,28]
	3505	[29,30]
	3501	[31]
LiNbO ₃ (neutron-irradiated)	3500, 3550	[32]

C OH ABSORPTION IN UNDOPED LiNbO₃

Lithium niobate is a typical non-stoichiometric material. The congruently melting composition corresponds to Li/Nb = 0.945 [33]. Other melt compositions result in inhomogeneous distribution of the crystal composition along the growth axis. Several properties of lithium niobate, including the shape of the OH absorption bands, are dependent on the composition.

C1 OH Absorption in Congruent LiNbO₃

The first detailed study of OH absorption in congruent LiNbO₃ was reported in 1973 [14]. It was found that the absorption band had a maximum at 3491 cm⁻¹ and a shoulder at 3478 cm⁻¹ (TABLE 2). A full width at half maximum (FWHM) of about 30 cm⁻¹ was observed. The band was completely polarised perpendicular to the crystallographic c-axis. The spectrum was measured at room temperature, 77 K and 6 K, but apart from the increased resolution the positions and the relative intensities of the two peaks were independent of temperature in this range.

In view of the above observations the authors concluded that the band is caused by the 0 - 1 stretching vibration of OH defects. The optical anisotropy of the band is produced by the OH bond being directed toward its nearest oxygen neighbours. The structure of the band was explained by the

existence of two slightly inequivalent configurations for the OH⁻ defect in the plane perpendicular to the c-axis.

In contradiction to the low temperature observations, heating of the crystal resulted in a significant change of the OH absorption band shape [23]. The main component broadened and shifted toward lower wavenumbers; its intensity decreased, while the parameters of the shoulder remained practically unchanged. On cooling the crystal back to room temperature the band returned to its initial state with a rather long relaxation time constant (several months).

C2 Stoichiometry Dependence of the OH Band in LiNbO₃

The incorporation of OH ions in LiNbO₃ crystals of different stoichiometry was studied [16]. It was assumed that in a congruent crystal the main defects for the charge compensation of lithium deficiency are oxygen vacancies, while for crystals with Li/Nb > 1 oxygen interstitials exist. In the experiments the position of the OH absorption maximum was 3491 cm⁻¹ for Li/Nb < 1 and 3478 cm⁻¹ for Li/Nb > 1. As a consequence the components of the absorption bands at 3491 cm⁻¹ and 3478 cm⁻¹ were attributed to vibrating OH substituting oxygen vacancies and occupying interstitial positions, respectively.

The absorption of OH in LiNbO₃ as a function of stoichiometry was also investigated [15]. The absorption band of the congruent crystal was found to be essentially similar to those observed earlier [14,16]. The decomposition of the spectrum of nearly stoichiometric crystals showed, however, that the OH band consists of three components. The presence of three components was confirmed in [21] and (for both congruent and near-stoichiometric lithium niobate) in [45]. TABLE 3 shows the results of a Gaussian fitting for the OH absorption in crystals of different composition [15].

TABLE 3 Location, FWHM and absorption coefficient data for OH vibrations in LiNbO₃ with different Li/Nb mole ratios. Li/Nbm is the mole ratio in the melt, while Li/Nbc is the mole ratio in the crystal determined using the data from [33].

Li/Nbm	Li/Nbc	Band (cm ⁻¹)	FWHM	α (cm ⁻¹)
0.818	0.899	3487	31	2.08
		3467	12	0.14
0.945	0.945	3485	28	2.43
		3468	11	0.60
1.000	0.959	3493	16	1.63
		3482	13	1.89
		3470	11	1.34
1.200	0.989	3492	10	0.86
		3481	10	2.12
		3467	9	3.21

The presence of three peaks in the absorption bands was interpreted by the existence of the three different O-O distances in the plane perpendicular to the c-axis. On the basis of the well-known relationship for hydrogen bonding in solids [34], longer O-O bonds result in higher stretching frequencies for the OH vibration. The wavenumbers and half-widths of the bands indicate, however, only a very weak hydrogen bonding in LiNbO₃. It can also be established from the spectra that the stronger the Li deficiency in the crystal, the broader the main absorption near 3485 cm⁻¹. This broadening is probably caused by the large structural disorder resulting in numerous slightly modified surrounds for the OH in these crystals.

D OH ABSORPTION IN DOPED LiNbO₃

Dopants are usually added to LiNbO₃ from a technological point of view or for practical applications. A small amount of magnesium is often added to the melt in order to improve the growth conditions. Transition metal elements increase the susceptibility of the crystal for hologram recording; rare earth (e.g. Nd, Er) doped crystals can be used as laser materials.

Dopants have negligible influence on the OH absorption band up to about 10³ mole/mole concentrations. The OH band at 3485 cm⁻¹ in Mg, Ti, Fe, Cr, Cu or Mn-doped congruent LiNbO₃ was practically unchanged compared to that of the pure crystal [35]. In Fe, Cu and Mn-doped crystals [19] the OH content is by no means correlated to the impurity content or to the valence states of the impurities. The changes of the OH band shape after water vapour annealing, however, can be used as an indicator of the fact that Bi³⁺, Mg²⁺ and Ni⁺ ions are incorporated at Li and Nb sites [36].

D1 OH Absorption in Mg-Doped LiNbO₃

High concentrations of magnesium can be incorporated into the LiNbO₃ crystal because its effective distribution coefficient is close to 1. Above about 5 mol% of Mg several abruptly changing properties can be observed, e.g. the appearance of the OH absorption band peaking at about 3534 cm⁻¹ [22].

The Mg concentration dependence of the OH band and the threshold effect as a function of Li/Nb ratio were studied for a wide range of crystal composition [23,37]. The band shape including the FWHM of about 30 cm⁻¹ was found to be equal to that in pure congruent crystals for Mg doping levels of up to 3 × 10⁻² mole/mole. In the crystal containing about 5 mol% of Mg the OH band became narrower (about 20 cm⁻¹) suggesting less structural lattice disorder, similar to the nearly stoichiometric crystal [15].

On further increasing the Mg concentration added to the congruent LiNbO₃, the OH absorption band appears at 3540 cm⁻¹ instead of 3485 cm⁻¹ as found in pure LiNbO₃ [23]. Changing the Li/Nb ratio of the melt to 1.1 or 1.2, the 3540 cm⁻¹ band is already present in the crystal at Mg concentrations of 3.5 and 2.7 mol%, respectively. The higher the Li/Nb ratio, the lower the threshold level of Mg above which the OH absorption switches over from 3485 to 3540 cm⁻¹. The shape of the 3540 cm⁻¹ band attributed to some kind of Mg-OH complexes is characterised by a main maximum with an FWHM of about 9 cm⁻¹ and a shoulder at 3530 cm⁻¹.

In contrast to the band at 3585 cm⁻¹ found in pure LiNbO₃, which is completely polarised perpendicular to the c-axis, the Mg-OH band has some absorption parallel to c as well [38]. The direction of the OH bond involved in the Mg-OH complex deviates by 14° ± 2° from the plane of oxygens perpendicular to the c-axis [23]. Similar polarisation dependence was reported in [39].

The OH absorption band at 3540 cm⁻¹ was also measured at 9 K but no essential improvement in resolution could be achieved [23]. On heating the crystal to 150°C the band maximum shifted by 3 cm⁻¹ to lower wavenumbers, the intensity decreased and the FWHM increased by about 20%, keeping the area constant. In contrast to pure congruent LiNbO₃ the equilibrium state was reached immediately after cooling back to room temperature.

D2 OH Absorption in Double-Doped LiNbO₃

Above the threshold concentration of magnesium the photorefractivity is strongly reduced in LiNbO₃ while transition metal elements increase the susceptibility to laser damage. The study of Mg and Cr or Mg and Fe double-doped crystals seems to be important in understanding both mechanisms.

Besides the absorption band at 3539 cm⁻¹ associated with Mg-OH complexes, an OH band was observed at 3506 cm⁻¹ in a crystal grown from the melt with Li/Nb = 1.1 containing 4 mol% Mg and

9.6 IR spectral presence of OH ions in LiNbO₃

3.5×10^{-2} mol% Cr [26] (see TABLE 2). It was confirmed by visible absorption measurements that this band can be attributed to some kind of Mg-OH-Cr complex. The OH⁻ ion lies perpendicular to the c-axis and is assumed to be situated between an Mg²⁺ and a Cr³⁺ ion, which are substituting lithium and niobium ions respectively. This complex can be regarded as locally neutral.

The same observations were made in the case of co-doping with Nd [46]. For crystals doped with 2 mol% or 5 mol% Mg (in melt) and co-doped with 0.5 mol% Nd (in melt), an additional OH band is identified at 3522 cm⁻¹, besides the 3539 cm⁻¹ band found in pure LiNbO₃ [46]. The 3522 cm⁻¹ band is considered to be related to the Nd³⁺-OH⁻-Mg²⁺ complex.

Two absorption bands were also found in congruent LiNbO₃ doped with 5 mol% Mg and 0.1 mol% Fe [24]. Both the 3507 and 3537 cm⁻¹ bands were considered as an Mg²⁺-OH association taking into account that the Mg concentration is fifty times higher than that of Fe. From polarisation dependence data a value of 58° was obtained for the angle between the OH bond and the c axis. It should be noted that this value differs strongly from those found in [23,29] and quoted in Section D1.

The infrared absorption of LiNbO₃ co-doped with magnesium and iron was also studied in [25]. It was shown that the 3504 cm⁻¹ band is present in the crystal doped with 6 mol% Mg and 530 ppm Fe, but is absent in LiNbO₃ doped only with 6 mol% Mg. It was concluded from EPR measurements that Fe³⁺ should substitute for Nb in heavily Mg-doped crystals, in contrast to congruent LiNbO₃ where Fe ions are assumed to occupy lithium sites. As a consequence the appearance of the 3504 cm⁻¹ band may be caused by the iron substituting for Nb⁵⁺. The 3504 cm⁻¹ band is certainly equivalent to the 3507 cm⁻¹ band reported in [24] and associated with the Mg-OH complex.

The OH absorption bands have also been investigated in congruent LiNbO₃ doped with Hf and Mg impurities, and a simple theoretical model for the OH vibration modes has been proposed [47].

E OH ABSORPTION IN PROTON-EXCHANGED LiNbO₃

Planar optical waveguides in LiNbO₃ can be fabricated by the proton-exchange method [40]. Crystals are treated near 200°C in an acid, such as benzoic acid, producing a thin surface layer of a few microns depth in which lithium ions are exchanged by protons.

The IR spectrum of proton-exchanged Li_{1-x}H_xNbO₃ shows an absorption band at 3510 cm⁻¹ [27,28] in addition to the 3480 cm⁻¹ band found in pure LiNbO₃ (see TABLE 2). The width of the 3510 cm⁻¹ peak increases with increasing x. The band is polarised perpendicular to the c axis indicating that the proton sites must lie within the hexagonally closest packed oxygen layers. The same conclusion was reached in [14,15] for the OH in the as-grown LiNbO₃ crystals.

It should be noted that in acid-reacted crystals a broad unpolarised band is also present at about 3280 cm⁻¹ [28]. This band was identified as OH vibration in cubic HNbO₃ in a very thin layer at the surface of the crystal. The frequency and FWHM of the band are typical of hydrogen-bonded systems. Two absorption bands after proton exchange in LiNbO₃ were also identified in [29]. One is a strong peak at 3505 cm⁻¹ which is polarisation-dependent, while the other is a broad, smaller, and polarisation-independent band at about 3250 cm⁻¹. The authors were unable, however, to detect a new crystalline structure pertaining to the HNbO₃ structure by X-ray diffraction methods.

The exchange process in deuterated benzoic acid results in the appearance of an intense OD absorption at 2590 cm⁻¹ [30,41] instead of an OH band at about 3505 cm⁻¹, corresponding to the isotopic substitution. It was concluded from the comparison of proton- and deuterium-exchanged LiNbO₃, however, that they cannot be regarded as structurally identical [30].

9.6 IR spectral presence of OH ions in LiNbO₃

In [39] the LiNbO₃ crystals were treated at 250°C in benzoic acid, with 2 - 3% Li₂CO₃ added to prevent surface damage, for up to 100 h using the proton-exchange method. This procedure yields an OH band position at about 3500 cm⁻¹ with an absorption coefficient of 10 - 100 cm⁻¹. A subsequent tempering at 600°C leads to an increase of the absorption band at 3483 cm⁻¹, while simultaneously the band at about 3500 cm⁻¹ disappears. Therefore one can assume that a large fraction of the hydrogen in the surface layer did diffuse into the bulk of the crystal [31]. This surface band shows some fine structure depending on the proton-exchange treatment. If no Li₂CO₃ is added the bandwidth is almost twice that of the samples treated with the addition of 2 - 3% Li₂CO₃ to the benzoic acid.

The proton-exchange method was also used to fabricate optical waveguides in Mg-doped LiNbO₃ [42]. Before exchange, the OH absorption was located at 3535 cm⁻¹. After exchange in benzoic acid, the considerably increased absorption appeared at about 3500 cm⁻¹, similar to the case for the pure crystal.

F RAMAN SPECTRA OF OH IN LiNbO₃

Raman scattering of the OH stretching vibration in as-grown, hydrogen-doped and 6 mol% Mg-doped congruent LiNbO₃ crystals was investigated [43]. The observed band of the right-angle scattering in as-grown congruent LiNbO₃ has a half-width and peak position which are in agreement with the IR absorption data. Equal scattering due to the diagonal elements (xx) and (yy) is observed. Considerably lower signals were obtained for the configuration (zz) and the off-diagonal components.

The samples doped with hydrogen by applying an electric field showed two deviations from the results for as-grown crystals. First, the scattering intensities in the (xx) and (yy) configurations are no longer equal. Second, an increase of the off-diagonal component (xy) compared to the diagonal ones was found.

Very similar behaviour was observed for strong Mg doping. The equality of (xx) and (yy) scattering is preserved but the off-diagonal element (xy) is increased, when compared to the case of as-grown and hydrogen-doped samples. Therefore it was concluded that both H doping and Mg doping increase the scattering efficiency for off-diagonal elements of the Raman tensor. Model calculations for the Raman tensor components based on symmetry arguments were also performed. Inequivalent scattering for (xx) and (yy) in H-doped crystals, however, suggests the destruction of the threefold rotational symmetry for the OH dipole.

G ANHARMONIC OSCILLATOR MODEL OF OH VIBRATION

IR absorption bands due to the fundamental and the overtone of OH and OD stretch modes were investigated in undoped, Mg-doped and benzoic-acid-treated LiNbO₃ [39]. The spectroscopic parameters were determined independently from the isotope shift and the overtone frequencies using the anharmonic oscillator model. The results are shown in TABLE 4.

Two important conclusions can be drawn from the results collected in TABLE 4. First, the anharmonicity constants for the different bands are similar, consistent with the local mode picture and small coupling to the lattice vibrations. Second, the parameters calculated by the two independent methods are close to each other indicating that the substitution of hydrogen by deuterium may be described almost completely by the mass exchange. The anharmonicity found is comparable to that of OH in other ABO₃ crystals and in alkali halides.

9.6 IR spectral presence of OH ions in LiNbO₃

TABLE 4 Frequencies of the fundamental and overtones, and anharmonicity parameter ($\omega_e \chi_e$) of the different bands in LiNbO₃ for both OH and OD [39].

	H-doped	Mg-doped	Surface band	Uncertainty
OH v(0,1)	3483	3529	3501	±2
v(0,2)	6778	6881	6829	±4
OD v(0,1)	2575	2606	2589	±2
v(0,2)	5050	5121	5081	±4
Anharmonicity parameter ($\omega_e \chi_e$) obtained from:			$\omega_e \chi_e$	
Isotope shift of the fundamental	99	93	101	±9
OH overtone	94	88.5	86.5	±4
Isotope shift of the overtone	97	94	92	±6
OD overtone	50	45.5	48.5	±4

H HYDROGEN ISOTOPES IN LiNbO₃

The protons forming OH ions with the oxygens are always present in air-grown LiNbO₃. Deuterons, partially exchanging protons, can be incorporated into the LiNbO₃ by treating the crystal in D₂ [17] or D₂O vapour [44] atmosphere at elevated temperatures. The OD⁻ spectroscopy has been used successfully in determining the anharmonicity parameters of the OH vibration in various LiNbO₃ crystals (see TABLE 4). The diffusivity of deuterium has also been calculated from the growth rate of the OD⁻ absorption band [44].

Tritium ions have also been produced. Transmutation of Li⁶ isotopes is obtained by irradiating LiNbO₃ crystals with thermal neutrons, Li⁶ + n = T³ + He⁴ [32]. After the neutron irradiation, the original OH band was absent and two new bands at 3500 and 3550 cm⁻¹ appeared. In addition, two very weak bands at 2180 and 2211 cm⁻¹ were observed. Heat treatments in air or in flowing D₂O vapour helped to assign these two bands to OT⁻ stretching vibrations. The tritium concentration was estimated as being given by

$$n(OT^-) = 1.4 \times 10^{16} (\text{cm}^{-2}) \times \alpha(OT^-) (\text{cm}^{-1})$$

where α is the maximum absorption coefficient at 2211 cm⁻¹. TABLE 5 summarises the wavenumbers and FWHM of the absorption bands found in neutron-irradiated LiNbO₃.

TABLE 5 Frequencies (v) and bandwidths (Δ) of the OH⁻, OD⁻ and OT⁻ bands in LiNbO₃ (all in units of cm⁻¹) [32].

v(OH ⁻)	Δ (OH ⁻)	v(OD ⁻)	Δ (OD ⁻)	v(OT ⁻)	Δ (OT ⁻)
3550	20	2615	9	2211	7
3547	15	2570	22	2180	15
		3545	15		
		3500	40		
		3480	30		

REFERENCES

- [1] L.C. Bobb, I. Lefkowitz, L. Muldawer [*Solid State Commun. (USA)* vol.7 (1969) p.937]
- [2] S. Singh, H.J. Levinstein, L.G. van Uitert [*Appl. Phys. Lett. (USA)* vol.16 (1970) p.176]
- [3] I. Laulicht, L. Benguigui [*Solid State Commun (USA)* vol.32 (1979) p.771]
- [4] S. Kapphan, G. Weber [*Ferroelectrics (UK)* vol.37 (1981) p.673]
- [5] F.G. Wakim [*J. Chem. Phys. (USA)* vol.49 (1968) p.3738]

- [6] S. Kapphan, G. Weber [*Ferroelectrics (UK)* vol.25 (1980) p.585]
- [7] S. Jandi, D. Houde, Y. Lepine, J.L. Brebner [*Ferroelectrics (UK)* vol.38 (1981) p.805]
- [8] H. Engstrom, J.B. Bates, L.A. Boatner [*J. Chem. Phys. (USA)* vol.73 (1980) p.1073]
- [9] A. Forster, H. Hesse, S. Kapphan, M. Wohlecke [*Solid State Commun. (USA)* vol.57 (1986) p.373]
- [10] G.M. Loiacono [*Appl. Opt. (USA)* vol.7 (1968) p.555]
- [11] R.G. Smith, D.B. Fraser, R.T. Denton, T.C. Rich [*J. Appl. Phys. (USA)* vol.39 (1968) p.4600]
- [12] R. Gonzalez, R. Hantehzadeh, C.Y. Chen, L.E. Halliburton, Y. Chen [*Phys. Rev. B (USA)* vol.39 (1989) p.1302]
- [13] L.M. Guseva, V. Kljuiev, I.S. Rez, S.A. Fedulov, A. Ljbimov, Z.I. Tatarov [*Izv. Akad. Nauk SSR Ser. Fiz. (USSR)* vol.31 (1967) p.1161]
- [14] J.R. Herrington, B. Dischler, A. Rauber, J. Schneider [*Solid State Commun. (USA)* vol.12 (1973) p.351]
- [15] L. Kovacs, V. Szaly, R. Capelletti [*Solid State Commun. (USA)* vol.52 (1984) p.1029]
- [16] W. Bollman, H.-J. Stohr [*Phys. Status Solidi A (Germany)* vol.39 (1977) p.477]
- [17] J.L. Ketchum, K.L. Sweeney, L.E. Halliburton, A.F. Armington [*Phys. Lett. A (Netherlands)* vol.94 (1983) p.450]
- [18] W. Bollman, K. Schlothauer, O.J. Zogal [*Krist. Tech. (Germany)* vol.11 (1976) p.1327]
- [19] H. Vormann, G. Weber, S. Kapphan, E. Kratzig [*Solid State Commun. (USA)* vol.40 (1981) p.543]
- [20] O.W. Johnson, J. DeFord, J.W. Shaner [*J. Appl. Phys. (USA)* vol.44 (1973) p.3008]
- [21] Feng Xi-Qi, Ying Ji-Feng, Wang Jin-Chang, Liu Jian-Cheng [*Acta Phys. Sin. (China)* vol.37 (1988) p.2062]
- [22] D.A. Bryan, R. Gerson, H.E. Tomaschke [*Appl. Phys. Lett. (USA)* vol.44 (1984) p.847]
- [23] L. Kovacs, K. Polgar, R. Capelletti [*Cryst. Lattice Defects Amorphous Mater. (UK)* vol.15 (1987) p.115]; see also Feng Xi-Qi, Zhang Qi-Ren, Ying Ji-Feng, Liu Jian-Cheng, Yin Zi-Wen [*Sci. China A (China)* vol.33 (1990) p.108]
- [24] Ma.J. de Rosendo, L. Arizmendi, J.M. Cabrera, F. Agullo-Lopez [*Solid State Commun. (USA)* vol.59 (1986) p.499]
- [25] Feng Xi-Qi, Ying Ji-Feng, Wu Yao-An, Liu Jian-Cheng [*Chin. Sci. Bull. (China)* vol.36 (1991) p.297]
- [26] L. Kovacs, I. Foldvari, I. Cravero, K. Polgar, R. Capelletti [*Phys. Lett. A (Netherlands)* vol.133 (1988) p.433]
- [27] C.E. Rice [*J. Solid State Chem. (USA)* vol.64 (1986) p.188]
- [28] J.L. Jackel, C.E. Rice [*Ferroelectrics (UK)* vol.38 (1981) p.801]
- [29] C. Canali et al [*J. Appl. Phys. (USA)* vol.59 (1986) p.2643]
- [30] A. Loni, R.M. De La Rue, J.M. Winfield [*J. Appl. Phys. (USA)* vol.61 (1987) p.64]
- [31] S.E. Kapphan [*Advances in Ceramics* vol.23 (Non-stoichiometric compounds) (1987)]
- [32] R. Gonzalez, Y. Chen, M.M. Abraham [*Phys. Rev. B (USA)* vol.37 (1988) p.6433]
- [33] J.R. Carruthers, G.E. Peterson, M. Grasso, P.M. Bridenbaugh [*J. Appl. Phys. (USA)* vol.42 (1971) p.1846]
- [34] A. Novak [*Structure and Bonding* vol.18 (1984) p.177]
- [35] L. Kovacs [unpublished results]
- [36] W. Bollman [*Cryst. Res. Technol. (Germany)* vol.17 (1982) p.K48]
- [37] K. Polgar, L. Kovacs, I. Foldvari, I. Cravero [*Solid State Commun. (USA)* vol.59 (1986) p.375]
- [38] D.A. Bryan, R.R. Rice, R. Gerson, H.E. Tomaschke, K.L. Sweeney, L.E. Halliburton [*Opt. Eng. (USA)* vol.24 (1985) p.138]
- [39] A. Forster, S. Kapphan, M. Wohlecke [*Phys. Status Solidi B (Germany)* vol.143 (1987) p.755]
- [40] J.L. Jackel, C.E. Rice, J.J. Veselka [*Appl. Phys. Lett. (USA)* vol.41 (1982) p.607]
- [41] C.E. Rice, J.L. Jackel, W.L. Brown [*J. Appl. Phys. (USA)* vol.57 (1985) p.4437]
- [42] J.L. Jackel [*Electron. Lett. (UK)* vol.21 (1985) p.509]

9.6 IR spectral presence of OH ions in LiNbO₃

- [43] A. Jovanovic, S. Kapphan, M. Wohlecke [*Cryst. Lattice Defects Amorphous Mater.* (UK) vol.15 (1987) p.137]
- [44] R. Gonzalez, Y. Chen, K.L. Tsang, G.P. Summers [*Appl. Phys. Lett. (USA)* vol.41 (1982) p.739]
- [45] Y. Kong, W. Zhang, X. Chen, J. Xu, G. Zhang [*J. Phys., Condens. Matter (UK)* vol.11 (1999) p.2139]
- [46] J. Li, B. Li, H.-F. Wang [*Phys. Lett. A (Netherlands)* vol.205 (1995) p.112]
- [47] V.G. Babajanyan, G.G. Demirkhanyan, E.P. Kokanyan [*J. Contemp. Phys. (USA)* vol.34 (1999) p.18]

9.7 Stark effect for rare-earth dopants in LiNbO₃

A.P. Skvortsov; updated by C. Florea

September 2001

A INTRODUCTION

A discussion is given of absorption and luminescence spectra of LiNbO₃ doped with various rare-earth ions. Properties of both impurities and defects can be studied using the Stark effect. An inverse piezoelectric effect is also possible in these materials.

B SPECTRA OF RARE-EARTH DOPANTS IN LiNbO₃

A number of papers [1-5] are devoted to the study of absorption and luminescence spectra of LiNbO₃ crystals doped with rare-earth (RE) ions (Nd, Ho, Er, Tm, Dy, Pr, Eu, Yb). These crystals can serve as sources of stimulated emission with trivalent ions being used as activators. The absorption of these rare-earths is located in the region of transparency of the LiNbO₃ crystals, from 350 nm to 1800 nm [3]. At 77 K and 4.2 K the spectra consist of partly and completely polarised lines. A temperature decrease causes freezing of a series of lines corresponding to the transitions from higher sublevels of the ground-state multiplet, and the intensities of the other lines are also redistributed. The spectral positions of the majority of lines remain practically unchanged on temperature decrease from 77 K to 4.2 K.

The number of absorption lines observed at 4.2 K for some transitions is larger than that predicted by theory [4,6]. It is known that RE³⁺ can replace both Li⁺ and Nb⁵⁺, which have octahedral oxygen surroundings in the LiNbO₃ lattice. Moreover, the LiNbO₃ structure contains vacant octahedral voids. Point symmetry of both substitution positions for RE ions is trigonal C3 [7]. At sufficiently high concentrations, the formation of impurity ions or more complicated aggregates is possible. All this brings about a multitude of non-equivalent centres and can cause an observed increase in the number of lines in the spectra.

C STARK EFFECT IN CRYSTALS WITH IMPURITIES AND DEFECTS

One of the most important methods for the determination of the impurity symmetry in crystals is the study of Stark splitting of the zero-phonon (i.e. purely electronic) lines in the optical spectra. The character of the influence of an external electric field on the electronic levels of an impurity centre in a crystal decisively depends on the type of the inversion symmetry of the centre. The Stark effect should be quadratic or linear in the field strength [8], depending on whether the point group of the impurity centre symmetry involves the inversion or not. Note that this is strictly true only for deep small-radius centres and transitions between sufficiently isolated levels.

The traditional method of analysis of the spectral splitting pattern in the static electric field [9] is not very sensitive. In many cases, even at very high static fields (2×10^5 V cm⁻¹), the magnitude of the Stark splitting is less than the linewidth.

A more sensitive method involves a modulation technique [10,11], which can be used for revealing and studying the Stark splitting otherwise unresolvable from within the linewidth. The technique uses an alternating electric field instead of a static field and the differential signal K(E) - K(0) is recorded,

where $K(E)$ and $K(0)$ are the spectral lines in the presence and, respectively, in the absence of the field.

As has been shown in [10], in the case of centrosymmetric crystals the spectral profile of the differential signal is quite different for linear and quadratic Stark effects. For impurity centres with inversion symmetry, the differential signal will be observed as the first derivative of the line shape with respect to the frequency (the absorption spectrum). For inversionless centres the differential signal will represent the second derivative of the line shape with respect to the frequency. Thus, the inversion symmetry can be easily determined from the spectral dependence of the differential signal. Moreover, the analysis of the Stark effect properties allows one to establish the magnitude and the direction of the transition electric dipole moment, the symmetry of the levels participating in the transition, and the multipole nature of the transition.

D STARK EFFECT FOR THE f-f TRANSITION SPECTRA OF RARE-EARTH DOPED LiNbO_3

In principle, the linear Stark effect is expected for the impurity ions situated in the inversionless crystal field C_3 of LiNbO_3 . However, in the case of the screened f-f transition spectra this effect is very small in magnitude. The magnitude of the line shifts is in the range of 0.5 cm^{-1} for a field of 10^5 V cm^{-1} and the typical line halfwidth is about 10 cm^{-1} . These values are of the same order of magnitude as in the case of trivalent RE ions in other crystal systems [14-16].

Due to the small values of the shifts, the modulation technique mentioned above must be used for revealing and studying the Stark effect in the case of $\text{RE}^{3+}\text{-LiNbO}_3$. The spectral response of the differential signal should reproduce the first derivative of the absorption spectrum with respect to the frequency. This is characteristic of the linear Stark effect in non-centrosymmetric crystals and indicates the shift of the 'centre of gravity' of the spectral lines. Moreover, the amplitude value of the differential signal depends linearly on the strength of the external field.

Also, one must note that in non-centrosymmetric crystals, such as LiNbO_3 , the spectral picture of splitting is dependent on the direction of the external electric field.

For RE^{3+} ions with an odd number of electrons (such as Er^{3+}) only non-degenerate electronic states are possible in the trigonal crystal field C_3 . For RE^{3+} ions with an even number of electrons, both non-degenerate and two-fold degenerate electronic states are possible. The influence of an external electric field on orbitally non-degenerate and two-fold degenerate states is different [9]. The non-degenerate levels are influenced only by the field directed along the trigonal centre's axis. The level shift in this case is linear with the field strength. The degenerate levels will be influenced by the field directed along the trigonal centre's axis (experiencing a shift) but also by the field oriented perpendicular to this axis (splitting into a symmetric doublet).

E EXPERIMENTAL RESULTS

The Stark effect has been studied in LiNbO_3 crystals doped with Er [6], Ho and Tm [12], and Nd [17]. The experiments were carried out at 77 K with polarised light in Czochralski-grown crystals [13], in an external electric field of strength up to 10^5 V cm^{-1} .

In crystals doped with Er^{3+} or with Nd^{3+} the differential signal was observed for most absorption lines in various regions of the spectrum in the case of the external field directed along the trigonal centre's axis. No effect was found in the case of the external field perpendicular to the axis, as expected since the $4f^1$ electronic configuration has only non-degenerate levels. This behaviour indicates that the

9.7 Stark effect for rare-earth dopants in LiNbO_3

constant electric dipole moment of the Er^{3+} and Nd^{3+} centres is oriented along the trigonal crystal axis, which confirms the trigonal C_3 symmetry of the RE^{3+} centres in the LiNbO_3 .

In the crystals doped with Ho^{3+} (electronic structure $4f^{10}$) the differential signal was observed on some lines in the case of the external field being oriented perpendicular to the trigonal axis. This is caused by the splitting of the orbitally degenerate levels in the external field.

The analysis of the differential spectra of $\text{Ho}^{3+}:\text{LiNbO}_3$ obtained for different directions of the external electric field and of the light polarisation allows one to conclude that the lowest sublevel of the ground state is non-degenerate. The transitions between the non-degenerate states and the transitions implicating the two-fold degenerate levels were also identified [12].

The properties of the Stark effect observed in $\text{Tm}^{3+}:\text{LiNbO}_3$ are similar to those observed in the spectra of the $\text{Ho}^{3+}:\text{LiNbO}_3$ crystals.

F INVERSE PIEZOELECTRIC EFFECT

It should be noted that for the crystals of C_{3v} class of symmetry in an external field, the inverse piezoelectric effect is possible. The crystal deformation caused by the action of the external field, in principle, can induce the shift of centre levels and consequently the shift of transition frequencies. Estimates show [6] that the relative crystal deformation in electric fields of up to 10^5 V cm^{-1} is of the order of 10^{-5} . The direct experimental study of the influence of the uniaxial stress on the impurity spectra has revealed no line shift or splitting [6]. Hence, we conclude that the line shifts observed in external electric fields are mainly caused by the direct action of the applied external field.

G CONCLUSION

This Datareview has presented results of both absorption and luminescence spectra of LiNbO_3 crystals, doped with a range of rare-earth ions, at various temperatures. Experimental results of the Stark effect are given for Er, Ho, Tm and Nd ions in Czochralski-grown crystals. Demonstration of an inverse piezoelectric effect on application of an external field is described.

REFERENCES

- [1] L.I. Ivleva, A.A. Kaminskii, Yu.S. Kuzminov, V.N. Shpakov [*Dokl. Akad. Nauk SSSR (Russia)* vol.183 (1968) p.1068]
- [2] N.F. Evlanova [*JETP Lett. (USA)* vol.5 (1967) p.291]
- [3] L.F. Jonson, A.A. Ballman [*J. Appl. Phys. (USA)* vol.40 (1967) p.297]
- [4] V.T. Gabrielyan, A.A. Kaminskii, L. Li [*Phys. Status Solidi A (Germany)* vol.3 (1970) p.K37]
- [5] K.G. Belabaev, A.A. Kaminskii, S.E. Sarkisov [*Phys. Status Solidi A (Germany)* vol.28 (1975) p.K17]
- [6] K. Polgar, A.P. Skvortsov [*Opt. Spektrosk. (Russia)* vol.58 (1985) p.229]
- [7] S.C. Abrahams, J.M. Reddy, J.L. Bernstein [*J. Phys. Chem. Solids (UK)* vol.27 (1966) p.997]
- [8] A.W. Overhauser, H. Ruchradt [*Phys. Rev. (USA)* vol.112 (1958) p.722]; N. Bloembergen [*Science (USA)* vol.133 (1961) p.3461]
- [9] A.A. Kaplyanskii, V.N. Medvedev [*Opt. Spektrosk. (Russia)* vol.23 (1967) p.404]
- [10] A.A. Kaplyanskii, V.N. Medvedev, A.P. Skvortsov [*Opt. Spektrosk. (Russia)* vol.29 (1970) p.481]

9.7 Stark effect for rare-earth dopants in LiNbO_3

- [11] A.A. Kaplyanskii, V.N. Medvedev, A.P. Skvortsov [*Surf. Sci. (Netherlands)* vol.37 (1973) p.650]
- [12] K. Polgar, A.P. Skvortsov [*Opt. Spektrosk. (Russia)* vol.64 (1988) p.947]
- [13] F. Schmidt, R. Voszka [*Cryst. Res. Technol. (Germany)* vol.16 (1981) p.K127]
- [14] A.A. Kaplyanskii, V.N. Medvedev, A.P. Skvortsov [*Opt. Spektrosk. (Russia)* vol.36 (1974) p.213 and vol.39 (1975) p.437]
- [15] A.A. Kaplyanskii, V.N. Medvedev, A.P. Skvortsov [*Sov. Phys.-Solid State (USA)* vol.17 (1975) p.1578]
- [16] V.N. Medvedev, A.P. Skvortsov [*Opt. Spektrosk. (Russia)* vol.48 (1980) p.418]
- [17] K. Polgar, A.P. Skvortsov, A.M. Tveritinov [*Phys. Solid State (USA)* vol.36 (1994) p.1810]

CHAPTER 10

ACOUSTIC WAVE PROPAGATION AND PROPERTIES

- 10.1 Velocity of ultrasonic bulk waves in LiNbO₃
- 10.2 Attenuation of ultrasonic bulk waves in LiNbO₃
- 10.3 SAWs in LiNbO₃: properties of common orientations
- 10.4 Attenuation of SAWs in LiNbO₃
- 10.5 Velocity of SAWs in proton-exchanged waveguides in LiNbO₃
- 10.6 Velocity of SAWs on LiNbO₃: anisotropy, temperature and composition dependence
- 10.7 Velocity of SAWs on LiNbO₃: Ti-indiffused, PE and ion-implanted

10.1 Velocity of ultrasonic bulk waves in LiNbO₃

R.C. Peach; updated by D. Craig

August 2001

A INTRODUCTION

Lithium niobate is a material widely used for bulk acoustic wave delay lines, resonators, transducers and acousto-optic devices, and for all of these components a knowledge of the bulk wave velocities is essential.

The velocity of ultrasonic bulk waves in an anisotropic elastic material can be computed, for any direction of propagation, from the elastic stiffnesses at constant electric field, cE_{ij} , the piezoelectric stress constants, e_{ij} , the dielectric permittivities at constant strain, ϵ_{ij} , and the mass density, ρ . In the low-frequency range, which covers all practical ultrasonic devices, the adiabatic constants should be chosen in preference to the isothermal ones.

When selecting data for acoustic velocity calculations, it is necessary to consider not only the accuracy of the individual constants but also the probable consistency of the entire data set. Some, or all, of the above constants for lithium niobate have been measured by various workers, including Warner et al [1], Yamada et al [2], Smith and Welsh [3], Nakagawa et al [4], Graham [5], Tomono and Matsumura [6], and Dankov et al [7]; of these, the data sets of Warner et al [1] and of Smith and Welsh [3] are the most complete and consistent.

The constants determined by Smith and Welsh [3] were derived principally from pulse echo velocity measurements, having a claimed error of 1 in 10^4 , on certain specific orientations within a single lithium niobate block. However, this level of measurement accuracy requires a number of experimental corrections that are not mentioned in the paper, and the possibility of there being systematic errors outside the claimed error limits cannot be discounted. The data given by Warner et al [1] are based on resonance measurements on small specimens of lithium niobate, and some of the measured parameters could only be determined to 1 in 10^3 ; the constants are, therefore, quoted to one less significant figure than those of Smith and Welsh [3].

Both pulse echo and resonance measurements provide direct information on acoustic-wave velocities, and the corresponding data sets should be consistent in the sense that they will make valid velocity predictions for those orientations on which measurements were originally made. Piecemeal alterations to a data set can destroy this consistency and reduce the accuracy of velocity predictions; for this reason, the tabulations given in Section C use the unmodified data sets of Warner et al [1] and of Smith and Welsh [3], even though some individual parameters, such as Warner's value for the density (4.7×10^3 kg/m³), are of questionable validity.

Variations in the composition of the lithium niobate employed are a likely cause of measurement discrepancies between various workers. Commercially supplied lithium niobate is now almost invariably of the congruently melting composition (Li/Nb 0.945), and is, as a result, a far more consistent product than that available for the original measurements. The compositions of the specimens used by Warner et al [1] and by Smith and Welsh [3] are not known, but Smith and Welsh quote a value of 1165°C for the Curie temperature of their sample.

B METHOD OF CALCULATION

The stiffness constants (cE_{ij} , $i,j = 1, \dots, 6$) and the piezoelectric constants (e_{ij} , $i = 1,2,3$, $j = 1, \dots, 6$) are invariably listed using contracted index notation, but for the description of the calculation procedure the full tensor notation is preferable (cE_{ijkl} , $i,j,k,l = 1,2,3$ and e_{ij} , $i,j,k = 1,2,3$). The correspondence between the two notations is given by:

<u>Tensor indices</u>	<u>Contracted Index</u>
11	1
22	2
33	3
23,32	4
31,13	5
12,21	6

Indices 1 and 2 and indices 3 and 4 of the fourth-order stiffness tensor are replaced by their corresponding contracted values to obtain the contracted form; for the third-order piezoelectric tensor only indices 2 and 3 are replaced; e.g. cE_{1131} becomes cE_{15} , e_{312} becomes e_{36} .

With this rule, any tensor component is easily determined if the values of the contracted components are known. It should be noted that the conversion rules for the compliance constants and the piezoelectric strain constants are more complex as certain additional multiplying factors are required.

If the direction of propagation of plane waves in an unbounded medium is described by the unit vector n_i , $i = 1,2,3$, relative to the crystallographic (X,Y,Z) axes, then the 3×3 matrix C_{ij} may be defined (Dieulesaint and Royer [8]):

$$C_{ij} = \left[\frac{cE_{ijkl} + (e_{pik} \times n_p) \times (e_{qjl} \times n_q)}{\epsilon_{rs} \times n_r \times n_s} \right] \times n_k \times n_l \quad (1)$$

with implied summations over repeated indices. The three eigenvalues of this matrix may be identified as $\rho \times (V_i)^2$, $i = 1,2,3$, where V_i is one of the possible acoustic-wave velocities for the chosen direction of propagation. The associated eigenvectors of C_{ij} give the polarisations (directions of particle displacement) of the waves. In general, one of the polarisations will be approximately parallel to n_i , and the other two will be approximately perpendicular; the corresponding waves are referred to as quasi-longitudinal (QL) and quasi-shear (QS), respectively. For certain special directions of propagation, one or more waves may be exactly longitudinal or exactly shear. From the fundamental symmetry conditions of the material constants it follows that C_{ij} is symmetrical; the three possible polarisations therefore form a mutually orthogonal set for any choice of n_i . For lithium niobate, and for most other materials, the quasi-longitudinal wave is faster than either of the two quasi-shear waves for any direction of propagation. Because the Z-axis in lithium niobate has threefold rotation symmetry, waves propagating along Z are pure longitudinal or pure shear, and the two shear waves have equal velocities.

From EQN (1), it can be seen that the acoustic velocities are principally determined by the stiffness constants; however, for a strong coupling material such as lithium niobate, the piezoelectric and dielectric constants also make a significant contribution. It can be shown that the inclusion of the piezoelectric terms necessarily increases the predicted wave velocities, and the effect is therefore referred to as ‘piezoelectric stiffening’; it may be regarded as being due to the additional stress produced, via the piezoelectric effect, by the electric field associated with the wave.

C TABULAR VELOCITY DATA

In the following tables the direction of propagation, $n(i)$, is specified by the polar angle θ and the azimuth angle ϕ ; θ is the angle between $n(i)$ and the Z-axis, and ϕ is the angle between the X-axis and the plane containing both the Z-axis and $n(i)$, e.g. X-axis propagation $\theta = 90$, $\phi = 0$, Y-axis propagation $\theta = 90$, $\phi = 90$, Z-axis propagation $\theta = 0$, ϕ arbitrary.

The velocity of the waves is not affected by a reversal of the direction of propagation, and, hence, θ may be restricted to the range [0,90] (deg). The Z-axis has a threefold rotation symmetry and the Y-Z plane is a mirror plane; ϕ may therefore be restricted to the range [30,90]. The tables give the velocities of each wave at 5° intervals over the chosen range. Values have been computed using the data sets both of Warner et al [1] and of Smith and Welsh [3]. Warner et al [1] do not specify temperature coefficients, and the corresponding velocity data are assumed to apply at room temperature; however, velocities are computed at 0°C, 25°C, 50°C and 100°C using the data of Smith and Welsh [3]. Unfortunately, the stoichiometry of the material used is not known for either data set. The velocities (m/s) are quoted to six digits accuracy for convenience in performing numerical interpolations, and not because the experimental data warrant such precision.

D CONCLUSION

It can be seen from the tables that quite large discrepancies exist (1%) between the two chosen data sets for certain velocity predictions. Practical experience on surface-wave devices suggests that the data of Warner et al [1] often give the best velocity values (Hartmann et al [9]), although this superior agreement is probably fortuitous.

Due to the uncertainties about the composition of the test samples and to the possible existence of systematic errors, the existing data sets are not adequate for high-precision velocity predictions. It would, therefore, be extremely valuable if a new set of constants could be measured for congruently melting lithium niobate, preferably using a pulse echo technique; such a set should include: elastic stiffness constants, piezoelectric stress constants, dielectric constants, expansion coefficients and mass density, all determined over a range of temperatures.

Slow Quasi-Shear Bulk Wave Velocities

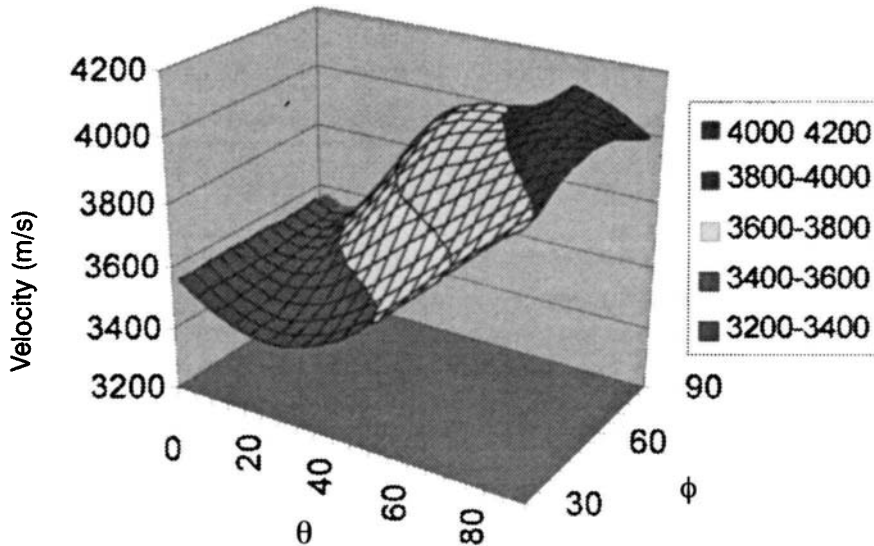


FIGURE 1 Bulk wave velocities (m/s), acoustic wave - slow quasi-shear; data set - Warner et al [1]; temperature - room temperature; stoichiometry - unknown (see TABLE 1).

TABLE 1 Bulk wave velocities (m/s), acoustic wave - slow quasi-shear; data set - Warner et al [1]; temperature - room temperature; stoichiometry - unknown.

$\theta\backslash\phi$ (degrees)	30.0	35.0	40.0	45.0	50.0	55.0	60.0	65.0	70.0	75.0	80.0	85.0	90.0
0.0	3572.95	3572.95	3572.95	3572.95	3572.95	3572.95	3572.95	3572.95	3572.95	3572.95	3572.95	3572.95	3572.95
5.0	3529.54	3529.78	3530.48	3531.60	3533.08	3534.86	3536.83	3538.86	3540.82	3542.56	3543.94	3544.82	3545.13
10.0	3493.69	3494.81	3497.54	3501.94	3507.83	3514.93	3522.88	3531.26	3539.55	3547.15	3553.37	3557.50	3558.95
15.0	3467.32	3469.34	3475.31	3484.94	3497.76	3513.15	3530.38	3548.60	3566.83	3583.92	3598.41	3608.45	3612.11
20.0	3450.86	3454.35	3464.60	3481.02	3502.67	3528.37	3556.76	3586.44	3615.97	3643.81	3668.07	3685.84	3692.71
25.0	3445.15	3450.39	3465.72	3490.04	3521.65	3558.51	3598.40	3639.16	3678.81	3715.61	3747.83	3772.73	3783.37
30.0	3450.43	3457.59	3478.43	3511.13	3552.97	3600.72	3651.06	3700.91	3747.74	3789.66	3825.34	3853.30	3866.81
35.0	3466.48	3475.57	3501.87	3542.65	3593.93	3651.10	3709.62	3765.55	3815.86	3858.63	3892.94	3918.38	3930.78
40.0	3492.68	3503.50	3534.59	3582.18	3640.84	3704.54	3767.63	3825.56	3875.24	3915.02	3944.43	3963.48	3970.71
45.0	3528.00	3540.14	3574.76	3626.87	3689.54	3755.36	3817.87	3872.46	3916.65	3949.82	3972.45	3985.50	3989.75
50.0	3571.13	3584.06	3620.56	3674.40	3737.15	3800.31	3857.27	3904.26	3940.28	3966.14	3983.38	3993.30	3996.56
55.0	3620.51	3633.72	3670.59	3723.72	3783.49	3841.06	3890.54	3929.59	3958.52	3978.83	3992.15	3999.73	4002.20
60.0	3674.40	3687.53	3723.72	3774.64	3830.04	3881.41	3924.06	3956.91	3980.92	3997.73	4008.80	4015.16	4017.27
65.0	3731.02	3743.85	3778.76	3826.76	3877.44	3923.02	3960.04	3988.30	4009.22	4024.59	4036.15	4045.21	4049.79
70.0	3788.57	3800.94	3834.21	3878.88	3924.65	3964.69	3996.57	4020.78	4038.98	4053.12	4065.54	4079.81	4100.61
75.0	3845.28	3857.08	3888.32	3929.13	3969.52	4003.62	4029.93	4049.30	4063.23	4073.09	4080.02	4084.72	4086.70
80.0	3899.52	3910.57	3939.26	3975.40	4009.49	4036.75	4056.44	4069.44	4076.68	4078.50	4074.92	4067.91	4064.01
85.0	3949.77	3959.82	3985.22	4015.56	4042.15	4061.46	4073.37	4078.57	4077.30	4069.27	4055.14	4039.91	4033.08
90.0	3994.68	4003.39	4024.46	4047.55	4065.35	4075.80	4079.18	4075.80	4065.35	4047.55	4024.46	4003.39	3994.68

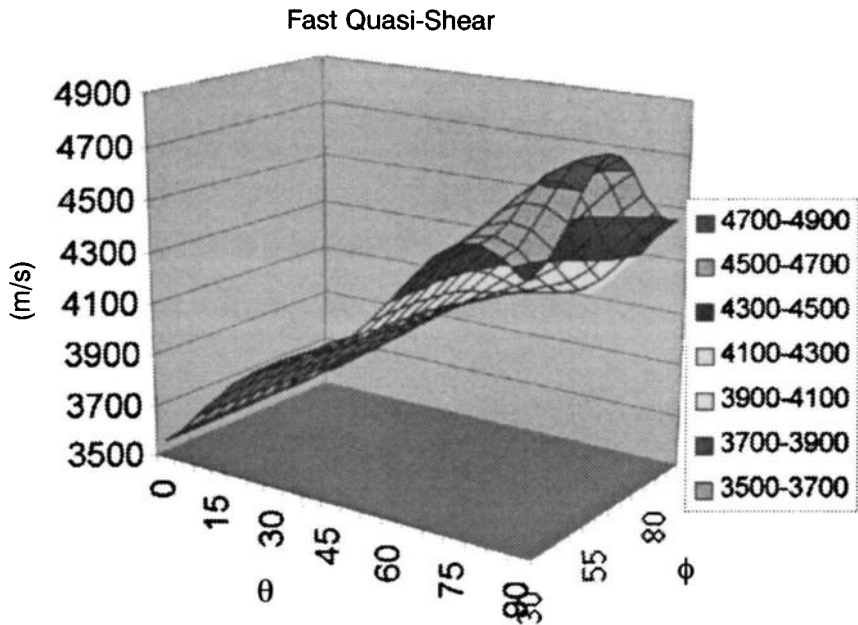


FIGURE 2 Bulk wave velocities (m/s), acoustic wave - fast quasi-shear; data set - Warner et al [1]; temperature - room temperature; stoichiometry - unknown.

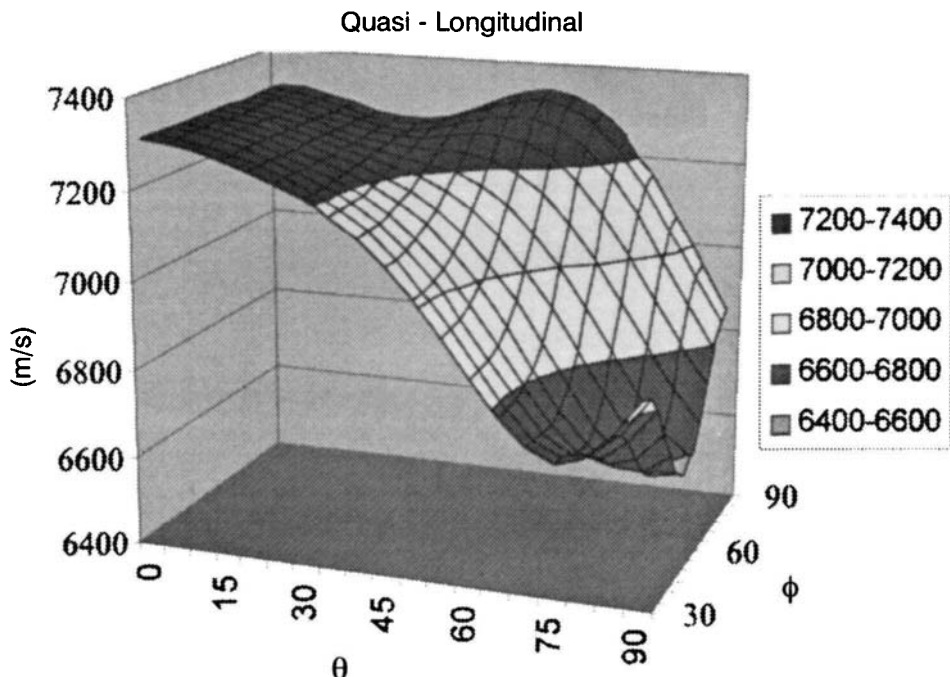


FIGURE 3 Bulk wave velocities (m/s), acoustic wave - quasi-longitudinal; data set Warner et al [1]; temperature - room temperature; stoichiometry - unknown.

TABLE 2 Bulk wave velocities (m/s), acoustic wave - fast quasi-shear; data set - Warner et al [1]; temperature - room temperature; stoichiometry - unknown.

$\theta \setminus \phi$ (degrees)	30.0	35.0	40.0	45.0	50.0	55.0	60.0	65.0	70.0	75.0	80.0	85.0	90.0
0.0	3572.95	3572.95	3572.95	3572.95	3572.95	3572.95	3572.95	3572.95	3572.95	3572.95	3572.95	3572.95	3572.95
5.0	3634.59	3634.41	3633.89	3633.05	3631.93	3630.58	3629.07	3627.49	3625.96	3624.58	3623.48	3622.77	3622.53
10.0	3715.32	3714.85	3713.45	3711.14	3707.98	3704.07	3699.52	3694.55	3689.42	3684.53	3680.39	3677.57	3676.56
15.0	3798.81	3798.16	3796.22	3792.98	3788.46	3782.69	3775.74	3767.75	3759.00	3750.03	3741.74	3735.58	3733.26
20.0	3872.07	3871.44	3869.52	3866.30	3861.71	3855.70	3848.19	3839.17	3828.68	3817.04	3805.11	3795.04	3790.80
25.0	3928.63	3928.13	3926.63	3924.09	3920.41	3915.49	3909.19	3901.31	3891.67	3880.17	3867.06	3854.06	3847.45
30.0	3969.32	3968.96	3967.88	3966.05	3963.42	3959.92	3955.43	3949.76	3942.65	3933.74	3922.71	3909.94	3901.56
35.0	4000.91	4000.59	3999.63	3998.05	3995.84	3993.03	3989.61	3985.54	3980.70	3974.85	3967.55	3958.52	3951.62
40.0	4033.26	4032.89	4031.79	4029.96	4027.45	4024.30	4020.60	4016.48	4012.11	4007.61	4003.07	3998.69	3996.30
45.0	4076.13	4075.74	4074.55	4072.53	4069.62	4065.80	4061.09	4055.63	4049.73	4043.94	4038.99	4035.62	4034.43
50.0	4136.20	4135.97	4135.23	4133.75	4131.15	4126.91	4120.45	4111.45	4100.19	4087.83	4076.35	4068.09	4065.05
55.0	4215.01	4215.30	4215.92	4216.17	4214.71	4209.62	4198.90	4181.52	4158.48	4132.99	4109.68	4093.31	4087.41
60.0	4307.97	4309.24	4312.52	4316.08	4316.70	4309.97	4291.92	4261.30	4220.93	4177.13	4137.89	4110.70	4100.97
65.0	4404.38	4407.28	4415.02	4424.31	4429.08	4421.45	4395.13	4349.07	4288.55	4223.34	4164.52	4122.02	4105.40
70.0	4488.75	4494.09	4508.64	4527.29	4540.38	4535.62	4503.79	4444.06	4364.61	4278.86	4200.84	4140.96	4103.86
75.0	4544.10	4552.59	4576.29	4608.53	4635.98	4641.07	4610.52	4543.26	4450.63	4350.64	4262.12	4201.05	4179.00
80.0	4557.59	4569.49	4603.48	4652.34	4699.91	4723.32	4703.92	4638.90	4542.32	4437.17	4346.99	4289.22	4270.05
85.0	4526.26	4541.13	4584.54	4649.84	4719.72	4767.62	4769.34	4718.03	4628.39	4527.08	4440.50	4385.67	4367.49
90.0	4458.08	4475.03	4525.44	4603.77	4692.84	4765.06	4793.09	4765.06	4692.84	4603.77	4525.44	4475.03	4458.08

TABLE 3 Bulk wave velocities (m/s), acoustic wave - quasi-longitudinal; data set Warner et al [1]; temperature - room temperature; stoichiometry - unknown.

$\theta \backslash \phi$ (degrees)	30.0	35.0	40.0	45.0	50.0	55.0	60.0	65.0	70.0	75.0	80.0	85.0	90.0
0.0	7316.29	7316.29	7316.29	7316.29	7316.29	7316.29	7316.29	7316.29	7316.29	7316.29	7316.29	7316.29	7316.29
5.0	7312.09	7312.09	7312.08	7312.07	7312.06	7312.05	7312.04	7312.02	7312.01	7312.00	7311.99	7311.99	7311.99
10.0	7300.52	7300.51	7300.48	7300.44	7300.38	7300.31	7300.23	7300.16	7300.09	7300.04	7299.99	7299.96	7299.96
15.0	7283.73	7283.71	7283.67	7283.61	7283.54	7283.46	7283.38	7283.31	7283.26	7283.22	7283.19	7283.17	7283.17
20.0	7263.62	7263.65	7263.72	7263.85	7264.05	7264.32	7264.66	7265.04	7265.45	7265.83	7266.14	7266.35	7266.42
25.0	7240.79	7240.94	7241.42	7242.22	7243.38	7244.87	7246.64	7248.61	7250.61	7252.46	7253.96	7254.95	7255.29
30.0	7213.98	7214.40	7215.71	7217.94	7221.13	7225.26	7230.19	7235.67	7241.25	7246.43	7250.65	7253.41	7254.37
35.0	7180.53	7181.38	7183.98	7188.47	7194.99	7203.53	7213.87	7225.42	7237.31	7248.38	7257.42	7263.35	7265.42
40.0	7137.44	7138.81	7143.05	7150.50	7161.51	7176.20	7194.25	7214.67	7235.83	7255.65	7271.87	7282.51	7286.22
45.0	7082.58	7084.47	7090.40	7101.05	7117.22	7139.32	7166.97	7198.66	7231.75	7262.85	7288.33	7305.04	7310.87
50.0	7015.75	7017.99	7025.18	7038.60	7059.76	7089.64	7127.91	7172.41	7219.23	7263.32	7299.43	7323.09	7331.33
55.0	6939.43	6941.63	6949.06	6963.87	6988.72	7025.54	7074.23	7131.88	7193.03	7250.73	7297.94	7328.82	7339.55
60.0	6859.25	6860.79	6866.71	6880.41	6906.26	6947.68	7005.08	7074.79	7149.57	7220.32	7278.16	7315.91	7329.01
65.0	6784.36	6784.37	6786.24	6795.07	6817.57	6859.42	6922.09	7001.20	7087.50	7169.61	7236.74	7280.51	7295.68
70.0	6727.02	6724.45	6719.20	6718.25	6731.34	6767.38	6829.80	6913.84	7008.11	7098.76	7173.10	7221.57	7238.37
75.0	6700.41	6694.33	6679.05	6663.22	6659.75	6681.79	6736.13	6818.54	6915.62	7010.85	7089.57	7141.04	7158.89
80.0	6713.91	6703.92	6677.11	6642.98	6616.77	6616.05	6652.64	6724.68	6817.58	6912.20	6991.66	7043.98	7062.18
85.0	6768.04	6754.51	6716.94	6664.67	6613.57	6584.10	6593.57	6645.12	6725.15	6812.57	6888.30	6938.85	6956.53
90.0	6853.68	6837.53	6791.83	6725.14	6652.45	6594.46	6572.02	6594.46	6652.45	6725.14	6791.83	6837.53	6853.68

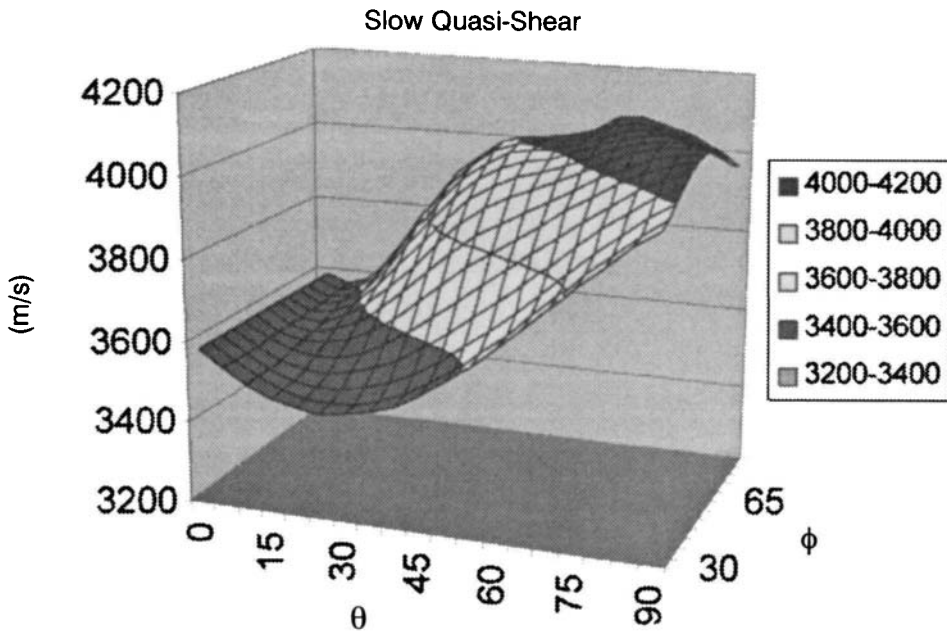


FIGURE 4 Bulk wave velocities (m/s), acoustic wave - slow quasi-shear; data set - Smith and Welsh [3]; temperature - 0.0°C; stoichiometry - unknown.

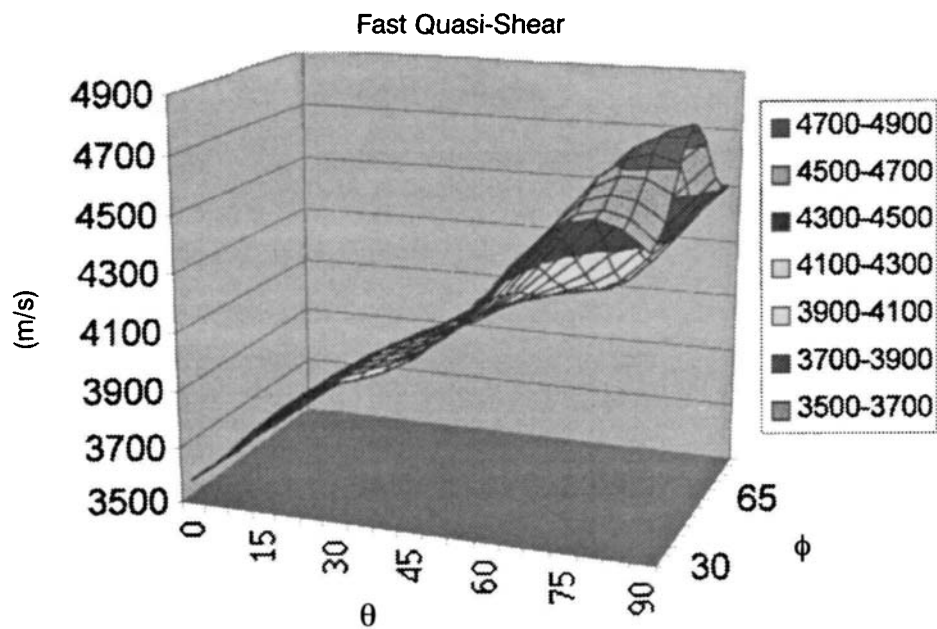


FIGURE 5 Bulk wave velocities (m/s), acoustic wave - fast quasi-shear; data set - Smith and Welsh [3]; temperature - 0.0°C; stoichiometry - unknown.

TABLE 4 Bulk wave velocities (m/s), acoustic wave - slow quasi-shear; data set - Smith and Welsh [3]; temperature - 0.0°C; stoichiometry - unknown.

$\theta\backslash\phi$ (degrees)	30.0	35.0	40.0	45.0	50.0	55.0	60.0	65.0	70.0	75.0	80.0	85.0	90.0
0.0	3588.36	3588.36	3588.36	3588.36	3588.36	3588.36	3588.36	3588.36	3588.36	3588.36	3588.36	3588.36	3588.36
5.0	3546.64	3546.89	3547.62	3548.81	3550.40	3552.30	3554.41	3556.60	3558.72	3560.62	3562.13	3563.10	3563.44
10.0	3511.90	3512.86	3515.71	3520.32	3526.49	3533.95	3542.34	3551.25	3560.15	3568.41	3575.26	3579.87	3581.51
15.0	3485.44	3487.53	3493.68	3503.60	3516.84	3532.77	3550.68	3569.74	3589.00	3607.35	3623.30	3634.73	3639.00
20.0	3468.26	3471.82	3482.27	3499.02	3521.11	3547.36	3576.44	3606.97	3637.57	3666.88	3693.23	3713.79	3722.41
25.0	3461.02	3466.31	3481.82	3506.41	3538.38	3575.65	3616.02	3657.32	3697.66	3735.47	3769.47	3798.01	3813.16
30.0	3463.99	3471.19	3492.14	3525.01	3567.04	3614.98	3665.49	3715.48	3762.44	3804.57	3840.85	3870.99	3893.84
35.0	3477.07	3486.17	3512.50	3553.32	3604.63	3661.81	3720.30	3776.13	3826.26	3868.75	3902.78	3928.39	3943.09
40.0	3499.75	3510.55	3541.60	3589.13	3647.77	3711.50	3774.71	3832.85	3882.79	3922.87	3952.67	3972.94	3983.99
45.0	3531.15	3543.26	3577.79	3629.87	3692.67	3758.91	3822.21	3877.98	3923.68	3958.51	3982.85	3997.60	4002.88
50.0	3570.12	3583.02	3619.50	3673.48	3736.78	3801.09	3859.83	3909.04	3947.36	3975.18	3993.74	4004.28	4007.69
55.0	3615.25	3628.47	3665.45	3719.07	3780.02	3839.59	3891.71	3933.66	3965.27	3987.75	4002.59	4011.03	4013.78
60.0	3664.95	3678.14	3714.65	3766.48	3823.69	3877.75	3923.59	3959.65	3986.60	4005.96	4019.37	4028.09	4031.62
65.0	3717.58	3730.52	3765.97	3815.29	3868.26	3916.93	3957.28	3988.65	4012.19	4029.69	4043.28	4055.89	4068.73
70.0	3771.44	3784.00	3818.00	3864.31	3912.72	3955.96	3990.94	4017.62	4037.27	4051.47	4061.71	4069.25	4072.98
75.0	3824.88	3836.92	3869.09	3911.84	3955.09	3992.32	4021.24	4042.11	4055.92	4063.35	4064.60	4061.01	4058.28
80.0	3876.33	3887.68	3917.54	3955.96	3993.12	4023.35	4045.07	4058.60	4064.42	4062.52	4053.35	4041.24	4035.41
85.0	3924.33	3934.80	3961.72	3994.81	4024.72	4046.83	4060.20	4065.13	4061.67	4049.74	4031.15	4012.77	4004.92
90.0	3967.57	3976.91	4000.08	4026.62	4048.07	4061.09	4065.37	4061.09	4048.07	4026.62	4000.08	3976.91	3967.57

TABLE 5 Bulk wave velocities (m/s), acoustic wave - fast quasi-shear; data set - Smith and Welsh [3];
temperature - 0.0°C; stoichiometry - unknown.

$\theta\backslash\phi$ (degrees)	30.0	35.0	40.0	45.0	50.0	55.0	60.0	65.0	70.0	75.0	80.0	85.0	90.0
0.0	3588.36	3588.36	3588.36	3588.36	3588.36	3588.36	3588.36	3588.36	3588.36	3588.36	3588.36	3588.36	3588.36
5.0	3648.78	3648.59	3648.04	3647.13	3645.92	3644.46	3642.82	3641.10	3639.41	3637.89	3636.67	3635.88	3635.60
10.0	3729.38	3728.88	3727.39	3724.94	3721.57	3717.37	3712.46	3707.04	3701.38	3695.91	3691.19	3687.92	3686.74
15.0	3812.87	3812.19	3810.14	3806.74	3801.96	3795.84	3788.41	3779.79	3770.19	3760.11	3750.48	3743.01	3740.09
20.0	3885.54	3884.87	3882.88	3879.50	3874.70	3868.38	3860.45	3850.84	3839.50	3826.58	3812.70	3799.94	3793.97
25.0	3940.77	3940.25	3938.66	3935.96	3932.08	3926.91	3920.28	3911.98	3901.76	3889.32	3874.49	3857.87	3846.76
30.0	3979.77	3979.36	3978.13	3976.06	3973.13	3969.28	3964.43	3958.40	3950.91	3941.56	3929.75	3914.70	3896.94
35.0	4009.93	4009.51	4008.27	4006.23	4003.43	3999.93	3995.79	3991.04	3985.65	3979.42	3971.92	3962.41	3953.09
40.0	4041.74	4041.20	4039.59	4036.93	4033.29	4028.76	4023.53	4017.82	4011.91	4006.07	4000.35	3994.28	3987.90
45.0	4085.38	4084.71	4082.68	4079.26	4074.42	4068.17	4060.61	4052.03	4042.98	4034.22	4026.62	4020.99	4018.57
50.0	4147.66	4147.02	4145.00	4141.38	4135.76	4127.72	4116.92	4103.44	4088.06	4072.41	4058.71	4049.31	4045.95
55.0	4230.11	4229.79	4228.61	4225.79	4220.07	4209.81	4193.57	4170.98	4143.56	4114.79	4089.32	4071.74	4065.46
60.0	4327.92	4328.39	4329.26	4328.77	4323.92	4310.93	4286.71	4250.74	4206.17	4159.19	4117.37	4087.77	4076.61
65.0	4430.12	4432.03	4436.75	4441.05	4439.32	4424.72	4392.14	4341.26	4277.48	4210.16	4149.63	4103.89	4079.14
70.0	4520.75	4524.92	4535.92	4548.76	4554.54	4542.43	4504.73	4441.40	4360.62	4275.62	4200.73	4148.28	4128.51
75.0	4582.03	4589.24	4609.02	4634.87	4654.41	4652.02	4616.29	4547.03	4455.51	4359.59	4278.35	4226.69	4209.74
80.0	4600.01	4610.59	4640.50	4682.65	4722.05	4738.10	4714.36	4648.96	4555.66	4456.70	4374.36	4323.21	4306.51
85.0	4570.81	4584.34	4623.59	4682.07	4743.88	4784.87	4783.18	4732.95	4648.21	4554.09	4474.84	4425.09	4408.60
90.0	4502.08	4517.61	4563.63	4635.00	4716.35	4782.49	4808.18	4782.49	4716.35	4635.00	4563.63	4517.61	4502.08

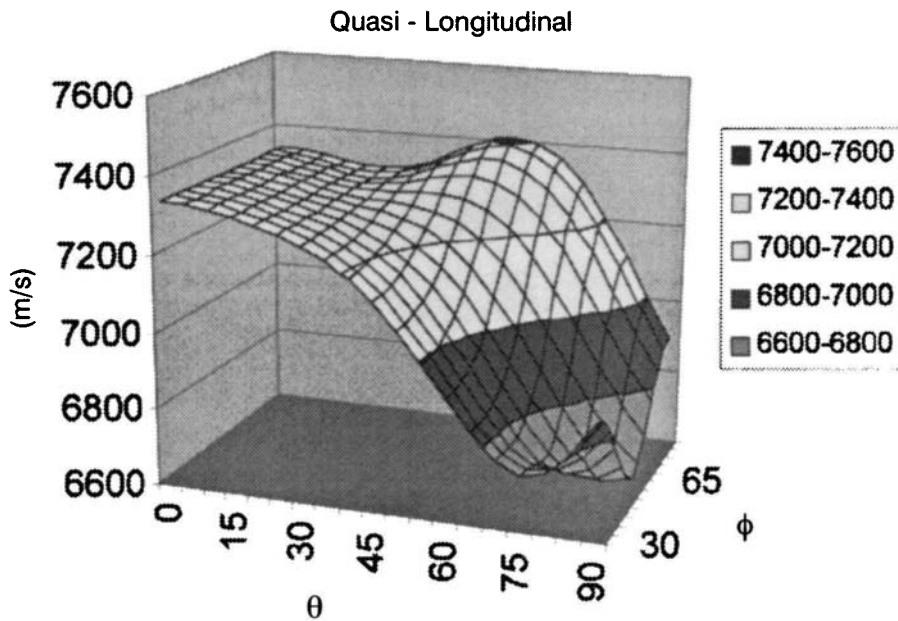


FIGURE 6 Bulk wave velocities (m/s), acoustic wave - quasi-longitudinal; data set - Smith and Welsh [3]; temperature - 0.0°C; stoichiometry - unknown.

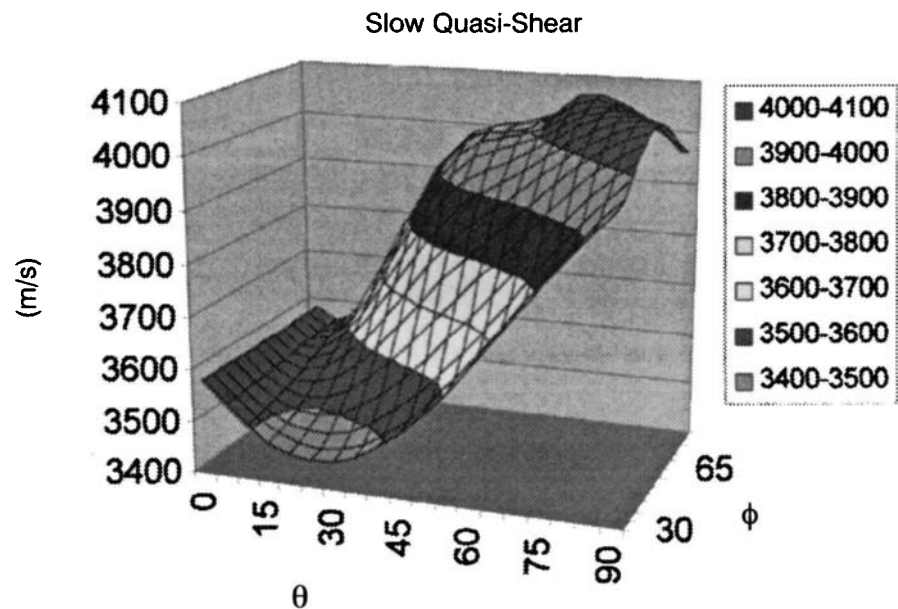


FIGURE 7 Bulk wave velocities (m/s), acoustic wave - slow quasi-shear; data set - Smith and Welsh [3]; temperature - 25.0°C; stoichiometry - unknown.

TABLE 6 Bulk wave velocities (m/s), acoustic wave - quasi-longitudinal; data set - Smith and Welsh [3]);
temperature - 0.0°C; stoichiometry - unknown.

$\theta\backslash\phi$ (degrees)	30.0	35.0	40.0	45.0	50.0	55.0	60.0	65.0	70.0	75.0	80.0	85.0	90.0
0.0	7340.91	7340.91	7340.91	7340.91	7340.91	7340.91	7340.91	7340.91	7340.91	7340.91	7340.91	7340.91	7340.91
5.0	7337.36	7337.36	7337.36	7337.35	7337.34	7337.33	7337.32	7337.32	7337.31	7337.30	7337.29	7337.29	7337.29
10.0	7327.71	7327.70	7327.69	7327.66	7327.63	7327.59	7327.55	7327.51	7327.47	7327.44	7327.42	7327.40	7327.40
15.0	7314.00	7314.00	7314.01	7314.02	7314.04	7314.07	7314.12	7314.17	7314.23	7314.28	7314.33	7314.36	7314.37
20.0	7297.94	7298.00	7298.19	7298.50	7298.94	7299.50	7300.14	7300.83	7301.52	7302.15	7302.66	7302.99	7303.11
25.0	7279.71	7279.94	7280.64	7281.82	7283.45	7285.51	7287.90	7290.48	7293.06	7295.42	7297.31	7298.54	7298.97
30.0	7257.54	7258.10	7259.79	7262.63	7266.63	7271.72	7277.69	7284.20	7290.77	7296.79	7301.66	7304.83	7305.93
35.0	7228.24	7229.29	7232.46	7237.87	7245.59	7255.53	7267.37	7280.43	7293.72	7305.99	7315.94	7322.44	7324.70
40.0	7188.42	7190.06	7195.08	7203.76	7216.36	7232.90	7252.89	7275.21	7298.10	7319.35	7336.65	7347.96	7351.90
45.0	7135.72	7137.95	7144.86	7157.06	7175.19	7199.50	7229.42	7263.24	7298.18	7330.75	7357.30	7374.66	7380.69
50.0	7069.85	7072.50	7080.88	7096.14	7119.60	7151.97	7192.66	7239.30	7287.85	7333.21	7370.18	7394.33	7402.72
55.0	6993.25	6995.94	7004.79	7021.75	7049.20	7088.71	7139.82	7199.40	7261.92	7320.48	7368.17	7399.27	7410.07
60.0	6911.59	6913.72	6921.29	6937.48	6966.26	7010.51	7070.22	7141.48	7217.08	7288.13	7345.97	7383.64	7396.70
65.0	6834.13	6834.82	6838.62	6850.31	6876.09	6920.93	6985.73	7065.92	7152.39	7234.15	7300.77	7344.13	7359.16
70.0	6773.43	6771.61	6768.54	6770.83	6787.59	6826.83	6891.21	6975.80	7069.56	7159.21	7232.53	7280.29	7296.84
75.0	6743.33	6738.04	6725.06	6712.73	6713.27	6738.73	6794.92	6877.38	6973.28	7066.88	7144.11	7194.58	7212.09
80.0	6754.23	6745.01	6720.44	6689.80	6667.71	6670.54	6708.86	6780.49	6871.57	6963.96	7041.51	7092.58	7110.34
85.0	6807.56	6794.71	6759.16	6710.10	6662.88	6636.82	6647.85	6698.56	6776.15	6860.77	6934.16	6983.22	7000.39
90.0	6894.48	6878.92	6834.97	6771.06	6701.74	6646.77	6625.58	6646.77	6701.74	6771.06	6834.97	6878.92	6894.48

TABLE 7 Bulk wave velocities (m/s), acoustic wave - slow quasi-shear; data set - Smith and Welsh [3]; temperature - 25.0°C; stoichiometry - unknown.

$\theta\backslash\phi$ (degrees)	30.0	35.0	40.0	45.0	50.0	55.0	60.0	65.0	70.0	75.0	80.0	85.0	90.0
0.0	3580.96	3580.96	3580.96	3580.96	3580.96	3580.96	3580.96	3580.96	3580.96	3580.96	3580.96	3580.96	3580.96
5.0	3539.35	3539.60	3540.33	3541.52	3543.09	3544.97	3547.06	3549.23	3551.33	3553.21	3554.71	3555.67	3556.00
10.0	3504.78	3505.74	3508.56	3513.13	3519.25	3526.65	3534.98	3543.81	3552.63	3560.81	3567.59	3572.15	3573.77
15.0	3478.51	3480.58	3486.69	3496.54	3509.68	3525.50	3543.27	3562.18	3581.29	3599.48	3615.28	3626.57	3630.78
20.0	3461.55	3465.08	3475.46	3492.09	3514.03	3540.11	3568.99	3599.32	3629.71	3658.81	3684.94	3705.25	3713.72
25.0	3454.54	3459.80	3475.20	3499.63	3531.39	3568.44	3608.55	3649.62	3689.74	3727.34	3761.15	3789.42	3804.21
30.0	3457.76	3464.91	3485.73	3518.38	3560.15	3607.81	3658.04	3707.77	3754.52	3796.50	3832.69	3862.77	3884.93
35.0	3471.08	3480.12	3506.29	3546.86	3597.87	3654.72	3712.90	3768.46	3818.40	3860.79	3894.82	3920.58	3935.89
40.0	3493.99	3504.73	3535.59	3582.85	3641.15	3704.54	3767.43	3825.30	3875.06	3915.04	3944.87	3965.28	3976.95
45.0	3525.61	3537.65	3571.99	3623.78	3686.24	3752.14	3815.15	3870.71	3916.27	3951.03	3975.37	3990.15	3995.47
50.0	3564.77	3577.60	3613.87	3667.57	3730.55	3794.58	3853.09	3902.17	3940.43	3968.25	3986.82	3997.39	4000.82
55.0	3610.05	3623.20	3659.98	3713.32	3773.98	3833.30	3885.26	3927.11	3958.70	3981.19	3996.07	4004.54	4007.30
60.0	3659.87	3672.99	3709.30	3760.85	3817.77	3871.60	3917.28	3953.27	3980.18	3999.55	4013.00	4021.80	4025.38
65.0	3712.58	3725.44	3760.68	3809.71	3862.39	3910.83	3951.01	3982.29	4005.79	4023.29	4036.93	4049.64	4062.59
70.0	3766.48	3778.95	3812.72	3858.74	3906.84	3949.83	3984.65	4011.23	4030.85	4045.07	4055.42	4063.18	4067.11
75.0	3819.91	3831.86	3863.79	3906.23	3949.16	3986.15	4014.91	4035.70	4049.50	4057.02	4058.48	4055.19	4052.61
80.0	3871.32	3882.58	3912.18	3950.28	3987.12	4017.12	4038.70	4052.18	4058.06	4056.32	4047.43	4035.62	4029.92
85.0	3919.24	3929.62	3956.26	3989.02	4018.63	4040.53	4053.80	4058.73	4055.39	4043.69	4025.41	4007.32	3999.59
90.0	3962.38	3971.61	3994.50	4020.71	4041.88	4054.74	4058.97	4054.74	4041.88	4020.71	3994.50	3971.61	3962.38

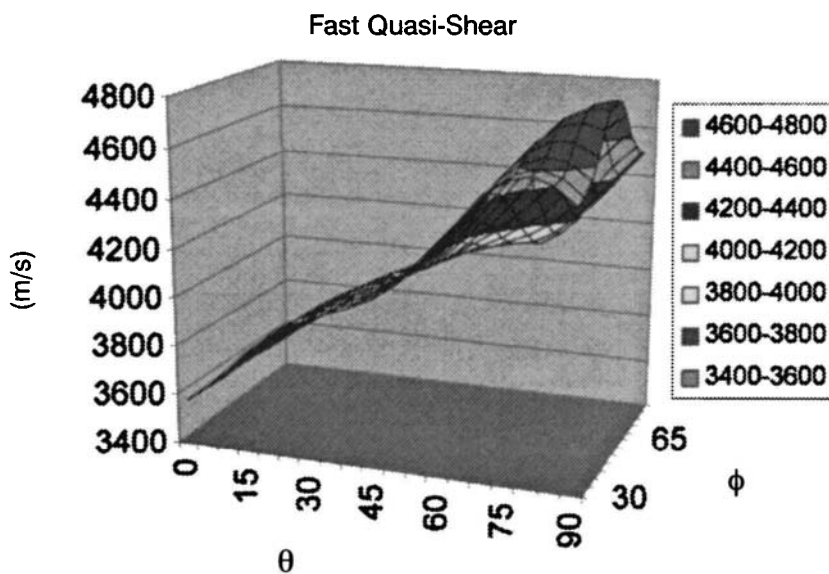


FIGURE 8 Bulk wave velocities (m/s), acoustic wave - fast quasi-shear; data set - Smith and Welsh [3]; temperature - 25.0°C; stoichiometry - unknown.

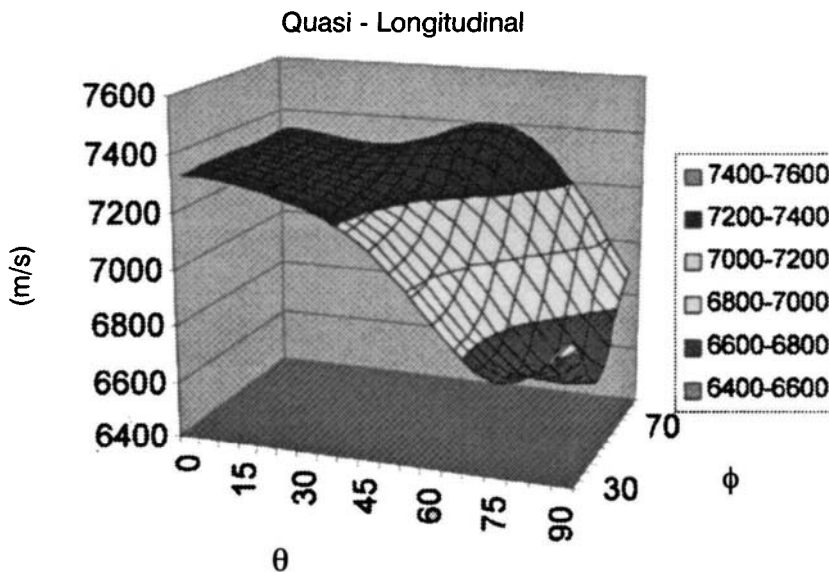


FIGURE 9 Bulk wave velocities (m/s), acoustic wave - quasi-longitudinal; data set - Smith and Welsh [3]; temperature - 25.0°C; stoichiometry - unknown.

TABLE 8 Bulk wave velocities (m/s), acoustic wave - fast quasi-shear; data set - Smith and Welsh [3]; temperature - 25.0°C; stoichiometry - unknown.

$\theta\backslash\phi$ (degrees)	30.0	35.0	40.0	45.0	50.0	55.0	60.0	65.0	70.0	75.0	80.0	85.0	90.0
0.0	3580.96	3580.96	3580.96	3580.96	3580.96	3580.96	3580.96	3580.96	3580.96	3580.96	3580.96	3580.96	3580.96
5.0	3641.18	3640.99	3640.44	3639.54	3638.34	3636.89	3635.27	3633.56	3631.89	3630.38	3629.17	3628.39	3628.12
10.0	3721.50	3721.00	3719.52	3717.08	3713.74	3709.56	3704.69	3699.31	3693.70	3688.28	3683.61	3680.37	3679.21
15.0	3804.81	3804.13	3802.10	3798.70	3793.95	3787.85	3780.45	3771.87	3762.34	3752.33	3742.80	3735.43	3732.55
20.0	3877.54	3876.88	3874.88	3871.50	3866.68	3860.36	3852.43	3842.83	3831.53	3818.67	3804.90	3792.31	3786.47
25.0	3933.10	3932.57	3930.96	3928.23	3924.32	3919.10	3912.42	3904.08	3893.82	3881.36	3866.57	3850.11	3839.33
30.0	3972.62	3972.20	3970.93	3968.82	3965.82	3961.90	3956.95	3950.81	3943.22	3933.76	3921.84	3906.72	3889.61
35.0	4003.37	4002.94	4001.67	3999.57	3996.69	3993.09	3988.83	3983.95	3978.40	3972.00	3964.29	3954.50	3944.53
40.0	4035.75	4035.20	4033.55	4030.83	4027.10	4022.47	4017.11	4011.25	4005.19	3999.17	3993.24	3986.91	3979.88
45.0	4079.84	4079.15	4077.08	4073.60	4068.66	4062.27	4054.56	4045.82	4036.60	4027.67	4019.93	4014.18	4011.70
50.0	4142.43	4141.77	4139.70	4135.99	4130.25	4122.04	4111.04	4097.36	4081.79	4065.96	4052.13	4042.65	4039.27
55.0	4225.05	4224.71	4223.47	4220.55	4214.68	4204.23	4187.76	4164.97	4137.38	4108.48	4082.91	4065.28	4058.98
60.0	4322.93	4323.38	4324.19	4323.59	4318.58	4305.40	4280.97	4244.83	4200.13	4153.08	4111.21	4081.54	4070.33
65.0	4425.12	4427.02	4431.69	4435.89	4434.01	4419.23	4386.47	4335.46	4271.62	4204.28	4143.72	4097.92	4073.07
70.0	4515.69	4519.86	4530.84	4543.62	4549.27	4537.00	4499.14	4435.71	4354.89	4269.88	4194.94	4142.33	4122.38
75.0	4576.84	4584.07	4603.87	4629.70	4649.17	4646.65	4610.78	4541.43	4449.86	4353.90	4272.53	4220.65	4203-58
80.0	4594.62	4605.23	4635.21	4677.42	4716.82	4732.79	4708.94	4643.45	4550.08	4451.02	4368.51	4317.16	4300.36
85.0	4565.16	4578.74	4618.10	4676.72	4738.60	4779.59	4777.84	4727.53	4642.71	4548.47	4469.03	4419.10	4402.53
90.0	4496.18	4511.78	4557.95	4629.50	4710.96	4777.16	4802.87	4777.16	4710.96	4629.50	4557.95	4511.78	4496.18

TABLE 9 Bulk wave velocities (m/s), acoustic wave - quasi-longitudinal; data set - Smith and Welsh [3]; temperature - 25.0°C; stoichiometry - unknown.

$\theta \backslash \phi$ (degrees)	30.0	35.0	40.0	45.0	50.0	55.0	60.0	65.0	70.0	75.0	80.0	85.0	90.0
0.0	7333.81	7333.81	7333.81	7333.81	7333.81	7333.81	7333.81	7333.81	7333.81	7333.81	7333.81	7333.81	7333.81
5.0	7330.28	7330.28	7330.28	7330.27	7330.27	7330.26	7330.25	7330.24	7330.24	7330.23	7330.22	7330.22	7330.22
10.0	7320.65	7320.65	7320.63	7320.61	7320.58	7320.55	7320.51	7320.48	7320.45	7320.42	7320.40	7320.39	7320.39
15.0	7306.91	7306.92	7306.93	7306.95	7306.99	7307.04	7307.10	7307.17	7307.24	7307.31	7307.37	7307.40	7307.42
20.0	7290.71	7290.78	7290.98	7291.32	7291.79	7292.37	7293.04	7293.77	7294.49	7295.15	7295.68	7296.02	7296.14
25.0	7272.22	7272.46	7273.18	7274.39	7276.06	7278.17	7280.61	7283.24	7285.86	7288.25	7290.18	7291.42	7291.85
30.0	7249.67	7250.24	7251.95	7254.84	7258.90	7264.04	7270.08	7276.65	7283.26	7289.32	7294.22	7297.40	7298.51
35.0	7219.91	7220.97	7224.18	7229.65	7237.43	7247.44	7259.35	7272.47	7285.79	7298.09	7308.06	7314.57	7316.83
40.0	7179.59	7181.24	7186.31	7195.06	7207.74	7224.35	7244.41	7266.78	7289.70	7310.96	7328.26	7339.57	7343.50
45.0	7126.38	7128.62	7135.59	7147.88	7166.10	7190.51	7220.50	7254.36	7289.32	7321.88	7348.40	7365.74	7371.77
50.0	7060.00	7062.67	7071.13	7086.50	7110.08	7142.56	7183.33	7230.02	7278.56	7323.90	7360.84	7384.96	7393.33
55.0	6982.91	6985.64	6994.58	7011.67	7039.28	7078.93	7130.13	7189.76	7252.28	7310.81	7358.45	7389.52	7400.30
60.0	6900.80	6902.97	6910.65	6927.01	6955.96	7000.39	7060.22	7131.55	7207.16	7278.17	7335.96	7373.59	7386.63
65.0	6822.93	6823.66	6827.58	6839.46	6865.46	6910.50	6975.46	7055.73	7142.22	7223.95	7290.52	7333.84	7348.85
70.0	6761.90	6760.12	6757.17	6759.66	6776.65	6816.12	6880.69	6965.38	7059.18	7148.79	7222.07	7269.79	7286.33
75.0	6731.60	6726.35	6713.48	6701.33	6702.08	6727.78	6784.16	6866.74	6962.68	7056.26	7133.45	7183.88	7201.37
80.0	6742.48	6733.28	6708.80	6678.29	6656.37	6659.39	6697.89	6769.63	6860.75	6953.12	7030.64	7081.67	7099.42
85.0	6795.93	6783.11	6747.62	6698.64	6651.52	6625.58	6636.72	6687.50	6765.11	6849.71	6923.05	6972.07	6989.23
90.0	6883.08	6867.53	6823.63	6759.77	6690.50	6635.56	6614.38	6635.56	6690.50	6759.77	6823.63	6867.53	6883.08

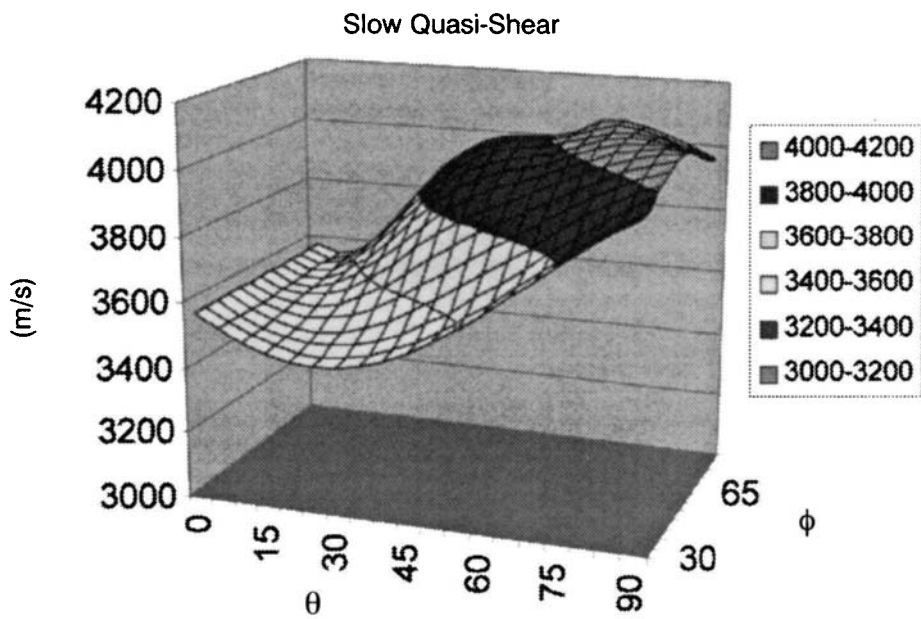


FIGURE 10 Bulk wave velocities (m/s), acoustic wave - slow quasi-shear; data set - Smith and Welsh [3]; temperature - 50.0°C; stoichiometry - unknown.

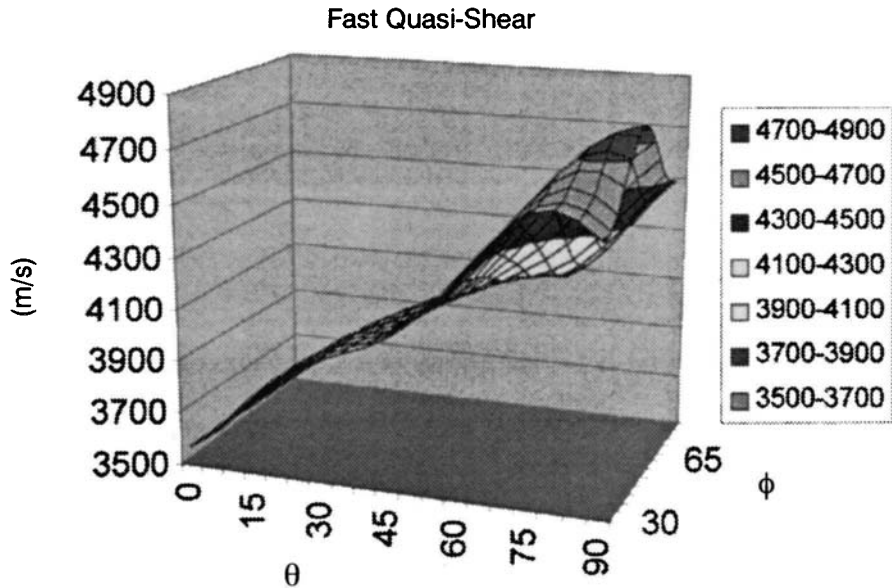


FIGURE 11 Bulk wave velocities (m/s), acoustic wave - fast quasi-shear; data set - Smith and Welsh [3]; temperature - 50.0°C; stoichiometry - unknown.

TABLE 10 Bulk wave velocities (m/s), acoustic wave - slow quasi-shear; data set - Smith and Welsh [3];
temperature - 50.0°C; stoichiometry - unknown.

$\theta\backslash\phi$ (degrees)	30.0	35.0	40.0	45.0	50.0	55.0	60.0	65.0	70.0	75.0	80.0	85.0	90.0
0.0	3573.53	3573.53	3573.53	3573.53	3573.53	3573.53	3573.53	3573.53	3573.53	3573.53	3573.53	3573.53	3573.53
5.0	3532.05	3532.29	3533.02	3534.19	3535.75	3537.62	3539.69	3541.84	3543.92	3545.78	3547.26	3548.22	3548.55
10.0	3497.63	3498.58	3501.38	3505.92	3511.99	3519.33	3527.60	3536.36	3545.10	3553.20	3559.92	3564.43	3566.02
15.0	3471.56	3473.61	3479.67	3489.46	3502.50	3518.21	3535.85	3554.62	3573.58	3591.61	3607.26	3618.42	3622.58
20.0	3454.81	3458.32	3468.63	3485.15	3506.94	3532.84	3561.54	3591.66	3621.86	3650.75	3676.66	3696.74	3705.06
25.0	3448.04	3453.27	3468.56	3492.83	3524.40	3561.21	3601.09	3641.92	3681.82	3719.23	3752.83	3780.85	3795.30
30.0	3451.51	3458.61	3479.29	3511.75	3553.26	3600.65	3650.59	3700.07	3746.61	3788.44	3824.53	3854.53	3876.07
35.0	3465.07	3474.06	3500.06	3540.39	3591.10	3647.64	3705.51	3760.81	3810.55	3852.84	3886.86	3912.75	3928.67
40.0	3488.22	3498.89	3529.57	3576.55	3634.53	3697.58	3760.15	3817.77	3867.34	3907.23	3937.06	3957.61	3969.88
45.0	3520.06	3532.02	3566.17	3617.67	3679.80	3745.37	3808.10	3863.44	3908.86	3943.56	3967.89	3982.71	3988.06
50.0	3559.40	3572.16	3608.24	3661.66	3724.32	3788.06	3846.36	3895.30	3933.50	3961.31	3979.90	3990.50	3993.93
55.0	3604.84	3617.91	3654.50	3707.57	3767.94	3827.00	3878.79	3920.56	3952.12	3974.62	3989.52	3998.03	4000.81
60.0	3654.78	3667.82	3703.93	3755.20	3811.84	3865.43	3910.96	3946.86	3973.74	3993.12	4006.62	4015.49	4019.12
65.0	3707.56	3720.35	3755.38	3804.12	3856.51	3904.71	3944.73	3975.91	3999.37	4016.87	4030.56	4043.36	4056.43
70.0	3761.50	3773.89	3807.44	3853.15	3900.95	3943.69	3978.34	4004.82	4024.40	4038.65	4049.11	4057.10	4061.23
75.0	3814.94	3826.79	3858.48	3900.60	3943.22	3979.96	4008.55	4029.26	4043.06	4050.67	4052.35	4049.35	4046.92
80.0	3866.30	3877.46	3906.81	3944.57	3981.11	4010.87	4032.30	4045.74	4051.67	4050.10	4041.50	4029.98	4024.41
85.0	3914.14	3924.41	3950.79	3983.21	4012.52	4034.21	4047.38	4052.31	4049.08	4037.62	4019.66	4001.86	3994.24
90.0	3957.17	3966.29	3988.90	4014.78	4035.68	4048.37	4052.54	4048.37	4035.68	4014.78	3988.90	3966.29	3957.17

TABLE 11 Bulk wave velocities (m/s), acoustic wave - fast quasi-shear; data set - Smith and Welsh [3];
temperature - 50.0°C; stoichiometry - unknown.

$\theta\backslash\phi$ (degrees)	30.0	35.0	40.0	45.0	50.0	55.0	60.0	65.0	70.0	75.0	80.0	85.0	90.0
0.0	3573.53	3573.53	3573.53	3573.53	3573.53	3573.53	3573.53	3573.53	3573.53	3573.53	3573.53	3573.53	3573.53
5.0	3633.55	3633.37	3632.82	3631.93	3630.74	3629.30	3627.69	3626.00	3624.34	3622.85	3621.65	3620.87	3620.60
10.0	3713.61	3713.11	3711.64	3709.21	3705.89	3701.74	3696.90	3691.56	3686.00	3680.62	3676.00	3672.80	3671.65
15.0	3796.75	3796.08	3794.05	3790.66	3785.92	3779.84	3772.48	3763.94	3754.47	3744.54	3735.10	3727.83	3724.99
20.0	3869.55	3868.88	3866.87	3863.49	3858.67	3852.34	3844.41	3834.82	3823.55	3810.75	3797.09	3784.67	3778.94
25.0	3925.42	3924.88	3923.26	3920.50	3916.55	3911.29	3904.56	3896.18	3885.88	3873.41	3858.65	3842.35	3831.88
30.0	3965.45	3965.02	3963.73	3961.57	3958.51	3954.50	3949.46	3943.23	3935.53	3925.96	3913.94	3898.77	3882.25
35.0	3996.80	3996.36	3995.05	3992.89	3989.94	3986.24	3981.86	3976.84	3971.14	3964.57	3956.66	3946.62	3936.01
40.0	4029.74	4029.18	4027.49	4024.70	4020.88	4016.15	4010.66	4004.66	3998.44	3992.25	3986.13	3979.55	3971.88
45.0	4074.28	4073.58	4071.47	4067.91	4062.87	4056.35	4048.49	4039.59	4030.20	4021.11	4013.22	4007.34	4004.81
50.0	4137.19	4136.51	4134.39	4130.59	4124.72	4116.34	4105.16	4091.27	4075.49	4059.50	4045.54	4035.98	4032.57
55.0	4219.98	4219.63	4218.33	4215.31	4209.28	4198.64	4181.96	4158.95	4131.19	4102.15	4076.50	4058.81	4052.48
60.0	4317.94	4318.37	4319.12	4318.42	4313.25	4299.87	4275.23	4238.92	4194.10	4146.97	4105.03	4075.30	4064.04
65.0	4420.14	4422.02	4426.65	4430.75	4428.72	4413.75	4380.81	4329.67	4265.75	4198.38	4137.80	4091.93	4066.98
70.0	4510.66	4514.82	4525.79	4538.50	4544.02	4531.58	4493.56	4430.03	4349.16	4264.14	4189.15	4136.36	4116.23
75.0	4571.69	4578.92	4598.75	4624.58	4643.97	4641.31	4605.30	4535.85	4444.23	4348.21	4266.71	4214.61	4197.41
80.0	4589.26	4599.89	4629.95	4672.23	4711.63	4727.52	4703.56	4637.96	4544.51	4445.35	4362.66	4311.10	4294.20
85.0	4559.53	4573.15	4612.65	4671.39	4733.36	4774.35	4772.55	4722.16	4637.24	4542.86	4463.23	4413.11	4396.46
90.0	4490.29	4505.95	4552.29	4624.01	4705.61	4771.88	4797.61	4771.88	4705.61	4624.01	4552.29	4505.95	4490.29

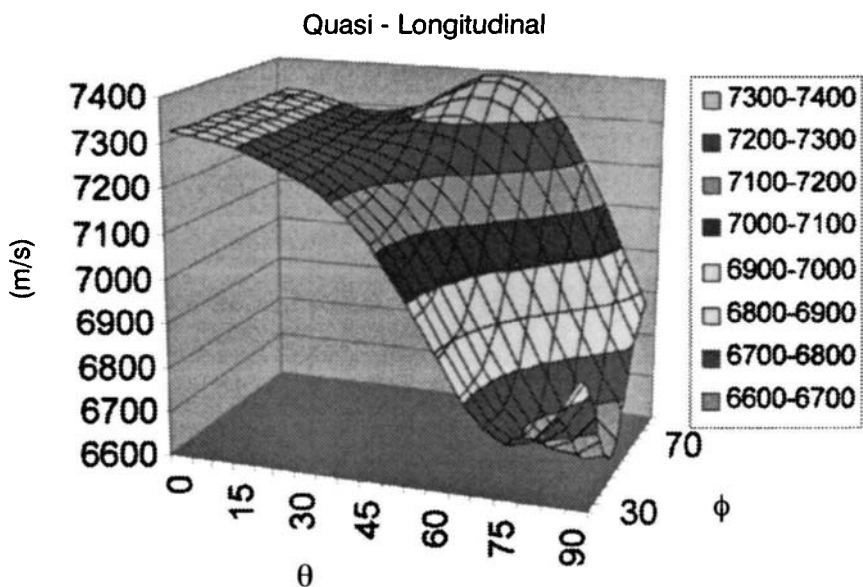


FIGURE 12 Bulk wave velocities (m/s), acoustic wave - quasi-longitudinal; data set - Smith and Welsh [3]; temperature - 50.0°C; stoichiometry - unknown.

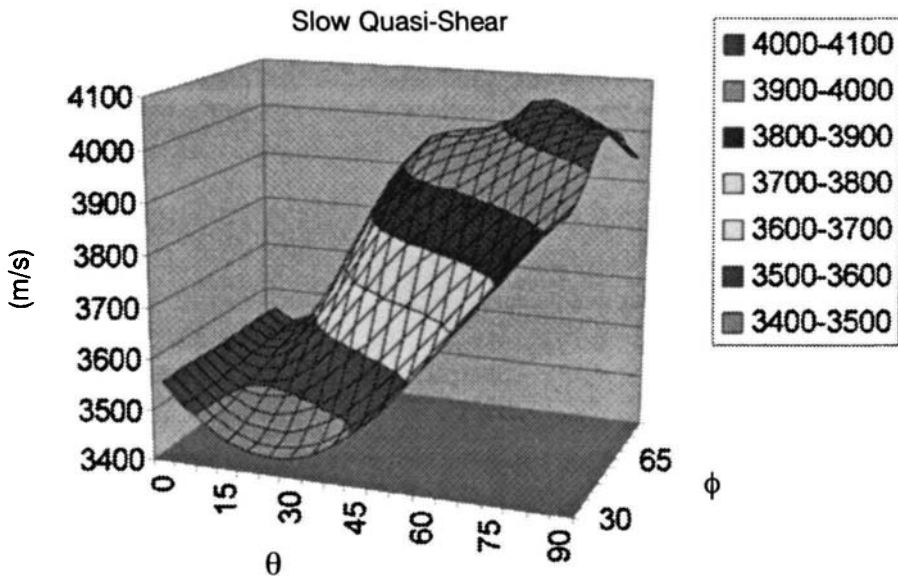


FIGURE 13 Bulk wave velocities (m/s), acoustic wave - slow quasi-shear; data set - Smith and Welsh [3]; temperature - 100.0°C; stoichiometry - unknown.

TABLE 12 Bulk wave velocities (m/s), acoustic wave - quasi-longitudinal; data set - Smith and Welsh [3]; temperature - 50.0°C; stoichiometry - unknown.

$\theta\backslash\phi$ (degrees)	30.0	35.0	40.0	45.0	50.0	55.0	60.0	65.0	70.0	75.0	80.0	85.0	90.0
0.0	7326.72	7326.72	7326.72	7326.72	7326.72	7326.72	7326.72	7326.72	7326.72	7326.72	7326.72	7326.72	7326.72
5.0	7323.20	7323.20	7323.20	7323.19	7323.19	7323.18	7323.17	7323.16	7313.16	7323.15	7323.15	7323.14	7323.14
10.0	7313.59	7313.58	7313.57	7313.55	7313.53	7313.50	7313.47	7313.44	7313.42	7313.40	7313.38	7313.37	7313.37
15.0	7299.81	7299.82	7299.84	7299.87	7299.92	7299.99	7300.06	7300.15	7300.24	7300.32	7300.39	7300.43	7300.45
20.0	7283.48	7283.55	7283.76	7284.12	7284.61	7285.23	7285.94	7286.70	7287.45	7288.13	7288.68	7289.03	7289.15
25.0	7264.72	7264.96	7265.71	7266.95	7268.67	7270.82	7273.30	7275.98	7278.65	7281.08	7283.03	7284.29	7284.73
30.0	7241.78	7242.36	7244.11	7247.04	7251.16	7256.36	7262.46	7269.08	7275.75	7281.85	7286.77	7289.97	7291.08
35.0	7211.57	7212.64	7215.89	7221.41	7229.26	7239.35	7251.32	7264.50	7277.87	7290.19	7300.18	7306.70	7308.97
40.0	7170.74	7172.41	7177.52	7186.34	7199.11	7215.81	7235.93	7258.35	7281.30	7302.58	7319.88	7331.19	7335.12
45.0	7117.02	7119.28	7126.31	7138.68	7157.01	7181.51	7211.58	7245.48	7280.46	7313.02	7339.53	7356.85	7362.87
50.0	7050.13	7052.83	7061.37	7076.85	7100.55	7133.15	7174.01	7220.74	7269.30	7314.61	7351.52	7375.61	7383.98
55.0	6972.55	6975.32	6984.35	7001.58	7029.34	7069.14	7120.45	7180.14	7242.66	7301.16	7348.77	7379.80	7390.57
60.0	6889.98	6892.19	6899.98	6916.50	6945.65	6990.25	7050.22	7121.63	7197.24	7268.23	7325.97	7363.57	7376.60
65.0	6811.70	6812.46	6816.51	6828.58	6854.80	6900.06	6965.19	7045.55	7132.06	7213.76	7280.29	7323.58	7338.57
70.0	6750.33	6748.60	6745.77	6748.46	6765.69	6805.39	6870.15	6954.96	7048.79	7138.39	7211.63	7259.32	7275.83
75.0	6719.84	6714.62	6701.86	6689.88	6690.86	6716.79	6773.38	6856.09	6952.07	7045.65	7122.80	7173.20	7190.68
80.0	6730.70	6721.53	6697.12	6666.74	6644.99	6648.21	6686.88	6758.75	6849.92	6942.29	7019.76	7070.76	7088.50
85.0	6784.29	6771.48	6736.05	6687.15	6640.13	6614.30	6625.54	6676.41	6754.05	6838.63	6911.94	6960.93	6978.07
90.0	6871.66	6856.14	6812.27	6748.46	6679.24	6624.31	6603.14	6624.31	6679.24	6748.46	6812.27	6856.14	6871.66

TABLE 13 Bulk wave velocities (m/s), acoustic wave - slow quasi-shear; data set - Smith and Welsh [3];
temperature - 100.0°C; stoichiometry - unknown.

$\theta\backslash\phi$ (degrees)	30.0	35.0	40.0	45.0	50.0	55.0	60.0	65.0	70.0	75.0	80.0	85.0	90.0
0.0	3558.59	3558.59	3558.59	3558.59	3558.59	3558.59	3558.59	3558.59	3558.59	3558.59	3558.59	3558.59	3558.59
5.0	3517.35	3517.60	3518.31	3519.46	3521.00	3522.84	3524.87	3526.99	3529.03	3530.86	3532.31	3533.25	3533.57
10.0	3483.26	3484.20	3486.96	3491.43	3497.41	3504.64	3512.78	3521.40	3529.99	3537.95	3544.53	3548.95	3550.52
15.0	3457.58	3459.60	3465.58	3475.23	3488.09	3503.58	3520.97	3539.47	3558.14	3575.88	3591.23	3602.15	3606.21
20.0	3441.27	3444.73	3454.90	3471.20	3492.71	3518.28	3546.61	3576.35	3606.16	3634.65	3660.14	3679.78	3687.85
25.0	3434.97	3440.13	3455.24	3479.20	3510.37	3546.74	3586.16	3626.53	3666.00	3703.02	3736.24	3763.76	3777.61
30.0	3438.94	3445.95	3466.38	3498.44	3539.46	3586.30	3635.71	3684.70	3730.83	3772.34	3808.22	3838.05	3858.46
35.0	3453.00	3461.88	3487.57	3527.42	3577.55	3633.46	3690.75	3745.53	3794.89	3836.95	3870.94	3897.02	3914.15
40.0	3476.62	3487.17	3517.49	3563.94	3621.27	3683.66	3745.62	3802.73	3851.94	3891.64	3921.47	3942.23	3955.68
45.0	3508.89	3520.73	3554.49	3605.43	3666.91	3731.84	3794.00	3848.92	3894.07	3928.63	3952.95	3967.85	3973.26
50.0	3548.62	3561.24	3596.93	3649.79	3711.84	3775.00	3832.86	3881.53	3919.61	3947.40	3966.04	3976.68	3980.15
55.0	3594.37	3607.30	3643.50	3696.02	3755.81	3814.38	3865.82	3907.40	3938.90	3961.41	3976.37	3984.96	3987.78
60.0	3644.55	3657.45	3693.15	3743.87	3799.95	3853.07	3898.28	3933.99	3960.81	3980.20	3993.78	4002.80	4006.54
65.0	3697.50	3710.13	3744.73	3792.89	3844.71	3892.42	3932.11	3963.09	3986.46	4003.98	4017.75	4030.76	4044.04
70.0	3751.51	3763.73	3796.83	3841.92	3889.12	3931.37	3965.66	3991.95	4011.45	4025.76	4036.42	4044.87	4049.41
75.0	3804.94	3816.61	3847.82	3889.29	3931.29	3967.53	3995.79	4016.33	4030.13	4037.92	4040.03	4037.62	4035.50
80.0	3856.22	3867.19	3896.02	3933.12	3969.02	3998.31	4019.46	4032.81	4038.84	4037.62	4029.58	4018.67	4013.35
85.0	3903.91	3913.97	3939.81	3971.55	4000.26	4021.53	4034.49	4039.43	4036.43	4025.42	4008.11	3990.89	3983.50
90.0	3946.71	3955.61	3977.67	4002.87	4023.21	4035.57	4039.63	4035.57	4023.21	4002.87	3977.67	3955.61	3946.71

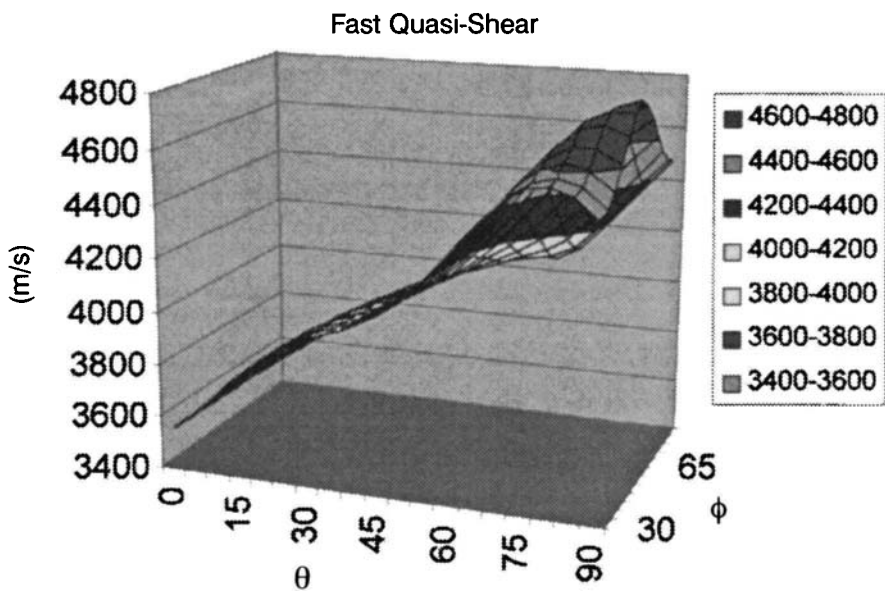


FIGURE 14 Bulk wave velocities (m/s), acoustic wave - fast quasi-shear; data set - Smith and Welsh [3]; temperature - 100.0°C; stoichiometry unknown.

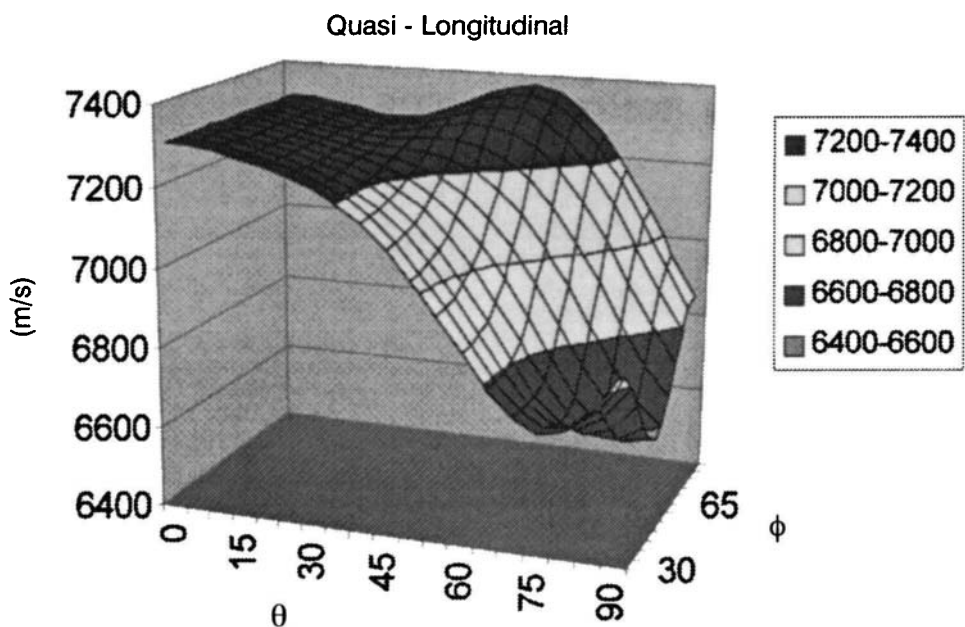


FIGURE 15 Bulk wave velocities (m/s), acoustic wave - quasi-longitudinal; data set - Smith and Welsh [3]; temperature - 100.0°C; stoichiometry unknown.

TABLE 14 Bulk wave velocities (m/s), acoustic wave - fast quasi-shear; data set - Smith and Welsh [3]; temperature - 100.0°C; stoichiometry unknown.

$\theta\backslash\phi$ (degrees)	30.0	35.0	40.0	45.0	50.0	55.0	60.0	65.0	70.0	75.0	80.0	85.0	90.0
0.0	3558.59	3558.59	3558.59	3558.59	3558.59	3558.59	3558.59	3558.59	3558.59	3558.59	3558.59	3558.59	3558.59
5.0	3618.23	3618.05	3617.51	3616.63	3615.46	3614.04	3612.45	3610.79	3609.16	3607.70	3606.52	3605.76	3605.49
10.0	3697.77	3697.28	3695.82	3693.43	3690.14	3686.04	3681.27	3676.00	3670.52	3665.24	3660.71	3657.58	3656.46
15.0	3780.61	3779.94	3777.92	3774.55	3769.84	3763.80	3756.50	3748.04	3738.68	3728.91	3719.65	3712.55	3709.79
20.0	3853.54	3852.87	3850.85	3847.45	3842.62	3836.28	3828.35	3818.79	3807.57	3794.90	3781.44	3769.32	3763.81
25.0	3910.03	3909.48	3907.83	3905.02	3900.99	3895.64	3888.83	3880.36	3870.00	3857.51	3842.82	3826.83	3816.89
30.0	3951.07	3950.62	3949.27	3947.02	3943.84	3939.69	3934.47	3928.04	3920.13	3910.37	3898.18	3882.95	3867.47
35.0	3983.59	3983.13	3981.75	3979.48	3976.37	3972.49	3967.88	3962.60	3956.60	3949.71	3941.43	3930.95	3919.05
40.0	4017.66	4017.06	4015.30	4012.39	4008.40	4003.45	3997.71	3991.43	3984.90	3978.38	3971.88	3964.86	3955.95
45.0	4063.11	4062.38	4060.18	4056.47	4051.23	4044.46	4036.30	4027.07	4017.34	4007.92	3999.73	3993.61	3990.96
50.0	4126.66	4125.94	4123.72	4119.74	4113.62	4104.91	4093.34	4079.04	4062.87	4046.53	4032.31	4022.58	4019.10
55.0	4209.83	4209.44	4208.02	4204.80	4198.48	4187.44	4170.33	4146.90	4118.77	4089.47	4063.62	4045.80	4039.42
60.0	4307.97	4308.37	4309.00	4308.09	4302.60	4288.82	4263.76	4227.09	4182.01	4134.71	4092.64	4062.76	4051.40
65.0	4410.22	4412.07	4416.61	4420.53	4418.19	4402.84	4369.52	4318.10	4254.02	4186.57	4125.92	4079.90	4054.75
70.0	4500.66	4504.82	4515.74	4528.33	4533.61	4520.83	4482.47	4418.70	4337.72	4252.64	4177.52	4124.37	4103.87
75.0	4561.45	4568.71	4588.59	4614.41	4633.66	4630.72	4594.41	4524.74	4432.98	4336.84	4255.05	4202.49	4185.04
80.0	4578.59	4589.30	4619.52	4661.94	4701.36	4717.10	4692.90	4627.07	4533.44	4434.04	4350.97	4298.96	4281.87
85.0	4548.31	4562.05	4601.80	4660.84	4722.98	4763.99	4762.08	4711.51	4626.38	4531.70	4451.66	4401.14	4384.33
90.0	4478.55	4494.34	4541.02	4613.13	4695.01	4761.44	4787.23	4761.44	4695.01	4613.13	4541.02	4494.34	4478.55

TABLE 15 Bulk wave velocities (m/s), acoustic wave - quasi-longitudinal; data set - Smith and Welsh [3]; temperature - 100.0°C; stoichiometry unknown.

$\theta\backslash\phi$ (degrees)	30.0	35.0	40.0	45.0	50.0	55.0	60.0	65.0	70.0	75.0	80.0	85.0	90.0
0.0	7312.51	7312.51	7312.51	7312.51	7312.51	7312.51	7312.51	7312.51	7312.51	7312.51	7312.51	7312.51	7312.51
5.0	7309.02	7309.02	7309.01	7309.01	7309.01	7309.00	7308.99	7308.99	7308.98	7308.98	7308.97	7308.97	7308.97
10.0	7299.43	7299.43	7299.42	7299.41	7299.39	7299.38	7299.36	7299.34	7299.33	7299.32	7299.31	7299.30	7299.30
15.0	7285.58	7285.59	7285.62	7285.68	7285.75	7285.85	7285.96	7286.08	7286.20	7286.31	7286.40	7286.46	7286.48
20.0	7268.96	7269.04	7269.28	7269.68	7270.23	7270.91	7271.68	7272.51	7273.32	7274.06	7274.64	7275.02	7275.15
25.0	7249.67	7249.93	7250.72	7252.02	7253.82	7256.07	7258.66	7261.44	7264.20	7266.70	7268.70	7270.00	7270.45
30.0	7225.98	7226.57	7228.38	7231.41	7235.63	7240.97	7247.19	7253.93	7260.70	7266.88	7271.86	7275.10	7276.22
35.0	7194.84	7195.93	7199.26	7204.90	7212.89	7223.13	7235.25	7248.54	7262.01	7274.41	7284.44	7290.98	7293.25
40.0	7153.00	7154.71	7159.92	7168.88	7181.82	7198.69	7218.97	7241.51	7264.54	7285.85	7303.17	7314.47	7318.40
45.0	7098.24	7100.55	7107.71	7120.26	7138.80	7163.50	7193.73	7227.75	7262.79	7295.35	7321.84	7339.13	7345.14
50.0	7030.34	7033.09	7041.78	7057.49	7081.45	7114.30	7155.35	7202.20	7250.79	7296.09	7332.95	7357.00	7365.35
55.0	6951.77	6954.60	6963.82	6981.34	7009.43	7049.53	7101.07	7160.90	7223.46	7281.92	7329.46	7360.44	7371.19
60.0	6868.26	6870.54	6878.57	6895.43	6924.97	6969.95	7030.21	7101.79	7177.45	7248.40	7306.07	7343.60	7356.61
65.0	6789.13	6789.98	6794.29	6806.74	6833.42	6879.12	6944.60	7025.18	7111.76	7193.43	7259.90	7303.12	7318.09
70.0	6727.09	6725.44	6722.87	6725.95	6743.67	6783.87	6849.04	6934.10	7028.03	7117.61	7190.79	7238.41	7254.91
75.0	6696.21	6691.07	6678.52	6666.89	6668.32	6694.74	6751.76	6834.75	6930.86	7024.43	7101.53	7151.86	7169.32
80.0	6707.04	6697.93	6673.68	6643.55	6622.14	6625.75	6664.80	6736.94	6828.23	6920.60	6998.03	7048.96	7066.68
85.0	6760.94	6748.16	6712.83	6664.08	6617.25	6591.63	6603.10	6654.14	6731.87	6816.45	6889.69	6938.62	6955.74
90.0	6848.80	6833.30	6789.50	6725.78	6656.62	6601.73	6580.56	6601.73	6656.62	6725.78	6789.50	6833.30	6848.80

REFERENCES

- [1] A.W. Warner, M. Onoe, G.A. Coquin [*J. Acoust. Soc. Am. (USA)* vol.42 no.6 (1967) p.1223-31]
- [2] T. Yamada, N. Niizeki, H. Toyoda [*Jpn. J. Appl. Phys. (Japan)* vol.6 no.2 (1967) p.151-5]
- [3] R.T. Smith, F.S. Welsh [*J. Appl. Phys. (USA)* vol.42 no.6 (1971) p.2219-30]
- [4] Y. Nakagawa, K. Yamanouchi, K. Shibayama [*J. Appl. Phys. (USA)* vol.44 no.9 (1973) p.3969-74]
- [5] R.A. Graham [*J. Appl. Phys. (USA)* vol.48 (1977) p.2153-63]
- [6] I. Tomono, S. Matsumura [*J. Phys. Soc. Jpn. (Japan)* vol.56 no.1 (1987) p.163-77]
- [7] I.A. Dankov, E.F. Tokarev, G.S. Kudryashov, K.G. Belobaev [*Inorg. Mater. (USA)* vol.19 no.7 (1983) p.1049-54]
- [8] E. Dieulesaint, D. Royer [*Elastic Waves in Solids* (John Wiley, 1980)]
- [9] C.S. Hartmann, S. Jen, M.A. Domalewski, J.C. Andle [*IEEE Ultrasonics Symposium Proc.* Denver, Colorado, USA, 14-16 October 1987, Ed. B.R. McAvoy (IEEE, New York, USA, 1988) p.161-7]

10.2 Attenuation of ultrasonic bulk waves in LiNbO₃

M.F. Lewis and C.L. West; updated by D. Craig

August 2001

This Datareview discusses ultrasonic waves in the frequency range from about 100 MHz to 10 GHz. At lower frequencies the losses are usually too low to measure accurately by ultrasonic techniques. At higher frequencies the losses are very high, and additionally transduction is difficult.

The attenuation of bulk acoustic waves in a solid can arise through a wide variety of mechanisms. These include both scattering and absorption mechanisms. The former category includes scattering losses due to specimen boundaries, dislocations, impurities and inclusions, and by electric/magnetic domain boundaries in ferroelectric/ferromagnetic media, LiNbO₃ being in the ferroelectric class. In the second category come absorption processes due to interactions of the ultrasonic wave with, for example, free electrons in metals, spin waves in magnetic media, and thermal phonons in all media. Further, in piezoelectric media such as LiNbO₃ an ultrasonic wave is, in general, accompanied by electric fields, and so is subject to dielectric losses. However, in the case of good single crystals of dielectric media such as well-poled highly insulating LiNbO₃ the attenuation of bulk acoustic waves in the frequency range of interest is normally dominated by a single mechanism, namely the interaction with thermal phonons. The relevant material parameters responsible for the phonon-phonon interactions are the third-order elastic constants [1]. At low temperatures ($T < 100$ K) the condition $\omega\tau \gg 1$ is satisfied, where ω is the ultrasonic frequency and τ the thermal phonon relaxation time. In these circumstances it is possible to describe the ultrasonic loss as arising from microscopic three-phonon collisions that individually conserve energy and wavevector. In this low-temperature regime the acoustic attenuation typically varies as ω^4 , the τ^4 factor largely reflecting the growth of the thermal phonon population with increasing temperature. In the case of longitudinal ultrasonic waves the variation with temperature may be even more rapid than τ^4 , as a result of the inability of any three-phonon collisions to satisfy precisely the conservation conditions [2]. Measurements on LiNbO₃ in this low-temperature regime have been reported by, for example, Smith et al [3] and Spencer and Lenzo [4].

At high temperatures, including room temperature, the condition $\omega\tau < 1$ is satisfied. As a consequence, the loss is best described as an interaction with the thermal phonon assembly as a whole, rather than with individual phonons. In this regime the ultrasonic attenuation varies as ω^2 and is only weakly dependent on temperature. One such loss mechanism that is readily visualised is the thermoelastic mechanism that arises from the irreversible spatial conduction of heat between the compressed and rarefied regions of the medium in the presence of a longitudinal ultrasonic wave. However, this mechanism is weak, and does not arise at all in the case of shear waves. Instead, the attenuation of all ultrasonic waves is believed to arise predominantly by a mechanism first proposed by Akheizer and discussed by Oliver and Slack [5] in which the disturbed thermal phonon distribution relaxes back towards local thermodynamic equilibrium through phonon-phonon interactions with a time constant τ . A useful phenomenological approach, which is valid for the Akheizer mechanism, is to add an imaginary term to the second-order elastic constants, c_{ijkl} , which then assume the form $c_{ijkl} + j\omega \eta_{ijkl}$ where η is a generalised phonon viscosity tensor. The attenuation α then takes the form

$$\alpha = \frac{\omega^2 \eta}{2\rho V^3} \text{ nepers/unit distance} \quad (1 \text{ neper} = 8.68 \text{ dB})$$

where ρ is the mass density, and V the ultrasonic velocity. This viscosity tensor approach is economical, as the knowledge of a small number of independent constants (six in the case of LiNbO_3 , ignoring piezoelectric complications) allows the attenuation of any bulk acoustic wave to be calculated, just as knowledge of the six independent second-order elastic constants enables the velocity of any wave to be calculated. In addition, this knowledge also allows one to calculate the inherent material attenuation of any other acoustic wave, for example surface acoustic waves. The effective phonon viscosity tensor elements of LiNbO_3 have been measured by Bajak et al [6] and in matrix notation are given by:

$$\eta_{11} = 0.6547$$

$$\eta_{12} = 0.2275$$

$$\eta_{13} = 0.2499$$

$$\eta_{14} = -0.0687$$

$$\eta_{33} = 0.3377$$

$$\eta_{44} = 0.1765$$

$$\eta_{66} = \frac{1}{2} (\eta_{11} - \eta_{12})$$

in units of $10^{-3} \text{ N/m}^2 \text{ s}$.

Typical bulk ultrasonic wave attenuation coefficients in lithium niobate at room temperature are 0.7 dB/cm at a frequency of 1 GHz. Of course, in poor-quality samples the attenuation may be higher due to a variety of other attenuation mechanisms, as discussed earlier.

REFERENCES

- [1] Y. Cho, K. Yamanouchi [Data review in this book: 4.3 Third-order elastic coefficients of LiNbO_3]
- [2] H.J. Maris [*Philos. Mag. (UK)* vol.9 (1964) p.901-10]
- [3] A.B. Smith, M. Kestigian, R.W. Kedzie, M.I. Grace [*J. Appl. Phys. (USA)* vol.38 (1967) p.4928-9]
- [4] E.G. Spencer, P.V. Lenzo [*J. Appl. Phys. (USA)* vol.38 (1967) p.423-4]
- [5] D.W. Oliver, G.A. Slack [*J. Appl. Phys. (USA)* vol.37 (1966) p.1542-8]
- [6] I.L. Bajak, A. McNab, J. Richter, C.D.W. Wilkinson [*J. Acoust. Soc. Am. (USA)* vol.69 no.3 (1981) p.689-95]

10.3 SAWs in LiNbO₃: properties of common orientations

D.F. Morgan; updated by D. Craig

August 2001

A INTRODUCTION

The commonest orientation for SAW devices is Y-Z lithium niobate, meaning that the active surface is normal to the crystal Y-axis and SAW propagation is along the crystal Z-axis. Compared with other materials, this orientation is advantageous for its strong piezoelectric coupling, low attenuation and low diffraction spreading of the waves. A disadvantage is that bulk waves can also be generated, that is, a transducer for surface-wave generation also generates waves in the bulk of the material, and those bulk waves travelling close to the surface can excite the output transducer and so produce an unwanted output signal. Y-Z lithium niobate is worse than most other SAW materials in this respect, and for this reason the 128° rotated orientation [1] is sometimes used. For this case the surface normal makes an angle of 128° with the crystal Y-axis, and propagation is along the crystal X-axis. Compared with the Y-Z orientation, the 128° orientation gives much less excitation of bulk waves, but more diffraction spreading of the surface waves; the choice of orientation therefore depends on the application.

This Datareview gives the properties of these two orientations of relevance in linear SAW devices such as delay lines, bandpass filters and pulse-compression filters. Important propagation parameters are the velocity, temperature coefficient of delay, attenuation, and parameters relating to diffraction. In addition, some details are given on perturbations due to surface structures such as metal strips (which occur in transducers and multi-strip couplers) and grooves (which occur in resonators).

It should be noted that all of the parameters are dependent on crystal orientation, owing to the anisotropy of the crystal. Thus, different orientations give different parameters. In addition, parameters for a particular orientation may show an apparent variation in practice owing to inaccuracies in the orientation. This applies particularly to the SAW velocity. Velocity variations not associated with orientation errors have also been observed, and these are often attributed to minor variations of stoichiometry.

Unless otherwise noted, the surface waves referred to here are piezoelectric Rayleigh waves, the commonest type of SAW used in devices. Parameter values quoted are valid in the SAW device frequency range (10 - 1000 MHz), and at lower frequencies down to zero.

B BASIC PROPAGATION PARAMETERS

B1 Velocity and Coupling Constant

Propagation parameters are most commonly quoted for the 'free-surface' case, that is, there are no structures on the surface and the space above the substrate is a vacuum. In practice, there is usually air or gas present, but this has negligible effect except for a small increase of SAW attenuation (see below). Another case often considered theoretically is the 'metallised' case, where an idealised metal film is present on the surface, thin enough for its mechanical properties (elastic constants, mass) to have no effect but with infinite electrical conductivity. This nullifies the parallel electric field, which is otherwise present due to piezoelectricity, and consequently the velocity and other parameters are changed. The velocity change is an important measure of the piezoelectric coupling between the wave

and electrical structures such as transducers or multi-strip couplers. It is expressed by the parameter dv/v, defined by

$$\frac{dv}{v} = \left(\frac{v_0 - v_m}{v_0} \right)$$

where v_0 and v_m are, respectively, the free-surface and metallised velocities. This is usually expressed as a percentage.

Theoretically, both velocities can be calculated from the elastic and piezoelectric constants of the material, and its density [2]. The results are independent of frequency. Such 'theoretical' results are, however, subject to the accuracies of the material constants, which are usually taken from experiments using bulk acoustic waves. Experimental measurements, i.e. measurements using SAWs directly, have shown sample-to-sample velocity variations of about 1 part in 2000, thought to be due to variations of stoichiometry [3]. Theoretical and experimental values are given in TABLE 1 below.

Although the free-surface SAW velocity is theoretically non-dispersive, a small amount of dispersion has been observed in wide-band measurements [4]. A typical velocity change was 1 part in 1500 per GHz of frequency change, though there were substantial variations between samples. This dispersion is negligible for most purposes, but has a significant bearing on non-linear effects (see below). The dispersion is thought to arise from imperfections near the surface due to the crystal preparation.

Responses due to bulk-wave excitation are sometimes observed in SAW devices. The appropriate bulk-wave velocities are given in the Datareview by Peach [22].

B2 Surface Dielectric Constant

This constant is defined by

$$\epsilon_p = \sqrt{\epsilon_{z,z} \times \epsilon_{x,x} - \epsilon_{x,z}^2}$$

where $\epsilon_{z,z}$ etc. are the components of the dielectric tensor rotated according to the orientation; z is the surface normal direction and x the SAW propagation direction. With the constants $\epsilon_{z,z}$ etc. defined as constant-stress values, ϵ_p can be used to deduce approximately the capacitances needed for analysis of transducers and multi-strip couplers. For Y-Z lithium niobate, $\epsilon_p = 50.2 \epsilon_0$, where ϵ_0 is the dielectric constant of free space [6].

B3 Temperature Coefficient of Delay

For any two points on the crystal surface separated by a distance D the delay for a wave launched at one point and received at the other is $t = D/v$, where v is the wave velocity. Here, D and v both vary with temperature, the variation of D being the linear expansion. The temperature coefficient of delay, TCD, is defined as

$$TCD = \frac{1}{t} \times \frac{dt}{dT}$$

$$= \frac{1}{D} \times \frac{dD}{dT} - \frac{1}{v} \times \frac{dv}{dT}$$

where T is the temperature. Thus TCD gives the variation of the delay between two transducers, allowing for the fact that the transducer separation changes due to expansion. More generally, all propagation paths in the same direction are affected in the same way, so the device impulse response is simply scaled in time by a factor given by TCD and the temperature change. The differentials dD/dT and dv/dT can be deduced from the measured bulk material constants and their temperature coefficients, giving a 'theoretical' value for TCD. For the lithium niobate orientations considered here, TCD is almost independent of temperature. Results are usually quoted for free-surface propagation (as in TABLE 1). The surface structures used in practical SAW devices usually have little effect on the delay variation.

TABLE 1 Basic SAW propagation parameters.

	Y-Z LiNbO ₃	128° rot. LiNbO ₃	Ref
Velocity (m/s) (free-surface)	3487.7 (W)	3990 (W,N)	[5]
	3485.6 ± 3 (E) ¹		[3]
	3487 ± 3 (E)	3977 ± 2 (E)	[5]
	3488.3 (E)		[7]
dv/v (%)	2.41 (T)		[6]
		2.9 (N), 2.7 (W)	[5]
	2.15 (E)		[8]
Temp. coeff. of delay, TCD (ppm) (free-surface)		2.8 (E)	[5]
	94 (T)		[6]
		75 (T)	[1]

Notes: T = theory, W = theory using Warner constants [10], N = theory using Nakagawa constants [11], E = expt., ¹scatter is partly due to sample variations.

B4 Free-Surface Propagation Loss

The term 'propagation loss' refers to attenuation of a propagating wave, but excluding losses due to diffraction or non-linear effects; the data for it are therefore valid for a relatively wide SAW beam with relatively low power level. To minimise losses, surface imperfections such as pits or scratches must be avoided. Slobodnik [6] has studied these losses using lithium niobate crystals of varied quality. However, for well-polished crystals the losses due to imperfections are not usually significant, and the loss is mainly due to two causes. Firstly, if the crystal is in air the surface wave generates an acoustic disturbance in the air, carrying energy away. This effect, known as 'air loading', contributes an attenuation proportional to the frequency f, though this disappears if the crystal is in a vacuum. Secondly, interactions with thermal phonons within the crystal give rise to an attenuation contribution roughly proportional to f², present irrespective of whether the crystal is in air or in a vacuum. For Y-Z lithium niobate, Slobodnik [6] has measured the loss at room temperature, giving an attenuation coefficient (in dB per microsecond of propagation path) of approximately

$$\alpha = 0.19f + 0.88f^{1.9} \text{ (dB/}\mu\text{s)}$$

where f is the frequency in GHz. The first term is due to air loading and is omitted for a crystal in vacuo. Thus a crystal in air gives 0.03 dB/μs at 100 MHz and 1.1 dB/μs at 1 GHz; for a crystal in vacuo the corresponding values are 0.01 dB/μs and 0.88 dB/μs.

At lower temperatures the propagation loss decreases markedly. For example, a measurement at 970 MHz in vacuo gave a loss of 0.32 dB/μs at 100 K [6]. However, this is not significant for practical SAW devices. None the less, studies at very low temperature (~30 K) are useful for measuring loss mechanisms [23].

At relatively high power levels, the wave amplitude is affected by non-linear effects in the material. Harmonic surface waves are generated at frequencies equal to multiples of the frequency of the launched fundamental wave, and the power of the fundamental is reduced [6,12]. The harmonics can also combine at a more distant point to regenerate the fundamental. This situation is further complicated by the presence of a very small amount of dispersion, mentioned above [4,6,12], which tends to reduce the effect of the non-linearities. Owing to the lack of reproducibility of the dispersion it is not possible to give reliable data for the resulting losses. However, from measurements on many Y-Z lithium niobate samples, Williamson [4] notes that for a 1 dB depletion of the fundamental the SAW power level is typically given by

$$\frac{P}{W \times LAM} = 4 \text{ to } 8 \text{ W/mm}^2$$

where W is the SAW beam width and LAM is the SAW wavelength. This gives a rough guide for the power limitation needed to avoid non-linear effects for free-surface propagation.

B5 Free-Surface Diffraction and Beam Steering

Diffraction of surface waves is, in many respects, similar to optical diffraction in free space, but with complications arising from the anisotropy of the material. To analyse propagation of a surface wave beam [9], information is needed on the variation of SAW velocity for a range of angles near the beam axis, since a finite-width beam can be regarded as a sum of infinite-width waves with varying propagation directions. There are two distinct topics to consider: beam steering in the near field, and the diffraction pattern as a whole.

B5.1 Beam steering in the near field

In the near field the surface-wave beam launched by a transducer propagates with little distortion. However, owing to the crystal anisotropy the beam propagation direction may not be perpendicular to the wavefronts, which for an interdigital transducer are parallel to the transducer electrodes. In consequence, a beam intended to propagate perpendicular to the electrodes does not fully illuminate the output transducer, and some power is lost. The angle γ between the beam propagation direction and the normal to the electrodes is, for wide beams, given by

$$\tan(\gamma) = \frac{1}{v} \times \frac{dv}{d\theta}$$

where v is the velocity of an infinite-width SAW propagating at an angle θ to the electrode normal. The right side is to be evaluated at $\theta = 0$.

For SAW devices, the material orientation is usually chosen such that v is a symmetrical function of θ , and γ is then zero. This applies for the orientations considered here. However, a misalignment error such that the transducer electrodes are not quite parallel to the required direction in the crystal lattice causes γ to be non-zero. The resulting beam steering can then be assessed from the differential $dy/d\theta$, since for a small misorientation θ , the value of γ is approximately $\theta \times dy/d\theta$.

For Y-Z lithium niobate the value of $dy/d\theta$ is -1.08 [6].

B5.2 Overall diffraction pattern

For an isotropic material, diffraction shows the features given by free-space optical diffraction, including a near-field region in which the beam maintains its profile and a far-field region in which it spreads out radially. Anisotropy modifies this picture. For many SAW materials the diffraction behaves in a similar way to the isotropic case, but with the diffraction pattern scaled in the propagation direction. This applies when the 'parabolic approximation' is valid for the material, that is, when a polar plot of the slowness $1/v$ is well approximated by a parabola. This is convenient for analysis as the known formulae for an isotropic material can be simply scaled for an anisotropic material.

For Y-Z lithium niobate the parabolic approximation is not valid; a parabola approximating $1/v$ does not give adequate accuracy for diffraction calculations [6]. A particular feature of this orientation is that diffraction spreading is much less than that found for an isotropic material, and this case is therefore known as a 'minimal-diffraction orientation'. It can be shown that low diffraction spreading occurs when the parameter $dy/d\theta$ is close to -1, and for Y-Z lithium niobate this parameter is -1.08.

Calculation of the diffraction pattern can be done using the 'angular spectrum of plane waves' theory [9,13], using data on the variation of velocity v with propagation direction. The velocity can be deduced theoretically from the measured bulk constants such as those in [10,11], but for Y-Z lithium niobate this is found to give inadequate accuracy as the diffraction pattern is sensitive to small velocity errors. However, Murray and Ash [7] have obtained more accurate velocity data by analysing experimental free-surface diffraction patterns. Their results were fitted to the polynomial

$$v = \sum_n A_n \times \theta^{2n}$$

with θ in degrees. The coefficients $A(n)$ were, in m/s:

n	0	1	2	3	4
A_n	3488.3	-3.85×10^{-1}	-1.64×10^{-3}	4.55×10^{-6}	5.54×10^{-9}

These coefficients are valid for values of θ in the range -18 to +18°, and for a temperature of 21.5°C. Repeated measurements on one sample gave a velocity repeatability of about 0.1 m/s.

C PROPAGATION DISTURBED BY SURFACE STRUCTURES

SAW devices make use of metal electrodes (for transducers or multi-strip couplers), grooves (in resonators and reflective array compressors, RACs) and sometimes continuous metal films. These structures all cause perturbations of the wave propagation, and appropriate data are given here. The metal used in practice is usually aluminium, as this has elastic properties somewhat similar to those of lithium niobate and so causes less perturbation than most other suitable metals.

C1 Continuous Metal Films

The presence of a metal film on the surface causes the (ideally) non-dispersive surface wave to become dispersive. For film thicknesses much less than the SAW wavelength the velocity v varies linearly with frequency and with film thickness, and can be written in the form

$$v = v_m \times \left(1 - \frac{A \times H}{LAM} \right)$$

where H is the film thickness, LAM is the free-surface SAW wavelength, v_m is the metallised SAW velocity and A is a constant. For aluminium films on Y-Z lithium niobate, Penunuri and Lakin [14] give the theoretical value of A = 0.287. For the same metal on the 128° rotated orientation the measured value [5] is A = 0.023. These values are valid for H/LAM less than 0.01.

Metal films also increase the SAW propagation loss. For aluminium films on Y-Z lithium niobate, measurements by Davis and Weller [15] give an attenuation coefficient of approximately

$$\alpha = K \times f^{2.2} (\text{dB}/\mu\text{s})$$

with the frequency f in GHz. The constant K varied from 3.0 for a film thickness H = 0.05 μm to 5.2 for H = 0.2 μm.

C2 Propagation in Grooves

Resonators use arrays of grooves arranged parallel to the SAW wavefronts, reflecting the waves through 180°. In RACs arrays of inclined grooves are used to reflect the waves through 90°. The SAW perturbations due to the grooves are called 'topographic effects' since they are caused only by the geometry of the surface. For Y-Z lithium niobate, a variety of measurements on reflection and transmission by grooves are reported by Melngailis et al [16]. For a shallow groove parallel to the SAW wavefront the reflection coefficient has the form

$$r = -2jC \times \frac{H}{LAM} \times \sin(a \times k)$$

where j = sqrt(-1), H is the groove depth, LAM is the free-surface wavelength of the incident wave, a is the groove width, k is the free-surface wavenumber of the incident wave and C is a constant. For a groove reflecting the incident wave through 90° the same formula applies except that k is replaced by k/2 and a is taken to be the groove width measured in the propagation direction of the incident wave. The phase of the reflected wave is referenced to the centre of the groove. For a groove parallel to the wavefronts, measurements give C = 0.33. For reflection through 90°, C = 0.51 ± 0.03.

Grooves also affect the phase of the wave transmitted through them, an effect known as 'stored energy'. At each groove edge there is a phase shift equal to -B/2 radians, where

$$B = 2C' \times \left(\frac{H}{LAM} \right)^2$$

and C' is a constant. In a periodic array of grooves this gives an effective wavenumber k' = k + B/p, where p is the groove pitch, and thus changes the SAW velocity. For reflection through 90°, measurements gave C' = 4.5 ± 0.4. For a groove parallel to the wavefront, C' = 21.

Properties of arrays of grooves, as used in resonators or RACs, can be deduced from the above data on reflection and transmission properties of individual grooves. The free-surface propagation loss (see above) must be added, and, in addition, there can be two other sources of loss. Firstly, it is possible in some circumstances for the grooves to scatter surface waves coherently into bulk waves. This occurs mainly when the groove pitch is larger than the wavelength. Substantial losses can occur, but this does not affect most SAW devices except for up-chirp dispersive devices with wide bandwidths. For groove arrays in which coherent bulk wave scattering does not occur, it is still found that propagation losses can be greater than the expected free-surface values, and the excess loss is described as

'non-synchronous scattering loss' (NSSL). This loss is ascribed to incoherent scattering of surface waves into bulk waves. Otto and Gerard [17] made measurements on Y-Z lithium niobate RACs and found the NSSL to be consistent with the formula

$$\frac{dP}{P} = - \left(\frac{\mathbf{K} \times \mathbf{H}}{\text{LAM}} \right)^2$$

where P is the power of the incident wave and dP is the power lost per groove. The constant K was found to be 2.3.

C3 Propagation in Metal Electrodes

Metal electrodes are used mainly in SAW transducers and multi-strip couplers. They reflect surface waves, modify the SAW velocity (giving dispersion), and increase the propagation loss. For simplicity, this section is restricted to periodic arrays of electrodes, with the electrodes parallel to the wavefronts. The electrodes are assumed to be either electrically disconnected, or electrically connected together (shorted) by a connector outside the SAW beam. Disconnected electrodes are used in multi-strip couplers. In a transducer, the electrodes are not all connected together, but it can be shown that the results for shorted electrodes are sufficient for transducer analysis. It is also assumed here that the width of each electrode is equal to the width of each gap, i.e. the 'metallisation ratio' is 0.5. This is approximately valid for most SAW devices.

Although the perturbations produced by individual electrodes are generally small, large reflections can be built up in an array of many electrodes when the electrode pitch is close to half the SAW wavelength. This condition is known as a stop band, and occurs at the stop-band frequency

$$f(s) = \frac{v}{2p}$$

where p is the electrode pitch and v is the SAW velocity. For this reason SAW devices generally use frequencies below f(s), except for resonators and some transducers with relatively few electrodes.

The perturbations due to the electrodes arise from 'electrical loading' (i.e. the perturbation of the electrical boundary conditions at the surface), and 'mechanical loading' (i.e. mechanical effects at the surface). For lithium niobate, which has relatively strong piezoelectric coupling, the effects of electrical loading are often significant. The severity of mechanical loading depends on the electrode thickness. Usually the electrodes are of aluminium, and for devices with relatively thin electrodes the perturbations are mainly due to electrical loading.

Little quantitative information is available for mechanical loading on lithium niobate. Skeie [21] has given experimental and theoretical results for gold electrodes, which give much larger perturbations than aluminium, but this is not relevant to most practical devices. The following account is therefore restricted to electrical loading.

For analysis of electrical loading, it is assumed that the electrodes are thin enough for mechanical loading to be insignificant. It is also usually assumed that the electrode resistivity is negligible (a reasonable approximation in practice) and losses are ignored. In an array of electrodes each electrode will reflect surface waves, though it should be noted that the reflection coefficient is affected by the presence of neighbouring electrodes because of electrostatic and other interactions. Complex formulae for the reflection coefficient of one electrode are given in [9,18]. For a frequency $f = f(s)$ the reflection coefficient is

$$\begin{aligned} r &= -0.718 j \frac{dv}{v} && \text{for shorted electrodes} \\ &= 0.718 j \frac{dv}{v} && \text{for disconnected electrodes} \end{aligned}$$

where the phase of r is referenced to the centre of the electrode. Thus, for Y-Z lithium niobate with dv/v taken to be 2.15%,

$$\begin{aligned} r &= -0.0154 j && \text{for shorted electrodes} \\ &= 0.0154 j && \text{for disconnected electrodes} \end{aligned}$$

These values have been confirmed experimentally [19].

The electrode transmission coefficient t can be deduced from r , because for no losses the squared moduli of r and t must sum to give unity, and it is known [9] that in this case r and t must be in phase quadrature. This implies that t is real, which in turn implies that the electrodes do not affect the SAW velocity. This is in fact an erroneous conclusion, due to approximations made in the derivation of r . However, a separate theory [9,20] gives the following results for the velocity v , as a function of the frequency f , ignoring perturbations localised in the stop bands. For shorted electrodes,

$$\begin{aligned} v &= v(m) && \text{at } f = 0 \\ &= (v_0 + v_m)/2 && \text{at } f = 2f_s \end{aligned}$$

For disconnected electrodes,

$$\begin{aligned} v &= v_0 && \text{at } f = 0 \\ &= (v_0 + v_m)/2 && \text{at } f = 2f_s \end{aligned}$$

where v_0 and v_m are the free-surface and metallised velocities, respectively. For frequencies between 0 and $2f_s$, both velocities vary approximately linearly. For frequencies between $2f_s$ and $4f_s$, both velocities remain constant. The forms of these relations were confirmed experimentally by Williamson [3].

D CONCLUSION

This Datareview covers the properties of both Y-Z and 128° oriented LiNbO_3 useful in linear SAW devices. All these parameters are dependent on crystal orientation. The surface waves discussed are normally piezoelectric Rayleigh waves. Parameter values are valid in the SAW device frequency range of 10 - 1000 MHz and at frequencies down to zero. Data are given on the effects of metal electrodes, grooves and metal films on wave propagation.

REFERENCES

- [1] K. Shibayama, K. Yamanouchi, H. Sato, T. Meguro [*Proc. IEEE (USA)* vol.64 no.5 (1976) p.595-7]
- [2] J.J. Campbell, W.R. Jones [*IEEE Trans. Sonics Ultrason. (USA)* vol.SU-15 (1968) p.209-17]
- [3] R.C. Williamson [*IEEE Ultrasonics Symp. USA* (1972) p.323-7]
- [4] R.C. Williamson [*IEEE Ultrasonics Symp. USA* (1974) p.321-8]
- [5] J. Temmyo, I. Kotaka, T. Inamura, S. Yoshikawa [*IEEE Trans. Sonics Ultrason. (USA)* vol.SU-27 no.4 (1980) p.218-9]

- [6] A.J. Slobodnik Jr. [in *Acoustic Surface Waves* Ed. A.A. Oliner (Springer-Verlag, Berlin, 1978) p.225-303]
- [7] D. Murray, E.A. Ash [*IEEE Ultrasonics Symp.* Phoenix, AZ, USA, 26-28 Oct 1977 (IEEE, New York, USA, 1978) p.823-6]
- [8] M.B. Schultz, J.H. Matsinger [*Appl. Phys. Lett. (USA)* vol.20 no.9 (1972) p.367-9]
- [9] D.P. Morgan [*Surface Wave Devices for Signal Processing* (Elsevier, 1985)]
- [10] A.W. Warner, M. Onoe, G.W. Coquin [*J. Acoust. Soc. Am. (USA)* vol.42 (1967) p.1223-31]
- [11] Y. Nakagawa, K. Yamanouchi, K. Shibayama [*J. Appl. Phys. (USA)* vol.44 no.9 (1973) p.3969-74]
- [12] E.G. Lean, C.G. Powell [*Appl. Phys. Lett. (USA)* vol.19 no.9 (1971) p.356-9]
- [13] M.S. Kharusi, G.W. Farnell [*IEEE Trans. Sonics Ultrason. (USA)* vol.SU-18 no.1 (1971) p.34-42]
- [14] D. Penunuri, K.M. Lakin [*IEEE Trans. Sonics Ultrason. (USA)* vol.SU-21 no.4 (1974) p.293-5]
- [15] K.L. Davis, J.F. Weller [*IEEE Ultrasonics Symp.* New Orleans, LA, USA, 22-28 Sept 1979 (IEEE, New York, USA, 1979) p.659-62]
- [16] J. Melngailis, R.C. Williamson, J. Holtham, R.C.M. Li [*Wave Electron. (Netherlands)* vol.2 no.1-3 (1976) p.177-98]
- [17] O.W. Otto, H.M. Gerard [*IEEE Ultrasonics Symp.* Phoenix, AZ, USA, 26-28 Oct 1977 (IEEE, New York, USA, 1978) p.596-601]
- [18] S. Datta, B.J. Hunsinger [*J. Appl. Phys. (USA)* vol.51 no.9 (1980) p.4817-23]
- [19] F. Barman, G.L. Matthaei [*Wave Electron. (Netherlands)* vol.4 no.4 (1983) p.251-72]
- [20] K. Blotekjaer, K.A. Ingebrigtsen, H. Skeie [*IEEE Trans. Electron Devices (USA)* vol.ED-20 no.12 (1973) p.1133-8]
- [21] H. Skeie [*J. Acoust. Soc. Am. (USA)* vol.48 (1970) p.1098-109]
- [22] R. Peach [Datareview in this book: *10.1 Velocity of ultrasonic bulk waves in LiNbO_3*]
- [23] A. El Habti, F. Bastien, E. Bigler, T. Thorvaldsson [*J. Acoust. Soc. Am. (USA)* vol.100 no.1 (1996) p.272-7]

10.4 Attenuation of SAWs in LiNbO₃

M.F. Lewis and C.L. West; updated by D. Craig

August 2001

The inherent material attenuation of surface acoustic waves in good single crystals of dielectric media is closely related to that of bulk waves in the same material, and arises from interactions with thermal phonons. However, as the disturbance is localised at the surface, rather than within the medium, it can be subject to various additional attenuation mechanisms as discussed below. First, we discuss the inherent attenuation of surface waves propagating on an ideal plane surface of a semi-infinite crystal of LiNbO₃ in contact with a vacuum.

At low temperatures, the dominant attenuation mechanism is by microscopic three-phonon collisions, in which energy and wavevector are conserved. An interesting difference from the bulk-wave interaction is the relaxation of the need for wavevector conservation perpendicular to the surface. Nevertheless the measured and calculated attenuations still vary as ωT^4 (ω = ultrasonic frequency, T = absolute temperature), and are similar in magnitude to those of slow shear bulk waves in the same material [1,2,7]. At higher temperatures, including room temperature, the attenuation can be calculated from the phonon-viscosity tensor, the independent components of which are listed in [5] for lithium niobate. The procedure for calculating the effective viscosity coefficient, η_{eff} , for a given surface acoustic wave is described by King and Sheard [3]. The resulting attenuation coefficient, α , is given by

$$\alpha = \frac{\omega^2 \eta_{\text{eff}}}{2\rho V^3} \text{ neper/unit distance (1 neper} = 8.68 \text{ dB)}$$

where ρ is the mass density and V the SAW velocity. In quartz, it has been found that η_{eff} never differs greatly from η_{44} [3]. It should be emphasised that the attenuation calculated in this manner is the lowest attenuation that can be expected for a given SAW. The attenuation measured in practice will be higher than this value due to a variety of additional attenuation mechanisms that are peculiar to SAWs, and which are discussed below. An approximate value for the room-temperature attenuation of SAWs on Y-cut Z-propagating LiNbO₃ is 2.5 dB/cm at a frequency of 1 GHz, and varies closely as the square of the frequency [2].

In addition to this intrinsic attenuation coefficient, which can be calculated reliably from the viscosity coefficients, SAWs on LiNbO₃ may encounter attenuation through any or all of the following mechanisms, many of which are described in more detail by Slobodnik [2]:

- (i) Surface damage incurred in polishing, and which typically extends into the substrate by a few micrometres.
- (ii) Surface contamination (e.g. due to failure to remove all the photoresist in the photolithographic SAW transducer fabrication process) and the surface adsorption of gases and/or moisture.

A further possible ultrasonic attenuation mechanism concerns the loss of oxygen, e.g. if the LiNbO₃ substrate is heated in vacuo; this undoubtedly modifies the mechanical properties, and can additionally induce a surface electrical conductivity; see (iii) below.

- (iii) Since SAWs on LiNbO₃ are accompanied by electric fields within and just above the surface, SAW attenuation through electrical conduction losses can arise if the surface is metallised, or if a metallic or semiconducting substrate is suspended just above the SAW substrate. In fact, this mechanism can also be used to amplify SAWs, e.g. if a silicon substrate is suspended just above the LiNbO₃ and the carriers are drifted faster than the SAW velocity [4].
- (iv) Since a surface acoustic wave is only a normal mode of a semi-infinite substrate, there is a finite energy density at the lower surface of any real substrate. As this lower surface is ordinarily roughened and/or covered with adhesive for mounting purposes, a measurable SAW attenuation can arise if the substrate is less than about five wavelengths thick.
- (v) If the SAW substrate is encapsulated in air or any other gas, there will be some loss of energy by the excitation of a phase-matched compressional wave in the gas. The SAW attenuation is given by [2]

$$\alpha \text{ (neper/unit length)} = \frac{f P}{\rho V^2} \left[\frac{\gamma M}{R T} \right]^{1/2}$$

where f is the frequency, ρ the mass density, V the SAW velocity, P the gas pressure, R the universal gas constant, γ the ratio of the specific heats at constant pressure and volume, and M the molecular weight. Clearly, gases of low molecular weight are preferable from this point of view.

The effects (i) to (iv) above vary from substrate to substrate and are very difficult to quantify. From extensive studies, Slobodnik [2] gives the overall attenuation on Y-Z LiNbO₃ arising from the phonon-phonon loss and mechanism (v) above in air as

$$\alpha \text{ (dB/microsecond)} = 0.88 f^{1.9} + 0.19f$$

where f is the frequency in GHz.

REFERENCES

- [1] P.J. King, F.W. Sheard [*Proc. R. Soc. Lond. Ser. A (UK)* vol.320 (1970) p.175-86]
- [2] A.J. Slobodnik Jr. [*Top. Appl. Phys. (Germany)* vol.24 (1978) ch.6]
- [3] P.J. King, F.W. Sheard [*J. Appl. Phys. (USA)* vol.40 no.13 (1969) p.5189-90]
- [4] J.H. Collins, K.M. Lakin, C.F. Quate, H.J. Shaw [*Appl. Phys. Lett. (USA)* vol.13 (1968) p.314-6]
- [5] M.F. Lewis, C.L. West [Datareview in this book: 10.2 Attenuation of ultrasonic bulk waves in LiNbO₃]
- [6] A. El Habti, F. Bastien, E. Bigler, T. Thorvaldsson [*J. Acoust. Soc. Am. (USA)* vol.100 no.1 (1996) p.272-7]

10.5 Velocity of SAWs in proton-exchanged waveguides in LiNbO₃

V.A. Fedorov, Yu.N. Korkishko, D. Ciplys and R. Rimeika

August 2001

A INTRODUCTION

The use of surface acoustic waves (SAWs) in integrated acousto-optic devices is stimulated by a variety of promising applications in the field of optical communications and radio frequency (RF) signal processing. LiNbO₃ is one of the materials most commonly used not only in optics, especially in integrated optics, but also in acoustics. It is now well recognised that lithium niobate is one of few materials inside which longitudinal acoustic waves may propagate with a relatively small attenuation at GHz frequencies. Large electromechanical coupling coefficients, high electro-optic coefficients, small propagation losses for acoustic waves and strong piezoelectricity are some of the features making LiNbO₃ so attractive for many acoustic applications, such as acoustic wave filter devices and radar signal processing devices. And taking its acousto-optic properties into account, lithium niobate is a good candidate for the fabrication of UHF frequency range acousto-optic devices.

Waveguides provide several advantages, such as acoustic and optical beam confinement, prolongation of delay time, and high acoustic intensity for the acoustic devices. Proton exchange (PE) is a convenient method for the fabrication of optical and acoustic waveguides and devices in LiNbO₃ substrates. Therefore, the characteristics of SAWs in PE LiNbO₃ waveguides deserve considerable interest. Investigations of the SAW properties have shown that proton exchange alters the phase velocity as well as the group velocity of SAWs, and thus can be used for constructing SAW waveguides [1]. This has several advantages [2]: first, the large velocity changes will result in a strong field confinement. This means that narrower guides and curved guides with smaller curvature radius are feasible, which should result in a better use of the substrate surface. Such waveguides can find high efficiency application in non-linear acoustics, in constructing low-loss curved guides, etc. On the other hand, weakly guiding structures can also be produced by simply changing the proton-exchange process. They can also be combined with optical strip guides to largely increase the efficiency of the collinear interaction between guided optical and acoustic waves. In this way, integrated optics can be combined with integrated acoustics on the same substrate using strip or planar guides for both types of waves or even combined guides [2]. This offers new applications of PE-waveguides in the fields of acousto-optic and guided SAW devices. Devices have already been described in the literature that take advantage of the special optical and acoustical properties of PE-waveguides as reviewed in [3]. The acoustic and acousto-optical properties of proton-exchanged waveguides in LiNbO₃ are summarised in this Datareview.

B ACOUSTIC AND ACOUSTO-OPTIC PROPERTIES OF PROTON-EXCHANGED LiNbO₃

There have been many reports of investigations of the acoustic and acousto-optic properties of proton-exchanged lithium niobate [1-44]. Much work has been done in order to determine quantitatively the SAW-velocity perturbation due to the ion-exchanged protons. Two dominant causes of the velocity change have been found: the piezoelectric activity is strongly diminished and obviously due to a drastic reduction of the corresponding elastic constants in the PE volume. Handa et al [4] reported at first greatly increased insertion loss (approximately 30 dB greater) for a SAW delay line in which the transducers were deposited directly on the PE region. They attributed this primarily to reduced piezoelectricity. Subsequent work [5] indicated that piezoelectric activity is reduced to near zero in

the PE layer by investigations of the electromechanical coupling coefficient. A large decrease in the SAW velocity (up to 20% at a frequency of 180 MHz) has been observed for propagation in the X-direction on Y- and Z-cut surfaces [1]. The variation of SAW phase velocity as well as group velocity of SAWs and attenuation with propagation direction on X-, Y-, and Z-cut PE LiNbO_3 has been measured using Brillouin scattering at acoustic frequencies of the order of 10 GHz [6] and by means of line-focus acoustic microscopy at 215 MHz [7] and by the acousto-optical diffraction method at 180 and 420 MHz for Y-cut samples [2]. The very substantial reduction of the elastic constants has been estimated at up to 40% [6]. Strong SAW guiding in PE-waveguides has been proved [2] and for various fabrication conditions and propagation directions the values of the velocity change have been summarised by Hinkov [8]. The detailed investigations of dispersion characteristics of the SAWs in the frequency range from 100 MHz up to over 1 GHz in Y-cut PE LiNbO_3 and an attempt to determine the elastic stiffness constants of the $\text{H}_x\text{Li}_{1-x}\text{NbO}_3$ layer have been reported [9]. The 128° rotated Y-cut LiNbO_3 substrate possessing the highest electromechanical coefficient, $K^2 = 0.055$, for X-propagating SAWs is very popular for fabrication of many acousto-electric devices, such as filters, resonators and oscillators. For this particular cut, PE waveguides have been fabricated and efficient acousto-optic diffraction of guided optical modes by surface acoustic waves has been demonstrated [10]. The characteristics of surface acoustic waves on PE 128°-rotated Y-cut LiNbO_3 were investigated at a frequency of 100 MHz [11], using the acousto-optical diffraction method in the SAW frequency range 30 - 600 MHz [12] and in a wide frequency range in metallised PE LiNbO_3 with Al and Cu-film deposited [13]. Strong velocity decreases were observed due to proton exchange and were strongly affected by the post-exchange annealing. Temperature-dependent attenuation of SAWs in proton-exchanged and annealed 128°-rotated Y-cut LiNbO_3 has been studied experimentally in [14]. As a result, PE 128°-rotated Y-cut LiNbO_3 can be expected to be applicable in low-loss SAW waveguides and high-efficiency acousto-optic devices. The characteristics of SAWs on PE and annealed PE Z-cut Y-propagated LiNbO_3 waveguides using pure benzoic [15], pyrophosphoric [16] and octanoic [17,18] acids were investigated and compared. The results obtained in these studies show that the characteristics of SAWs on PE Z-cut are comparable to those of PE Y-cut and 128°-rotated Y-cut LiNbO_3 and can be adopted for applications to acoustic waveguides, lenses and reflective gratings. Surface acoustic wave sensors on PE Z-cut LiNbO_3 for dilute electrolyte sensing have been realised recently [19].

One report [20] showed that the bulk wave that is radiated to the inside of the substrate in the excitation and propagation of a leaky surface acoustic wave (LSAW) can be suppressed by forming a proton-exchanged layer on the surface of the substrate. It was theoretically shown that, even if the electrical condition of the propagation path is a free surface, the particle displacement distribution of the LSAW particle is concentrated at the substrate surface by PE, as in the case of a metallised surface. This result suggests that the bulk wave radiation in LSAW excitation can be suppressed. The bulk wave radiation loss was examined by measuring the insertion loss between the input and the output IDT on the 41° Y-X LiNbO_3 substrate, and it was shown that the bulk wave can be reduced to zero by proton exchange. It was shown experimentally that the leak loss in the propagation due to the bulk-wave radiation can be reduced to approximately one-third by the PE [20].

An interesting phenomenon, in the case of the phase velocity of SAWs propagating on a PE substrate, was observed experimentally in [21]. The phase velocity on PE 128° Y-X LiNbO_3 was measured as a function of the exchange depth using parallel comb filters. Unlike the ordinary dispersive phase velocity for the free-surface case, the phase velocity for the case of the metallised surface maintained a constant value when the exchange depth was greater than a certain value. In this region, a reversal phenomenon was observed, indicating that the phase velocity in the case of the metallised surface became faster than that in the case of the free surface.

The SAW properties of PE and APE Z-cut LiNbO_3 samples were investigated in [22]. The phase velocity (V_p) and electromechanical coupling coefficient (K^2) of PE samples were significantly decreased by the increase of k_d . The insertion loss (IL) of PE samples was increased by the increase of k_d and became nearly constant at $k_d > 0.064$. The temperature coefficient of frequency (TCF) of

PE samples showed an apparent increase with $k\text{d}$, reaching a maximum at $k\text{d} = 0.292$, then slightly decreased at higher $k\text{d}$. The effects of annealing resulted in a restoration of V_p and an improvement of IL [22].

Summarising all these studies, here we will note the following interesting features of the acoustic properties of proton-exchanged lithium niobate:

- (i) The proton exchange results in creation of an $\text{H}_x\text{Li}_{1-x}\text{NbO}_3$ layer at the surface with altered elastic and piezoelectric properties of the crystal. This is why the velocity of the Rayleigh SAWs becomes frequency dependent. The velocity change in the PE LiNbO_3 layers is also anisotropic: for Z-cut only decreases in SAW velocity are observed, while in X- and Y-cut LiNbO_3 both increases and decreases are possible, being much greater for SAWs propagating along the x-axis than for SAWs propagating parallel to the z-axis.
- (ii) The absolute value of the velocity change decreases with a dilution of the proton source. Proton exchange in diluted sources generally reduces SAW propagation velocity along the X- and Y-directions and generally results in smaller increases in velocity for waves propagating along the Z-direction.
- (iii) The proton exchange allows us to control the acoustic birefringence. In fact, PE in a diluted source largely decreases the higher SAW velocity in the X direction and increases the lower SAW velocity in the Z direction. By properly choosing the dilution of the melt it is possible to produce even isotropic samples or to reverse the sign of the acoustic birefringence of the crystal [2]. Annealing of the samples also leads to a large reduction of the acoustic birefringence. Clearly, the exchange process affects the various elastic constants to a different degree. The proton exchange not only softens the shear stiffness of the crystal but also affects the compressional elastic constants.
- (iv) The proton exchange generally increases the SAW propagation losses. For Z-propagating SAWs the attenuation is similar to that of the bulk, pure LiNbO_3 . However, for Y- and X-propagating SAWs on X- and Y-cut LiNbO_3 , respectively, an increase in attenuation accompanies the decrease in SAW velocities noted above. This increase is larger for Y-cut, X-propagating samples than for X-cut, Y-propagating samples.
- (v) The acoustic dispersion and SAW propagation losses grow with increasing exchange temperature or time (and thus with the waveguide depth) and strongly decrease with post-exchange annealing.

Rather naturally, there has also been work on the acousto-optic interaction in and acousto-optic properties of proton-exchanged lithium niobate. Planar acoustic deflectors can be divided into guided-to-guided mode coupling and coupling of guided waves to radiation modes. Acousto-optic devices of both types, which take advantage of the special optical and acoustic properties of PE waveguides, have already been described in the literature. Successful acousto-optic diffraction was first reported in [23,24]. Strong dependence of the non-collinear acousto-optic interaction efficiency on the diffusion depth has been found in [24,25], which could, at least qualitatively, be explained by a drastic reduction of the electro-optic activity due to the PE. In comparison with Ti: LiNbO_3 waveguides, much more efficient collinear acousto-optic diffraction employing combined optical/acoustical PE-stripe-waveguides has been demonstrated in [26]. The authors of [27] have described investigations of various processing techniques to increase acousto-optic diffraction efficiency in proton-exchanged guides, and an efficient acousto-optic Bragg deflector, which is resistant to optical damage, has been reported. Saiga and Ichioka [10] reported that the Bragg diffraction efficiency resulting from an acousto-optic interaction in PE 128°-rotated Y-cut LiNbO_3 reached 50% at the acoustic power of 18 mW. Experimental results on acousto-optic interaction at 520 MHz in PE waveguides in Y- LiNbO_3 were reported in [28]. The acousto-optic diffraction

efficiency, for an electrical input of 300 mW, was 39% in proton-exchanged devices, as compared to 22% in titanium-indiffused ones. The dynamic range observed in PE and Ti-indiffused acousto-optic devices was 22 and 25 dB, respectively [28]. Acousto-optic collinear TE-TM mode conversion was investigated in a two-layer Ti-indiffused and PE waveguide structure in LiNbO_3 [29]. A very narrowband interaction of only 130 kHz (0.31 nm optical bandwidth) was achieved with about 25 mW acoustic power for 96% conversion efficiency. This structure is especially suitable for constructing novel-type acousto-optical gas sensors [30]. The acousto-optic interaction in PE LiNbO_3 waveguides has been studied in [31]. Collinear deflection in PE waveguides was found to be very efficient. Compared to titanium-diffused waveguides up to three orders of magnitude higher coupling coefficients have been obtained [31]. The efficiency of acousto-optic interaction in YZ-cut PE LiNbO_3 waveguides was theoretically analysed in [32] determining the overlap between the optical and acoustic field distributions. The overlap was found to be significant up to very high acoustic frequencies of the order of 5 GHz. A guided-wave two-dimensional acousto-optic scanner using PE LiNbO_3 waveguide has been realised recently [33]. A collinear acousto-optic deflector for an optical pickup application has been fabricated on PE LiNbO_3 [34]. The acousto-optic interaction on PE 128°-rotated Y-cut LiNbO_3 was investigated to evaluate the photoelastic constants [35]. The experimental and theoretical analysis, using a surface acoustic wave of 200 MHz and a He-Ne laser beam, showed the photoelastic constants of the PE layer are 76% of those in unexchanged LiNbO_3 [35]. The propagation of horizontal shear SAWs (Love waves) with a purely shear polarisation in the propagation plane in PE Z-cut LiNbO_3 was studied in [36]. This wave causes the effective collinear diffraction of TM-guided optical modes with a polarisation rotation.

Recently, the acousto-optic diffraction of guided optical modes by SAWs at the frequency of 78 MHz in the Raman-Nath regime in a single-mode optical waveguide formed by PE in 128°-rotated Y-cut LiNbO_3 has been studied in [37]. The measured dependences of the light intensity diffracted into the zeroth, first and second orders on the driving voltage were in good agreement with the theoretical calculations. The values for the acousto-optic figure of merit $M_2 = 9.5 \times 10^{-15} \text{ s}^3/\text{kg}$ and the effective photoelastic coefficient $p_{\text{eff}} = 0.14$ have been evaluated showing the efficiency of the acousto-optic interaction in PE LiNbO_3 being comparable to that in the pure crystal.

The results of a detailed theoretical study on collinear guided wave to leaky wave acousto-optic interactions in PE: LiNbO_3 planar waveguides by the induced diffraction grating were presented in [38], using a generalised multimode formulation of the coupled mode theory. Mode-conversion efficiency and AO bandwidth have been calculated as functions of acoustic frequency, interaction length, guiding-layer thickness, and acoustic drive power density for three cuts of the LiNbO_3 substrate. High-performance configurations that are desirable for application to demultiplexing and switching in optical communication systems are identified, and the corresponding channel capacity and frequency resolution are determined. For example, it was shown that the X-cut configuration features the highest mode-conversion efficiency. However, a relatively small AO bandwidth is associated with this configuration. Both high mode conversion efficiency and large AO bandwidth can be accomplished at the guiding layer thickness of 1.0 μm . A $\text{TM} \rightarrow \text{TE}$ mode conversion efficiency as high as 42% together with an AO bandwidth of approximately 70 MHz can be achieved in the Z-cut waveguide at the guiding layer thickness of 1.0 μm , acoustic drive power density of 50 mW/mm, interaction length of 40 mm, and acoustic frequency of 460 MHz [38]. The corresponding channel capacity and frequency resolution are 745 and 0.09 MHz, respectively. Measured mode conversion efficiencies as high as 90 and 78% obtained at the acoustic frequencies of 107 and 367 MHz using the X-cut substrate and the Y-propagation SAW have verified the theoretical prediction on the mode-conversion efficiencies [38].

A knowledge of both SAW velocity and attenuation is essential if the performance and design of SAW devices are to be optimised. However, the available data are very scarce and the observed velocity changes are strongly dependent on the technological treatment of the samples, e.g. exchange in pure or diluted acid, annealing, etc.

C VELOCITY OF SAWs IN DIFFERENT $\text{H}_x\text{Li}_{1-x}\text{NbO}_3$ PHASES

Our recent studies, reviewed in [39], have shown that the seven different crystallographic phases of $\text{H}_x\text{Li}_{1-x}\text{NbO}_3$, the α , κ_1 , κ_2 , β_1 , β_2 , β_3 and β_4 phases, can be realised in proton-exchanged LiNbO_3 layers depending on exchange and annealing conditions, but the relationships between the phase composition and the resulting acoustic properties of PE LiNbO_3 waveguides are not well known. Therefore, for the design, fabrication and optimising of acoustic and acousto-optical devices it is essential to determine the SAW properties of proton-exchanged waveguides with different $\text{H}_x\text{Li}_{1-x}\text{NbO}_3$ phases and correlate them to the processing conditions and their optical properties. In the present Datareview the important parameter for the design of SAW devices, phase velocity of SAWs on different phases in proton-exchanged LiNbO_3 waveguides, is investigated [40,41]. The SAW velocity was measured using the acousto-optic probe technique. The Rayleigh waves were excited by interdigital transducers, which were deposited on areas protected from the proton exchange. Transducers with a grating period of 30 μm and 60 μm were used, and they could operate at their fundamental and higher harmonics, thus covering the range of frequencies from 60 to about 400 MHz. The input transducer was fed by RF pulses of about 1 μs duration, and the propagation of the SAW was monitored by the probe beam from a He-Ne laser with the wavelength 0.6328 μm . The angle 2Δ between +1 and -1 orders of the acousto-optic diffraction was measured, and the SAW velocity was determined from the relation

$$V = \frac{f\lambda}{\left(1 - \frac{\sin^2 \theta_0}{\cos^2 \Delta}\right)^{1/2} \sin \Delta}$$

where θ_0 was the angle of incidence of the light. The measurement of the angles was performed by a precise goniometer, and the error in the velocity value typically did not exceed 0.1% (approximately 4 m/s).

The dependences of SAW velocity upon frequency in the proton-exchanged samples are presented in FIGURE 1 for SAW propagation along X- and Y-axes [40,41]. In accordance with the previous studies, well-expressed dispersion is observed. The velocity decreases with the frequency for both the X- and Y-directions. At $f \rightarrow 0$, the SAW velocity tends to its value in pure LiNbO_3 . At the highest frequencies, about 400 MHz, no saturation is attained since the SAW energy is still distributed between a layer and a substrate. The acoustic wavelength (and the characteristic penetration depth) at 400 MHz is of the order of 10 μm , whereas the thickness of the proton-exchanged layers did not

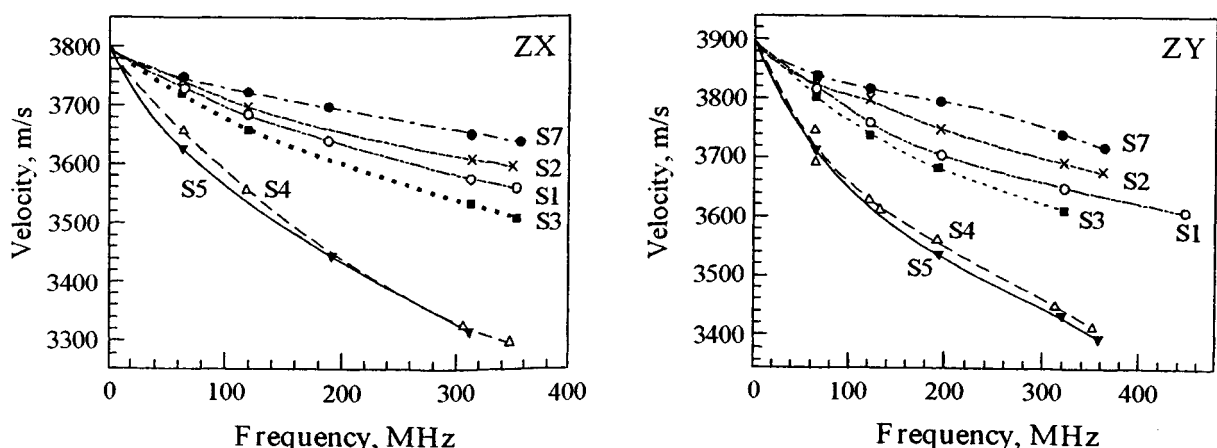


FIGURE 1 Experimental dependences of the SAW velocity on frequency in PE Z-cut LiNbO_3 samples for (a) X and (b) Y propagation direction.

exceed 5 μm . The reason for the SAW dispersion observed is the existence of the layer at the sample surface that has acoustic properties (mainly, tensor of elastic constants, C_{ij}) different from those of the bulk of the sample.

In as-exchanged β_i -phase samples S1 (β_1), S3 (β_2), S4 (β_3) and S5 (β_4) the index profiles are close to a step-like function, while, on the contrary, they are graded in annealed κ_i -phase samples S2 (κ_2^{LT}) and S7 (κ_1^{LT}) [41]. Nevertheless, in order to compare the results obtained in different samples, a common parameter could be defined. Let us define the effective layer thickness d as follows: it is the thickness of the step which has a height equal to the refractive index value at the surface, and an area equal to the area under the real profile. It is evident that such a definition is a good approximation for the samples S1, S3, S4 and S5, and it serves only as a rough approximation for S2 and S7. Using the effective layer thickness thus obtained we were able to normalise the experimental results shown in FIGURE 1 with respect to the common parameter kd , where k is the acoustic wavenumber. The dependences of the relative velocity change $\Delta V/V$ (with respect to the velocity V in pure LiNbO_3) upon kd are shown for both X- and Y-directions in FIGURE 2. One can see from FIGURE 2 that the dependences $V(kd)$ for samples S1, S3 and S4 coincide for both the X- and Y-directions. This is evidence that the layers of different thickness in S1, S3 and S4 have the same acoustic properties, hence, the phases β_1 , β_2 and β_3 cannot be acoustically distinguished. Thus, the layers can be characterised by the single set of acoustic parameters that under certain assumptions may be evaluated from the best fit of the measured and calculated values of the SAW velocity. A stronger dispersion is observed in sample S5, and this can be treated as an effect of the acoustically different β_4 sublayer. Weaker dispersion is observed in samples S2 and S7, which were post-exchange annealed. This shows that, in general, the acoustic properties (elastic constants, in particular) in annealed waveguides are closer to those of the pure crystal in comparison with the samples S1, S3, S4 and S5.

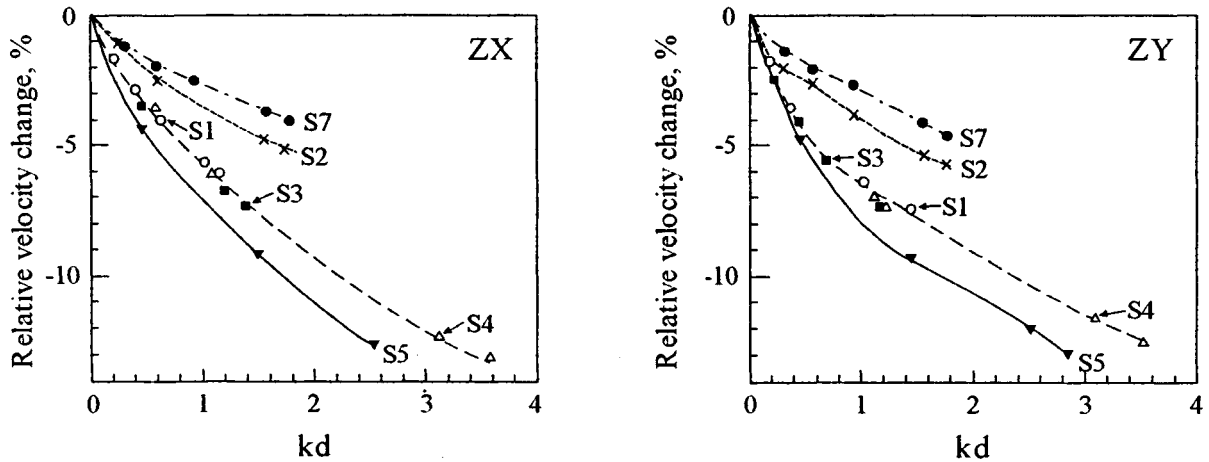


FIGURE 2 Relative SAW velocity reduction versus wavenumber-thickness product for various PE samples: (a) X propagation, (b) Y propagation.

Summarising these results, the formation of a proton-exchanged $\text{H}_x\text{Li}_{1-x}\text{NbO}_3$ layer causes strong acoustic dispersion. No differences in the dispersion were observed in the samples with the β_1 , β_2 and β_3 phases, showing that they are identical from an acoustic point of view, whereas the appearance of β_4 phase leads to stronger dispersion. The κ_i phases, exhibited in annealed samples, are characterised by much weaker dispersion.

D ELECTROMECHANICAL COUPLING COEFFICIENT

Progress in the applications of SAWs in integrated optical devices based on PE lithium niobate stimulates further studies of the material properties that determine the acoustic wave propagation characteristics. The factor of primary importance for many SAW devices is the electromechanical

coupling coefficient defined as twice the fractional change in the SAW velocity produced by short-circuiting the free surface of the substrate with a thin conducting film

$$K^2 = 2 \frac{\Delta V}{V}$$

The electromechanical coupling coefficient K² reflects the piezoelectric properties of both LiNbO₃ substrate and H_xLi_{1-x}NbO₃ layer. The measurements of K² in PE LiNbO₃ have been reported as a loss of piezoelectricity in the H_xLi_{1-x}NbO₃ layer [5,15-18]. The electromechanical coupling coefficient almost decreased with the increase of kd [15-18]. The characteristics of surface acoustic waves on PE 128°-rotated Y-cut LiNbO₃ were investigated in [11]. The decrease of the electromechanical coupling coefficient K² in PE 128°-rotated Y-cut LiNbO₃ as a function of the proton-exchange depth was measured in [11]. The electromechanical coupling coefficient for SAWs in PE 128°-rotated Y-cut LiNbO₃ has also been found to be reduced practically to zero with increasing thickness of the protonated layer and acoustic frequency [42]. In order to obtain a high-efficiency collinear acousto-optic deflector on PE LiNbO₃ with the objective of achieving high-speed seeking and track-following in optical disk drives, the electromechanical coupling coefficient K² in X-cut PE LiNbO₃ was studied experimentally in [34]. It was found that PE greatly reduces K², but annealing can gradually restore the value of K². The changes of the phase velocity V_p and the electromechanical coupling coefficient K² as a function of the proton-exchange depth were measured [34]. Recently the electromechanical coupling coefficient for SAWs in PE Z-cut X-propagation LiNbO₃ has been investigated experimentally by the method of evaporating a thin metal film and measuring in-situ the SAW attenuation [43]. An enhancement in K² value as large as twice that caused by the proton exchange has been observed. This is attributed to the redistribution of electric potential of the acoustic wave due to formation of an H_xLi_{1-x}NbO₃ layer at the surface. The change of electromechanical coupling coefficient in samples fabricated in different conditions depends on the acoustic wavelength-layer thickness product kd (TABLE 1). The increase in electromechanical coupling coefficient can be applied for enhancement of the SAW interdigital transducer efficiency. The influence of annealing on electromechanical coupling coefficient in proton-exchanged 128°-rotated Y-cut X-SAW propagation LiNbO₃ has also been studied in [44].

TABLE 1 Values of squared electromechanical coupling coefficient K² measured for proton-exchanged Z-cut X-propagation LiNbO₃ waveguides at different frequencies f for samples characterised by protonated layer thickness d and surface acoustic wave velocity V [43].

Sample (phase)	d (μm)	f (MHz)	V (m/s)	K ² (10 ⁻²)
Non-exchanged		94	3795	0.46
S1 (β_1)	1.85	31	3780	0.48
		93	3720	0.81
S2 (κ_2^{LT})	2.85	75	3740	0.84
S3 (β_2)	2.14	93	3690	0.8
S5 (β_4)	4.3	74	3626	0.7
		91	3570	0.65
		114	3541	0.47
S7 (κ_1^{LT})	2.9	32	3780	0.53
		63	3760	0.67
		75	3747	0.83
		94	3735	0.81
		117	3725	0.7

E CONCLUSION

The acoustic and acousto-optical properties of proton-exchanged waveguides in different H_xLi_{1-x}NbO₃ phases are summarised in this Datareview. The results obtained are believed to be useful for the design, fabrication and optimisation of SAW and acousto-optical devices in LiNbO₃.

REFERENCES

- [1] V. Hinkov, E. Ise [*J. Phys. D, Appl. Phys. (UK)* vol.18 (1985) p.L31]
- [2] V. Hinkov [*J. Appl. Phys. (USA)* vol.62 (1987) p.3573]
- [3] Yu.N. Korkishko, V.A. Fedorov [*Ion Exchange in Single Crystals for Integrated Optics and Optoelectronics* (Cambridge International Science Publishing, Cambridge, UK, 1999)]
- [4] Y. Handa, M. Miyawaki, S. Ogura [*Proc. SPIE (USA)* vol.460 (1984) p.101]
- [5] F.S. Hickernell, K.D. Ruehle, S.J. Joseph, G.M. Reese, J.F. Weller [*Proc. IEEE Ultrasonics Symp. (IEEE, New York, 1985)* p.237; *IEEE Trans. Ultrason. Ferroelectr. Freq. Control (USA)* vol.33 (1986) p.110]
- [6] V. Hinkov, M. Barth, K. Dransfeld [*Appl. Phys. A (Germany)* vol.3B (1985) p.269]
- [7] P.J. Burnett, G.A.D. Briggs, S.M. Al-Shukri, J.F. Duffy, R.M. De La Rue [*J. Appl. Phys. (USA)* vol.60 (1986) p.2517]
- [8] V. Hinkov [in *Properties of Lithium Niobate* (INSPEC, IEE, London, UK, 1989) ch.3.4 p.94]
- [9] M.E. Biebl, P. Russer [*IEEE Trans. Ultrason. Ferroelectr. Freq. Control (USA)* vol.39 (1992) p.330]
- [10] N. Saiga, Y. Ichioka [*J. Appl. Phys. (USA)* vol.61 (1987) p.1230]
- [11] S. Kakio, J. Matsuoka, Y. Nakagawa [*Jpn. J. Appl. Phys. (Japan)* vol.32 (1993) p.2359]
- [12] J. Paškauskas, R. Rimeika, D. Ciplys [*J. Phys. D, Appl. Phys. (UK)* vol.28 (1995) p.1419]
- [13] D. Ciplys, R. Rimeika [*Electron. Lett. (UK)* vol.34 (1998) p.1707]
- [14] D. Ciplys, R. Rimeika [*Appl. Phys. A (Germany)* vol.64 (1997) p.523]
- [15] Y.C. Chen, C.C. Cheng [*IEEE Trans. Ultrason. Ferroelectr. Freq. Control (USA)* vol.43 (1996) p.417]
- [16] C.C. Cheng, Y.C. Chen, S.T. Wang, B.W. Tsai [*Jpn. J. Appl. Phys. (Japan)* vol.34 (1995) p.1627]
- [17] C.C. Cheng, Y.C. Chen, S.T. Wang [*J. Phys. D, Appl. Phys. (UK)* vol.29 (1996) p.589]
- [18] C.C. Cheng, Y.C. Chen, S.T. Wang, B.W. Tsai [*Jpn. J. Appl. Phys. (Japan)* vol.34 (1995) p.5732]
- [19] C.Y. Shen, Y.T. Shen, R.S. Horng [*Jpn. J. Appl. Phys. (Japan)* vol.38 (1999) p.1438]
- [20] S. Kakio, K. Aoyama, Y. Nakagawa [*Electron. Commun. Jpn. 3 (USA)* vol.83 (2000) p.44]
- [21] S. Kakio, H. Nakamura, Y. Kanamori, Y. Nakagawa [*Jpn. J. Appl. Phys. (Japan)* vol.38 (1999) p.3261]
- [22] C.C. Cheng, R.C. Horng, Y.C. Chen [*IEEE Trans. Ultrason. Ferroelectr. Freq. Control (USA)* vol.48 (2001) p.387]
- [23] E.M. Koralev, Yu.L. Kopylov, V.V. Proklov [*Tech. Digest IEEE Int. Workshop on Integrated Optical and Related Technologies for Signal Processing Florence, Italy, 1984, addendum, paper PD-4*]
- [24] A. Dawar, S.M. Al-Shukri, R.M. De La Rue [*Tech. Digest IEEE Int. Workshop on Integrated Optical and Related Technologies for Signal Processing Florence, Italy, 1984, addendum, paper PD-3*]
- [25] R.L. Davis [*Proc. SPIE (USA)* vol.517 (1984) p.74]
- [26] V. Hinkov, U. Nolte, W. Sohler [*Integr. Guided-Wave Optics Tech. Dig. Series (USA)* vol.4 (1989) p.196]
- [27] M. Miyawaki, S. Ogura [*Appl. Phys. Lett. (USA)* vol.47 (1985) p.918]
- [28] A.L. Dawar, J.C. Joshi [*IEEE Photon. Technol. Lett. (USA)* vol.2 (1990) p.815]
- [29] I. Hinkov, V. Hinkov [*Opt. Quantum Electron. (Netherlands)* vol.25 (1993) p.195]

10.5 Velocity of SAWs in proton-exchanged waveguides in LiNbO_3

- [30] I. Hinkov, V. Hinkov [*Sens. Actuators B, Chem. (Switzerland)* vol.11 (1993) p.227]
- [31] E.M. Biebl, P. Russer [*Proc. IEEE Ultrasonics Symposium USA* (1990) p.604]
- [32] P. Annachelvi, A. Selvarajan, G.V. Anand [*Pramana J. Phys. (India)* vol.41 (1993) p.209]
- [33] C.S. Tsai, Q. Li, C.L. Chang [*Fiber Integr. Opt. (USA)* vol.17 (1998) p.157]
- [34] K. Ito, K. Kawamoto [*Jpn. J. Appl. Phys. (Japan)* vol.37 (1998) p.4858]
- [35] S. Kakio, Y. Nakagawa [*Jpn. J. Appl. Phys. (Japan)* vol.36 (1997) p.3064]
- [36] F. Dobrovolskis, D. Ciplys, R. Rimeika, J. Paškauskas [*Ultragarsas (Lithuania)* no.1(26) (1996) p.33]
- [37] R. Rimeika, D. Ciplys, S. Balakauskas [*Phys. Status Solidi A (Germany)* vol.184 (2001) p.217]
- [38] A.R. Matteo, C.S. Tsai, N. Do [*IEEE Trans. Ultrason. Ferroelectr. Freq. Control (USA)* vol.47 (2000) p.16]
- [39] Yu.N. Korkishko, V.A. Fedorov [Datareview in this book: 3.1 Structural phase diagram of proton-exchanged waveguides in LiNbO_3]
- [40] V.A. Fedorov, Yu.N. Korkishko, D. Ciplys, R. Rimeika [*Proc. 9th Europ. Conf. Integrated Optics Torino, Italy, April 1999*, p.131]
- [41] D. Ciplys, R. Rimeika, Yu.N. Korkishko, V.A. Fedorov [*Ultragarsas (Lithuania)* no.1(29) (1998) p.24]
- [42] D. Ciplys, R. Rimeika [*Appl. Phys. Lett. (USA)* vol.73 (1998) p.2417]
- [43] D. Ciplys, R. Rimeika, Yu.N. Korkishko, V.A. Fedorov [*Appl. Phys. Lett. (USA)* vol.76 (2000) p.433]
- [44] R. Rimeika, D. Ciplys [*Phys. Status Solidi A (Germany)* vol.168 (1998) p.R5]

10.6 Velocity of SAWs on LiNbO₃: anisotropy, temperature and composition dependence

V. Hinkov

This Datareview appeared in *Properties of Lithium Niobate* (INSPEC, IEE, London, UK, 1989) and is reproduced here for the reader's convenience.

Data relevant to the acoustic surface wave velocity in lithium niobate can be found in [1-18]. The elastic constants used in computing the velocity of the surface acoustic waves on LiNbO₃ are given in [1-3]. The SAW velocities for some sample orientations of interest are given in TABLE 1 in units of m/s together with the reference sources.

TABLE 1

Sample orientation	YZ	41.5° X	38° X	16.5° DR	YX
Velocity and ref	3487 ± 3* [11] 3485.6 ± 3* [6] 3487.7 [4] 3491 [7,14]	3995.5 [5] 3966* [11] 3948* [12] 3982 [12] 4003.6 [14]	3977* [11] 3955* [12] 3990 [12]	3503 [10]	3710* [6] 3769 [6] 3769 [4]

An asterix (*) indicates the experimentally measured velocities. Extensive computed velocity data for different substrate geometries can be found in [4,18].

Due to the intrinsic anisotropy of LiNbO₃ the velocity of the surface acoustic waves is directionally dependent. In TABLE 2 the velocity in units m/s is given for waves propagating in different directions on a Y-cut plate [4].

TABLE 2

Angle (°) from X	0 (YX)	10	20	30	40	50	60	70	80	90 (YZ)
Velocity (m/s)	3769	3757	3718	3653	3557	3496	3443	3430	3455	3488

TABLE 3 presents the velocity of an X-propagating surface acoustic wave (in units m/s) as a function of the plate normal direction measured in degrees from the Z-axis [5].

TABLE 3

Plate normal direction (°)	0 (ZX)	10	20	30	40	50	60
Velocity (m/s)	3798	3842	3893	3948	3995	3971	3919
Plate normal direction (°)	70	80	90 (YX)	100	110	120	130
Velocity (m/s)	3860	3813	3769	3735	3706	3686	3673
Plate normal direction (°)	140	150	160	170	180 (ZX)		
Velocity (m/s)	3675	3692	3722	3756	3798		

All the data cited above are assumed to be relevant for LiNbO₃ crystals grown from congruent melt composition (48.6 Li₂O mol%) and at room temperature. In most of the papers the temperature and the crystal composition are not specified.

The temperature stability of the surface acoustic wave velocity is very poor, e.g. the temperature coefficient for the most widely used YZ plates is $94 \times 10^{-6}/^\circ\text{C}$ [7,14,16]. The temperature coefficient has its lowest value of $72 \times 10^{-6}/^\circ\text{C}$ [7,14,16] for 41.5° X-rotated samples. Attempts are made to reduce the temperature sensitivity, e.g. with thin SiO_2 overlayers [17].

The velocity of the surface acoustic waves on LiNbO_3 is also composition dependent. Experiments performed with 128° -rotated Y-cut X-propagating (128 Y-X) samples are reported in [19]. TABLE 4 presents the results obtained in [19], i.e. the velocity of the surface acoustic waves in units m/s as a function of the crystal composition.

TABLE 4

Composition (Li_2O mol%)	Velocity (m/s)
47.55	3940
47.92	3956
48.37	3976
48.60	3986
48.67	3989
48.77	3994
48.93	4000

The dependence presented in TABLE 4 is linear and the coefficient dV/dC (in (m/s)/mol%) has the value of 43.

REFERENCES

- [1] A.W. Warner, M. Onoe, G.A. Coquin [*J. Acoust. Soc. Am. (USA)* vol.42 (1967) p.223]
- [2] Y. Nakagawa, K. Yamanouchi, K. Shibayama [*J. Appl. Phys. (USA)* vol.44 no.9 (1973) p.3966-74]
- [3] A.P. Korolynk, L.Y. Matsakov, V.V. Vasilichenko [*Kristallografiya (USSR)* vol.15 (1970) p.1028]
- [4] J.J. Campbell, W.R. Jones [*IEEE Trans. Sonics Ultrason. (USA)* vol.SU-15 (1968) p.209]
- [5] A.J. Slobodnik Jr., E.D. Conway [*Electron. Lett. (UK)* vol.6 (1970) p.171]
- [6] R.C. Williamson [*1972 Ultrasonics Symp. Proc. (IEEE, New York, USA, 1972)* p.323]
- [7] M. Feldmann, J. Henaff [*Rev. Phys. Appl. (France)* vol.12 no.11 (1977) p.1755-88]
- [8] R.V. Spraight, G.G. Koerber [*IEEE Trans. Sonics Ultrason. (USA)* vol.SU-18 (1971) p.237]
- [9] D. Murray, E.A. Ash [*Proc. Ultrasonics Symp. Phoenix, Arizona, USA, 26-28 Oct. 1977 (IEEE, New York, USA, 1977)* p.823-6]
- [10] A.J. Slobodnik Jr., T.L. Szabo [*Electron. Lett. (UK)* vol.7 (1971) p.257]
- [11] J. Temmyo, I. Kotaka, T. Iramura, S. Yoshikava [*IEEE Trans. Sonics Ultrason. (USA)* vol.SU-27 (1980) p.218]
- [12] K. Shibayama, K. Yamanouchi, H. Sato, T. Meguro [*Proc. IEEE (USA)* vol.64 (1976) p.595]
- [13] M.F. Lewis, C.L. West, J.M. Deacon, R.F. Humphreys [*IEE Proc. A (UK)* vol.131 (1984) p.186]
- [14] J. Henaff, M. Feldmann, M.A. Kirov [*Ferroelectrics (UK)* vol.42 no.1-4 (1982) p.161-85]
- [15] R.T. Smith, F.S. Welsh [*J. Appl. Phys. (USA)* vol.42 (1971) p.2219]
- [16] R.W. Whatmore [*J. Cryst. Growth (Netherlands)* vol.48 no.4 (1980) p.530-47]
- [17] K. Yamanouchi, S. Hayama [*IEEE Trans. Sonics Ultrason. (USA)* vol.SU-31 (1981) p.51]
- [18] A.J. Slobodnik, E.D. Conway, R.T. Delmonico [*Microwave Acoustics Handbook, vol.1a, Surface Acoustic Wave Velocities (AFCRL, Hanscom AFB, MA 01731, USA, TR-73-0597, 1973)*]
- [19] K. Yamaka, H. Takemura, Y. Inoue, T. Omi, S. Matsumura [*Jpn. J. Appl. Phys. Suppl. (Japan)* vol.26 suppl.26-2 (1987) p.219]

10.7 Velocity of SAWs in LiNbO₃: Ti-indiffused, PE and ion-implanted

V. Hinkov

February 1999

A INTRODUCTION

In this Datareview the influence of different impurities introduced into LiNbO₃ by diffusion or ion implantation on the SAW velocity will be discussed. The effects observed can be used to construct acoustic waveguides.

B EXPERIMENTAL DATA

Indiffusion of some metals in LiNbO₃ leads to a small change (in most cases an increase) of the surface acoustic wave velocity [1-3]. YZ samples were investigated in greater detail. The relative changes of the phase velocity V_p at two frequencies are given in TABLE 1, together with some diffusion parameters [1].

TABLE 1 Relative changes of the SAW phase velocity in metal-indiffused samples at two acoustic frequencies [1].

Metal	Film thickness (nm)	Diffusion depth (μm)	Δ(V _p /V) (80 MHz)	Δ(V _p /V) (412 MHz)
Ti	100	3	0.0030	0.0115
Ti	150	3	0.0029	0.0138
Ni	100	100	0.0043	0.0047
Cr	50	/	0.0039	0.0075
Cr	80	/	0.0045	0.1040

In [3] the relative velocity change produced by the metal indiffusion is given by the following expression:

$$\frac{\Delta V}{V} = \chi \left(\frac{W_m}{W_l} \right) \quad (1)$$

where χ is characteristic of the metal diffused, W_m is the weight per unit area of the metal deposited and W_l is the weight per unit area of the LiNbO₃ contained in the volume of depth

$$0.5(\sqrt{\pi})b$$

Here b is a measure of the diffusion depth

$$b = \sqrt{(4Dt)}$$

where D is the diffusion coefficient and t is the diffusion time. Expression (1) is only valid if b is much larger than the surface wave penetration depth. The value of χ is given in [3] for two metals: 2.1 for Ni and -1.5 for Zn. In contrast to all other metals investigated, the Zn produces a velocity decrease.

Unusual surface wave velocity changes were observed on Ti-diffused +ZY samples [4]. A group velocity decrease of ~5% at about 100 MHz was observed for a sample indiffused with 80 nm Ti at 1000°C for nine hours. At frequencies higher than 200 MHz an increase is observed of no more than 3%. The exact frequency behaviour of the velocity is a function of the preparation technology. A plausible explanation for the anomalous velocity change is that an inversion layer of ferroelectric domains is formed by the diffusion of Ti into +YZ-LiNbO₃ [4]. No unusual velocity changes were observed on Ti-diffused -Z samples, i.e. they behave like the YZ samples [4].

The observed effects are of interest in microacoustics and integrated optics. They were used for constructing waveguides for surface acoustic waves [2]. Ti-diffused regions are nowadays widely used as cladding for SAW waveguides in combined guiding structures for surface acoustic and optical waves to optimise the collinear acousto-optic interactions. The first experiments were performed several years ago on YZ-samples [5]. Today the preferred interaction geometry is based on XY-samples [6-8].

Proton exchange (exchange of Li-ions with protons) leads to very significant velocity changes for the surface acoustic waves [9-15]. This effect was observed for waves propagating in all directions on X-, Y- and Z-cut samples, as well as on 128°-rotated Y-cut [15,16]. The absolute value of the changes is larger for surface acoustic waves propagating along the X- and Y-axis and much smaller for those propagating along the Z-axis [9,10,12]. As a result, a change in the sign of the acoustic birefringence of the LiNbO₃ crystal is observed [10,12].

In [10], Y-cut samples exchanged in pure benzoic acid were investigated by means of Brillouin scattering involving surface acoustic waves with a wavelength of only 0.25 μm. This small wavelength allowed observation of the properties of the 4 μm deep, proton-exchanged region alone. Results for samples exchanged in 0.25 mol% Li-diluted benzoic acid were published in [12]. X-, Y- and Z-cut samples were investigated in that study at an acoustic frequency of 215 MHz. Since the penetration depth of the surface acoustic waves was greater than the depth of the proton-exchanged layer, the 'true' velocity in the latter was computed from the measurements by assuming the substrates and the layer were isotropic. Whereas in [10] a velocity decrease is observed for all propagation directions, in [12] a velocity increase is also observed for waves propagating in the Z-direction. This sign reversal in the velocity change is a consequence of the use of a Li-diluted proton source, as subsequent investigations have shown [14].

TABLE 2 summarises the results presented in [10] and [12] for Y-cut substrates. The experiments were performed at room temperature with LiNbO₃ crystals grown from congruent melt composition (48.6 Li₂O mol%). The unperturbed velocity is also given for comparison as taken from [17]. All velocity data are given in units of m/s.

The observed velocity changes are strongly dependent on the technological treatment of the samples, e.g. exchange in pure or diluted acid, annealing, etc. The reduction of the strength of the proton exchange, e.g. by using diluted acid or post-exchange annealing, also leads to a reduction of the size of the observed effects [9,14-16]. There is as yet no physical model to explain the experimental data. The velocity depends on the density p and on an effective elastic constant c as

$$\sqrt{(c/p)}$$

TABLE 2 SAW velocity changes after proton exchange in Y-cut LiNbO₃.

Propagation direction, degrees from X	SAW velocity (m/s) unexchanged LiNbO ₃ [17]	SAW velocity (m/s) after exchange in pure acid [10]	SAW velocity (m/s) after exchange in 0.25 mol% Li-diluted acid [12]
X ... 0	3769	2972	2744
10	3757	2989	2755
20	3718	2975	2837
30	3653	2955	3126
40	3557	2916	3383
50	3496	2942	3672
60	3443	3011	3621
70	3430	3110	3517
80	3455	3162	3476
Z ... 90	3488	3189	3682

Since the density of LiNbO₃ is only slightly perturbed (~1% decrease) by the proton exchange, the observed velocity changes can only be caused by a dramatic change of the effective elastic constant of up to about 40%. The elastic properties of proton-exchanged layers on Y-cut LiNbO₃ samples were investigated in [18] in greater detail.

The decrease of the SAW velocity by the proton exchange is accompanied by an increase of the acoustic attenuation for waves propagating in Y- and X-directions as reported in [9,10,12]. No pronounced changes in the attenuation were observed for waves propagating in the Z-direction [9,12]. A more detailed study of the attenuation of the SAWs, as well as its temperature dependence for PE 128°-rotated Y-cut LiNbO₃ samples, is given in [15,16,19]. It is suggested in [16] that the attenuation enhancement can be attributed to the large number of defects introduced during the exchange. Post-exchange annealing reduces the attenuation significantly, parallel to the reduction of the velocity changes [9,15,16].

The proton exchange also leads to a reduction of the SAW velocity in LiTaO₃ crystals, as reported in [20-23].

Strongly guiding waveguides for the surface acoustic waves were fabricated on LiNbO₃ [14], making use of the large velocity change produced by the proton exchange. Waveguides that can simultaneously guide surface optical and acoustic waves were also reported [13]. The latter are important in integrated optics, since they allow a large increase in the efficiency of the collinear acousto-optic interactions [24].

Implantation of ions in LiNbO₃ leads to a decrease of the SAW velocity as measured on YZ samples. Experiments have been performed with ⁴He⁺ beams [25-28] or Ar⁺ beams [29,30] at 100 keV. Inert gas ions have been used in order to avoid the formation of new chemical compounds in the surface layer, so the effects observed are mainly determined by the defects the implanted ions generate.

Experimental results on the velocity perturbation obtained for two (⁴He⁺) ion doses are summarised in TABLE 3, as taken from the graphs published in [26]. The velocity decrease is given in % from the unperturbed velocity for five different SAW frequencies. The results obtained with Ar⁺ ions [30] indicate the same effects. Several ion doses, from 10¹²/cm² to 10¹⁶/cm², have been used in this study. Additionally, it was observed that the decrease of the SAW velocity is coupled with an increase of the acoustic attenuation [30].

TABLE 3 SAW velocity perturbation by ion implantation [26].

SAW frequency →	$\Delta V/V (\%)$				
	100 MHz	200 MHz	300 MHz	400 MHz	500 MHz
Ion doses ↓					
$2.5 \times 10^{15} \text{ ions/cm}^2$	-0.5	-0.9	-1.2	-1.3	-1.4
$10^{16} \text{ ions/cm}^2$	-0.9	-1.5	-2.1	-2.2	-2.5

The frequency dependence of the velocity change (see TABLE 3) is due to the dispersion introduced by the implanted layer with a thickness of about 0.9 μm . At lower ion doses of up to $2 \times 10^{14}/\text{cm}^2$ (Ar^+) a gradual decrease of the SAW velocity to 1.2% is observed with an insignificant increase in the attenuation. The point defects introduced by the implantation and the stresses they produce in the surface layer are responsible for these effects. For higher ion doses, the crystalline structure is strongly perturbed up to a complete amorphisation above $2 \times 10^{14}/\text{cm}^2$ and generation of microcracks at and above $10^{16}/\text{cm}^2$. The velocity changes observed at these ion doses are governed by the reduction of the effective electromechanical coupling coefficient of lithium niobate. A strong increase of the SAW attenuation is caused by the microscopic defects [30].

Guides for SAWs fabricated on YZ LiNbO_3 with ion implantation have also been reported [26].

C CONCLUSION

Data are presented on the changes in SAW velocity on introduction of various impurities into LiNbO_3 . These impurities are introduced by indiffusion, proton exchange and ion implantation. The frequency dependence of the velocity change in the latter case is also tabulated.

REFERENCES

- [1] R.V. Schmidt [*Appl. Phys. Lett. (USA)* vol.27 (1975) p.8]
- [2] J.F. Weller, J.D. Crowley, T.G. Giallorenzi [*Appl. Phys. Lett. (USA)* vol.31 (1977) p.146]
- [3] G.D. Boyd, R.V. Schmidt, F.G. Storz [*J. Appl. Phys. (USA)* vol.48 (1977) p.2880]
- [4] Shu-yi Zhang, Zhang-nan Lu, Jun Yu, Wen-bo Yuan [*Appl. Phys. A (Germany)* vol.40 (1986) p.119]
- [5] L.N. Binh, J. Livingstone [*IEEE J. Quantum Electron. (USA)* vol.QE-16 (1980) p.964]
- [6] D.A. Smith, J.J. Johnson [*IEEE Photon. Technol. Lett. (USA)* vol.3 (1991) p.923F]
- [7] I. Hinkov, V. Hinkov, E. Wagner [*Electron. Lett. (UK)* vol.30 (1994) p.1884]
- [8] F. Tian et al [*IEEE J. Lightwave Technol. (USA)* vol.12 (1994) p.1192]
- [9] V. Hinkov, E. Ise [*J. Phys. D (UK)* vol.18 (1985) p.31]
- [10] V. Hinkov, M. Barth, K. Dransfeld [*Appl. Phys. A (Germany)* vol.38 (1985) p.269]
- [11] F.S. Hickernell, K.D. Ruehle, S.J. Joseph, G.M. Reese, J.F. Weller [*Ultrasonics Symp. Proc.* San Francisco, CA, USA, 16-18 Oct. 1985, Ed. B.R. McAvoy (IEEE, New York, USA, 1985) p.110]
- [12] P.J. Burnett, G.A.D. Briggs, S.M. Al-Shukri, J.F. Duffy, R.M. De La Rue [*J. Appl. Phys. (USA)* vol.60 (1986) p.2517]
- [13] V. Hinkov, R. Opitz, W. Sohler [*Proc. 4th European Conf. Integrated Optics* Glasgow, Scotland, 11-13 May 1987, Eds. C.D.W. Wilkinson, J. Lamb (Glasgow Univ., Dept. Electron. & Electr. Eng., UK, 1987) p.112]
- [14] V. Hinkov [*J. Appl. Phys. (USA)* vol.62 (1987) p.3573]
- [15] Sh. Kakio, J. Matsuoka, Y. Nakagawa [*Jpn. J. Appl. Phys. (Japan)* vol.32 (1993) p.2359]
- [16] J. Paskauskas, R. Rimeika, D. Ciplys [*J. Phys. D, Appl. Phys. (UK)* vol.28 (1995) p.1419]

10.7 Velocity of SAWs in LiNbO_3 : Ti-indiffused, PE and ion-implanted

- [17] J.J. Cambell, W.R. Jones [*IEEE Trans. Sonics Ultrason. (USA)* vol.SU-15 (1968) p.209]
- [18] E.M. Biebl, P. Russer [*IEEE Trans. Ultrason. Ferroelectr. Freq. Control (USA)* vol.39 (1992) p.330]
- [19] D. Ciplys, R. Rimeika [*Appl. Phys. A (Germany)* vol.64 (1997) p.523]
- [20] K. Hano, N. Chubachi, T. Sannomiya [*Electron. Lett. (UK)* vol.28 (1992) p.2306]
- [21] M. Hirabayashi, T. Yamasaki, Y. Komatsu [*Jpn. J. Appl. Phys. (Japan)* vol.32 (1993) p.2355]
- [22] J. Kushibiki, M. Miyashita, N. Chubachi [*IEEE Photon. Technol. Lett. (USA)* vol.8 (1996) p.1516]
- [23] D. Ciplys, R. Rimeika [*Phys. Status Solidi A (Germany)* vol.163 (1997) p.R13]
- [24] V. Hinkov, R. Opitz, W. Sohler [*J. Lightwave Technol. (USA)* vol.LT-6 (1988) p.903]
- [25] P. Hartemann, M. Morizot [*Ultrasonics Symp. Proc.* Milwaukee, WI, USA, 11-13 Nov 1974 (IEEE, New York, USA, 1974) p.307]
- [26] P. Hartemann [*Appl. Phys. Lett. (USA)* vol.27 (1975) p.263]
- [27] P. Hartemann, P. Canvard, D. Desbois [*Appl. Phys. Lett. (USA)* vol.32 (1978) p.266]
- [28] P. Hartemann [*Ultrasonics Symp. Proc.* New Orleans, LA, USA, 26-28 Sept 1979, Eds. J. de Klerk, B.R. McAvoy (IEEE, New York, USA, 1979) p.649]
- [29] R.Yu. Valatka, S.A. Ionelyunas, L.I. Pranyavichyus [*Sov. Phys.-Acoust. (USA)* vol.26 (1980) p.454]
- [30] V.M. Basin, A.V. Petrov, G.B. Pranyavichene, D.Yu. Eidukas [*Sov. Phys.-Acoust. (USA)* vol.30 (1984) p.160]

CHAPTER 11

BASIC PROCESSING TECHNIQUES

- 11.1 Poling of LiNbO₃
- 11.2 Preparation of LiNbO₃ wafers
- 11.3 Chemical etching of LiNbO₃
- 11.4 Ion beam milling and reactive ion beam etching of LiNbO₃
- 11.5 Reactive ion etching of LiNbO₃
- 11.6 Excimer laser treatment of LiNbO₃

11.1 Poling of LiNbO₃

D.H. Jundt

September 2000

A INTRODUCTION

Even though lithium niobate crystallises in the paraelectric phase (non-polar) at the growth temperature, it is a ferroelectric material at room temperature. When cooled below the Curie temperature in the absence of an electric field, a multi-domain structure normally develops [1,2]. Conversion to the generally desired single-domain crystal structure is typically done by application of an electric field, while simultaneously cooling the crystal below the Curie temperature, a process called 'poling'.

B AS-GROWN DOMAIN STRUCTURE

When cooling a crystal without applying an electric field, the crystal will spontaneously orient itself into a variety of domains. Such domains can be made visible by polishing the faces with subsequent etching. Domains on X-faces will not show up because of the mirror symmetry resulting in equal polish and etch rates for both domain orientations. Etching can be performed with a mixture of one part of HF and two parts of HNO₃ at the boiling point [1]. Concentrated HF at room temperature has also been utilised successfully. A small gradient in stoichiometry or impurity concentration will often lead to a domain preference [2]. This effect can be utilised in the growth of periodically poled crystals [3,4]. During poling, such grown-in biases must be overcome by applying a field large enough to overpower them.

The point symmetry in the various domains is the same, but the crystallographic Y- and Z-axis have their signs reversed. This is equivalent to a rotation by 180° around the X-axis. Because the X-planes are mirror planes, this can also be thought of as a point inversion. Symmetric second-order tensors are not affected, but all tensor elements of a third-order tensor such as electro-optics or piezo-optics will change sign as one moves from one domain to the next.

Neighbouring domains are separated by domain walls. As the crystal is heated or cooled, pyroelectric charges accumulate at those boundaries. This leads to a refractive index modulation via the electro-optic effect. As a result, an unpoled crystal looks somewhat milky when cooled to room temperature. The protonic conductivity of lithium niobate (LN) decreases the boundary charges over a time period of several weeks, after which the crystal appears clear.

C POLING OF CRYSTALS

Crystals can be poled anywhere below the Curie temperature, even though the required field becomes very large as the temperature drops significantly below the transition temperature [5]. The Curie temperature depends on the crystal composition, and the impurity content. Lithium-rich, or MgO-doped crystals, for example, have a higher Curie temperature than the pure, congruent composition. For undoped lithium niobate with varying composition $c = \text{Li}/(\text{Li} + \text{Nb})$, the Curie temperature T_c can be calculated according to:

$$T_c = -746.73 + 39.064c \quad (1)$$

where the lithium composition c is given in mol % [6].

In the most straightforward implementation, poling is performed during growth, before the crystal is cooled to room temperature. A voltage is applied between the seed mount and the crucible, and a small current is sent through the crystal. This can lead to single-domain crystals even though the crystal does not cool through the phase-transition temperature while the current is being applied (annealing is typically performed at temperatures higher than the Curie point). It appears that the current sets up impurity or compositional gradients that lead to spontaneous ordering on cooling. Even though this method is simple, it poses some difficulties. Czochralski growth systems generally have high thermal gradients, and the electric field has to be applied for quite a long time. The resistivity in the seed (which is coolest) is high, and the applied current displaces lithium ions, often damaging the seed [7].

A more controlled method of poling has been described by Nassau et al [7]. The multi-domain crystal is harvested from the growth furnace after having cooled to room temperature. Depending on the crystal orientation, the field must be applied in different ways. In a Z-crystal or a crystal grown close to a Z-orientation, the field can be applied from top to bottom of the crystal. In some cases, it is advantageous to crop the ends so that flat areas can be contacted. In X- or Y-oriented crystals, the field is applied from the sides of the cylindrical crystal. To ensure adequate and uniform contact, the areas where the voltage is applied are often covered with a platinum paste (suspension of platinum particles in a solvent). After the paste has dried, the electrodes are connected, and the crystal is heated above the Curie temperature. On firing, the platinum forms a continuous cover and ensures good contact. A small electric field, 0.2 - 5 V/cm [7], is then applied, as the crystal is cooled below the Curie temperature. Since lithium niobate is conductive (mostly ionic) at those temperatures, a current density of about 2 - 5 mA/cm² typically results [8]. The conductivity is strongly temperature dependent and is shown in FIGURE 1. Poling is typically performed in a flowing oxygen atmosphere in order to avoid reduction of the material.

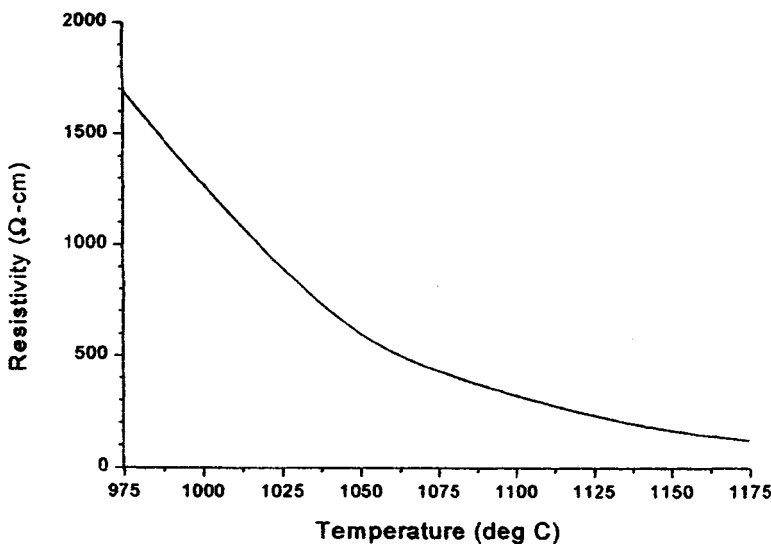


FIGURE 1 DC conductivity of lithium niobate at high temperature.

Poling can also be achieved at room temperature, as long as the coercive field of about 21 kV/mm is exceeded [9]. At elevated temperature, the coercive field is lower, and vanishes at the Curie point. In order to get an estimate on when the field can be switched off during normal poling, it is instructive to estimate the coercive field in the neighbourhood of the Curie point.

The phase-transition in LN can be modelled as a second-order phase transition with Gibbs free energy [10]

$$G = \frac{\beta(T - T_c)}{2} D^2 - \frac{\gamma}{4} D^4 \text{ with } \beta > 0, \text{ and } \gamma > 0 \quad (2)$$

where β and γ are material specific constants.

The applied electric field E as a function of D is calculated by taking the derivative of EQN (2). Above the Curie temperature T_c , the function $E(D)$ has only one root at $D = 0$. At temperatures T below T_c , there are two new roots at the spontaneous polarisation value $D = P_s$. The permittivity ϵ , the spontaneous polarisation P_s , and the coercive field E_c can be derived from EQN (2):

$$P_s = \sqrt{\frac{\beta(T_c - T)}{\gamma}} \quad (3a)$$

$$\frac{1}{\epsilon} = 2\epsilon_0\beta(T_c - T) \quad (3b)$$

$$E_c = \frac{2\beta}{3} \sqrt{\frac{\beta}{3\gamma}} [(T_c - T)]^{3/2} \quad (3c)$$

Published measurements of permittivity [11] and spontaneous polarisation [12,13] have shown the predicted temperature dependence of EQNS (3a) and (3b), and allow the determination of β and γ .

$$2\epsilon_0\beta = 1.63 \times 10^{-5} \frac{1}{\text{K}} \text{ and thus } \beta = 9.20 \times 10^5 \frac{\text{V m}}{\text{K C}} \quad (4a)$$

$$\frac{\beta}{\gamma} = \frac{P_s^2}{T_c - T} = \frac{0.002008}{\text{K}} P_s^2 \text{ (300 K) and thus } \gamma = 9.09 \times 10^8 \frac{\text{V m}^5}{\text{C}^3} \quad (4b)$$

Inserting those values into EQN (3c) yields an expression for the coercive field close to, but below T_c :

$$E_c = 113 \frac{\text{V}}{\text{cm}} \times \left(\frac{T_c - T}{\text{K}} \right)^{3/2} \quad (4c)$$

At T_c , successful poling can be achieved with very small applied electric fields; just one degree below T_c , over 100 V/cm are necessary to reverse the polarisation of domains. Once the crystal has cooled a few degrees below the transition temperature, the field can be switched off without any danger of depolarisation. The time required for the voltage to be applied is mainly determined by the crystal temperature uncertainty and the cooling rate.

D CONCLUSION

The desired single-domain form of LiNbO_3 is obtained by applying an electric field while cooling below the Curie point, a process known as poling. Poling can be carried out on the crystal after growth, as it is cooling to room temperature. A more controlled route is to apply the field, to a grown multi-domain crystal, in various directions depending on the crystal orientation. The phase transition can be modelled as a second-order transition.

REFERENCES

- [1] K. Nassau, H.J. Levinstein, G.M. Loiacono [*J. Phys. Chem. Solids (UK)* vol.27 (1966) p.983]
- [2] P.F. Bordui, R.G. Norwood, C.D. Bird, G.D. Calvert [*J. Cryst. Growth (Netherlands)* vol.113 (1991) p.61]
- [3] G.A. Magel, M.M. Fejer, R.L. Byer [*Appl. Phys. Lett. (USA)* vol.56 (1990) p.108]
- [4] D.H. Jundt, G.A. Magel, M.M. Fejer, R.L. Byer [*Appl. Phys. Lett. (USA)* vol.59 (1991) p.2657]
- [5] L.E. Myers, R.C. Eckardt, M.M. Fejer, R.L. Byer, W.R. Bosenberg, J.W. Pierce [*J. Opt. Soc. Am. B (USA)* vol.12 (1995) p.2102]
- [6] P.F. Bordui, R.G. Norwood, D.H. Jundt, M.M. Fejer [*J. Appl. Phys. (USA)* vol.71 (1992) p.875]
- [7] K. Nassau, H.J. Levinstein, G.M. Loiacono [*J. Phys. Chem. Solids (UK)* vol.27 (1966) p.989]
- [8] A. Räuber [*Curr. Top. Mater. Sci.* vol.1 Ed. E. Kaldis (North-Holland, Amsterdam, 1978) p.481]
- [9] L.E. Myers, W.R. Bosenberg [*J. Quantum Electron. (USA)* vol.33 (1997) p.1663]
- [10] M.E. Lines, A.M. Glass [*Principles and Applications of Ferroelectrics and Related Materials* (Clarendon Press, Oxford, 1977) p.680]
- [11] [Landolt-Börnstein, *Zahlenwerte und Funktionen aus Naturwissenschaften und Technik*, Neue Serie, Eds. K.-H. Hellwege, A.M. Hellwege (Springer-Verlag, Berlin, 1987)]
- [12] D. Birnie [*J. Mater. Res. (USA)* vol.5 (1990) p.1933]
- [13] S.H. Wemple, J.M. DiDomenico, M. Camlibel, I. Camlibel [*Appl. Phys. Lett. (USA)* vol.12 (1968) p.209]

11.2 Preparation of LiNbO₃ wafers

T. Fang, L. Gordon and D.H. Jundt

June 2001

A INTRODUCTION

Lithium niobate wafers are used in many different products such as surface acoustic wave (SAW) filters, integrated optic devices, birefringent elements in optical read heads, and blur-filters for digital cameras. Smaller volume uses include non-linear and electro-optic devices, and transducers for acousto-optic cells. As of this writing, over 80 tons of lithium niobate per year are grown and fabricated into wafers worldwide.

Wafers are ideally suited for mass fabrication processes involving lithography with subsequent coating steps. These technologies have been pioneered and refined for VLSI manufacturing on silicon. As the device scale continues to get smaller, the requirements for surface quality, cleanliness, and wafer flatness become more demanding. To satisfy the requirement of decreasing chip cost, the wafer size must increase so that more chips can be processed together in the same processing steps. Lithium niobate is undergoing the same evolution as silicon, albeit somewhat delayed in time. The most commonly used wafer diameter in lithium niobate today is 100 mm, with some customers making the transition to 125 mm (silicon fabs are currently moving to 300 mm wafers).

B TRADITIONAL FABRICATION METHODS

Crystals used in bulk form are typically produced with equipment commonly used in custom glass fabrication shops. Unlike glass, LN is an anisotropic crystal with material properties very dependent on orientation. Therefore, an X-ray goniometer is used in all production to accurately align the cut faces with respect to the crystalline lattice. The key fabrication steps are X-ray orientation, sawing, lapping, and polishing. The crystals are typically mounted using waxes or epoxies [1,2]. The choice of the mounting medium depends on two factors: the workpiece should be held without slipping or shifting so that crystal orientation and flatness are not compromised. The mounting medium also should be removed easily after de-mounting in order to minimise the burden on subsequent cleaning processes. Care must be taken when heating and cooling lithium niobate. Large thermal gradients may fracture the crystal, and a large pyroelectric charge build-up during cool-down can spontaneously discharge, leading to domain inversion.

Cutting is performed with peripheral saws or annular saws with diamond fixed-abrasive blades. Depending on the cut depth and the finish desired, the diamond abrasive size and the speed may vary. The cutting lubricants are normally aqueous-based.

Lapping can be done using either fixed or loose abrasives, with a variety of types and sizes available. Fixed abrasive comes as a wheel or a sheet; loose abrasive is typically suspended in water. The most common abrasive types are SiC, diamond and Al₂O₃, with the most common sizes ranging from 3 to 20 µm. The desired surface characteristics dictate which abrasive type and size are chosen. Larger abrasives remove material faster, but result in a rougher surface with deeper subsurface damage requiring longer polishing time. A multi-step lapping process with consecutively finer abrasives often gives the lowest subsurface damage in the shortest time.

Polishing is usually performed using an alkaline colloidal silica slurry on a polyurethane pad. To achieve a flat surface polish, the pad must be well maintained, and it is necessary to mount the LN

piece surrounded by ‘blocking’ material, made either of glass with a similar polishing rate, or lithium niobate. To prevent the silica slurry from drying on the polished surface, the mounted part may be dipped into a dilute NaOH solution followed by spraying with DI water and drying with nitrogen [2].

C HIGH-VOLUME WAFER MANUFACTURING

For high-volume wafer manufacturing, the material utilisation needs to be optimised and the process automated as much as possible. Luckily, silicon wafer manufacturing demands have resulted in machine development that can be utilised for LN wafer manufacturing with minor modifications. LN wafers manufactured today are most commonly produced in 3” (76.2 mm), 100 mm and 125 mm diameters. The wafer thickness varies depending on the application. Thicker wafers (typically 1 mm) are more costly, but are more rigid with a smaller chance of handling-induced breakage. The most commonly used thicknesses for SAW wafers are 0.35 and 0.5 mm. Most lithographic applications do not require the back surface to be polished. Many wafers therefore are polished on one side only, with the back surface typically in an as-lapped state. However, inspection for front-surface cleanliness is hindered by the large amount of light scattered from the rough backside. Therefore, demanding high-end applications typically prefer wafers that are polished on both sides.

The crystals of cylindrical shape are grown in the orientation most suitable for efficient wafer manufacturing. For example, in the case of the common 128° RY wafer orientation, the wafer normal and the cylinder axis are perpendicular to the crystallographic (10.4) plane. After growth and poling, the crystals are ground into a perfect cylindrical shape with a diameter slightly larger than the finished wafer diameter. This is done on fixed diamond abrasive wheels using aqueous coolant. Orientation flats are then ground along the cylinder sides with similar equipment.

There are two technologies used for wafer slicing: annular saws and wire saws. In an annular saw, the saw blade is held and tension applied around its outside perimeter. This gives the thin blade the required stiffness. The inner rim of the central hole in the saw blade is coated with electrophoretically deposited diamond. Using this saw, each wafer is cut individually in a process that takes several minutes. To ensure good cutting quality, the blade sharpness and deflection must be monitored, and selective dressing is required to correct for asymmetrical cutting. FIGURE 1 shows the geometry and reference frame of the slicing using an annular saw [3].

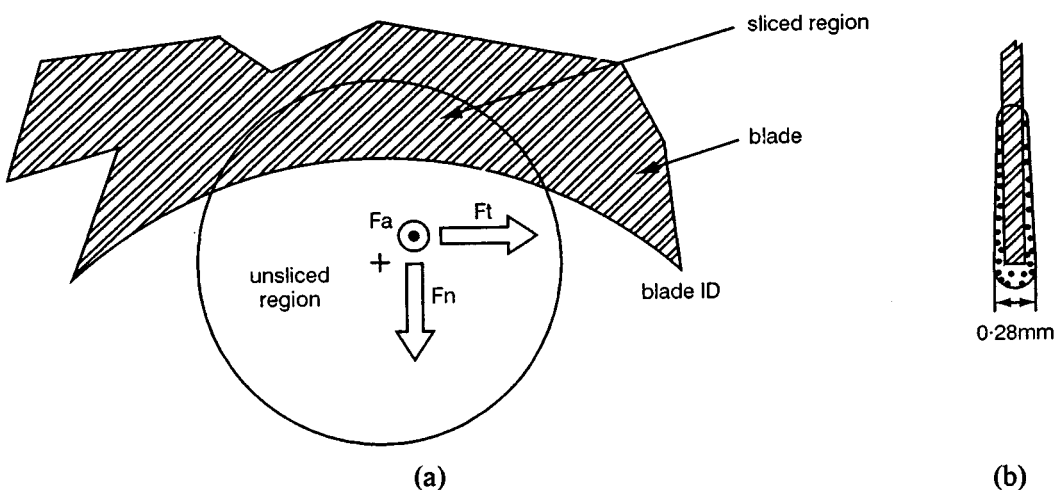


FIGURE 1 (a) Geometry of sliced crystal and saw blade; (b) cross-section of blade.

FIGURE 2 shows the forces the saw blade exerts on the material as it is being cut. The material is a (10.4) crystal with a cylinder diameter of 3 inches. The tangential and radial forces are linearly

related, and both vary with the length of arc of material being sliced as the cylindrical crystal is fed into the blade at constant speed. The axial force ideally is zero, and its magnitude is an indication of the asymmetry of the blade condition.

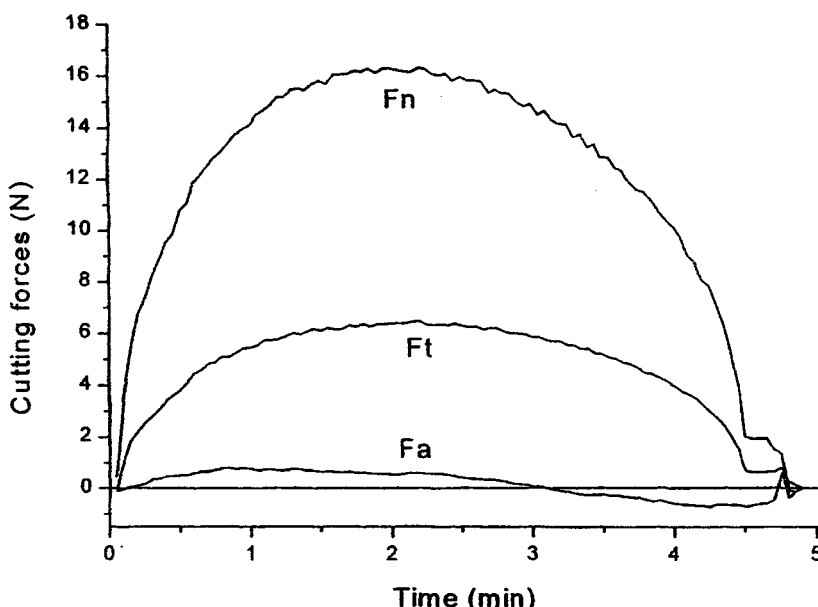


FIGURE 2 Measured forces during the cut of one wafer.

Wire slicing was developed for large diameter silicon wafers that cannot be cut on annular saws. In this process, a continuous wire is wound around several grooved guide-rolls. The resulting 'web' between two of those guide-rolls can be up to 400 mm long consisting of hundreds of wire segments. As the steel wire is stretched with high tension and transported at speeds up to 15 m/s, cutting is performed by loose abrasive (SiC) delivered in a suspended slurry of either glycol or oil [4]. Wire slicing has the advantage of smaller kerf loss, it can be scaled to larger wafer sizes, and it has the potential for lower warp and better surface finish of the sliced wafers. Several hundred wafers can be sliced in a single run taking a few hours. The kerf loss is typically smaller than in annular saws because a thin wire can be used.

Normally, after the wafers are sliced, the perimeter is re-machined to avoid having edge cracks propagate in subsequent processing steps. A high-quality edge is also important for reducing wafer breakage in processing steps involving rapid temperature changes. This operation can either be done by hand (bevelling), or by automated edge-grinding machines. Typical edge-grinding machines have a cassette-to-cassette operation. The wafers are taken from the supply cassette to an alignment chuck where the previously defined flat is sensed in order to assure precise re-grinding of the orientation flat. Then, the wafer is passed onto the grinding chuck. A grinding wheel with embedded diamond and grooves of the desired contour is used in the actual grinding operation. The grinding of the circular perimeter, the orientation flat, and auxiliary flats is controlled by a program stored in the machine's memory. If a very smooth finish is required, a multiple-step process with consecutively finer diamond abrasive must be used.

The sliced surface is not well suited to be polished directly. ID sliced wafers may have extensive subsurface damage, and the thickness may not be well controlled. Wire-sawn wafers often display ridges corresponding to the reciprocating wire transport (wire feed direction changes approximately every 10 s) typically used for wire slicing. A lapping step is therefore used to ensure reproducible roughness and good thickness control. The finer the abrasive used for the lapping step, the less material has to be removed in the time-intensive polishing process. Lapping can be performed in

multiple steps with decreasing abrasive size; however, since each finer abrasive requires cleaning of both the wafers and the lapping machine, high-volume production houses will usually choose one abrasive to optimise removal and minimise subsurface damage. Fixed abrasive grinding machines are cassette-to-cassette and grind one wafer and one surface at a time. They can be set up with multiple wheels with different abrasive sizes; however, throughput is low, with one cassette (25 wafers) taking 30 - 45 min. Most common in production are double-sided lapping machines, using a loose abrasive slurry. The wafers are held inside carriers, which are rotated by the sun and ring gears as the upper and lower plates rotate separately from the carriers. With these four parameters, the plate speeds can be optimised with respect to the wafer surfaces for equal removal from both sides of the wafer. Wafer batches of tens to hundreds of wafers (depending on the machine and wafer sizes) are typically processed simultaneously in one run of 10 - 15 min.

Lapping creates a rough layer with a partially amorphous orientation, resulting in a highly stressed surface. This stress can be relieved by etching the wafer before further processing. Since LN is quite inert, hydrofluoric acid (HF) is typically used. This stress-relief is particularly important for polished wafers where one side remains unpolished.

As with lapping, the polishing process uses machines that have been developed for the silicon processing industry. Single-side polishing machines mount the wafers onto flat plates that are then rotated against the polishing pad. Wafers are either wax mounted or positioned by templates and held in place by capillary action between the wafer and the template backing. Wax mounting permits the production of very flat wafers; however, mounting, demounting and cleaning is tedious. In contrast, the template system is extremely fast for mounting and demounting, and introduces no hindrances to cleaning. Double-side polishing machines are similar in design, size and capacity to double-side lapping machines, and can achieve better parallelism than the single-side polishing machines. As with lapping, the wafers are held in place and rotated by carriers. These carriers can be made from a variety of materials: reinforced fibreglass, steel, or stainless steel, depending on the thickness and stiffness of the carrier required. The choice of mounting and polishing supplies as well as the polishing parameters such as pressure and rotation rates have a very large influence on the removal rate, surface quality and flatness of the wafers. LN polishes much more slowly than silicon, requiring larger pressures. This can lead to non-elastic deformation in the polishing pad and template backing, resulting in significant roll-off (thinner edges). As wafer users make the transition to high-throughput projection lithography systems, the flatness and parallelism requirements for LN wafers are increasing. Vendors and manufacturers are constantly developing new products and techniques optimised for LN polishing, to achieve flatter, higher-quality wafer surfaces in high-volume production.

High-volume cleaning of LN wafers also borrows from the silicon industry. Traditionally scrubbers have been used for the final cleaning step; however, the increasing demands for better cleanliness, coupled with recent advances in sonic cleaning technology, favour the implementation of non-contact ultrasonic and megasonic systems. These sonic systems permit the removal of very fine particles simultaneously from all surfaces and edges of the wafers.

D CONCLUSION

Although most LN processing techniques have originated in silicon manufacturing, as the LN industry is maturing and moving to very high volume, new technology is continually being developed that is specific to LN material properties and wafer requirements. While any wafer manufacturing will always be compared to that of silicon, the challenge has been to employ the available high-volume equipment, but to optimise the techniques for LN production.

REFERENCES

- [1] D.F. Horne [*Optical Production Technology* (Adam Hilger, London, 1972)]
- [2] G.W. Fynn, W.J.A. Powell [*The Cutting and Polishing of Electro-Optical Materials* (Adam Hilger, London, 1983)]
- [3] T. Fang, D.H. Jundt, J.C. Lambropoulos [*Proc. ASME Int. Mech. Eng. Congress and Exposition* vol.EEP-vol.28 (2000) p.227]
- [4] J. Li, I. Kao, V. Prasad [*J. Electron. Packag. (USA)* vol.120 (1998) p.123]

11.3 Chemical etching of LiNbO₃

C.W. Pitt; updated by K.A. Green

August 2001

Wet etching, using aqueous-acid and other solutions, has been found to be almost impossible to use for device shaping, since it is both slow at room temperature (less than tens of Å/min, depending on etchant and concentration), and imprecise in delineating masked edges. The poor edge acuity may result from preferential attack on defects in the bulk crystal, so that wet chemistry has found some application with other chemically based procedures for revealing the structure and defect topography [1-5]. Domain polarity, the effect of dopants, and crystal-axis direction all affect the etch rate [6]. Wet etching has also been employed as part of a cleaning procedure, for example before using crystallographic structural examination techniques such as electron diffraction [7,8]. Common formulations include concentrated and dilute HF, HF with HNO₃, and orthophosphoric acid. Reactivity has been enhanced by using heated solutions, for example 1 part HF + 2 parts HNO₃ at the boiling point for 2 min [1], to reveal etch pits and domain boundaries.

Due to the low chemical reactivity of lithium niobate, technology development for device shaping through chemical etching has focused on enhancing reactivity through, for example, plasma processes [15]. Since some structural defects appear to etch rapidly, one approach to accelerating the chemical attack, and to some extent improving the etched-wall acuity, has been to induce large numbers of defects to the point of amorphising the crystal in selected areas. Implantation of gas ions has been studied as a means of disrupting the crystal bonds and thus reducing the energy required to chemically remove atoms. In an early comparison between etch rates achieved by ion milling [9], dilute HF etching and ion-enhanced wet etching, the ion dose transfers ~5 eV to each atom in the lattice region, which is comparable to the binding energy of the crystal. A detailed general study [10] determined the minimum dose for accelerated etching, and highlighted one of the difficulties of the process: the etch rate varies with the buried damage profile as the removal of material proceeds into the crystal. This difficulty appears to have been overcome [11] by the use of multiple-energy implants; smoothly etched walls were produced as the overlapping damage regions in the crystal tended to give a more uniform etch rate versus depth relationship. TABLE 1 shows a comparison of some of the reported results.

Laser-enhanced chemical etching either in molten salts [12] or in gas atmospheres [13,14] is a relatively recent innovation that offers a potential alternative to the ion implantation approach. In the salt-fusion process [12], powdered KF was sprinkled on the surface. It absorbed water by deliquescence and was heated to the fusion reaction temperature by pulses from a 270 nm Nd-YAG-pumped frequency-doubled dye laser (1200 pulses, power density of, for example, 800×10^8 W/cm²). The reaction products were removed by rinsing in water. The material removal rate was given as 10 µm/min. Another combined chemical/ablation process exposes z-cut lithium niobate layers, in an atmosphere of 500 torr Cl₂, to a frequency-doubled argon-ion laser (257 nm, 50 mW, 1.4 MW/cm² on substrate, beam scanned at 0.5 to 10 µm/s) [13]. The etch rate for a 1.5 µm 1/e diameter laser beam, 21 mW, 10 s exposure, is described as a hole 0.8 µm deep. A purely ablative process [14] has been achieved by XeCl excimer laser exposure of lithium niobate (308 nm, full-width-half-maximum pulses of 11 ns, 10 Hz, energy density varied from <1 to ~3 J/cm², up to 1000 pulses). The results indicated a threshold for ablation at ~1 J/cm², and, at higher energy densities, a dependence on both the optical energy density and the irradiated area. The latter effect appeared to be due to ablated material attenuating the laser beam, particularly apparent for larger exposed areas. The ablation rate per laser pulse varied

TABLE 1 Etching characteristics of ion-damaged lithium niobate.

Crystal cut	Ion beam parameters			Subs. temp. (°C)	Etching characteristics			Ref and comments				
	Type	Energy (keV)	Dose ($10^{15}/\text{cm}^2$)		Time (min)	Solution	Temp. (°C)					
Y	H^+	60	No etch rate increase at any dose							[9] cf. etch rate of 80 Å/min in same HF etch at 50°C		
	He^+	150	No etch rate increase at any dose									
	N^+	60	20	-	9	1 pt. 47% HF + 8 pt. H_2O	RT	145				
	N^+	60	20	-	-		40	1450				
	Ar^+	150	30	-	6		RT	217				
	Ar^+	60	3	-	2		RT	300				
Y	N^+	150	<1	RT	No etch rate increase			[10]; error bars are ± 17 Å/min				
	N^+	150	20	RT	6	3% HF in H_2O	RT	130				
					12			173				
					18			90				
					50			19				
Y & Z	He^+	30+		25	-	8% HF in H_2O	-	None	[11]; multiple implants in one substrate			
		60+		25	10	24.5% HF	-	300				
		90+		25	40	24.5% HF	-	33				
		120+		25	4	49% HF	-	1250				
		150		25	36	49% HF	-	16				

from $\sim 0.02 \mu\text{m}$ per pulse (1 J/cm^2 ; 83 and $156 \mu\text{m}$ diameter holes) to $0.14 \mu\text{m}$ per pulse (3 J/cm^2 ; $24 \mu\text{m}$ diameter hole). Note that the etched surface roughness achieved by the laser-enhanced processes to date is poor compared with gas-etched lithium niobate.

REFERENCES

- [1] S. Miyazawa [*Appl. Phys. Lett. (USA)* vol.23 no.4 (1973) p.198]
- [2] V.A. Meleshina et al [*Phys. Status Solidi A (Germany)* vol.62 (1980) p.475]
- [3] G.S. Jeen, C.S. Kim, M.S. Jang [*New Phys. (Korean Phys. Soc.) (South Korea)* vol.23 (1963) p.279]
- [4] N.G. Bocharova, E.V. Rakova, S.A. Semiletov [*Kristallografiya (Russia)* vol.30 (1985) p.114; transl. in *Sov. Phys.-Crystallogr. (USA)* vol.30 no.1 (1985) p.63]
- [5] V.P. Sergeev, E.A. Budovskikh, L.B. Zuev, G.I. Goldenberg [*Kristallografiya (Russia)* vol.31 (1986) p.612; transl. in *Sov. Phys.-Crystallogr. (USA)* vol.31 (1986) p.361]
- [6] Z.E. Alekseeva, L.B. Vorob'eva, N.F. Evlanova [*Inorg. Mater. (USA)* vol.22 (1986) p.1213]
- [7] M. Petrucci, C.W. Pitt [*Electron. Lett. (UK)* vol.22 (1986) p.637]
- [8] E. Muller, G. Pflug, U. Burghoff [*Cryst. Res. Technol. (Germany)* vol.22 (1987) p.KI2]
- [9] M. Kawabe, M. Kubota, K. Masuda, S. Namba [*J. Vac. Sci. Technol. (USA)* vol.15 no.3 (1978) p.1096]
- [10] G. Gotz, H. Karge [*Nucl. Instrum. Methods Phys. Res. (Netherlands)* vol.209/210 pt.2 (1983) p.1079]
- [11] C.I.H. Ashby, G.W. Arnold, P.J. Brannon [*J. Appl. Phys. (USA)* vol.65 no.1 (1989) p.93]
- [12] C.I.H. Ashby, P.J. Brannon [*Mater. Res. Soc. Symp. Proc. (USA)* vol.75 (1987) p.419]
- [13] K.W. Beeson, V.H. Houlding, R. Beach, R.M. Osgood Jr. [*J. Appl. Phys. (USA)* vol.64 no.2 (1988) p.835]
- [14] M. Eyett, D. Bauerle [*Appl. Phys. Lett. (USA)* vol.51 no.24 (1987) p.2054]
- [15] C.W. Pitt [Datareview in this book: 11.4 Ion beam milling and reactive ion beam etching of LiNbO_3]

11.4 Ion beam milling and reactive ion beam etching of LiNbO₃

C.W. Pitt; updated by C. Florea

May 2001

The increasing use of LiNbO₃ in acousto-optics and integrated optics starting in the 1970s created the need for a reliable and precise etching technology, which was not satisfied at the time by chemical solution etching (see Datareview 11.3 in this book). Therefore a focused research effort was directed toward passive and reactive ion beam etching of LiNbO₃ that continues to attract attention to this day.

Ion beam milling in the case of LiNbO₃ is a difficult process in that it yields very low etch rates and the by-products are not easily removable during the milling leading to undesirable redeposition. Also, the etch selectivity between the mask and the niobate depends strongly on the residual partial pressures in the chamber (for example the oxygen will oxidise a metal mask or it will ash a photoresist mask). This might be why some of the earlier reported etch-rate results tend to vary quite widely. The repeatability of the process has improved since as a result of equipment development.

The most frequently used commercial ion beam millers employ Kaufman gun sources in which Ar gas is injected at low pressure (circa 3 mtorr) into a plasma-arc discharge between a hot filament cathode and a surrounding cylindrical anode. Optically aligned grids serve to extract the positive ions and shape them in a collimated mono-energetic beam. Beam diameters of several centimetres have been achieved with current densities of mA cm⁻² and energies from a few tens to several thousand eV.

An alternative beam-forming system is the saddle ion source. Cold cathode sources tend to produce smaller overall beam currents than the Kaufman source, but beam shaping and direction can usually be achieved more easily by means of shaped apertures.

Reactive ion beam etching can provide better results than inert-gas milling since additional material removal is obtained through a chemical reaction involving the reactive gas used. Argon gas may be employed to help maintain the reactive plasma (in which case the reactive gas can be either injected into the extracted inert beam or into the discharge chamber and formed into a beam by the grids) or the reactive gas may be the sole beam constituent.

Milling and etching rates along with the conditions employed are presented in TABLE 1 and TABLE 2. Most of the reported work was performed on Y- and Z-cut plates, but there is little difference in the etch rates between the two cuts so the crystal orientation has been omitted from the Datareview.

The milling rates are relatively low compared with most masking materials such as photoresists or oxide layers, implying thick masking and shallow etch features. Only modest etch selectivity (between the mask and niobate) enhancement was gained by using reactive species because of the momentum transfer.

The milling and etch rates can be increased dramatically by directing the ion beam at non-normal incidence angles to the sample [7]. This is so because the sputter yield curve of removed atoms per incident ion depends on both incident ion energy and the depth at which the lattice bond is broken. However, this technique may result in faceting of the etched face if the starting surface is featured [12].

Several authors [8,13] note that the inert gas milling of LiNbO₃ produces a dark grey surface due to induced oxygen deficiency in the surface layers after etching; sheet resistivity appears to be reduced by this effect.

11.4 Ion beam milling and reactive ion beam etching of LiNbO_3

TABLE 1 Argon milling rates (the beam is at normal incidence unless otherwise indicated).

Beam parameters		Pressure	Source type	Etch rate (\AA min^{-1})	Ref
I (mA cm^{-2})	U (V)				
0.65	500	-	Kaufman	276	[1]
0.6	1000	0.1 mtorr	-	240	[2]
0.45	500	-	-	78	[3]
1.2	1000	0.08 mtorr	Kaufman	500	[4]
0.4	500	-	-	80	[5]
1.15	1000	1.3 mPa	Kaufman	350	[6]
0.85	600	-	Kaufman	200	[8]
0.6 - 1.0	1000	-	-	400	[9]
0.5	500	0.03 mPa	Kaufman	150	[10]
1.0	1000	same	same	280	
30 $\mu\text{A}^{(a)}$	7000	0.4 mtorr	Saddle	0.75 (10°) ^(b) 1.09 (30°) 0.75 (40°)	[11]
1.2	1000	0.002 mtorr	Kaufman	350	[14]

^(a)No area given. ^(b)The angle is with respect to the normal to the sample face; the indicated rates are the selectivity ratio between niobate and Shipley 1405J photoresist (at the given chamber pressure, the etch rate of this type of photoresist is between 100 \AA min^{-1} and 500 \AA min^{-1} depending on the partial pressure of oxygen in the residual chamber atmosphere).

TABLE 2 RIBE rates (the beam is at normal incidence unless otherwise indicated).

Beam parameters		Gas	Source type	Etch rate (\AA min^{-1})	Ref
I (mA cm^{-2})	U (V)				
0.4	500	CF_4	-	140	[5]
0.4	500	CHF_3	-	130	
0.2	500	C_2F_6	Kaufman	200	
0.4	500	same	same	290 (90°) 400 (45°)	[7]
0.5	500	same	same	310	
0.85	600	25% O_2 + 75% Ar	Kaufman	130	[8]
0.5	500	20% O_2 + 80% Ar	Kaufman	50	[10]
1.0	1000	same	same	220	
40 $\mu\text{A}^{(a)}$	5000	30% CHF_3 + 70% Ar	Saddle	3.5 (10°) ^(b) 7.0 (30°) 2.5 (40°)	[11]
0.3	300	CHF	Kaufman	60	
0.3	900	CHF	same	135	
0.3	1200	CHF	same	190	[13]
0.3	300	CF	same	270	
0.3	900	CF	same	180	
0.3	1200	CF	same	310	
1.2	1000	$\text{SF}_6 + \text{Ar}^{(c)}$	Kaufman	650	[14]
0.6	400	$\text{O}_2 + \text{Ar}^{(d)}$	-	12	[15]

^(a)No area given. ^(b)See TABLE 1 note. ^(c)The extracted Ar beam was injected with reactive gas to comprise approximately 10% of the beam composition. ^(d)No mixture details given.

REFERENCES

- [1] H.I. Smith, J. Melngailis, R.C. Williamson, W.T. Brogan [*J. Vac. Sci. Technol. (USA)* vol.10 (1973) p.1127]
- [2] M. Cantagrel [*J. Vac. Sci. Technol. (USA)* vol.12 (1975) p.1340]

11.4 Ion beam milling and reactive ion beam etching of LiNbO_3

- [3] M. Kawabe, M. Kubota, K. Masuda, S. Namba [*J. Vac. Sci. Technol. (USA)* vol.15 (1978) p.1096]
- [4] S.P. Singh, C.W. Pitt [*Proc. Ion Plating & Allied Techniques Conf.* London (1979) p.37]; C.W. Pitt [*J. Non-Cryst. Solids (Netherlands)* vol.47 (1982) p.159]
- [5] S. Matsui, T. Yamato, H. Aritome, S. Namba [*Jpn. J. Appl. Phys. (Japan)* vol.19 (1980) p.L463]
- [6] P.S. Chung [*Opt. Laser Technol. (UK)* vol.15 (1983) p.263]
- [7] B. Zhang, S. Forouhar, S.Y. Huang, W.S.S. Chang [*J. Lightwave Technol. (USA)* vol.2 (1984) p.528]
- [8] R.E. Chapman [*Vacuum (UK)* vol.34 (1984) p.417]
- [9] A.C.G. Nutt, J.P.G. Bristow, A. McDonach, P.J.R. Laybourn [*Opt. Lett. (USA)* vol.9 (1984) p.463]
- [10] D.A. Darbyshire, A.P. Overbury, C.W. Pitt [*Vacuum (UK)* vol.36 (1986) p.55]
- [11] M. Belanger, G.L. Yip [*J. Lightwave Technol. (USA)* vol.5 (1987) p.1252]
- [12] M.A. Venables, S.S. Makh [*J. Mater. Sci. Lett. (UK)* vol.6 (1987) p.1254]
- [13] R. Congxin, Y. Jie, Z. Yanfang, C. Lizhi, C. Guoliang, T. Sichang [*Nucl. Instrum. Methods Phys. Res. B (Netherlands)* vol.19/20 (1987) p.1018]
- [14] D.A. Darbyshire to C.W. Pitt [private communication (1989)]
- [15] J. Sochtig [*Electron. Lett. (UK)* vol.24 (1988) p.844]

11.5 Reactive ion etching of LiNbO₃

C.W. Pitt; updated by C. Florea

May 2001

Plasma etching is a well-known etching technique and it has been applied to lithium niobate in both its forms: direct plasma etching and reactive ion etching. Due to the interest in LiNbO₃-based integrated optics devices, plasma etching of this material still attracts great interest.

In order to sustain an acceptable etch rate the plasma must be of sufficiently high density to supply many ions (the chamber pressure of the reactive gas is usually tens to hundreds of Pa) and the sample must form non-volatile compounds with the etching gas. Lithium niobate is rather non-chemically reactive when etched through direct plasma etching (etch rates from a few angstroms to tens of angstroms per minute). It seems probable that the Li in the niobate tends to form non-volatiles since the removal rate of niobium pentoxide, both Cl and F plasmas, is significantly higher than that of the LiNbO₃.

Somewhat better results can be obtained through reactive ion etching (RIE), in which lower-pressure plasma is used and the sample is placed in a DC bias. In this way the sample experiences not only the chemical reaction with the plasma ions but also some directional energetic ion bombardment by plasma ions accelerated across the cathode dark space. The physical process may sputter away non-volatile monolayers as they form, so maintaining the removal rate. Due to this added physical process, the RIE process is analogous to reactive ion beam etching (RIBE, see Datareview 11.4 in this book), but with ion energies usually of tens to a few hundred eV.

It should be noted that the etch rates are still modest: around 70 - 80 Å min⁻¹ (see TABLE 1). One exception is the hollow cathode configuration [2] which gave up to 2000 Å min⁻¹ etch rates. This suggests that commercial parallel-plate etchers might be improved by enhanced confinement of the plasmas and somewhat higher electrode voltages. Such a configuration might resemble that of the magnetron sputter-etch electrode.

Enhancement of the etch rate has been observed when the (Y-cut) LiNbO₃ samples were bombarded with MeV O²⁺ ions [8]. The etch rate was increased by two to three times when etching in CF₄ or CF₄:CHF₃ plasmas after the bombardment. The enhancement factor was dependent on the implant dose with the rate significantly increasing for doses larger than about 3×10^{14} ions cm⁻². No enhancement in the etch rate in an Ar plasma was observed after the bombardment.

It might be expected that an essentially chemical etching process would exhibit etch-rate variation with the crystal cut. However, little mention is made of the crystal cuts in the RIE literature.

Finally, it is noted from [4] that plasmas containing no oxidising agent are likely to produce the characteristic darkening of the etched surface, especially at higher ion energies (see Datareview 11.4 in this book).

The results presented in TABLE 1 are some of the most significant in this field of research. Several of the papers mention gas flow rates, but without the associated chamber volume and the pumping rates of the system. Therefore this information has been omitted and the chamber pressure given in each case (although it must be noted that in some systems the base pressure may be a significant fraction of the operational pressure).

TABLE 1 RIE rates.

Chamber details	Excitation frequency (MHz)	Electrode spacing (cm)	Gas and pressure	Power input	Etch rate (\AA min^{-1})	Ref
(Tegal Plasmaline 211)	-	-	CF_4 550 mtorr	300 W	70	[1]
Planar sputter-etch electrode	8	-	CF_4 20 Pa	$U = 600 \text{ V}$	15	[2] ^(a)
			CF_4 15 Pa	$U = 1000 \text{ V}$ $U = 800 \text{ V}$ $U = 1800 \text{ V}$	50 100 2000	
(PlasmaTech PE80) parallel plate (24 cm dia.)	13.56	3 - 6	$\text{CF}_4 + 5\% \text{ O}_2$ 3 Pa	0.2 W cm^{-2}	80	[3]
			SF_6 25 - 100 mtorr	0.2 W cm^{-2}	70	
(STS 320 RIE) (dia. 380 cm, capacity $1.5 \times 10^5 \text{ cm}^3$)	13.56	3 - 6	$\text{CF}_4:\text{CHF}_3^{(c)}$ 50 mtorr	75 - 580 W (self bias $\sim 185 - 700 \text{ V}$)	10 - 150	[6]
(PlasmaTech?)	-	-	SF_6 3 mtorr	300 W	160	[7]

^(a)For the power input, in this paper V is given, which is the peak-to-peak RF voltage applied to the excited planar electrode. ^(b)The planar sputter-etch and the hollow cathode electrode etch rate results appear to be presented for comparable electrode sizes. ^(c)A variety of gas ratios, chamber pressures and flow rates were tried but did not influence the etch rate; the etching has been largely attributed to a physical sputtering process.

REFERENCES

- [1] C.L. Lee, C.L. Lu [*Appl. Phys. Lett. (USA)* vol.35 (1979) p.756]
- [2] P.S. Chung, C.M. Horwitz, W.L. Guo [*Electron. Lett. (UK)* vol.22 (1986) p.484]
- [3] D.A. Darbyshire, A.P. Overbury, C.W. Pitt [*Vacuum (UK)* vol.36 (1986) p.55]
- [4] N.A. Astakhova, M.V. Streltsov, Yu.V. Tsvetkova [*Phys. Chem. Mater. Treat. (UK)* vol.21 (1987) p.327]
- [5] D.A. Darbyshire to C.W. Pitt [private communication (1989)]
- [6] P.W. Leech [*J. Vac. Sci. Technol. A (USA)* vol.16 (1998) p.2037]
- [7] J. Sochtig, H. Schultz, R. Widmer, H.W. Lehmann, R. Groß [*Proc. SPIE (USA)* vol.2213 (1998) p.98]
- [8] P.W. Leech, M.C. Ridgway [*J. Vac. Sci. Technol. A (USA)* vol.17 (1999) p.3358]

11.6 Excimer laser treatment of LiNbO₃

C. Florea

October 2001

A INTRODUCTION

Due to the sustained interest in LiNbO₃-based integrated optics devices, practical techniques of etching the LiNbO₃ are still being investigated. Dry and wet etching, as well as the RIE and RIE-like processes have been known for quite some time and some of the main results have been presented elsewhere in this book.

Part of the larger field of UV laser ablation, the UV excimer laser treatment of the LiNbO₃ has emerged as an alternative to the typical etching techniques. In itself, the UV laser ablation of LiNbO₃ can be used as a thin film growth technique, which is known as pulsed laser deposition.

B EXCIMER LASER ABLATION AND SURFACE RELIEF STRUCTURES

Excimer laser surface etching of LiNbO₃ can be used for the fabrication of surface relief structures either by itself or as a complementary step in more involved processes.

The ablation process of LiNbO₃ is, in general, described as a combination of thermal fusing and air annealing processes [1,2]. A thin layer of material is fused and ablated by the excimer pulse. Depending on the etching geometry, material redeposition on the surface will limit the etch depth.

It was found that the exposed area is Nb-rich [3] as LiO₂ evaporates preferentially, having a higher vapour pressure than Nb₂O₅. Also, the illuminated area will present higher wet-etching rates in HF [4].

Etching with a CW laser at 257 nm (in Cl₂ atmosphere) and with 15 ns laser pulses at 248 nm have been compared and it was found that the etch rate is much higher when using the pulsed laser [1]. A study of the ablation dynamics in the picosecond regime has also been performed [5], which supports the idea that the excimer laser pulse creates an ablation plume that will shield the substrate from an eventual second pulse [5]. This shielding is observed within a few picoseconds of the first pulse and therefore the ablation dynamics are quite sensitive to the repetition rate. The ablation process is considered to be mainly due to single-photon absorption [5].

The ablation threshold is dependent on the pulse width and on the wavelength. It has been measured to be about 0.9 J cm⁻² in the case of 11 ns pulses at 308 nm [6], 0.6 J cm⁻² in the case of 15 ns pulses at 248 nm [1], and 0.05 J cm⁻² in the case of 500 fs pulses at 248 nm [5]. Etching experiments were performed in Cl₂, O₂, N₂, H₂ and air and it was found that the threshold fluences are nearly identical [1]. The influence of the beam size on the ablation rates in the nanosecond regime has also been investigated [6].

Some of the experimental conditions and ablation rates are presented in TABLE 1 below.

The main application of the excimer laser treatment has been the generation of surface relief gratings on either X-cut or Z-cut wafers. Gratings 110 nm deep and with 2 μm periods have been achieved by simple ablation [2]. Submicrometer gratings with periods of 350 - 500 nm and depths of up to

TABLE 1 UV excimer laser ablation rates.

Laser	Pulse width	Repetition rate	Fluence/energy per pulse	Ablation rate per pulse	Notes	Ref
248 nm	15 ns	1 pulse	Up to 1.2 J cm^{-2}	Up to 50 nm	Y- and Z-cut wafers $\text{Cl}_2, \text{O}_2, \text{N}_2, \text{H}_2$ and air	[1]
248 nm	30 ns	1 pulse	400 mJ cm^{-2}	110 nm (total depth)	X-cut wafer	[2]
248 nm	0.5 ps	1 pulse-pair with variable delay	Around 115 mJ cm^{-2} per pulse	Up to 20 nm per pulse-pair	Pulses have different fluences	[5]
248 nm	0.5 ps	1 pulse	170 mJ cm^{-2}	80 nm (180 nm after 5 pulses)	X-cut wafer; no ablation enhancement after the fifth pulse	[7]
248 nm	see [7]	see [7]	Below ablation threshold	-	X- and Z-cut wafers; wet etching followed the excimer exposure	[8]

180 nm have also been obtained by small-area exposure (for high fluence) [7,8] or by exposure below the ablation threshold followed by wet etching in an HF-HNO₃ mixture [8]. For submicrometer structures, pulse durations less than 1 ns should be used such that the thermal diffusion length in the material is negligible compared to the dimension of the structure to be fabricated [7]. When exposing under the ablation threshold, the UV irradiation will induce surface relief structures due to either volume expansion [9] or higher concentrations of crystal point defects in the exposed areas [4].

Atomic force microscopy (AFM) studies of the surface morphology of the ablated gratings suggest that the morphology is comparable to that obtained with the dry etching technique [7,10]. Surface smoothness of less than 0.25 μm was measured for fluences up to around 1 J cm^{-2} [3]. Redeposition of the molten material on the LiNbO₃ surface might actually help when trying to build surface relief gratings as it will enhance the relative depth of the grating [7].

C EXCIMER PULSED LASER DEPOSITION

The UV excimer laser treatment of the LiNbO₃ is also a topic of interest in the field of thin film growth. Good-quality LiNbO₃ films would allow complex functions to be integrated on planar structures, which are of great commercial potential. In particular, pulsed laser deposition (PLD) using excimer lasers has become a widely used tool for LiNbO₃ thin film growth. Typical values for the PLD process parameters are given in TABLE 2. For more details on the PLD process see [11-14] and references therein.

TABLE 2 Process parameters for PLD of LiNbO₃ thin films - typical values.

Laser line (nm)	Pulse width (ns)	Repetition rate (Hz)	Pulse energy density	Temperature and atmosphere	Target	Substrates
248/193	10 - 30	1 - 15	$1 - 5 \text{ J cm}^{-2}$	$400 - 800^\circ\text{C}$ O_2	LiNbO ₃ single crystals or Li-Nb-O ceramics	Sapphire, Si

D CONCLUSION

This Datareview has described the technique of excimer laser surface etching of LiNbO₃, which can be used as an alternative to the more traditional wet etching processes. Ablation rates, and their dependence on key process parameters, are summarised. The main application is in the generation of surface relief gratings. Excimer pulsed lasers can also be used to deposit thin films of LiNbO₃ on sapphire and silicon substrates.

REFERENCES

- [1] K.W. Beeson, N.S. Clements [*Mater. Res. Soc. Symp. Proc. (USA)* vol.129 (1989) p.321]
- [2] G.P. Luo et al [*Appl. Phys. Lett. (USA)* vol.69 (1996) p.1352]
- [3] N. Omori, M. Inoue [*Appl. Surf. Sci. (Netherlands)* vol.54 (1992) p.232]
- [4] K.I. Avdienko et al [*Sov. Tech. Phys. Lett. (USA)* vol.14 (1988) p.442]
- [5] S. Preuss, M. Spath, Y. Zhang, M. Stuke [*Appl. Phys. Lett. (USA)* vol.62 (1993) p.3049]
- [6] M. Eyett, D. Bauerle [*Appl. Phys. Lett. (USA)* vol.51 (1987) p.2054]
- [7] K. Chen, J. Ihlemann, P. Simon, I. Baumann, W. Sohler [*Appl. Phys. (Germany)* vol.65 (1997) p.517]
- [8] S. Mailis, G.W. Ross, L. Reekie, J.A. Abernethy, R.W. Eason [*CLEO 2000, Conf. on Lasers and Electro-Optics* paper CWK46 (2000)]
- [9] B. Wu, P.L. Chu, H. Hu, Z. Xiong [*IEEE J. Quantum Electron. (USA)* vol.35 (1999) p.1369]
- [10] J. Sochtig, H. Schutz, R. Widmer, R. Lehmann, R. Gross [*Proc. SPIE (USA)* vol.2213 (1994) p.98]
- [11] G. Balestrino et al [*Appl. Phys. Lett. (USA)* vol.78 (2001) p.1204]
- [12] D. Ghica et al [*Appl. Surf. Sci. (Netherlands)* vol.138-139 (1999) p.617]
- [13] K. Matsubara, S. Niki, M. Watanabe, P. Fons, K. Iwata, A. Yamada [*Appl. Phys. A (Germany)* vol.69 (1999) p.S679]
- [14] Y. Shibata, K. Kaya, K. Akashi, M. Kanai, T. Kawai, S. Kawai [*Appl. Phys. Lett. (USA)* vol.61 (1992) p.1000]

CHAPTER 12

RARE-EARTH DOPING

- 12.1 Erbium doping of LiNbO₃ by thin film diffusion**
- 12.2 Erbium doping of LiNbO₃ by the ion exchange process**
- 12.3 Study of erbium-doped LiNbO₃ waveguides by the beam propagation method**

12.1 Erbium doping of LiNbO₃ by thin film diffusion

F. Caccavale and F. Segato

August 1999

A INTRODUCTION

In recent years, several studies have been conducted on the thermal diffusion of erbium from metal film into lithium niobate (LiNbO₃) crystals ([1-3] and references therein). In this Datareview, a systematic review on the Er diffusion process is reported. Thermal diffusion is investigated as a function of crystal cut direction, process parameters (temperature and time) and initial film thickness. Erbium concentration profiles are obtained by secondary ion mass spectrometry (SIMS).

The diffusion process is investigated in two distinct regimes: (i) diffusion from an infinite source to evaluate the lower limit of the solid solubility of erbium in LiNbO₃, (ii) thin film diffusion regime, with complete depletion of the erbium source. Combining experimental data with the diffusion theory, relevant parameters such as diffusion coefficient, diffusion constant and activation energy are derived.

B EXPERIMENT

Erbium is deposited as a metallic film on the surface of cleaned optical grade X-cut and Z-cut LiNbO₃ wafers by electron beam evaporation in vacuum. Deposition of Er in oxygen atmosphere (at a partial pressure of about 10⁻² Pa) leads to the formation of an Er₂O₃ film, more suitable for photolithographic processes. Film thickness ranges from 5 to 15 nm for complete diffusion. For the infinite source regime, a 100 nm thick film has been deposited.

The diffusion process is performed in a tubular quartz furnace, with a flow of dry oxygen at a rate of about 0.5 dm³/min. Diffusion temperatures varying from 1000 to 1100°C and times varying from 72 to 120 h are used. Investigations have also been performed at lower (down to 920°C) and higher (up to 1150°C) temperatures. The Curie temperature of lithium niobate (1142°C) represents a natural upper limit for thermal processes, in order to preserve the ferroelectric structure of the crystal.

Erbium concentration profiles are measured using a CAMECA ims4f ion microscope, equipped with a normal incidence electron gun used to compensate charge build-up while profiling insulating samples [4]. The erosion speed is evaluated by measuring the depth of the crater at the end of the analysis by a Tencor Alpha-Step profilometer. Calibration of the Er profiles is made by measuring the total Er dose in the as-deposited films using Rutherford backscattering spectrometry (RBS), and invoking mass conservation during the diffusion process.

C DIFFUSION THEORY

The theoretical description of the thermal diffusion process of metals in lithium niobate crystals is made by Fick's law, which is derived from the general diffusion equation [5] under the assumption that the diffusion coefficient D is independent of the erbium concentration profile c:

$$\frac{\partial c(y,t)}{\partial t} = D \frac{\partial^2 c(y,t)}{\partial y^2} \quad (1)$$

12.1 Erbium doping of LiNbO_3 by thin film diffusion

where y is the diffusion direction normal to the crystal surface and t is time. In the infinite source regime, the contour conditions and the solution of EQN (1) can be expressed as follows:

$$\begin{cases} c(y=0, t) = c_0 \\ c(y > 0, t=0) = 0 \end{cases} \quad (2)$$

$$c(y, t) = c_0 \operatorname{erfc}\left(\frac{y}{d}\right) \quad (3)$$

where c_0 is the erbium concentration at the crystal/film interface, and

$$d = 2\sqrt{Dt}$$

is the diffusion depth. c_0 represents also the lower limit of solid solubility, as it asymptotically approaches its maximum value after long diffusion time, the erbium ions not being completely exhausted at the surface.

For a finite film of initial thickness τ , the depletion time t_d for the complete diffusion can be calculated analytically from the mass conservation law:

$$t_d = \left(\frac{\rho N_{AV} \tau}{2M c_0} \right) \frac{\pi}{D} \quad (4)$$

where ρ is the mass density of the film, N_{AV} is the Avogadro number, and M is the molecular weight of erbium.

In the thin film diffusion regime ($t \gg t_d$), the solution of EQN (1) can be approximated by a Gaussian function with a surface concentration

$$\hat{c} = \frac{\tau c_0}{\sqrt{\pi D t}}$$

below the solid solubility limit:

$$c(y, t) = \hat{c}_0 \exp\left(-\frac{y^2}{d^2}\right) \quad (5)$$

The diffusion coefficient D depends on the temperature according to the Arrhenius relation:

$$D(T) = D_0 \exp\left(-\frac{Q}{k_B T}\right) \quad (6)$$

where D_0 is the diffusion constant, Q is the activation energy, k_B is the Boltzmann constant and T is the absolute temperature.

D RESULTS AND DISCUSSION

FIGURE 1 shows erbium concentration profiles in X- and Z-cut LiNbO_3 samples obtained at different diffusion temperatures. Both the surface concentration and the diffusion depth increase with temperature, as expected. Depth profiles follow an erfc-like behaviour, confirming the validity of Fick's theory for Er diffusion in LiNbO_3 .

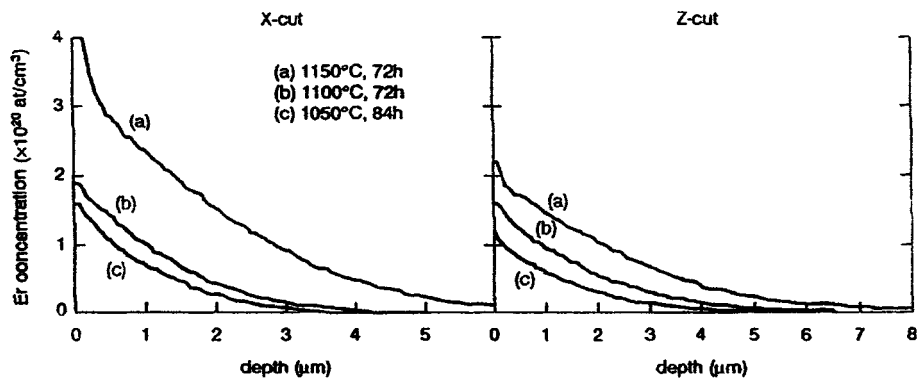


FIGURE 1 Erbium concentration profiles in X- and Z-cut samples for different diffusion temperatures.

It is worth noting that the diffusion process is anisotropic, with the Z-cut diffusivity higher than the X-cut one. Moreover, the surface concentration is systematically different and it is lower for Z-cut samples. It turns out that the total amount of Er diffused,

$$2c_0 \sqrt{\frac{Dt}{\pi}},$$

is the same, within experimental error, for both orientations, suggesting that the rate of dissolution of erbium from the deposited film into the crystal lattice is orientation-independent and limited by a surface energy barrier. As a consequence, the difference in Er surface concentration for different crystal cuts can be attributed to the relative ease with which Er ions further penetrate into LiNbO_3 along the Z-axis. The solid solubility of erbium in lithium niobate can therefore be evaluated from X-cut samples. Baumann et al [2] reported the isotropic behaviour of the Er surface concentration in LiNbO_3 on the basis of a couple of samples, whereas in our paper [1] the anisotropy can be seen for three pairs of crystals. Nevertheless, the reported solid solubility values are equal, within experimental error, in both papers: $c_0 = (1.85 \pm 0.09) \times 10^{20} \text{ at}/\text{cm}^3$ at 1100°C. In TABLE 1 are reported the diffusion constants and the activation energies for X- and Z-cut samples.

TABLE 1 Diffusion constants and activation energies for erbium diffusion in LiNbO_3 [2].

Diffusion direction	$D_0 (10^8 \mu\text{m}^2/\text{h})$	$Q (\text{eV})$
X	1.7 ± 0.2	2.28 ± 0.04
Z	4.3 ± 0.7	2.44 ± 0.04

A two-step process can describe thermal diffusion of erbium into lithium niobate: the first corresponds to the formation of a mixed layer of erbium and niobium oxides. Similar processes take place during erbium doping of LiNbO_3 by the ion exchange process [6,7], and titanium diffusion [8]. Second, the Er-Nb oxides phase acts as a source for the migration of erbium ions into the crystal. Atomic force microscopy (AFM) measurements show [2] that the oxide layer covers the LiNbO_3 crystal surface in the form of islands, which disappear when diffusion time becomes longer than the depletion time t_d . The presence of Er-Nb oxides induces a surface roughness, with an undesired enhancement of optical scattering in light waveguides.

12.1 Erbium doping of LiNbO_3 by thin film diffusion

From the technological point of view, the Er thin film diffusion regime is of interest, where waveguides with good optical quality are produced.

For diffusion times much longer than t_d , the source is exhausted, and the erbium concentration profile gradually assumes a Gaussian form (EQN (5)), in good agreement with Fick's law.

FIGURE 2 shows a Gaussian erbium concentration profile, obtained by diffusion of a 5 nm thick film for 99 h at 1150°C ($t_d \approx 10$ h).

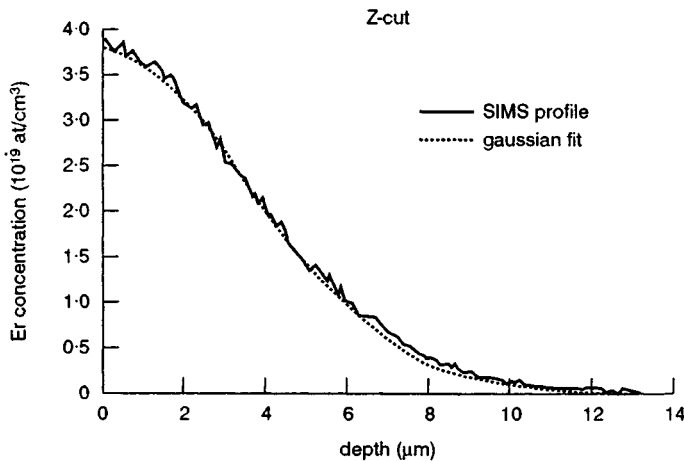


FIGURE 2 Erbium concentration profile in the thin film regime
(5 nm thick film diffused at 1150°C for 99 h).

In the thin film regime, the diffusion process is also anisotropic, and it is faster along the Z-axis compared with the X one. The diffusion coefficients are the same as for the infinite source regime. FIGURE 3 shows the relation between initial film thickness and erbium surface concentration. In this case a good linearity is observed, indicating that no saturation occurs when the concentration of Er remains under the solid solubility limit.

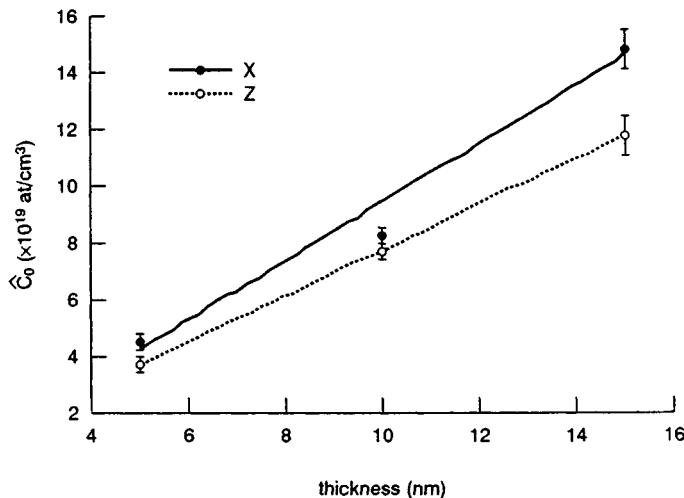


FIGURE 3 Erbium surface concentration as a function of initial film thickness.

E CONCLUSION

Thermal diffusion of erbium into lithium niobate has been reviewed. The dependence of the process on initial film thickness, diffusion parameters (temperature, time) and crystal cut directions has been investigated by secondary ion mass spectrometry (SIMS).

The lower limit of the solid solubility of Er in LiNbO_3 has been determined, and the conditions for complete film diffusion have been derived. Diffusion depth along the Z-axis of LiNbO_3 has been found to be about 30% greater than that along the X-axis, under the same diffusion conditions. The diffusion parameters have been determined for two crystal cut directions, for both infinite source and thin film diffusion regimes.

REFERENCES

- [1] F. Caccavale, F. Segato, I. Mansour, J.M. Almeida, A.P. Leite [*J. Mater. Res. (USA)* vol.13 (1998) p.1672-8]
- [2] I. Baumann et al [*Appl. Phys. A (Germany)* vol.64 (1997) p.33-44]
- [3] F. Caccavale, F. Segato, I. Mansour, P. Chakraborty [*Proc. Int. Conf. on Fibre Optics and Photonics "PHOTONICS-96"* Madras, India, 9-13 Dec. 1996, Eds J.P. Raina, P.R. Vaya (Tata McGraw-Hill, New Delhi, India, 1997) p.261-6]
- [4] F. Caccavale [*Critical Reviews of Optical Science and Technology* vol.CR69 (SPIE Press, Bellingham, 1997) p.423-59]
- [5] J. Crank [*The Mathematics of Diffusion* (Clarendon, 1975)]
- [6] F. Caccavale, C. Sada, F. Segato [Data review in this book: 12.2 Erbium doping of lithium niobate by the ion exchange process]
- [7] C. Sada et al [*Appl. Phys. Lett. (USA)* vol.72 (1998) p.3431-3]
- [8] M.N. Armenise, C. Canali, M. De Sario, A. Carnera, P. Mazzoldi, G. Celotti [*J. Appl. Phys. (USA)* vol.54 (1983) p.6223-31]

12.2 Erbium doping of LiNbO₃ by the ion exchange process

F. Caccavale, C. Sada and F. Segato

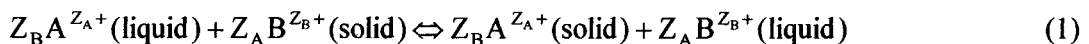
August 1999

A INTRODUCTION

During the last decade, the trivalent erbium ion has been the subject of increasing interest as one of the most promising dopants for photonic materials [1-6], with application in integrated optoelectronics technology. Travelling wave amplifiers [7] and waveguide lasers [8] have been made in Er³⁺-doped lithium niobate (LiNbO₃). Among different hosts, LiNbO₃ has drawn particular attention, owing to its good intrinsic electro-optic behaviour and its excellent non-linear optical properties. Several ways are currently under investigation for the doping of LiNbO₃ with Er³⁺ ions, with the aim to control erbium distribution and concentration in the host crystal, as well as its site location. Bulk doping of LiNbO₃ during crystal growth has been extensively investigated [9,10]. Local doping by erbium diffusion from Er film has been demonstrated [3-5] and erbium implantation has been studied [1,11,12]. Ion exchange is a well-established process, widely used for creating optical planar, channel and buried waveguides. Ion exchange in LiNbO₃ has been extensively investigated in the case of H⁺-Li⁺ ([13] and references therein), and for Ag⁺-Li⁺, Tl⁺-Li⁺, Cu⁺-Li⁺, Mn²⁺-2Li⁺ ion exchanges ([14] and references therein). More recently [15,16], we have demonstrated that such a method is suitable for the Er-doping of LiNbO₃ crystal, with the possibility of tailoring optical performance of the material through preparation parameters. In this Datareview the most important aspects of the ion exchange process will be given and it will be shown how this process can be exploited for the local doping of LiNbO₃ single crystals.

B THEORY OF THE ION EXCHANGE PROCESS

The ion exchange process consists of a transfer of different species between phases brought into contact. The chemical potential gradient drives the species exchange between the two phases in order to maintain their charge neutrality. In this case the general process regarding the ion exchange of a species B (valence state Z_B) belonging to a solid phase (LiNbO₃ crystal) and the species A (valence state Z_A) belonging to a liquid phase will be considered. As a consequence, modification of the solid phase composition and structure is generated in a region near the surface. The ion exchange process at the interface can be described in terms of a chemical reaction:



The chemical reaction (1) is limited by the kinetics at the interface and it depends on the species transport inside the solid and the liquid phases. In the case of the liquid phase the mass transfer is driven by diffusion and convection processes, the first being the most relevant in the region closer to the interface. In the solid solution the mass transfer is mainly due to diffusion. At the interface the process occurs faster than the other transport phenomena described here. For this reason, the equilibrium state condition expressed in EQN (1) establishes the interface boundary conditions to be fulfilled by the diffusion of the species into the solid phase. The concentration gradient and electric potential gradient V, induced by the local imbalance of charges, give the driving force of ionic species exchange. The ionic flux J is given by the Nernst-Plank model:

$$J_{A,B} = \hat{D}_{A,B} \left(\frac{\partial C_{A,B}}{\partial z} + \frac{C_{A,B} F_{A,B}}{z} \frac{\partial V}{\partial z} \right) \quad (2)$$

where the z-axis is normal to the surface and it is directed towards the solid solution. C represents the concentration of each species, $F_{A,B}$ is the activity coefficient and $\hat{D}_{A,B}$ represents the diffusion coefficient of the species A and B, respectively. The last depends on the temperature and the diffusion time.

From the conditions of electrical neutrality

$$Z_A C_A + Z_B C_B = \text{constant} \quad (3)$$

It is possible to correlate the concentration with the time and the thickness relevant to the exchange process:

$$\frac{\partial C_{A,B}}{\partial t} = \frac{\partial}{\partial z} \left(D_{AB} \frac{\partial C_{A,B}}{\partial z} \right) \quad (4)$$

where the interdiffusion coefficient D_{AB} is expressed by

$$D_{AB} = \frac{\hat{D}_A \hat{D}_B (C_A Z_A^2 + C_B Z_B^2)}{\hat{D}_A C_A Z_A^2 + \hat{D}_B C_B Z_B^2} \quad (5)$$

By solving EQN (4) with numeric procedures, it is possible to determine the in-depth profile of the exchanged species. FIGURE 1 shows, as an example, erbium profiles as a result of the Er^{3+} - Li^+ ion exchange for different $D_{\text{Er}}/D_{\text{Li}}$ values, assuming that the erbium concentration at the surface is maximum.

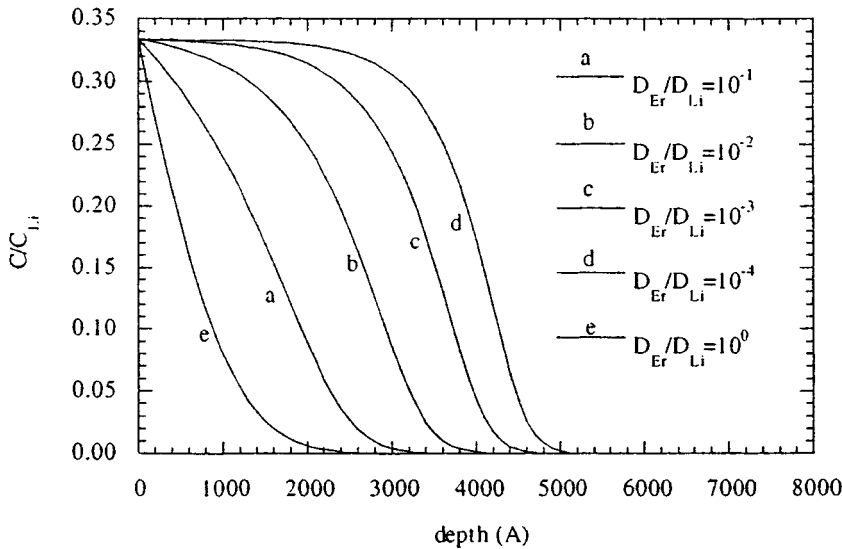


FIGURE 1 Trivalent dopant in depth profile calculated from EQN (4) for different $D_{\text{Er}}/D_{\text{Li}}$.

FIGURE 2 shows the dependence of the erbium depth profile on Er surface concentration for a specified relative diffusion coefficient.

In the case of non-isovalent ion exchange, because the diffusion coefficient depends on various parameters, it is not easy to predict the dopant profile. Moreover, in the case of single crystal, the elastic potential gradient induced by the lattice mismatch between the exchanged layer and the substrate should be taken into account. The exchange process involves complex rearrangement of the crystal structure, and a complete model is still lacking.

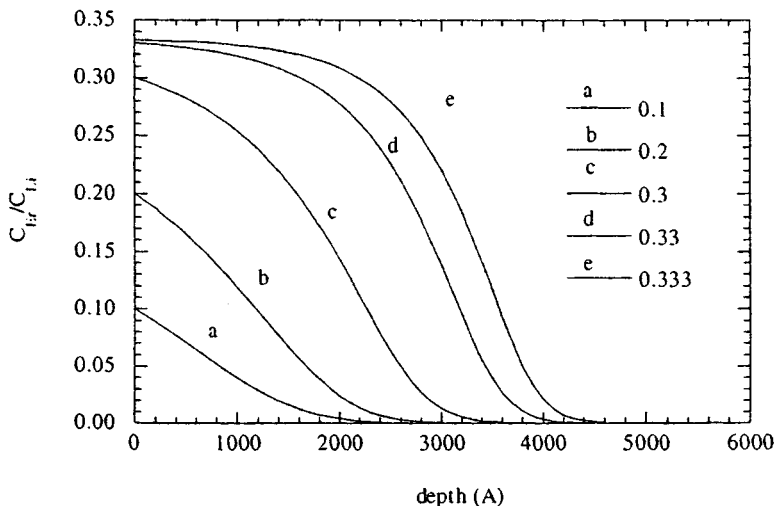


FIGURE 2 Trivalent dopant in depth profile calculated from EQN (4) for different surface dopant concentration and a given $D_{\text{Er}}/D_{\text{Li}}$.

C EXPERIMENT

Ion exchange was performed by immersing X- and Z-cut crystal plates in a molten salt bath at temperatures ranging from 560°C to 700°C and processing times varying from 5 h to several days. The starting bath composition was $\text{K}_2\text{SO}_4:\text{Na}_2\text{SO}_4:\text{Li}_2\text{SO}_4$ (19.4:9.9:70.7 wt.%), to which $\text{Er}_2(\text{SO}_4)_3$ was added in various percentages, varying from 0.002 wt.% to 5 wt.%. Compositional and structural analyses were performed by secondary ion mass spectrometry (SIMS), Rutherford backscattering spectrometry (RBS) and X-ray diffraction methods. Spectroscopic analysis was performed at room temperature by means of a spectrofluorometer. The experimental details are reported elsewhere [15,16]. A systematic study has been performed in order to evaluate the role of the most important parameters that could influence the ion exchange process, i.e. temperature, processing time and crystal orientation. Moreover, different erbium profiles can be obtained by changing the warming rate of the salt mixture used as the erbium source. Results obtained for fast (300°C/h) and slow (150°C/h) warming up processes will be discussed.

D RESULTS

Compositional analysis has pointed out that the Er penetration takes place under different regimes dependent on the ion exchange parameters, especially processing temperature and time. Erbium and lithium profiles are reported in FIGURE 3 for X-cut LiNbO_3 , and in the case of processing time and temperature of 24 h and 560°C, respectively ($\text{Er}_2(\text{SO}_4)_3 = 4.7$ wt.%). The presence of two distinct regions, separated by a thinner ‘transition’ layer, can be observed. In the most superficial region (about 0.2 μm thick) complete lithium depletion occurs. RBS analysis has suggested a stoichiometry close to $\text{Er}_1\text{Nb}_1\text{O}_{4.5}$, corresponding to the presence of a mixture of erbium and niobium oxides. In the second region, in the depth range from 0.3 to about 1 μm , the multivalent Er^{3+} - 3Li^+ ion exchange process takes place.

By comparing the shape of erbium profiles for different processing times, it appears that the superficial region plays the role of erbium reservoir for the further indiffusion of erbium into the substrate. This effect is evident in FIGURE 4, where a decrease of erbium concentration at the surface and the appearance of a plateau are observed for increasing processing time. In this case, the erbium concentration at the surface increases until erbium diffusion into the substrate takes place [15].

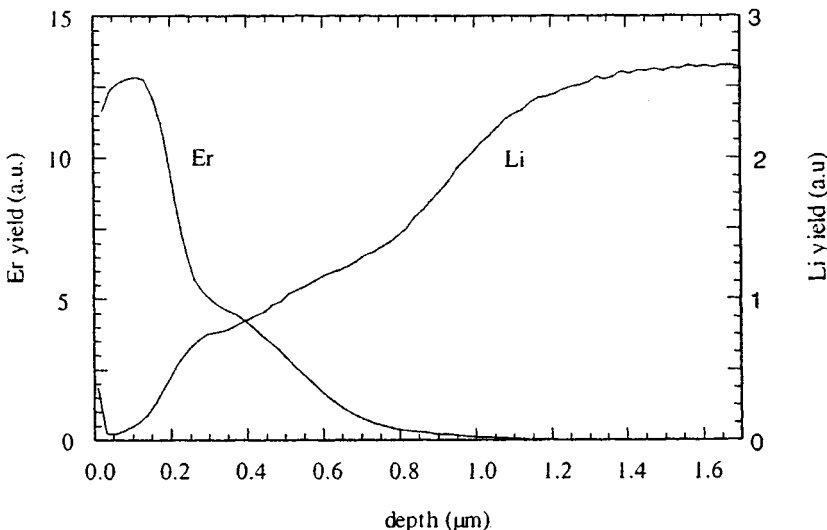


FIGURE 3 Secondary ion mass spectrometry profiles of an X-cut Er:LiNbO_3 ion-exchanged sample ($t = 24 \text{ h}$, $T = 560^\circ\text{C}$, $\text{Er}_2(\text{SO}_4)_3 = 4.7 \text{ wt.\%}$).

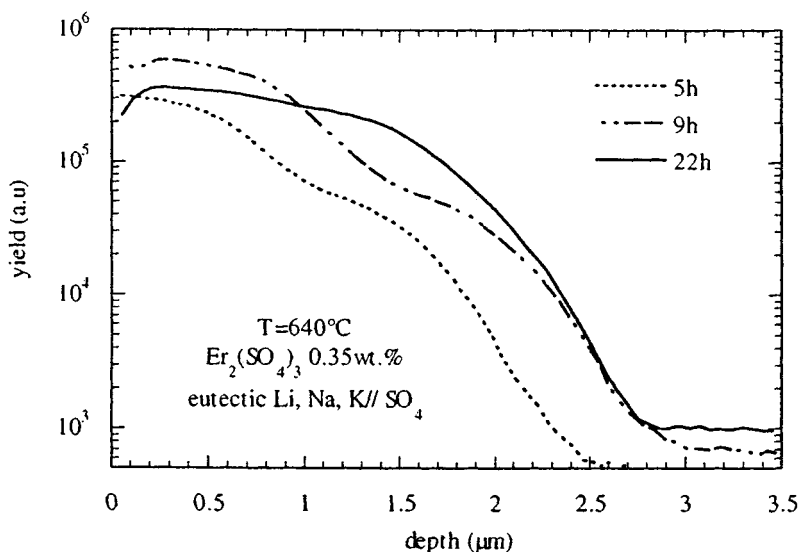


FIGURE 4 Erbium profiles for ion exchange performed at 640°C and $\text{Er}_2(\text{SO}_4)_3$ concentration of about 0.35 wt.%.

A systematic study on erbium content inside the salt mixtures has pointed out that [16]:

- when erbium sulphate is less than 0.002 wt.%, ion exchange is not effective even for long processing times (up to 200 h) and high temperatures (up to 700°C);
- large erbium concentrations in the molten salts are not favourable for the process, as can be seen in FIGURE 4, where erbium profiles have been reported for different ion exchange parameters;
- depths of a few microns could be obtained with low erbium sulphate concentration (less than 0.6 wt.%), limited processing time (below 10 h) and low temperature with respect to the thermal diffusion process [5];
- if the $\text{Er}_2(\text{SO}_4)_3$ concentration increases from 0.1 wt.% to 5 wt.%, the exchange depth is reduced by a factor of two;
- the ion exchange appears to be anisotropic (see FIGURE 5). The thickness relevant to the process is greater in X-cut crystals than in Z-cut ones ($d_x \approx 2d_z$) [15].

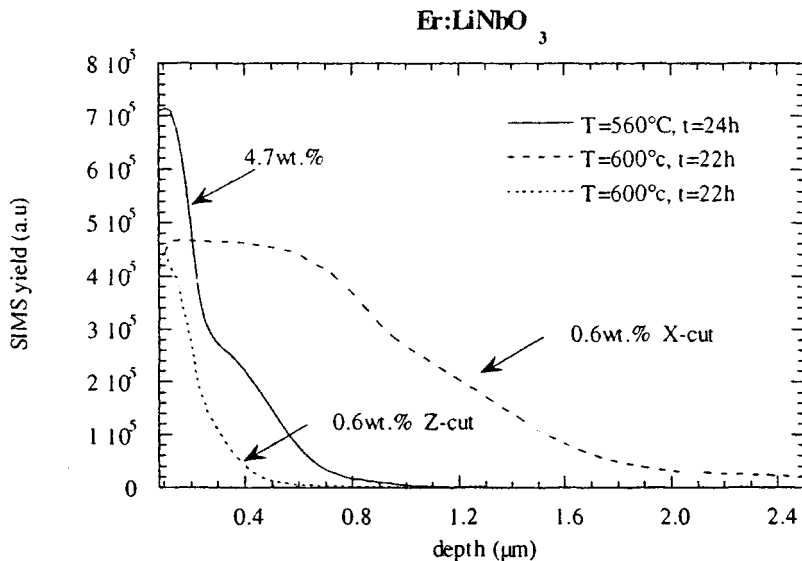


FIGURE 5 Erbium profiles for different ion exchange parameters.

From the structural point of view, XRD analyses have revealed the presence of various phases different from the LiNbO_3 one (the LiNb_3O_8 phase together with a few not yet recognised [16]). The comparison with RBS analysis suggests that the unidentified phases can be attributed to the mixture of erbium and niobium oxides [14,17]. It is worth noting that both the shape and position of the XRD peaks on rocking curves are independent of the exchange time, thus suggesting that the structure modification inside the LiNbO_3 crystals is the same.

We claim that, due to the larger mobility of lithium with respect to erbium, local charge imbalance limits the further diffusion of erbium into the matrix. The concentration gradient of the species leads to the formation of barrier layers which block the diffusion of the species involved in the process. A possible explanation of the fact that in X-cut LiNbO_3 the thickness of the exchanged layer is greater than that in Z-cut crystals, could be found in the greater wettability of X-cut LiNbO_3 with respect to Z-cut [18]. In the latter case, erbium incorporation is energetically less favoured due to the smaller erbium surface concentration.

Spectroscopic measurements were performed in order to understand how the optical properties of erbium are affected by concentration quenching. Room temperature PL spectra of all ion-exchanged samples have been measured at various excitation wavelengths. The luminescence spectrum for excitation at 379 nm ($^4\text{I}_{15/2} \rightarrow ^4\text{G}_{11/2}$) is shown for a crystal doped by ion exchange together with an Er:LiNbO₃ bulk doped one (with Er concentration of 0.8 at.%) in FIGURE 6.

The lines of the spectra are due to transitions between Er^{3+} state manifolds, corresponding to crystal field splitting into $(J + 1/2)$ Stark levels of the free ion $4f^1$ electronic configuration [19-22]. A direct identification of the states can be obtained by results reported in [22]. A linear dependence of luminescence intensity on erbium concentration was observed for erbium sulphate contents below 0.6 wt.%, suggesting that, in this range, concentration quenching is not appreciable. Moreover, it is well known that the internal strain, due to the presence of defects and impurities in the crystal, induces an inhomogeneous broadening of the lines corresponding to centres occupied by erbium, which consist of a convolution of subbands due to ions in a slightly different strain environment [23]. The inhomogeneous line broadening observed in the spectra can therefore be attributed both to internal strain and to the presence of different sites occupied by Er^{3+} ions [23]. The former was evidenced by XRD analysis and is usually present in charge-mismatched substitution and in ferroelectricity with domains. The latter can be inferred due to the observation of changes in the emission spectra while slowly varying the excitation wavelength [23]. It is also worth noting that different spectroscopic

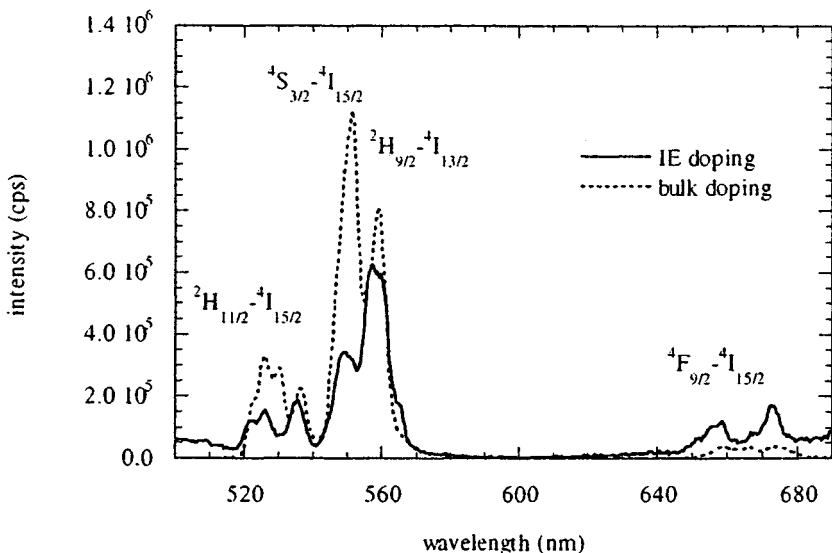


FIGURE 6 Luminescence spectra of Er:LiNbO_3 ($t = 600^\circ\text{C}$, $t = 22\text{ h}$, $\text{Er}_2(\text{SO}_4)_3 = 0.6\text{ wt.\%}$) for excitation at 379 nm (corresponding to the $^4\text{I}_{15/2} \rightarrow ^4\text{G}_{11/2}$ transition) and of a bulk doped Er:LiNbO_3 (erbium concentration = 0.8%).

features are present in bulk and ion-exchanged samples. This suggests that the surroundings of the dopant ion differs in the two cases, whereas appreciable differences are not evident by comparing samples doped by thermal diffusion and bulk doping (in agreement with [9]).

For slower warming up processes of the salts mixture, and for the same processing parameters, erbium incorporation takes place in a different way. In FIGURE 7 are reported SIMS erbium and lithium depth profiles in an ion-exchanged LiNbO_3 sample for a processing time of 20 h, temperature of 600°C and $\text{Er}_2(\text{SO}_4)_3$ concentration of about 0.2 wt.%.

It can be observed that the ion exchange process involves small thickness (below 1 μm) and the erbium profile is close to the shapes predicted by theoretical calculations. Only the region where non-isovalent ion exchange occurred could be identified. In this case, we suggest a different reactivity of the species at the interface, thus limiting the modification of the substrate nature and preventing the formation of blocking forces. Work is in progress to clarify this aspect.

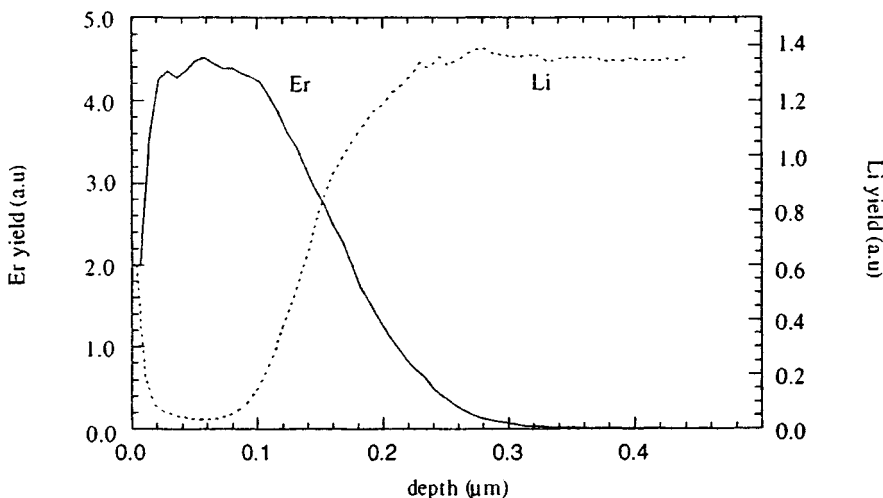


FIGURE 7 Erbium profiles for ion exchange performed at 600°C , processing time up to 20 h and $\text{Er}_2(\text{SO}_4)_3$ concentration of about 0.2 wt.%.

E CONCLUSION

In this Datareview erbium local doping of LiNbO_3 single crystal by the ion exchange process has been presented. It has been shown that the Er penetration takes place under different regimes, dependent on the ion exchange parameters. A step-like dopant distribution with time dependence can be obtained in the first layer, preserving a better matching between the doping profile and the optical mode field profile [5]. Higher Er concentration values are achievable, if compared with the thin Er film diffusion method, without appreciable quenching effects. Moreover, lower processing temperature and time are requested. Due to the complexity of structural rearrangements during the (inter)diffusion process, a comprehensive phenomenological model of the ion exchange process in LiNbO_3 is still lacking. Nevertheless, the method is suitable for Er-doping of LiNbO_3 crystals, with the possibility of tailoring the optical performance of the material through the preparation parameters.

REFERENCES

- [1] A. Polman [*J. Appl. Phys. (USA)* vol.82 (1997) p.1]
- [2] M.P. Hehlen, N.J. Cockcroft, T.R. Gosnell [*Phys. Rev. B (USA)* vol.56 (1997) p.9302]
- [3] I. Baumann et al [*Appl. Phys. A (Germany)* vol.64 (1997) p.33-44]
- [4] F. Caccavale, F. Segato, I. Mansour, J.M. Almeida, A.P. Leite [*J. Mater. Res. (USA)* vol.13 (1998) p.1672-8]
- [5] F. Caccavale, F. Segato [Datareview in this book: 12.1 *Erbium doping of lithium niobate by thin film diffusion*]
- [6] C. Mignotte, A. Traverse, P. Moretti, M. Monchanin [*Nucl. Instrum. Methods Phys. Res. B (Netherlands)* vol.120 (1996) p.81]
- [7] R. Brinkmann, I. Baumann, M. Dinand, W. Sohler, H. Suche [*IEEE J. Quantum Electron. (USA)* vol.30 (1994) p.2356]
- [8] I. Baumann, R. Brinkmann, M. Dinand, W. Sohler, S. Westenhöfer [*IEEE J. Quantum Electron. (USA)* vol.32 (1996) p.1695]
- [9] D.M. Gill, J.C. Wright, L. McCaughan [*Appl. Phys. Lett. (USA)* vol.64 (1994) p.2483]
- [10] J. Amin, B. Dussardier, T. Schweitzer, M. Hempstead [*J. Lumin. (Netherlands)* vol.69 (1996) p.17]
- [11] M. Fleuster, Ch. Buchal, E. Snoeks, A. Polman [*J. Appl. Phys. (USA)* vol.75 (1994) p.173]
- [12] Ch. Buchal, S. Mohr [*J. Mater. Res. (USA)* vol.6 (1991) p.134]
- [13] V.A. Ganshin, Yu.N. Korkishko [*Opt. Commun. (USA)* vol.86 (1991) p.523]
- [14] V.Sh. Ivanov, V.A. Ganshin, Yu.N. Korkishko [*Vacuum (UK)* vol.43 (1992) p.317]
- [15] C. Sada et al [*Appl. Phys. Lett. (USA)* vol.72 (1998) p.3431]
- [16] F. Caccavale, C. Sada, F. Segato, Yu.N. Korkishko, V.A. Fedorov, T.V. Morozova [*J. Non-Cryst. Solids (Netherlands)* vol.245 (1999) p.135]
- [17] Yu.N. Korkishko, V.A. Fedorov [*IEEE J. Sel. Top. Quantum Electron. (USA)* vol.2 (1996) p.187]
- [18] J. Hradilová, P. Kolárova, J. Schröfel, J. Ctyroky, J. Vacík, V. Perina [*Proc. SPIE (USA)* vol.2775 (1996) p.647]
- [19] A.M. Glass [*J. Chem. Phys. (USA)* vol.50 (1969) p.1501]
- [20] S.C. Abrahams, J.M. Reddy, J.L. Bernsten [*J. Phys. Chem. Solids (UK)* vol.27 (1966) p.997]
- [21] L. Rebouta et al [*Appl. Phys. Lett. (USA)* vol.70 (1997) p.9]
- [22] V.T. Gabrielyan, A.A. Kaminskii, L. Li [*Phys. Status Solidi A (Germany)* vol.3 (1970) p.K37]
- [23] D.L. Huber, D.S. Hamilton, B.B. Barnet [*Phys. Rev. B (USA)* vol.16 (1977) p.4642]
- [24] L. Nunez, B. Herreros, R. Duchowicz, G. Lifante, J.O. Tocho, F. Cusso [*J. Lumin. (Netherlands)* vol.60&61 (1994) p.81]

12.3 Study of erbium-doped LiNbO₃ waveguides by the beam propagation method

F. Caccavale and F. Segato

August 1999

A INTRODUCTION

Numerical methods are now widely used in photonics in order to simulate the behaviour of real systems operating under different conditions. It is possible to calculate and optimise the performance of an optical device as a function of the design parameters, without realising different samples of it.

In this Datareview, the numerical simulation of active waveguides made by erbium doping of Ti:LiNbO₃ channel waveguides is described. The simulation algorithm is based on the vectorial beam propagation method (BPM) [1]. The numerical model is applied for the optimisation of signal gain in Er:Ti:LiNbO₃ optical amplifiers, working at 1.55 μm wavelength, with respect to the erbium-doping process. The flexibility of the developed active-BPM (ABPM) algorithm enables one to find the best parameters for consolidated doping methods, such as thermal diffusion or ion implantation [2], and to direct the research toward innovative doping methods [3].

B MATHEMATICAL FRAMEWORK

B1 Propagation Equations

Let z be the propagation axis of the waveguide. Light propagation is described by the vectorial Helmholtz equation [1]. In the case of steady-state solutions with harmonic time dependence of the fields, the electric field can be expressed as:

$$\vec{E}(x, y, z) = \vec{A}(x, y, z)e^{\gamma z} \quad (1)$$

where \vec{A} is called the envelope field, and $\gamma = \alpha + j\beta$ where α is the gain (or absorption) coefficient,

$$\beta = \frac{\omega}{c} n_{\text{eff}}$$

is the effective wavenumber, and ω and c are the light frequency and light speed in vacuum, respectively. A weak dependence of the envelope field on the propagation distance (slowly varying envelope approximation - SVEA) [4] has been assumed

$$\left| \frac{\partial^2 A_\mu}{\partial z^2} \right| \ll 2 \left| \frac{\partial A_\mu}{\partial z} \right| \quad (2)$$

where μ represents the x or y direction. The physical meaning of SVEA is that the gain (or absorption) of the electric field is weak along a distance of the order of the wavelength. Typical gain values are a few dB per centimetre, i.e. less than 1% at 1.5 μm, so the SVEA condition is completely fulfilled.

Using SVEA and for a linear dielectric isotropic medium with losses and no magnetic susceptibility¹, one gets the following equation, which describes the evolution of the transverse components of \vec{A} along z:

$$\frac{\partial A_\mu}{\partial z} = -\frac{1}{2\gamma} \left[\nabla_t^2 + \left(\gamma^2 + \frac{\omega^2}{c^2} \epsilon_r \right) A_x + \frac{\partial}{\partial \mu} \left(A_x \frac{\partial \ln \epsilon_r}{\partial x} + A_y \frac{\partial \ln \epsilon_r}{\partial y} \right) \right] \quad (3)$$

where ∇_t^2 is the Laplacian operator along the transverse coordinates, and

$$\epsilon_r = \left[n + \frac{i\alpha c}{2\omega} \right]^2$$

is the complex dielectric function.

EQN (3) is a first-order differential equation, and it can be numerically integrated in a more simple way, if compared with the second-order Helmholtz equation.

B2 Optical Amplification Equations

In the theoretical description of optical amplification of Er ions in LiNbO_3 monomode waveguides, laser pumping and emission near 1480 nm and 1530 nm are considered, respectively. Therefore, a 'quasi-two-level' model [5,6] is applied in ABPM. The lower laser level is the Er^{3+} ground state, namely ${}^4\text{I}_{15/2}$, while both excited state and pump level belong to the ${}^4\text{I}_{13/2}$ multiplet. The energy fine structure is taken into account by wavelength-dependent absorption and emission cross-sections.

Gain coefficients α of propagating modes can be described as follows:

$$\alpha(x,y,z,\lambda) = -\alpha_s(\lambda) + \sigma_{21}(\lambda)N_2(x,y,z) - \sigma_{12}(\lambda)N_1(x,y,z) \quad (4)$$

where α_s is the scattering coefficient, N_1 and N_2 are the populations of lower and upper laser states, and σ_{12} and σ_{21} are the absorption and emission cross-sections, respectively. The polarisation state, TE or TM, is omitted for the sake of clarity. Populations N_1 and N_2 are obtained from transition rates between the laser levels, and from rate equations

$$\begin{aligned} \frac{dN_1}{dt} &= - \left(R_{12} + W_{12} + W_{12}^{\text{ASE}} \right) N_1 + \left(R_{21} + W_{21} + W_{21}^{\text{ASE}} + A_{21} \right) N_2 \\ \frac{dN_2}{dt} &= - \frac{dN_1}{dt} \end{aligned} \quad (5)$$

where R_{ij} , W_{ij} and W_{12}^{ASE} are the transition rates for pump, signal and amplified spontaneous emission (ASE) radiation, respectively. $A_{21} = \tau^{-1}$ is the spontaneous transition rate, where τ is the lifetime of the upper laser level. Steady-state solutions of EQN (5) yield for N_1 :

$$N_1 = \frac{A_{21} + R_{21} + W_{21} + W_{21}^{\text{ASE}}}{A_{21} + R_{21} + W_{21} + W_{21}^{\text{ASE}} + R_{12} + W_{12} + W_{12}^{\text{ASE}}} c_{\text{Er}} \quad (6)$$

where c_{Er} is the local concentration of erbium ions, and N_2 is obtained directly from:

¹ The anisotropy of lithium niobate has not been considered, and it is taken into account only by the change of the substrate refractive index for different crystal cut directions.

$$N_1(x,y,z) + N_2(x,y,z) = c_{\text{Er}}(x,y) \quad (7)$$

Transition rates for pump, signal and ASE depend on the local intensity of the pump $I_p(x,y,z,\lambda)$, signal $I_s(x,y,z,\lambda)$ and ASE $I_{\text{ASE}}^{\text{TE,TM}}(x,y,z,\lambda)$ (the ASE has a random polarisation):

$$\begin{aligned} U_{\text{lm}}(x,y,z) &= \frac{1}{hc} \int \lambda \sigma_{\text{lm}}(\lambda) I_j(x,y,z,\lambda) d\lambda \\ W_{\text{lm}}^{\text{ASE}}(x,y,z) &= \frac{1}{hc} \int \lambda \sigma_{\text{lm}}^{\text{TE,TM}}(\lambda) I_{\text{ASE}}^{\text{TE,TM}}(x,y,z,\lambda) d\lambda \end{aligned} \quad (8)$$

where $U = R$ or W when $j = s$ or p , and h is Planck's constant.

As a consequence, from the local intensity of electromagnetic fields it is possible to calculate the transition rates (EQN (8)); from these one gets the population of the amplifier levels (EQN (6)), and then the gain coefficients (EQN (4)). The intensity of the propagating fields is updated accordingly, and the procedure starts again.

B3 Numerical Implementation

The analytical model of the coupled differential equations (EQN (3)) together with the gain coefficients (EQN (4)) is used in a vectorial BPM code [7]. A finite differences numerical scheme, with the alternated direction implicit (ADI) technique, has been adopted. This procedure leads to an increase of the calculation speed, to a reduction in memory requirements, to a direct implementation of transparent boundary conditions [8], and to an increased freedom in the choice of the longitudinal step (typically 0.2 μm).

The full analytical model, however, requires very long calculation times. A simplification can be made when the gain is lower than 20 - 25 dB, neglecting ASE and considering both the pump and the signal monochromatic ($\lambda_{\text{pump}} = 1480 \text{ nm}$, $\lambda_{\text{signal}} = 1532 \text{ nm}$) [4]. Other approaches [6] consider the mode profiles invariant in order to explore the wavelength dependence of signal gain. However, in this case the effect of erbium ion distribution is averaged over an (x,y) section of the waveguide. Direct comparison of the results obtained with the two methods applied under the same conditions shows a good agreement. Further calculation speed is obtained by updating the gain α every 20 steps. The parameter β is obtained by minimising the oscillations of the envelope vector along the z axis².

C SIMULATIONS

The results of a study for the optimisation of signal gain in active waveguides, as a function of the erbium concentration profile, will be presented. For the numerical simulations [4], we consider a Z-cut Ti:LiNbO₃ channel waveguide, realised in a 7 μm wide and 95 nm thick titanium stripe, diffused at 1030°C for 9 h. The waveguide length is supposed to be enough to reach the maximum signal gain, where the pump power becomes lower than the threshold level $P_{p \text{ max}}$, after a distance L_{opt} from the launching point. The titanium concentration determines the refractive index profile, and the guided modes intensity. The waveguide is monomodal both at the pump and the signal frequency. Only TE modes are considered, both for pump and signal. We assume that refractive index, scattering coefficients, lifetime and cross-sections are independent of the erbium concentration profile and of the doping method. These values are reported in TABLE 1.

² It is worth remembering that for a mode in a passive optical waveguide the envelope vector is uniform along the propagation axis.

TABLE 1 Optical parameters used in the modelling of active waveguides.

	$\sigma_{12} (10^{-24} \text{ m}^2)$	$\sigma_{21} (10^{-24} \text{ m}^2)$	$\alpha_s (\text{dB/cm})$	$\tau (\text{ms})$	n
Signal	2.55	2.41	0.16	2.63	2.138
Pump	0.59	0.20	0.16	-	2.138

Erbium concentration profiles obtained from thermal diffusion [2], ion implantation [9] and bulk doping are considered. Moreover, step-like profiles, which could be obtained by the ion exchange technique, are considered [3].

D RESULTS

D1 Thermal Diffusion

The erbium concentration profile is given by the solution of the diffusion equation. For a complete diffusion of a $2w$ -wide Er strip, the solution is given by:

$$c(x, y) = \frac{c_0}{2} \exp\left(-\frac{y^2}{d_y^2}\right) \left[\operatorname{erf}\left(\frac{x+w}{d_x}\right) - \operatorname{erf}\left(\frac{x-w}{d_x}\right) \right] \quad (9)$$

where y is the diffusion axis perpendicular to the crystal surface,

$$d_y = \sqrt{2D_z t}$$

is the diffusion depth (y is parallel to the Z -axis of the crystal), D_z is the diffusion coefficient along Z , t is the diffusion time,

$$d_x = \sqrt{2D_x t}$$

is the lateral diffusion width and D_x is the diffusion coefficient along X . Therefore, the ratio d_x/d_y has been kept constant to the square root of the ratio of the diffusion coefficients (about 0.7). Launched pump and signal power are 100 mW and 0.1 mW, respectively. The Er surface concentration is $c_0 = 6.6 \times 10^{19} \text{ at/cm}^3$. FIGURE 1 shows the maximum signal gain as a function of diffusion depth d_y and initial width w . The best value is 19.3 dB for $d_y = 8 \mu\text{m}$ and $w = 1 \mu\text{m}$. To reach such a gain, a propagation length of 22.4 cm is needed. This is quite a non-realistic value, as practical lengths of devices are of the order of 5 cm (10 cm in double-pass configuration [10]). If one considers a maximum length of 5 cm, the signal gain increases with both d_y and w , so bulk doped waveguides present better performance as compared with diffused ones.

If the surface concentration c_0 increases up to $18.5 \times 10^{19} \text{ at/cm}^3$, which is the solid solubility of Er in LiNbO_3 [2], the best gain is reached for the same values of d_y and w , but it is now equal to 23.2 dB. In this case the threshold pump power is about 17 mW.

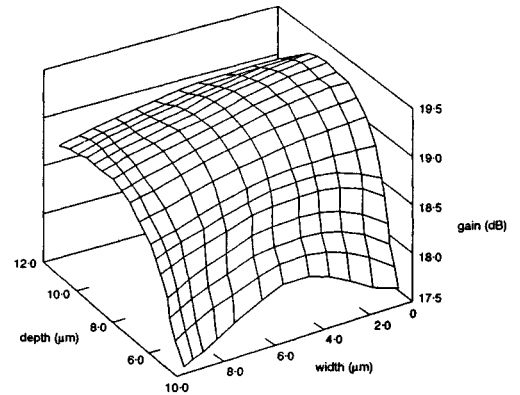


FIGURE 1 Maximum signal gain as a function of diffusion depth and lateral width in Er-diffused waveguides.

D2 Ion Implantation and Step-Like Profiles

In the case of erbium ion implantation in LiNbO_3 , the Er concentration profile is modelled from experimental data [9] and TRIM simulations [11]. The in-depth behaviour is described by two half-Gaussian functions related to the asymmetry of the implantation profile. A systematic study of signal gain as a function of profile depth and width has been made. The best signal gain is obtained with a profile depth and width similar to that of the intensity profile of the signal optical mode, and it gives 24.2 dB ($c_0 = 18.5 \times 10^{19} \text{ at/cm}^3$). The optimal length is 15.7 cm and the threshold pump power is 14.6 mW.

MeV-implanted waveguides, however, should be thermally annealed to restore the crystalline structure damaged by the implantation process. The annealing leads to a smoothing of the erbium profile, and to a decrease of the maximum gain of about 1 dB.

Step-like concentration profiles in lithium niobate could be obtained by the ion exchange process [12]. Typical examples are the hydrogen (proton) distribution, but also metals like silver. Recently, some results have been obtained on erbium by ion exchange [2]. In the model presented, the erbium profile has a plateau near the surface, and decays in depth with a short tail. In analogy with the implantation case, the best signal gain is obtained with a profile depth and width similar to that of the intensity profile of the signal optical mode. In this case, however, the maximum gain is 25.1 dB ($c_0 = 18.5 \times 10^{19} \text{ at/cm}^3$), the optimal length is 10.5 cm and the threshold pump power is 14.5 mW.

FIGURE 2 shows the signal power evolution along the propagation axis for the optimal profile of the different doping methods, at a distance of 10 cm. In all cases, the maximum erbium concentration is $18.5 \times 10^{19} \text{ at/cm}^3$. TABLE 2 summarises the amplification characteristics. It can be seen that the best performing Er profile is the step-like one, even for 5 cm-long devices. Moreover, the step-like profile requires the minimum threshold power, and a 10 cm-long waveguide is enough to reach the maximum gain.

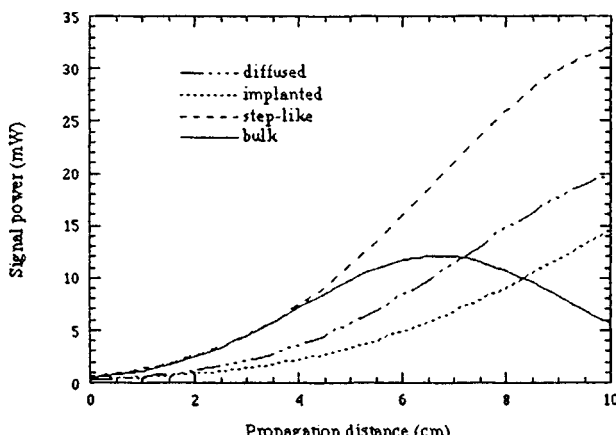


FIGURE 2 Signal power evolution as a function of propagation distance for different erbium concentration profiles.

TABLE 2 Amplification characteristics for different concentration profiles.

	Bulk	Diffusion	Implantation	Step-like
Signal gain (dB)	20.8	23.2	24.2	25.1
Threshold pump power (mW)	23.2	17.4	14.6	14.5
Optimal length (cm)	6.7	11.3	15.7	10.5

E CONCLUSION

The application of a vectorial beam propagation method to active optical devices realised by erbium doping of Ti:LiNbO_3 waveguides enables one to optimise the realisation process, and to focus on the most promising doping method. This synergy between numerical simulations and experimental processes is one of the keys to research in materials science today. Current investigations on erbium ion exchange have been simulated by the results presented, with the aim of creating a new class of high-performance optical amplifiers.

ACKNOWLEDGEMENTS

Dr. I. Mansour of the Electrical Engineering Department of the University of Jordan is gratefully acknowledged for his great help and competence in numerical simulation.

REFERENCES

- [1] R. März [*Integrated Optics: Design and Modeling* (Artech House, 1995)]
- [2] F. Caccavale, F. Segato [Datareview in this book: 12.1 *Erbium doping of lithium niobate by thin film diffusion*]
- [3] F. Caccavale, C. Sada, F. Segato [Datareview in this book: 12.2 *Erbium doping of lithium niobate by the ion exchange process*]
- [4] F. Caccavale, F. Segato, I. Mansour [*J. Lightwave Technol. (USA)* vol.15 (1997) p.2294-300]
- [5] E. Desurvire [*Erbium-Doped Fiber Amplifiers: Principles and Applications* (Wiley & Sons, 1994)]
- [6] M. Dinand, W. Sohler [*J. Quantum Electron. (USA)* vol.30 (1994) p.1267-76]
- [7] I. Mansour, A.D. Capobianco, C. Rosa [*J. Lightwave Technol. (USA)* vol.14 (1996) p.908-13]
- [8] G.R. Hadley [*IEEE J. Quantum Electron. (USA)* vol.28 (1992) p.363-70]
- [9] Ch. Buchal, S. Mohr [*J. Mater. Res. (USA)* vol.6 (1991) p.134-7]
- [10] R. Brinkmann, I. Baumann, M. Dinand, W. Sohler, H. Suche [*IEEE J. Quantum Electron. (USA)* vol.30 (1994) p.2356-60]
- [11] J. Biersack, L. Haggmark [*Nucl. Instrum. Methods (Netherlands)* vol.174 (1980) p.275-80]
- [12] Yu.N. Korkishko, V.A. Fedorov [*Ion Exchange in Single Crystals for Integrated Optics and Optoelectronics* (Cambridge Int. Sci., 1999)]

CHAPTER 13

TECHNIQUES FOR MATERIAL STUDIES

- 13.1 Uniformity studies of congruent LiNbO₃ by Maker fringe analysis**
- 13.2 Secondary ion mass spectrometry of LiNbO₃**
- 13.3 Near field method for the characterisation of channel waveguides in LiNbO₃**
- 13.4 M-lines spectroscopy for the characterisation of slab waveguides in LiNbO₃**
- 13.5 Microanalytical techniques for waveguide examination in LiNbO₃**

13.1 Uniformity studies of congruent LiNbO₃ by Maker fringe analysis

N.A. Sanford and J.A. Aust

July 2002

A INTRODUCTION

In recent years, LiNbO₃ has taken on increased importance in optoelectronics for the manufacture of high-speed modulators for telecommunications, the expanded use of this material for realising optical-frequency synthesis via periodically poled (PPLN) components, and for the continued adoption of multifunction LiNbO₃ integrated optical components for guidance and control [1-3]. The material has also been used with great success as a spectroscopic host for the rare-earth ions Er, Yb and Nd, thereby offering additional functionality, including lasing and amplification, to the suite of applications available to the integrated optical device engineer [4-6].

It may be argued that while continued improvements with crystal growth and quality control in the large-scale production of LiNbO₃ boules have certainly occurred, they may not be keeping pace with new demands imposed by high-volume manufacture of integrated optical devices. For example, there are reports of irregular yields for waveguide components fabricated from different batches of LiNbO₃ wafers even with the greatest possible care and precautions taken during device fabrication [7-9].

B EXPERIMENTAL STUDIES

The most common methods for waveguide fabrication in LiNbO₃ involve the diffusion of Ti stripes, ion-exchange processes, or some combination of the two [10,11]. Of course, even with the most careful fabrication control, there will always be problems associated with unintentional fluctuations in processing arising from operator error, variations in process chemicals, or variations in process equipment, to name but a few. However, irregularities in device yield and performance will also arise from non-uniformity in the LiNbO₃ wafers themselves and variations between different batches of wafers cut from different boules. For example, there have been reports associating composition fluctuations in the material to changes in the diffusivity of Ti whereby a 0.02 mol% variation in Li₂O will change the Ti diffusivity by 2% [12]. Such effects, in addition to Ti concentration fluctuations, can impact the performance of directional couplers [13]. We shall illustrate in the following discussion that composition variations of this order are not uncommon in commercially available LiNbO₃. With these issues in mind, it is beneficial for the continued evolution of LiNbO₃ integrated-optical technology to develop new non-destructive methods of full-wafer mapping and inspection that supplement existing metrologies such as interferometry and X-ray topography analysis. New methods of wafer inspection that can be adopted to the manufacturing floor and used at various stages of wafer processing could potentially prevent wasting costly fabrication effort on substrates that will inherently not yield acceptable devices.

It was suggested in the mid-1980s that second-harmonic generation (SHG) could offer a convenient method for examining LiNbO₃ wafer uniformity [14,15]. In this regard, we focus exclusively on SHG in the form of Maker fringes with the pump and SHG transmitted through the sample [16]. Maker fringes are defined as the oscillation of the SHG intensity produced when the pump beam angle of incidence is continuously varied. The oscillation in SHG intensity results from the pump and SHG

13.1 Uniformity studies of congruent LiNbO₃ by Maker fringe analysis

moving in and out of phase as the optical path length for both changes with the varying angle of incidence. Detailed analysis of Maker fringes has been given elsewhere and interested readers should consult these earlier publications [17-21]. As a specific example, consider an x-cut LiNbO₃ rotated about the y-axis with the pump beam polarised parallel to the y-axis (o-polarised pump). With the pump beam at 1064 nm, the z-polarised SHG intensity (e-polarised SHG) at 532 nm is sensitive to small changes in wafer birefringence. This fortuitously occurs near room temperature because the natural birefringence and dispersion of the material forces the ordinary refractive index at 1064 nm very close to the extraordinary refractive index at the SHG wavelength 532 nm. Ignoring Fabry-Perot resonances of the pump and SHG in the wafer under test, the intensity of the e-polarised Maker fringes may be represented by a function of the form

$$A + B \cos[2\pi L(n_o^p - n_e^{\theta_s})/\lambda_s]$$

where L is the thickness of the plate, n_o^p is the ordinary index at 1064 nm, and n_e^{θs} is the extraordinary index at λ_s = 532 nm that depends upon the angle of propagation in the plate. At normal incidence n_e^{θs} = n_e where n_e is the extraordinary index at 532 nm. Explicit expressions for the factors A and B have been published elsewhere [17]. The coherence length

$$l_c^{(o,e)} = \lambda/2|n_o^p - n_e|$$

for this pump-SHG case is defined as the length over which power is fed from the pump to the SHG. Near room temperature l_c^(o,e) ~ 115 μm. With modern cutting and polishing procedures one would expect that the thickness of typical production LiNbO₃ wafers should vary by no more than a few micrometres across an entire wafer (this will be confirmed in more detail later in the discussion). Therefore, the variation in the e-polarised Maker fringes taken at different locations on a wafer arises more from variations in birefringence rather than variations in sample thickness. In fact, careful examination of the e-polarised Maker fringe patterns reveals that birefringence variations as small as 5 × 10⁻⁶ are readily resolved in commercially produced x-cut wafers [17,19].

LiNbO₃ can exist over a fairly wide range of the solid solution from nearly stoichiometric to Li-depleted compositions as low as roughly 45 mol% Li₂O at 1200°C. Composition fluctuations may occur during crystal growth. The Li/Nb mole ratio may change sufficiently such that the Li₂O content can vary by as much as ±0.02 mol% during the growth of a single LiNbO₃ boule and may differ by at least this amount between separately grown boules [22]. Such a change in composition will result in a variation in the extraordinary index n_e of approximately 2 × 10⁻⁴ at 632 nm while the ordinary index n_o remains nearly invariant to composition fluctuations [23]. Thus, Maker fringe patterns collected at many locations on a single substrate can reveal variations in wafer birefringence and therefore wafer composition.

A schematic of an apparatus used to generate and record Maker fringes is illustrated in FIGURE 1. The mode-locked (82 MHz), Q-switched (800 Hz) Nd:YAG laser indicated was attenuated so that the average power falling on the sample was roughly 25 mW. The lens L1 focused the pump beam to a diameter of approximately 70 μm on the sample wafer. Since the Maker fringe analysis was performed entirely in transmission, accurate simulations of the fringe patterns arising from the e-polarised SHG requires knowledge of the wafer thickness at each location on the wafer being examined. Conveniently, wafer thickness maps can also be generated using Maker fringe analysis. Consider o-polarised (y-polarised in the coordinate system of the wafer) Maker fringes arising from the o-polarised pumping scheme described earlier. Ignoring Fabry-Perot resonances of the pump and SHG in the wafer, the intensity of these fringes may be expressed by the function

$$C + D \cos[2\pi L(n_o^p - n_o)/\lambda_s]$$

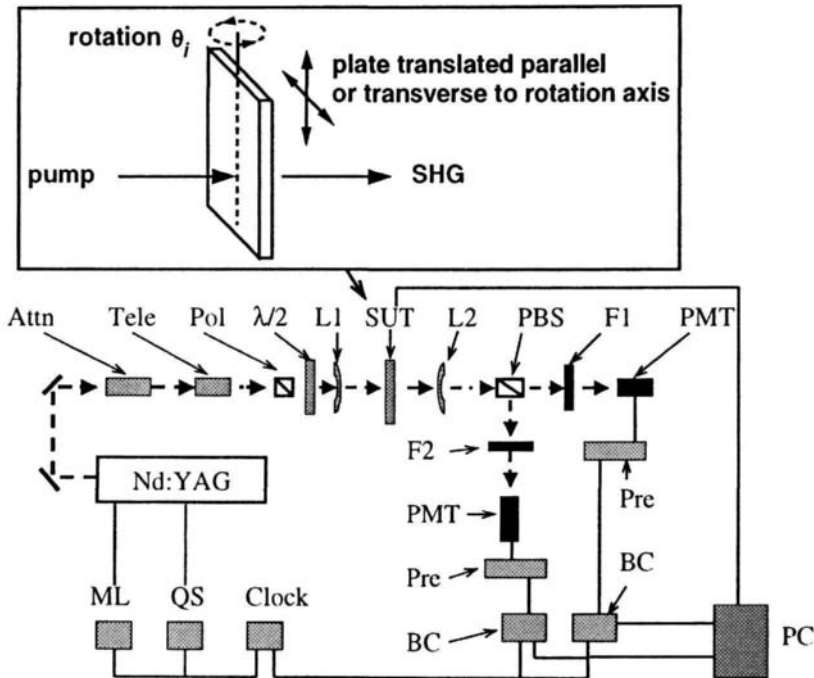


FIGURE 1 An illustration of the apparatus used to generate and record Maker fringes. The automated x-y stage assembly is mounted on the rotation stage that is fixed with respect to the laboratory reference frame, and the pump beam is aligned to fall on the rotation axis. In this way, Maker fringes can be collected at arbitrary locations on a wafer under test. Wafers that are x-cut are aligned such that the y-axis conforms with the laboratory rotation axis. The pump beam can either be o-polarised (parallel to the rotation axis) or e-polarised (perpendicular to the rotation axis). Similarly, either o- or e-polarised SHG may be collected. The components of the apparatus labelled in the block diagram are: optical attenuator (Attn), telescope (Tele), polariser (Pol), half-wave plate ($\lambda/2$), pump focusing lens (L1), sample under test (SUT), SHG collection lens (L2), polarising beam splitter to separate o- and e-polarised SHG (PBS), pump rejecting filters (F1, F2), photomultiplier tube (PMT), current-sensitive preamplifier (Pre), boxcar averager (BC), crystal oscillator and countdown electronics (Clock), mode-lock driver (ML), Q-switch driver (QS), Nd:YAG laser (Nd:YAG), personal computer (PC).

where explicit forms of the factors C and D have been given in a previous publication [17]. The coherence length for this interaction is

$$l_c^{(o,o)} = \lambda/2 |n_o^p - n_o|$$

where n_o is the ordinary refractive index at 532 nm. In this case, the coherence length is rather short with $l_c^{(o,o)} \sim 2.9 \mu\text{m}$. This indicates that there will be substantial differences in the o-polarised Maker fringes collected at locations on a wafer that differ in thickness by a few micrometres. As mentioned earlier, the ordinary index of refraction displays only negligible variation with composition. Thus, fitting simulation codes to the o-polarised Maker fringes by using L as an adjustable parameter allows for the computation of the wafer thickness at the location of the Maker fringe scan. For these simulations, it was assumed that the ordinary refractive index n_o , as computed from the temperature-dependent Sellmeier equations of Edwards and Lawrence [24], was correct. An example of fitting the simulation to o-polarised Maker fringes is illustrated in FIGURE 2. Note that inclusion of Fabry-Perot resonances of the pump and SHG in the solution code would return a precision of 0.01 μm in the calculation of L. Neglecting these effects would reduce the computed precision in L to 0.1 μm . The simulation displayed in FIGURE 2 used the higher-precision method. The accuracy in L (and ultimately the accuracy of n_e obtained by fitting the simulations to the e-polarised Maker fringes) is

13.1 Uniformity studies of congruent LiNbO₃ by Maker fringe analysis

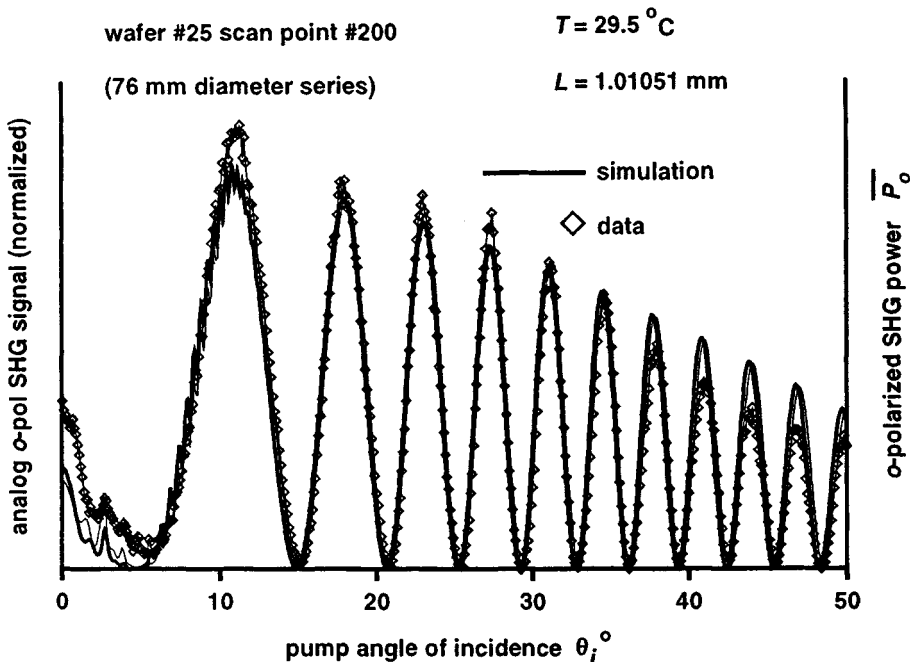


FIGURE 2 An example of a simulation for fitting o-polarised Maker fringes to o-polarised data collected at a temperature of 29.5°C. The computed sample thickness $L = 1.01051 \text{ mm} \pm 0.01 \mu\text{m}$.

determined entirely by the accuracy in the Sellmeier equation for n_o and the negligible dependence of n_o on composition variations. The accuracy of the Sellmeier equations is believed to be $\pm 2 \times 10^{-4}$ and is limited by the accuracy of the refractive index data used to generate the equations [25].

Therefore, simultaneously collecting both e- and o-polarised Maker fringes at a single location allows computation of wafer thickness and birefringence where the thickness is used as input in the computation of the birefringence. In this fashion, maps of these quantities may be built up for entire wafers.

FIGURE 3 illustrates fitting a numerical simulation to e-polarised Maker fringe data and includes the effect of Fabry-Perot resonances of the pump and SHG, as has been described in more detail in earlier publications [17-19]. The factor $\Delta^S n_e = n_e - n_e^S$ represents the deviation of n_e from the extraordinary index n_e^S computed from the Sellmeier equations [24]. As previously discussed, LiNbO₃ can exist over a range of solid solutions, and the composition of a single boule may vary spatially with growth. Therefore, the factor $\Delta^S n_e$ can vary between wafers cut from different portions of a boule. Indeed, we have measured $\Delta^S n_e \sim 0$ in some wafers and as low as roughly -7×10^{-4} in others. The composition of the wafers we examined was expected to fall within $\pm 0.02 \text{ mol\% Li}_2\text{O}$ from the now-accepted congruent compositions of 48.38 mol% Li₂O [22]. The extraordinary index of LiNbO₃ will increase with reduced Li concentration [23]. Therefore, the composition of the wafers where $\Delta^S n_e \sim 0$ must be close to the composition of the LiNbO₃ samples originally studied by Nelson and Mikulyak [25], whose refractive index data were used by Edwards and Lawrence to derive their Sellmeier equations. The preponderance of wafers we examined exhibit $\bar{n}_e < n_e^S$, and one may therefore conclude that the Li content of these wafers is greater than that of the samples used by Nelson and Mikulyak. These observations, in conjunction with the results described by Byer et al [26] and Carruthers et al [27], lead us to conclude that the samples used by Nelson and Mikulyak were composed of roughly 48.30 mol% Li₂O rather than the 48.60 mol% value that they estimated.

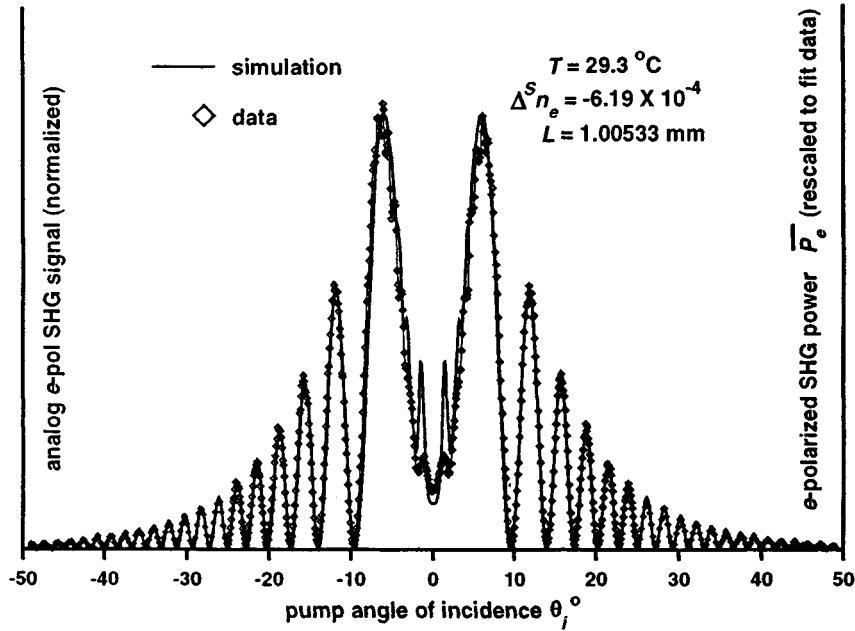


FIGURE 3 An example of a simulation fitting e-polarised Maker fringes to e-polarised data resulting in $\Delta^S n_e = -6.19 \times 10^{-4} \pm 5 \times 10^{-6}$. The value for L was computed from fitting the companion o-polarised Maker fringes collected at the same location on the sample.

Examples of maps for wafer thickness and birefringence are illustrated in FIGURE 4(a) and 4(b), respectively. Over a typical span of 44 mm on a wafer the thickness maps commonly show a variation in L of 3 - 5 μm and the birefringence maps show variations in n_e of a few parts in 10^{-5} . A notable feature of the birefringence map is an apparent grading running along the z-axis. This effect is observed in many wafers and is thought to arise as an artefact of Li migration occurring during the poling of the boule [19,22]. Furthermore, by examining wafers cut sequentially from a boule, the trend in composition can be traced along the direction of growth. This feature is illustrated in FIGURE 5 and shows for this particular case that the top of the boule is lithium depleted with respect to the bottom by approximately 0.013 mol% Li₂O.

The intensity of the e-polarised SHG is larger than that of the o-polarised SHG by roughly a factor of $10^3 - 10^4$, corresponding to $(l_c^{(o,e)} / l_c^{(o,o)})^2$. Consequently, recording o-polarised Maker fringes that are not corrupted by the more intense e-polarised fringes requires careful alignment of the wafer under test. It is important to ensure that the plate is rotated about its y-axis during the Maker fringe scans such that the rotation axis conforms to the transmission axis of the output polariser that is used to separate the orthogonally polarised SHG components. However, if the wafer contains static strains, photoelastic effects can produce a mixing of the o- and e-polarised SHG components since the wafer would unavoidably behave as an arbitrarily oriented waveplate located between crossed polarisers. Regardless of the care taken for this alignment, all wafers examined show some degree of intermixing of the o- and e-polarised SHG. This effect is illustrated in FIGURE 6(a), which shows that the o-polarised Maker fringes display extra structure that conforms to the e-polarised fringes simultaneously collected at the same location on the sample. As illustrated in FIGURE 6(b), these effects suggest indirect evidence for the presence of photoelastic strain in the material whereby the collective effects of axial (S_1 , S_2) and shear (S_4) strains may contribute to slight rotations of the optic axis (z-axis) about the x-axis in the material [17,19]. To a first approximation, such a slight axial rotation would project a small component of the dominant e-polarised SHG onto the transmission axis of the output polariser that is oriented to pass only the o-polarised SHG in the detection system. Thus, an axial rotation ζ of a few milliradians corresponding to an aggregate strain on the order of $10^{-4} - 10^{-3}$

13.1 Uniformity studies of congruent LiNbO_3 by Maker fringe analysis

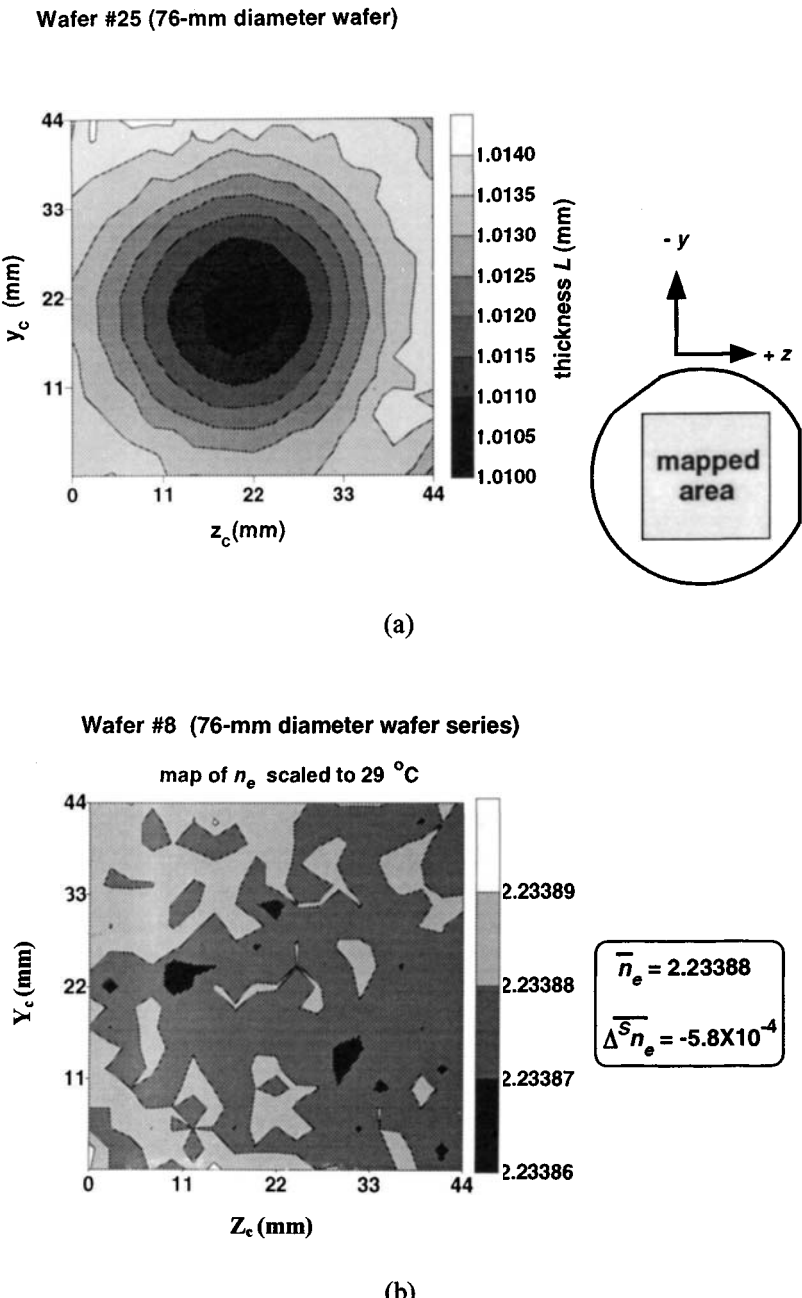


FIGURE 4 (a) An example of a map of wafer thickness compiled by fitting the simulation code for o-polarised Maker fringes to data collected in a grid over the wafer. The square data collection grid was composed of 361 points with adjacent separation of 2.444 mm. The axes y_c and z_c are parallel to the associated crystal axes, as indicated on the inset that illustrates the mapped area with respect to the orientation of the wafer. The enumeration of the grid points is left-to-right, bottom-to-top such that point #1 is located at $y_c = 0$ mm, $z_c = 0$ mm, point #19 at $y_c = 0$ mm, $z_c = 44$ mm and point #361 at $y_c = 44$ mm, $z_c = 44$ mm.

(b) A map of wafer birefringence variation compiled by fitting the simulation code for e-polarised data taken over a grid of the same dimensions previously given. The factors \bar{n}_e and $\bar{\Delta}^S n_e$ represent the average values of n_e and $\Delta^S n_e$, respectively.

Both x-cut wafers used in (a) and (b) were 76 mm in diameter.

Variation of index and composition in LiNbO₃boule #124

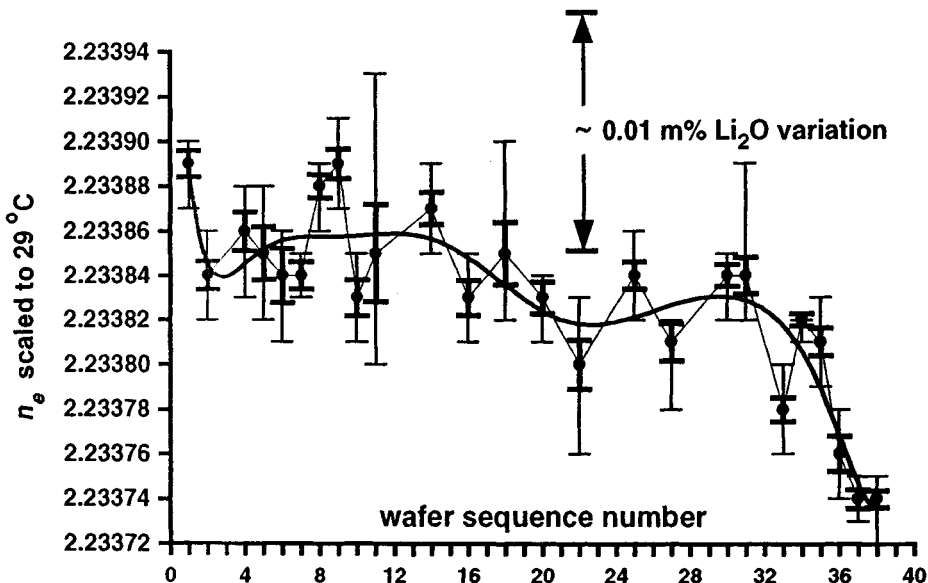


FIGURE 5 Trend in n_e for 25 x-cut wafers taken sequentially from a single boule. The heavy error bars indicate the standard deviation of n_e and the light error bars show the maximum and minimum values of n_e for each wafer. The polynomial curve is included only as an aid to the eye. The data indicate that the top of the boule is depleted in Li from the bottom of the boule by roughly 0.013 mol% Li₂O.

would be effective in projecting a component $\zeta E_z^{(T_2)_o}$ of the e-polarised SHG, of comparable magnitude to the o-polarised SHG $E_y^{(T_2)_o}$, onto the output polariser oriented to pass only the o-polarised SHG. This results in a total SHG field

$$E_{y_L}^{(T_2)_o} \sim E_y^{(T_2)_o} + \zeta E_z^{(T_2)_o}$$

that is polarised parallel to the laboratory axis y_L and exits the wafer to be detected as o-polarised SHG. The primed axes y' and z' appearing in FIGURE 6(b) refer to the transformed y and z crystal axes under the action of the strain. Strains in LiNbO₃ of approximate magnitude 10^{-4} , as inferred from linear interferometry, are not unexpected [28]. Simulation codes were developed to model the Maker fringes resulting from the vector addition of the o- and e-polarised SHG as a function of ζ , and results of these simulations are illustrated in FIGURE 6(c). It should be emphasised that this analysis is approximate and there is insufficient information to extract the contributions of the axial and shear components of the strain. Only an estimation of the aggregate effects of the photoelastic strain may be deduced. The annular distribution of this o-e SHG mixing effect illustrated in FIGURE 6(c) is fairly typical. However, more singular behaviour has been observed in some wafers [29].

C CONCLUSION

In summary, Maker fringe analysis may be used to study the homogeneity of LiNbO₃ wafers in terms of composition, birefringence, thickness and strain. The use of non-linear optics rather than linear optics to evaluate these quantities is unique since effects of variations in sample thickness can be completely accounted for without separate mechanical or interferometric measurements to establish a thickness map of the wafer. For example, accurately accounting for sample thickness variations has frustrated efforts to examine wafer uniformity using maps of linear birefringence [7]. Furthermore, the Maker fringe analysis is completely non-destructive and may be adapted to a manufacturing

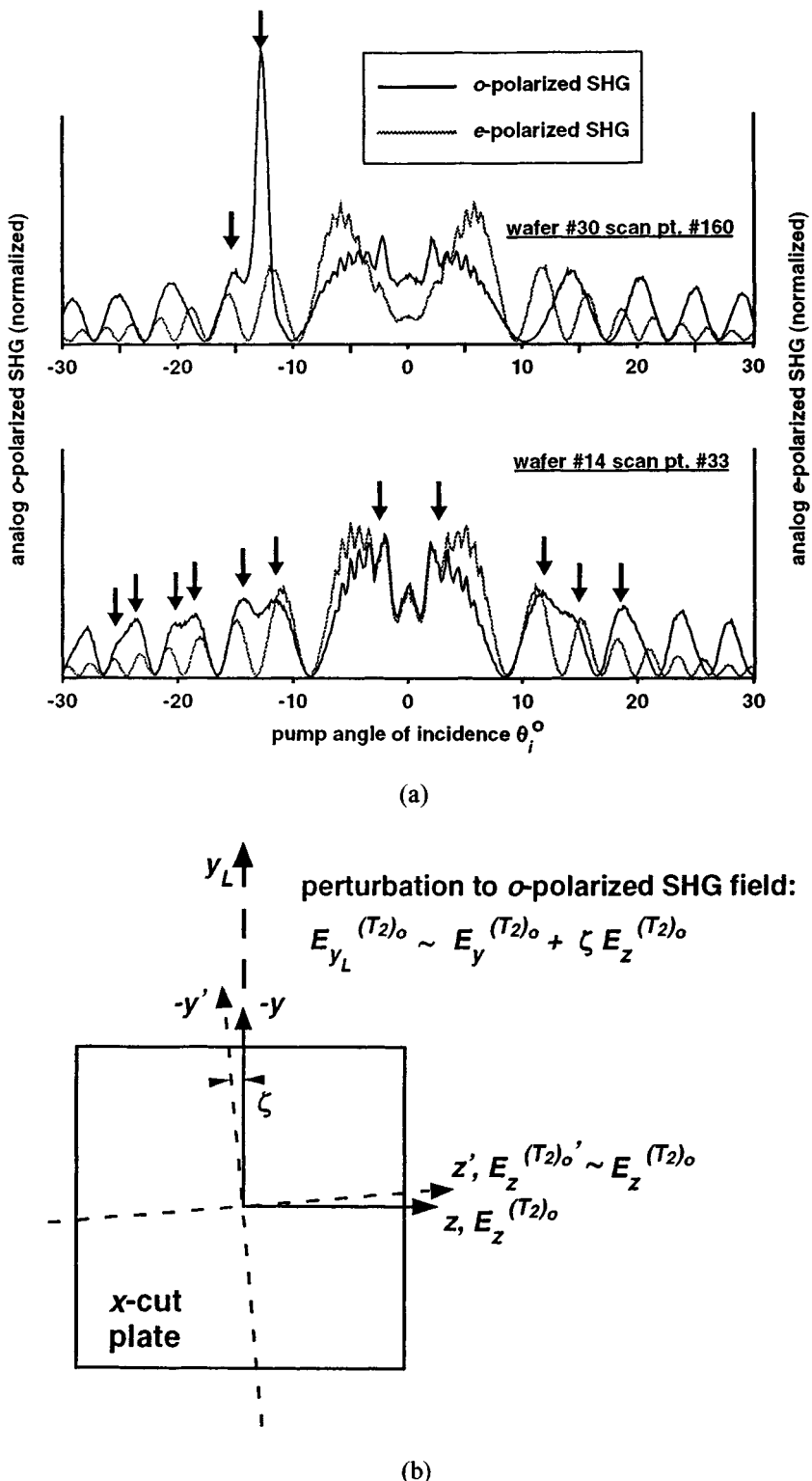


FIGURE 6 (a) Examples of o-polarised Maker fringes showing significant corruption by e-polarised SHG where both are produced at common locations on the samples. The arrows indicate how extra structure in the o-polarised fringes corresponds to the angular location of various e-polarised fringes. (b) A schematic illustrating the interpretation that the intermixing of the e- and o-polarised Maker fringes arises in part from a strain-induced rotation of the optic axis (z-axis) about the x-axis.

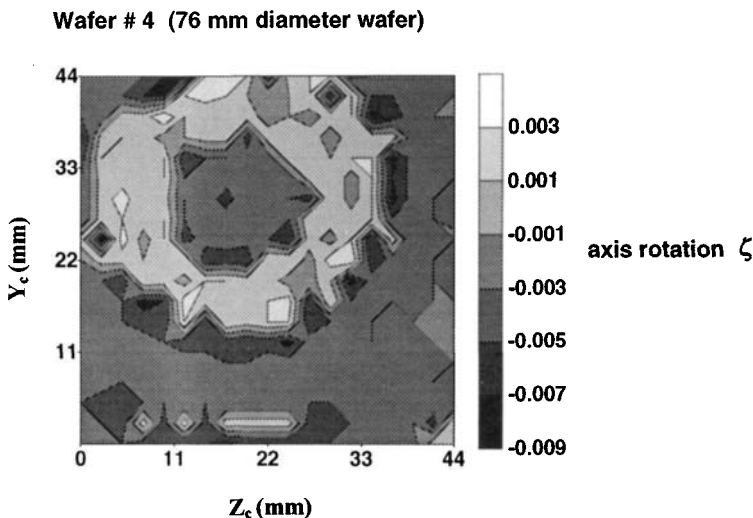


FIGURE 6 (c) A map of the axis rotation angle ζ compiled by simulating the vector addition of e- and o-polarised SHG required to fit the resulting o-polarised Maker fringes recorded. The square data grid was composed of 361 points separated by 2.444 mm with the same orientation and grid enumeration as described in the caption of FIGURE 4(a).

environment to examine wafer uniformity at virtually any stage of device manufacture. This is true even for examining the uniformity of diffused layers. Recall that the non-linear optical interaction is sensitive on a length scale of the coherence length $l_c^{(o,o)}$ or $l_c^{(o,e)}$. Therefore, diffused waveguide layers (typically several micrometres in depth) could be examined for uniformity via the type of methods described herein.

In their recent work on the optimisation of integrated tunable narrow-linewidth filters, Chollet et al [30] have shown that the best result to date for filter bandwidth is 0.7 nm. Furthermore, they also point out that the birefringence fluctuations revealed by Maker fringe mapping (as surveyed in this review) imposes a lower limit for filter bandwidth of 0.6 nm.

ACKNOWLEDGEMENTS

A number of people have contributed useful comments and insights during the course of this work. We would like to thank Dieter Jundt and Peter Bordui of Crystal Technology, Bruce Steiner of NIST (now retired), Alexana Roshko of NIST and K.K. Wong of Codeon Corporation.

REFERENCES

- [1] R. Stubbe, G. Edwall, B. Sahlgren, L. Svahn [*J. Lightwave Technol. (USA)* vol.10 (1992) p.1489]
- [2] L.E. Myers, W.R. Bosenberg [*IEEE J. Quantum Electron. (USA)* vol.33 (1997) p.1663]
- [3] R.S. Moyer, R. Grenavich, F.F. Judd, R.C. Kershner, W.J. Minford, R.W. Smith [*IEEE Trans. Compon. Packag. Manuf. Technol. B, Adv. Packag. (USA)* vol.21 (1998) p.130]
- [4] A. Grisard, E. Lalier, G. Garry, P. Aubert [*IEEE J. Quantum Electron. (USA)* vol.33 (1997) p.1627]
- [5] J. Amin, J.A. Aust, N.A. Sanford [*Appl. Phys. Lett. (USA)* vol.69 (1996) p.3785]
- [6] K. Schäfer, I. Baumann, W. Sohler, H. Suche, S. Westenhöfer [*IEEE J. Quantum Electron. (USA)* vol.33 (1997) p.1636]

13.1 Uniformity studies of congruent LiNbO₃ by Maker fringe analysis

- [7] H. Nagata [*Opt. Eng. (USA)* vol.37 (1998) p.1612]
- [8] H. Nagata, S. Oikawa, M. Yamada [*Opt. Eng. (USA)* vol.36 (1977) p.283]
- [9] E.J. Murphy et al [*J. Lightwave Technol. (USA)* vol.14 (1996) p.352]
- [10] N. Dagli [*IEEE Trans. Microw. Theory Tech. (USA)* vol.47 (1999) p.1151 and references therein]
- [11] K.K. Wong, A.C.G. Nutt, D.F. Clark, J. Winfield, P.J.R. Laybourn, R.M. De La Rue [*IEE Proc. J. Optoelectron. (UK)* vol.133 (1986) p.113]
- [12] R.J. Holmes, W.J. Minford [*Ferroelectrics (UK)* vol.75 (1987) p.63]
- [13] L. McCaughan, K.D. Choquette [*IEEE J. Quantum Electron. (USA)* vol.22 (1986) p.947]
- [14] S.R. Lunt, G.E. Peterson, R.J. Holmes, Y.S. Kim [*Proc. SPIE (USA)* vol.578 (1985) p.22]
- [15] S.R. Lunt, G.E. Peterson [*Ferroelectrics (UK)* vol.75 (1987) p.87]
- [16] P.D. Maker, R.W. Terhune, M. Nisenhoff, C.M. Savage [*Phys. Rev. Lett. (USA)* vol.8 (1962) p.21]
- [17] N.A. Sanford, J.A. Aust [*J. Opt. Soc. Am. B (USA)* vol.15 (1998) p.2885]
- [18] J.A. Aust [PhD Thesis, University of Colorado, Boulder, Department of Electrical and Computer Engineering, 1999]
- [19] V. Gopalan, N.A. Sanford, J.A. Aust, K. Kitamura, Y. Furukawa [*Handbook of Advanced Electronic and Photonic Materials and Devices* vol.4 *Ferroelectrics and Dielectrics* Ed. H.S. Nalwa (Academic Press, San Diego, 2001)]
- [20] I. Shoji, T. Kondo, A. Kitamoto, M. Shirane, R. Ito [*J. Opt. Soc. Am. B (USA)* vol.14 (1997) p.2268]
- [21] Y.R. Shen [*The Principles of Nonlinear Optics* (Wiley, New York, 1984)]
- [22] P.F. Bordui, R.G. Norwood, C.D. Bird, G.D. Calvert [*J. Cryst. Growth (Netherlands)* vol.113 (1991) p.61]
- [23] J.G. Bergman, A. Ashkin, A.A. Ballman, J.M. Dziedzic, H.J. Levinstein, R.G. Smith [*Appl. Phys. Lett. (USA)* vol.12 (1968) p.92]
- [24] G.J. Edwards, M. Lawrence [*Opt. Quantum Electron. (UK)* vol.16 (1984) p.373]
- [25] D.F. Nelson, R.M. Mikulyak [*J. Appl. Phys. (USA)* vol.45 (1974) p.3688]
- [26] R.L. Byer, J.F. Young, R.S. Feigelson [*J. Appl. Phys. (USA)* vol.41 (1970) p.2320]
- [27] J.R. Carruthers, G.E. Peterson, M. Grasso, P.M. Bridenbaugh [*J. Appl. Phys. (USA)* vol.42 (1971) p.1846]
- [28] P. Bordui [personal communication, 1997]
- [29] N.A. Sanford, J.A. Aust [in *Lasers and Optics for Manufacturing* vol.9 of 1997 OSA Trends in Optics and Photonics Series, Ed. C. Tam (Optical Society of America, Washington DC, 1997) p.23-32]
- [30] F. Chollet, J.-P. Goedgebuer, G. Ramantoko [*Opt. Eng. (USA)* vol.40 (2001) p.2763]

13.2 Secondary ion mass spectrometry of LiNbO₃

F. Caccavale

August 1999

A INTRODUCTION

Many of the complex new materials developed today derive their unique properties from the presence of multiple phases or from local variations in elemental concentration. Simply performing a bulk analysis of the materials is not sufficient to achieve a true understanding of their nature. One method that has met with a great deal of success in materials characterisation is the surface analytical technique known as secondary ion mass spectrometry (SIMS).

It has become a frequently used analytical technique because it can detect impurities at atom densities less than one part per million atomic (ppma) for almost all elements, and 10 ppba for some elements. Moreover, a depth resolution of a few nanometres can be achieved.

In a typical SIMS analysis a solid sample is bombarded in vacuum by a several-keV focused beam. The final result of the ion-solid interaction is the emission of particles from the surface. A small fraction (~1%) of these particles is in an ionised state and can be subsequently analysed by a mass spectrometer - magnetic sector, quadrupole, time-of-flight - and then detected. The obtained mass spectrum gives information about the chemical elements present on the surface, in particular on the first atomic layers from where most of the secondary ions come. If one studies the peak intensity of one or more detected elements as a function of the erosion time, i.e. as a function of the depth of the eroded material, the depth behaviour of the concentration can be obtained [1].

In this Datareview the basic concepts and instrumental aspects, as well as the applications and trends of the SIMS technique will be presented. Particular attention will be devoted to the analysis of the LiNbO₃ crystals.

B FUNDAMENTALS OF SECONDARY ION MASS SPECTROMETRY

B1 Secondary Ion Production

Secondary ion mass spectrometry is based on the fact that charged atomic and molecular species are ejected from the surface of a condensed phase (liquid or solid) under particle bombardment. During this bombardment by ions or neutral particles - in general in the energy range of some keV - surface particles are sputtered and the primary bombarding particle is implanted into the condensed phase (FIGURE 1). Sputtering is one of the various processes that happen during this kind of surface bombardment [2].

The impact of a primary particle on a surface causes an energy and momentum transfer to a limited area around the point of particle impact, resulting in (i) a change of the lattice structure, and (ii) the loss of surface material by sputtering. The ion-bombardment-induced emission processes include electron and photon emission and the emission of surface particles (atoms or molecules) in charged, uncharged and also excited states. All these emission products are emitted with a certain angular distribution.

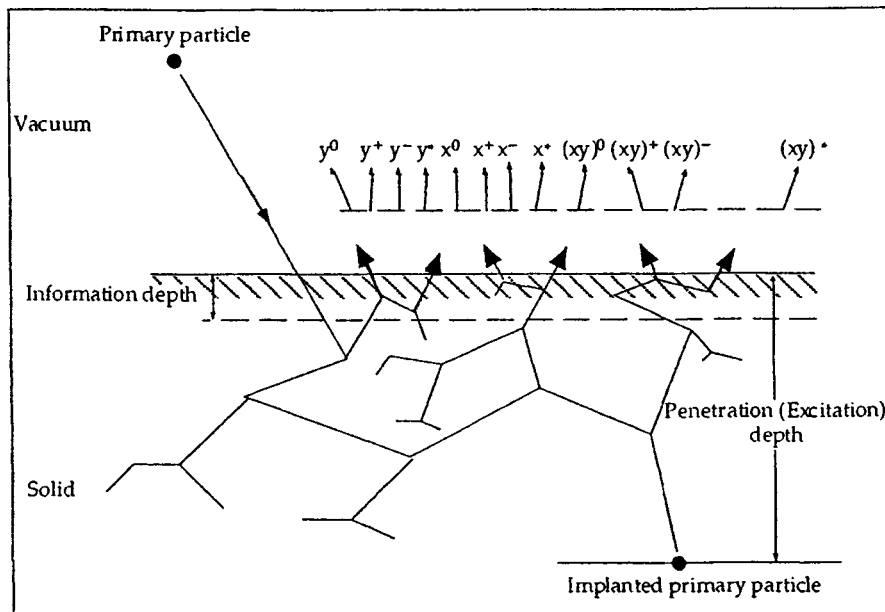


FIGURE 1 Schematic layout of the sputtering process.

The secondary ion emission includes all emitted ionised surface particles in the ground state as well as in the excited state. These secondary ions may be separated easily by different types of mass analysers.

Virtually all secondary ions originate from the uppermost atomic layers of the bombarded surface. This results in one of the most important features of secondary ion mass spectrometry - its surface sensitivity.

B2 Quantification

The secondary ion current measured by a SIMS instrument is a function of many factors, and the equation that describes the intensity of the secondary ion signal of an element, M, present in the sample under analysis is given by:

$$I_{M\pm} = I_p S C_M \beta_{M\pm} \eta \gamma \quad (1)$$

where $I_{M\pm}$ is the secondary ion current of the element M, I_p is the primary ion current, S represents the sputtering yield, i.e. the amount of emitted particles per incident ion, C_M is the atomic concentration of the element M in the matrix, $\beta_{M\pm}$ is the ionisation efficiency, i.e. the ratio of the number of emitted ions M to the number of emitted neutral atoms of M per second.

As a consequence, the number of emitted ions per incident ion is given by:

$$n_{M\pm} = S C_M \beta_{M\pm} \quad (2)$$

η is a factor including all the instrumental effects for the detected isotope and it represents the ratio of the measured current to that emitted from the sample, and γ represents the isotopic abundance of the element M.

EQN (1) can be considered the basic formula in the secondary ion mass spectrometry. There are two different SIMS regimes.

The first - static SIMS - has low primary current density ($\leq 1 \text{ nA/cm}^2$) and erosion speeds less than a few \AA/h and allows one to analyse the first surface layer and, in general, to detect the chemically adsorbed particles on the surface.

The second method - dynamic SIMS - is characterised by current densities above several mA/cm^2 and erosion speeds that allow one to analyse the distribution of an element in depth (up to several micrometres) in a reasonable time ($< 1 \text{ h}$).

The ionisation efficiency, $\beta_{M\pm}$, is the most relevant parameter to make a quantitative SIMS analysis and it depends mainly on four factors: (i) the element to be studied, (ii) the matrix of the analysed sample, (iii) the chemical nature of the species already present or introduced in the sample, and (iv) the residual gas pressure in the analysed region.

The factors determining the measured signal are, in general, dependent on C_M ; in particular, due to the matrix effects, $\beta_{M\pm}$ is a strong function of C_M .

It follows that quantitative SIMS analyses are valid only in those cases when the standard sample and the sample under analysis have a similar composition, i.e. in the case of the same matrix, or when $\beta_{M\pm}$ is certainly independent of C_M . The last condition is satisfied in the case of analysis of impurities diluted in the sample - for example in the analyses of dopants in semiconductors. Generally speaking, a given element can be considered diluted in a matrix if a small variation of its concentration does not change significantly the concentration of the reactive species (oxygen or caesium) present in the sample.

There are several quantification methods in the literature [3], all using first principles and standards. The most useful and accurate method is the employment of standard samples obtained by ion implantation [4], in which the main uncertainty is related to the current integration system used for the control of the implantation dose. In this case, analyses with a reproducibility and accuracy less than 10% can be obtained.

C ANALYTICAL CONDITIONS AND INSTRUMENTATION

A typical SIMS block-diagram is shown in FIGURE 2. Its basic components are: (a) the primary column, which produces and spatially controls the bombarding particles, (b) the sample chamber, and (c) the extraction, transmission, selection and detection system of the secondary ions.

- (a) The ions created in the source are extracted and focalised by a system of electrostatic lenses. To ensure the purity of the beam the last is filtered through a magnetic field. The control of positioning and of the sputtered area is obtained by the use of deflection plates, and the entire primary column is differentially pumped in order to remove the un-ionised gas particles.
- (b) The vacuum chamber, which contains the analysing sample, can usually be heated up to 250°C in order to get a vacuum of the order of 10^{-10} torr . At 10^{-6} torr one second is enough to create an adsorbate atomic layer of residual gas on the sample surface, with a sticking coefficient equal to one. It follows that static SIMS requires a vacuum better than 10^{-9} torr during the analysis. In the case of dynamic SIMS, i.e. with erosion speeds of the order of hundreds of \AA/h , a partial pressure of residual gas of about $10^{-7} - 10^{-9} \text{ torr}$ is enough.
- (c) SIMS instruments can be divided into two large groups as a function of the employed mass analyser.

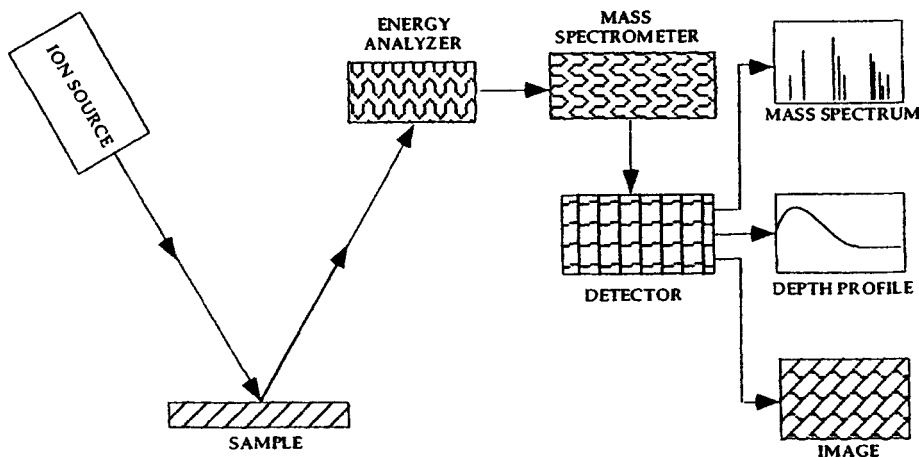


FIGURE 2 SIMS technique block diagram [2].

- (i) In systems using a magnetic sector [5] the secondary ions extracted from the sample pass through a magnetic field and undergo a deflection that is proportional to the mass-to-charge ratio (M/e).
- (ii) Another kind of SIMS instrument employs as a mass analyser a quadrupole [6]. In this case, an oscillating electric field is applied to four parallel metallic plates with a hyperbolic section.
- (iii) Sometimes a third type of mass spectrometer is used: the time-of-flight (TOF) analyser [7]. TOF analysers generally have high transmission and a mass range that can extend up to thousands of amu. High mass resolution is also achievable with this type of analyser.

D APPLICATIONS

Three basic forms of data acquisition are commonly performed on SIMS instruments: (a) mass spectra, (b) depth profiles, and (c) secondary ion images (see FIGURE 2).

- (a) A mass spectrum consists of the secondary ion intensities of the species detected as a function of mass. Sputtering a sample while the mass spectrometer scans the mass range produces a mass spectrum. If the sample surface is sputtered very lightly, removing less than 1% of the uppermost monolayer of atoms while the mass spectrometer is scanned, the spectrum will contain information as to which elements are present on the sample surface and will contain peaks that are indicative of higher mass molecular species present on the sample surface.
- (b) Depth profiles are obtained if, instead of scanning the mass spectrometer as the sputtering continues, one or more masses are monitored sequentially by a rapid switching among masses. The detected signal from the chosen species occurs from increasingly greater depths beneath the original sample surface. Accurate depth profiling requires uniform bombardment of the analysis area and no contribution of ions from the crater walls, adjacent sample surfaces, or nearby instrument surfaces.

Depth profiles and mass spectra are complementary. Mass spectra provide helpful information about mass interferences needed to make decisions as to which species (isotope, elemental, or molecular ion) gives the best profile or best detection limit in a depth profile.

One of the major uses for SIMS during the last decade has been semiconductor analysis. SIMS is the only surface-sensitive technique that can detect the low levels of dopants and impurities critical to semiconductor performance.

- (c) SIMS can also be used in a mode of data collection that is analogous to scanning electron microscopy (SEM), but, instead of obtaining images of the sample by using a focused electron beam and detection of secondary electrons emitted from the sample, one bombards with a focused ion beam and records an image formed by secondary ions emitted from the sample that are detected with a mass spectrometer. In this way, element-specific images or maps can be generated. Ion images can be taken almost continuously in an image depth profile to provide a three-dimensional picture.

The analysis by SIMS of samples with a high dielectric constant presents special problems due to the electrical charging of the sample surface due to the particle bombardment and the subsequent emission from the surface of secondary electrons. An electrostatic analyser allows only ions with certain energies to enter into the magnetic analyser. If, during the analysis, the sample surface is not at a fixed potential the energy distribution of the emitted secondary ions is out of the energy range to be analysed. The secondary-ion current therefore becomes unstable (for weak charging) or even reduced; the fast growth of the charging can lead to the deflection of the primary beam or to a discharge between the sample surface and the sample holder. In addition, it can promote field-enhanced migration of those ions released inside the solid insulator by irradiation with charged-particle beams, thereby leading to erroneous depth profiles [8].

When an insulating specimen is etched away by the primary beam, a source of electrons is required to prevent charge build-up at the sample surface [9].

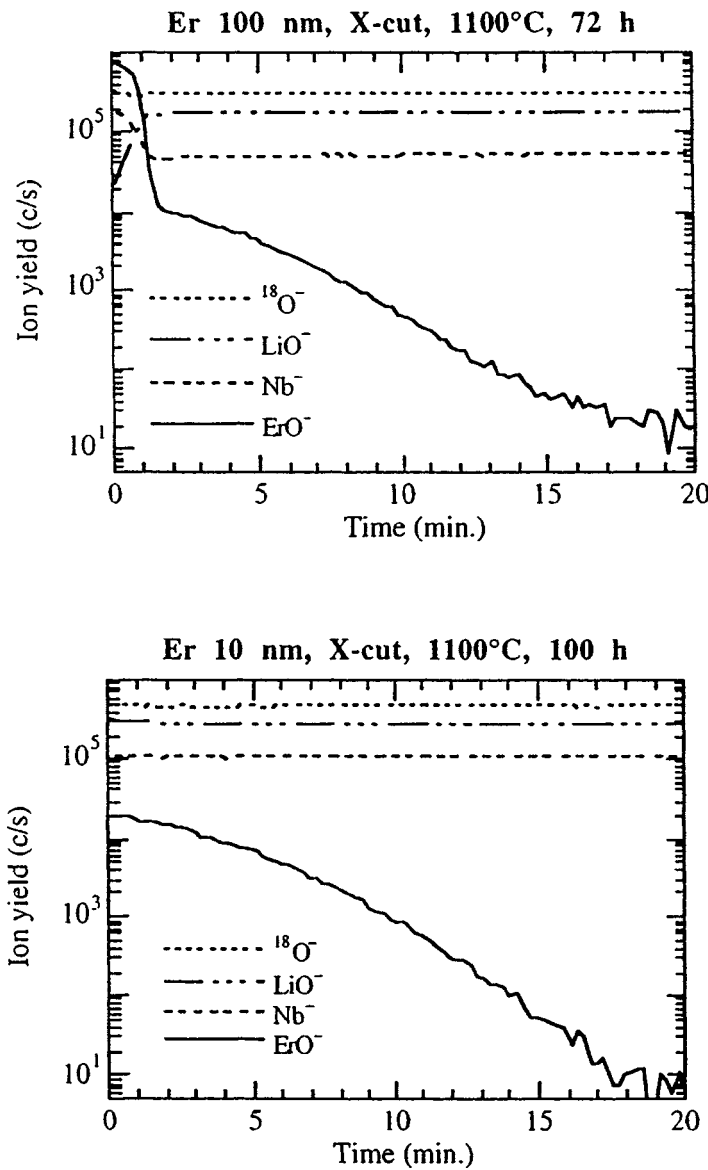
E THE APPLICATION OF SIMS FOR THE CHARACTERISATION OF LITHIUM NIOBATE

Due to its high sensitivity, good depth resolution and achievable high mass resolution, the SIMS technique has been successfully applied to the study of various doping methods in optical materials [1]. In particular, results obtained on diffusion of metals, rare earths and protons in lithium niobate will be presented.

E1 Local Doping of Lithium Niobate Crystals

Detailed studies of Mg, Ti, Cr and Er diffusion in LiNbO_3 from deposited thin metal/metal oxide films have been performed using SIMS [10-17]. The high sensitivity and remarkable depth resolution of the technique permitted detailed investigation of the in-depth behaviour of the mentioned elements as a function of diffusion parameters, like temperature, time and film thickness, for different crystal cut directions. Starting from the experimental SIMS data, the diffusion process has been analysed in terms of the classical mathematical diffusion model. Consequently, diffusion constants and activation energies have been derived.

SIMS measurements of the diffused samples were performed using a CAMECA IMS4f ion microscope equipped with a normal incidence electron gun used to compensate the surface charge build-up while profiling insulating samples like LiNbO_3 crystals. Concentration profiles were obtained using 14.5 keV Cs^+ bombardment and negative secondary ion detection. The erosion speed was evaluated by measuring the depth of the crater at the end of each analysis by means of a Tencor Alpha-step profilometer. Constancy of the bulk signals with depth during the analysis indicated the complete surface-charge compensation. FIGURE 3 shows, as an example, typical SIMS raw spectra of Er-doped LiNbO_3 by thermal diffusion from thick and thin erbium films, respectively.

FIGURE 3 Raw SIMS spectra of Er:LiNbO₃.

E2 Reverse Proton Exchange for Buried Waveguides in LiNbO₃

One of the basic methods to realise optical waveguides in LiNbO₃ is H⁺ \leftrightarrow Li⁺ proton exchange (PE). There are some exchange and annealing conditions to produce best waveguides in LiNbO₃ characterised by low optical losses, negligible decrease of electro-optical and non-linear coefficients, and high power handling capability. However, since the depth index profile for the conventional PE LiNbO₃ waveguides is asymmetric, the waveguide depth mode is also quite asymmetric. On the other hand, single-mode fibres have circular symmetric mode profiles. Thus, depth-index symmetrising is essential to reduce the fibre to waveguide coupling loss. Making buried proton-exchanged waveguides can solve this problem. Such waveguides can be produced by the Li⁺ \leftrightarrow H⁺ reverse proton exchange (RPE) method [18]. The RPE method also allows the realisation of symmetric mode waveguides with high conversion efficiency in non-linear processes due to a better overlap between the interacting modes and lower losses due to a reduction of the influence of surface imperfections. Moreover, ordinary waveguides are created at the surface using the PE region as an index barrier.

SIMS is used to measure, with good accuracy and high depth resolution, compositional profiles of PE and RPE systems.

SIMS measurements of the PE and RPE samples were performed using the CAMECA IMS4f ion microscope (see the previous section). In this case, a quantification can be obtained by the use of a hydrogen-implanted standard of LiNbO_3 or by the measurement of the total hydrogen dose retained in the sample after the direct proton exchange by means of nuclear reaction analysis (NRA) or elastic recoil detection (ERDA).

FIGURE 4 shows the SIMS depth profiles in Z-cut LiNbO_3 samples, as-exchanged and after the reverse exchange.

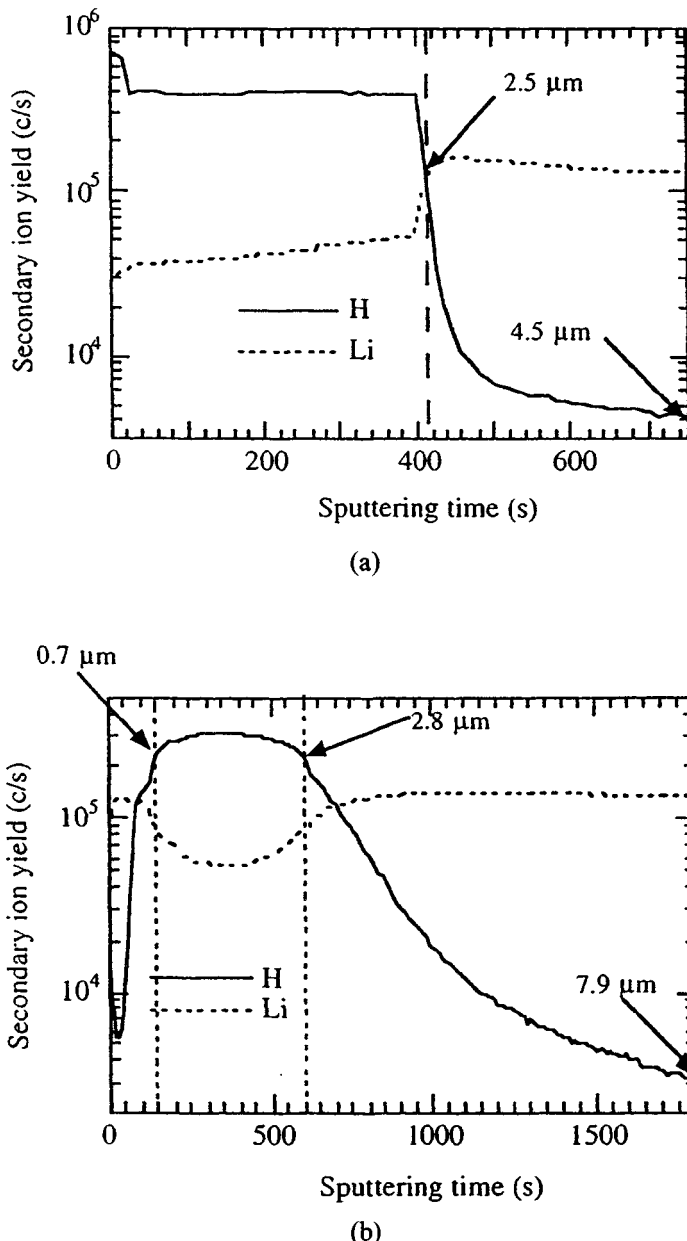


FIGURE 4 (a) SIMS depth profiles of Z-cut PE LiNbO_3 sample,
(b) SIMS depth profiles of Z-cut RPE LiNbO_3 sample.

In the first case, the hydrogen profile consists of a plateau of constant H density, followed by a sharp decrease to the SIMS signal corresponding to the bulk hydrogen level in pure LiNbO_3 . The Li signal is complementary to that of H, showing that direct exchange $\text{H}^+ \leftrightarrow \text{Li}^+$ has been obtained. After reverse proton exchange a buried H profile is realised. It is worth mentioning that in the last case the lithium signal at the surface is close to that in the bulk region, and therefore one can expect that pure lithium niobate is realised on the top of the RPE LiNbO_3 waveguide. During the RPE process the hydrogen distribution at the diffusion front becomes graded due to the annealing process proceeding simultaneously with reverse proton exchange. The mode profiles of the analysed PE and RPE follow the hydrogen concentration profiles, as obtained by m-lines and near-field measurements [18].

F CONCLUSION

The peculiarities of the SIMS technique have been outlined. It has been shown how SIMS can be applied to the characterisation of optical materials such as lithium niobate. SIMS has permitted a study of the diffusion of doping elements like Er in LiNbO_3 from thin film in the frame of classical diffusion theory, as well as characterisation of LiNbO_3 buried-index waveguides obtained by proton ion exchange. In the characterisation of optical materials SIMS has been demonstrated to be effective for the correlation between compositional modifications and optical properties. The need of complementary techniques for the quantification of the obtained data has been underlined.

The main advantages and disadvantages of SIMS are summarised below.

Main advantages: (1) detection limits of parts per million atomic for most elements and parts per billion atomic for favourable elements, (2) all elements detectable, (3) isotopes can be distinguished, (4) depth resolution of 2 - 5 nm possible, and 10 - 20 nm typical, (5) lateral resolution of 20 nm - 1 μm , depending on primary ion source, (6) insulators analysable.

Disadvantages: (1) mass interferences, (2) secondary ion yields vary by more than six orders of magnitude over the periodic table, (3) secondary ion yields are often matrix dependent, (4) numerous secondary standards or complementary techniques are required to quantify data, (5) flat surface required for best depth resolution and for ion microscopy, (6) destructive analysis.

REFERENCES

- [1] F. Caccavale [*Materials Characterization and Optical Probe Techniques* vol.CR69 (SPIE, 1997) p.423-59]
- [2] R.G. Wilson, F.A. Stevie, Ch.W. Magee [*Secondary Ion Mass Spectrometry: A Practical Handbook for Depth Profiling and Bulk Impurity Analysis* (John Wiley & Sons, 1989) ch.1]
- [3] H.W. Werner [*Surf. Interface Anal. (UK)* vol.2 (1980) p.56]
- [4] D.P. Leta, G.H. Morrison [*Anal. Chem. (USA)* vol.52 (1980) p.277]
- [5] [*CAMECA IMS4f User's Guide* Paris, 1988]
- [6] P.H. Dowson [*Int. J. Mass. Spectrom. Ion. Phys. (Netherlands)* vol.17 (1975) p.447]
- [7] S. Miyagawa [*J. Appl. Phys. (USA)* vol.44 (1973) p.5617]
- [8] H.W. Werner, A.E. Morgan [*J. Appl. Phys. (USA)* vol.47 (1976) p.1232]
- [9] H.N. Migeon, M. Schuhmacher, G. Slodzian [*Surf. Interface Anal. (UK)* vol.16 (1990) p.9]
- [10] F. Caccavale, P. Chakraborty, I. Mansour, G. Gianello, M. Mazzoleni, M. Elena [*J. Appl. Phys. (USA)* vol.76 (1994) p.7552-8]
- [11] F. Caccavale, P. Chakraborty, A. Capobianco, G. Gianello, I. Mansour [*J. Appl. Phys. (USA)* vol.78 (1995) p.187-93]
- [12] F. Caccavale et al [*J. Appl. Phys. (USA)* vol.78 (1995) p.5345-50]
- [13] F. Caccavale, F. Gonella, A. Quaranta, I. Mansour [*Electron. Lett. (UK)* vol.31 (1995) p.1054-6]

- [14] J.M. Almeida et al [*J. Appl. Phys. (USA)* vol.78 (1995) p.2193-7]
- [15] F. Caccavale, F. Segato, I. Mansour, J.M. Almeida, A.P. Leite [*J. Mater. Res. (USA)* vol.13 (1998) p.1672-8]
- [16] F. Caccavale [Datareview in this book: 8.10 *Chromium doping of LiNbO_3 by thin film diffusion*]
- [17] F. Caccavale, F. Segato [Datareview in this book: 12.1 *Erbium doping of LiNbO_3 by thin film diffusion*]
- [18] Yu.N. Korkishko, V.A. Fedorov, T.M. Morozova, F. Caccavale, F. Gonella, F. Segato [*J. Opt. Soc. Am. A (USA)* vol.15 (1998) p.1838-42]

13.3 Near field method for the characterisation of channel waveguides in LiNbO₃

F. Caccavale, C. Sada and F. Segato

August 1999

A INTRODUCTION

Design and fabrication of optical waveguides with specific features are nowadays two fields of theoretical, experimental and technological study that still require great efforts for the optimisation of devices. The development of accurate techniques able to determine the main properties of such structures is an essential goal. In particular, the precise knowledge of the refractive index of an optical waveguide is necessary to create structures with the desired spot size, bandwidth, efficiency of fibre-to-guide coupling, and satisfaction of single-mode condition.

In this Datareview, the near field (NF) technique for the reconstruction of refractive-index profiles of light waveguides, based on the measurement of the transmitted intensity pattern, will be presented. The experimental set-up and the reconstruction algorithms are presented and discussed.

B EXPERIMENTAL

The NF technique is based on the measurement of the intensity profile of the light transmitted from a waveguide. The light source is a linearly polarised laser with a wavelength ranging from visible (He-Ne laser at 633 nm) to infrared (laser diodes at 1.3 - 1.5 μm). Laser light is usually coupled to the waveguide through the butt-coupling, also called end-fire method. By this method, the radiation coming directly from the laser or transported through an optical fibre is focused onto the optically polished face of the waveguide. At the end of the waveguide, an output objective focuses the image of the bright spot of the waveguide onto a video camera, which digitises and records the image. The set-up is shown in FIGURE 1.

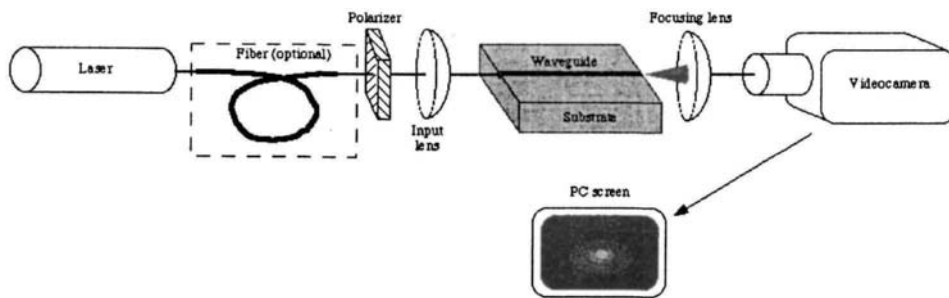


FIGURE 1 Typical set-up for near field measurements.

In this set-up, different modes are excited in a multi-mode waveguide. For the reconstruction of the refractive index profile, only the fundamental mode has to be excited. In many cases, however, the coupling between the incident laser beam and the high-order modes can be neglected.

13.3 Near field method for the characterisation of channel waveguides in LiNbO_3

An alternative coupling method that ensures an excellent selectivity of the modes in waveguides is given by using prism coupling, in a scheme analogous to m-lines spectroscopy [1]. Prism coupling works well with both slab and channel waveguides. Its set-up is shown in FIGURE 2.

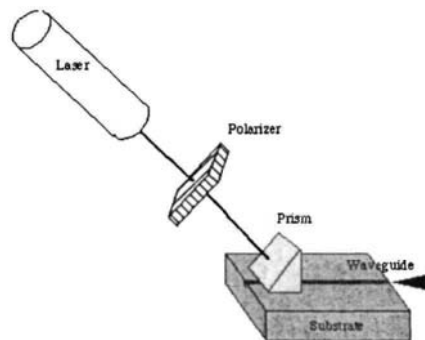


FIGURE 2 Alternative coupling scheme for single-mode excitation.

The normalised electric field profile $E(x,y)$ is calculated from the intensity profile of the fundamental mode $I(x,y)$,

$$E(x,y) = \sqrt{\frac{I(x,y)}{I_{\max}}}$$

[2], where x and y are the coordinates of the transverse section of the waveguide and I_{\max} is the maximum value of the intensity. FIGURE 3 shows the near field profile of a Ti: LiNbO_3 waveguide (TE mode, $\lambda = 633$ nm).

Near field images are affected by several noise sources such as mechanical vibrations and misalignment, image defocusing, non-linearity of the video camera and electronic and quantisation noise. Helms et al [3] carefully studied the influence of the errors in the reconstructed index profile. Accurate preparation of the experimental set-up enables one to eliminate most of the error sources. Repeated measurements are useful to reduce the fluctuations due to the electronic noise. The quantisation noise is due to the low depth of the digital image provided by the control unit of the video camera, typically 256 levels of grey, i.e. an 8-bit image. A small variation in intensity between adjacent pixels of the same order of the quantisation step may result in abrupt non-physical changes after the digitalisation process. This happens mainly on the mode tails and affects the reconstruction process (see next section).

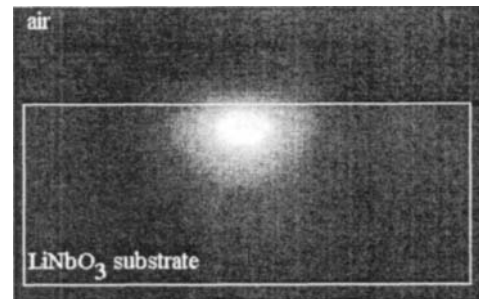


FIGURE 3 Near field image of the fundamental mode in a Ti: LiNbO_3 waveguide.

C RECONSTRUCTION ALGORITHMS

The link between the refractive index profile $n(x,y)$ and the electric field is given by the Helmholtz equation. For a TE mode in a smoothly varying index profile, the Helmholtz equation is reduced to the scalar form

13.3 Near field method for the characterisation of channel waveguides in LiNbO₃

$$\nabla_t^2 E(x, y) + \frac{\omega^2}{c^2} n^2(x, y) E(x, y) = \frac{\omega^2}{c^2} n_{\text{eff}}^2 E(x, y) \quad (1)$$

where ∇_t^2 is the Laplacian operator on the coordinates x and y, ω and c are the light frequency and speed in vacuum, respectively, and n_{eff} is the effective refractive index of the fundamental mode. In general, n_{eff} is an unknown quantity, unless measured by independent techniques such as m-lines spectroscopy [1].

The simplest algorithm for the calculation of the refractive index profile is the inversion of EQN (1) [2]:

$$n(x, y) = \sqrt{n_{\text{eff}}^2 - \frac{c^2}{\omega^2} \frac{\nabla_t^2 E(x, y)}{E(x, y)}} \quad (2)$$

Although this method is numerically simple, it is very sensitive to noise sources, in particular near the tails of the mode, where the electric field vanishes. Moreover, the Laplacian operator amplifies the high spatial frequency noise [3]. For this reason, it is not possible to calculate n_{eff} from EQN (2), because in the regions where the Laplacian is small, i.e. on the tails of the mode, the electric field is very small and the second term inside the square root of EQN (2) tends to diverge. As the relative index variations are usually small, n_{eff} is approximated by the substrate value of the refractive index, thus inducing a slight underestimation of the refractive index variation.

Several techniques have been developed to reduce the noise effects in EQN (2). The most relevant are:

- (i) to calculate the second term of EQN (2) from the experimental profile and to fit it with a suitable function to recover $n(x, y)$ [3];
- (ii) the application of noise-reduction techniques to the measured intensity profile such as a spline fit [3], a tailored low-pass filter in the spatial frequency domain like a third-order Butterworth filter [4] or a Gaussian filter [5];
- (iii) the measurement of mode tails at high power, with a saturation of the central intensity peak, in order to increase the signal-to-noise ratio (SNR) [5].

The application of low-pass filters limits the spatial resolution of the NF technique, already limited by the finite numerical aperture of the lenses and objectives. An accurate tailoring in the filters design is required, due to the strong competition between low-pass attenuation (typically 6 - 8 dB per octave) and noise amplification due to the Laplacian operator (9 dB per octave) [6]. Good results have been shown by Mansour and Caccavale [4] and Brooks and Ruschin [5] in the case of Ti:LiNbO₃, Mg:Ti:LiNbO₃ channel waveguides and optical fibres, respectively.

A more refined algorithm for the calculation of the refractive-index profile has been developed by Caccavale et al [7]. Based on the knowledge of the fabrication process of the waveguide, an hypothesis on the analytical form of the index profile $n(x, y; a_1, \dots, a_N)$ can be made, in which a_1, \dots, a_N are parameters representing the depth, the width of the profile, and the maximum index change. Starting from the expected values for these parameters, the electric profile of the fundamental mode $E_c(x, y; a_1, \dots, a_N)$ is calculated by a finite-differences scheme, and compared to the measured field $E_m(x, y)$. The error function $F(a_1, \dots, a_N)$ is evaluated by:

$$F(a_1, \dots, a_N) = \int |E_m(x, y) - E_c(x, y; a_1, \dots, a_N)|^2 dx dy \quad (3)$$

and then minimised with respect to parameters a_1, \dots, a_N . High-frequency noise is averaged out in EQN (3) by this method, and no low-pass filters are needed. The averaging of several near-field images is recommended to increase the signal-to-noise ratio (SNR). Another advantage of this method is given by the possibility of reducing the image resolution if the pixel size is smaller than the optical resolution of the system, by averaging adjacent pixels. In this way, the SNR is increased. The last method is not useful when using EQN (2), as the calculation of derivatives would become quite inaccurate. An effective increase of the image depth is obtained by reducing both the image resolution and the stochastic noise. Moreover, the grid matrices used in the numerical implementation of the method have reasonable dimensions. In the finite differences scheme, if the waveguide is represented by an $M \times M$ grid, the matrices for the calculation of the normal mode have $M^2 \times M^2$ dimension (typical values are $M = 60$ and $M^2 = 3600$).

The drawback of this method is given by the heaviness in terms of numerical calculations. Large matrices, although sparse, require large amounts of memory and CPU time. Moreover, the calculation of the normal mode for the minimisation process is repeated tens or hundreds of times, thus requiring some hours of CPU on a fast, dedicated workstation.

D APPLICATIONS

The results of the near field characterisation of two identical parallel channel waveguides realised by thermal diffusion of two lithographically patterned titanium strips in lithium niobate are presented [8]. From the diffusion theory and from the experimental relation between optical and compositional properties in Ti:LiNbO_3 waveguides [9], the following expression can be used for the refractive index profile of each waveguide:

$$n(x, y \geq 0; \Delta n, d_x, d_y) = n_s + \Delta n \exp\left[-\left(\frac{x}{d_x}\right)^2\right] \exp\left[-\left(\frac{y}{d_y}\right)^2\right] \quad (4)$$

$$n(x, y < 0) = 1$$

where n_s is the refractive index of the substrate (pure lithium niobate), Δn is the maximum index variation, d_x is the lateral width of the index profile and d_y is its depth. The region for $y < 0$ represents the air layer over the waveguide.

NF measurements have been performed using a polarised He-Ne laser at 633 nm, and by using the prism-coupling scheme. Several images have been recorded and averaged. The image resolution has been decreased, as described in the previous section.

FIGURE 4 shows lateral and in-depth profiles of the measured intensity pattern for one waveguide, together with the matched calculated profile.

A good agreement can be seen between the measured and calculated profiles. Similar results have been obtained for the second waveguide. TABLE 1 summarises the calculated parameters, together with their error obtained from the minimisation procedure [10].

TABLE 1 Minimisation results.

	Δn	$d_x (\mu\text{m})$	$d_y (\mu\text{m})$
Guide 1	0.0081 ± 0.0002	3.98 ± 0.03	3.3 ± 0.2
Guide 2	0.0084 ± 0.0005	4.13 ± 0.07	3.6 ± 0.3

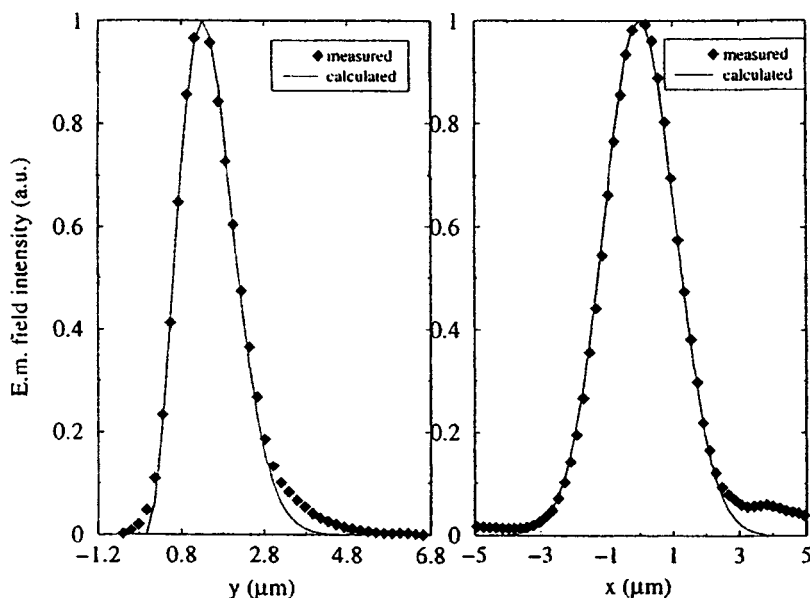


FIGURE 4 In-depth (left) and lateral (right) profiles of measured and calculated NF intensity.

The two waveguides turn out to be equal within the experimental errors, thus confirming that the reconstruction method gives good results. Relative errors less than 6%, 2% and 8% are achieved in the maximum index variation, profile width and depth, respectively. The major error in the profile depth with respect to the width is due to the uncertainty in the position of the air/waveguide interface. Nevertheless, these errors are lower than those obtained by using EQN (2), which are typically around 10 - 25% [4].

E CONCLUSION

The near field technique has been reviewed. Particular attention has been dedicated to the reconstruction methods to obtain the refractive-index distribution from the measured intensity profiles. A method, based on the hypothesis of the refractive index profile analytical form, and on the minimisation of the difference between the measured and calculated intensity profile, has been presented. The good results in terms of small relative errors of this method have been outlined.

ACKNOWLEDGEMENTS

We would like to thank Dr. I. Mansour from the University of Jordan, Dr. A. Morbiato from our Department, and Dr. M. Gianesin of Italtel company, for their valuable contributions in both the experimental and numerical activity.

REFERENCES

- [1] F. Caccavale, C. Sada, F. Segato [Data review in this book: 13.4 M-lines spectroscopy for the characterisation of slab waveguides in LiNbO_3]
- [2] L. McCaughan, E.E. Bergman [*J. Lightwave Technol. (USA)* vol.LT-1 (1983) p.241-4]
- [3] J. Helms, J. Schmidtchen, B. Schüppert, K. Petermann [*J. Lightwave Technol. (USA)* vol.8 (1990) p.625-33]
- [4] I. Mansour, F. Caccavale [*J. Lightwave Technol. (USA)* vol.14 (1996) p.423-8]

13.3 Near field method for the characterisation of channel waveguides in LiNbO₃

- [5] D. Brooks, S. Ruschin [*IEEE Photonics Technol. Lett. (USA)* vol.8 (1996) p.254-6]
- [6] A.V. Oppenheim, R.V. Schafer [*Discrete-Time Signal Processing* (Prentice Hall Int., 1989)]
- [7] F. Caccavale, F. Segato, I. Mansour, M. GIANESIN [*J. Lightwave Technol. (USA)* vol.16 (1998) p.1348-53]
- [8] F. Caccavale et al [*J. Appl. Phys. (USA)* vol.78 (1995) p.5345-50]
- [9] F. Caccavale, C. Sada, F. Segato, F. Cavuoti [*Appl. Surf. Sci. (Netherlands)* vol.150 (1999) p.195-201]
- [10] F. James [*MINUIT Reference Manual* (CERN, 1994)]

13.4 M-lines spectroscopy for the characterisation of slab waveguides in LiNbO₃

F. Caccavale, C. Sada and F. Segato

August 1999

A INTRODUCTION

New developments in modern optoelectronics are due to the combination of physics, optics, electronics, chemistry and material science studies, with the aim of developing more efficient ways of acquiring, storing and transmitting information. Planar waveguides have attracted great interest for providing the next generation of optical circuits after those which employ optical fibres.

A waveguide consists of a region having a higher refractive index than the surrounding material; thus the light is guided through the high-index region by means of total internal reflection. As a consequence of reflection conditions, only the electromagnetic field with a particular phase velocity, which corresponds to a discrete number of guided optical modes, can propagate inside the waveguide. An accurate knowledge of the refractive index is fundamental for characterising waveguide optical properties.

M-lines spectroscopy is a useful technique for the evaluation of waveguide optical parameters, such as effective refractive indexes, from which it is possible to reconstruct the refractive index of the waveguide. In this review, the m-lines spectroscopy technique for slab waveguide characterisation will be described.

B WAVEGUIDE THEORY

It is well known that electromagnetic wave propagation can be described by the Maxwell equations. In the case of a birefringent, non-magnetic medium and in the absence of free charges the equations are:

$$\nabla^2 \mathbf{E} + \tilde{\epsilon}_r \frac{\omega^2}{c^2} \mathbf{E} + \nabla \left(\mathbf{E} \cdot \nabla \ln \epsilon_r^o + \frac{\epsilon_r^e - \epsilon_r^o}{\epsilon_r^o} \frac{\partial E_z}{\partial z} \right) = 0 \quad (1)$$

(optical axis // z-axis)

$$\nabla^2 \mathbf{E} + \tilde{\epsilon}_r \frac{\omega^2}{c^2} \mathbf{E} + \nabla \left(\mathbf{E} \cdot \nabla \ln \epsilon_r^e + \frac{1}{\epsilon_r^e} \frac{\partial (\Delta \epsilon_r E_x)}{\partial x} + \frac{1}{\epsilon_r^e} \frac{\partial (\Delta \epsilon_r E_z)}{\partial z} \right) = 0 \quad (2)$$

(optical axis // y-axis)

where \mathbf{E} represents the electric field. The third-rank tensor $\tilde{\epsilon}_r^{o,e}$ indicates the relative dielectric function of the medium with respect to vacuum for the ordinary (o) and extraordinary (e) axes, respectively. The term containing $\Delta \epsilon_r$ is related to the birefringence, and it can be neglected in order to reduce the complexity of EQNS (1) and (2). Such an approach is correct for small dielectric function gradient.

As a consequence, EQN (1) is applied to a medium of constant dielectric function ϵ_r^o :

$$\nabla^2 \mathbf{E} + \tilde{\epsilon}_r \frac{\omega^2}{c^2} \mathbf{E} + \nabla(\mathbf{E} \cdot \nabla \ln \epsilon_r^o) = 0 \quad (3)$$

and EQN (2) corresponds to a medium of dielectric function ϵ_r^e :

$$\nabla^2 \mathbf{E} + \tilde{\epsilon}_r \frac{\omega^2}{c^2} \mathbf{E} + \nabla(\mathbf{E} \cdot \nabla \ln \epsilon_r^e) = 0 \quad (4)$$

EQNS (3) and (4) are well known as Helmholtz equations. For the sake of simplicity, the system shown in FIGURE 1 will be considered. The waveguide (second region) is embedded between two regions with lower refractive indices, corresponding to the first and the third regions, respectively. If the dielectric function is constant along the propagation direction, the solution for EQN (3) and EQN (4) can be assumed in the following form:

$$\mathbf{E}(x, y, z, \omega) = \mathbf{E}'_k(x, y, \omega) e^{ikz} \quad (5)$$

In this way, Helmholtz equations are an eigenvalues problem for the operator H:

$$H \mathbf{E}'_k = k^2 \mathbf{E}'_k \quad (6)$$

where:

$$H = \nabla_t^2 + \epsilon_r \frac{\omega^2}{c^2} + \nabla_t (\nabla_t \ln \epsilon_r) \text{ and } \nabla_t = \left(\frac{\partial}{\partial x}, \frac{\partial}{\partial y} \right) \quad (7)$$

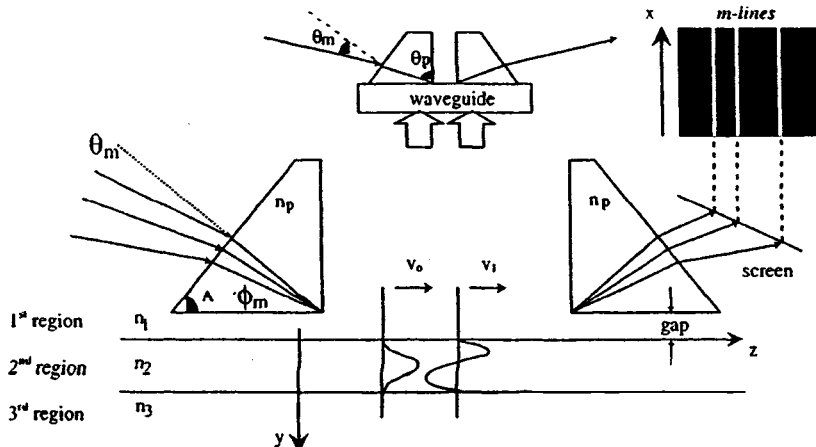


FIGURE 1 Scheme of light propagation inside a waveguide and prism coupling.

Only the discrete (and positive) part of the H spectrum corresponds to the guided modes in which the electromagnetic field is confined inside the region with higher refractive index. The relative eigenstates are called normal modes, i.e. electromagnetic field profiles propagating in the waveguide with invariant shapes. Guided modes are allowed only if

$$k_o n_3 < k < k_o n_2 \quad (8)$$

The mth mode propagates inside the waveguide with a particular phase velocity and, therefore, we see an effective refractive index $n_{eff,m} = k_m/k_o = c/v_m$ where $k_o (= \omega/c)$ is the wavenumber in vacuum.

$$\nabla^2 \mathbf{E} + \tilde{\epsilon}_r \frac{\omega^2}{c^2} \mathbf{E} + \nabla(\mathbf{E} \cdot \nabla \ln \epsilon_r^e) = 0 \quad (3)$$

and EQN (2) corresponds to a medium of dielectric function ϵ_r^e :

$$\nabla^2 \mathbf{E} + \tilde{\epsilon}_r \frac{\omega^2}{c^2} \mathbf{E} + \nabla(\mathbf{E} \cdot \nabla \ln \epsilon_r^e) = 0 \quad (4)$$

EQNS (3) and (4) are well known as Helmholtz equations. For the sake of simplicity, the system shown in FIGURE 1 will be considered. The waveguide (second region) is embedded between two regions with lower refractive indices, corresponding to the first and the third regions, respectively. If the dielectric function is constant along the propagation direction, the solution for EQN (3) and EQN (4) can be assumed in the following form:

$$\mathbf{E}(x, y, z, \omega) = \mathbf{E}'_k(x, y, \omega) e^{ikz} \quad (5)$$

In this way, Helmholtz equations are an eigenvalues problem for the operator H:

$$H \mathbf{E}'_k = k^2 \mathbf{E}'_k \quad (6)$$

where:

$$H = \nabla_t^2 + \epsilon_r \frac{\omega^2}{c^2} + \nabla_t (\nabla_t \ln \epsilon_r) \text{ and } \nabla_t = \left(\frac{\partial}{\partial x}, \frac{\partial}{\partial y} \right) \quad (7)$$

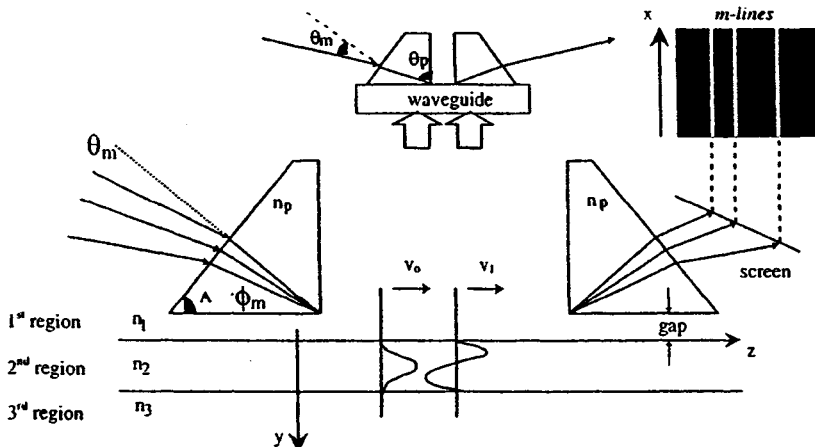


FIGURE 1 Scheme of light propagation inside a waveguide and prism coupling.

Only the discrete (and positive) part of the H spectrum corresponds to the guided modes in which the electromagnetic field is confined inside the region with higher refractive index. The relative eigenstates are called normal modes, i.e. electromagnetic field profiles propagating in the waveguide with invariant shapes. Guided modes are allowed only if

$$k_o n_3 < k < k_o n_2 \quad (8)$$

The mth mode propagates inside the waveguide with a particular phase velocity and, therefore, we see an effective refractive index $n_{eff,m} = k_m/k_o = c/v_m$ where $k_o (= \omega/c)$ is the wavenumber in vacuum.

that of the waveguide, is pressed to the waveguide and geometric conditions are checked until a total internal reflection occurs on the prism base. Therefore, a stationary wave is formed along the x-direction (the wave propagates in the z-direction), and an evanescent field fills the prism-waveguide gap. If this gap is thin enough (about 0.1 μm), the evanescent field can excite the guided modes inside the waveguide. Mode excitation occurs when the phase velocity, v_p , of the incident electromagnetic field equals the mth mode phase velocity, v_m , supported by the waveguide in the propagation direction

$$v_p = \frac{c}{n_p \sin \phi} \quad (12)$$

It follows that the coupling is obtained if

$$n_{\text{eff},m} = \frac{k_m}{k_o} = n_p \sin \phi_m \quad (13)$$

ϕ_m can be evaluated by measuring the angle of incidence of the light on the prism, θ_m ,

$$\phi_m = A + \arcsin\left(\frac{\sin \theta_m}{n_p}\right) \quad (14)$$

where A represents the prism angle at the base.

Therefore, the effective refractive index of a given optical mode can be correlated to the relative angle of incidence on the prism:

$$n_{\text{eff},m} = n_p \sin\left(A + \arcsin\left(\frac{\sin \theta_m}{n_p}\right)\right) \quad (15)$$

It is, therefore, possible to selectively excite the normal modes in the waveguide by properly varying the angle of incidence of the light on the prism or by varying the coupling angle. Each optical guided mode can be ‘decoupled’ with a second prism, so that relative lines can be observed on a screen (see FIGURE 1). Alternatively, it is possible to record the intensity of the guided light as a function of the incidence angle by means of a photodetector, thus demonstrating when the best coupling has been reached. After the calculation of the effective refractive index relative to each guided mode by EQN (15), an inverse WKB procedure can be exploited for the reconstruction of the refractive index profile of the waveguide.

D M-LINES SPECTROSCOPY: SET-UP

The m-lines experimental set-up is quite simple and its block-diagram is reported in FIGURE 2. A laser beam (usually He-Ne at 632.8 nm) is polarised for the selection of TE and TM polarisations, and is directed towards the incident prism. Two prisms are mechanically pushed to the waveguide: the first at the incident light, the second at the waveguide exit. Both the prism and the waveguide are put on a platform, which rotates with a high degree of precision (0.002°). A chopper and a lock-in are used to reduce the noise level. The guided light that comes out from the waveguide is then recorded by a photodetector. The accuracy in the effective refractive index determination using this set-up is about 10^{-4} , the errors deriving from the evaluation of the synchronous angles (in the worst condition, about 20×10^{-3} deg), and from the zero angle adjustment (0.002°) [6].

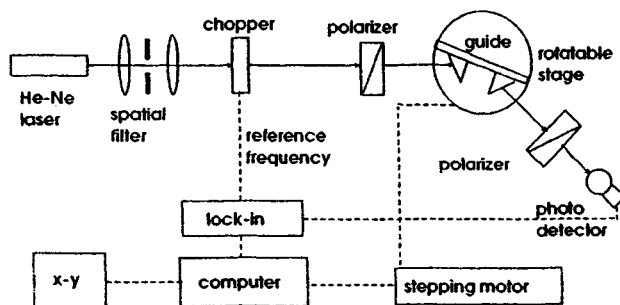


FIGURE 2 M-lines experimental set-up.

Once the effective indices are known, an inverse WKB method can be exploited for the reconstruction of the refractive-index profile of the waveguide.

E APPLICATIONS

Local doping of crystals or glasses by means of thermal diffusion, ion-exchange processes and various thin-film deposition techniques can achieve an increase of the refractive index for the realisation of an optical waveguide. In the present Datareview optical waveguides obtained in LiNbO₃ by means of thermal diffusion from thin metal film will be considered. As is well known, lithium niobate is a birefringent crystal (the ordinary and the extraordinary refractive indices are equal to n_o = 2.2020 and n_e = 2.2865, respectively, at λ = 632.8 nm). Although the above-mentioned processing technique is widely used [8], a careful study on the inter-relationship between the refractive-index variation and the dopant concentration is necessary for the tailoring of optical waveguide properties. Therefore, optical measurements such as m-lines and near field [9] methods have attracted great interest.

The diffusion of various doping elements has been studied in the literature to achieve high refractive index changes in LiNbO₃. Among them, titanium has played an important role. Although the Ti indiffusion technique is widely used for the realisation of technological and commercial devices, a complete understanding of the relationship between Ti concentration and the corresponding optical properties induced in the medium is still not clear. Some papers have dealt with the problem of determining the refractive-index changes in Ti:LiNbO₃ optical waveguides obtained with low titanium concentration (up to 1.2×10^{21} at/cm³) [10-12]. In [12] a 10 nm thick Ti film has been thermally diffused in X- and Z-cut LiNbO₃ slides and a Gaussian doping profile with surface concentration up to 7.2×10^{20} at/cm³ for X-cut and 5.17×10^{20} at/cm³ for Z-cut has been obtained. M-lines spectroscopy measurements have been performed on both X- and Z-cut samples for both TE and TM polarisation. The guided light intensity, measured as a function of the incidence synchronous angle (see FIGURE 3), leads to effective index evaluation by means of EQN (15). A rutile prism with base angle A = $49.64 \pm 0.01^\circ$ has been used, and refractive indices n_p = 2.86568 (TE) and n_p = 2.58385 (TM) at λ = 632.8 nm have been obtained. FIGURE 4 shows the reconstructed refractive index obtained by ISA-FDM, Chiang and White-Heidrich methods, respectively. The relationships between dopant concentration and refractive index change can be given by

$$\begin{aligned} \Delta n_o &\propto C^{0.51} \text{ (Z-cut, TE)} & \Delta n_o &\propto C^{0.53} \text{ (X-cut, TM)} \\ \Delta n_e &\propto C^{1.07} \text{ (Z-cut, TM)} & \Delta n_e &\propto C^{0.85} \text{ (X-cut, TE)} \end{aligned}$$

The relationship between extraordinary refractive index change and Ti concentration is an approximately linear function, whereas for the ordinary index it is proportional to the square root of Ti concentration.

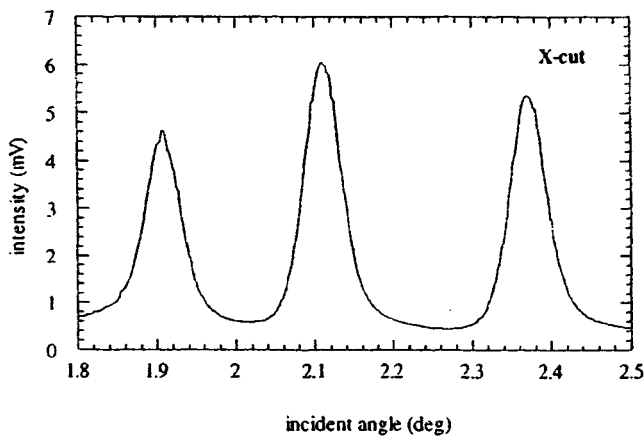


FIGURE 3 Guided light intensity measured as a function of incidence synchronous angle for a Ti:LiNbO_3 (X-cut) slab waveguide.

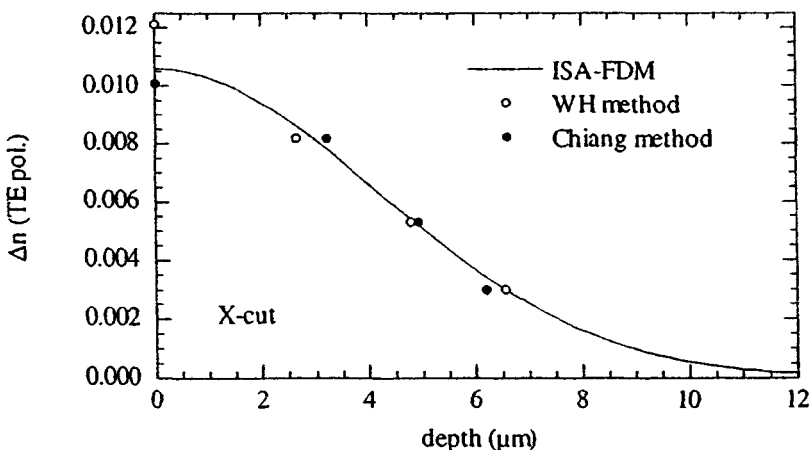


FIGURE 4 Reconstructed refractive-index profile by ISA-FDM, Chiang and White-Heidrich methods for a Ti:LiNbO_3 (X-cut) slab waveguide.

Recently [13], a study on slab and channel LiNbO_3 waveguides obtained by high titanium concentration exploited for better light confinement has been performed. In that work, effective refractive indexes have been obtained by m-lines spectroscopy and the refractive-index profiles have been reconstructed by the Chiang method. Typical refractive-index profiles for ordinary and extraordinary indices together with Ti concentration profile for a Ti:LiNbO_3 waveguide are shown in FIGURE 5. Errors on the measured effective index were estimated to be ± 0.0002 , and the error on the surface index to be ± 0.0010 .

FIGURE 6 shows the surface index variation with respect to the bulk refractive index as a function of surface titanium concentration (dots and squares for ordinary and extraordinary index, respectively), together with data from [11] (continuous line).

It is evident that the extrapolation of these data to higher concentration values (dashed line) does not agree with measured data, showing a saturation in the dependence of surface refractive indices on Ti concentration to the maximum values of $\Delta n_o = 0.0111$ and $\Delta n_e = 0.0284$, for ordinary and extraordinary index, respectively. This saturation can be explained by considering that at high concentration titanium ions are surrounded not only by the neighbour atoms of the host matrix

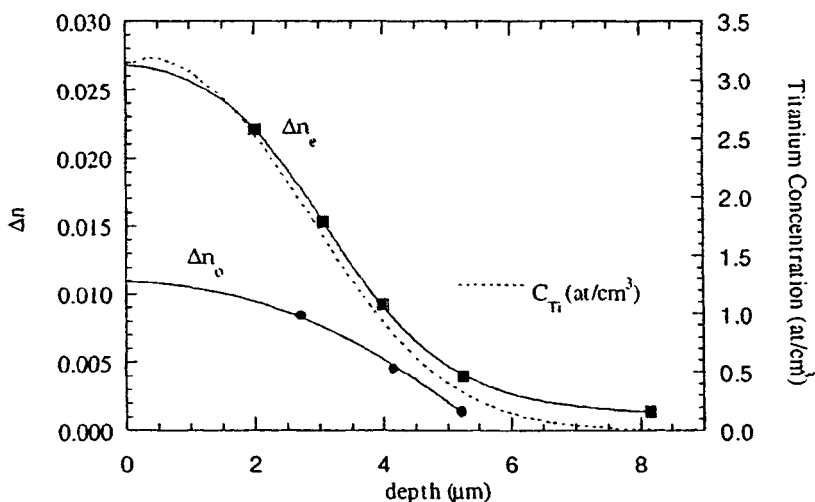


FIGURE 5 Ordinary and extraordinary refractive-index profiles together with Ti concentration profile in a Ti:LiNbO_3 (X-cut) slab waveguide.

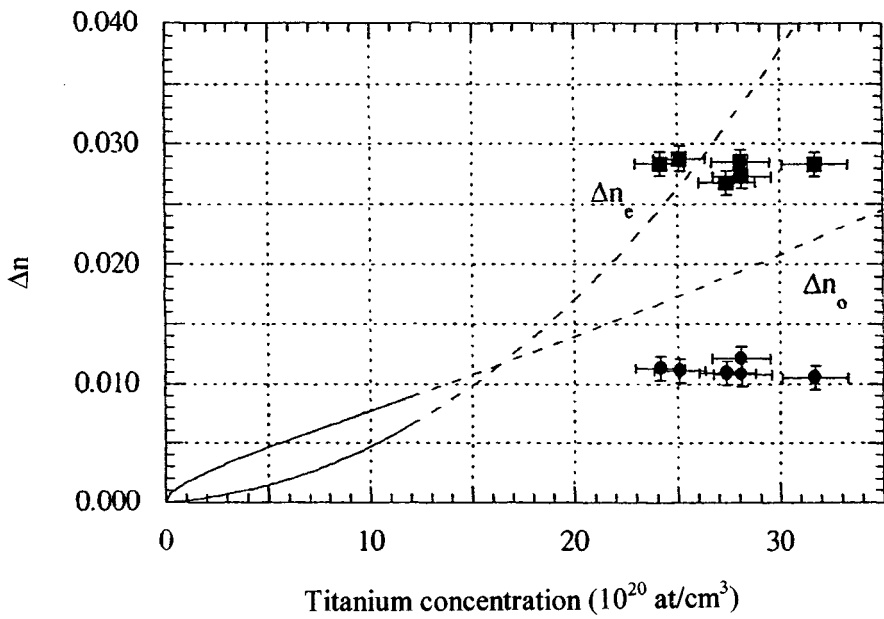


FIGURE 6 Surface refractive-index saturation as a function of surface titanium concentration (dots and squares for ordinary and extraordinary index respectively) together with data from [11] (continuous line).

LiNbO_3 , but also by other Ti ions. The increase of polarisability due to the increase of concentration is therefore partially compensated by some sort of ‘shielding’ of Ti ions on themselves. Moreover, the diffusion of Ti into LiNbO_3 creates sufficient stresses to generate both misfit dislocations and cracks within the diffused layer [14]. Another mechanism for the refractive index change in the diffused layer is given by the photoelastic effect caused by the lattice contraction, which increases non-linearly with titanium concentration, explaining the non-linear behaviour of the relation between Δn and C_{Ti} .

F CONCLUSION

In this Datareview m-lines spectroscopy has been presented as a useful technique for the optical characterisation of LiNbO₃ waveguides. Some applications on Ti indiffused waveguides have been presented with special attention to the relationship between compositional and optical properties.

REFERENCES

- [1] K.S. Chiang [*IEEE J. Lightwave Technol. (USA)* vol.LT-3 (1985) p.385]
- [2] J.M. White, P.F. Heidrich [*Appl. Opt. (USA)* vol.15 (1976) p.151]
- [3] F. Caccavale, F. Gonella, G. Caneva, I. Mansour [*IEEE J. Lightwave Technol. (USA)* vol.14 no.8 (1996) p.1825]
- [4] J. Janta, J. Ctyroky [*Opt. Commun. (Netherlands)* vol.25 (1978) p.49]
- [5] A. Gedeon [*Opt. Commun. (Netherlands)* vol.12 (1974) p.329]
- [6] F. Gonella, A. Quaranta [*Pure Appl. Opt. (UK)* vol.2 (1993) p.405]
- [7] P.K. Tien, R. Ulrich [*J. Opt. Soc. Am. (USA)* vol.60 (1970) p.1325]
- [8] F. Caccavale, F. Segato [Datareview in this book: 12.1 Erbium doping of LiNbO₃ by thin film diffusion]
- [9] F. Caccavale, C. Sada, F. Segato [Datareview in this book: 13.3 Near field method for the characterisation of channel waveguides in LiNbO₃]
- [10] M. Minakata, S. Saito, M. Shibata, S. Miyazawa [*J. Appl. Phys. (USA)* vol.49 (1978) p.4667]
- [11] S. Fouchet, A. Carencio, C. Daguet, R. Guglielmi, L. Riviere [*IEEE J. Lightwave Technol. (USA)* vol.LT-5 (1987) p.700]
- [12] F. Caccavale et al [*J. Appl. Phys. (USA)* vol.78 (1995) p.5345]
- [13] F. Caccavale, C. Sada, F. Segato, F. Cavouti [*Appl. Surf. Sci. (Netherlands)* vol.150 (1999) p.195]
- [14] K. Sugii, M. Fukuma, H. Iwasaki [*J. Mater. Sci. (UK)* vol.13 (1978) p.523]

13.5 Microanalytical techniques for waveguide examination in LiNbO₃

C.E. Geosling

December 1998

A INTRODUCTION

The goal of any waveguide formation process is to attain a waveguide depth, width, refractive index and crystalline phase with low optical loss and good electro-optical properties. In order to control these properties, one must be able to observe them. In this Datareview several analytical techniques for observing and measuring waveguides in lithium niobate are described. The intent is not to be exhaustive but rather to describe some of the most valuable techniques reported in the literature and practised in the author's laboratory. The emphasis is on evaluating proton-exchanged waveguides, although others, such as titanium indiffused waveguides, lend themselves readily to most of the techniques. The techniques to be described are: prism coupling, SIMS (secondary mass ion spectrometry), infrared spectroscopy, phase contrast (Nomarski) microscopy, AFM (atomic force microscopy).

B PRISM COUPLING

Prism coupling has been a research tool for almost thirty years [1-3] and has gradually evolved into the foundry essential that it is today. Commercial instruments from several companies allow measurement of waveguide depth and index profile that are automated, or nearly so. A typical instrument consists of a stable, aligned laser beam impinging on one face of a prism, reflecting from the base, and exiting the second face to a detector. A thin film or planar waveguide on a substrate is made to impinge on the base face of the prism and is held with a steady pressure. Either the laser beam or the prism and sample are rotated such that the angle between the beam and the input face (and thus also the base face) of the prism is continuously varied (FIGURE 1). At certain discrete angles, the light becomes totally internally reflecting at the base film interface, and a portion of the light tunnels into the waveguide in optical propagation modes. At these mode angles, which are defined solely by the waveguide depth and index for a given substrate, the detector sees and records a drop in intensity (FIGURE 2). In simplified terms, the measurement consists of: (1) a plot of laser intensity versus the angle between the beam and the prism base, (2) determination of the discrete

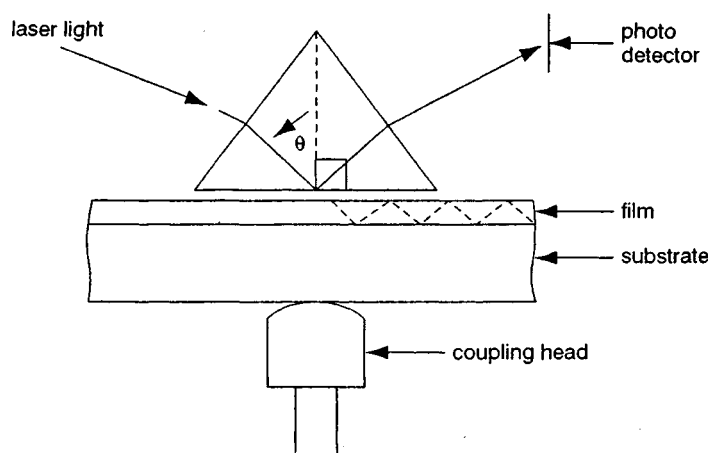


FIGURE 1 Prism coupling light path (courtesy Metricon, Inc.).

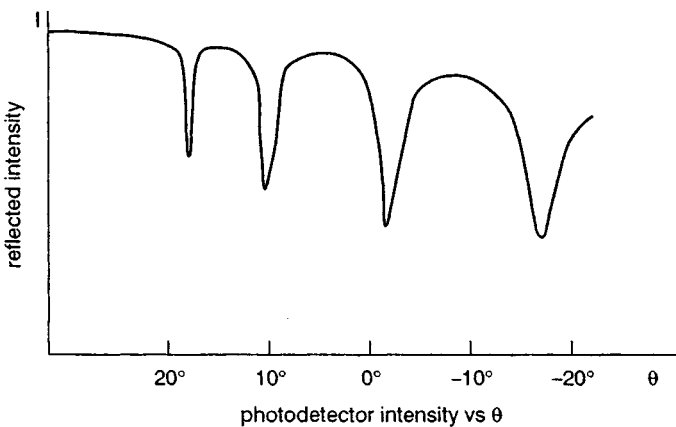


FIGURE 2 Dark modes for single layer film (courtesy Metricon, Inc.).

mode angles, and (3) a calculation of the waveguide depth and refractive index. Quite a bit of work has been reported in the literature on increasingly precise methods for carrying out these calculations. The iWKB (inverse Wentzel, Kramers, Brillouin) method and variations thereof are currently used [4-11]. For annealed proton-exchanged waveguides, the index profile with depth is Gaussian or nearly so, and a fit must be made to the data. Referring to Fick's law of diffusion, a Gaussian fit is used where the guides are formed under a 'limited source' condition. For a 'constant surface concentration' condition, an error function complement gives a better fit. Once the best fit is obtained, the depth and Δn at the $1/e$ or $1/e^2$ point can be defined. Where the waveguide can support multiple modes at several available laser wavelengths, added precision can be obtained in the results [12,13].

C SIMS (SECONDARY ION MASS SPECTROMETRY)

Although SIMS is a destructive analytical technique, its results have been found to correlate well with those from prism coupling. SIMS gives a concentration profile of the dopant material, which has been found to match the refractive index profile in a number of studies [9,14-18] (FIGURES 3 and 4).

It has been used to probe concentration depths in waveguides formed of protons [19] as well as titanium ions [20]. SIMS is an ion sputtering and detection technique in vacuo. When a primary beam of energetic ions, usually Ar^+ , O_2^+ , or Cs^+ , is aimed at the selected analysis spot (on the order of 30 - 50 μm), both neutral and charged 'secondary' atoms and clusters are ejected. The uncharged species are identified and counted with the use of any one of several types of mass spectrometer - quadrupole, sector, or time-of-flight. Many commercial instruments and analytical services are available in this mature technology. Since secondary ion yields vary widely from element to element and also because of a strong matrix effect, the best analyses result when standards with equivalent matrices are employed. This is particularly important in the analysis of APE (annealed proton-exchange) waveguides. Extensive work by Korkishko et al ([21-23] and references therein) has revealed a number of distinct crystallographic phases produced in lithium niobate as a result of the proton-exchange and anneal processes. The proton-exchange (PE) step, when carried out in a melt of concentrated acid or acid with a small amount of the corresponding lithium salt, produces a layer of protonated lithium niobate, $\text{H}_x\text{Li}_{(1-x)}\text{NbO}_3$, in an altered crystalline phase, identified as the β -phase for the benzoic acid system. This phase (which consists of several sub-phases, β_1 - β_4) is high loss, with poor electro-optic properties. Creation of low-loss waveguides with good electro-optic properties is achieved by thermal annealing and diffusing the protons deeper into the substrate. At the same time, this causes several crystalline phase transitions (from higher to lower order β -phases to κ_2 - to κ_1 -

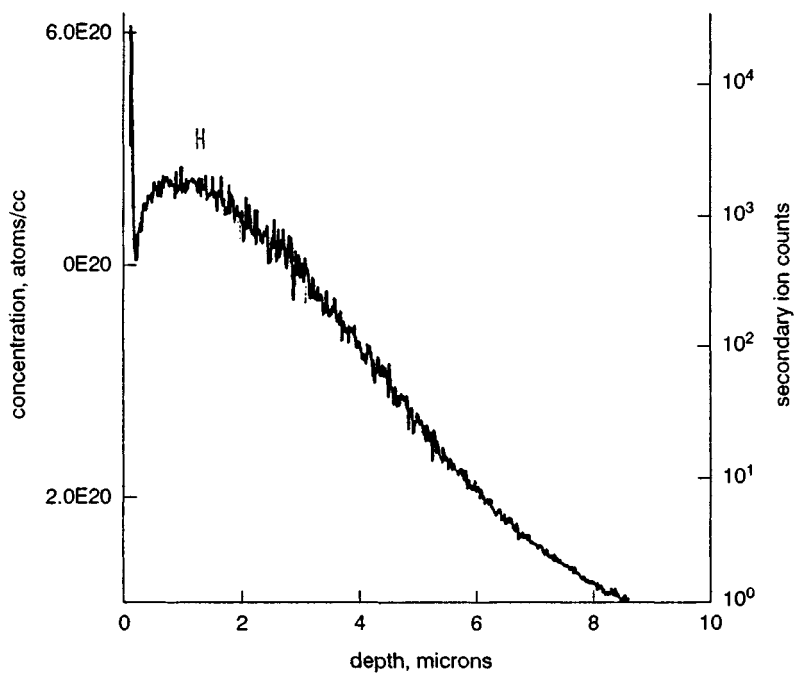


FIGURE 3 SIMS profile of APE slab waveguide on LiNbO_3 .

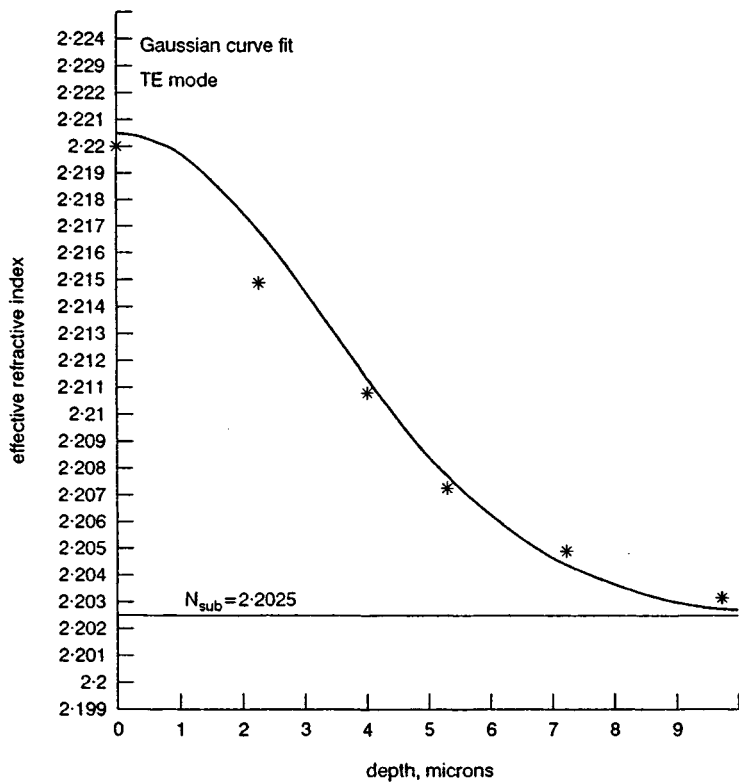


FIGURE 4 Gaussian fit to prism-coupler data for waveguide of FIGURE 3.

phases to α -phase). The SIMS matrix effect in each phase will be different. Ion implantation standards are available for most of the important elements in lithium niobate, but further quantification accuracy can be attained by combining SIMS with other analytical techniques to obtain the SIMS relative sensitivity factors (RSFs) for the particular phases of interest. For example, a step-profile waveguide layer can be produced by proton exchange where the phase is well defined [21]. The concentration of protons in this layer can be independently established by RBS (Rutherford backscattering spectroscopy). This defines the dosage of the layer. If the assumption is made that the dosage does not change through the anneal process, then RSFs can be determined for the intermediate phases. If a single phase (κ or α) endpoint is reached, then RBS can be used again to obtain the RSF for that phase.

D INFRARED SPECTROSCOPY

The OH^- stretching band is quite sensitive to the crystalline phase of the proton-exchanged waveguide as well as to impurities in the lattice. Much work has been reported in the literature on this topic, and it is well summarised in the excellent review paper 'Hydrogen in Lithium Niobate' by Cabrera et al [24]. The highly polarised (perpendicular to the c-axis) OH^- stretching band maximum is found at about 3507 cm^{-1} in waveguides proton exchanged in pure benzoic acid; this corresponds to an $\text{H}_x\text{Li}_{(1-x)}\text{NbO}_3$ structure consisting of β_1 - and β_2 -phases [21]. Two distinct peaks can be seen in FIGURE 5(a), the one at higher energy being assigned to protons in the β_2 -phase. After annealing, the peak has shifted to about 3486 cm^{-1} , this now corresponding primarily to a κ_1 -phase (FIGURE 5(c)). Intermediate peaks, corresponding to intermediate crystalline phases, are seen in FIGURE 5(b), where the waveguide has been only partially annealed. One may expect waveguides in the α -phase to exhibit an OH^- stretching band in the 3482 cm^{-1} region, near that for protons in undoped, congruent LiNbO_3 . It can thus be seen that the OH^- stretching band can be a sensitive indicator of progress in a proton-exchanged waveguide annealing process. This band was also used to determine the hydroxyl content in commercial lithium niobate wafers [25]. In this work, the authors documented a gradient in the hydroxyl content along the Z-axis of commercial X-cut LiNbO_3 wafers. Infrared spectroscopy has also been used in investigations of proton-exchanged waveguides where a layer of differing structure has been inferred from a small unpolarised absorption in the 3280 cm^{-1} region [26]. Recent work by Korkishko et al [27] relates physical and crystallographic properties of the various $\text{H}_x\text{Li}_{(1-x)}\text{NbO}_3$ phases in Z-cut lithium niobate to changes in the reflectance spectra in the 580 cm^{-1} to 900 cm^{-1} region.

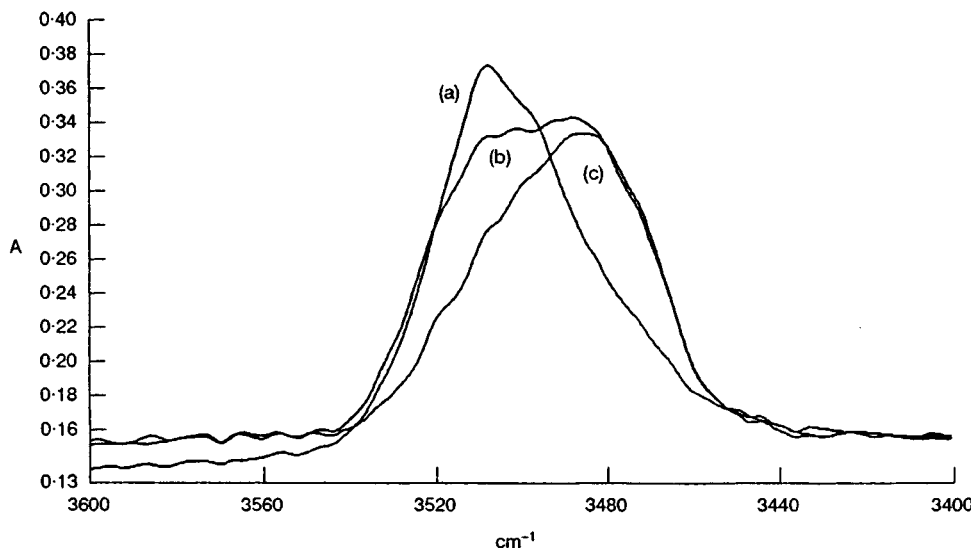


FIGURE 5 FTIR spectra of slab waveguide in LiNbO_3 (a) after proton exchange, (b) approximately midpoint in the anneal, (c) after anneal to the κ_1 phase.

E NOMARSKI MICROSCOPY

Nomarski microscopy is a differential interference contrast (DIC) imaging technique. In one form, an adjustable polariser/analyser couple in combination with a birefringent prism illuminates a surface with two orthogonally polarised beams. The prism causes the beams to be offset at the surface. Surface variations in height and refractive index result in a relative phase shift between the polarisation components of the reflected light. The reflected light recombines with the incoming beam, and the polariser is adjusted to maximise constructive interference of desired features in the image plane. This is shown in the simplified sketch of FIGURE 6. A number of papers dealing with phase contrast and DIC imaging have been incorporated in a volume of the SPIE Proceedings [28]. A review of Nomarski microscopy is included in that volume [29].

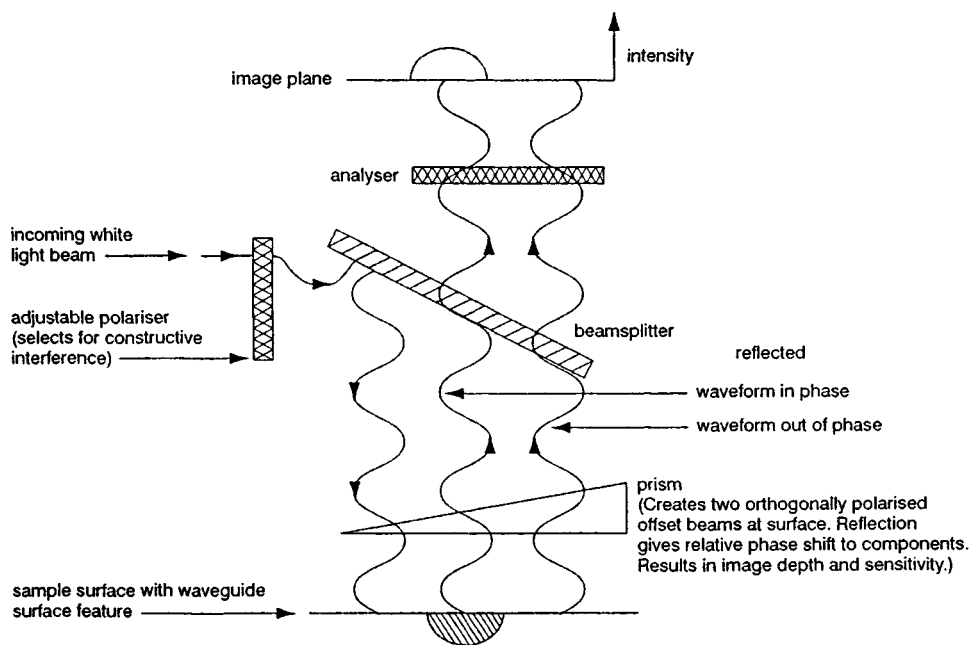


FIGURE 6 Schematic drawing of Nomarski microscopy set-up.

Nomarski microscopy has proven useful to visually image proton-exchanged and titanium indiffused waveguides on lithium niobate. The image in FIGURE 7 is the boundary of a planar waveguide formed by an extended proton-exchange process. It was obtained in an optical system similar to that shown in FIGURE 6 with a prism at the objective lens. Surface buckling caused by phase change stresses is readily imaged. Added image contrast can be gained with loss of three-dimensional information by removing the objective prism. This is shown in FIGURE 8, which is the image of a lithography-defined proton-exchanged waveguide on lithium niobate.

F ATOMIC FORCE MICROSCOPY

Atomic force microscopy (AFM) is now a mature technique for imaging surface structure on dielectric materials. AFM is similar to scanning tunnelling microscopy (STM) except that a tunnelling current is not required. Instead, the monitored deflection of a cantilevered tip is due to interatomic repulsion between atoms on the tip and those on the surface. The tip is scanned very close to the sample surface, and the cantilever's deflection increases or decreases as peaks and valleys are traversed. Surface structural changes in lithium niobate due to various processing or environmental conditions can be seen. FIGURE 9 shows a step structure formed on the surface of an X-cut wafer after heating above 1000°C. The step heights were about 2.8 Å. This height is about a half unit cell

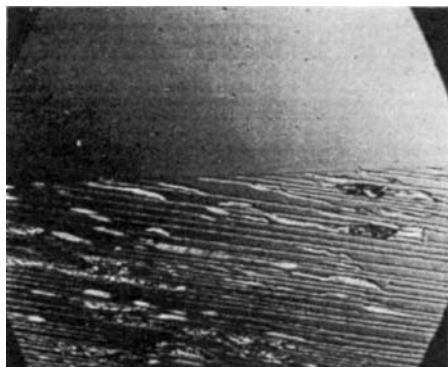


FIGURE 7 Nomarski microscope image of damaged slab waveguide boundary.

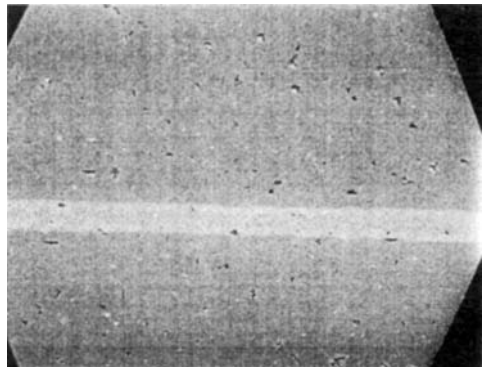


FIGURE 8 Nomarski microscope image of APE waveguide on LiNbO_3 .

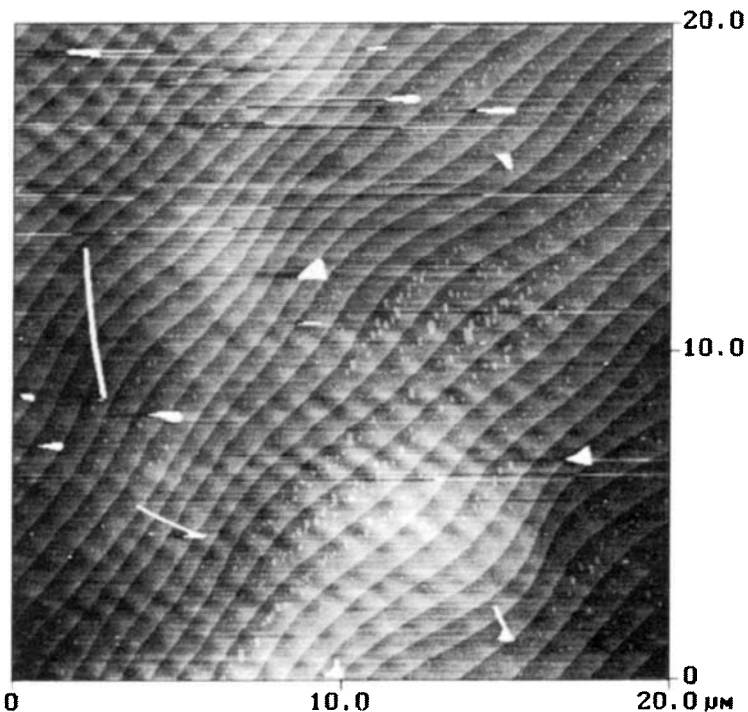


FIGURE 9 AFM image of LiNbO_3 surface after exposure to a temperature typical for Ti indiffusion. The white features are particles.

along the a (or X) axis. Similar step formation has been seen in Z-cut crystals, with the height reported to be about half the Z-axis unit cell [30].

G CONCLUSION

This Datareview summarises the most commonly used microanalytical techniques applied to waveguides made in LiNbO₃. Although the main emphasis is placed on proton-exchanged waveguides, Ti indiffused ones are also discussed.

ACKNOWLEDGEMENT

It is a pleasure to thank Metricon Corporation for allowing reprint of FIGURES 1 and 2 from their Model 2010 Operating Guide.

REFERENCES

- [1] P.K. Tien, R. Ulrich, R.J. Martin [*Appl. Phys. Lett. (USA)* vol.14 (1969) p.291]
- [2] P.K. Tien [*Appl. Opt. (USA)* vol.10 (1971) p.2395]
- [3] R. Ulrich, R. Torge [*Appl. Opt. (USA)* vol.12 (1973) p.2901]
- [4] J.M. White, P.F. Heidrich [*Appl. Opt. (USA)* vol.15 (1976) p.151]
- [5] Y.M. Dikaev, Yu.A. Kopylov, I.M. Kotelyanskii [*Kvantovaya Elektron. (USSR)* vol.8 (1981) p.378]
- [6] E.A. Kolosovskii, D.V. Petrov, A.V. Tzaryov [*Sov. J. Quantum Electron. (USA)* vol.8 (1981) p.2557]
- [7] K.S. Chiang [*IEEE J. Lightwave Technol. (USA)* vol.3 (1985) p.385]
- [8] P. Hertel, H.P. Menzler [*Appl. Phys. B (Germany)* vol.44 (1987) p.75]
- [9] R. Richter, T. Bremer, P. Hertel, E. Krätzig [*Phys. Status Solidi A (Germany)* vol.114 (1989) p.189]
- [10] R. Oven, S. Batchelor, D.G. Ashworth, D. Gelder, J.M. Bradshaw [*Electron. Lett. (UK)* vol.31 (1995) p.229]
- [11] J.F. Offersgaard, T. Veng, T. Skettrup [*Appl. Opt. (USA)* vol.35 (1996) p.2602]
- [12] F. Xiang, G.L. Yip [*J. Lightwave Technol. (USA)* vol.12 (1994) p.443]
- [13] K.S. Chiang, C.L. Wong, H.P. Chan, Y.T. Chow [*J. Lightwave Technol. (USA)* vol.14 (1996) p.827]
- [14] S.T. Vohra, A.R. Mickelson, S.E. Asher [*J. Appl. Phys. (USA)* vol.66 (1989) p.5161]
- [15] S.W. Wilson, S.W. Novak, J.M. Zavada, A. Loni, R.M. De La Rue [*J. Appl. Phys. (USA)* vol.66 (1989) p.6055]
- [16] A. Loni, R.M. De La Rue, J.M. Zavada, S.W. Wilson, S.W. Novak [*Electron. Lett. (UK)* vol.27 (1991) p.1245]
- [17] J.M. Zavada, H.C. Casey Jr., Ch.-Ho Chen, A. Loni [*Appl. Phys. Lett. (USA)* vol.62 (1993) p.2769]
- [18] J.M. Zavada, H.C. Casey Jr., R.J. States, S.W. Novak, A. Loni [*J. Appl. Phys. (USA)* vol.77 (1995) p.2697]
- [19] K.M. Kiss, P.G. Suchoski, D.K. Lewis [*IEEE J. Lightwave Technol. (USA)* vol.13 (1995) p.1521]
- [20] F. Caccavale et al [*J. Appl. Phys. (USA)* vol.78 (1995) p.5345]
- [21] Yu.N. Korkishko, V.A. Federov, V.N. Nosikov, S.M. Kostritskii, M.P. De Micheli [*Proc. SPIE (USA)* vol.2997 (1997) p.188]
- [22] Yu.N. Korkishko, V.A. Federov [*J. Appl. Phys. (USA)* vol.82 (1997) p.1010]
- [23] Yu.N. Korkishko [*IEEE J. Sel. Top. Quantum Mech. (USA)* vol.2 (1996) p.187]
- [24] J.M. Cabrera, J. Olivares, M. Carrascosa, J. Rams, R. Müller, E. Diéguez [*Adv. Phys. (UK)* vol.45 (1996) p.349]
- [25] H. Nagata [*Opt. Eng. (USA)* vol.37 (1998) p.1612]
- [26] M. Kunova, V. Krastev [*Appl. Phys. A (Germany)* vol.63 (1996) p.391]

13.5 Microanalytical techniques for waveguide examination in LiNbO₃

- [27] Yu.N. Korkishko, V.A. Federov, S.M. Kostritskii [*J. Appl. Phys. (USA)* vol.84 (1998) p.2411]
- [28] M. Pluta, M. Szyjer (Eds) [*Proc. SPIE (USA)* vol.1846 (1994)]
- [29] M. Pluta [*Proc. SPIE (USA)* vol.1846 (1994) p.10]
- [30] H. Nagata, K. Shima [*Jpn. J. Appl. Phys. (Japan)* vol.35 (1996) p.4040]

CHAPTER 14

SPECIAL EFFECTS AND HOLOGRAPHIC PROCESSES

- 14.1 Radiation effects in LiNbO₃**
- 14.2 Basics of holographic processes in LiNbO₃**
- 14.3 Dynamic properties of LiNbO₃, optical-damage-related issues and stabilisation techniques**

14.1 Radiation effects in LiNbO₃

E.W. Taylor

August 2001

A INTRODUCTION

The systematic study of radiation effects in LiNbO₃ has spanned approximately three decades and while it would be of historical interest to trace and discuss the complete evolutionary process by which the study of radiation effects occurred, this Datareview will summarise only the most important findings. The reader is referred to the reference literature for details and a greater understanding of the reported data and underlying principles governing the interaction of light, matter and radiation. In order to accomplish a succinct overview of the known radiation effects and mechanisms responsible, the induced effects are discussed in two distinct areas: radiation responses intrinsic to bulk materials and responses arising from a combination of bulk and component geometry effects. The effects of doping fabrication of components from LiNbO₃ lead to a myriad of radiation-induced effects, which include the usual bulk effects and the effects arising from the fabrication of the component structure. As examples, effects in LiNbO₃-based technologies such as thin film integrated optic devices and bulk acousto-optic modulators will be highlighted to illustrate widely differing radiation induced responses that can occur in present-day component technologies. Attention is called to the radiation sensitivity of LiNbO₃ in either its 'pure' or doped states. As the reader will learn, depending on the application, LiNbO₃ can assume the role of serving as a sensitive sensor of radiation, or as a material quite resistant to radiation.

Thus, in the sections that follow the critical characteristics and material parameters that are affected by radiation are discussed in respect to low dose and enhanced dose radiation environments. These induced effects include changes to bulk and component LiNbO₃ properties such as absorption, polarisation, coupling coefficients, propagation constants and refractive indices. The latter parameter is of paramount importance since any changes to the extraordinary and ordinary indices in LiNbO₃ optical components such as directional couplers, phase modulators and optically guided or coupled wave structures can corrupt operational functions performed by the device. In particular, the relationship between the known photorefractivity of LNO and its corresponding propensity for sensitivity to radiation will be discussed.

B EFFECTS IN BULK LiNbO₃

In the early 1970s McDowell and Lefkowitz [1] reported that LiNbO₃ irradiation by neutrons at 60°C resulted in increasing the unit cell volume while the dielectric loss factor ($\tan \delta$) remained essentially constant, suggesting that the density of free charge carriers remained unchanged. Their work suggested that the room-temperature dielectric constant increased with neutron dose up to $10^{17} \text{ n cm}^{-2}$ and did not result in the formation of absorption bands. They also advanced the assertion that irradiated LiNbO₃ was more polarisable than in the non-irradiated state. In 1970, a study by Primak et al [2] also reported on the dilatational effects induced by 1.3 MeV electron irradiation of Z- and Y-cut plates of LiNbO₃. They reported a broad optical absorption band ($<0.1 \text{ mm}^{-1}$) which occurred from the middle of the visible to the ultraviolet cut-off. Their study also reported material dilatations on the order of 10^{-5} along with small changes to the electro-acoustical properties: -7% in the electromechanical coupling coefficient and -6% in the electrical permittivity. They concluded that the induced effects were attributed to storage of charge in a piezoelectric material, which annealed partially at room temperature within weeks, or responded to rapid annealing, by heating of the samples.

14.1 Radiation effects in LiNbO_3

In a later study by Micheron [3] $\text{LiNbO}_3:\text{Fe}^{3+}$ crystals were irradiated by 3 MeV electrons causing the partial ionisation of $\text{Fe}^{3+} + \text{e}^- \rightarrow \text{Fe}^{2+}$ leading to the formation of traps and optical absorption. He reported that under the illumination of the irradiated crystals at a wavelength of $\lambda = 488$ nm, the absorption (α) decreased exponentially with time and was given by the expression

$$\alpha(t) = \alpha_0 + \alpha_1 \exp{-(t/\tau)} \quad (1)$$

where α_0 and α_1 represent the initial and time-dependent absorptions, and τ is a time constant dependent on the absorbed photon density. He concluded that holographic read-write characteristics were improved in Fe^{3+} LiNbO_3 compared to reduced $\text{LiNbO}_3:\text{Fe}$, since the crystals were more absorbent during writing and transparent during reading. This observation was confirmed and treated in a further study by Staebler and Phillips [4].

In 1977, Ohmori et al [5] presented arguments for resolving the issue of whether the optical damage in Fe-doped and undoped LiNbO_3 was attributable to the photo-excited electrons migrating to positions determined by the internal field [6-8], diffusion or via the bulk photovoltaic effect originating from the local asymmetry of the pyroelectric host as proposed by Glass et al [9]. They concluded that local changes to the extraordinary and ordinary refractive indices by X-ray irradiation ($\Delta n \sim 10^{-4}$) were not due to radiation-induced lattice disorder or the formation of defects, but rather that the changes were due to the same phenomena as in optical damage caused by intense light, with the doped material showing less sensitivity to the radiation than the undoped material. Their data led to a direct contradiction based on the process set forth by Glass et al [9] since they maintained that mechanisms other than the bulk photovoltaic effect were necessary to explain the optical damage. In contrast, Volk et al [10] challenged certain of the findings reported by Ohmori et al [5] by providing data indicating that Fe-doped LiNbO_3 showed greater sensitivity to X-ray radiation than undoped LiNbO_3 . However, Volk agreed with Ohmori et al [5] that the X-ray-induced damage could not be explained solely by the carrier transport arising from a static photovoltaic effect. These and other data presented by researchers [11,12] in the late 1970s eventually culminated in a paper by Vartanyan et al [13] that is generally accepted as the most viable explanation of certain of the radiation-induced effects in bulk LiNbO_3 . Their data convincingly showed that LiNbO_3 irradiated by gamma rays resulted in a prolonged transient current due to the optical annealing relaxation of radiation centres. The current was attributed to the radiation-induced spontaneous polarisation of the LiNbO_3 . They went on to explain that the increase in photorefractive sensitivity arising from gamma-ray irradiation was due to the increase in the Glass coefficient, which could also be interpreted or defined for a photorelaxation current.

In 1982, Rosa et al [14] reported that X-ray and gamma-ray exposures of pure and Ni-doped LiNbO_3 were observed to induce ESR, optical absorption and electrical conductivity changes observable at room and liquid nitrogen temperatures. Their studies concentrated on examining the processes by which irradiation induced a higher concentration of defect centres in Ni-doped LiNbO_3 than in the pure samples of LiNbO_3 . They were able to show that Ni impurities in LiNbO_3 resulted in increased sensitivity of the material to radiation, while reducing the effects of optical bleaching. These effects were increased at liquid-nitrogen temperatures. Shortly thereafter, Pareja et al [15] reported that LiNbO_3 single crystals irradiated by 1.5 MeV electrons near or above room temperature resulted in the growth of a broad optical absorption band at 510 nm. They concluded that the centres responsible for absorption were not attributable to positron trapping centres, but rather to oxygen vacancies bound to impurities. Many other researchers have reported radiation effects via radiolysis, displacement and electron rearrangement. The reader is directed to the references for a brief overview of these and other related findings including an excellent paper by Hodgson and Agullo-Lopez [16] that clearly identified a broad structured absorption band in LiNbO_3 irradiated by 2.0 MeV electrons. The absorption was believed to be due to oxygen ion vacancies within the lattice and the formation of Nb^{+4} clusters causing rearrangement of the crystal lattice.

C EFFECTS IN DOPED LiNbO₃

LiNbO₃ has long been used in a variety of applications, and showed great promise for application to non-linear guided-wave devices. Well-known processes for the alteration of the material refractive indices, its large electro-optic coefficients, ease of poling, stability, and low voltage requirements indeed make LiNbO₃ components such as modulators, directional couplers, phase modulators, filters and other guided-wave structures viable and commercially available from a wide variety of sources. However, certain LiNbO₃ materials can display photorefractivity, which can seriously limit the performance in many optical device applications. Photorefractivity arising from ferrous LiNbO₃ has been a concern and the basis of much study. Many applications require that the photorefractive response be suppressed. As early as 1980, it was reported that LiNbO₃ doped with moderate amounts of MgO (~5%) resulted in a significant reduction of photorefractive response. A later study reported a factor of two improvement in optical damage threshold (~70 kW/cm², at 0.5145 nm) in a proton-exchanged (PE) LiNbO₃ waveguide compared to an undoped LiNbO₃ waveguide. As will be shown in the sections that follow, the presence of transition ion impurities in LiNbO₃ can lead to strong radiation-induced photorefractive-like effects. Fortunately, there is ample evidence that these effects can be greatly suppressed by doping (e.g. with MgO) or by employing other manufacturing processes such as proton exchange (PE) during the growth and formation of waveguide structures. As will be shown, the radiation response of a sample of LiNbO₃ can be related to or depend on its degree of photorefractivity, the energy and type of radiation, irradiation dose, operational optical power, applied electric fields, polarisation sensitivity, temperature and the time domain of interest.

D RADIATION-INDUCED EFFECTS IN LiNbO₃ SLAB AND SINGLE CHANNEL WAVEGUIDES

The development of LNO slab and single-channel waveguides moved the focus of radiation studies from strictly bulk effects to new effects arising from the geometry of the structure. Radiation-induced absorption can be important where propagation of light within the waveguide for more than a few millimetres is required. For waveguides that are formed near the surface, interaction with low-energy ionising radiation can change the refractive index quite easily, and affect the confinement of light within the waveguide. As will be shown in the next section, coupled waveguides can experience radiation-induced crosstalk. The first to quantify and model X-ray-induced absorption in a titanium in-diffused single channel waveguide was Taylor [17] and the data are shown in FIGURE 1. The device was composed of a Z-cut, X propagating single mode channel waveguide operating at $\lambda = 1300$ nm.

The data in FIGURE 1 resulted from a dose of 3 krad (Si) deposited by a 20 ns (FWHM) X-ray pulse at a dose rate of 1.5×10^{11} rad (Si) s⁻¹. The X-ray pulse was composed of energies ranging to 1.8 MeV and peaked at 238 keV. The waveguide was operated at a wavelength of $\lambda = 1300$ nm and the measurements were performed over a temperature range of T = 23 - 25°C. The peak transient-induced attenuation in the guided wave region was observed to range from 0.07 to 0.14 dB cm⁻¹ and recovery from the ionisation event was observed to be ~ 66% of the pre-irradiation intensity when measured at 500 μs following cessation of the irradiation pulse (shown in FIGURE 1). The response behaviour was repeated for some twenty exposures, with total recovery observed in ~592 ms. Recovery was observed to be independent of dose up to 60 krad (Si) for the dose rate and limited temperature range investigated. The data were fitted to a kinetic model for geminate-ion recombination shown by the dashed line in FIGURE 1. The model was based on the diffusion process leading to ion neutralisation via relaxation processes for glasses [18] and is given by the expression

$$G(t) = G_0(1/\pi\lambda t)^{1/2} \quad (2)$$

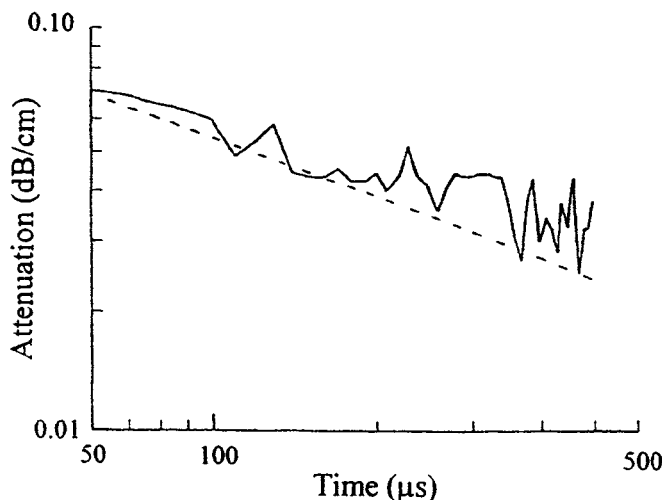


FIGURE 1 Comparison of geminate recombination model (dashed line) with experimental data.

where $G(t)$ represents the number of ion pairs existing at time t , λ represents a constant or a measure of the recombination rate, and G_0 is the initial number of geminate-ion pairs. In the geminate-ion recombination process, $G(t)$ is dependent on temperature and independent of dose. The data shown in FIGURE 1 indicate that the geminate-ion recombination kinetics apply for the irradiated doped LiNbO_3 waveguide within the recovery times, temperature range and doses examined. However, temperature-independent recovery via tunnelling is also possible as advanced by Mattern [19], where, following the irradiation, free electrons are trapped and recombine in proportion to the concentration and distribution of the available acceptor ions. Interestingly, Mattern et al [19] reported a similar $1/t^{1/2}$ dependence in doped optical fibres and a $1/t^{1/4}$ dependence for pure fused silica optical fibres. Trapped electrons (or trapped hole centres) formed by radiation processes can be bleached by heating the irradiated material, exposing the material to light of sufficient intensity (energy) at the appropriate wavelength. In this scenario, a free electron combines with a trapped hole and similarly a free hole can combine with a trapped electron and experience annihilation.

Attempts to compare radiation effects in pure (impurity level less than a few ppm) and in doped (MgO:LiNbO_3) material operating at $\lambda = 1061 \text{ nm}$ irradiated by a mixture of fission gamma rays (1 - 3 MeV) and neutrons from a nuclear reactor were reported in 1994 by Brannon [20]. For a gamma-ray dose of 7.5 krad (neutron contribution was assumed to be negligible) he reported peak absorption coefficients of 0.032 and 0.240 cm^{-1} for MgO -doped and undoped lithium niobate, respectively. These data compared favourably with the average peak absorption coefficient of $0.105 \pm 0.035 \text{ dB cm}^{-1}$ first reported by Taylor for the Ti-doped channel waveguide data shown in FIGURE 1. Considering that the measurements of these two studies were performed at different wavelengths, in bulk samples and integrated structures, and that the radiation energies and species used by the experimenters were different, the convergence of the response data is reasonable. Brannon also reported the observation of a non-exponential time constant in the undoped samples, but used a non-linear fit to the data using the sum of three exponentials, which yielded three time constants for the undoped sample ranging from 0.183 to 37.5 ms, indicating the presence of absorption centres with different time-relaxation dependence. The recovery time behaviour was observed to follow a $1/t^{1/4}$ dependence in the undoped sample, while no recovery time dependence could be ascertained from the data reported from the MgO -doped sample. Clearly, the extent of radiation-induced optical damage and the differences in absorption relaxation times reported for doped and undoped LiNbO_3 are strongly dependent on the dopants, defects present, radiation type and energy, wavelength of operation, and, as will be shown in the next paragraphs, the additional factors of polarisation and optical intensity.

D1 Radiation-Induced Effects in Integrated Optic Coupled Waveguides

In 1988, the first observed radiation-induced non-linear and non-equivalent absorption in $\text{LiNbO}_3:\text{Ti}$ directional coupler waveguides was reported by Taylor and co-workers [21-26]. The introduction of transient radiation-induced carriers and the formation of colour centres within and near the guiding regions was believed to have reduced the coupler effective refractive indices through the creation of a transient space charge. This resulted in increased scattering, reduction of effective guiding and alteration of the directional coupling efficiency. The induced space-charge effects were believed to be similar to or identical with those caused by strictly photorefractive processes. Irradiation of the coupled waveguides by electrons changed the waveguide refractive indices, propagation constants, coupling coefficients and phase synchronisation. Shown in FIGURE 2 is an example of these responses.

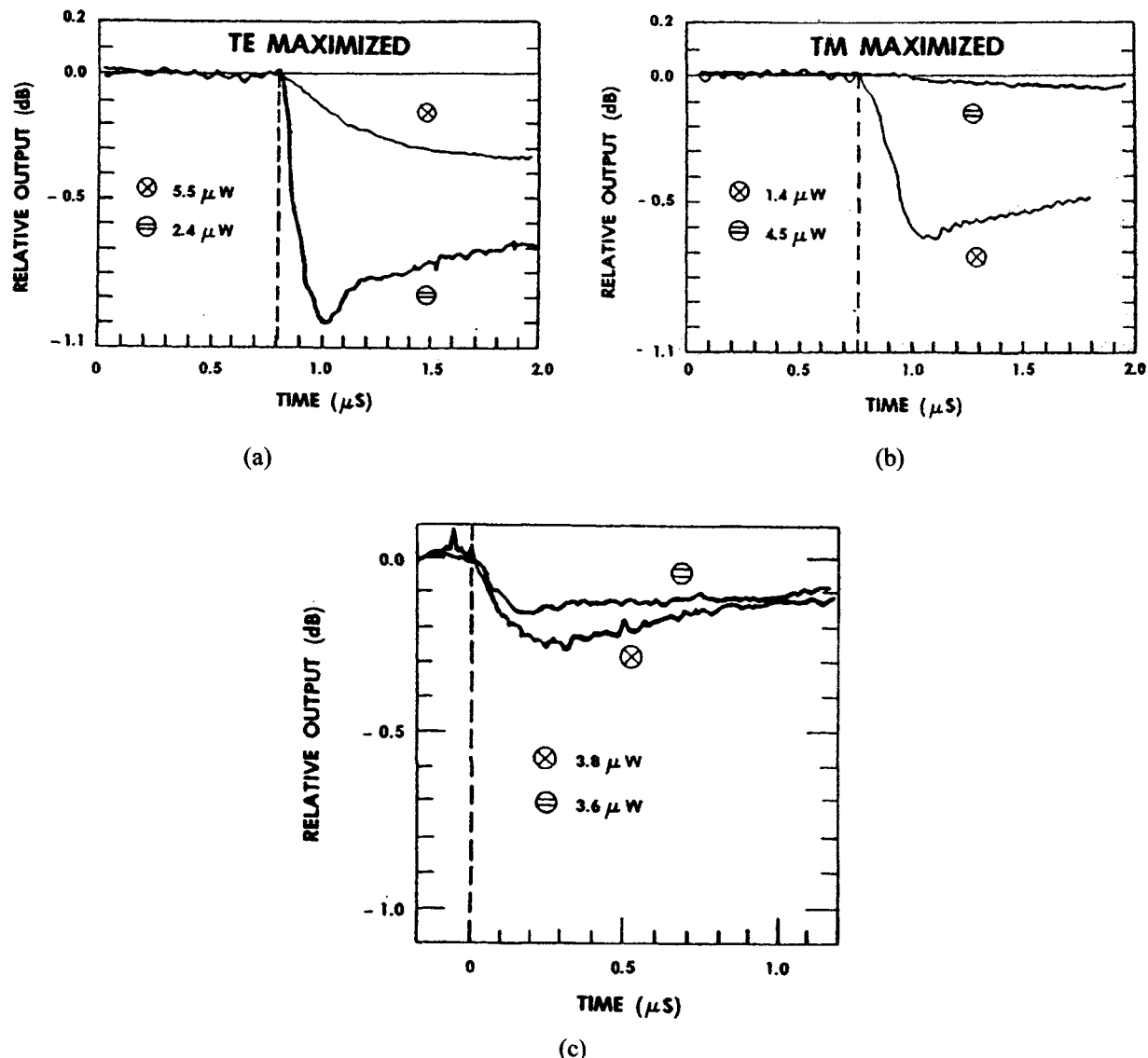


FIGURE 2 Ionisation-induced non-equivalent and non-linear absorption and crosstalk in $\text{LiNbO}_3:\text{Ti}$ channel waveguides [22].

In FIGURES 2(a) - 2(c), the different responses exhibited under TE and TM maximised signal conditions are readily apparent. In FIGURE 2(a), the propagation of TE polarised light ($\lambda = 1300 \text{ nm}$) was maximised in the coupler, prior to irradiation by 16 MeV electrons, which resulted in a total

detected power output from the coupler waveguides of $7.9 \mu\text{W}$. Of this amount, $5.5 \mu\text{W}$ was detected in the crossover waveguide, while $2.4 \mu\text{W}$ exited the throughput waveguide. Next, a TM polarisation was maximised and the power level distribution changed as shown in FIGURE 2(b). Finally, in FIGURE 2(c), nearly equal polarisation and optical power levels were achieved in the coupled waveguides prior to electron irradiation. The vertical dotted lines in FIGURES 2(a) - 2(c) represent the electron pulse width ($\sim 12 - 17 \text{ ns FWHM}$), which resulted in a total integrated dose of 15 krad (Si) over the $2 \text{ mm} \times 4 \text{ mm}$ elliptical exposure area of the coupled waveguide region.

As shown in FIGURE 2(a), following the electron pulse, two distinct responses are noted: that of non-equivalent attenuation of the optical signal among the crossover and throughput waveguides, and the initiation of an earlier relaxation (recovery) of the signal propagating in the throughput waveguide. A third response that was noted for the first time, and will be more fully discussed in the section that follows, was the onset of radiation induced crosstalk between the coupled waveguides. In FIGURE 2(a) this is suggested by the onset of apparent recovery of signal in the throughput waveguide for $t > 1.0 \mu\text{s}$, while the crossover waveguide appears to continue to undergo signal loss for $t > 2.0 \mu\text{s}$. In FIGURE 2(b), these processes and observations are reversed when the optical power signal is TM polarised, and the larger optical power is contained in the throughput waveguide. In FIGURE 2(c), the TE and TM light power levels prior to irradiation were set approximately equal. Irradiation of the device under this set of conditions resulted in the observation of nearly equivalent induced absorption. The relaxation times from the induced absorption are observed to differ since the throughput optical power recovery is plateaued while the recovery of the crossover channel continues at a linear rate. In actuality, this behaviour suggests the occurrence of increased crosstalk via weak photorefractive-like processes.

The optical power densities in the coupled waveguides shown for the data in FIGURE 2 ranged from 24 to 32 W cm^{-2} for the $7 \mu\text{m} \times 4.0 \mu\text{m}$ channel waveguides. In a baseline study performed on the directional coupler prior to the irradiations, no photorefractive damage was observed at a power density level of 32 W cm^{-2} and $\lambda = 1300 \text{ nm}$ over an $\sim 3 \text{ h}$ period on several occasions. This was consistent with the observations of Harvey et al [29] reporting little or no photorefractive damage for investigations conducted to 50 kW cm^{-2} at $\lambda = 1300 \text{ nm}$. However, the data in FIGURE 2 clearly show both linear and non-linear responses long after cessation of the electron pulse. This suggests that refractive-index changes are occurring that are dependent on the instantaneous light power and polarisation states in the guided regions. The introduction of radiation-induced transient carriers into the guiding and coupling regions as well as ionisation of the waveguide/substrate interface locales, caused the formation of relatively long-lived colour centres. Since the optical intensities and wavelength of light used in the acquisition of data in FIGURES 2(a) - 2(c) fell out of the energy density-wavelength criteria for known photoexcitation of Fe^+ donors present in the channel waveguides, it is reasonable to attribute the responses to the introduction and generation of transient carriers. These carriers resulted in the formation of colour centres, and space-charge regions that agree with trapping schemes reported by Micheron [3]. Kurz and Von der Linde [30] have reported multi-photon absorption induced in Fe-doped and undoped LiNbO_3 using 25 ps optical pulses at 10^8 W cm^{-2} at $\lambda = 532 \text{ nm}$, resulting in the formation of absorbing defects and short-lived non-linear absorption effects (approximately the time of the pulse duration).

The above data strongly support the hypothesis that radiation-induced colour centres can sensitise non-centrosymmetric materials such as LiNbO_3 into photorefractive states without the application of an electric field. Therefore, depending on the defect population in the LiNbO_3 prior to irradiation, the concentration of transition ion impurities, the wavelength, polarisation and intensity of the optical signal, energy and particle type of the irradiation source and the temperature, the extent of radiation-caused photorefractive-like behaviour will vary.

Under the proper conditions, guided-wave structures can efficiently support the propagation of light with minimal absorption or distortion of the form and function of the optical signal. Manipulation of light signals between coupled waveguide regions allows useful functions such as precisely controlled

14.1 Radiation effects in LiNbO_3

energy exchanges, modulation, beam steering, mode filtering and other index-dependent operations. In his treatment of mode coupling theory, Marcuse [31] addressed the nature and extent of energy changes (crosstalk) between two parallel dielectric waveguides. His work showed that the underlying principle for efficiently guiding optical energy within bounded media was a function of the varying refractive indices composing the media and the transparency of the media at the optical wavelength of interest. This is best illustrated by considering the coupled waveguide (directional coupler) structure shown in FIGURE 3.

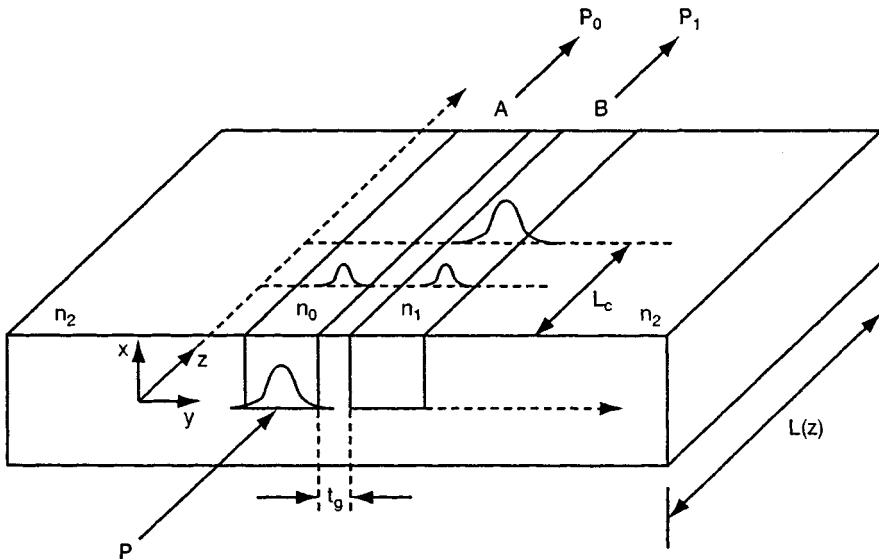


FIGURE 3 Energy exchanges between waveguides A and B in an unswitched ($V = 0$) $\text{LiNbO}_3:\text{Ti}$ directional coupler. Separation of the channel waveguides is given by $t_g = 6 \mu\text{m}$, $L(z) = 20 \text{ mm}$, and the critical coupling length (first energy crossover) is $L_c = 10 \text{ mm}$. The refractive indices of this device for synchronous TM propagation are $n_0 = n_1 > n_2$.

In FIGURE 3, the titanium in-diffused LNO channel waveguides exhibit energy exchanges given by [32]

$$P_0(z) = \{\cos^2(gz) + [(\Delta\beta/2)^2/g^2] \sin^2(gz)\} e^{-\alpha z} \quad (3)$$

$$P_1(z) = [(k^2/g^2) \sin^2(gz)] e^{-\alpha z} \quad (4)$$

where

$$g^2 = k^2 + (\Delta\beta/2)^2 \quad (5)$$

In FIGURE 3, the energies in the guided regions are defined as $P_0 = 1$ (energy exiting channel waveguide A) for $P_1 = 0$ (energy exiting channel waveguide B). The coupling coefficient (k) determines the strength of the coupling, while for synchronous coupling the propagation constants β_0 and β_1 are equivalent resulting in $\Delta\beta = |\beta_0 - \beta_1| = 0$. Under synchronous coupling, and no material transmission loss ($\alpha = 0$), all the energy in waveguide A is transferred to waveguide B in the length $L_c = \pi/2k = m\pi/k$, where $m = 0, 1, 2, \dots$. However, exposure of the coupled waveguide regions to sufficiently high levels of ionising radiation results in the alteration of the waveguide properties that degrade the phase synchronisation of the optical fields and change the critical coupling length, as may be observed in FIGURE 4.

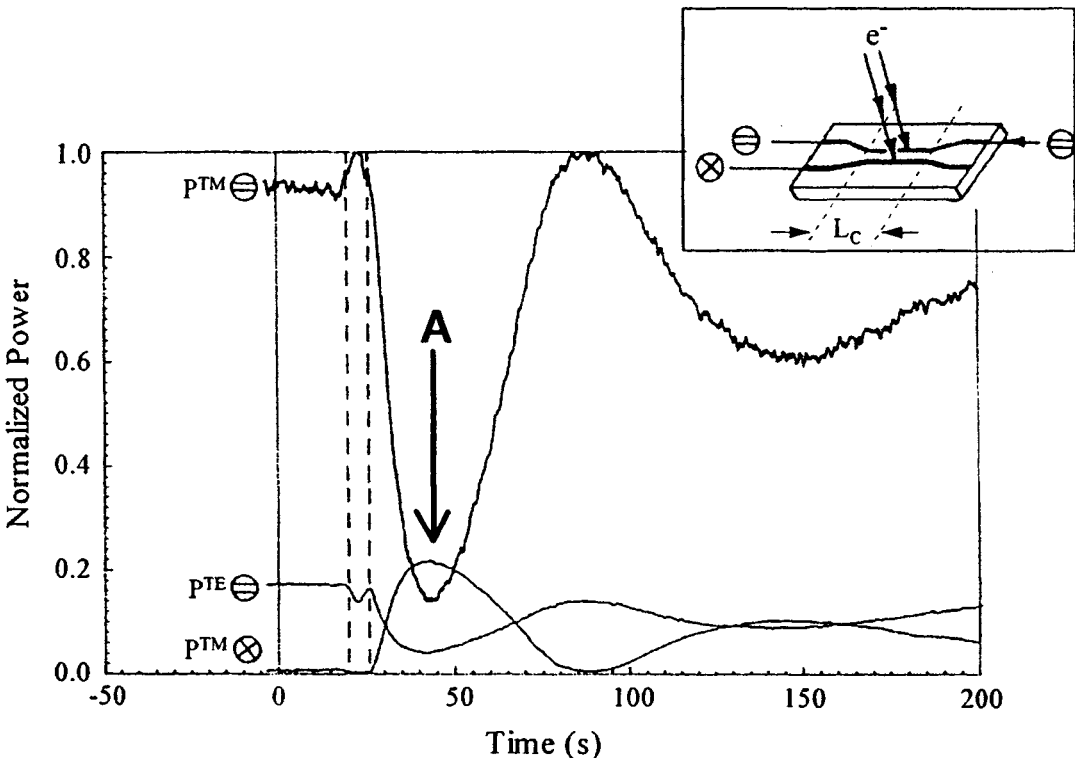


FIGURE 4 Electron (e^-)-induced non-synchronous coupling in a LiNbO_3 directional coupler [26,35]. Irradiation of the coupling region occurred over the time interval shown by the dashed vertical lines. The unwanted transfer (crosstalk) of transverse magnetic (TM) and transverse electric (TE) power (P) from the pre-irradiated switched throughput (Θ) and cross (\otimes) states is observed during and after the coupler irradiation by 15 MeV electrons (time interval between dashed vertical lines) for a dose of 75 krad(Si). Changes to the device coupling length (L_c) optical intensity, refractive index, coupling coefficients and propagation constants were transiently affected by the irradiation.

FIGURE 4 illustrates the conclusive data first reported by Taylor and co-workers [21-26] demonstrating the long term ($t > 200$ s) radiation-induced crosstalk of a coupled-wave LiNbO_3 ferroelectric device irradiated by pulsed electrons. As may be observed in FIGURE 4, a relatively low level electron irradiation (dose ~ 75 krad(Si)) of a Z-cut, Y propagating LiNbO_3 optical directional coupler optimised for TM signal propagation was observed to undergo asynchronous, oscillatory energy exchanges, deviating from its stable (switched, $V = 0$ V) pre-irradiated TE-TM baseline signals. Electron-induced crosstalk between the coupled waveguides is observed during and long after the cessation of irradiation. An enhancement to the throughput baseline TM power level was observed during the irradiation period and persisted during the first maxima following cessation of the irradiation. In contrast, the light power level in the throughput TE signal was diminished by an approximate or lesser amount, indicating mode conversion from $\text{TE} \rightarrow \text{TM}$. This effect arises since the electrons induce changes to the local refractive indices in the device guiding and gap regions. The magnitude of the index change resulting in the asynchronous energy exchanges (crosstalk) for the device response shown in FIGURE 4 may be calculated [26] from the expression

$$\Delta n = -(n_1)^3 r_{ij} E / 2 \quad (6)$$

where n_1 is the guide principal refractive index ($n_1 = 2.28$), $r_{ij} = r_{33} = 30 \times 10^{-12}$ m/V and E is the electric field between the coupled regions. The data shown in FIGURE 4 were obtained from a directional coupler device with an interaction length $L = 20$ mm, critical coupling length of

14.1 Radiation effects in LiNbO_3

$L_c = 10 \text{ mm}$, $\alpha = 0.1 \text{ dB mm}^{-1}$, $k = 0.155 \text{ mm}^{-1}$ and $t_g = 6 \mu\text{m}$. The device was measured to efficiently switch TM polarised light at an applied voltage of $V = 6 \text{ V DC}$. Using EQN (6), the change in index required to switch the optical energy from guide A to guide B in FIGURE 3 may be calculated as $\Delta n = -1.778 \times 10^{-4}$ (pre-irradiated state).

FIGURE 4 confirms that TM energy coupled energies from the throughput and crossover guides in an oscillatory and asynchronous manner during, and for a long period after cessation of, the irradiation. The efficient, orderly exchange of energy was disrupted due to the formation of space-charge regions induced by the free electrons that lead to refractive-index changes in the waveguides and the gap region between the channel waveguides. An estimate of the decrease in coupler efficiency and crosstalk is possible by examining an isolated instant in time for the coupler response shown in FIGURE 4. The coupling efficiency (η^{TM}) for the TM power component is given by

$$\eta^{\text{TM}} = P^{\text{TM}\otimes}/(P^{\text{TMO}} + P^{\text{TM}\otimes}) \quad (7)$$

and the energy coupled into the crossover channel waveguide over the length $z = L$ is given by EQN (3). By combining EQNS (3) and (5), we can obtain the α -independent expression of the coupling efficiency given by

$$\eta^{\text{TM}} = [(k^2/g^2) \sin^2 gL] \quad (8)$$

The radiation-induced index change or change in phase may be calculated at point A ($t = 15.7 \text{ s}$ following cessation of the irradiation) in FIGURE 4 by using EQNS (2) - (4) and the relationship

$$\Delta\beta = 2\pi \Delta n/\lambda_0 \quad (9)$$

where λ_0 is the optical wavelength in free space. The calculation results in a value of $\Delta n = -0.509 \times 10^{-4}$, approximately 28.6% of the required index change for complete switching of the optical power in waveguide A to waveguide B. The incomplete exchange of energy is evident in FIGURE 4 at point A.

As shown in FIGURE 4, the oscillatory and damping behaviour of the TM and TE throughput and crossover powers (crosstalk) was recorded for $\sim 200 \text{ s}$. With time limitations imposed by the experimental data-acquisition system the effect was observed to repeatably persist for 6 - 7 min. Garmire [32] has shown that during the photorefractive-induced process, a fraction of the total energy in a two-channel directional coupler oscillates between the throughput and crossover channels, and is never totally transferred to the crossover channel when $\Delta\beta \neq 0$. However, the energy can return to the throughput channel when $gL = \pi$. Examination of the data in FIGURE 4 also shows that the effective or critical coupling length of the device is decreased due to the irradiation ($L_c \sim 8.0 \text{ mm}$ at point A) [26].

The above data exemplify the myriad of radiation-induced effects possible on a LiNbO_3 directional coupler. The coupler was believed to contain transition ion impurities of the order of several ppm. It was advanced that certain of the observed effects resulted from the ionisation of Fe^{+2} and Fe^{+3} ion impurities in the device guiding regions which give rise to excess space-charge photorefractive-like driven processes, which in turn alter the refractive index. Similar results have recently been reported confirming the data [33]. As observed and predicted by Taylor [22], the magnitude of the radiation-induced effects is diminished with the application of the proper electric field. This has recently been confirmed by similar data presented by d'Hose et al [34] for Mach-Zehnder modulators irradiated by 17 MeV electron pulses.

In 1995, Taylor et al [35] reported the results of an electron irradiation study comparing the induced responses between the titanium in-diffused coupler shown in FIGURE 4 and that of a proton-exchanged directional coupler. The proton-exchanged coupler was observed to be less crosstalk sensitive to pulsed electron irradiation even when exposed to a higher dose (D_e) delivered in a shorter time period ($D_e = 94 \text{ krad(Si)}$, $t = 0.62 \text{ s}$). (Note: the transition ion content in the proton-exchanged coupler was specified to be <2 ppm compared to >>2 ppm for the coupler shown in FIGURE 4.) The power exchanges and oscillatory behaviour in the proton-exchanged coupler were greatly diminished compared to the responses observed in the Ti in-diffused coupler of FIGURE 4. However, the electron-induced absorption of the TE and TM modes in the throughput and crossover waveguides of the proton-exchanged device was very apparent for time scales of $t < 0.67 \text{ s}$. Relaxation of the induced absorption was measured to be 8 - 10 ms for TM-polarised signals, and 90 ms to 7.0 min for TE-polarised signals. The temperature increase experienced by the coupler as a result of the electron irradiation ($\Delta T = 0.7^\circ\text{C}$) was believed to contribute significantly in sustaining the long term crosstalk.

D2 Radiation Effects in Acousto-Optic Devices

Recent applications of acousto-optic (AO) Bragg cells have necessitated studies of radiation-induced effects in AO modulators and deflectors [35-41]. While ionisation-induced changes to the refractive index occur, these effects, in most instances, are secondary to thermo-optic effects induced by electron heating of the LiNbO_3 crystal. Shown in FIGURE 5 is a representation of an AO Bragg cell modulator and the orientation of the device with respect to radiation exposures (x-direction). Applying a modulated voltage signal to the device transducer results in the generation of a strain in the AO crystal portion of the device, which alters the crystal's refractive index in accordance with the modulating waveform. If the acoustically induced strain is periodic (e.g. sinusoidal), an index grating is formed which serves to diffract a portion of the incident optical beam (I_0).

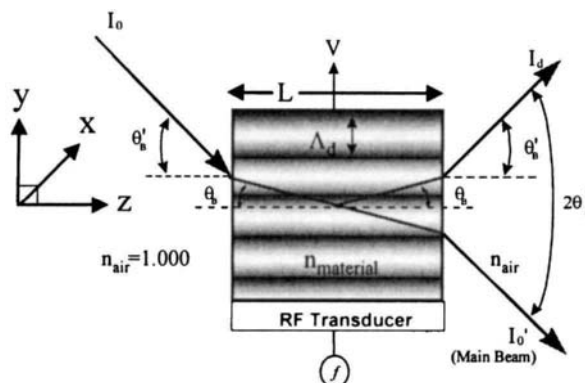


FIGURE 5 Acousto-optic Bragg modulator diffraction of a single side order (I_d) occurs when the light input (I_0) is incident within the AO crystal at the Bragg angle (θ_B) and interacts with an acoustic grating of frequency f and spacing A_d , length L , and where V represents the magnitude and direction of the sound velocity in the crystal.

The magnitude of the diffracted beam (I_d) intensity relative to I_0' is a measure of the modulator's diffraction efficiency (η) and is given as

$$\eta = I_d / (I_d + I_0') \quad (10)$$

where I_0' represents the intensity of the incident optical beam as it exits the crystal as depicted in FIGURE 5. In FIGURE 5, maximum diffraction efficiency with only one diffracted side order is realised for Bragg angle diffraction and is represented by the expression

14.1 Radiation effects in LiNbO₃

$$\theta_B = \sin^{-1}(\lambda_0/2\Lambda_d n) \quad (11)$$

Here, θ_B represents the Bragg angle expressed in terms of the free-space optical signal wavelength (λ_0), the acoustic grating spacing (Λ_d), and the crystal refractive index (n). Irradiation of AO devices can induce changes in the device acoustic velocity, absorption band and refractive index or phase-grating amplitude (Δn). As a result, changes to the AO device bandwidth response and transmission efficiency, displacement of the spatial intensities, changes to the degree and states of polarisation, alteration of the deflection angle and changes to the diffraction efficiency have been reported [34-40]. For example, reduction in the diffraction efficiency as a function of irradiation dose can be related to the diffraction efficiency of EQN (10) by the expression

$$\Delta n = (\lambda_0/\pi L) \sin^{-1}(n^{1/2}) \quad (12)$$

A change in diffraction efficiency can be directly attributed to perturbations of the crystal refractive index-phase grating strength (Δn). Not all radiation species affect the AO modulator equivalently. For example, gamma-ray irradiations to 1 Mrad (Si) were not observed to affect the diffraction efficiency or absorption spectra of a LiNbO₃ AO modulator operating over a bandwidth of 360 MHz [38]. However, the same device exposed to a neutron fluence of 1×10^{15} n cm⁻² resulted in permanent changes to the diffraction efficiency (-10.77%) and to the absorption (0.09 dB) at $\lambda = 6328$ nm. Thus, the effects of ionisation and displacement must be considered on an individual basis to predict induced phenomena.

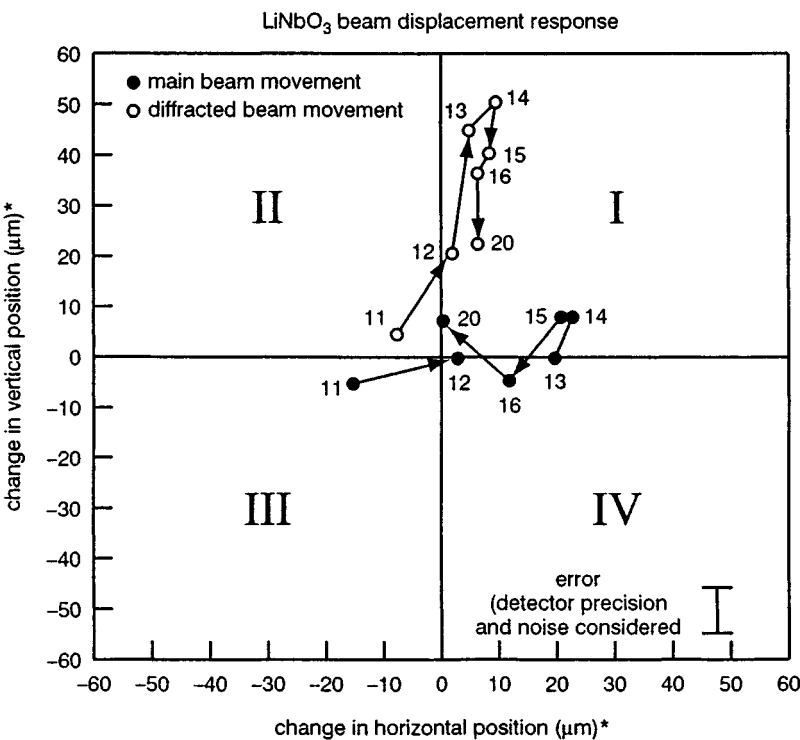
The data shown in TABLE 1 and plotted in FIGURE 6 depict the thermo-optic effects induced by radiation heating of a LiNbO₃ crystal. The peak induced heating (ΔT) resulting from the electron-pulse irradiation resulted in temperature gradients that varied the spatial intensities of the main (I_0') and diffracted (I_d) light beams. Values for ΔT were measured at the back and front faces of the crystal away from the electron-irradiated regions.

TABLE 1 AO spatial intensity displacement data.

Exposure	Pulses	Dose (rad [Si])	ΔT_1 (°C)	ΔT_2 (°C)
11	100	46600	0	1.073
12	200	124500	0	2.334
13	500	298100	4.269	5.261
14	750	464000	5.583	7.076
15	600	362000	4.835	6.615
16	400	244000	3.628	4.544
20	300	167000	2.430	3.440

In FIGURE 6 the electron-radiation-induced heating effects observed in a LiNbO₃ AO modulator-deflector were first explained by Taylor et al [35] to depend on ionisation-induced transient changes to the refractive index, and to a greater degree on the longer-term temperature gradients arising from radiation-induced thermo-optic effects. The latter effect is due to the temperature dependence of the crystal static birefringence, altered by the temperature gradients arising from the radiation-induced heating changes to the sonic velocity of the LiNbO₃ crystal.

Heating is evidenced in FIGURE 6 by the displacements of the main and diffracted beam intensities for increasing and decreasing levels of electron irradiation. The reader is referred to additional literature regarding the reported effects of radiation-induced changes to the deflection angle and polarisation states in AO devices [38-41].



*Position normalised to 1 AOD-detector baseline
Normalisation factor = 0.6765

FIGURE 6 Electron-induced thermo-optic effects in a LiNbO_3 AO Bragg deflector.

E CONCLUSION

This Datareview summarised the effects of both low and high radiation doses on the properties and critical device characteristics of LiNbO_3 . Both bulk undoped and doped materials are discussed. Applications covered include waveguides and acousto-optic devices.

REFERENCES

- [1] M.B. McDowell, I. Lefkowitz [*J. Phys. Soc. Jpn. (Japan)* vol.28 suppl. (1970) p.442-4]
- [2] W. Primak, T.T. Anderson, S.L. Halverson [*Nucl. Technol. (USA)* vol.10 (1971) p.76-84]
- [3] F. Micheron [*Ferroelectrics (UK)* vol.21 (1978) p.627-9]
- [4] D.L. Staebler, W. Phillips [*Appl. Phys. Lett. (USA)* vol.24 no.6 (1974) p.268-70]
- [5] Y. Ohmori, M. Yanaguchi, K. Yoshino, Y. Inuishi [*Jpn. J. Appl. Phys. (Japan)* vol.16 no.1 (1977) p.181-2]
- [6] F.S. Chen [*J. Appl. Phys. (USA)* vol.40 (1969) p.3389]
- [7] Y. Ohmori, Y. Yasojima, Y. Inuishi [*J. Appl. Phys. (USA)* vol.25 (1974) p.716]
- [8] Y. Ohmori, Y. Yasojima, Y. Inuishi [*Jpn. J. Appl. Phys. (Japan)* vol.14 (1975) p.1291]
- [9] A.M. Glass, D. von der Linde, T.J. Negran [*Appl. Phys. Lett. (USA)* vol.25 (1974) p.233]
- [10] T.R. Volk, S.A. Shramchenko, L.A. Shulalov [*Ferroelectr. Lett. Sect. (UK)* vol.2 (1984) p.55-8]
- [11] R.Y. Azimzade, A.K. Zeinally, L.S. Kogan, A.L. Timofeev [*Sov. Phys.-Tech. Phys. (USA)* vol.24 no.9 (1979) p.1143]

14.1 Radiation effects in LiNbO_3

- [12] K.K. Shvarts, P.A. Agustov, A.O. Ozols, A.K. Popelis [*Ferroelectrics (UK)* vol.22 (1978) p.655-7]
- [13] E.S. Vartanyan, R.K. Ovsepyan, A.R. Pogosyan, A.L. Timofeev [*Sov. Phys.-Solid State (USA)* vol.26 no.8 (1984) p.1464-7]
- [14] J. Rosa, L. Polak, J. Kubatova [*Phys. Status Solidi B (Germany)* vol.111 (1982) p.K85]
- [15] R. Pareja, R. Gonzalez, M.A. Pedrosa [*Phys. Status Solidi A (Germany)* vol.84 (1984) p.179-83]
- [16] E.R. Hodgson, F. Agullo-Lopez [*Solid State Commun. (USA)* vol.64 no.6 (1987) p.965-8]
- [17] E.W. Taylor [*J. Opt. Commun. (Germany)* vol.9 no.2 (1988) p.64-6]
- [18] S.J. Rzad, P.P. Infelta, J.M. Warman, R.H. Schuler [*J. Chem. Phys. (USA)* vol.52 no.8 (1970) p.3971-83]
- [19] P. Mattern, L. Watkins, C. Skoog, E. Barsis [*IEEE Trans. Nucl. Sci. (USA)* vol.NS-22 (1965) p.2468]
- [20] P.J. Brannon [*IEEE Trans. Nucl. Sci. (USA)* vol.41 no.3 (1994) p.642-7]
- [21] E.W. Taylor [*Proc. SPIE (USA)* vol.1314 (1990) p.155-67]
- [22] E.W. Taylor [*J. Lightwave Technol. (USA)* vol.9 no.3 (1991) p.335-40]
- [23] E.W. Taylor [*Proc. European Space Agency/IEEE Radiat. Eff. Compon. Devices (USA)* vol.15 (1991)]
- [24] E.W. Taylor, R.J. Padden, A.D. Sanchez, S.P. Chapman, J. Berry, S.A. DeWalt [*Proc. SPIE (USA)* vol.1474 (1991) p.126-31]
- [25] R.J. Padden et al [*Proc. SPIE (USA)* vol.1474 (1991)]
- [26] E.W. Taylor [*Proc. SPIE (USA)* vol.1794 (1992) p.54-61]
- [27] R.V. Schmidt, P.S. Cross, A.M. Glass [*J. Appl. Phys. (USA)* vol.51 no.1 (1980) p.90-3]
- [28] C.T. Mueller, E. Garmire [*Appl. Opt. (USA)* vol.23 no.23 (1984) p.4348-51]
- [29] G.T. Harvey, G. Astfalk, Y. Feldblum, B. Kassabrun [*J. Appl. Phys. (USA)* vol.22 (1986) p.939]
- [30] H. Kurz, D. Von der Linde [*Ferroelectrics (UK)* vol.21 (1978) p.621-2]
- [31] D. Marcuse [*Bell Syst. Tech. J. (USA)* vol.50 no.6 (1971)]
- [32] E. Garmire [*Topics in Applied Physics, Vol. 7, Integrated Optics* Ed. T. Tamir 3rd (Springer-Verlag, Berlin, Germany, 1982) p.266-71]
- [33] R.H. West, S. Dowling [*Electron. Lett. (UK)* vol.29 no.11 (1993) p.970-1]
- [34] C. d'Hose, E. Cassan, J. Baggio, O. Musseau, J.L. Leray [*IEEE Trans. Nucl. Sci. (USA)* vol.45 no.3 (1998) p.1524-30]
- [35] E.W. Taylor, S.P. Chapman, A.D. Sanchez, M.A. Kelly, J. Stohs, D.M. Craig [*Proc. SPIE (USA)* vol.2482 (1995) p.99-108]
- [36] E.W. Taylor, A.D. Sanchez, S.A. DeWalt [*Proc. SPIE (USA)* vol.1794 (1992) p.217-24]
- [37] E.W. Taylor et al [A Study of Radiation Induced Effects in Photonic Devices: Acousto Optic Modulators and Deflectors - Preliminary Results, PL-TR-94-1141, June 1995]
- [38] E.W. Taylor, J.E. Winter, A.D. Sanchez, S.J. McKinney [*J. Opt. Eng. (USA)* vol.36 (1997) p.1901-9]
- [39] E.W. Taylor et al [A Study of Radiation Induced Effects in Photonic Devices: Acousto Optic Modulators and Deflectors AFRL-VS-TR-1998-1028, Jan. 1998]
- [40] E.W. Taylor, R. Ewart [*AIP Conf. Proc. (USA)* vol.458 (1999) p.582-96]
- [41] E.W. Taylor [*Proc. IEEE Aerospace Conf.* ISBN5427-3, March 1999]

14.2 Basics of holographic processes in LiNbO₃

K.H. Ringhofer

February 1999

A INTRODUCTION

The holographic process comprises the steps necessary to record a hologram. There must be a signal wave and a reference wave crossing each other and there must be some medium to store the interference pattern. Very often that will be a high-quality photoresist which, after exposure, will be handled to store one and the same hologram 'for all time'.

The kind of holograms described above are abundant nowadays. They are not what we have in mind in this Datareview. We shall discuss 'volume holograms', holograms stored in the volume of a photorefractive crystal, to be precise. There are other storage materials with other storage mechanisms (polymers, etc.) which we shall not discuss here.

The main characteristics of 'thick' volume holograms, as opposed to the usual 'thin' holograms, are the following:

- Reconstruction, that is, reading the hologram out with the reference wave, must use the reference wave under the same (Bragg-)angle as under recording.
- The stored hologram is not fixed (although there are methods available for hologram fixing). Indeed, the signal wave may carry temporal information, and fast materials that can follow the temporal information are of great interest in optical data processing.

Trivially, the amount of optical information that can be stored in a thick hologram is far larger than that storable in a thin hologram.

The fundamental paper about how a hologram is stored in a photorefractive crystal is by Kukhtarev et al [1]; it exploits the band structure of photorefractive crystals. In this Datareview we shall follow, however, a simpler and purely phenomenological derivation of the basic equations, namely the recent paper by Sturman et al [2]. The most complete reference to all kinds of holographic processes is the book by Solymar et al [3] which has become an indispensable tool for everybody working in the field.

This Datareview will end with a short section about absorption. This effect is basic in the sense that under certain circumstances it changes primarily the space-charge field.

B PHENOMENOLOGICAL THEORY

The phenomenological theory does not refer to a specific model of the photorefractive crystal. It is a macroscopic theory in which the current density is related in the simplest possible way to the electric field and to the light intensity. For simplicity we restrict ourselves to the one-dimensional case, where all variables are only functions of the time t and the spatial variable z , measuring distance in the direction of the polar axis of a photorefractive ferroelectric (the general case, using the appropriate tensors, is developed in [2]). Then

$$j = \sigma E + \beta I + q \frac{\partial I}{\partial z} \quad (1)$$

This equation may be considered as the start of an expansion of the electric current, j , in a power series in the electric field, E , the light intensity, I , and the gradient of the light intensity, $\partial I / \partial z$.

The first term describes ohmic conduction and the coefficient σ is the conductivity, $\sigma = \sigma_d + \sigma_{ph}$, with σ_d the dark conductivity and $\sigma_{ph}(I)$ the photoconductivity.

The second term on the right-hand side of EQN (1) describes the volume photovoltaic effect, i.e. the photogeneration of a current along the polar axis of the crystal in the absence of an electric field and of spatial gradients [4,5]. This effect is inherent in any photosensitive ferroelectric.

The third term, finally, describes diffusion of photoexcited carriers. Assuming them to be electrons, we equate it with the diffusion current:

$$q \frac{\partial I}{\partial z} = eD \frac{\partial n}{\partial z} \quad (2)$$

where e is the electron charge and D is the diffusion constant for the mobile electrons. Using now the Einstein relation $D = \mu k_B T / e$, where μ is the electron mobility, k_B the Boltzmann constant, and T the absolute temperature, and also using the defining relation for the photoconductivity, $\sigma = \mu e n$, where n is the density of the mobile carriers, we work out the meaning of the third parameter:

$$q = \frac{\sigma_{ph} k_B T}{eI} \quad (3)$$

Reviewing EQN (2) we are satisfied that, at least in the long-scale limit and for a slow temporal change of the light intensity, the profile of $n(z)$ will follow the profile of the intensity $I(z)$.

C SPACE-CHARGE FIELD

To obtain the total electric field, E , in the crystal, we need Gauss's law and the continuity equation for the total charge density, ρ :

$$\frac{\partial E}{\partial z} = \frac{\rho}{\epsilon \epsilon_0} \left(\frac{\partial \rho}{\partial t} + \frac{\partial j}{\partial z} \right) \quad (4)$$

where $\epsilon \epsilon_0$ is the dielectric constant. Elimination of ρ allows us to integrate these equations:

$$\frac{\partial E}{\partial t} + \frac{j}{\epsilon \epsilon_0} = C \quad (5)$$

where $C = C(t)$ is an integration constant to be defined by the proper conditions for the electric field at opposite faces of the crystal. The most natural boundary conditions are the following:

- Open circuit. The integration constant is zero, as can be seen by crossing the boundary face of the crystal.
- Closed circuit. The integration constant is found by spatial averaging over the current density, $C = \langle j \rangle / \epsilon \epsilon_0$.

The simplest light pattern has the form

$$I = I_0 (1 + m \cos Kz) \quad (6)$$

with I_0 the average intensity, m the contrast and K the fundamental grating vector. It may be obtained by the interference of two light beams of the same frequency and polarisation. We shall also assume that the period of the light pattern, $\Lambda = 2\pi/K$, is small in comparison with the crystal length or, equivalently, that the crystal is ‘infinitely’ long in the z -direction. The space-charge field, that is, the spatially oscillating part of the total electric field, can then be written as a Fourier series:

$$\tilde{E} = \sum_{n=1}^{\infty} E_{nK} e^{inKz} + \text{c.c.} \quad (7)$$

where c.c. means the complex conjugate. For most applications the fundamental amplitude, $E_K = E'_K + iE''_K$, is of main importance. Its real part, E'_K , is called the unshifted (with respect to the light pattern) component of the photorefractive grating; its imaginary part, E''_K , is called the $\pi/2$ -shifted component. Both can be calculated easily in linear approximation in the contrast m .

D FUNDAMENTAL COMPONENT FOR OPEN CIRCUIT

In the case of an open circuit, the total field includes not only the oscillating space-charge field E but also a uniform component $\langle E \rangle(t)$, which is due to the photovoltaic effect. Assuming that the electric field is initially zero we calculate first the spatially constant contributions, neglecting thereby oscillating parts:

$$\langle E \rangle = -\frac{\beta I_0}{\sigma_0} [1 - e^{-vt_d}] \quad t_d = \frac{\epsilon \epsilon_0}{\sigma_0} \quad (8)$$

where t_d is the dielectric relaxation time and σ_0 is the spatially constant part of the conductivity. Introducing the photovoltaic field

$$E_{phv} = \frac{\beta I_0}{\sigma_{ph,0}} \quad (9)$$

where $\sigma_{ph,0}$ is the spatially constant part of the photoconductivity, this formula can be written more elegantly:

$$\langle E \rangle = -\frac{E_{phv}}{1 + v} [1 - e^{-vt_d}] \quad v = \frac{\sigma_d}{\sigma_{ph,0}} \quad (10)$$

In the steady state, if the dark conductivity is small compared to the photoconductivity, the uniform component of the electric field does not depend on the light intensity, while the dielectric relaxation time is inversely proportional to I_0 .

The uniform component of the electric field affects the fundamental component of the space-charge field via the modulated part of the photoconductivity:

$$\sigma = \sigma_d + \sigma_{ph,0} (1 + m \cos Kz)$$

so that

$$\sigma E = (\sigma_d + \sigma_{ph,0}) E_K + \sigma_{ph,0} m \cos Kz \langle E \rangle$$

From this, we find that the fundamental component of the space-charge field is built up according to the law

$$\left(t_d \frac{\partial}{\partial t} + 1 \right) E_K = - \frac{\bar{m}}{2} \left[\frac{E_{phv}}{1+v} (v + e^{-vt_d}) + iE_D \right] \quad (11)$$

where $\bar{m} = m/(1+v)$ is the reduced modulation and $E_D = k_B T/e$ is the diffusion field. The response time is again t_d . For the steady state EQN (11) simplifies to

$$E_K = - \frac{\bar{m}}{2} \left(\frac{vE_{phv}}{1+v} + iE_D \right) \quad (12)$$

and if the dark conductivity can be neglected, this result simplifies further to

$$E_K = -i \frac{m}{2} E_D \quad (13)$$

Clearly, the drift current and the photovoltaic current have compensated each other so that the fundamental component of the space-charge field has become purely imaginary.

E FUNDAMENTAL COMPONENT IN THE PRESENCE OF AN EXTERNAL FIELD

Next, we consider an externally applied electric field, E_{ex} , so that a closed circuit has to be considered. Repeating the argument of the last section, it will affect the fundamental component of the space-charge field, which is now built up according to the law

$$\left(t_d \frac{\partial}{\partial t} + 1 \right) E_K = \frac{\bar{m}}{2} (E_{ex} + E_{phv} + iE_D) \quad (14)$$

The steady-state value is obtained as

$$E_K = \frac{\bar{m}}{2} (E_{ex} + E_{phv} + iE_D) \quad (15)$$

so that even for negligible dark conductivity both the shifted and the unshifted components are contained in the photorefractive response.

F ABSORPTION

In most experimental situations the influence of absorption is trivial, insofar as signal and reference wave and therefore also the intensity are just exponentially damped on their way into the crystal. Assuming small dark conductivity, the intensity enters only via the dielectric relaxation time, τ_d . Therefore, the intensity does not enter in the steady state, in general.

Often, however, one has a slightly more complicated situation, when one applies a small detuning frequency between signal and reference wave to make use of the ensuing resonance enhancement of the space-charge field [6]. In this situation the dielectric relaxation time does not drop out of the materials equations [7].

What to do in this situation has been known for a long time: the space-charge field divided by the modulation, E_K/m , must be replaced by its average value over the crystal, so that E_K is to be replaced by

$$\overline{E_K / m} \times m$$

where the bar means spatial averaging [8]. Although a formal proof of this has still not been published, the statement is correct. Following the averaging procedure, the ‘shape asymmetry’ of the diffraction efficiency as a function of the frequency detuning has been explained [7].

G CONCLUSION

All the results obtained are simplified versions of the results of the band structure theory, worked out in detail by Kukhtarev et al [1]. Only those features that are connected with the densities of ionised and non-ionised impurities are missing, such as space-charge limitation by exhaustion of certain impurities. As a basic access to the holographic process, however, the present phenomenological theory serves exceedingly well. It can be extended to describe hole transport and other features [2].

We have added a few remarks about absorption which is basic in the sense that it affects primarily the space-charge field.

ACKNOWLEDGEMENTS

The author thanks B.I. Sturman for permission to study his manuscript prior to publication. The support of Volkswagen-Stiftung (I/72072) is gratefully acknowledged.

REFERENCES

- [1] N.V. Kukhtarev, V.B. Markov, S.G. Odulov, M.S. Soskin, V.L. Vinetskii [*Ferroelectrics (UK)* vol.22 (1979) p.949 and p.961]
- [2] B.I. Sturman, F. Agullo-Lopez, M. Carrascosa, L. Solymar [*Appl. Phys. B (Germany)* feature issue (1999) Photorefractive Materials: Properties and Applications]
- [3] L. Solymar, D.J. Webb, A. Grunnet-Jepsen [*The Physics and Applications of Photorefractive Materials* (Clarendon Press, Oxford, UK, 1996)]
- [4] A.M. Glass, D. von der Linde, T.J. Negran [*Appl. Phys. Lett. (USA)* vol.25 (1974) p.233]
- [5] B.I. Sturman, V.M. Fridkin [*The Photovoltaic and Photorefractive Effect in Noncentrosymmetric Materials* (Gordon and Breach, Philadelphia, USA, 1992)]
- [6] P. Refregier, L. Solymar, H. Rajbenbach, J.P. Huignard [*J. Appl. Phys. (USA)* vol.58 (1985) p.45]
- [7] E. Shamonina, K.H. Ringhofer, P.M. Garcia, J. Frejlich [*Opt. Commun. (Netherlands)* vol.141 (1997) p.132]
- [8] T.J. Hall, R. Jaura, L.M. Connors, P.D. Foote [*Prog. Quantum Electron. (UK)* vol.10 (1985) p.77]

14.3 Dynamic properties of LiNbO₃, optical-damage-related issues and stabilisation techniques

K.H. Ringhofer

February 1999

A INTRODUCTION

The basic holographic processes dealt with in Datareview 14.2 are, in general, time dependent. This, however, is not what is meant when one speaks of 'dynamic holography'. The latter concept refers to the fact that signal and reference wave, while storing the volume hologram as described in the preceding Datareview, are themselves changed by the hologram, which is itself in the process of being built up. This is a consequence of the electro-optic effect [1], that is, the change of the refractive index, or, more accurately, the dielectric tensor, by an electric field:

$$(\Delta\epsilon)^{-1} = r_{ikl} E_l \quad (1)$$

Here, $(\Delta\epsilon)^{-1}$ is the inverse dielectric tensor, E is the electric field, and \hat{r} is the electro-optic tensor. In effect, the modulated space-charge field is now accompanied by a modulated refractive index grating. This is what one usually calls the hologram or the holographic grating. It diffracts signal wave and reference wave and is thereby the origin of the dynamic effects.

The present Datareview will concentrate on the dynamic properties of holography in the sense explained above. This is a vast field of research and there will be no chance to explain the details as accurately as the basic holographic process itself.

B RECONSTRUCTION AND BEAM COUPLING IN FERROELECTRICS

From the point of view of volume holography, ferroelectrics like lithium niobate (LiNbO₃) or barium titanate (BaTiO₃) are the simplest materials. They are characterised by large birefringence with the effect that the wave surfaces for two light eigenmodes (often ordinary and extraordinary waves) are here well separated in k -space. For this reason, wave interactions in ferroelectrics may successfully be described by coupled equations for the scalar wave amplitudes. The polarisation properties of the wave coupling are here uncoupled from the effects of energy and phase exchange.

The standard method in this case is the approximation of slowly varying amplitudes: the amplitudes of the eigenmodes are considered to vary slowly in space and time, so that the second derivative in Maxwell's equations may be neglected. Assuming that the stationary state has already been obtained, one derives the following pair of differential equations for the amplitudes S and R of signal and reference waves [2]:

$$R' + \alpha R = -\frac{i}{2} \bar{n}^3 k_0 r E_K S \quad S' + \alpha S = -\frac{i}{2} \bar{n}^3 k_0 r E_K^* R \quad (2)$$

Here, E_K is the amplitude of the space-charge field, \bar{n} is the constant part of the appropriate refractive index, $k_0 = 2\pi/\lambda$ is the vacuum wavenumber with λ the vacuum wavelength, and r is the appropriate component of the electro-optic tensor. In deriving this formula, it has been assumed that signal and reference waves impinge symmetrically onto the normal of the crystal surface and nearly perpendicular to the crystal surface. Furthermore, α is the absorption constant with the effect of

letting signal and reference waves decay exponentially. Knowing this behaviour in advance, it can simply be transformed away, as long as there is no detuning (see Datareview 14.2).

The main information from EQN (2) is easily obtained. One derives first the differential equations for the intensities I_R and I_S of signal and reference waves. Solving them, one has to keep in mind that the space-charge amplitude E_K is proportional to the contrast $m = 2S^*R/I$ with I the total intensity, so that the differential equations are by no means linear. Nevertheless, their solution is easily obtained [2]:

$$\frac{I_R}{I} = \frac{I_R(0)e^{-\frac{\Gamma_d}{2}d}}{I_R(0)e^{-\frac{\Gamma_d}{2}d} + I_S(0)e^{\frac{\Gamma_d}{2}d}} \quad \frac{I_S}{I} = \frac{I_S(0)e^{\frac{\Gamma_d}{2}d}}{I_R(0)e^{-\frac{\Gamma_d}{2}d} + I_S(0)e^{\frac{\Gamma_d}{2}d}} \quad (3)$$

Here d is the crystal thickness. This equation describes beam coupling or coherent amplification. Signal and reference waves exchange their intensities. We shall assume that the logarithmic amplification, $\Gamma = -2\bar{n}^3k_0r\Re(E_K/m)$, is positive. Then the signal wave gains more intensity the thicker the crystal. In the limit of an infinitely thick crystal the signal wave would have gathered all the intensity.

Another important parameter that can be obtained from EQN (2) is the diffraction efficiency. The dynamic grating written by signal and reference waves can be read out by a probing wave. The intensity of the diffracted wave at the rear side of the crystal, divided by the intensity of the probing wave at the crystal front, is the diffraction efficiency, η . It is not obtained by putting the intensity $I_S(0)$ of the signal wave at the crystal front equal to zero. In this case, there would be no grating at all. The correct calculation is not quite trivial; the result can be found in [2]:

$$\eta = 2 \frac{I_R(0)I_S(0)}{I} \frac{\cosh \frac{\Gamma}{2}d - \cos \frac{\gamma}{2}d}{I_R(0)e^{-\frac{\Gamma_d}{2}d} + I_S(0)e^{\frac{\Gamma_d}{2}d}} \quad (4)$$

Here, $\gamma = -2\bar{n}^3k_0r\Re(E_K/m)$. For a thin crystal, $|\Gamma d|, |\gamma d| \ll 1$, we find

$$\eta \approx \left| \frac{1}{2} \bar{n}^3 k_0 r E_K d \right|^2 \quad (5)$$

This is essentially Kogelnik's formula [3] with

$$\sin^2 \left(\frac{1}{2} \bar{n}^3 k_0 r E_K d \right)$$

simply replaced by

$$\left| \frac{1}{2} \bar{n}^3 k_0 r E_K d \right|^2$$

It is derived under the assumption of a constant grating amplitude which is only reasonable for a thin crystal. In this case also, the sine function does not play any role.

C CUBIC CRYSTALS

The situation changes drastically when we consider crystals of cubic symmetry, which are not birefringent and, therefore, in the absence of an external field, do not hinder the free movement of the polarisation vectors of the light waves. There are two main classes of such crystals: the sillenites with symmetry 23 and semiconductors with symmetry $\bar{4}3m$. The sillenites show optical activity, the semiconductors do not.

Clearly, the vectorial properties of the wave amplitudes must be taken into account. The situation is a little simplified if one assumes the usual experimental situation of the beams impinging symmetrically and at a small angle to the normal to the crystal front surface. Then, the component of the polarisation vector perpendicular to the front surface may be neglected and only two-dimensional vectors come into play, and the formalism of Pauli matrices with them [4].

We shall now list a few effects that, in principle, are of interest for all photorefractive crystals, but which have been investigated up to now mainly in cubic crystals.

- Optical activity. This is the rotation of the polarisation plane during the propagation of a lightwave. Experimentalists try to choose initial polarisations of the waves so that the influence of optical activity does not become detrimental to the experiment. It is not often tried to really take into account the influence of optical activity, although it is known that optical activity in $\text{Bi}_{12}\text{SiO}_{20}$ (BSO) is quite large, rotatory power $\rho \approx 628 \text{ m}^{-1}$ for $\lambda = 514.5 \text{ nm}$, in contrast to $\text{Bi}_{12}\text{TiO}_{20}$ (BTO) with rotatory power $\rho \approx 200 \text{ m}^{-1}$ for the same wavelength. Only recently has it turned out that optical activity in BSO is easy to handle because it dominates, while optical activity in BTO is an unpleasant feature because its strength corresponds to the strength of the holographic coupling [5].

We would like to stress that rotation of the polarisation plane during the propagation of lightwaves is also possible in semiconductors (of symmetry $\bar{4}3m$) which do not exhibit optical activity. The change of the polarisation vectors is here achieved by the coupling of signal and reference waves by the hologram [6].

- Birefringence. Application of an external electric field induces birefringence also in cubic crystals. If the external field is strong enough, the polarisation vector will freeze again. The situation is especially intriguing if the external field is an AC field. There is birefringence while the external field is positive as well as when it is negative, and the sign of the induced dielectric tensor depends on the sign of the external field. But there is no birefringence while the external field goes through zero [7].

The switching of the applied square-wave field produces strong and short pulses of the outgoing signal. The effect allows combination of the processes of non-perturbing recordings in a large AC field with an effective pulsed readout [7].

- Photoelastic effect. The importance of this effect was stressed a long time ago [8] and the theory has been worked out in [9,10]. The point is that the ‘primary’ electro-optic effect is only observed when the crystal is clamped, that is, fixed so that it cannot be deformed. This, however, is not the usual experimental situation where the inverse piezo-electric effect acts like electro-striction: an electric field deforms the crystal. As a consequence, the elasto-optic effect changes the dielectric tensor, adding, in effect, an extra term to the electro-optic tensor, which strongly depends on the orientation of the grating vector (‘secondary electro-optic effect’).

The effect is quite complicated insofar as it acts differently for homogeneous and inhomogeneous electric fields. For a homogeneous electric field the clamped electro-optic coefficient, r_{41} , is

renormalised. For inhomogeneous electric fields there is an additional tensor with a different structure.

Taking into account elasto-optic properties has recently allowed us to explain the three-lobe structure of the fanning light in BaTiO_3 [11] and the strong dependence of the optimum crystal orientation on the crystal thickness for two-wave mixing in selenite crystals [12].

D OPTICAL DAMAGE AND HOW TO AVOID IT

When the photorefractive effect was detected in 1966 by Ashkin, Boyd and others [13] it was first considered as ‘optical damage’, something that should be avoided. In the meantime one has learned to make use of the effect, but still there is an aspect of photorefraction that is considered as optical damage: the build-up of unwanted ‘noise gratings’. Signal and reference waves are scattered from inhomogeneities of the crystal and by interference of one of the scattered waves with signal or reference waves the noise gratings build up. Although even these spurious gratings have found a certain use (certain photovoltaic coefficients are most easily determined from noise gratings [14,15]) the tendency is to avoid them. A number of methods of doing so can be found in [16] and we shall not repeat them. We restrict ourselves to mention of one new method that is connected with the following section. The stabilisation technique to be described there, in essence, introduces a small detuning frequency with the effect of moving the hologram with a small velocity [17]. Thereby, the noise holograms, which are generated very slowly because of the low intensities involved, are partly erased [18].

E ACTIVE STABILISATION

Stabilisation of the holographic set-up is a subject of importance in two-wave mixing, phase-conjugation, pattern recognition, optical information processing, hologram fixing and other techniques. In this section, we concentrate on a promising technique using phase modulation that seems to have been introduced first by MacQuigg [19] and then has been further developed at the University of Campinas in Brazil [20].

The essence of the method is the following. To stabilise the position of a hologram against the influence of small changes in the environment one needs a ‘handle’ with which to hold the hologram at a fixed position. Furthermore, the ‘fixing’ of the hologram by this handle should occur automatically: each movement of the handle should be compensated for immediately. A feedback system seems best to serve this purpose.

The nature of this handle is not terribly important. In [20] a certain parameter, characteristic for the hologram, has been chosen and the feedback loop does nothing else but fix this parameter. This ‘feedback angle’ is defined as the phase difference between the transmitted signal wave and the diffracted reference wave, both waves moving in the same direction. The value of this parameter may be chosen at will [21].

We shall not describe here the exact nature of the feedback loop. Suffice it to say that the signal wave is phase modulated with small amplitude and high frequency and that the first and second harmonic in the transmitted signal wave and diffracted reference wave are used to keep a mirror in the path of the input signal wave at exactly the right velocity (corresponding to a certain detuning frequency) to guarantee the stability of the chosen feedback angle.

It is important to note that the time-development of the system under feedback conditions differs from the time-development without feedback; the system is no longer the same. As in mechanics one can speak of different ‘orbits’ chosen by the system when it is subject to different conditions.

The potential of the method is great and only the first steps have been taken. It is clear that there are experiments for which the method is essential. The unstable behaviour of reflection holograms is well known. This is caused by the small grating constant. A small shift in the environment can shift the hologram a full wavelength. Nothing has been done in this direction. Likewise, four-wave mixing has not yet been investigated. In the following, we shall list a few cases in which the method has already been proven useful.

- Crystal parameters. The method has been used to determine crystal parameters like dielectric response time and quantum efficiency in GaAs [22].
- 100% diffraction efficiency. Experiments in lithium niobate (LiNbO_3) [23,24] have shown that it is possible to stabilise the system so that it is held fixed at a diffraction efficiency of 100%.
- Scattering reduction. In [18] it is shown that in addition to the 100% diffraction efficiency possible in lithium niobate scattering from parasitic gratings is reduced by a factor of 3 to 4.
- Incremental holographic recording of angular multiplexed holograms (that is, recording of each hologram with the same recording time and repetition of the recording cycle until the diffraction efficiency is no longer increased) in iron-doped lithium niobate using active stabilisation has been shown to work in [25].
- Thermal fixing is another process where active stabilisation is most important to fight movement or vibrations of the interference pattern during long-time writing at enhanced temperatures [26].

F CONCLUSION

In conclusion, we have given a short overview of new developments in dynamic holography. Special attention has been given to the behaviour of the polarisation vector of the lightwaves in cubic crystals and to a successful new technique of actively stabilising a hologram while it is stored.

ACKNOWLEDGEMENTS

The support of Volkswagen-Stiftung (I/72072) is gratefully acknowledged.

REFERENCES

- [1] I.P. Kaminov [*An Introduction to Electrooptic Devices* (Academic Press, Orlando, 1984)]
- [2] N.V. Kukhtarev, V.B. Markov, S.G. Odulov, M.S. Soskin, V.L. Vinetskii [*Ferroelectrics (UK)* vol.22 (1979) p.949 and p.961]
- [3] H. Kogelnik [*Bell Syst. Tech. J. (USA)* vol.48 (1969) p.2910]
- [4] B.I. Sturman, D.J. Webb, R. Kowarschik, E. Shamonina, K.H. Ringhofer [*J. Opt. Soc. Am. B (USA)* vol.11 (1994) p.1813]
- [5] E. Shamonina et al [*Opt. Commun. (Netherlands)* vol.146 (1998) p.62]
- [6] Y. Hu, K.H. Ringhofer, B.I. Sturman [*Appl. Phys. B (Germany)* feature issue (1999) Photorefractive Materials: Properties and Applications]
- [7] E. Shamonina, K.H. Ringhofer, B.I. Sturman, V. Kamenov [*Opt. Lett. (USA)* vol.23 (1998) p.1435]
- [8] S. Stepanov, S.M. Shandarov, N.D. Khat'kov [*Sov. Phys.-Solid State (USA)* vol.29 (1987) p.1754]
- [9] A.A. Izvanov, A.E. Mandel, N.D. Khat'kov, S.M. Shandarov [*Optoelectron. Instrum. Data Process. (USA)* vol.2 (1986) p.80]

14.3 Dynamic properties of LiNbO_3 , optical-damage-related issues and stabilisation techniques

- [10] G. Pauliat, P. Mathey, G. Roosen [*J. Opt. Soc. Am. B (USA)* vol.8 (1991) p.1942]
- [11] G. Montemezzani, A.A. Zozulya, L. Czaia, D.Z. Anderson, M. Zgonik, P. Günter [*Phys. Rev. A (USA)* vol.52 (1995) p.1791]
- [12] E. Shamonina, B. Kamenov, K.H. Ringhofer, G. Cedilnik, A. Kießling, R. Kowarschik [*J. Opt. Soc. Am. B (USA)* vol.15 (1998) p.2552]
- [13] A. Ashkin et al [*Appl. Phys. Lett. (USA)* vol.9 (1966) p.72]
- [14] S.G. Odoulov, M. Soskin [*Photorefractive Materials and their Applications* Eds. P Guenter, J.-P. Huignard (Springer-Verlag, Berlin, 1989) ch.2]
- [15] B.I. Sturman, S.G. Odoulov, M.Y. Goul'kov [*Phys. Rep. (Netherlands)* vol.275 (1996) p.197]
- [16] L. Solymar, D.J. Webb, A. Grunnet-Jepsen [*The Physics and Applications of Photorefractive Materials* (Clarendon Press, Oxford, UK, 1969)]
- [17] J. Frejlich, P.M. Garcia, L. Cescato [*Opt. Lett. (USA)* vol.14 (1989) p.1010]
- [18] P.M. Garcia, A.A. Freschi, J. Frejlich, E. Krätzig [*Appl. Phys. B (Germany)* vol.63 (1996) p.207]
- [19] D. MacQuigg [*Appl. Opt. (USA)* vol.16 (1977) p.291]
- [20] A.A. Kamshilin, J. Frejlich, L. Cescato [*Appl. Opt. (USA)* vol.25 (1986) p.2375]
- [21] A.A. Freschi, J. Frejlich [*Opt. Lett. (USA)* vol.20 (1995) p.635]
- [22] S. Bian, J. Frejlich [*Opt. Lett. (USA)* vol.19 (1994) p.1702]
- [23] A.A. Freschi, J. Frejlich [*J. Opt. Soc. Am. B (USA)* vol.9 (1994) p.1837]
- [24] P.M. Garcia, K. Buse, D. Kip, J. Frejlich [*Opt. Commun. (Netherlands)* vol.117 (1995) p.236]
- [25] K. Peithmann, A. Wiebrock, K. Buse [*Opt. Lett. (USA)* vol.23 (1998) p.1927]
- [26] S. Breer, K. Buse, K. Peithmann, H. Vogt, E. Krätzig [*Rev. Sci. Instrum. (USA)* vol.69 (1998) p.1591]

CHAPTER 15

OPTICAL WAVEGUIDE TECHNOLOGIES

- 15.1 Proton exchange in undoped LiNbO₃ (concentrated melt)
- 15.2 Proton exchange in undoped LiNbO₃ (dilute melt)
- 15.3 Proton exchange in Ti-indiffused and MgO-doped LiNbO₃
- 15.4 Kinetics of Ti-indiffusion in LiNbO₃
- 15.5 Characteristics of LiNbO₃ optical waveguides
- 15.6 Ion implantation in LiNbO₃

15.1 Proton exchange in undoped LiNbO₃ (concentrated melt)

K.K. Wong

March 2002

A INTRODUCTION

The proton exchange method, originally used as a means of preparing new cubic perovskites from LiNbO₃ and LiTaO₃ [1,2], was found to be a very convenient and fast technique for the formation of optical waveguides in LiNbO₃ by Jackel et al [3]. Since then, optical waveguide studies have been carried out in X- [4,5], Y- [6-8] and Z-cut [9-12] LiNbO₃ using concentrated benzoic acid melts or pyrophosphoric acid as the protonic source. A number of review papers on the subject of proton-exchange waveguide technology for integrated optics applications have also been written [13-15].

The main advantage of the process is that fabrication of waveguides is quick and simple. The temperature required for the waveguide formation is low, between 160°C and 249°C [5]. The end result is a waveguide with a high index change of around 0.12, i.e. $\Delta n = 0.12$ [5]. However, the refractive index change is not isotropic as only the extraordinary refractive index is increased. There is a significant but smaller decrease in the ordinary refractive index [16]. This implies that only TE-modes are guided in proton-exchanged (PE) X- and Y-cut LiNbO₃ and TM-modes in PE Z-cut LiNbO₃. Another important advantage of proton-exchange waveguides in LiNbO₃ is that they have been found to be more resistant to optical damage [17-19] than titanium-diffused waveguides. Also the ability to temperature tune the refractive index profiles of waveguides formed by the proton-exchange method is a very important property of this technique [20].

B WAVEGUIDE FORMATION

The proton exchange process in LiNbO₃ can be described broadly as the depletion of lithium and the replacement of hydrogen in the crystal. This occurs when the substrate is immersed in a protonic source, i.e. an acid (e.g. benzoic acid, palmitic acid, stearic acid, cinnamic acid, and mixtures) or a hydrate melt (e.g. Mg(NO₃)₂.6H₂O), at the appropriate temperature. The exchange process can be complete, i.e. with all the lithium replaced [2], or it can be partial, depending on the acidity of the medium. However the effect of 'acidity' has by no means yet been fully and properly investigated. For optical waveguide fabrication, only partial exchange is of interest since total exchange will cause the LiNbO₃ crystal to change from its hexagonal structure to a cubic perovskite. This volume change will result in cracking of the surface of the LiNbO₃ crystal. However, totally proton-exchanged layers cannot be obtained on large area LiNbO₃ single crystal substrates because the enormous stress introduced by this phase transformation does not allow any epitaxial adhesion of the new HNbO₃ phase on the substrate.

It has been established by some researchers that for the proton exchange process to be useful for optical waveguide formation, the general composition of the exchanged regions is H_xLi_{1-x}NbO₃ with x up to 0.12. One of the most commonly used protonic sources for partial exchange is benzoic acid [3]. In general the overall reaction between acid and LiNbO₃ can be described by the equation below:



The effects of optical waveguides formed using titanium indiffusion followed by PE in LiNbO₃ [16,21-24] in relation to the refractive index change and the refractive index profile have been studied and identified to be potentially useful in the improvement of present Ti:LiNbO₃ waveguide devices.

15.1 Proton exchange in undoped LiNbO_3 (concentrated melt)

Also, phosphoric acid has been employed to form optical waveguides with Δn values of 0.13 [12] and 0.15 [25,26]. The annealing of the PE waveguides has shown that the refractive index profile of the optical waveguide can be modified from an almost step-index profile to a graded-index profile [15,20,27]. The modification is dependent upon the annealing time, temperature and atmosphere in which the process is carried out [28].

C WAVEGUIDE STUDIES

The prism coupling technique [29] with single-crystal rutile prisms was employed by researchers in general to evaluate the optical properties of the PE waveguides. Results from the literature indicated that the refractive index profiles of the as-fabricated PE waveguides were step-like [4,5,10]. It was confirmed experimentally by researchers that only TE modes were excited in PE waveguides formed in X- and Y-cut LiNbO_3 [4-6] and only TM modes were excited in waveguides formed in Z-cut LiNbO_3 [10,12].

By using the IWKB technique [30] for approximating the refractive index profiles of the PE waveguides, the depth of the optical waveguides can be determined. Diffusion coefficients can then be established from plots of optically estimated diffusion depth versus time. TABLE 1 shows the diffusion coefficients for concentrated benzoic acid melt experiments in X- [5] and Z-cut [10] LiNbO_3 at various temperatures. In addition the use of thermal annealing to modify the refractive index profile and the Δn change is critical in the successful fabrication of high performance single-mode devices [15,16,28].

TABLE 1 Diffusion coefficients at various temperatures.

Temperature of exchange (°C)	Diffusion coefficient ($\mu\text{m}^2/\text{h}$) for X-cut LiNbO_3 [5]	Diffusion coefficient ($\mu\text{m}^2/\text{h}$) for Z-cut LiNbO_3 [10]
160	0.032	0.008
170	0.054	0.015
180	0.089	0.027
190	0.144	0.046
200	0.229	0.077
210	0.356	0.126
220	0.544	0.202
230	0.818	0.318
240	1.210	0.493

Several researchers have employed Rutherford backscattering spectrometry (RBS), nuclear reactions, secondary ion mass spectrometry, scanning electron microscopy and X-ray diffraction (by double crystal and topograph) to identify the structure, thickness and strain in the lattice of the exchanged layers [31-36]. Some of the results from the above analytical studies are summarised below:

- There was close agreement between optical waveguide thicknesses estimated from prism coupling measurements and estimates from resonant nuclear interaction and RBS [31]. From all three measurements, it was found that the refractive index profile is step-like for waveguides formed without annealing.
- The results from the X-ray diffractometry study indicated that the PE regions had undergone a positive lattice strain. For Z-cut PE crystals it was found that the strain was $\Delta c/c = 0.45\%$ (with $\Delta a/a$ being negligible) [36].
- Lee and co-workers [35] indicated that there was possible formation of Nb_2O_5 or LiNb_3O_8 in annealed PE waveguide regions examined using transmission electron microscopy. In

15.1 Proton exchange in undoped LiNbO₃ (concentrated melt)

addition small cavities were also seen in the PE channels after annealing. They suggested that this could be caused by a dehydration reaction.

Work reported by Loni et al employing hydrogen-isotopic effects in proton-exchanged and deuterium-exchanged LiNbO₃ may prove to be useful as an investigational tool in the understanding of the proton exchange process, in terms of the changes in the crystal stoichiometry, waveguide stability and ionic conduction effects on acousto-optic and electro-optic device performance [14,37,38].

D OBSERVED PROBLEMS WITH PE WAVEGUIDES

Unfortunately, some important problems have been identified in PE waveguides fabricated using pure benzoic acid melts. The problems include refractive index instability [39,40], a DC extinction effect [41], reduced electro-optic activity [36,42,43] and reduced acousto-optic interaction efficiency [44].

The measured effect mode indices on a day-to-day basis reveal an oscillatory [39] and in some reports a general reduction in values [5]. This implies that the refractive index profile of the PE LiNbO₃ waveguides evolves with time after fabrication. Researchers have attributed these short- and long-term refractive index instabilities to continuous migration of protons within the thickness of the waveguiding layer [40], relaxation of the metastable structure H_xLi_{1-x}NbO₃, and possibly a phase separated surface layer caused by dehydration of the PE regions [35].

In electro-optic devices (phase modulators and Mach-Zehnder interferometers) it was found that the electro-optic activity was reduced in some device demonstrations [36,38,42]. Evidence exists where the r₃₃ electro-optic coefficient of LiNbO₃ was found to be ten times smaller in proton-exchange devices when compared to titanium-indiffused devices [36]. However, successful demonstrations of proton-exchange optical frequency translators and cut-off modulators with no measured reduction in electro-optic activity have been reported [45,46]. The optical frequency translators formed by pure PE however were sensitive to non-zero DC voltages [41]. On the other hand Mach-Zehnder interferometers in LiNbO₃ formed by concentrated-melt PE with some form of annealing were found to preserve the electro-optic coefficients and were not sensitive to DC bias voltages [17,47,48].

AO devices in proton-exchange waveguides have also been found to have reduced interaction efficiency. Variations in SAW velocities and increases in acoustic wave attenuation have been reported [49].

E PASSIVE AND ACTIVE DEVICES

The high refractive index change that can be achieved with PE in LiNbO₃ suggests that this method can be used to realise high performance passive structures such as gratings and lenses of various types. A 3 micron period grating with approximately 90% deflection efficiency was fabricated in X-cut LiNbO₃ by Pun et al [50]. This was then followed by a demonstration of a chirp grating lens by Warren et al [51]. Yu [52] demonstrated planar equivalents of aspheric bulk lens structures.

The use of PE regions as passive polarising elements in conjunction with titanium-indiffused stripe waveguides has been demonstrated [53-56]. In these devices, both the TE and TM modes are supported in the Ti:LiNbO₃ stripe waveguides. The PE insets however only support the TE or the TM modes, depending on the crystal cut used. High performance polarisers using appropriate lengths of PE inset have been demonstrated with TE/TM mode rejection ratios of as high as 50 dB and low optical excess insertion losses of the order of 1 dB [55,56].

Other passive structures demonstrated to date include ring-resonators [57,58], and an interferometric temperature sensor in Z-cut LiNbO₃. In the latter structure, the large change in refractive index was

used to realise low-loss waveguide bends and hence enable a large interferometer arm length difference to be realised in a compact structure [59]. This implies that highly sensitive temperature sensing applications can be accomplished, in this case, in Z-cut LiNbO_3 and could be digitised using several structures with different pathlength differences.

The use of PE optical waveguides in LiNbO_3 in non-linear optical interactions such as second harmonic generation (SHG) has also been demonstrated by a number of workers. SHG has been observed as a guided wave in LiNbO_3 waveguides at Nd:YAG laser wavelength, i.e. 1060 nm [60,61]. However, for the GaAs laser diode wavelength, i.e. 830 nm, phase matching to guided waves was not possible (e.g. without employing a periodic phase-matching structure) but it was possible to radiate plane waves into the LiNbO_3 substrate. This type of SHG radiation was observed in the form of Cerenkov radiation and in this case both the fundamental optical wave and the second harmonic wave were extraordinary waves [26,62]. The non-linear coupling here is obtained via the non-linear coefficient d_{33} , which is the largest in the case of LiNbO_3 .

Electro-optic and acousto-optic devices have been demonstrated by various researchers. Their results indicated variations in performance, with some indicating performance comparable with Ti: LiNbO_3 counterparts while others reported reductions in electro-optic and acousto-optic interaction strength of as much as three times. It has been shown in those experiments that optical frequency translators made by PE had similar performance to Ti: LiNbO_3 frequency translators [45]. Work by Becker [42] on PE and titanium-indiffused Mach-Zehnder interferometers at 830 nm and 1300 nm concluded that the electro-optic activity was reduced by at least a factor of 2.7 in the case of the PE Mach-Zehnder interferometer devices. Work by Minakata and co-workers showed that the r_{33} electro-optic constant values in their PE Z-cut LiNbO_3 phase modulators were reduced to one-tenth of published r_{33} values for virgin crystals [36].

The use of PE X-, Y-, 128° rotated Y-, and Z-cut LiNbO_3 waveguides in acousto-optic (AO) devices has been investigated by a number of researchers [8,28,44,63-71]. The general conclusions from all these papers were that there was a measured reduction in AO interaction efficiency, an increase in acoustic wave propagation losses and substantial changes in the surface acoustic wave velocity. For example, Dawar and co-workers demonstrated that in reducing the in-plane scattering levels of the PE Y-cut LiNbO_3 waveguides, a drastic reduction in AO interaction efficiency was observed [28].

F OTHER PROMISING PROTONIC SOURCES

In recent years researchers have identified other inorganic and organic protonic sources such as pyrophosphoric [72], phosphoric [73,81], octanic [74,79], cinnamic [75,76], stearic [77,80], tollic [78,83] and adipic acid [82] to fabricate optical waveguides in LiNbO_3 with results similar to those realised using molten benzoic acid. The advantages in using these alternative organic protonic sources are that they are non-toxic, non-corrosive and safe. Recently a novel protonic source consisting of a mixture of adipic and benzoic acids was used to fabricate optical waveguides with interesting waveguide properties [84]. Further use of such mixture concepts to tailor waveguide properties may result in novel optical devices.

The rate of diffusion varies from acid to acid, and the stronger acid tends to have a higher rate of diffusion because the proton concentration H^+ available for replacement of Li^+ at the surface of the LiNbO_3 substrate is higher. Comparison of the rate of diffusion for the different acids is shown in FIGURE 1. It can be deduced that among the protonic sources used, stearic acid has the lowest rate of diffusion and phosphoric acid has the highest. It is noted that the acidity constant for stearic acid is the lowest (i.e. 1.28×10^{-5}).

15.1 Proton exchange in undoped LiNbO_3 (concentrated melt)

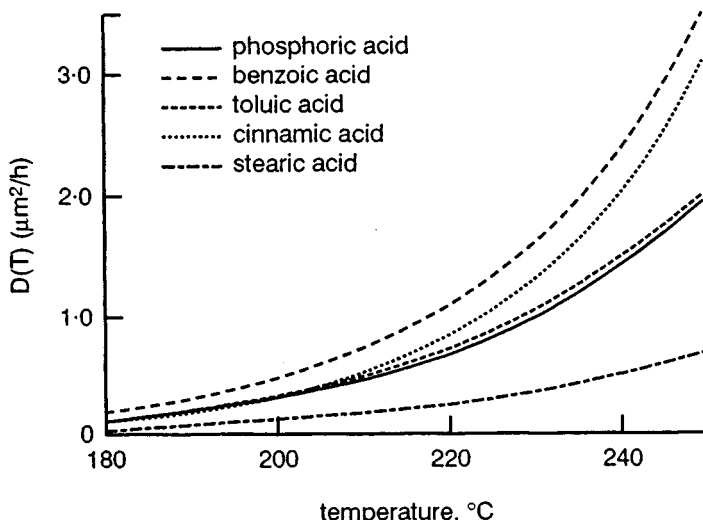


FIGURE 1 Comparison of $D(T)$ as a function of exchange temperature for difference proton sources.

REFERENCES

- [1] J.L. Jackel, C.E. Rice [*Ferroelectrics (UK)* vol.38 no.1-4 (1981) p.801-4]
- [2] C.E. Rice, J.L. Jackel [*J. Solid State Chem. (USA)* vol.41 no.3 (1982) p.308-14]
- [3] J.L. Jackel, C.E. Rice, J.J. Veselka [*Topical Meeting on Integrated and Guided-Wave Optics* Pacific Grove, CA, USA, 6-8 Jan. 1982, Technical Digest Post-Deadline Papers (Opt. Soc. America, Washington DC, 1982) p.PDP1.1-PDP1.4]
- [4] J.L. Jackel, C.E. Rice, J.J. Veselka [*Appl. Phys. Lett. (USA)* vol.41 no.7 (1982) p.607-8]
- [5] K.K. Wong, A.C.G. Nutt, D.F. Clark, P.J.R. Laybourn, R.M. De La Rue [*IEE Proc. J (UK)* vol.133 no.2 (1986) p.113-7]
- [6] M. Goodwin, C. Stewart [*Electron. Lett. (UK)* vol.19 no.6 (1983) p.223-5]
- [7] A. Campari et al [*J. Appl. Phys. (USA)* vol.58 no.12 (1985) p.4521-4]
- [8] N. Saiga, Y. Ichioka [*J. Appl. Phys. (USA)* vol.61 no.3 (1987) p.1230-3]
- [9] A.C.G. Nutt, K.K. Wong, D.F. Clark, P.J.R. Laybourn, R.M. De La Rue [*2nd European Conf. on Integrated Optics* Florence, Italy, 17-18 Oct. 1983 (IEE, London, 1983) p.53-6]
- [10] D.F. Clark, A.C.G. Nutt, K.K. Wong, P.J.R. Laybourn, R.M. De La Rue [*J. Appl. Phys. (USA)* vol.54 no.11 (1983) p.6218-20]
- [11] S.T. Vohra, A.R. Mickelson [*J. Lightwave Technol. (USA)* vol.6 no.12 (1988) p.1848-53]
- [12] N. Goto, G.L. Yip [*Appl. Opt. (USA)* vol.28 no.1 (1989) p.60-5]
- [13] J.L. Jackel, C.E. Rice, J.J. Veselka [*Ferroelectrics (UK)* vol.50 no.1-4 (1983) p.491-6]
- [14] R.M. De La Rue et al [*Proc. 4th European Conf. on Integrated Optics* Glasgow, Scotland, 11-13 May 1987, Eds C.D.W. Wilkinson, J. Lamb (Scottish Electron. Technol. Group, Glasgow, 1987) p.48-53]
- [15] K.K. Wong [*Proc. SPIE - Int. Soc. Opt. Eng. (USA)* vol.993 (1988) p.13-25]
- [16] M. De Micheli, J. Botineau, P. Sibillot, D.B. Ostrowsky [*Opt. Commun. (Netherlands)* vol.42 no.2 (1982) p.101-3]
- [17] K.K. Wong [*GEC J. Res. (UK)* vol.3 no.4 (1985) p.243-50]
- [18] J.L. Jackel, A.M. Glass, G.E. Peterson, C.E. Rice, D.H. Olson, J.J. Veselka [*J. Appl. Phys. (USA)* vol.55 no.1 (1984) p.269-70]
- [19] Y. Fujii, S. Tanikoshi [*Trans. Inst. Electron. Inf. Commun. Eng. E (Japan)* vol.69 no.2 (1986) p.95-6]
- [20] M. De Micheli, J. Botineau, S. Neveu, P. Sibillot, D.B. Ostrowsky [*Opt. Lett. (USA)* vol.8 no.2 (1983) p.114-5]

- [21] A.L. Dawar, S.M. Al-Shukri, R.M. De La Rue, A.C.G. Nutt, G. Stewart [*Appl. Opt. (USA)* vol.25 no.9 (1986) p.1495-8]
- [22] V. Hinkov, E. Ise [*J. Lightwave Technol. (USA)* vol.LT-4 no.4 (1986) p.444-8]
- [23] A.C.G Nutt, E. Sudo, K. Nishizawa [*OFC/IOOC'87 USA* (1987) p.64]
- [24] A.L. Dawar, S.M. Al-Shukri, R.M. De La Rue, A.C.G. Nutt, G. Stewart [*Opt. Commun. (Netherlands)* vol.61 no.2 (1987) p.100-4]
- [25] K. Yamamoto, T. Taniuchi [*1st Optoelectronic Conf. OEC 86* Post-Deadline Technical Digest (Japan, 1986) paper B11-4 p.16-7]
- [26] T. Taniuchi, K. Yamamoto [*Proc. Conf. on Lasers and Electro-Optics USA*, 1986, p.230]
- [27] S.M. Al-Shukri et al [*7th Topical Meeting on Integrated and Guided-Wave Optics* Kissimmee, FL, USA, 24-26 Apr. 1984, Technical Digest, Post-Deadline Papers (Opt. Soc. America, Washington DC, 1984) p.PD7.1-PD7.4]
- [28] A. Dawar, S.M. Al-Shukri, R.M. De La Rue [*Int. Workshop on Integrated Optical and Related Technologies for Signal Processing* (IEEE, New York, USA, 1984)]
- [29] P.K. Tien, R. Ulrich [*J. Opt. Soc. Am. (USA)* vol.60 no.10 (1970) p.1325-37]
- [30] J.M. White, P.F. Heidrich [*Appl. Opt. (USA)* vol.15 no.1 (1976) p.151-5]
- [31] C. Canali, A. Carnera, G. Della Mea, R.M. De La Rue, A.C.G. Nutt, J.R. Tobin [*Proc. SPIE - Int. Soc. Opt. Eng. (USA)* vol.460 (1984) p.49-55]
- [32] A. Yi-Yan, J. Primot, J. Burgeat, R. Guglielmi [*2nd European Conf. on Integrated Optics* Florence, Italy, 17-18 Oct. 1983, Post-Deadline Papers (IEE, London, 1983) 3pp]
- [33] N.A. Sanford, W.C. Robinson [*Opt. Lett. (USA)* vol.10 no.4 (1985) p.190-2]
- [34] C. Canali et al [*J. Appl. Phys. (USA)* vol.59 no.8 (1986) p.2643-9]
- [35] W.E. Lee, N.A. Sanford, A.H. Heuer [*J. Appl. Phys. (USA)* vol.59 no.8 (1986) p.2629-33]
- [36] M. Minakata, K. Kumagai, S. Kawakami [*Appl. Phys. Lett. (USA)* vol.49 no.16 (1986) p.992-4]
- [37] A. Loni, R.M. De La Rue, J.M. Winfield [*J. Appl. Phys. (USA)* vol.61 no.1 (1987) p.64-7]
- [38] A. Loni, R.M. De La Rue, J.M. Winfield [*Topical Meeting on Integrated and Guided-Wave Optics* (Opt. Soc. America, Washington DC, 1988) p.MD3.1-MD3.4]
- [39] A. Yi-Yan [*Appl. Phys. Lett. (USA)* vol.42 no.8 (1983) p.633-5]
- [40] J.L. Jackel, C.E. Rice [*Proc. SPIE - Int. Soc. Opt. Eng. (USA)* vol.460 (1984) p.43-8]
- [41] K.K. Wong, R.M. De La Rue [*1st Int. Conf. on Optical Fibre Sensors* London, UK, 26-28 Apr. 1983 (IEE, London, 1983) p.72-4]
- [42] R.A. Becker [*Appl. Phys. Lett. (USA)* vol.43 no.2 (1983) p.131-3]
- [43] M. Rottschalk, A. Rasch, W. Karthe [*J. Opt. Commun. (Germany)* vol.9 no.1 (1988) p.19-23]
- [44] R.L. Davis [*Proc. SPIE - Int. Soc. Opt. Eng. (USA)* vol.517 (1984) p.74-81]
- [45] K.K. Wong, R.M. De La Rue, S. Wright [*Opt. Lett. (USA)* vol.7 no.11 (1982) p.546-8]
- [46] R. Chen, C.S. Tsai [*Opt. Lett. (USA)* vol.11 no.8 (1986) p.546-8]
- [47] N.J. Parsons, K.K. Wong, A.C. O'Donnell [*Topical Meeting on Integrated and Guided-Wave Optics USA*, 1986, Post-Deadline Paper]
- [48] P.G. Suchoski, M.M. Abou el leil, T.K. Findakly, F.J. Leonberger [*Integrated and Guided-Wave Optics Conf.* USA, 1988, p.MD4.1-MD4.4]
- [49] P.J. Burnett, G.A.D. Briggs, S.M. Al-Shukri, J.F. Duffy, R.M. De La Rue [*J. Appl. Phys. (USA)* vol.60 no.7 (1986) p.2517-22]
- [50] E.Y.B. Pun, K.K. Wong, I. Andonovic, P.J.R. Laybourn, R.M. De La Rue [*Electron. Lett. (UK)* vol.18 no.17 (1982) p.740-2]
- [51] C. Warren, S. Forouhar, W.S.C. Chang, S.K. Kao [*Appl. Phys. Lett. (USA)* vol.43 no.5 (1983) p.424-6]
- [52] Z.D. Yu [*Opt. Commun. (Netherlands)* vol.47 no.4 (1983) p.248-50]
- [53] M. Papuchon [*Electron. Lett. (UK)* vol.19 no.16 (1983) p.612-3]
- [54] T. Findakly, B. Chen [*Electron. Lett. (UK)* vol.20 no.3 (1984) p.128-9]
- [55] J.J. Veselka, G.A. Bogert [*Electron. Lett. (UK)* vol.23 no.1 (1987) p.29-31]
- [56] P.G. Suchoski, T.K. Findakly, F.J. Leonberger [*Opt. Lett. (USA)* vol.13 no.2 (1988) p.172-4]
- [57] A. Mahapatra, W.C. Robinson [*Appl. Opt. (USA)* vol.24 no.15 (1985) p.2285-6]

15.1 Proton exchange in undoped LiNbO₃ (concentrated melt)

- [58] A. Mahapatra, W.C. Robinson [*Proc. SPIE - Int. Soc. Opt. Eng. (USA)* vol.578 (1985) p.70-4]
- [59] M. Haruna, H. Nakajima, H. Nishihara [*Appl. Opt. (USA)* vol.24 no.16 (1985) p.2483-4]
- [60] M. De Micheli, J. Botineau, S. Neveu, P. Sibillot, D.B. Ostrowsky, M. Papuchon [*Opt. Lett. (USA)* vol.8 no.2 (1983) p.116-8]
- [61] S. Neveu, J.P. Barety, M. De Micheli, P. Sibillot, D.B. Ostrowsky [*7th Topical Meeting on Integrated and Guided-Wave Optics* Kissimmee, FL, USA, 24-26 Apr. 1984 (Opt. Soc. America, Washington DC, 1984) Post-Deadline Papers p.PD6.1-PD6.3]
- [62] T. Taniuchi, K. Yamamoto [*12th European Conf. on Optical Communication* Barcelona, Spain, 22-25 Sept. 1986, Technical Digest, vol.1 (Telefonica, Madrid, Spain, 1986) p.171-4]
- [63] E.M. Korablev, Y.L. Kopylov, V.V. Proklov [*IEEE Int. Workshop on Integrated Optical and Related Technologies for Signal Processing* (IEEE, New York, USA, 1984)]
- [64] A. Dawar, R.M. De La Rue, G.F. Doughty, N. Finlayson, S.M. Al-Shukri, J. Singh [*Proc. SPIE - Int. Soc. Opt. Eng. (USA)* vol.517 (1984) p.64-73]
- [65] V. Hinkov, E. Ise [*J. Phys. D (UK)* vol.18 no.6 (1985) p.L31-4]
- [66] V. Hinkov, E. Ise, W. Sohler [*Proc. 3rd European Conf. on Integrated Optics* Berlin, Germany, 6-8 May 1985 (Springer-Verlag, Berlin, 1985) p.169-73]
- [67] M. Miyawaki, S. Ogura [*Appl. Phys. Lett. (USA)* vol.47 no.9 (1985) p.918-20]
- [68] A.L. Dawar, S.M. Al-Shukri, R.M. De La Rue [*Appl. Phys. Lett. (USA)* vol.48 no.23 (1986) p.1579-81]
- [69] C.S. Tsai, D.Y. Zang, P. Le [*Appl. Phys. Lett. (USA)* vol.47 no.6 (1985) p.549-51]
- [70] F.S. Hickernell, K.D. Ruehle, S.J. Joseph, S.M. Reese, J.F. Weller [*Proc. IEEE Ultrasonics Symp.* San Francisco, CA, USA, 16-18 Oct. 1985, vol.1 (IEEE, New York, USA, 1985) p.237-40]
- [71] V. Hinkov, R. Opitz, W. Sohler [*Proc. 4th European Conf. on Integrated Optics* Glasgow, Scotland, 11-13 May 1987 (Scottish Electron. Technol. Group, Glasgow, Scotland, 1987) p.111-4]
- [72] E.Y.B. Pun, T.C. Kong, P.S. Chung, H.P. Chan [*Electron. Lett. (UK)* vol.26 no.2 (1990) p.81-2]
- [73] E.Y.B. Pun, K.K. Loi, P.S. Chung [*Electron. Lett. (UK)* vol.27 no.2 (1991) p.168-70]
- [74] E.Y.B. Pun, Y.O. Tse, P.S. Chung [*IEEE Photonics Technol. Lett. (USA)* vol.3 no.6 (1991) p.522-3]
- [75] E.Y.B. Pun, K.K. Loi, P.S. Chung [*Electron. Lett. (UK)* vol.27 no.14 (1991) p.1282-3]
- [76] E.Y.B. Pun, K.K. Loi, S.A. Zhao, P.S. Chung [*Appl. Phys. Lett. (USA)* vol.59 no.6 (1991) p.662-4]
- [77] E.Y.B. Pun, K.K. Loi, S.A. Zhao, P.S. Chung [*IEEE Photonics Technol. Lett. (USA)* vol.3 no.11 (1991) p.1006-8]
- [78] K.K. Loi, E.Y.B. Pun, P.S. Chung [*Electron. Lett. (UK)* vol.28 no.6 (1992) p.546-8]
- [79] E.Y.B. Pun, C.K. Chan, P.S. Chung [*Jpn. J. Appl. Phys. (Japan)* vol.31 no.5B (1992) p.1591-2]
- [80] E.Y.B. Pun, K.K. Loi, P.S. Chung [*Microw. Opt. Technol. Lett. (USA)* vol.5 no.10 (1992) p.490-3]
- [81] E.Y.B. Pun, K.K. Loi, P.S. Chung [*J. Lightwave Technol. (USA)* vol.11 no.2 (1993) p.277-84]
- [82] E.Y.B. Pun, K.K. Loi, C.F. Mak, P.S. Chung [*J. Appl. Phys. (USA)* vol.73 no.6 (1993) p.3114-6]
- [83] K.K. Loi, E.Y.B. Pun, P.S. Chung [*Microw. Opt. Technol. Lett. (USA)* vol.6 no.6 (1993) p.378-81]
- [84] V.M.N. Passaro, M.N. Armenise, D. Nesheva, I.T. Savatinova, E.Y.B. Pun [*J. Lightwave Technol. (USA)* vol.20 no.1 (2002) p.71-7]

15.2 Proton exchange in undoped LiNbO₃ (dilute melt)

K.K. Wong

March 2002

A WAVEGUIDE FORMATION AND STUDIES

The overall rate of the proton exchange process in LiNbO₃ can be controlled by: (1) the concentration of solvated protons available at the LiNbO₃ surface and (2) the outdiffusion rate of lithium ions. Researchers have chosen to introduce extra lithium ions into the protonic source, i.e. mixing benzoic acid with lithium benzoate as defined by the equation below:

$$X_d = (\text{mole of lithium benzoate}) / (\text{mole of benzoic acid}) \times 100\%$$

where X_d can range from 0.1 to 5% [1-8]. The process has since been called the dilute melt proton exchange (DMPE) method. Optical waveguides and devices fabricated by the DMPE method in X-[3,4,6,7], Y- [5] and Z-cut [3,4,6,7] LiNbO₃ have been reported with very promising results. Problems such as refractive index instability, DC extinction effect and reduced electro-optic activity which are associated with optical waveguides fabricated by concentrated benzoic acid melts were eliminated or reduced in magnitude when diluted benzoic acid melts were used instead [3,6,7].

Both infrared spectroscopy and optical prism coupling methods have been used by a number of researchers to partially or fully characterise the DMPE process in both X- and Z-cut LiNbO₃ [3,4,8]. TABLE 1 shows the values of diffusion coefficients for various X_d values at exchange temperatures of 215°C and 235°C obtained by Loni et al [8]. TABLE 2 shows the values of diffusion coefficients at various exchange temperatures with an X_d value of 0.5% [4].

In general, it can be concluded that the diffusion of a protonic source slows the proton exchange process by three to twenty times, depending also on the cut of lithium niobate used. TABLE 3 shows a summary of a comparison of diffusion coefficients for 0.5% and 1.0% dilutions for both X- and Z-cut LiNbO₃ [3].

The results of TABLES 1, 2 and 3 indicate that there are differences in the diffusion coefficients of the DMPE results from the various researchers. A possible explanation for the differences may be due to the actual container or vessel in which the diluted benzoic acid was held since a container that holds a small volume of diluted benzoic acid which is not properly sealed can lose a significant amount of benzoic acid and hence will result in a different X_d dilution value. The best method for DMPE experiments is to carry out the exchange in a sealed ampoule.

It was confirmed experimentally that only TE and TM modes were excited in DMPE waveguides fabricated in X- and Z-cut LiNbO₃, respectively [1-8]. The DMPE optical waveguides were found to be stable over a measured period of ten months, i.e. no variation of effective refractive index with respect to time after fabrication [3]. The Δn values for the fabricated waveguides were around 0.12 at dilutions less than 1.0% [3,8]. For larger dilutions of 2% and 5% the Δn values were reported to be 0.08 and 0.01, respectively [1]. Optical propagation losses of the DMPE waveguides were found to be low, i.e. less than 1.0 dB/cm at 633 nm [3], and with appropriate annealing, losses of 0.2 dB/cm and 0.15 dB/cm at 633 nm and 820 nm, respectively, have been reported [6,7]. In-plane scattering results of DMPE (X_d = 0.5% and 1.0%) slab waveguides were measured to be between 21 dB and 35 dB for a scattering angle of 0.5° [3]. In general, there is no trend in increase of in-plane scatter losses with increase in dilution or temperature [3]. Optical power densities of 40 kW/cm² and

15.2 Proton exchange in undoped LiNbO₃ (dilute melt)

TABLE 1 Variation in diffusion coefficients with various Xd values (X-cut LiNbO₃) [8].

Temperature of exchange (°C)	Xd (%)	Diffusion coefficient (μm ² /h)
215	0	0.495
	0.28	0.123
	0.51	0.063
	0.73	0.049
	1.04	0.028
235	0	1.119
	0.23	0.224
	0.57	0.138
	0.73	0.099
	1.12	0.054

TABLE 2 Diffusion coefficients at various temperatures (Xd = 0.5%, X-cut LiNbO₃) [4].

Temperature of exchange (°C)	Diffusion coefficient (μm ² /h)
160	0.004
170	0.007
180	0.011
190	0.016
200	0.024
210	0.036
220	0.052
230	0.074
240	0.103

TABLE 3 Diffusion coefficients for different DMPE fabrication conditions [3].

LiNbO ₃ cut	Dilution %	D _d , μm ² /h (235°C, dilute melt)	D _c , μm ² /h (235°C, conc. melt)	R = D _c /D _d
X	0.5	0.201	0.997	4.96
	1.0	0.103	0.997	9.68
Z	0.5	0.129	0.397	3.08
	1.0	0.067	0.397	5.93

35.2 kW/cm² were propagated in DMPE waveguides at 633 nm and 514.5 nm without any measurable optical damage effects [3].

B ELECTRO-OPTIC ACTIVITY AND OPTICAL DEVICES

The electro-optic effect in single-mode DMPE waveguides was studied by a number of researchers. Loni et al [6] measured the r₃₃ electro-optic coefficient of slab DMPE waveguides and deduced that it was essential to anneal the waveguides to restore the electro-optic activity. TABLE 4 summarises the measured r₃₃ electro-optic coefficients of a number of Z-cut DMPE LiNbO₃ waveguides.

Other researchers fabricated integrated optical Mach-Zehnder interferometers in both X- and Z-cut LiNbO₃ using the DMPE method. The measured V(pi) values were consistent with an r₃₃ value of around 30 × 10⁻¹² m/V [3,7]. Again in both cases, the devices were annealed at temperatures in the range 350°C to 400°C.

15.2 Proton exchange in undoped LiNbO_3 (dilute melt)

TABLE 4 Measured (at 633 nm) r_{33} values of Z-cut proton-exchanged LiNbO_3 waveguides [6].

Fabrication conditions	r_{33} (10^{-12} m/V)	r_{33}^* (10^{-12} m/V)
PE, 0%	2.46	9.25
PE, 0.94%	1.64	22.33
PE, 0%	2.01	16.09
PE, 0.55%	2.02	23.16
PE, 1.01%	1.43	24.58

PE: proton-exchange was carried out at 235°C.

*After annealing at 275°C for 30 min and 375°C for 15 min.

As a specific example, a number of travelling-wave optical Mach-Zehnder interferometers operating with a 3 dB bandwidth of 10 GHz were fabricated using a 1% dilute benzoic acid melt in X-cut LiNbO_3 [10,11]. The devices have a waveguide width of 4 microns and an active length of 8 mm. The measured $V(\pi)$ of the devices at an operating wavelength of 830 nm was 1.7 V (similar devices fabricated in Ti:LiNbO₃ waveguides yielded devices with a $V(\pi)$ of 1.8 V). These results suggest that the electro-optic activity in dilute melt devices is preserved. In addition these devices have been annealed as part of the buffer layer (SiO_2) deposition process using a chemical vapour deposition system operated at around 350°C.

Burnett et al studied the acoustic properties of X-, Y- and Z-cut DMPE ($X_d = 0.25\%$) optical waveguides using acoustic microscopy in the $V(z)$ mode [9]. The acoustic properties of all crystals were found to be modified by the DMPE process. For X- and Y-cut DMPE LiNbO_3 waveguides, both increases and decreases in surface acoustic wave (SAW) propagation velocity are possible, while in Z-cut DMPE LiNbO_3 waveguides only decreases are observed. It was also found that decreases in SAW velocity are accompanied by increases in the measured acoustic attenuation for waves propagating in the Y- and X-directions on X- and Y-cut DMPE LiNbO_3 waveguides, respectively. In addition, the sign of the acoustic birefringence can be reversed by the DMPE process. No acousto-optic devices have been demonstrated using the DMPE process.

C IN-PLANE SCATTERING MEASUREMENTS

In-plane scattering of dilute melt optical waveguides in X- and Z-cut LiNbO_3 was studied using a scanning photodetector (with a 5 micron slit) and a lock-in amplifier arrangement [3]. The study indicated that there is no trend in increase of in-plane scatter losses with increase in dilution or temperature. This is best described in TABLES 5 and 6 which show measured in-plane scatter levels of X- and Z-cut LiNbO_3 substrates fabricated in a 1.0% diluted benzoic acid melt at 235°C. Here the only variation is the time of exchange. Such results indicate that high performance spectrum analysis optical circuits can be fabricated in LiNbO_3 .

TABLE 5 Summary of in-plane scatter results for an in-plane angle of 0.5°, Z-cut, 235°C, 1%, $\lambda_0 = 632.8 \text{ nm}$.

Exchange time (hours)	TM_0 (dB)	TM_1 (dB)	TM_2 (dB)	TM_3 (dB)	TM_4 (dB)
18.0	28	27	23	21	18
11.0	21	27	28	30	-
6.0	27	24	27	-	-

15.2 Proton exchange in undoped LiNbO_3 (dilute melt)

TABLE 6 Summary of in-plane scatter results for an in-plane angle of 0.5° , X-cut, 235°C , 1%, $\lambda_0 = 632.8 \text{ nm}$.

Exchange time (hours)	TE ₀ (dB)	TE ₁ (dB)	TE ₂ (dB)	TE ₃ (dB)	TE ₄ (dB)	TE ₅ (dB)
18.0	22	21	23	29	26	25
11.0	30	30	29	29	27	-
6.0	29	29	28	28	-	-

REFERENCES

- [1] M. De Micheli, J. Botineau, S. Neveu, P. Sibillot, D.B. Otrowsky, M. Papuchon [*Opt. Lett.* (USA) vol.8 no.2 (1983) p.114-5]
- [2] J.L. Jackel, C.E. Rice, J.J. Veselka [*Electron. Lett.* (UK) vol.19 no.10 (1983) p.387-8]
- [3] K.K. Wong [*GEC J. Res.* (UK) vol.3 no.4 (1985) p.243-50]
- [4] S.M. Al-Shukri, J. Duffy, R.M. De La Rue, M.N. Armenise, C. Canali, A. Carnera [*Proc. SPIE - Int. Soc. Opt. Eng.* (USA) vol.578 (1985) p.2-6]
- [5] M. Varasi, A. Annunzi, A. Vannucci, S. Reid [*Proc. SPIE - Int. Soc. Opt. Eng.* (USA) vol.866 (1987) p.110-6]
- [6] A. Loni, R.M. De La Rue, J.M. Winfield [*Integrated and Guided Wave Optics Conf.* USA, 1988, p.MD3-1 - MD3-4]
- [7] P.G. Suchoski, M.M. Abou el leil, T.K. Findakly, F.J. Leonberger [*Integrated and Guided Wave Optics Conf.* USA, 1988, p.MD4-1 - MD4-4]
- [8] A. Loni, R.M. De La Rue, J.M. Winfield [*J. Lightwave Technol.* (USA) vol.7 no.6 (1989)]
- [9] P.J. Burnett, G.A.D. Briggs, S.M. Al-Shukri, J.F. Duffy, R.M. De La Rue [*J. Appl. Phys.* (USA) vol.60 no.7 (1986) p.2517-22]
- [10] A.C. O'Donnell, K.K. Wong, N.J. Parsons [*IEE Colloquium on Optical Control and Generation of Microwave Signals* UK, 14 January 1986]
- [11] N.J. Parsons, K.K. Wong, A.C. O'Donnell [*Topical Meeting on Integrated and Guided-Wave Optics* Atlanta, GA, USA, 26-28 February 1986, post-deadline paper]

15.3 Proton exchange in Ti-indiffused and MgO-doped LiNbO₃

V. Hinkov

This Datareview appeared in *Properties of Lithium Niobate* (INSPEC, IEE, London, UK, 1989) and is reproduced here for the reader's convenience.

A INTRODUCTION

Proton exchange (in this Datareview, benzoic acid is understood as the proton source) can be performed not only on normal LiNbO₃ but also on doped crystals, which adds to the versatility of this technology. Up to now, the influence of two dopants on the proton exchange process has been investigated, namely Ti and MgO. The results of these investigations are published in [1-16].

B Ti-INDIFFUSED LiNbO₃

Ti-indiffusion is performed prior to the proton exchange as its processing temperature is much higher. The waveguides produced in this combined process are called TIPE (titanium indiffused proton exchanged) [1]. The most pronounced physical effect of the Ti-doping consists in reducing the proton diffusion rate. Y-cut samples have been investigated in greater detail [1,4,9,10], but the same effect is observed on X-cut samples as well [1]. The decrease of the proton diffusion coefficient D(T) with the increase of the amount of the Ti-indiffusion is given in TABLE 1 in units of μm²/h for Y-cut samples [7].

TABLE 1

Initial thickness of titanium before diffusion, nm	D (220°C)	D (250°C)
0	0.65	1.60
30	0.40	1.20
50	0.30	0.90

No exact conditions for the Ti-indiffusion are given in this paper. In [10] 25 nm of titanium were indiffused for ten hours in a wet atmosphere at 1000°C resulting in the following proton diffusion coefficients for Y-cut samples, again expressed in μm²/h:

$$\begin{aligned}D(160^\circ\text{C}) &= 0.048 \\D(180^\circ\text{C}) &= 0.082 \\D(200^\circ\text{C}) &= 0.144 \\D(220^\circ\text{C}) &= 0.29\end{aligned}$$

The diffusion constant and the activation energy are found in this study to be $9.5 \times 10^{-9} \mu\text{m}^2/\text{h}$ and 0.5432 eV, respectively. In [9] D (250°C) = 0.55 μm²/h was measured for Y-cut samples prediffused with 25 nm Ti at 1060°C for eight hours in dry argon.

Ti-doping prevents the surface destruction of Y-cut samples exchanged in pure benzoic acid [1]. This destruction is due to the large positive strain ($\Delta a/a = 1.56\%$) produced by the proton exchange [16]. Since titanium indiffusion causes a negative strain, a compensation occurs preventing the surface destruction. TIPE waveguides combine to some extent the properties of Ti-indiffused and proton-exchanged waveguides: large index change [1], higher resistance to optical damage [5], guidance of extraordinary as well as ordinary modes [1,2,9,15]. The latter property is very important. It allows

for example the extension of the second-harmonic phase matching range in LiNbO₃ to well over 2 μm [2,3]. In [9] it has been shown that the waveguide birefringence can be precisely controlled in the range 0 - 5 × 10⁻².

TIPE waveguides have been used in a collinear acousto-optic mode converter [13], an acousto-optic deflector [11], waveguide lenses [6,12,14], second harmonic generation [2,3] and combined optical and acoustic strip waveguides for efficient collinear acousto-optical interactions [15].

C MgO-DOPED LiNbO₃

The effect of MgO doping on proton exchange was investigated for crystals pulled from a congruent melt to which 5% MgO had been added. X- and Y-cut samples have been investigated [7,8]. Both cuts have shown approximately the same diffusion coefficient D (250°C) = 0.81 μm²/h whereas the value measured in undoped crystals is 1.37 μm²/h.

MgO-doped Y-cut samples did not suffer the surface etch [8] of the undoped samples when exchanged in pure acid.

Proton-exchanged waveguides produced in undoped LiNbO₃ from pure benzoic acid are unstable, i.e. their effective indices fluctuate with time. No fluctuation was observed in waveguides produced on MgO-doped substrates [7]. Furthermore, such guides show an improvement of factor 2 in field photorefractive sensitivity as compared to undoped LiNbO₃ [8]. The same large index change and the same step-like profile as found in normal LiNbO₃ have been observed in MgO-doped samples exchanged in pure benzoic acid [7,8].

REFERENCES

- [1] M. de Micheli, J. Botineau, P. Sibillot, D.B. Ostrowsky [*Opt. Commun. (Netherlands)* vol.42 no.2 (1982) p.101-3]
- [2] M. de Micheli et al [*Opt. Lett. (USA)* vol.8 no.2 (1983) p.116-8]
- [3] M. de Micheli [*J. Opt. Commun. (Germany)* vol.4 no.1 (1983) p.25-31]
- [4] M. Goodwin, C. Stewart [*Electron. Lett. (UK)* vol.19 no.6 (1983) p.223-5]
- [5] J.L. Jackel et al [*J. Appl. Phys. (USA)* vol.55 no.1 (1984) p.269-70]
- [6] D.Y. Zang [*Opt. Commun. (Netherlands)* vol.47 no.4 (1983) p.248-50]
- [7] J.L. Jackel [*Electron. Lett. (UK)* vol.21 no.11 (1985) p.509-11]
- [8] M. Digonnet, M. Fejer, R. Byer [*Opt. Lett. (USA)* vol.10 no.5 (1985) p.235-7]
- [9] V. Hinkov, E. Ise [*J. Lightwave Technol. (USA)* vol.LT-4 no.4 (1986) p.444-8]
- [10] A.L. Dawar, S.M. Al-Shukri, R.M. De La Rue, A.C.G. Nutt, G. Stewart [*Appl. Opt. (USA)* vol.25 no.9 (1986) p.1495-9]
- [11] M. Miyawaki, S. Ogura [*Appl. Phys. Lett. (USA)* vol.47 no.9 (1985) p.918-9]
- [12] D.Y. Zang, C.S. Tsai [*Appl. Phys. Lett. (USA)* vol.46 no.8 (1985) p.703-5]
- [13] V. Hinkov, E. Ise, W. Sohler [*Springer Ser. Opt. Sci. (Germany)* vol.48 (1985)]
- [14] D.Y. Zang, C.S. Tsai [*Appl. Opt. (USA)* vol.25 no.14 (1986) p.2264-71]
- [15] V. Hinkov, R. Optiz, W. Sohler [*Proc. 4th European Conf. on Integrated Optics* Glasgow, Scotland, 11-13 May 1987, Eds C.D.W. Wilkinson, J. Lamb (Scottish Electron. Technol. Group, Glasgow, 1987) p.111-4]
- [16] A. Campari et al [*J. Appl. Phys. (USA)* vol.58 no.12 (1985) p.4521-4]

15.4 Kinetics of Ti-indiffusion in LiNbO₃

M.N. Armenise

This Datareview appeared in *Properties of Lithium Niobate* (INSPEC, IEE, London, UK, 1989) and is reproduced here for the reader's convenience.

Ti indiffusion into lithium niobate produces a surface layer a few microns thick with higher refractive indices than the substrate: $\Delta n(e) < 0.04$; $\Delta n(o) < 0.02$.

The formation of low-loss slab and stripe waveguides in LiNbO₃ by means of titanium indiffusion has been extensively investigated since 1974 when it was first demonstrated [1]. Many guided-wave devices both passive and active have been demonstrated. The characteristics and the performance of integrated optic devices are strongly related to a complete knowledge of the Ti indiffusion mechanism. However, despite various efforts the relationships between structural and optical properties in Ti:LiNbO₃ waveguides have not yet been well established.

Diffusion of sputtered or evaporated thin films (100 - 1000 Å) of titanium in lithium niobate is generally carried out, in reactive or inert atmosphere, at temperatures ranging from 900 to 1150°C. While the lower limit depends mainly on the possible formation of more or less stable compounds, the upper limit is related to the Curie temperature and to the increase of optical losses due to lithium evaporation and structure modifications. Diffusion times range from 0.5 to 30 hours. In [2] some fabrication parameters are reported.

Electron microprobe measurements of Ti concentration profile as a function of depth in the diffused layers showed a good approximation to Gaussian distribution when the Ti diffusion can be considered as a limited source process, in the absence of outdiffusion of lithium or lithium oxide [3-6], and the diffusion time is longer than the time interval in which Ti is entirely penetrated into the substrate. While similar values of activation energy are reported in the literature, large discrepancies in the published values of the depth diffusion coefficients may be found. The comparison of self-consistent sets of values shows that the differences may be due to the crystal composition and the measurement technique. In [7] some values of the diffusion coefficient obtained under the same fabrication conditions by different techniques in samples of different orientations (y- and z-cut) are reviewed. The values of the Ti diffusion coefficient D at 1050°C in x-, y- and z-cut LiNbO₃ crystals with a composition slightly different from the congruent one (48.6 mol% Li₂O) are reported in TABLE 1 [8].

TABLE 1 Titanium diffusivity at 1050°C as a function of crystal orientation and composition.

Cut	Mol% Li ₂ O	D (10 ⁻¹² cm ² /s)
z	48.1	2.22
x	48.3	1.39
y	48.3	1.47
x	50.0	0.44
y	50.0	0.39
z	50.0	0.42

The Ti diffusivity in crystals having a congruent composition, at 1050°C, is about 1.1×10^{-12} cm²/s for all orientations. The corresponding activation energy, which may be evaluated from Arrhenius plots, is about 2.2 eV.

Since Ti ions substitute for Nb ions in the lithium niobate lattice, the refractive index change has been attributed to the increase of polarisability and to the photoelastic effect caused by the different ionic radii of Ti and Nb ions [3]. Another hypothesis [9] is that the refractive index change is due partly to the polarisability change and partly to a structure rearrangement (rotation of oxygen octahedra) to accommodate Ti ions. A reduction of lattice parameter, $a(h)$, is produced. However, this lattice contraction does not significantly affect the waveguiding action when diffusion time is sufficiently prolonged [10]. Although a conclusive work on index change sources is not yet available, the relationships between refractive index changes and Ti concentrations have been established. In particular, Minakata et al [11] determined, in y-cut samples, a linear variation only for the extraordinary index change $\Delta n(e)$, and $\Delta n(o) = \Delta n(e) = 4.5 \times 10^{-3}$ at 0.75% Ti concentration.

Since the electron microprobe technique has a finite resolution capability, thin guiding layers cannot be accurately studied. So, various microanalytical techniques have been used to carry out more detailed observations of Ti concentration profile and compound formed during the thermal process. Burns et al [12], using the secondary ion mass spectroscopy (SIMS) technique, determined a Gaussian in-depth Ti profile with an additional peak attributed to the formation of the compound LiTiO_3 . No evidence for that compound was found by Armenise et al [13,14] who analysed the sample morphology, the compound formation, the atomic composition profiles and the structural characteristics of the phases formed, using various techniques such as scanning electron microscopy (SEM), Rutherford backscattering spectroscopy (RBS), Auger electron spectroscopy (AES), SIMS and glancing angle X-ray diffraction.

For thermal diffusion in a dry O_2 atmosphere the main interaction between Ti and LiNbO_3 is the formation of a mixed oxide $\text{Ti}_x\text{Nb}_{1-x}\text{O}_2$. The intermediate stages of the process can be summarised as follows:

- For low temperature thermal treatments Ti oxidation occurs. The Ti oxidation process starts at temperatures higher than 300°C. At temperatures around 500°C Ti oxidises, forming a small-grained polycrystalline TiO_2 ($x = 1$) layer. The oxidation mechanism occurs by capturing oxygen atoms both from the surrounding atmosphere and from the LiNbO_3 substrate. This last effect produces an accumulation of Nb at the Ti/LiNbO_3 interface, while Li, because of its high mobility, diffuses through Ti or Ti oxide film. The change of O concentration in the diffusion gas (O_2 , Ar or air) only causes a change of the amount of the O atoms captured by the bulk.
- The LiNb_3O_8 phase has been detected as large epitaxial crystallites at temperatures from 600 to 800°C in both Ti-coated and uncoated samples. Its precipitation is consistent with the $\text{Nb}_2\text{O}_5/\text{Li}_2\text{O}$ phase diagram, as observed in [15]. For temperatures higher than 800°C the compound LiNb_3O_8 decomposes and vanishes. Its formation induces large stress and microfractures in TiO_2 films appearing as a possible source of the Ti inhomogeneities in the guiding layer.
- The LiNb_3O_8 formation is followed by the growth of the $\text{Ti}_{0.65}\text{Nb}_{0.35}\text{O}_2$ epitaxial compound which continuously grows with temperature up to 1000°C when it is the only phase present at the crystal surface and, consequently, it may be considered as the real source of Ti indiffusion. When the annealing time increases at 1000°C a decomposition of the $\text{Ti}_{0.65}\text{Nb}_{0.35}\text{O}_2$ phase occurs.

During the diffusion process a simultaneous outdiffusion of Li or Li_2O from the lithium niobate crystal surface occurs. This outdiffusion constitutes a serious problem which affects the performance of stripe waveguide devices because it produces an unwanted surface guiding layer for the extraordinary wave. Several attempts to compensate for the extraordinary index increase due to lithium outdiffusion have been made. They have been critically reviewed by Jackel [16]. Ti indiffusion in wet atmosphere (pure O_2 bubbling through a fixed volume of pure water at 80 - 90°C) is the most recent technique to avoid the formation of outdiffused guiding layers. The presence of water

vapour inhibits and decomposes the LiNb_3O_8 compound, and causes an indiffusion of protons in LiNbO_3 . Protons form (OH)- defects and $\text{Li}_{1-y}\text{H}_y\text{NbO}_3$ molecules, which can destroy the LiNb_3O_8 phase when it is present [17]. In samples annealed in a wet atmosphere the ternary compound $\text{Ti}_x\text{Nb}_{1-x}\text{O}_2$ forms at temperatures higher than in the dry atmosphere case. In particular, for z-cut substrates, the titanium oxide TiO_2 ($x = 1$) keeps constant up to 800°C. The x value decreases only at temperatures >850°C and reaches $x = 0.65$ before its decomposition. Recently Read et al [18], using the elastic recoil detection analysis (ERDA) and the RBS technique, inferred that during the early stages of diffusion both H and Ti assume a similar depth profile. They postulated also the formation of a titanate phase Li_2TiO_3 or LiTi_3O_7 not detectable by X-ray analysis because of its low level.

REFERENCES

- [1] R.V. Schmidt, I.P. Kaminow [*Appl. Phys. Lett. (USA)* vol.25 no.8 (1974) p.458-60]
- [2] G.J. Griffiths, R.J. Esaile [*IEEE J. Quantum Electron. (USA)* vol.QE-20 no.2 (1984) p.149-59]
- [3] K. Sugii, M. Fukuma, H. Iwasaki [*J. Mater. Sci. (UK)* vol.13 no.3 (1978) p.523-33]
- [4] H. Naitoh, M. Nunoshita, T. Nakayama [*Appl. Opt. (USA)* vol.16 (1977) p.2546-9]
- [5] M. Fukuma, J. Noda, H. Iwasaki [*J. Appl. Phys. (USA)* vol.49 no.7 (1978) p.3693-8]
- [6] M. Minakata, S. Saito, M. Shikata [*J. Appl. Phys. (USA)* vol.50 no.5 (1979) p.3063-7]
- [7] J. Ctyroky, M. Hofman, J. Janta, J. Schrofel [*IEEE J. Quantum Electron. (USA)* vol.QE-20 no.4 (1984) p.400-9]
- [8] R.J. Holmes, D.M. Smyth [*J. Appl. Phys. (USA)* vol.55 no.10 (1984) p.3531-5]
- [9] A.D. McLachlan, R.M. De La Rue, J.A.H. Wilkinson [*Proc. 1st European Conf. Integrated Optics* London, England, 14-15 Sept. 1981 (IEE, London, 1981) p.4-7]
- [10] R.J. Esaile, A.D. McLachlan, R.M. De La Rue [*Proc. 5th Topical Meeting on Integrated and Guided-Wave Optics* Incline Village, Nevada (Jan. 1980) p.WB3-1/4]
- [11] M. Minakata, S. Saito, M. Shibata, S. Miyazawa [*J. Appl. Phys. (USA)* vol.49 no.9 (1978) p.4677-82]
- [12] W.K. Burns, P.H. Klein, E.J. West, L.E. Plew [*J. Appl. Phys. (USA)* vol.50 no.10 (1979) p.6175-82]
- [13] M.N. Armenise, C. Canali, M. De Sario, A. Carnera, P. Mazzoldi, G. Celotti [*J. Appl. Phys. (USA)* vol.54 no.1 (1983) p.62-70]
- [14] M.N. Armenise et al [*J. Appl. Phys. (USA)* vol.54 no.11 (1983) p.6223-31]
- [15] R.J. Esaile [*J. Appl. Phys. (USA)* vol.58 no.2 (1985) p.1070-1]
- [16] J.L. Jackel [*J. Opt. Commun. (Germany)* vol.3 no.3 (1982) p.82-5]
- [17] M. De Sario et al [*J. Appl. Phys. (USA)* vol.57 no.5 (1985) p.1482-8]
- [18] P.M. Read, S.P. Speakman, M.D. Hudson, L. Considine [*Nucl. Instrum. Methods Phys. Res. B (Netherlands)* vol.15 (1986) p.398-403]

15.5 Characteristics of LiNbO₃ optical waveguides

M.N. Armenise

This Datareview appeared in *Properties of Lithium Niobate* (INSPEC, IEE, London, UK, 1989) and is reproduced here for the reader's convenience.

Recent developments in hybrid integrated optics technology confirmed lithium niobate as appropriate material for applications in the area of telecommunications as well as signal processing and sensing. Several waveguide devices in lithium niobate have been demonstrated in the last few years [1-3]. The performance of guided-wave devices strongly depends on the characteristics of the waveguide which constitutes the essential element of such devices.

A complete characterisation of lithium niobate waveguides includes both the theoretical investigation, and structural and optical measurements to determine the optical parameters and relate them to the structural properties.

Several numerical methods have been used to evaluate the propagation characteristics of optical waveguides in lithium niobate.

The microwave network methods provide a physical insight into the electromagnetic problems by considering analogous transmission lines and lumped equivalent networks, and taking into account analytically the physical differences between microwave and optical waveguides [4].

The similarities between Schrodinger's equation and the scalar wave equation lead to a correspondence between the wave function and the electromagnetic field components in optical waveguides. Therefore various techniques used to solve quantum-mechanical problems have been applied for the determination of approximate solutions of electromagnetic problems in optical waveguides. Among them we mention the WKB analysis [5], perturbation theory [6] and the variational technique [7].

Besides these methods, other powerful methods based on the numerical integration of two coupled first-order differential equations have been reported [8,9].

Optical characterisation of optical waveguides includes the determination of the mode number and effective index, the in-depth index profile, the optical losses including scattering levels, and the induced photorefractive effects.

The number and effective index of guided modes can be easily found by the m-line technique [10] using rutile prism couplers.

The index profile in multimode guides may be obtained using a best fitting technique in combination with the inverse WKB method [11]. The evaluation of the index profile in monomode guides requires a number of measurements at different wavelengths and the comparison between experimental and calculated values of the effective index [12]. The numerical technique utilised in the mode calculation can affect the index profile evaluation to a considerable extent. The choice of the numerical procedure also depends on the waveguide fabrication technology. However, a systematic study of the theoretical analysis sensitivity to the waveguide fabrication conditions has not yet been carried out.

Optical losses may be measured by either evaluating the total throughput of the guide or measuring the scattered light as a function of distance along the waveguide. Several techniques have been proposed utilising each of these approaches [13-15]. Himel et al [16] proposed an accurate, non-

destructive and easy to use method employing a coherent optical fibre bundle to image the streak of light away from the waveguide.

Scattering of guided modes can remarkably affect the performance of integrated optics devices and systems, and therefore represents a fundamental element in the waveguide optical characterisation mainly for planar waveguides. In-plane [17] and out-of-plane [18] light scattering are the two basic types of scattering that can take place in a slab waveguide. Since the out-of-plane scattered light results in substrate radiation modes, and material absorption in lithium niobate at visible and near-IR is very low, in-plane scattering which is relative to the guided light represents the main source of loss in planar waveguides.

Various fabrication techniques of optical waveguides in lithium niobate have been tried [19-21]. Most of the guided-wave devices on lithium niobate have been fabricated on a waveguide formed by Ti indiffusion (TI) or proton exchange in benzoic acid (PE), because other waveguide fabrication processes are, so far, not well assessed.

Optical waveguides formed by indiffusion of Ti thin films into lithium niobate are preferred for a wide range of applications. Both TE and TM modes can propagate in Ti:LiNbO_3 guides which present small modifications in refractive indices (~ 0.01) and low optical damage resistance.

The dependence of the effective index of both TE and TM guided modes on diffusion time t_d , for samples prepared in dry O_2 ambient, consists of a decrease of the index with increasing t_d . Naitoh et al [22] showed the relationships between surface index change, diffusion depth and fabrication conditions. A review of Ti indiffusion fabrication parameters and an analysis of some characteristics of diffused waveguides are reported by Griffiths et al [23]. They indicated two different mechanisms for refractive index change in Y-cut waveguides inferring that the surface extraordinary index change is related to the titanium-to-niobium ratio, and is sensitive to the oxidation state of the crystal. Moreover they observed that for long diffusion times the index profile is better modelled by an exponential function rather than by a Gaussian function.

During Ti indiffusion a simultaneous outdiffusion of lithium oxide from the crystal surface occurs causing the formation of an unwanted surface guiding layer which strongly reduces the performance of devices utilising stripe waveguides.

Among the various methods proposed to suppress outdiffusion a very effective and simple method appears to be Ti diffusion in the presence of water vapour [24]. A wet atmosphere inhibits and decomposes the LiNb_3O_8 phase which affects the waveguide propagation characteristics [25], and then influences the formation mechanism of the Ti:LiNbO_3 guide [26]. However, no conclusive work has been done so far on extraordinary index changes induced by the presence of water vapour during the annealing. Eknayan et al [27] analysed the characteristics of deep Ti:LiNbO_3 waveguides diffused in dry and wet oxygen. They found larger diffusion coefficients and surface index changes in samples diffused in wet O_2 for both ordinary and extraordinary waves. They also observed outdiffused modes in the wet case.

Several microanalytical techniques have been used to study the kinetics of Ti indiffusion into lithium niobate [28]. Much effort was spent in understanding the Ti indiffusion mechanism [29-33], but, so far, the relationships between technological process and waveguide properties have not been established in a conclusive manner. Sugii et al [34] found a Gaussian Ti concentration depth profile when t_d is longer than the time interval required for the metal film to enter the crystal. A linear variation of the extraordinary index change with Ti concentration has been determined by Minakata et al [35] in Y-cut samples. They observed a Gaussian index profile with maximum index change $\Delta n(e) = 1.0 \times 10^{-2}$ and $\Delta n(o) = 7.7 \times 10^{-3}$ for a Ti concentration of 1.5% (initial thickness 500 Å) in samples annealed at 1000°C in air for ten hours. However, chemical compounds formed during the

diffusion process, electroneutrality of the Ti^{++++} inclusions, and impurities such as divalent iron strongly reduce the waveguide performance [36].

Photorefractive effects [37] in Ti:LiNbO_3 guides generate unacceptable instabilities in the devices. When such waveguides are exposed to high-intensity radiation in the visible and near-IR regions, the photoionisation of iron impurities in the Fe^{++} state to the Fe^{+++} state occurs, releasing a mobile electron which drifts in the positive optic axis direction out of the illuminated zone. The electric field relative to the mobile electrons produces modifications of the refractive index because of the electrooptic effect and phase velocity changes in the guided light. Therefore the photorefractive effect has both photovoltaic and photoconductive components, and depends on the wavelength and optical power. Becker [38] reviewed two methods for measuring the photorefractive susceptibility of Ti:LiNbO_3 waveguides. It has been well established that guides annealed in wet oxygen ambient show a considerably higher optical damage resistance than guides prepared in dry O_2 . This effect is mainly due to an indiffusion of protons in lithium niobate [39].

However, despite the decrease of photorefractive susceptibility due to the presence of water vapour, the optimum conditions for producing reproducible low loss Ti:LiNbO_3 waveguides are diffusion at high temperatures ($\sim 1100^\circ\text{C}$) in a dry O_2 atmosphere. These conditions, in fact, reduce surface roughness which causes attenuation and coupling loss, increase the optical damage resistance, as has just been observed, and reduce the uncertainty in the refractive index profile.

Measurements of in-plane scattering levels can easily be done by scanning an output mode line by an apertured photodetector.

Armenise et al [40] investigated by both microanalytical techniques and optical measurements the dependence of in-plane scattering levels on the diffusion time. An experimental study of in-plane scattering has been carried out by Singh et al [41]. They observed the dependence of scattering levels on the waveguide fabrication parameters inferring that the major sources of light scattering in the guiding layer are: (i) refractive index inhomogeneity; (ii) surface roughness. Other possible sources of scattering are strain and dislocations induced in the crystal by the diffusion process, and measuring conditions (i.e. prism pressure, dust or lumps on waveguide surface).

Good quality Ti:LiNbO_3 waveguides with losses $< 1 \text{ dB/cm}$ have been produced taking particular care in avoiding contamination during the Ti film deposition process.

Optical waveguides formed by proton exchange in pure or dilute benzoic acid show an increase of the extraordinary refractive index ($\Delta n(e) = 0.1$), a decrease of the ordinary index ($\Delta n(o) = -0.05$) and a higher optical damage resistance [42] relative to the ones prepared by Ti indiffusion. The extraordinary index assumes a very nearly step distribution.

Studies on the characterisation of X-, Y- and Z-cut proton-exchanged waveguides have been reported [43-45]. An anomalous sideshift out of the expected geometrical plane of the mode lines has been observed by De Micheli et al [46] in guides exchanged in molten benzoic acid. They postulated the existence of grating-like structures induced by the fabrication process in the guides.

An ageing effect on the effective index of waveguides exchanged in pure benzoic acid has been observed and related to continuous migration of protons within the guiding layer [47]. Other problems, such as extinction effect and reduced electrooptic and acoustooptic activity, have been detected in guides prepared in pure benzoic acid. However, some of these problems may be overcome by forming the waveguide layer in dilute ($\sim 1 \text{ mol\%}$ of lithium benzoate) benzoic acid [48,49]. Lowering of H concentration in the dilute melt inhibits face etching in Y-cut crystals where large lattice stress developing in a very short time occurs in pure benzoic acid.

Microanalytical techniques have been used to study the exchange mechanism and the proton in-depth profile [50,51]. Canali et al [52] demonstrated the reduction of lattice distortions which are due to the presence of protons, by annealing the samples after the exchange. In general, post-annealing provides very sharp mode lines. When the samples are annealed at high temperatures ($>400^\circ\text{C}$) the guiding layer becomes thicker, the step profile is lost and mode number increases. De Micheli et al [53] showed the possibility of controlling the index increase and index profile, by exchange in lithium-rich solutions and post-annealing, respectively.

At visible wavelengths no optical damage has been observed using energy densities up to 10^5 J/cm^2 , and good quality PE guides with optical losses of the order of 1 dB/cm have been produced by exchange in dilute benzoic acid.

However, much work on defects induced by the exchange process needs to be done to achieve a better understanding of the PE waveguide formation mechanism and relate it to the optical properties of the waveguides.

REFERENCES

- [1] I.P. Kaminow, V. Ramaswamy, R.V. Schmidt, E.H. Turner [*Appl. Phys. Lett. (USA)* vol.24 no.12 (1974) p.622-4]
- [2] R.V. Schmidt, L.L. Buhl [*Electron. Lett. (UK)* vol.12 no.22 (1976) p.575-7]
- [3] H. Sasaki, R.M. De La Rue [*Electron. Lett. (UK)* vol.12 no.10 (1977) p.295-6]
- [4] T. Tamir [*Appl. Phys. (Germany)* vol.25 no.3 (1981) p.201-10]
- [5] D. Gloge, E.A.J. Marcatili [*Bell Syst. Tech. J. (USA)* vol.52 (1973) p.1563]
- [6] J.F. Lotspeich [*Opt. Commun. (Netherlands)* vol.18 (1976) p.567]
- [7] P.M. Morse, H. Feshbach [*Methods of Theoretical Physics* (McGraw-Hill, New York, USA, 1953)]
- [8] M.N. Armenise, M. De Sario [*Fiber Integr. Opt. (USA)* vol.3 (1980) p.197]
- [9] M.D. Feit, J.A. Fleck [*Appl. Opt. (USA)* vol.17 no.24 (1978) p.3990-8]
- [10] P.K. Tien, R. Ulrich [*J. Opt. Soc. Am. (USA)* vol.60 no.10 (1970) p.1325-37]
- [11] D. Sarid [*Appl. Opt. (USA)* vol.19 no.10 (1980) p.1606-8]
- [12] A.N. Kaul, K. Thyagarajan [*Opt. Commun. (Netherlands)* vol.48 no.5 (1984) p.313-6]
- [13] Y.H. Won, P.C. Jaussaud, G.H. Chartier [*Appl. Phys. Lett. (USA)* vol.37 no.3 (1980) p.269-71]
- [14] J.E. Goell, R.D. Stanley [*Bell Syst. Tech. J. (USA)* vol.48 (1969) p.3445]
- [15] Y. Okamura, S. Sato, S. Yamamoto [*Appl. Opt. (USA)* vol.24 no.1 (1985) p.57-60]
- [16] M.D. Himel, U.J. Gibson [*Appl. Opt. (USA)* vol.25 no.23 (1986) p.4413-6]
- [17] D.G. Hall [*J. Opt. Soc. Am. A (USA)* vol.2 (1985) p.747]
- [18] M. Gottlieb, G.B. Brandt, J.J. Conroy [*IEEE Trans. Circuits Syst. (USA)* vol.CAS-26 (1979) p.1029]
- [19] R.V. Schmidt, I.P. Kaminow [*Appl. Phys. Lett. (USA)* vol.25 no.8 (1974) p.458-60]
- [20] J.L. Jackel, C.E. Rice, J.J. Veselka [*Appl. Phys. Lett. (USA)* vol.41 no.7 (1982) p.607-8]
- [21] M. De Micheli, J. Botineau, P. Sibillot, D.B. Ostrowsky [*Opt. Commun. (Netherlands)* vol.42 no.2 (1982) p.101-3]
- [22] H. Naitoh, M. Nunoshita, T. Nakayama [*Appl. Opt. (USA)* vol.16 no.9 (1977) p.2546-9]
- [23] G.J. Griffiths, R.J. Esdaile [*IEEE J. Quantum Electron. (USA)* vol.QE-20 no.2 (1984) p.149-59]
- [24] J.L. Jackel [*J. Opt. Commun. (Germany)* vol.3 no.3 (1982) p.82-5]
- [25] M.N. Armenise et al [*IEE Proc. H (UK)* vol.131 (1984) p.295]
- [26] M.N. Armenise, C. Canali, M. De Sario, A. Carnera, P. Mazzoldi, G. Celotti [*Proc. 7th Tech. Meet. on Processing of Guided-Wave Optoelectronics Materials* Los Angeles, 1984, paper 460-07]

- [27] O. Eknayan, A.S. Greenblatt, W.K. Burns, C.H. Bulmer [*Appl. Opt. (USA)* vol.25 no.5 (1986) p.737-9]
- [28] M.N. Armenise [EMIS Datareview RN=16003 (Nov. 1986) *Kinetics of Ti indiffusion in LiNbO_3*]
- [29] W.K. Burns, P.H. Klein, E.J. West, L.E. Plew [*J. Appl. Phys. (USA)* vol.50 no.10 (1979) p.6175-82]
- [30] M.N. Armenise, C. Canali, M. De Sario, A. Carnera, P. Mazzoldi, G. Celotti [*J. Appl. Phys. (USA)* vol.54 no.11 (1983) p.6223-31]
- [31] P.M. Read, S.P. Speakman, M.D. Hudson, L. Considine [*Nucl. Instrum. Methods Phys. Res. B (Netherlands)* vol.15 (1986) p.398-403]
- [32] M. Fontaine, A. Delage, D. Landheer [*J. Appl. Phys. (USA)* vol.60 no.7 (1986) p.2343-50]
- [33] C.E. Rice, R.J. Holmes [*J. Appl. Phys. (USA)* vol.60 no.11 (1986) p.3836-9]
- [34] K. Sugii, M. Fukuma, H. Iwasaki [*J. Mater. Sci. (UK)* vol.13 no.3 (1978) p.523-33]
- [35] M. Minakata, S. Saito, M. Shibata [*J. Appl. Phys. (USA)* vol.50 no.5 (1979) p.3063-7]
- [36] R.L. Holman, P.J. Cressman, J.A. Anderson [*Ferroelectrics (UK)* vol.27 (1980) p.77]
- [37] A.M. Glass [*Opt. Eng. (USA)* vol.17 (1966) p.470]
- [38] R.A. Becker [*Proc. SPIE - Int. Soc. Opt. Eng. (USA)* vol.578 (1985) p.12]
- [39] J.L. Jackel, G.E. Peterson, C.E. Rice, D.H. Olson, J.J. Veselka [*J. Appl. Phys. (USA)* vol.55 no.1 (1984) p.269-70]
- [40] M.N. Armenise et al [*Appl. Phys. Lett. (USA)* vol.45 no.4 (1984) p.326-8]
- [41] J.D. Singh, R.M. De La Rue [*J. Lightwave Technol. (USA)* vol.LT-3 (1985) p.67]
- [42] R.A. Becker [*Proc. SPIE - Int. Soc. Opt. Eng. (USA)* vol.460 (1984) p.95-100]
- [43] K.K. Wong, A.C.G. Nutt, D.F. Clark, J. Winfield, P.J.R. Laybourn [*IEE Proc. J (UK)* vol.133 (1986) p.113]
- [44] M. Goodwin, C. Stewart [*Electron. Lett. (UK)* vol.19 no.6 (1983) p.223-5]
- [45] D.F. Clark, A.C.G. Nutt, K.K. Wong, P.J. Laybourn, R.M. De La Rue [*J. Appl. Phys. (USA)* vol.54 no.11 (1983) p.6218-20]
- [46] M. De Micheli, P.St.J. Russell [*Appl. Opt. (USA)* vol.25 no.21 (1986) p.3896-8]
- [47] A. Yi-Yan [*Appl. Phys. Lett. (USA)* vol.42 no.8 (1983) p.633-5]
- [48] K.K. Wong, N.J. Parsons, A.R. Oldroyd, A.C. O'Donnell [*Proc. Int. Conf. Integrated Optics and Optical Fibre Communications and European Conf. Optical Communication* vol.1 (1985) p.59]
- [49] S.M. Al-Shukri, J.F. Duffy, R.M. De La Rue, G. Mazzi, A. Carnera, M.N. Armenise [*Proc. SPIE - Int. Soc. Opt. Eng. (USA)* vol.651 (1986) p.20-5]
- [50] A. Campari et al [*J. Appl. Phys. (USA)* vol.58 no.12 (1985) p.4521-4]
- [51] N.A. Sanford, W.C. Robinson [*Opt. Lett. (USA)* vol.10 no.4 (1985) p.190-2]
- [52] C. Canali et al [*J. Appl. Phys. (USA)* vol.59 no.8 (1986) p.2643-9]
- [53] M. De Micheli, J. Botineau, S. Neven, P. Sibillot, D.B. Ostrowsky, M. Papuchon [*Opt. Lett. (USA)* vol.8 no.2 (1983) p.114-5]

15.6 Ion implantation in LiNbO₃

G.T. Reed and B.L. Weiss

This Datareview appeared in *Properties of Lithium Niobate* (INSPEC, IEE, London, UK, 1989) and is reproduced here for the reader's convenience.

A INTRODUCTION

The implantation of ions into LiNbO₃ results in two effects, namely the production of radiation damage and the controlled introduction of dopant atoms into the crystal lattice. For the fabrication of optical waveguides in LiNbO₃ it is necessary to be able to modify the refractive index depth profile in a controlled manner. The ions of interest for such modifications are the light ions, such as He⁺ and H⁺, whose projected ranges for the ion energies normally available produce radiation damage at depths required for the fabrication of optical waveguides, and Ti⁺ whose effects are predominantly those of doping.

It is well known that ion implantation into LiNbO₃ causes a reduction in refractive index of a buried layer. The depth of the buried layer is determined by the incident ion species and their energy, and the magnitude of the index change is determined by the ion dose. Initial experimentation by Wei et al [1] in 1974 demonstrated an index reduction of approximately 10% realised by implantation of 60 keV argon ions to a dose of 10¹⁶/cm². The index change remained constant to a depth of approximately 140 nm. Later work by a number of other authors has yielded additional information. Destefanis et al [2] determined that ion implantation may be used to vary the birefringence of LiNbO₃ since the ordinary and extraordinary indices are affected to a differing degree. They also suggested that the index change was due to radiation damage caused by nuclear collisions, rather than a doping effect. These claims were supported by the work of Karge et al [3], who implanted a variety of species (N⁺, Ne⁺ and O⁺) at different energies such that approximately the same range was achieved for each ion, with three damage stages being identified for 150 keV nitrogen ions into LiNbO₃ [4]:

- (1) Up to 10¹⁵ N⁺/cm² - pre-damage due to point defects.
- (2) 10¹⁵ to 5 × 10¹⁵ N⁺/cm² - heavy damage stage, overlapping effect.
- (3) Above 5 × 10¹⁵ N⁺/cm² - saturation damage levels.

Similar dose dependences were observed for each suggesting that the refractive index change is independent of ion species. The hypothesis was further supported by Wenzlik et al [4] who measured good correspondence between refractive index and radiation damage profiles, for helium ion implantation into LiNbO₃.

B He⁺ IMPLANTED WAVEGUIDES

In order that ion implantation may be utilised for the manufacture of optical waveguides in LiNbO₃, an energetic light ion is required to achieve sufficient range to facilitate guiding. Consequently several workers have utilised He⁺ ions with energies up to 2 MeV (e.g. [6]).

In order to produce a buried layer of reduced refractive index, to act as the lower waveguide boundary, ions must pass through the guiding layer with high velocity. This causes minor crystal damage [4] which can be reduced by subsequent thermal annealing [2].

In 1981 King et al [7] measured the attenuation of ion-implanted planar waveguides, for various ion doses and ion energies, producing guides with a minimum attenuation of 0.7 dB/cm, utilising a

combination of implants. Gotz et al [6] also measured a range of planar guides determining an optimum implant energy. Naden and Weiss [8] produced a more thorough characterisation of the optical parameters of planar waveguides by studying the propagation constants together with the attenuation. Their results again suggested an optimum implant energy and dose for particular guide characteristics.

The first application of ion implantation to optical stripe waveguides was reported in 1982 when Heibei and Voges [9] combined the technique of Ti indiffusion with that of ion implantation to produce waveguides and modulators. The Ti indiffusion was used to form a planar guide, and the implantation used to produce laterally confining sidewalls. The resulting guides were compared to others of similar dimensions formed entirely by Ti indiffusion. The guides made by the combined technique exhibited fewer lateral modes which was interpreted as more precise control of the guide width.

In 1983 the work of Barfoot and Weiss [10] aided the design of ion-implanted optical waveguides when they produced a fifth order polynomial fit to determine radiation damage ranges in LiNbO₃ for ion energies up to 2 MeV. The results were based on the niobium damage profiles, determined by analysis with a high energy channelling beam. When corrected to the damage range, the polynomial fit is as follows:

$$RD = 0.975 \exp[K_0 + K_1(\ln E) + K_2(\ln E)^2 + K_3(\ln E)^3 + K_4(\ln E)^4 + K_5(\ln E)^5]$$

where

$$\begin{aligned}K_0 &= +1.970496 \\K_1 &= +9.840678 \times 10^{-1} \\K_2 &= +5.254263 \times 10^{-2} \\K_3 &= -2.615660 \times 10^{-2} \\K_4 &= +2.452610 \times 10^{-3} \\K_5 &= -3.028347 \times 10^{-5}\end{aligned}$$

In 1986 the first stripe waveguides fabricated entirely by ion implantation were reported by Reed and Weiss [11], demonstrating losses as low as 1 dB/cm for TM modes in Y-cut, X-propagating LiNbO₃. This work studied the variations in mode confinement and attenuation with implanted ion energy and dose. In particular the effect of waveguide sidewalls fabricated by multiple implants was established, resulting in waveguides of sufficiently good quality to rival Ti indiffused guides for one polarisation of the input beam. Unfortunately ion-beam-induced lithium loss from the sample surface (which has also been observed by ERDA [12]) remains a problem, changing the refractive index seen by the extraordinary wave, and may be the cause of the so called missing modes [13].

LiNbO₃ has been of particular interest for waveguiding applications due in part to its relatively large electrooptic coefficients, promising efficient optical modulation. Initial experimentation of Destefanis et al [2] showed that ion implantation reduced the electrooptic activity of LiNbO₃. They reported reductions in the r₁₃ and r₃₃ coefficients of approximately 40% and 70% of their original values respectively. Later work by Reed and Weiss [14], using a more optimised experimental arrangement, suggested more promising, lower reductions of the r₁₃ coefficient of only 20%.

The photorefractive properties of waveguides are very important and, whilst Ti indiffused waveguides show dramatic effects at visible wavelengths, both planar [13] and stripe [14] He⁺ implanted LiNbO₃ have been shown to be free of such unwanted effects at significantly higher power levels.

C PROTON IMPLANTED WAVEGUIDES IN LITHIUM NIOBATE

The implantation of protons into bulk and Ti-diffused LiNbO₃ has been found to produce highly absorbing structures which have developed for use with acoustooptic spectrum analysers. The experiments used 100 keV protons to doses from 10^{17} - 7×10^{17} H/cm² which produced transmission coefficients varying from about 0.4 to 0.9 for wavelengths from 0.5 micron to 1.0 micron in X-cut samples [15]. Optical densities of 0.05 to 3 were produced by varying the H⁺ dose from 10^{14} to 10^{17} H^{+/cm² at 100 keV for a TM mode in a 2 mm long Ti-indiffused waveguide for a wavelength of 0.63 micron.}

D Ti IMPLANTED WAVEGUIDES

The relatively high mass of Ti means that with the ion energies normally available sufficient depth and index change for waveguide fabrication cannot be obtained. However, highly doped surface layers can be produced which could act as diffusion sources. Solid phase epitaxy using LiNbO₃ implanted with 360 keV Ti at liquid nitrogen temperatures, and annealed at 400°C in water-saturated oxygen, produces epitaxial regrowth of the amorphous region, while temperatures above 600°C are required to remove all the implantation damage [18]. For a dose of 3×10^{16} Ti⁺/cm² the activation energy for regrowth is 2.0 eV whilst for higher doses the regrowth is slower and Ti segregates at the regrowth interface. Thus Ti-doped LiNbO₃ has been used to fabricate low loss optical waveguides and devices.

Ti implantation into Ti-indiffused waveguides has been used to selectively increase the refractive index of the LiNbO₃ [19]. After annealing at 400 - 600°C the depth of this increase is about 0.3 micron, the change in ordinary refractive index varies between 4 and 6×10^{-2} and the change in extraordinary refractive index between 3 and 7×10^{-2} . This change in refractive index may be used, for example, for the fabrication of gratings for signal processing devices.

REFERENCES

- [1] D.T.Y. Wei, W.W. Lee, L.R. Bloom [*Appl. Phys. Lett. (USA)* vol.25 no.6 (1974) p.329-31]
- [2] G.L. Destefanis et al [*J. Appl. Phys. (USA)* vol.50 no.12 (1979) p.7898-905]
- [3] H. Karge, G. Gotz, U. Jahn, S. Schmidt [*Nucl. Instrum. Methods (Netherlands)* vol.182-183 pt.2 (1981) p.777-80]
- [4] K. Wenzlik, J. Heibei, E. Voges [*Phys. Status Solidi A (Germany)* vol.61 no.2 (1980) p.K207-11]
- [5] G.L. Destefanis, P.D. Townsend, J.P. Gailliard [*Appl. Phys. Lett. (USA)* vol.32 no.5 (1978) p.293-4]
- [6] G. Gotz, H. Karge [*Nucl. Instrum. Methods Phys. Res. (Netherlands)* vol.209-210 pt.2 (1983) p.1079-88]
- [7] G.D.H. King, M.C. Bone, B.L. Weiss, D.W. Weeks [*Electron. Lett. (UK)* vol.17 no.23 (1981) p.897-8]
- [8] J.M. Naden, B.L. Weiss [*J. Lightwave Technol. (USA)* vol.LT-3 no.4 (1985) p.855-9]
- [9] J. Heibei, E. Voges [*IEEE J. Quantum Electron. (USA)* vol.QE-19 no.5 (1983) p.820-5]
- [10] K.M. Barfoot, B.L. Weiss [*J. Phys. D (UK)* vol.17 no.3 (1984) p.L47-52]
- [11] G.T. Reed, B.L. Weiss [*Nucl. Instrum. Methods Phys. Res. B (Netherlands)* vol.B19/20 pt.2 (1987) p.907-11]
- [12] S.A.M. Al-Chalabi, B.L. Weiss, K.M. Barfoot, G.W. Arnold [*J. Appl. Phys. (USA)* vol.63 no.4 (1988) p.1032-6]
- [13] P.J. Chandler, L. Zhang, J.M. Cabrera, P.D. Townsend [*Appl. Phys. Lett. (USA)* vol.54 no.14 (1989) p.1287-9]
- [14] G.T. Reed, B.L. Weiss [*Electron. Lett. (UK)* vol.23 no.8 (1987) p.424]

15.6 Ion implantation in LiNbO₃

- [15] E. Glavas, P.D. Townsend, G. Droungas, M. Dorey, K.K. Wong, L. Allen [*Electron. Lett.* (UK) vol.23 no.2 (1987) p.73]
- [16] B.L. Weiss, J.M. Naden [*Int. J. Electron. (UK)* vol.62 no.1 (1987) p.153-5]
- [17] W.K. Burns, J. Comas, R.P. Moeller [*Opt. Lett. (USA)* vol.5 no.2 (1980) p.45-7]
- [18] D.B. Poker, D.K. Thomas [*J. Mater. Res. (USA)* vol.4 no.2 (1989) p.412-6]
- [19] S. Fouchet, A. Carenco, N. Duhamel [*Proc. 4th European Conf on Integrated Optics* Glasgow, Scotland, 11-13 May 1987 (Scottish Electron. Technol. Group, Glasgow, 1987) p.54-7]

Index

<u>Index terms</u>	<u>Links</u>
A	
ablation	282
excimer laser	290 291
ablation rate	291
absorption edge	4
composition dependence	4
acoustic attenuation	241
acoustic birefringence	256 266
acoustic dispersion	258 259
acoustic shear waves	61
acoustic wave velocity	63
acoustic waveguides	265
<i>see also</i> surface acoustic waves	
acoustic waves	63
diffraction efficiency	63
<i>see also</i> surface acoustic waves	
acousto-optic Bragg cell modulator	368 369
diffraction efficiency	368 369
radiation effects	369
acousto-optic Bragg deflector	369 370
electron irradiation effects	369 370
acousto-optic devices	256 257 266 387 388
acousto-optic diffraction	256 257
acousto-optic interaction efficiency	388
acousto-optic materials	63
active beam propagation method algorithm	307 308
algorithms	307 335
anharmonic oscillator model	205 206
anharmonicity parameter	206
annealed proton exchange	46
annealed proton-exchanged waveguides	143 147 148 150 153
	158 349 353
atomic force microscopy	352 353
attenuated total reflection	161

Index terms**Links****B**

beam coupling	378
beam propagation method	307
bipolarons	16
birefringence	132 316 319 320 379
acoustic	256 266
Bragg angle	368 369

C

chemical etching	282
ion-damaged LN	282 283
laser-enhanced	282 284
Cherenkov generation	153 157 388
chromium doping of LN	175
concentration profile	177
diffusion coefficients	179
diffusion constant	179 180
codoping	18 19 203 204
coercive field	274 275
coherence length	316 317
coherent amplification	378
colour centres	16 364
compliance	57 59 63 101 108 216
constant electric field	59
constant polarization	59
temperature dependence	59
congruent composition	3 25
constitutional supercooling	26 28
coupled waveguide structure	365 366
critical resolved shear stress	68 69
crosstalk	363
crystal composition	3
congruent	3
melt composition dependence	3
crystal structure	8
proton-exchanged waveguides	43 50
Curie constant	129

<u>Index terms</u>	<u>Links</u>				
Curie temperature	3 73 295	5 102	6 129	35 215	68 273
composition dependence	3				
defect structure dependence	6				
cutting	277				
Czochralski growth	3	25	80	274	
double crucible	35				
iron-doped LN	30	31	34		
D					
Debye temperature	84				
defect structure	5	6			
defects	15				
density	5	10	215		
deuterium-exchanged LN	204				
dielectric constants	57	129	130		
frequency dependence	129				
neutron irradiation effects	359				
temperature dependence	129	130			
dielectric function	340	341			
dielectric loss	130				
dielectric permittivity	57	97	101	108	119
	215	275			
dielectric polarization	131				
dielectric relaxation time	375				
dielectric tensor	377				
differential interference contrast imaging	352				
diffusion coefficient	177	179	295	296	310
interdiffusion	301	302			
proton exchange	386	392	393		
titanium	398				
diffusion constant	179	180	296	297	373
chromium	179	180			
erbium	297				
diffusion current	373				
diffusion depth	296	297	310		
diffusion temperature	177				
dilute melt proton exchange	392				

Index terms**Links**

directional coupler waveguide	363				
coupling coefficient	365				
coupling efficiency	367				
electron irradiation effects	363	364	366		
dispersion	115	150			
domain structure	273				
doping	175	295			
chromium	175				
erbium	295				
double crucible Czochralski method	35				
dynamic holography	377				
 E					
elastic constants	57				
third-order	65				
elasto-optic effect	379	380			
electric polarization	11				
electrical conductivity	91	274	373		
activation energy	92				
doping effects	92				
frequency dependence	92				
high temperature	94				
hopping mechanism	91				
ionic	94				
mobile protons	93				
stoichiometry dependence	92				
temperature dependence	91	274			
electrical permittivity					
electron irradiation effects	359				
electroluminescence	185				
electromechanical coupling coefficients	108	255	268		
electron irradiation effects	359				
proton-exchanged waveguides	259	260			
temperature coefficients	111				
electron irradiation effects	359	360	363	364	366
	367	369	370		
electron nuclear double resonance	192	193			
electron paramagnetic resonance spectra	192				
electron spin resonance spectra	192				
3d ions	193	194			
4f ions	194	195			

Index terms**Links**

electron spin resonance spectra (<i>Continued</i>)						
radiation-induced defects	195					
temperature dependence	194					
electro-optic coefficients	131	164	165	167	407	
doping effects	136					
IR	139					
linear	131	133				
measurement	131	132				
polycrystalline LN	138					
proton-exchange devices	387	393	394			
quadratic	138	139				
stoichiometry dependence	135	136				
temperature dependence	136	137				
UV	133					
visible and near-IR	133					
wavelength dependence	135	136				
electro-optic devices	388					
electro-optic effect	62	131	163	164	377	
secondary	379					
electrostrictive constants	107					
epitaxial growth	38					
indiffusion regrowth	38					
liquid-phase	39					
melt-phase	38					
molecular beam epitaxy	39	40				
sputtering	39					
vapour transport technique	39					
erbium-doped waveguides	307					
amplification characteristics	311					
erbium concentration profile	310	311				
gain	310	311				
numerical simulation	307					
signal power evolution	311					
erbium doping of LN	295					
activation energy	297					
concentration profile	297	298	302			
diffusion constant	297					
ion exchange	300					
SIMS	329	330				
surface concentration	297	298	302	303		

Index terms**Links**

erbium doping of LN (<i>Continued</i>)					
thin film diffusion	295				
waveguides	307				
etch rate	283	285	286	288	
etching	280	282	288	289	
chemical	282				
ion beam milling	285	286			
reactive ion	288	289			
reactive ion beam	285	286			
wet	282				
excimer laser treatment	290	291			
excimer pulsed laser deposition	291				
exponential gain coefficient	35				
F					
ferroelectric oxides	200				
ferroelectric-paraelectric phase transition	188				
ferroelectric properties	165	377			
Fick's law	295				
figures of merit	63				
fluorescence spectra	180				
fracture	67				
G					
gamma ray irradiation effects	360	362	369		
geminate-ion recombination model	361	362			
Gibbs free energy	275				
glide	68				
graded index layers	40				
graded proton exchange	46				
graded proton-exchanged waveguides	157	158			
gratings	290	291	387	408	
growth					
Czochralski	25	30	31	34	35
epitaxial	38				
iron-doped LN	30				
Stepanov's technique	28	29			

Index terms**Links****H**

heat capacity	81				
Helmholtz equation	335	336	341	342	
high-temperature proton exchange	46				
holograms	142	372			
reflection	381				
stabilization	380	381			
thermal fixing	381				
volume	372	377			
holographic gratings	169	170	172	377	
diffraction efficiency	170	172	173	378	381
holographic sensitivity	172	173			
holographic processes	372				
absorption	375	376			
closed circuit	375				
dynamic	377	81			
open circuit	374	375			
space-charge field	373				
holographic read-write characteristics	360				
hydrogen isotopes in LN	206				
hydrostatic coupling factor	110				
hydrostatic strain coefficient	102				

I

Impermeability	101				
indiffusion regrowth	38	39			
insertion loss	255				
inverse piezoelectric effect	211				
ion beam milling	285	286			
ion exchange	300	311			
dopant profile	301	302			
ion implantation	406				
Ar into LN	406				
Er into LN	311				
He ⁺ into LN	406	407			
N ⁺ into LN	406				
Ti into LN	408				
ion implantation effects	267				
ion-implanted waveguides	406	407			
IR absorption bands	200				

Index terms**Links**

IR reflection spectra			
librational band	165		
proton-exchanged waveguides	161		
IR spectroscopy	351		
iron-doped LN	30		
congruent	30		
stoichiometric	34		
J			
Jahn-Teller effect	193	194	
K			
Kleinmann symmetry rule	135		
L			
lapping	277	279	280
laser action	175		
laser amplification	180	181	
laser damage resistance	198		
laser etching	290		
lattice constants	4	5	
lattice mismatch			
LN/lithium tantalate	38		
lattice structure	8		
atomic positions	9	10	
hexagonal	8	9	
perovskite	10	11	
rhombohedral	8	9	
lattice vectors	8		
composition dependence	10		
temperature dependence	10		
lattice vibration spectra			
proton-exchanged waveguides	161		
leaky surface acoustic waves	255		
lenses	387		
libration	165		
liquid phase epitaxy	39		
lithiation	6	7	
luminescence	185	186	
doping effects	185	304	

<u>Index terms</u>	<u>Links</u>	
luminescence (<i>Continued</i>)		
impurity effects	185 186	
intrinsic	185	
stoichiometry effects	185 186	
luminescence spectra		
rare-earth dopants	209 304 305	
M		
m-lines spectroscopy	340	
Ti:LN waveguides	344	
Mach-Zehnder interferometers	387 388 393 394	
magnetic resonance spectra	192	
Maker fringe analysis	142 315	
Maxwell equations	340 342	
melt composition	3 8	
melt-phase epitaxy	38	
melting point	25 38 81	
MgO-doped LN	397	
proton exchange	397	
microanalytical techniques	348	
microinclusions	28 29	
Miller-Bravais indices	8 9	
milling rate	285 286	
molecular beam epitaxy	39 40	
molecular weight	81	
multi-strip couplers	249	
N		
near field technique	334	
reconstruction algorithms	335	
Nernst-Plank model	300	
neutron irradiation effects	206 359 369	
noise holograms	380	
Nomarski microscopy	352 353	
non-destructive characterization	315	
non-equivalent centres	19 20	
non-linear optic coefficient	154 155	
non-linear susceptibility	153	
non-stoichiometry defects	15 20	

Index terms**Links****O**

OD vibration	205	206
OH absorption	200	
congruent LN	201	202
doping effects	203	204
double-doped LN	203	204
ferroelectric oxides	200	
proton-exchanged LN	204	205
stoichiometry dependence	202	
temperature dependence	201	202
undoped LN	201	202
OH incorporation into LN	200	201
doping effects	201	
OH vibration	205	206
optical absorption coefficient	35	116 197 198 202
electron irradiation effects	360	
gamma ray irradiation effects	362	
optical absorption spectra	197	198 200
doping effects	197	198
IR	200	
rare-earth dopants	209	
temperature dependence	197	
UV absorption edge	197	
optical activity	379	
optical amplification	180	181
optical amplifiers	312	
optical damage	141	142 360 362 380
optical damage resistance	142	
optical storage	30	
OT vibration	206	

P

paraelectric phase	8
passive devices	387
periodically poled LN	
photorefractive effects	143
periodically poled LN waveguides	154
phase contrast microscopy	348 352
phase diagram	43
phase modulator	388

<u>Index terms</u>		<u>Links</u>
phase transition temperatures	13	14
high temperature	13	
low temperature	13	14
phase transitions	73	83
phonon absorption	119	133
phonon-phonon interactions	241	
phonon viscosity tensor	241	242 252
photoconductivity	373	374
photo-elastic coefficients	61	132
photo-elastic effect	61	379
indirect	62	
photorefractive crystals	372	375 379 380
cubic	379	
photorefractive effect	16	17 30 141 142
	361	
optical waveguides	142	
surface	142	
photorefractive grating	374	
photorefractive sensitivity	35	141 143 170 397
photorefractive waveguides	142	169
photovoltaic effect	143	373
piezoelectric coefficients	11	101 132
second-order	101	
temperature dependence	103	
third-order	105	106
piezoelectric effect	62	
in verse	211	
piezoelectric Rayleigh waves	243	
piezoelectric stiffening	216	
piezoelectric strain constant	102	108 216
piezoelectric stress constant	57	102 105 215 216
plasma etching	288	
plastic deformation	67	68
point defects	15	
impurities	16	
intrinsic	15	16
rare-earth ions	17	
transition metal ions	17	
point group	131	
polarisability	115	

Index terms**Links**

polarization-optic coefficient	131	139			
polarisers	387				
polarons	16				
poling	273				
coercive field	274	275			
polishing	277	278	280		
prism coupling	348	349	386		
proton and copper exchange	169				
proton exchange	43	385			
annealed	46				
concentrated melt	385				
diffusion coefficients	392	393	396		
dilute melt	392	393			
graded	46				
high-temperature	46				
MgO-doped LN	397				
reverse	159	330			
soft	46				
Ti-indiffused LN	396	397			
proton-exchanged coupler	368				
proton-exchanged waveguides	43	50	146	153	161
	254				
acoustic attenuation	394				
acoustic birefringence	394				
acoustic properties	254				
acousto-optic properties	256	257			
characterization	403	404			
chromium-doped	180				
copper-exchanged	169				
crystal phase composition	50	154			
crystallographic phases	258	259			
dilute melt	392				
electromechanical coupling coefficient	259	260			
electron irradiation effects	368				
electro-optic activity	387	393	394		
fluorescence spectra	180				
formation	385	386	392	393	
in-plane scattering	394	395			
IR reflection spectra	161				
IR spectroscopy	351				
lattice strain	386				

Index terms**Links**

proton-exchanged waveguides (<i>Continued</i>)						
MgO-doped	397					
Nomarski spectroscopy	352	353				
non-linear optical properties	153					
OH absorption	204	205				
optical losses	158					
passive devices	387					
photorefractive effects	143	169				
prism coupling	349	350				
problems	387					
proton concentration	51					
refractive index	50	146	156	157	162	
refractive index instability	387					
refractive index profiles	386					
SAW velocity	254	266	267	394		
SIMS	330	349	350			
structural phase diagram	43	162				
Ti-indiffused	396	397				
proton-implanted waveguides	408					
prototypic sources	385	386	388	389		
diffusion rate	386	389				
pulsed laser deposition	290	291				
pyroelectric charges	273					
pyroelectric coefficients	97					

Q

quasi-extensional modes	108					
quasi-phase-matching technique	153	154				
quasi-shear modes	108					
fast	108					
slow	108					
quasimolecular model	163					

R

radiation effects	359					
acousto-optic devices	368					
bulk LN	359	360				
doped LN	360	361				
waveguides	361					
radiation heating	369	370				
radiation sensitivity	359					

Index terms**Links**

Raman spectra	188	190			
doping effects	190				
OH in LN	205				
pressure dependence	188				
temperature dependence	188				
rare-earth doping	295				
reactive ion beam etching	285	286			
reactive ion etching	288	289			
rectilinear coordinate system	11				
reflective array compressors	248				
refractive index	38	40	115		
amorphous LN	124				
composition dependence	117	118	124		
congruent LN	115	116	118	122	
doping dependence	124	344			
extraordinary	4	38	39	44	46
	50	116	120	316	318
	344				
IR	126	127			
Mg-doped LN	117				
microwave	127				
ordinary	38	39	52	116	120
	316	317	344		
polycrystalline LN	124				
proton-exchanged waveguides	146				
stoichiometric LN	117	118	120		
temperature dependence	116	117	121		
UV	120				
visible and near-IR	120				
wavelength dependence	115	119			
refractive index profile reconstruction	334	342			
algorithms	335				
minimization procedure	337				
noise effects	336	337			
relative sensitivity factor	351				
resonators	248				
reverse proton-exchange technique	147	148	159	330	
ring-resonator	387				

Index terms**Links****S**

Schmid number	68					
Schottky vacancies	5					
second-harmonic generation	88	153	315	321	388	
secondary ion mass spectrometry	325	349				
doped LN	329	330				
dynamic	327					
ionization efficiency	326	327				
proton-exchanged LN	330					
secondary ion production	325	326				
static	327					
Sellmeier equations	115	119	121	149	317	
	318					
shear	67					
shear modes	108					
slip systems	68	69				
slowly varying envelope approximation	307					
small polaron model	91					
soft proton exchange	46					
soft proton exchange waveguides	150					
solid solubility						
erbium in LN	297	310				
sonic cleaning	280					
space-charge field	373					
space group	8	11				
specific heat	81	86				
Mn-doped LN	83	84				
temperature dependence	82	83				
spontaneous polarization	5	11	97	163	164	
	167	275	360			
sputtering	39	325	326			
stabilization of holograms	380	381				
Stark effect	209					
rare-earth dopants	209					
Stepanov's technique	28	29				
stiffness	57	101	215	216		
constant electric field	57	58				
constant polarization	58	59				
hypersonic	59					
stoichiometry effects	59					

Index terms**Links**

stiffness (*Continued*)

temperature dependence	58	59			
stoichiometry	3	34			
structural phase diagram	43				
surface acoustic wave velocity	243	247	248	250	263
	264				
anisotropy effects	263				
composition dependence	264				
frequency dependence	256	258	268		
ion-implanted LN	267	268			
metal-indiffused LN	265				
mode-conversion efficiency	257				
orientation effects	263				
proton-exchanged LiTaO ₃	267				
proton-exchanged LN	266	267			
proton-exchanged waveguides	254	267			
temperature dependence	264				
surface acoustic waves	243	252	253		
air loading	245				
attenuation	252	253	267	268	
attenuation coefficient	245	248	252	253	
beam steering	246				
coupling constant	110	111	243		
diffraction	246	247			
effective viscosity coefficient	252				
grooves	248	249			
metal electrodes	249	250			
non-synchronous scattering loss	249				
propagation	247				
propagation loss	245	246	248	249	
reflection coefficient	248				
stop-band frequency	249				
surface dielectric constant	244				
surface structure effects	247				
temperature coefficient of delay	244	245			
<i>see also</i> surface acoustic wave velocity					
surface characterization	325	326	352	353	
surface relief structures	290	291			
symmetry	11	131			

Index terms**Links****T**

temperature sensor	387				
thermal conductivity	78	85	86		
congruent	79				
thermal diffusion	295	296	310		
thermal diffusivity	85				
congruent	86	87			
thermal expansion	6	10			
thermal expansion coefficients	73				
congruent	75				
regression data	74	75			
stoichiometric	75				
thermal runaway	80				
thermodynamic tension	105	107			
thermoluminescence	185	186			
thermo-optic effects	369	370			
thickness modes	108				
thin film diffusion	175	176	295		
chromium	175	176			
erbium	295				
threshold effect	18				
Ti-implanted waveguides	408				
Ti-indiffused LN	344	398	402		
kinetics	398				
outdiffusion	399	402			
proton exchange	396	397			
SAW velocity	265	266			
Ti-indiffused proton-exchanged waveguides	396	397			
Ti:LN waveguides	344	352	353	363	398
	399	402			
in-plane scattering	403				
photorefractive effects	403				
proton-exchanged	396	397			
refractive index	399	402			
Ti implantation	408				
transducers	246	247	249		
tritium concentration	206				
twinning	67	68			
ultrasonic bulk wave attenuation	241	242			
frequency dependence	241				
temperature dependence	241				

Index terms**Links**

ultrasonic bulk wave velocity	215				
fast quasi-shear	216	219	220	222	224
	228	229	231	233	237
	238				
quasi-longitudinal	216	219	221	225	226
	228	230	234	235	237
	239				
slow quasi-shear	216	222	223	225	227
	231	232	234	236	

U

uniformity studies	315				
unit cell volume	4	5	8		
composition dependence	5				
radiation effects	359				
UV laser ablation	290				

V

vacancies	5	15	16	94	
Schottky	5				
vapour transport technique	39				

W

wafer diameter	278				
wafer preparation	277				
cleaning	280				
edge grinding	279				
high-volume	278				
lapping	279	280			
polishing	280				
slicing	278	279			
wafer thickness	278				
mapping	319	320			
wafer uniformity	315				
waveguide characterization	401				
atomic force microscopy	352	353			
buried waveguides	330				
channel waveguides	334				
IR spectroscopy	351				
m-lines spectroscopy	340				
Maker fringe analysis	323				
microanalytical techniques	348				

Index terms**Links**

waveguide characterization (<i>Continued</i>)						
near field technique	334					
Nomarski microscopy	352					
optical	401					
prism coupling	348	349				
proton-exchanged waveguides	330	349	351			
SIMS	330	349				
slab waveguides	340					
Ti:LN waveguides	344	345				
waveguide theory	340					
waveguides						
chromium-doped	180	181				
erbium-doped	307					
fluorescence spectra	180					
He ⁺ -implanted	406	407				
non-linear optical properties	153					
numerical simulation	307					
optical amplification equations	308	309				
optical characteristics	401					
photorefractive effects	142	169				
propagation equations	307	308				
proton-exchanged	43	50	143	146	153	
	161	180	385	392	397	
proton-implanted	408					
radiation-induced effects	361					
refractive indices	146					
Ti-implanted	408					
Ti-indiffused	398	399				
Ti-indiffused proton exchanged	396	397				
wet etching	282					
WKB method	342					
inverse	342	349				
writing time	35					
X						
X-ray irradiation effects	360					
waveguides	361	362				
Y						
yield stress	67					
temperature dependence	68					